BEILSTEIN JOURNAL OF NANOTECHNOLOGY

Advanced hybrid nanomaterials

Edited by Andreas Taubert, Fabrice Leroux, Pierre Rabu and Verónica de Zea Bermudez

Imprint

Beilstein Journal of Nanotechnology
www.bjnano.org
ISSN 2190-4286
Email: journals-support@beilstein-institut.de

The *Beilstein Journal of Nanotechnology* is published by the Beilstein-Institut zur Förderung der Chemischen Wissenschaften.

Beilstein-Institut zur Förderung der Chemischen Wissenschaften
Trakehner Straße 7–9
60487 Frankfurt am Main
Germany
www.beilstein-institut.de

BEILSTEIN JOURNAL OF NANOTECHNOLOGY

Advanced hybrid nanomaterials

Andreas Taubert*[1], Fabrice Leroux[2], Pierre Rabu[3] and Verónica de Zea Bermudez[4]

Editorial

Open Access

Address:
[1]Institute of Chemistry, University of Potsdam, Karl-Liebknecht-Str. 24–25, D-14476 Potsdam OT Golm, Germany, [2]Chemical Institute of Clermont-Ferrand, UMR CNRS 6296, University Clermont Auvergne, 24 av. Blaise Pascal, Aubière, France, [3]Institute of Physics and Chemistry of Materials of Strasbourg, CNRS-University of Strasbourg, 23, rue du Loess, BP43, Strasbourg cedex 2, France and [4]Departamento de Química - Escola de Ciências da Vida e do Ambiente, Universidade de Trás-os-Montes e Alto Douro, 5001-801 Vila Real, Portugal

Email:
Andreas Taubert* - ataubert@uni-potsdam.de

* Corresponding author

Keywords:
colloidal chemistry; environmental remediation; hybrid nanomaterials; nanocomposite; nanofillers; nanomedicine; nanostructures; polymer fillers; pore templating; smart materials

Beilstein J. Nanotechnol. **2019,** *10,* 2563–2567.
doi:10.3762/bjnano.10.247

Received: 26 November 2019
Accepted: 11 December 2019
Published: 20 December 2019

This article is part of the thematic issue "Advanced hybrid nanomaterials".

Editor-in-Chief: T. Schimmel

The Maya blue pigment that was used in Mexico during the VIIIth century is often given as a prototypical example of a hybrid material in which an indigo derivative is stabilized into magnesium aluminum phyllosilicate. This material, palygorskite, was used to produce beautiful mural paintings that are still shining centuries later [1-3]. Since these origins, the field of hybrid materials has developed into a broad scientific and technological subject including important fields such as sol–gel chemistry [4,5], polymer nanocomposites [6,7], and hybrid nanomaterials [8,9]. Nowadays, hybrid materials are almost everywhere and provide a wide range of applications from biology and health, to photonic devices, catalysis and environment, smart coatings, energy, and electronics [10-17]. By essence, the hybrid approach consists of building new materials and devices by assembling elementary functional organic/inorganic, molecular or extended bricks to obtain materials with greatly improved or even completely new properties. This has been called a Lego©-like approach to materials synthesis [18]. The main issue in this approach is to monitor and control interactions between different bricks and to understand the physicochemical mechanisms involved at the interfaces between the individual building blocks as well as between different materials. Moreover, the implementation of hybrid systems in devices implies miniaturization. Therefore, nanostructuration or nanoarchitectonics is the core of current research in hybrid materials, and the analysis of advanced hybrid materials needs specialized experimental and theoretical techniques.

This thematic issue clearly shows that “advanced hybrid nanomaterials” is not just hype, it is a real and powerful toolbox towards advanced materials for highly diverse fields, such as polymer nanocomposite, health and environment.

Smart Materials and Nanostructures

As far as hybrid materials are concerned, significant effort is still focused on materials synthesis and characterization. This is most probably due to the endless number of combinations of different moieties that can be envisaged, as well as to the

increasingly complex, resulting structures with critical importance of interfaces. In the current issue, from "simple" to more elaborated, we here observe the importance of the polyol method, the non-hydrolytic or colloidal approach, and ordered mesopore templating techniques.

In "Tailoring the magnetic properties of cobalt ferrite nanoparticles using the polyol process" [19], the synthetic process was found to be of prime importance to shape the nanoparticles and to optimize their surface/volume ratio in relation to the magnetic behavior.

A one-step non-hydrolytic sol–gel synthesis of mesoporous TiO_2 phosphonate hybrid materials was applied to yield diverse materials, which were found to depend on the P/Ti atom ratio [20]. The ratio was found to determine the particle size and the aggregation state and thereby could strongly tune the porosity of the resulting materials.

Colloidal chemistry with patchy silica nanoparticles was employed to synthesize clusters, so-called colloidal molecules [21]. Nanospherical satellites were covalently bonded via amide groups within the dimples of valence-endowed patchy nanoparticles, allowing the tuning of their topology and self-assembling ability.

Polyion complex micelles formed by complexation between poly(ethylene oxide)-*b*-poly(acrylic acid) (PEO-*b*-PAA) and an oligo-chitosan-type polyamine was used as a structure-directing agent to prepare ordered mesoporous silica materials in the work "pH-mediated control over the mesostructure of ordered mesoporous materials templated by polyion complex micelles" [22]. The mesostructures are highly pH-sensitive, adopting 2D-hexagonal, wormlike or lamellar organization depending on the extent of the electrostatic complexing bonds and on the condensation rate.

More complex assemblies involving ternary compositions in "Ternary nanocomposites of reduced graphene oxide, polyaniline and hexaniobate: hierarchical architecture and high polaron formation" were explored for the promotion of synergistic effects expected at the nanoscale [23]. The resulting mixture between polyaniline chains with reduced graphene flakes and hexaniobate nanoscrolls may find application as coatings for sensing or corrosion protection.

To understand composite formation of a complex hybrid assembly, high quality characterization is paramount. An example is small angle X-ray scattering (SAXS), which was used in the work "Mechanism of silica–lysozyme composite formation unraveled by in situ fast SAXS" to identify and characterize subtle interparticle interactions [24]. This study shows that fast in situ synchrotron SAXS provides an understanding of lysozyme deformation molecules during aggregation. All these contributions indicate a marked interest of current research in hybrid materials for nanostructuration and related issues.

Nanofillers

Nanocomposites remain a vast playground for research into new hybrid systems. A common approach for polymer fillers presented in this thematic issue is their use as organo-modified layered double hydroxides (LDHs) or new layered calcium phenylphosphonates, as well as functionalized films with high dielectric constant, or, in the case of optical applications, this consists also in embedding different types of nanoparticles.

In the first example, "Co-intercalated layered double hydroxides as thermal and photo-oxidation stabilizers for polypropylene", the concomitant intercalation of both a thermal and a photo-oxidation stabilizer endows polypropylene with remarkable resistance against thermal degradation and photo-oxidation [25]. In the same vein, the protection of the polymer using organo-modified LDH was addressed in "Outstanding chain-extension effect and high UV resistance of polybutylene succinate containing amino-acid-modified layered double hydroxides" [26]. However, this time with a "green aspect", since the polymer studied is a bio-based polyester and the organo-modifying agent of the 2D-filler is an amino acid.

The same host structure (i.e., LDH) was employed in "Topochemical engineering of composite hybrid fibers using layered double hydroxides and abietic acid" [27]. In this work, a composite hybrid was formed using cellulose fibers with LDH particles growing on their surface and then covered by abietic acid. The fibers were tested against hydrophobicity and lipophilicity.

Exfoliated nanosheets of layered calcium phenylphosphonate assisted by solvent were used in "Layered calcium phenylphosphonate: a hybrid material for a new generation of nanofillers" to promote the mechanical properties and improve the barrier effect for applications such as fire retardancy and gas permeation in a low molecular weight epoxy resin [28].

Regarding specific applications, the dielectric properties were investigated by broadband dielectric spectroscopy (BDS) in "Nanocomposite–parylene C thin films with high dielectric constant and low losses for future organic electronic devices" [29]. A combination of deposition techniques was used, chemical vapor deposition for parylene and RF-magnetron sputtering for silver nanoparticles. The content and size of the latter influences the dielectric characteristics of the resulting hybrid films.

Such devices may find application as insulating gates in organic field-effect transistors (OFETs).

Optical properties are the focus in "Ceria/polymer nanocontainers for high-performance encapsulation of fluorophores" [30]. Here, an organic/inorganic system is based on a liquid core containing a fluorophore (terrylene diimide) within a polymer shell armored with an inorganic layer (cerium oxide nanoparticles). CeO_2 nanoparticles act as oxygen scavengers, protecting the organic fluorophore from molecular oxygen. A different approach to luminescent composite films is reported in "Towards rare-earth-free white light-emitting diode devices based on the combination of dicyanomethylene and pyranine as organic dyes supported on zinc single-layered hydroxide" [31]. In this article, two fluorescent organic dyes, dicyanomethylene and pyranine, emit visible light upon blue LED excitation and are tethered to single layer hydroxide platelets and then embedded into a silicone polymer. These coatings deliver white-light emission when placed above a blue LED.

Health

Functionalized nanoparticles are highly investigated as possible platforms for disease diagnosis and therapy, leading to potential applications in nanomedicine. The state-of-the-art, as well as potential further developments, are reviewed in "Targeting strategies for improving the efficacy of nanomedicine in oncology" [32]. Nanocarriers for drugs were also decorated with suitable moieties to tune their affinity with specific biological membranes. More sophisticated strategies, including double targeting, are also highlighted in several articles. Among others, nanoparticles are often used as specific agents in dual therapy and diagnostics (i.e., theranostics). In "Size-selected Fe_3O_4–Au hybrid nanoparticles for improved magnetism-based theranostics", a Fe_3O_4–Au hybrid nanomaterial is simultaneously employed as a contrast agent in magnetic resonance imaging (MRI) and for local heating therapy using magnetic particle hyperthermia [33]. In vitro hyperthermia tests showed efficiency in inoculating mouse breast cancer cells. Another study reports the use of alendronate-coated gold nanoparticles [34]. The resulting gold–alendronate nanoplatform combines antitumor activity through drug delivery and photothermal therapy, as illustrated in vitro on the inhibition of prostate cancer cells.

In the field of hybrid coordination networks, new lanthanide-based networks synthesized by a solvo-ionothermal reaction or organic ligands are reported in "Magnetic and luminescent coordination networks based on imidazolium salts and lanthanides for sensitive ratiometric thermometry" [35]. Compounds associating the imidazolium ligand with several rare earth ions behave as a ratiometric thermometer and operate in the physiological range with suitable sensitivity.

Another metal–organic framework (MOF) is studied in "The nanoscaled metal–organic framework ICR-2 as a carrier of porphyrins for photodynamic therapy" [36]. Phosphinate-based MOF nanoparticles are decorated with porphyrin-type molecules as photosensitizers for biological applications. In this work, it was found that the photodynamic efficacy of the system depends on the substituent at the porphyrin phosphinate groups.

Environmental

Hybrid nanomaterials may play a key role in the field of environmental research, in which environmental remediation and speciation can be targeted. For example, in the work "New micro/mesoporous nanocomposite material from low-cost sources for the efficient removal of aromatic and pathogenic pollutants from water", a hybrid kaolinite nanocomposite was assembled via Zn cations upon calcination, resulting in a low-cost porous material exhibiting both micro- and mesopores [37]. The material is efficient in adsorbing water micropollutants, as well as the pathogen *E. coli.*, lending itself for application in water remediation. For the same application, a silica matrix, onto which the conjugated β-ketoenol–pyridine–furan ligand is immobilized, has been studied in "Removal of toxic heavy metals from river water samples using a porous silica surface modified with a new β-ketoenolic host" [38]. The metal adsorption speciation is relevant for some divalent cations in aqueous medium, and the hybrid system is recyclable.

Finally, catalysis is the focus of an article reporting the performance of functionalized gold clusters deposited on ZrO_2 nanoparticles for benzyl alcohol oxidation in [39]. Interestingly, the defunctionalized gold nanoclusters exhibit full catalytic conversion.

Overall, this thematic issue clearly highlights not only the current trends in the field of hybrid materials but also a special focus on the comprehensive elaboration of new functional nanostructures. It also illustrates the consistently high potential of hybrid materials for numerous applications. We hope that readers will enjoy this reference work and find this thematic issue a source of inspiration for their own future research. It was an immense pleasure for us to edit this thematic issue of *Beilstein Journal of Nanotechnology* devoted to "Advanced hybrid nanomaterials".

Verónica de Zea Bermudez, Fabrice Leroux, Pierre Rabu, Andréas Taubert

Vila Real, Aubière, Strasbourg, Potsdam, November 2019

ORCID® iDs

Fabrice Leroux - https://orcid.org/0000-0002-4671-9630
Pierre Rabu - https://orcid.org/0000-0002-6779-1527

References

1. Jose-Yacaman, M.; Rendon, L.; Arenas, J.; Serra Puche, M. C. *Science* **1996,** *273,* 223–225. doi:10.1126/science.273.5272.223
2. Doménech, A.; Doménech-Carbó, M. T.; Vidal-Lorenzo, C.; Vázquez de Agredos-Pascual, M. L. *Angew. Chem., Int. Ed.* **2012,** *51,* 700–703. doi:10.1002/anie.201106562
3. Lima, E.; Guzmán, A.; Vera, M.; Rivera, J. L.; Fraissard, J. *J. Phys. Chem. C* **2012,** *116,* 4556–4563. doi:10.1021/jp207602m
4. Wen, J.; Wilkes, G. L. *Chem. Mater.* **1996,** *8,* 1667–1681. doi:10.1021/cm9601143
5. Sanchez, C.; Ribot, F.; Lebeau, B. *J. Mater. Chem.* **1999,** *9,* 35–44. doi:10.1039/a805538f
6. Schubert, U.; Huesing, N.; Lorenz, A. *Chem. Mater.* **1995,** *7,* 2010–2027. doi:10.1021/cm00059a007
7. Schottner, G. *Chem. Mater.* **2001,** *13,* 3422–3435. doi:10.1021/cm011060m
8. Leonel, A. G.; Mansur, H. S.; Mansur, A. A. P.; Caires, A.; Carvalho, S. M.; Krambrock, K.; Outon, L. E. F.; Ardisson, J. D. *Int. J. Biol. Macromol.* **2019,** *132,* 677–691. doi:10.1016/j.ijbiomac.2019.04.006
9. Zhao, N.; Yan, L.; Zhao, X.; Chen, X.; Li, A.; Zheng, D.; Zhou, X.; Dai, X.; Xu, F.-J. *Chem. Rev.* **2019,** *119,* 1666–1762. doi:10.1021/acs.chemrev.8b00401
10. Blanco-Andujar, C.; Walter, A.; Cotin, G.; Bordeianu, C.; Mertz, D.; Felder-Flesch, D.; Begin-Colin, S. *Nanomedicine (London, U. K.)* **2016,** *11,* 1889–1910. doi:10.2217/nnm-2016-5001
11. Ariga, K.; Leong, D. T.; Mori, T. *Adv. Funct. Mater.* **2018,** *28,* 1702905. doi:10.1002/adfm.201702905
12. Govindaraju, T.; Avinash, M. B. *Nanoscale* **2012,** *4,* 6102–6117. doi:10.1039/c2nr31167d
13. Lebeau, B.; Innocenzi, P. *Chem. Soc. Rev.* **2011,** *40,* 886–906. doi:10.1039/c0cs00106f
14. Ruiz-Hitzky, E.; Aranda, P.; Darder, M.; Rytwo, G. *J. Mater. Chem.* **2010,** *20,* 9306–9321. doi:10.1039/c0jm00432d
15. Lim, H.-R.; Kim, H. S.; Qazi, R.; Kwon, Y.-T.; Jeong, J.-W.; Yeo, W.-H. *Adv. Mater. (Weinheim, Ger.)* 1901924. doi:10.1002/adma.201901924
16. Suriano, R.; Ciapponi, R.; Griffini, G.; Levi, M.; Turri, S. *Surf. Coat. Technol.* **2017,** *311,* 80–89. doi:10.1016/j.surfcoat.2016.12.095
17. Wang, B.; Wilkes, G. L.; Hedrick, J. C.; Liptak, S. C.; McGrath, J. E. *Macromolecules* **1991,** *24,* 3449–3450. doi:10.1021/ma00011a063
18. Nicole, L.; Laberty-Robert, C.; Rozes, L.; Sanchez, C. *Nanoscale* **2014,** *6,* 6267–6292. doi:10.1039/c4nr01788a
19. Bibani, M.; Breitwieser, R.; Aubert, A.; Loyau, V.; Mercone, S.; Ammar, S.; Mammeri, F. *Beilstein J. Nanotechnol.* **2019,** *10,* 1166–1176. doi:10.3762/bjnano.10.116
20. Wang, Y.; Mutin, P. H.; Alauzun, J. G. *Beilstein J. Nanotechnol.* **2019,** *10,* 356–362. doi:10.3762/bjnano.10.35
21. Rouet, P.-E.; Chomette, C.; Adumeau, L.; Duguet, E.; Ravaine, S. *Beilstein J. Nanotechnol.* **2018,** *9,* 2989–2998. doi:10.3762/bjnano.9.278
22. Molina, E.; Mathonnat, M.; Richard, J.; Lacroix-Desmazes, P.; In, M.; Dieudonné, P.; Cacciaguerra, T.; Gérardin, C.; Marcotte, N. *Beilstein J. Nanotechnol.* **2019,** *10,* 144–156. doi:10.3762/bjnano.10.14
23. Silva, C. H. B.; Iliut, M.; Muryn, C.; Berger, C.; Coldrick, Z.; Constantino, V. R. L.; Temperini, M. L. A.; Vijayaraghavan, A. *Beilstein J. Nanotechnol.* **2018,** *9,* 2936–2946. doi:10.3762/bjnano.9.272
24. Stawski, T. M.; van den Heuvel, D. B.; Besselink, R.; Tobler, D. J.; Benning, L. G. *Beilstein J. Nanotechnol.* **2019,** *10,* 182–197. doi:10.3762/bjnano.10.17
25. Zhang, Q.; Gu, Q.; Leroux, F.; Tang, P.; Li, D.; Feng, Y. *Beilstein J. Nanotechnol.* **2018,** *9,* 2980–2988. doi:10.3762/bjnano.9.277
26. Marek, A. A.; Verney, V.; Taviot-Gueho, C.; Totaro, G.; Sisti, L.; Celli, A.; Leroux, F. *Beilstein J. Nanotechnol.* **2019,** *10,* 684–695. doi:10.3762/bjnano.10.68
27. Sobhana, L.; Kesavan, L.; Gustafsson, J.; Fardim, P. *Beilstein J. Nanotechnol.* **2019,** *10,* 589–605. doi:10.3762/bjnano.10.60
28. Kopecká, K.; Beneš, L.; Melánová, K.; Zima, V.; Knotek, P.; Zetková, K. *Beilstein J. Nanotechnol.* **2018,** *9,* 2906–2915. doi:10.3762/bjnano.9.269
29. Mokni, M.; Maggioni, G.; Kahouli, A.; Carturan, S. M.; Raniero, W.; Sylvestre, A. *Beilstein J. Nanotechnol.* **2019,** *10,* 428–441. doi:10.3762/bjnano.10.42
30. Katta, K.; Busko, D.; Avlasevich, Y.; Landfester, K.; Baluschev, S.; Muñoz-Espí, R. *Beilstein J. Nanotechnol.* **2019,** *10,* 522–530. doi:10.3762/bjnano.10.53
31. Nyalosaso, J. L.; Boonsin, R.; Vialat, P.; Boyer, D.; Chadeyron, G.; Mahiou, R.; Leroux, F. *Beilstein J. Nanotechnol.* **2019,** *10,* 760–770. doi:10.3762/bjnano.10.75
32. Villaverde, G.; Baeza, A. *Beilstein J. Nanotechnol.* **2019,** *10,* 168–181. doi:10.3762/bjnano.10.16
33. Efremova, M. V.; Nalench, Y. A.; Myrovali, E.; Garanina, A. S.; Grebennikov, I. S.; Gifer, P. K.; Abakumov, M. A.; Spasova, M.; Angelakeris, M.; Savchenko, A. G.; Farle, M.; Klyachko, N. L.; Majouga, A. G.; Wiedwald, U. *Beilstein J. Nanotechnol.* **2018,** *9,* 2684–2699. doi:10.3762/bjnano.9.251
34. Plan Sangnier, A.; Aufaure, R.; Motte, L.; Wilhelm, C.; Guenin, E.; Lalatonne, Y. *Beilstein J. Nanotechnol.* **2018,** *9,* 2947–2952. doi:10.3762/bjnano.9.273
35. Farger, P.; Leuvrey, C.; Gallart, M.; Gilliot, P.; Rogez, G.; Rocha, J.; Ananias, D.; Rabu, P.; Delahaye, E. *Beilstein J. Nanotechnol.* **2018,** *9,* 2775–2787. doi:10.3762/bjnano.9.259
36. Hynek, J.; Jurík, S.; Koncošová, M.; Zelenka, J.; Křížová, I.; Ruml, T.; Kirakci, K.; Jakubec, I.; Kovanda, F.; Lang, K.; Demel, J. *Beilstein J. Nanotechnol.* **2018,** *9,* 2960–2967. doi:10.3762/bjnano.9.275
37. Unuabonah, E. I.; Nöske, R.; Weber, J.; Günter, C.; Taubert, A. *Beilstein J. Nanotechnol.* **2019,** *10,* 119–131. doi:10.3762/bjnano.10.11
38. Tighadouini, S.; Radi, S.; Elidrissi, A.; Haboubi, K.; Bacquet, M.; Degoutin, S.; Zaghrioui, M.; Garcia, Y. *Beilstein J. Nanotechnol.* **2019,** *10,* 262–273. doi:10.3762/bjnano.10.25
39. Shahin, Z.; Ji, H.; Chiriac, R.; Essayem, N.; Rataboul, F.; Demessence, A. *Beilstein J. Nanotechnol.* **2019,** *10,* 228–237. doi:10.3762/bjnano.10.21

BEILSTEIN JOURNAL OF NANOTECHNOLOGY

Size-selected Fe_3O_4–Au hybrid nanoparticles for improved magnetism-based theranostics

Maria V. Efremova[‡1,2], Yulia A. Nalench[‡2], Eirini Myrovali[3], Anastasiia S. Garanina[1,2], Ivan S. Grebennikov[2], Polina K. Gifer[2], Maxim A. Abakumov[2,4], Marina Spasova[5], Makis Angelakeris[3], Alexander G. Savchenko[2], Michael Farle[5], Natalia L. Klyachko[1,2], Alexander G. Majouga[1,2,6] and Ulf Wiedwald[*2,5]

Full Research Paper

Open Access

Address:
[1]Department of Chemistry, Lomonosov Moscow State University, Moscow, 119991, Russia, [2]National University of Science and Technology «MISIS», Moscow, 119049, Russia, [3]Physics Department, Aristotle University of Thessaloniki, Thessaloniki, 54124, Greece, [4]Department of Medical Nanobiotechnology, Russian National Research Medical University, Moscow, 117997, Russia, [5]Faculty of Physics and Center for Nanointegration Duisburg-Essen, University of Duisburg-Essen (CENIDE), Duisburg, 47057, Germany and [6]D. Mendeleev University of Chemical Technology of Russia, Moscow, 125047, Russia

Email:
Ulf Wiedwald[*] - ulf.wiedwald@uni-due.de

* Corresponding author ‡ Equal contributors

Keywords:
hybrid nanoparticles; magnetic hyperthermia; magnetic resonance imaging; nanomagnetism; theranostics

Beilstein J. Nanotechnol. **2018,** *9,* 2684–2699.
doi:10.3762/bjnano.9.251

Received: 27 June 2018
Accepted: 17 September 2018
Published: 16 October 2018

This article is part of the thematic issue "Advanced hybrid nanomaterials".

Guest Editor: A. Taubert

Abstract

Size-selected Fe_3O_4–Au hybrid nanoparticles with diameters of 6–44 nm (Fe_3O_4) and 3–11 nm (Au) were prepared by high temperature, wet chemical synthesis. High-quality Fe_3O_4 nanocrystals with bulk-like magnetic behavior were obtained as confirmed by the presence of the Verwey transition. The 25 nm diameter Fe_3O_4–Au hybrid nanomaterial sample (in aqueous and agarose phantom systems) showed the best characteristics for application as contrast agents in magnetic resonance imaging and for local heating using magnetic particle hyperthermia. Due to the octahedral shape and the large saturation magnetization of the magnetite particles, we obtained an extraordinarily high r_2-relaxivity of 495 $mM^{-1}{\cdot}s^{-1}$ along with a specific loss power of 617 $W{\cdot}g_{Fe}^{-1}$ and 327 $W{\cdot}g_{Fe}^{-1}$ for hyperthermia in aqueous and agarose systems, respectively. The functional in vitro hyperthermia test for the 4T1 mouse breast cancer cell line demonstrated 80% and 100% cell death for immediate exposure and after precultivation of the cells for 6 h with 25 nm Fe_3O_4–Au hybrid nanomaterials, respectively. This confirms that the improved magnetic properties of the bifunctional particles present a next step in magnetic-particle-based theranostics.

Introduction

Biocompatible magnetite nanoparticles (NPs) are anticipated to provide new noninvasive therapies and early diagnostics for previously incurable diseases using a single, so-called "theranostics" platform [1-3]. The magnetic properties of Fe_3O_4 NPs give rise to novel therapeutic approaches such as magneto-mechanical cancer treatment [4] and magnetic particle hyperthermia (MPH) [5-7] as well as to improvements in diagnostic techniques like magnetic resonance imaging (MRI) [8-10] and magnetic particle imaging (MPI) [11,12]. For advanced functionality under real operational conditions, various approaches have been attempted, e.g., optimization of the NP surface using targeting molecules or specific polymers [13-15]. From the physics point of view, the strategically tailored design of structural and magnetic properties in biocompatible Fe_3O_4 NPs is of utmost importance for improved performance in MPH, MRI, or MPI [16,17]. It is essential to obtain Fe_3O_4 NPs of high crystallinity with bulk-like magnetic properties, which change with the NP size, shape and iron oxidation state [18-20]. These parameters can be adjusted by heterogeneous nucleation of NPs on noble metal seeds [21,22]. Additionally, such bifunctional Fe_3O_4–Au NPs are potentially applicable for targeted drug delivery, enhanced hyperthermia, multimodal imaging and theranostics [8,23-27].

In this work, we present the first size-dependent study of hybrid Fe_3O_4–Au NPs with Janus structure for application in theranostics where improvements in MRI and MPH were demonstrated. Increasing the magnetic NP diameter from 6 to 44 nm, we show the gradual transition of their lattice parameters from an intermediate value between maghemite γ-Fe_2O_3 and magnetite, to high-quality stoichiometric Fe_3O_4. We find a size-dependent transition from superparamagnetic to a stable ferrimagnetic response, a bulk-like saturation magnetization, and observe the Verwey transition at 123 K – all of which result in the superior magnetic properties for a particle diameter greater than 20–25 nm [28].

For theranostic application, we test the contrast enhancement of the developed materials in MRI and the heating potential in MPH. Importantly, these measurements are performed in both aqueous and agarose dispersions, i.e., phantoms, mimicking the conditions in cells and tissues. For the MRI tests, we observe the growth of the r_2-relaxivity from 159 to 495 $mM^{-1}{\cdot}s^{-1}$ in water and from 118 to 612 $mM^{-1}{\cdot}s^{-1}$ in agarose gel matrices with increasing NP diameter from 6 to 25 nm. Our best values are significantly enhanced in comparison to other Fe_3O_4–Au hybrids or commercial contrast agents due to the high crystallinity and large bulk-like saturation magnetization leading to larger field gradients in MRI. The MPH measurements reveal that the specific loss power (SLP) increases from 10 to 617 $W{\cdot}g_{Fe}^{-1}$ in water and from 12 to 327 $W{\cdot}g_{Fe}^{-1}$ in agarose with increasing NP diameter from 6 to 25 nm. The 25 nm and 44 nm diameter NPs show similar theranostic performance.

In in vitro experiments we detected the death of 4T1 mouse breast cancer cells at a rate of 79 ± 8% after exposure to 25 nm Fe_3O_4–Au hybrids for 30 min in an ac magnetic field (AMF) with 261–393 kHz and 25 mT, which resulted in heating up to 46 ± 1 °C. Preincubation of the cells with the hybrid NPs for 6 h further decreased the cell viability and led to complete (100%) cell death. Such multifunctional Fe_3O_4–Au Janus NPs combine the best characteristics for MRI and MPH and offer the highest potential for therapeutic and visualization capabilities in magnetism-based theranostics.

Results and Discussion

In this section, we start presenting the basic characterization of the size-selected NPs addressing dimensions and morphology, structure, and magnetic properties. This is followed by a discussion of the theranostic application of NPs in MRI and MPH. We conclude with a proof-of-principle in vitro study showing efficient induction of cell death.

Size and morphology

All Fe_3O_4–Au hybrid NPs were synthesized by the thermal decomposition of iron pentacarbonyl on the surface of Au NPs in a high-boiling solvent. Details regarding the synthesis are given in the Experimental section. In brief, Fe_3O_4 was grown on either in situ synthesized Au NPs (samples MNP-6 and MNP-15) or presynthesized Au seeds (samples MNP-25 and MNP-44). In addition, by using three different solvents (phenyl ether, benzyl ether, 1-octadecene), we vary the reaction temperature. The sample numbers reflect the mean magnetic NP diameter, i.e., the Fe_3O_4 part, in nanometers. After synthesis, all NPs were investigated by transmission electron microscopy (TEM).

Figure 1 shows the corresponding images of the four NP batches: magnetite and gold NPs are pairwise connected and form hybrid NPs. The magnetite NPs formed using the in situ synthesized Au seeds have a spherical or poorly facetted shape (Figure 1A and 1B), while NPs obtained using presynthesized Au seeds are highly facetted (Figure 1C and 1D). The formation of highly facetted magnetite with improved crystallinity in this case is likely due to the longer reflux time. To the best of our knowledge, only a few examples of Fe_3O_4–Au NPs with octahedral-like morphology have been reported in the literature [29,30]. We find that our hybrid NPs outperform previous

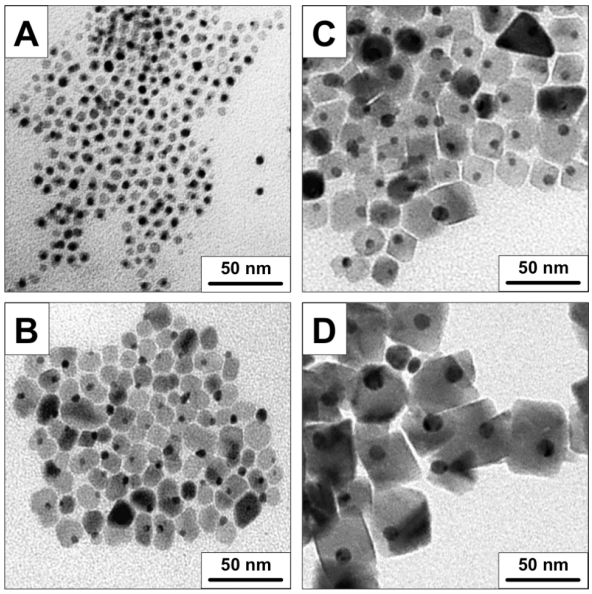

Figure 1: Bright-field TEM images of size-selected magnetite–gold NPs with in situ synthesized Au seeds: A) MNP-6; B) MNP-15; and with presynthesized Au seeds: C) MNP-25; D) MNP-44. The sample numbers reflect the Fe_3O_4 NP mean size in nanometers.

reports in terms of size selection, size distribution, degree of crystallinity and faceting.

The size distribution of the magnetite–gold NPs was measured based on a series of TEM images. The average NP diameter and standard deviation (SD) values are presented in Table 1. The size histograms are provided in Supporting Information File 1, Figure S1. The volume fraction of magnetite and gold can be evaluated using the average NP diameter (assuming spherical Au–Fe_3O_4 NPs) by TEM and from fitting by modified Rietveld refinement from XRD. Importantly, the ratio of Fe_3O_4 to Au is almost constant at about 97% for MNP-15, MNP-25, and MNP-44, while for the smallest NPs, we obtain a slightly lower Fe_3O_4 volume fraction of 91%. For optimized MRI and MPH properties, the Fe_3O_4 volume fraction should be high since the diamagnetic Au can only be considered as a minor contributor. In comparison to Fe_3O_4, Au does not modify the optimized collective magnetic response, which is a prerequisite for biomagnetic applications.

Structure and phase composition

The structure and phase composition of the Fe_3O_4–Au NPs was investigated by X-ray diffraction (XRD). Figure 2 presents the experimental data. All expected powder diffraction peaks of magnetite and gold are clearly observed. Rietveld refinement, combining the powder diffraction reference data of Fe_3O_4 (ICDD PDF-2 No. 00-019-0629) and Au (ICDD PDF-2 No. 03-065-8601), is applied (not shown). The extracted lattice constants, crystallite size and phase volume fractions are listed in Table 1.

Since magnetite (Fe_3O_4) and maghemite (γ-Fe_2O_3) are structurally similar, XRD alone does not provide an accurate discrimination between the two phases. As listed in Table 1, the lattice parameter approaches bulk Fe_3O_4 (a = 0.8397 nm) rather than bulk γ-Fe_2O_3 (a = 0.8347 nm) with increasing NP size [31]. The XRD results suggest that the structure of sample MNP-25 is bulk-like Fe_3O_4 and Au in the NPs. The TEM diameter and the XRD crystallite size measurements of Fe_3O_4 match well, except for the MNP-44 batch, where polycrystalline Fe_3O_4 is presumed. We conclude that the Fe_3O_4 crystallite size can be varied while holding the Fe_3O_4/Au phase volume ratio almost constant.

Additionally, the crystallographic orientation of Fe_3O_4 and Au for samples MNP-15 (with in situ synthesized Au seeds) and MNP-25 (with presynthesized Au seeds) was evaluated using bright-field high-resolution TEM (HRTEM) imaging (Figure 3A and 3B) and fast Fourier transform (FFT)

Table 1: Results of the structural and morphological characterization by TEM and XRD. The NP size distribution, volume fraction of Fe_3O_4 and Au, lattice parameter (a), and crystallite size are listed.

Sample	TEM				XRD					
	NP diameter (nm)		Volume fraction (%)		a (nm)		Crystallite diameter (nm)		Volume fraction (%)	
	Fe_3O_4	Au	Fe_3O_4	Au	Fe_3O_4	Au	Fe_3O_4	Au	Fe_3O_4	Au
MNP-6	6.3 ± 0.8	3.2 ± 0.6	91.4 ± 4.1	8.6 ± 4.1	0.8376 ± 0.0005	0.4060 ± 0.0005	4.0 ± 1.0	2.0 ± 1.5	92.9 ± 4.0	7.1 ± 4.0
MNP-15	14.6 ± 2.7	5.9 ± 1.0	96.9 ± 2.3	3.1 ± 2.3	0.8384 ± 0.0004	0.4068 ± 0.0004	15.0 ± 2.0	4.0 ± 1.0	95.5 ± 2.0	4.5 ± 2.0
MNP-25	25.1 ± 5.0	9.2 ± 2.1	97.2 ± 2.6	2.8 ± 2.6	0.8394 ± 0.0002	0.4076 ± 0.0002	26.0 ± 1.1	4.5 ± 0.4	95.3 ± 0.7	4.7 ± 0.7
MNP-44	43.9 ± 10.6	10.9 ± 2.3	97.1 ± 2.6	2.9 ± 2.6	0.8390 ± 0.0001	0.4082 ± 0.0002	16.8 ± 0.4	9.5 ± 0.6	95.0 ± 1.5	5.0 ± 1.5

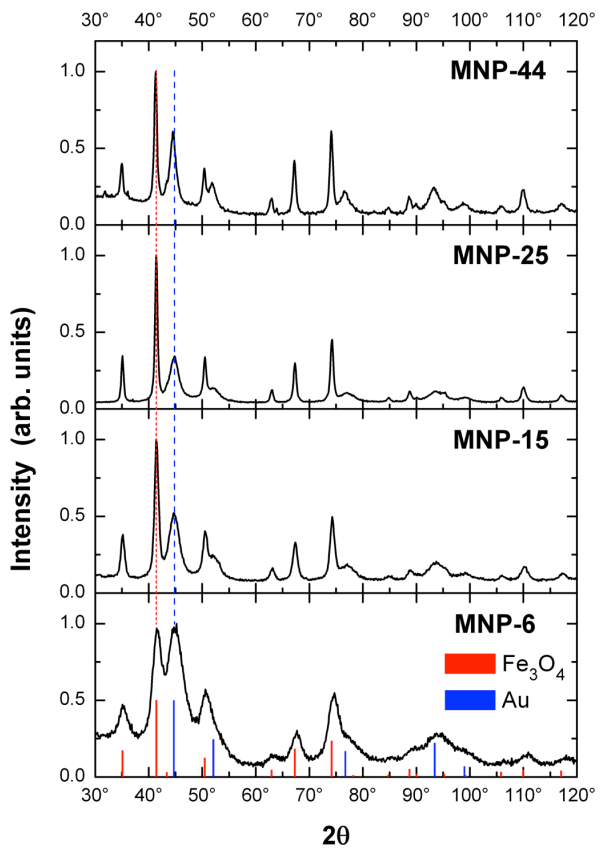

Figure 2: XRD patterns of Fe_3O_4–Au NPs. Panels are sorted by magnetic NP size from bottom to top – samples MNP-6, MNP-15, MNP-25 and MNP-44, respectively. The intensity of each diffractogram is normalized to the strongest peak. The red and blue vertical lines represent the angular position and relative intensity of reference bulk magnetite and gold phases.

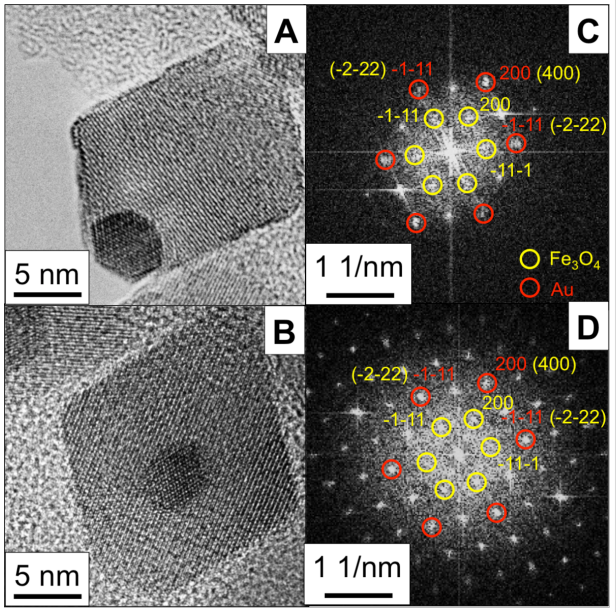

Figure 3: HRTEM and corresponding FTT images of size-selected magnetite–gold NPs: MNP-15 (A, C) and MNP-25 (B, D). Fe_3O_4 and Au indices are marked yellow and red, respectively. The [111] and [200] crystallographic directions of Fe_3O_4 and Au register to each other. The NPs are viewed along their [011] direction.

Table 2: Mass fraction of Fe_3O_4 and Au in the samples, as determined by XRD and AES analysis.

Sample	mass % (XRD)		mass % (AES)	
	Fe_3O_4	Au	Fe_3O_4	Au
MNP-6	78.0 ± 4.0	22.0 ± 4.0	84.7 ± 2.3	15.3 ± 2.3
MNP-15	85.2 ± 2.0	14.8 ± 2.0	82.9 ± 1.4	17.1 ± 1.4
MNP-25	84.6 ± 0.7	15.4 ± 0.7	85.3 ± 0.9	14.7 ± 0.9
MNP-44	83.8 ± 1.5	16.2 ± 1.5	87.5 ± 2.5	12.5 ± 2.5

(Figure 3C and 3D). It is clear that the Au NPs, acting as seeds in the synthesis, allow for epitaxial growth of Fe_3O_4 on Au, forming the Janus structure with Au (111) || Fe_3O_4 (111) and Au (200) || Fe_3O_4 (200), which is in agreement with the previous reports on similar hybrids and electrodeposited epitaxial films [32,33]. HRTEM images of samples MNP-6 and MNP-44 are presented in Supporting Information File 1, Figure S2. While MNP-44 shows a similar growth mode, the smallest hybrid NPs (MNP-6) show a rather spherical shape for the Au core and deteriorated Fe oxide parts attached to each other.

The composition (in terms of Fe_3O_4 and Au mass fraction) of the hybrid NPs is determined by XRD (assuming Fe_3O_4 and Au bulk densities of 5.2 g·cm^{-3} and 19.3 g·cm^{-3}, respectively) and additionally by atomic emission spectrometry (AES). The results are presented in Table 2. XRD and AES data for the samples MNP-15, MNP-25 and MNP-44 correlate well within 3%. The larger difference for MNP-6 can be explained by the presumably larger fraction of maghemite in this sample. For all further analysis we use the AES results.

Magnetic properties

The static magnetic properties are presented in this section. We measure zero-field cooling and field cooling (ZFC/FC) at an applied field of $\mu_0 H$ = 5 mT and hysteresis loops in the field range $\mu_0 H$ = ±9 T in the temperature interval 5–350 K for MNP-15 and MNP-25 and 5–390 K for samples MNP-6 and MNP-44. Figure 4A presents the ZFC/FC curves. With increasing NP size, the superparamagnetic blocking temperature (T_B) increases from 62 K for MNP-6 to 210 K for MNP-15, as identified by the maximum of the ZFC branch. However, the rather broad size distribution of 10–20% (Table 1) and corresponding volume distributions result in broad distributions of blocking temperatures, T_B. Thus, the T_B values should be taken as those of the larger NPs. For sample MNP-25, T_B is above ambient

and the ZFC curve suggests a T_B in the range 310–350 K while the T_B of sample MNP-44 is clearly larger than the experimentally accessible temperature range 5–390 K. For samples MNP-25 and MNP-44, a sudden increase of the ZFC curve is observed above 123 K and 100 K, respectively, after which a plateau develops. We identify this feature as the Verwey transition in Fe_3O_4 at T_V = 123 K in bulk material [34]. Sample MNP-25 shows the bulk T_V, revealing the high quality of the Fe_3O_4 nanocrystals. Instances of slightly off-stoichiometric Fe_3O_4 leads to rather large shifts of T_V towards lower temperatures [35]. Therefore, the Verwey transition could often not be identified in NP ensembles since the transition smears out over a broader temperature range [36]. For sample MNP-44, T_V is indeed shifted by more than 20 K, indicating that the Fe_3O_4 in this sample is of lower quality than for sample MNP-25. We ascribe this to the polycrystalline nature of the Fe_3O_4 NPs for this sample, as supported by the XRD results revealing a grain size of 17 nm compared to the TEM diameter of 44 nm. In contrast, the diameter of Fe_3O_4 in sample MNP-25, as determined by TEM and XRD, is the same within the error bar.

Figure 4B shows the magnetic hysteresis loops at T = 5 K and T = 300 K. All samples have an open hysteresis at T = 5 K while at ambient temperature only the larger NPs (MNP-25 and MNP-44) preserve their hysteretic behavior. Smaller NPs become superparamagnetic in accordance with the ZFC/FC curves in Figure 4A. Note that for Fe_3O_4 the transition from a single- to multidomain state is expected at a critical diameter of 30–90 nm, depending on the magneto-crystalline anisotropy and the saturation magnetization M_S as well as on the shape and morphology [37-39]. We thus expect that except for sample MNP-44 all magnetite hybrid samples are single domain.

The M_S (Table 3) is measured at large fields by extrapolation of a linear fit to the ordinate. The M_S increases with increasing particle size from 57.0 (47.6) $A{\cdot}m^2{\cdot}kg^{-1}$ (Fe_3O_4) for MNP-6 to 97.1 (86.8) $A{\cdot}m^2{\cdot}kg^{-1}$ (Fe_3O_4) at 5 (300) K for MNP-25 while MNP-44 only reaches 79.6 (73.6) $A{\cdot}m^2{\cdot}kg^{-1}$ (Fe_3O_4) at 5 (300) K probably due to the reduced grain size and resulting deterioration of the Fe_3O_4 lattice as well as partial oxidation to γ-Fe_2O_3, e.g., at the grain boundaries. The decrease of M_S for small particles has been ascribed to these features [40-42] and considering the bulk M_S values at 5 K (96.4 $A{\cdot}m^2{\cdot}kg^{-1}$ for magnetite) and 300 K (92.0 $A{\cdot}m^2{\cdot}kg^{-1}$ for magnetite and 76.0 $A{\cdot}m^2{\cdot}kg^{-1}$ for maghemite) our results follow the trends reported previously [43-46]. Note that M_S of sample MNP-25 matches the Fe_3O_4 bulk value within the error bar. The error is rather large due to the net weight of the samples (few milligrams) and the mass fraction of Fe oxide with respect to Au as determined by AES (Table 2).

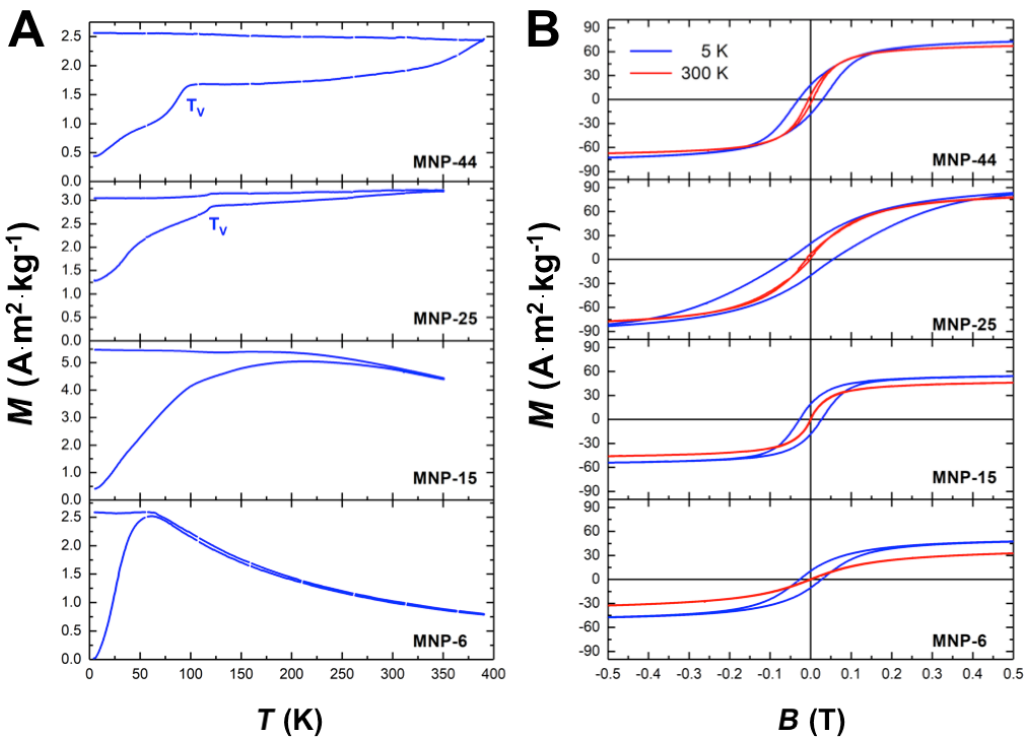

Figure 4: Magnetic properties of Fe_3O_4–Au hybrid NPs. ZFC/FC curves at B = 5 mT (A). T_V indicates the Verwey transition temperature for samples MNP-25 and MNP-44. Hysteresis loops at T = 5 K and T = 300 K (B).

Table 3: Overview of the size-dependent magnetic properties of Fe_3O_4–Au NPs. Saturation magnetization M_S at 9 T, T = 5 K and T = 300 K, coercive field $\mu_0 H_C$ at T = 5 K, and deduced blocking temperature, T_B, and effective magnetic anisotropy, K_{eff}. The bulk Fe_3O_4 reference values are listed for comparison and referenced in the text.

Sample	M_S (A·m^2·kg(Fe_3O_4)$^{-1}$)		$\mu_0 H_C$ (mT)	T_B (K)	K_{eff} (kJ·m^{-3})
	T = 5 K	T = 300 K	T = 5 K	ZFC	Sharrock model
MNP-6	57.0 ± 3.0	47.6 ± 2.4	27 ± 2	62	45 ± 18
MNP-15	70.4 ± 2.1	61.1 ±2.0	28 ± 2	210	11 ± 7
MNP-25	97.1 ± 2.4	86.8 ±2.1	55 ± 2	310	10 ± 6
MNP-44	79.6 ± 4.6	73.6 ± 4.2	30 ± 2	>390	–
bulk Fe_3O_4	96.4	92.0	–	–	13 (K_1)

The temperature dependence of the coercive field $H_C(T)$ allows us to estimate the effective magnetic anisotropy energy density K_{eff} (Table 3) by using Sharrock's equation for single domain, randomly oriented, non-interacting NPs [47-49]:

$$H_C(T) = H_C(T=0)\left[1-\left(\frac{T}{T_B}\right)^{\frac{2}{3}}\right].$$

Random orientation and single domain properties are guaranteed for the three smaller particle batches [37], while dipolar coupling in the powder sample is neglected in the following. This simple approach averages over all particle sizes of a distribution and does not overestimate the mean blocking temperature as the ZFC curves do for larger size distributions [50]. Fitting $H_C(T)$ yields an average blocking temperature T_B which can be translated into K_{eff} via $21 \cdot k_B T \approx K_{eff} \cdot V$ where k_B the Boltzmann constant and V the NP volume. The prefactor 21 accounts for an attempt frequency of 10^9 Hz and the VSM measurement time of 1 s [51].

Table 3 lists the extracted K_{eff} values while the uncertainty intervals have been estimated based on the volume distributions. We obtain 11 ± 7 kJ·m^{-3} and 10 ± 6 kJ·m^{-3} for MNP-15 and MNP-25, respectively. These values are in reasonable agreement with the first order anisotropy constant of bulk Fe_3O_4 K_1 = 13 kJ·m^{-3} [37]. For MNP-44 the model is not used since T_B is much larger than the accessible temperature range and presumably rather close to the temperature where this simple model cannot be applied. More interesting is the significantly enhanced K_{eff} = 45 ± 18 kJ·m^{-3} for MNP-6. Previous reports and our XRD results suggest that small particles (<10–15 nm) crystallize as a composite of magnetite and maghemite, and the anisotropy constant increases with decreasing size. Martinez et al. [52], for example, determined $K_1 \approx 70$ kJ·m^{-3} for about 15 nm maghemite NPs, which is strongly enhanced as compared to the bulk value of $K_1 \approx$ 4–5 kJ·m^{-3} [53]. The effective anisotropy of K_{eff} = 45 ± 18 kJ·m^{-3} for MNP-6 compares well with such an enhancement, and a mixture of magnetite and maghemite can explain our measured value for the smallest batch. The observed NP size for blocking at ambient temperature of about 25 nm compares well with the predictions for 25 nm Fe_3O_4 cuboids with an aspect ratio of 1.05–1.1 [54]. Such slight elongations are also present in the octahedra.

Overall, the static magnetic properties suggest that the smallest particles are of little interest for MRI and MPH applications. MNP-15 and larger NPs perform better under 100–1000 kHz ac magnetic fields [6,55]. For MRI in quasi-static fields, however, we expect that MNP-25 and MNP-44 will perform the best.

Magnetic resonance imaging

Knowing the structural and magnetic properties of our hybrid Fe_3O_4–Au NPs, in this section we discuss if such features have an impact on the NP performance in MRI. For this purpose, the NPs were stabilized in water by modification with a biocompatible derivative of polyethylene glycol and phospholipid (DSPE-PEG-COOH). The NPs with a polymer shell have a hydrodynamic diameter ranging from 95 to 160 nm, according to the dynamic light scattering data (Table S1, Supporting Information File 1).

The ability of magnetite NPs to increase the T_2-contrast in MRI arises from the creation of huge magnetic field gradients, accelerating the relaxation rate of water protons in the vicinity of the NPs [56]. The correlation of r_2-relaxivity with the size of Fe_3O_4 NPs and clusters of NPs has been thoroughly discussed in the literature. See for example [57-60]. These aggregates can be considered as magnetic volumes in which the dipole–dipole interaction between NPs produces a strong magnetic field gradient leading to the predominant T_2-effect. The r_2-relaxivity is affected by NP aggregation, and three different regimes can be distinguished. First, for small clusters, r_2 is given by the theory of the outer sphere. NPs are homogeneously dispersed, and water protons diffuse between the magnetic cores before becoming completely out-of-phase. At this point, r_2 increases

with the NP size. This regime is called the motional average regime (MAR). Therefore, MAR is predicted for relatively small iron oxide NPs, where water diffusion near NPs occurs on much faster timescales than the resonance frequency shift, resulting in increased r_2 values with increasing NP size [61]. For example, the variation of NP diameters from 4 nm to 6 nm, 9 nm, and 12 nm resulted in r_2 values of 78, 106, 130, and 218 $mM^{-1}·s^{-1}$, respectively [62]. When the diameter is increased further, the r_2 value is constant up to a certain size limit. The size and the corresponding stray field are so large that water molecules experience a nearly constant magnetic field during their T_2-relaxation. These NPs are then in the so-called static dephasing regime (SDR) [63], which determines the relaxivity limit, and the r_2 value reaches a plateau. In the SDR, the induced perturbing field around larger NPs is much stronger, and proton diffusion becomes nondominant for the signal decay. For instance, the r_2 values increased rapidly from 173 to 204 and 240 $mM^{-1}·s^{-1}$ at 7 T for NPs from 8 nm to 23 nm and 37 nm, respectively [63]. For larger 65 nm sized iron oxide NPs [64], the r_2-relaxivity only slightly increases further to 249 $mM^{-1}·s^{-1}$. Recently, Reguera et al. [65] reported a similar enhancement of $\Delta r_2 \approx 100$ $mM^{-1}·s^{-1}$ for increasing diameters from 16 nm to 20 nm Fe_3O_4–Au hybrid NPs. Finally, as the size further increases, r_2 decreases with increasing size. The decrease rate of r_2 depends on the echo time in the partial refocusing model [66].

In our experiments, the r_2 values of the Fe_3O_4–Au hybrid samples were measured for all particle sizes (Figure 5, Figure S3, Supporting Information File 1) in water and in 2% agarose NP solutions. The latter has a viscosity close to that of cell cytoplasm [6,67] thus mimicking the viscosity and microstructure of tissues [68,69]. We measure an increase of the r_2-relaxivity from 159 to 495 $mM^{-1}·s^{-1}$ in water (Figure 5A) and from 118 to 612 $mM^{-1}·s^{-1}$ in agarose (Figure 5B) for the sample series of MNP-6, MNP-15 and MNP-25 Fe_3O_4–Au hybrid samples, while for even larger, 44 nm Fe_3O_4–Au NPs (sample MNP-44) no significant increase in r_2 (514 and 620 $mM^{-1}·s^{-1}$ for water and agarose solutions, respectively) was observed. We ascribe this to the initial increase of the saturation magnetization M_S for

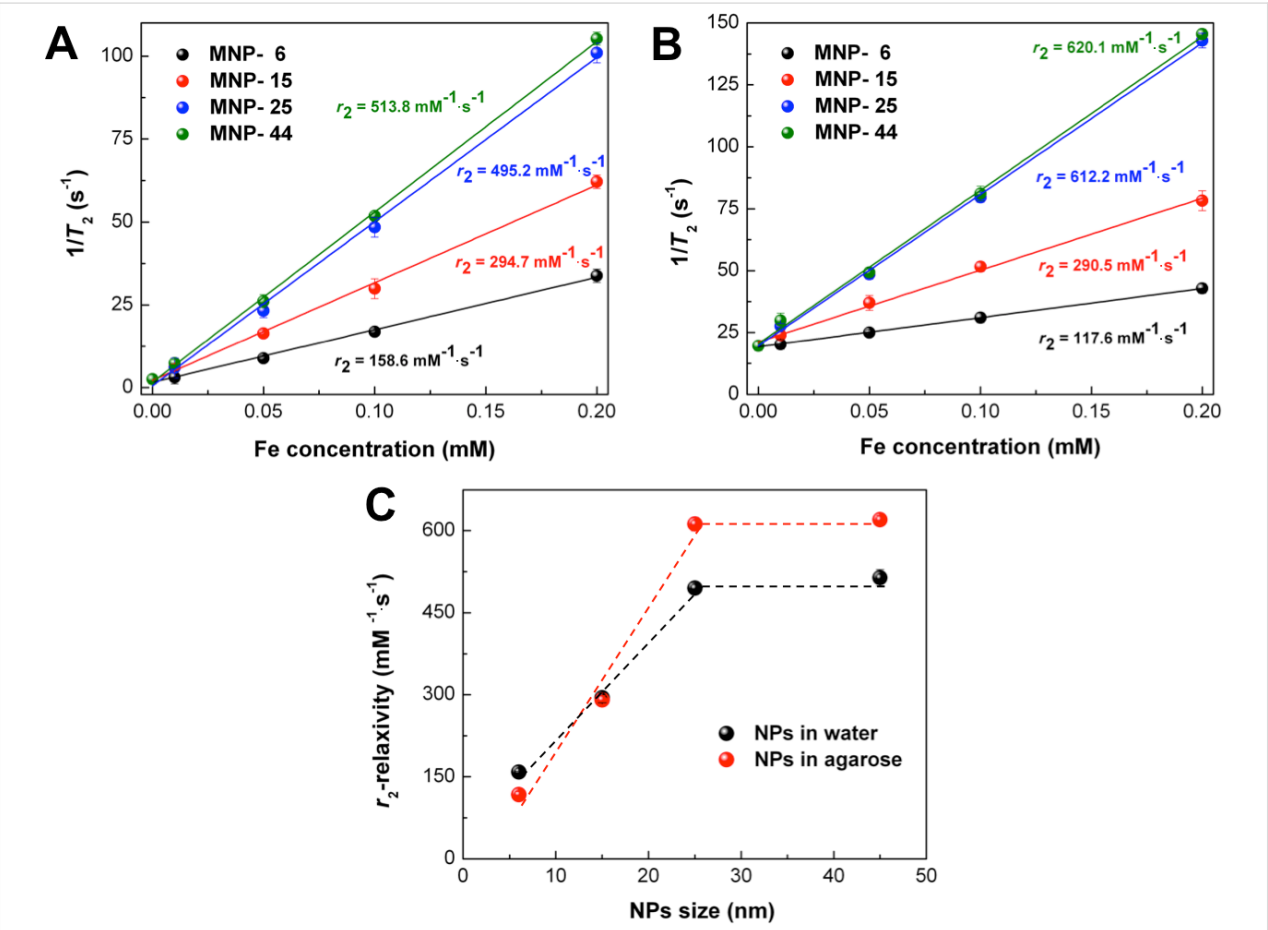

Figure 5: Inverse of the MRI proton T_2-relaxation time as a function of iron concentration for MNP-6, MNP-15, MNP-25 and MNP-44 in water (A) and 2% agarose (B). The r_2 values are determined by the slopes of the linear fits. C) r_2 values as a function of NP size in water and agarose. The SDs are smaller than the symbol size.

larger Fe_3O_4 NPs from 6 to 25 nm. For MNP-25 the bulk M_S value is reached and remains roughly constant for MNP-44. The T_2 behavior of samples MNP-6 and MNP-15 can be described as within MAR. Further increase of size (MNP-25) results in an intermediate state close to the SDR regime, while sample MNP-44 is presumably in SDR. It should be mentioned that the r_2-relaxivity of MNP-25 and MNP-44 samples is much higher as compared to other examples of Fe_3O_4–Au hybrid NPs (r_2 = 245–381 $mM^{-1}·s^{-1}$) [65,70] and commercial contrast agents, such as Feridex®, with an r_2 of 120.0 $mM^{-1}·s^{-1}$ [71] and Resovist®, with an r_2 of 150.0 $mM^{-1}·s^{-1}$ [72].

The most probable reasons for the extraordinarily high performance of our NPs are the perfect crystallinity and the resulting bulk-like M_S leading to a stronger local magnetic stray field [59]. Following Hwang and Freed's theory [73] the r_2 value is proportional to the square of two key parameters in highly magnetized nanomaterials: the M_S value and the effective magnetic radius R. In short, the M_S value determines the local magnetic field inhomogeneity induced by the NPs. The effective radius is responsible for the field perturbation volumes for water protons. Variations from a spherical shape of the NPs, especially significant for the present octahedra, increase the effective magnetic anisotropy by shape anisotropy which increases quadratically with M_S [59]. Experimentally, this was observed by Joshi et al. [74] and Smolensky et al. [75] when they compared spherical and faceted NPs. In both studies, a higher r_2-relaxivitiy was found for faceted NPs. These findings also correlate with the highest r_2 values ever reported (761 $mM^{-1}·s^{-1}$ for 22 nm cubic Fe_3O_4 NPs [76] and 679 $mM^{-1}·s^{-1}$ for Fe_3O_4 octapods [77]). Therefore, in addition to the stray field strength, the facets of MNP-25 and MNP-44 are likely to produce stronger stray field gradients ΔB in their vicinity, especially near the six corners and eight edges of the magnetic octahedrons.

The effective magnetic radius R of a nanoplate, for instance, has been determined to be much larger than its spherical counterpart with a similar solid volume [78], which leads to enhanced r_2 values. This principle may be applied to the octahedral particles of MNP-25 and MNP-44 samples as an explanation of increased r_2-relaxivity values. Zhou et al. [78] further argued that the strong T_1 and T_2 contrast enhancement of nanoplates could be explained by the large surface area of Fe_3O_4 (111) facets for efficient chemical exchange/interaction. This also holds for the present NPs with (111) facets (see Figure S2C, Supporting Information File 1). Finally, the functionalization of the NPs with DSPE–PEG–COOH further increases the r_2-relaxivity since the subunits of PEG chains are usually associated with two or three water molecules via complex formation and/or hydrogen bonds. These strong interactions slow down the diffusion of water molecules to some extent and increase the r_2 value [59].

Moreover, r_2 values are even higher for the larger NPs dispersed in agarose in comparison with water solutions (Figure 5C), while for the smaller NPs, lower r_2 values are observed. This splits the batches into two size regimes, namely SDR and MAR for the larger and smaller batches, respectively. According to these relaxation regimes, the NPs up to about 20–25 nm are in the MAR where the diffusion processes are the predominant factor for the r_2-relaxivity. This limit correlates well with the model predictions for the r_2 value described in [66] considering clusters of 4–5 NPs in the case of sample MNP-6 (modeled r_2 = 154 $mM^{-1}·s^{-1}$) and single NPs of MNP-15 (modeled r_2 = 255 $mM^{-1}·s^{-1}$) in MAR. The confinement of the NPs in an agarose matrix hinders or at least slows down the diffusion of water molecules near NPs and therefore decreasing r_2 values are obtained. Although the theoretical limit [66] for MNP-25 and MNP-44 in SDR of ≈1000 $mM^{-1}·s^{-1}$ (given their high M_S values) is not reached, an additional stabilization by agarose seems to play a decisive role for significantly enhanced r_2 values [57]. This means that the effectiveness of the hybrid materials as contrast agents increases under in vitro and in vivo operational conditions.

Magnetic hyperthermia

Next, we evaluate the heating efficiency of the hybrid NPs in MPH, measuring the heating rate in both water and agarose at various concentrations in AMF at the frequency of 765 kHz and amplitude $\mu_0 H$ = 30 mT, as shown in Figure 6. The relatively high AMF frequency has been chosen for better data acquisition. Figure 6A depicts a set of two hyperthermia sequences, composed of a heating (magnetic field is switched on) and a cooling stage (magnetic field is switched off), for two aqueous solutions, respectively. It is apparent that there is a critical magnetite size that renders such structures suitable for hyperthermia applications. Superparamagnetic 6 nm Fe_3O_4 are too small to induce a thermal shock within the hyperthermia window of 41–45 °C (shaded temperature band in the figure) while 25 nm Fe_3O_4 safely reach 42 °C within the first 35 s of AMF application. A similar, yet moderated situation is shown in the corresponding agarose samples in Figure 6B. Agarose is a polysaccharide matrix, widely accepted as an excellent phantom system since, with respect to its concentration, it may mimic both soft and hard tissues.

From the initial heating rates $\Delta T/\Delta t$ we determine the SLP for NPs of a certain size range for agarose medium and MNP-25 in aqueous medium as a reference. Table 4 summarizes the results. The experimental details and evaluations are explained in the Experimental part. For samples MNP-6 and MNP-15, the ob-

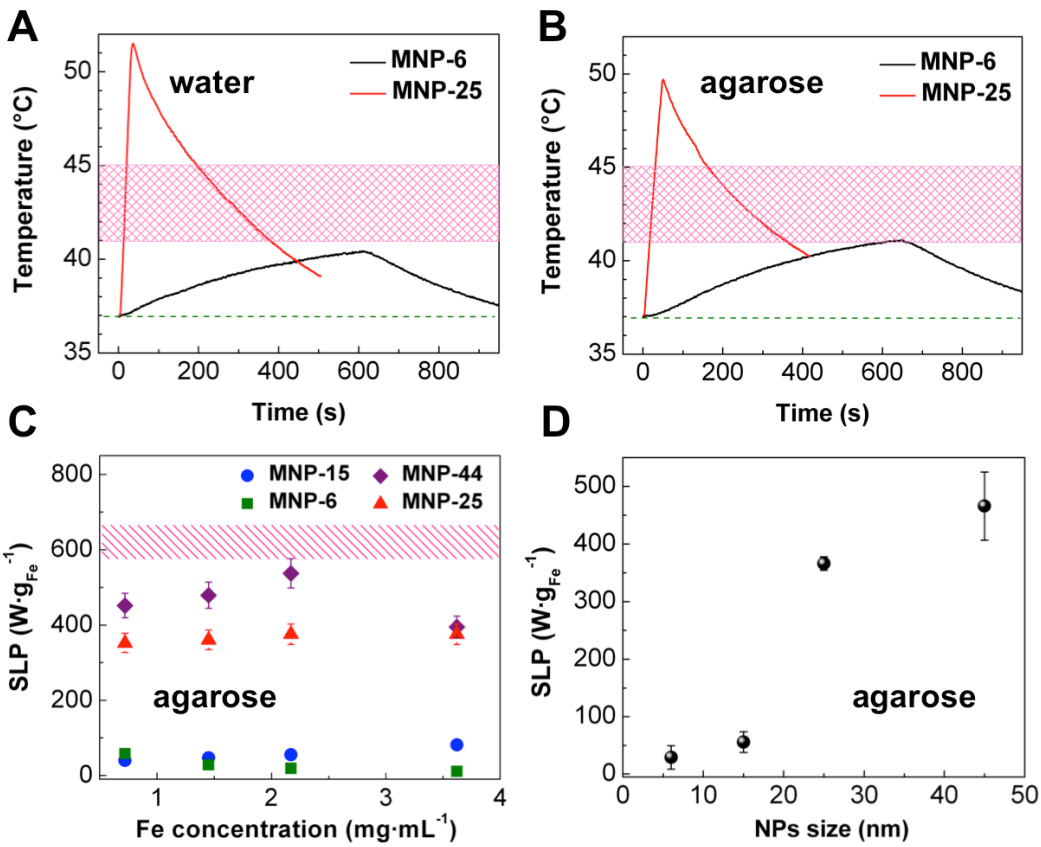

Figure 6: MPH experiments (765 kHz, 30 mT). The heating curves of MNP-6 and MNP-25 (3.6 mg·mL^{-1} Fe) in water (A) and agarose (B), the shaded bands show the 41–45 °C region; SLP values for MNP-6, MNP-15, MNP-25 and MNP-44 samples for various concentrations in agarose compared to the reference values for MNP-25 (3.6 mg·mL^{-1} Fe) in water shown by the shaded band (C); the comparison of concentration-averaged SLP values for the NPs of various size (D). The error bars in (C) and (D) correspond to the standard deviation.

Table 4: The heating rate $\Delta T/\Delta t$ and calculated SLP values for various NP concentrations and sizes in agarose and aqueous medium using MNP-25 as a reference.

Sample	Medium	Heating rate (K·s^{-1})	c(Fe_3O_4) (mg·mL^{-1})	c(Fe) (mg·mL^{-1})	SLP (W·g_{Fe}^{-1})
MNP-6	agarose	0.010	5	3.6	12 ± 1
MNP-15		0.070			81 ± 6
MNP-25		0.281			327 ± 24
MNP-44		0.342			398 ± 29
MNP-25	water	0.531	5	3.6	617 ± 44

tained SLP values are below 80 W·g^{-1}, which is insufficient for effective MPH. Reasonably high SLP values, however, are found for MNP-25 and MNP-44 (larger than 327 W·g^{-1}). We ascribe the observations to the transition from superparamagnetic to ferrimagnetic behavior between MNP-15 and MNP-25 together with the increasing M_S with NP size in agreement with literature [28]. In the blocked state, MPH additionally benefits from Néel losses, increasing the SLP. Diameters in the range of 20–25 nm Fe_3O_4 are considered to be optimal for iron-oxide-based MPH [79]. Despite this, the observed SLP values for MNP-44 are significantly higher than for MNP-25, which can at least partly be explained by the higher blocking temperature. Thus, all NPs in MNP-44 contribute to the temperature rise via Néel losses. Hysteresis losses prevail and stabilize the SLP values for MNP-25 and MNP-44 at 3.6 mg·mL^{-1} Fe concentration (Figure 6C). As a reference, the heating rate and corresponding SLP are also determined for MNP-25 in aqueous solution (3.6 mg·mL^{-1} Fe), which is used for in vitro hyperthermia experiments in the following. The SLP of 617 ± 44 W·g^{-1} for the MNP-25 sample is indicated by the shaded band in

Figure 6C. This value is comparable to the SLP of 524 $W \cdot g^{-1}$ for NP chains in magnetosomes with a 30 nm core size obtained by Hergt et al. [80]. The authors, however, used more moderate field conditions (12.5 mT, 410 kHz) in their experiments.

For each sample the SLP values are averaged over all concentrations since we only obtain minor variations with increasing relative amounts. Figure 6D presents the SLP values as a function of NP size. The strongly increasing SLP between MNP-15 and MNP-25 is attributed to the transition from superparamagnetic to the thermally blocked state in this size regime.

Our results are in good agreement with the relevant literature on gold/iron oxide nanoparticle dimers (Fe_3O_4–Au [81] and Fe_2O_3–Au [82]), where the heating efficiency is optimized at diameters of about 23 nm, and SLP values up to 1330 ± 20 $W \cdot g^{-1}$ (300 kHz, 30 mT) are reported. This high SLP value, however, is questionable, since the heating curve of this sample provided in the supplementary information of [82] for a Fe concentration in the 6–12 $mg \cdot mL^{-1}$ range, only delivers a heating rate of 0.640 $K \cdot s^{-1}$. This corresponds, according to our calculations, to 223–447 $W \cdot g^{-1}$ SLP (depending on the Fe concentrations used). Therefore, we can conclude that our Fe_3O_4–Au hybrids with 25 nm diameter provide high SLP values for MPH, which are at least in line with the values reported in [82]. In all cases nonadiabatic correction is performed within the SLP calculation to avoid erroneous overestimations due to heating transfers of nonmagnetic origin [83]. Eventually, a critical magnetite diameter (≥20 nm) is required to promote enhanced heating efficiency within the concentration range of 1–10 $mg\ mL^{-1}$.

Moreover, the dispersion of NPs in an agarose matrix results in the same SLP magnitudes for MNP-6 when compared to water solutions (see the heating curves, Figure 6A and Figure 6B) and leads to an almost two-fold decrease of SLP for the MNP-25 sample. This decrease is due to Brownian relaxation, which is dependent on the medium viscosity, and is at least partially suppressed in agarose due to the increased hydrodynamic diameter (Figure 6C). The good performance of MNP-25 is very important here since it affirms the application of the NPs for magnetic hyperthermia in conditions comparable to the intracellular environment. Moreover, the SLP values of the larger NPs are adequate to promote significant heating in the in vitro experiments following.

In vitro test of performance

The high contrast properties of 25 nm Fe_3O_4–Au hybrid NPs for in vitro MRI in 4T1 mouse breast adenocarcinoma cells have been recently demonstrated [84]. In summary, a r_2 value of 276.9 $mM^{-1} \cdot s^{-1}$ was obtained after 24 h of NP incubation with cell culture. Such an r_2 value is suitable for MRI, although it was found to decrease as compared to the hybrids in water or agarose in line with previous cell culture experiments [85].

Here, we focus on the hyperthermia function of the hybrid materials in the same cell line. For this purpose, polymer-coated MNP-25 NPs were dispersed in RPMI medium at 3.6 $mg \cdot mL^{-1}$ Fe concentration, resulting in the same hydrodynamic size as in water (Table S1, Supporting Information File 1) and added to 4T1 cells. The specimen was immediately exposed to 261–393 kHz, 25 mT AMF. The frequency is adjusted to keep the temperature constant at 46 ± 1 °C for 15 or 30 min. Afterwards, the cell viability is tested by several methods. Standard MTS assay (Figure 7, Table S2, Supporting Information File 1) was conducted to investigate the NP cytotoxicity. These results are supplemented with apoptosis/necrosis activation (Figures S4 and S6, Supporting Information File 1) and production of reactive oxygen species (ROS) (Figures S5 and S7, Supporting Information File 1). The ROS excess level is known to induce apoptosis [86-88]. The applied combination of techniques enables us to draw definite conclusions about the effect of NPs on cell viability [89].

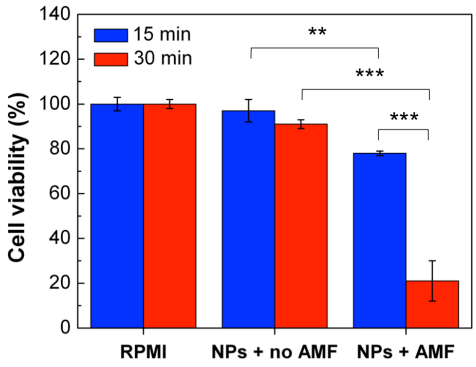

Figure 7: Cell viability study (MTS assay) of 4T1 cells after 15 and 30 min incubation with NPs during AMF exposure or without its application. RPMI: viability of cells cultivated at 37 °C in cell medium without NPs; NPs + no AMF: viability of cells cultivated at 37 °C in the presence of MNP-25 in cell medium for 15 or 30 min; NPs + AMF: viability of cells cultivated in the presence of MNP-25 in cell medium for 15 or 30 min of AMF exposure (heating up to 46 ± 1 °C in 261–393 kHz, 25 mT AMF). The results are shown as the mean ± SD, $^{**}p < 0.01$, $^{***}p < 0.001$ (one-way ANOVA).

In our experiments, 15 min AMF exposure of 4T1 cells incubated with NPs indicate the initial level of induced cell death (22 ± 1%, MTS assay) in comparison with cells, incubated at 37 °C with NPs in the absence of AMF and control samples without NPs in zero field or exposed to AMF. This is well in

line with the detection of apoptosis/necrosis as a positive staining of 4T1 cells is found only on the periphery of the cell monolayer. However, ROS activation is observed at this point of time – as indicated by an increased number of H2DCFDA-positive cells in the culture (Figure S5C, Supporting Information File 1). Exposure to AMF for 30 min is sufficient to kill 79 ± 8% of cells according to the MTS assay. Consistent with this finding, more pronounced apoptosis/necrosis activation is detected (Figure S5D, Supporting Information File 1).

Next, 4T1 cells are precultivated with NPs for 6 h before AMF exposure to increase NP–cell interactions. In this case, 15 min and 30 min of exposure to AMF led to similar, yet improved, results: 100% cell death detected by apoptosis/necrosis activation in cell culture (Figure S6, Supporting Information File 1). Accordingly, no ROS activation is detected (Figure S7C and S7D, Supporting Information File 1) due to the late stage of apoptosis.

The two sets of experiments, direct AMF treatments and precultivation for 6 h, both show clear apoptosis/necrosis of 4T1 cells induced by the hyperthermia treatment. The more efficient precultivation might help to decrease the concentration threshold for MPH in future studies. Furthermore, the results are in line with previous reports on polymer-coated Fe_3O_4 or $MnFe_2O_4$ NPs, where apoptosis/necrosis of various cell cultures along with ROS generation was observed [90-94] for the identical concentration range (1–10 $mg{\cdot}mL^{-1}$) and similar AMF conditions. Other experiments have shown a decrease of 4T1 cell viability down to 60–70% after initial incubation of cells with magnetic NPs [95,96]. In the current study, however, we achieve the same level of cell viability immediately after NP addition followed by AMF treatment. If the cells are first incubated with NPs for 6 h before field application, 100% cell death is observed. Therefore, the results demonstrate not only the general in vitro function of Fe_3O_4–Au hybrid NPs for MPH, but also the opportunity of reduced AMF treatment time leading to 100% cell death if an intermediate step of NP–cell co-cultivation is added. Corato et al. [81] have tested Fe_3O_4–Au NPs for hyperthermia treatment of so-called “minitumors”, consisting of SKOV-3 cells, which is the transitional step between in vitro and in vivo experiments. Considering the higher SLP values of the present hybrid NPs, the suggested approach may improve in vivo MPH in future experiments.

Conclusion

We have successfully synthesized Fe_3O_4–Au hybrid NPs with 6–44 nm diameter Fe_3O_4 and 3–11 nm diameter Au subunits, while maintaining an approximately constant Fe_3O_4/Au volume ratio. With the increase of size, the iron oxide lattice parameters change towards stoichiometric Fe_3O_4. Hybrids below 20 nm are superparamagnetic, while NPs of larger diameter are thermodynamically blocked, and the Verwey transition is observed in ZFC/FC curves as an indicator of high quality, bulk-like Fe_3O_4. The best combination of the r_2-relaxivity and SLP values for all samples, both in water and agarose mimicking tissues, is obtained for 25 nm diameter Fe_3O_4–Au NPs. This also allows for efficient NP visualization and heating in in vitro conditions, leading to the death of 4T1 mouse breast adenocarcinoma cells in high-frequency alternating magnetic fields. Therefore, these hybrid nanomaterials are demonstrated to exhibit an optimized theranostic response in magnetic resonance imaging and magnetic particle hyperthermia.

Experimental

Materials

Iron pentacarbonyl $Fe(CO)_5$, hydrogen tetrachloroaurate trihydrate (III) $HAuCl_4{\cdot}3H_2O$, oleic acid, oleylamine, phenyl ether, benzyl ether, 1-octadecene and 1,2-hexadecanediol were purchased from Sigma-Aldrich. 1,2-Distearoyl-*sn*-glycero-3-phosphoethanolamine-*N*-[carboxy(polyethylene glycol)-5000] ammonium salt (DSPE-PEG-COOH) was delivered by Avanti Polar Lipids. Isopropanol, hexane and chloroform were purchased from Reachim. Water used in the experiments was deionized (18.2 $M\Omega{\cdot}cm^{-1}$, Millipore Milli-Q Academic System).

Synthesis and functionalization of nanoparticles

The Au NPs were synthesized according to a previously published protocol [97]. Briefly, 35 mg $HAuCl_4{\cdot}3H_2O$ was dissolved in 80 mL deionized water (DI H_2O) and heated up to 80 °C. Then 200 µL oleylamine was added and the temperature was maintained during 3 h. After cooling down to room temperature, the water was evaporated, and the Au NPs were redispersed in hexane (2 mL).

The synthesis of MNP-6 and MNP-15 samples was performed as follows: Fe_3O_4–Au hybrid NPs with in situ synthesized Au seeds were obtained by thermal decomposition of $Fe(CO)_5$ and $HAuCl_4{\cdot}3H_2O$ at high temperatures following a modified protocol [98]. In brief, a mixture of 20 mL high-boiling solvent (phenyl ether for sample MNP-6 or 1-octadecene for sample MNP-15), 2.584 g 1,2-hexadecanediol, 2 mL oleylamine and 2 mL oleic acid was heated up to 120 °C under argon atmosphere and kept at this temperature for 30 min. Then, 0.28 mL of $Fe(CO)_5$ was added. Three minutes later, a mixture of $HAuCl_4{\cdot}3H_2O$ (45 mg), 5 mL solvent and 0.5 mL oleylamine was added, and the final solution was slowly (3 °C/min) heated up to reflux for 45 min. After cooling down to room temperature, the reaction mixture was oxidized by stirring for 1 h under ambient air. The NPs were isolated via centrifugation, washed several times with isopropanol and dispersed in hexane.

Fe_3O_4–Au hybrid NPs with presynthesized Au seeds (MNP-25 and MNP-44) were grown by thermal decomposition of $Fe(CO)_5$ in the presence of Au NPs following a modified protocol [84,99]. A mixture of 1 mL oleic acid and 20 mL solvent (phenyl ether for sample MNP-25 or benzyl ether for sample MNP-44) was heated up to 120 °C under argon atmosphere and kept at this temperature for 30 min. Then, 0.28 mL of $Fe(CO)_5$ was added. Five minutes later, the presynthesized Au NPs in 2 mL hexane and 500 µL oleylamine were added, and the final solution was slowly heated up to reflux at a rate of 3 °C/min for a total time of 3 h. After cooling down to room temperature, the reactants were oxidized by stirring for 1 h under ambient air. The NPs were isolated via centrifugation, washed with isopropanol and dispersed in hexane.

Oleic-acid-coated Fe_3O_4–Au NPs were transferred into water by modification with 1,2-distearoyl-*sn*-glycero-3-phosphoethanolamine-*N*-[carboxy(polyethylene glycol)-5000] ammonium salt (DSPE–PEG–COOH) [100]. Fe_3O_4–Au NPs (1 mg) and DSPE–PEG–COOH (2.45 mg) were mixed in 1 mL chloroform via ultrasonication. The mixture was left overnight for the slow evaporation of the solvent. Then DI H_2O was added to the precipitate, and the solution was sonicated for 15 min. After that, unbound polymer was removed by centrifugation (14500 rpm for 30 min) twice. Finally, the NPs were redispersed in 2 mL DI H_2O.

Characterization techniques

All particle batches were examined by a JEOL JEM-1400 transmission electron microscope operated at 120 kV acceleration voltage. Overview images were taken in conventional bright-field TEM mode. The samples were prepared by casting and evaporating a droplet of hexane solution onto a carbon-coated copper grid (300 mesh). The average diameter of NPs was calculated from TEM images by analysis of about 500 NPs for each sample using ImageJ software. Selected samples were investigated in bright-field high-resolution mode using a FEI Tecnai F20 microscope operated at 200 kV acceleration voltage. The Fe and Au concentrations in the samples were measured by microwave-coupled plasma atomic emission spectrometry (Agilent 4200 MP-AES, USA) for the NPs dissolved in aqua regia using the calibration curve for the standard samples in 0.1–1 $mg{\cdot}mL^{-1}$ concentration range.

X-ray diffraction patterns were measured from $2\theta = 30°$ to 120° at a scan rate of 0.1° per step and 3 s per point using the X-ray powder diffractometer Rigaku Ultima IV with Co Kα radiation and a graphite monochromator on the diffracted beam. Quantitative XRD analysis (including crystal size evaluation by determination of the coherent scattering region) was performed using the PHAN% and SPECTRUM programs developed by the Physical Materials Science Department of the National University of Science & Technology (NUST) "MISIS" that are a modification of the Rietveld method, based on the minimization of the difference between the experimental spectrum, taken from the points, and model (calculated) one. For fitting the spectra, the lattice parameters, the amount of each phase and their crystallite diameter are optimized.

Standard magnetometry at various temperatures and fields was measured in a Quantum Design PPMS DynaCool system. For this, about 10 mg of dried powder Fe_3O_4–Au NPs was put into synthetic capsules.

The hydrodynamic size of the NPs in water was measured by dynamic light scattering using a Zetasizer Nano ZS (Malvern Instruments). The average values with error bars were obtained from three measurements of each sample.

Magnetic resonance imaging (MRI) was measured at 18 °C in a ClinScan 7 T MRI system. The r_2-relaxivity of hydrogen protons in the presence of Fe_3O_4–Au NPs modified with DSPE–PEG–COOH was determined by linear fitting of various Fe concentrations from 0.01 to 0.2 mM in water and 2% w/w agarose. Image acquisition was performed in the spin echo mode with the following parameters: repetition time 10 s, echo times 16, 24, …, 256 ms, flip angle 180°, resolution 640 × 448 pixel, field of view 120 × 82.5 mm^2. The signal intensities were determined using ImageJ software, and the T_2-relaxation time was calculated by exponential fitting as a function of echo time. The r_2-relaxivity values were calculated from linear fitting of T_2^{-1} relaxation times as a function of Fe concentration.

Magnetic particle hyperthermia (MPH) experiments were performed using a commercial 4.5 kW inductive heater operating at 765 kHz under AC induction amplitudes of up to 30 mT. Each measurement cycle included a heating and a cooling stage. The temperature was continuously recorded (0.4 s steps) by a GaAs-based fiber optic probe immersed in the vial containing 1 mL of solution. The heating efficiency of the NPs is quantified by the specific loss power (SLP) determined from the power absorption per unit mass of magnetic material (in $W{\cdot}g_{Fe}^{-1}$) following a standardized procedure to estimate solely the magnetic heating contribution by using

$$\mathrm{SLP} = C\frac{\Delta T}{\Delta t}\frac{m_\mathrm{f}}{m_{\mathrm{MNP_s}}},$$

where C is the volumetric specific heat capacity of the sample, m_f the dispersion mass, $m_{\mathrm{MNP_s}}$ is the iron mass diluted in the

dispersion and $\Delta T/\Delta t$ is the maximal slope at initial time after switching on the heating AC field.

In vitro experiments

Cell culture. 4T1 mouse breast cancer cells were purchased from the American Type Culture Collection (ATCC, Manassas, VA, USA). They were cultured in RPMI-1640 medium (Gibco) supplemented with 10% fetal bovine serum (FBS) (Gibco) and 2 mM L-glutamine (Gibco) at 37 °C in a humidified incubator supplied with 5% CO_2.

MTS assay. The cells were plated in the wells of Stripwell 96-well plates (Corning) at a concentration of 6,000 cells per well. The cells were counted using the automatic cell counter EVE. After two days the medium from the cells was replaced by 200 μL of the Fe_3O_4–Au Janus NP solution in full culture medium (the final concentration of NPs was 3.6 mg·mL^{-1} Fe), and the obtained samples were exposed to high-frequency AMF (TOR Ultra HT, Nanomaterials LLC, Russia) for 15 min or 30 min immediately or 6 h after NP–cell co-cultivation. The AMF parameters of 261–393 kHz, 25 mT were used to keep a constant temperature of 46 ± 1 °C (checked by Seek Thermal camera and software). The cells, incubated in the full culture medium and in a medium with the same concentration of NPs at 37 °C without AMF, were used as controls. After hyperthermia treatment, the medium with NPs was replaced by 100 μL of new culture medium, and 20 μL of MTS reagent (CellTiter 96 aqueous non-radioactive cell proliferation assay, Promega, USA) was added to each well. Following 4 h of incubation at 37 °C in darkness, the wells were placed on a permanent magnet to remove the NPs from solution, and 100 μL of the obtained solution was carefully replaced in the new 96-well plate. The absorbance of the solution was measured at 490 nm using a Thermo Scientific Multiskan GO spectrometer.

Apoptosis/necrosis detection. In parallel with the preparation of samples for MTS assay we prepared samples for cell death detection using an apoptosis/necrosis detection kit (abcam). Apopxin deep red dye stained phosphatidylserine on the membrane of apoptotic cells and nuclear green dye – the cells with loss of plasma membrane integrity (i.e., cells at late stage apoptosis or necrotic cells). After the hyperthermia treatment, the cells were washed twice with HBSS (Gibco) supplemented with 2 mM L-glutamine (Gibco) and 10 mM HEPES (Helicon, pH 7.4 adjusted with 1 M NaOH), and intravitally stained with the apoptosis/necrosis detection kit for 40 min at room temperature in the darkness, and washed with full HBSS two times again. The cells, incubated in full culture medium and in medium with NPs at 37 °C without AMF, were used as controls. The obtained preparations were analyzed using a fluorescence microscope (EVOS, life technologies), with a PlanFluor objective 10×/0.3. The further processing of the photos was carried out by ImageJ software.

ROS detection by 2',7'-dichlorodihydrofluorescein diacetate (H2DCFDA). Reactive oxygen species (ROS) generation by cells was also investigated during hyperthermia in vitro experiments. In this case, unfixed cells (exposed to AMF and control cells) were washed twice with HBSS supplemented with 2 mM L-glutamine and 10 mM HEPES (pH 7.4 adjusted with 1 N NaOH), and stained with 2 μM H2DCFDA solution (life technologies) for 30 min at 37 °C in darkness. Then the cells were carefully washed with HBSS three times for 5 min. The obtained preparations were analyzed using the EVOS fluorescence microscope with a PlanFluor objective 10×/0.3. The further processing of the photos was also carried out by ImageJ software.

Statistical analysis. All data were obtained in three independent triplicate experiments. The percentage of live cells in the MTS assay was represented as the mean ± standard deviation (SD) (for 3 repetitions in each experiment). Plotting and calculation of the standard deviation values were made using Origin 8.0 software. The p-values were calculated using one-way ANOVA calculator. p-values <0.05 were considered significant (** for $p < 0.01$, *** for $p < 0.001$). A post-hoc Scheffe test was applied.

Supporting Information

Size distribution for all synthesized NPs (Figure S1), HRTEM images for MNP-6, MNP-44 and MNP-25 samples (Figure S2), T_2-weighted MRI-images of the NP solutions in water and 2% agarose (Figure S3), hydrodynamic size of NPs in water (Table S1), a cell viability study by MTS assay (Table S2), apoptosis/necrosis activation (Figures S4 and S6) as well as reactive oxygen species generation (Figures S5 and S7) in 4T1 cells cultivated with MNP-25 NPs followed by AMF application in comparison with control, are presented in the Supporting Information.

Supporting Information File 1

Additional experimental information.
[https://www.beilstein-journals.org/bjnano/content/supplementary/2190-4286-9-251-S1.pdf]

Acknowledgements

The authors gratefully acknowledge the financial support of the Ministry of Education and Science of the Russian Federation in the framework of Increase Competitiveness Program of NUST

"MISIS" No. K2-2018-008 (magnetic hyperthermia). M.E. gratefully acknowledges the DAAD scholarship program No. 57314023. U.W. gratefully acknowledges the financial support of the Ministry of Education and Science of the Russian Federation in the framework of Increase Competitiveness Program of NUST "MISIS" No. K3-2017-022 (magnetic characterization). The reported study was funded by Russian Foundation for Basic Research (RFBR) according to the research project No. 18-33-01232 (magnetic resonance imaging). MRI measurements were carried out by ClinScan 7T (Bruker Biospin) located at CKP "Medical Nanobiotechnology".

ORCID® iDs

Maria V. Efremova - https://orcid.org/0000-0002-5196-5596
Yulia A. Nalench - https://orcid.org/0000-0002-6031-8163
Natalia L. Klyachko - https://orcid.org/0000-0002-9357-8236
Ulf Wiedwald - https://orcid.org/0000-0002-3209-4078

References

1. Ferrari, M. *Nat. Rev. Cancer* **2005,** *5,* 161–171. doi:10.1038/nrc1566
2. Cho, K.; Wang, X.; Nie, S.; Chen, Z.; Shin, D. M. *Clin. Cancer Res.* **2008,** *14,* 1310–1316. doi:10.1158/1078-0432.CCR-07-1441
3. Ma, Y.; Huang, J.; Song, S.; Chen, H.; Zhang, Z. *Small* **2016,** *12,* 4936–4954. doi:10.1002/smll.201600635
4. Master, A. M.; Williams, P. N.; Pothayee, N.; Zhang, R.; Vishwasrao, H. M.; Golovin, Y. I.; Riffle, J. S.; Sokolsky, M.; Kabanov, A. V. *Sci. Rep.* **2016,** *6,* 33560. doi:10.1038/srep33560
5. Ortega, D.; Pankhurst, Q. A. Magnetic hyperthermia.. In *Nanoscience: Nanostructures through Chemistry;* O'Brien, P., Ed.; Royal Society of Chemistry: Cambridge, 2013; Vol. 1, pp 60–88. doi:10.1039/9781849734844-00060
6. Myrovali, E.; Maniotis, N.; Makridis, A.; Terzopoulou, A.; Ntomprougkidis, V.; Simeonidis, K.; Sakellari, D.; Kalogirou, O.; Samaras, T.; Salikhov, R.; Spasova, M.; Farle, M.; Wiedwald, U.; Angelakeris, M. *Sci. Rep.* **2016,** *6,* 37934. doi:10.1038/srep37934
7. Périgo, E. A.; Hemery, G.; Sandre, O.; Ortega, D.; Garaio, E.; Plazaola, F.; Teran, F. J. *Appl. Phys. Rev.* **2015,** *2,* 041302. doi:10.1063/1.4935688
8. Leung, K. C.-F.; Xuan, S.; Zhu, X.; Wang, D.; Chak, C.-P.; Lee, S.-F.; Ho, W. K.-W.; Chung, B. C.-T. *Chem. Soc. Rev.* **2012,** *41,* 1911–1928. doi:10.1039/C1CS15213K
9. Pu, F.; Salarian, M.; Xue, S.; Qiao, J.; Feng, J.; Tan, S.; Patel, A.; Li, X.; Mamouni, K.; Hekmatyar, K.; Zou, J.; Wu, D.; Yang, J. J. *Nanoscale* **2016,** *8,* 12668–12682. doi:10.1039/C5NR09071G
10. Tomitaka, A.; Arami, H.; Raymond, A.; Yndart, A.; Kaushik, A.; Jayant, R. D.; Takemura, Y.; Cai, Y.; Toborek, M.; Nair, M. *Nanoscale* **2017,** *9,* 764–773. doi:10.1039/C6NR07520G
11. Khandhar, A. P.; Ferguson, R. M.; Arami, H.; Krishnan, K. M. *Biomaterials* **2013,** *34,* 3837–3845. doi:10.1016/j.biomaterials.2013.01.087
12. Yu, E. Y.; Bishop, M.; Zheng, B.; Ferguson, R. M.; Khandhar, A. P.; Kemp, S. J.; Krishnan, K. M.; Goodwill, P. W.; Conolly, S. M. *Nano Lett.* **2017,** *17,* 1648–1654. doi:10.1021/acs.nanolett.6b04865
13. Lee, J.-H.; Lee, K.; Moon, S. H.; Lee, Y.; Park, T. G.; Cheon, J. *Angew. Chem., Int. Ed.* **2009,** *48,* 4174–4179. doi:10.1002/anie.200805998
14. Ulbrich, K.; Holá, K.; Šubr, V.; Bakandritsos, A.; Tuček, J.; Zbořil, R. *Chem. Rev.* **2016,** *116,* 5338–5431. doi:10.1021/acs.chemrev.5b00589
15. Fernandes Cardoso, V.; Francesko, A.; Ribeiro, C.; Bañobre-López, M.; Martins, P.; Lanceros-Mendez, S. *Adv. Healthcare Mater.* **2018,** *7,* 1700845. doi:10.1002/adhm.201700845
16. De Crozals, G.; Bonnet, R.; Farre, C.; Chaix, C. *Nano Today* **2016,** *11,* 435–463. doi:10.1016/j.nantod.2016.07.002
17. Mosayebi, J.; Kiyasatfar, M.; Laurent, S. *Adv. Healthcare Mater.* **2017,** *6,* 1700306. doi:10.1002/adhm.201700306
18. Wiedwald, U.; Ziemann, P. *Beilstein J. Nanotechnol.* **2010,** *1,* 21–23. doi:10.3762/bjnano.1.4
19. Guardia, P.; Labarta, A.; Batlle, X. *J. Phys. Chem. C* **2011,** *115,* 390–396. doi:10.1021/jp1084982
20. Baaziz, W.; Pichon, B. P.; Fleutot, S.; Liu, Y.; Lefevre, C.; Greneche, J.-M.; Toumi, M.; Mhiri, T.; Begin-Colin, S. *J. Phys. Chem. C* **2014,** *118,* 3795–3810. doi:10.1021/jp411481p
21. Brollo, M. E. F.; López-Ruiz, R.; Muraca, D.; Figueroa, S. J. A.; Pirota, K. R.; Knobel, M. *Sci. Rep.* **2014,** *4,* 6839. doi:10.1038/srep06839
22. Pineider, F.; de Julián Fernández, C.; Videtta, V.; Carlino, E.; al Hourani, A.; Wilhelm, F.; Rogalev, A.; Cozzoli, P. D.; Ghigna, P.; Sangregorio, C. *ACS Nano* **2013,** *7,* 857–866. doi:10.1021/nn305459m
23. Thi Thuy, N.; Mammeri, F.; Ammar, S. *Nanomaterials* **2018,** *8,* 149. doi:10.3390/nano8030149
24. Fazal, S.; Paul-Prasanth, B.; Nair, S. V.; Menon, D. *ACS Appl. Mater. Interfaces* **2017,** *9,* 28260–28272. doi:10.1021/acsami.7b08939
25. Schick, I.; Lorenz, S.; Gehrig, D.; Tenzer, S.; Storck, W.; Fischer, K.; Strand, D.; Laquai, F.; Tremel, W. *Beilstein J. Nanotechnol.* **2014,** *5,* 2346–2362. doi:10.3762/bjnano.5.244
26. Efremova, M. V.; Veselov, M. M.; Barulin, A. V.; Gribanovsky, S. L.; Le-Deygen, I. M.; Uporov, I. V.; Kudryashova, E. V.; Sokolsky-Papkov, M.; Majouga, A. G.; Golovin, Y. I.; Kabanov, A. V.; Klyachko, N. L. *ACS Nano* **2018,** *12,* 3190–3199. doi:10.1021/acsnano.7b06439
27. Rudakovskaya, P. G.; Lebedev, D. N.; Efremova, M. V.; Beloglazkina, E. K.; Zyk, N. V.; Klyachko, N. L.; Golovin, Y. I.; Savchenko, A. G.; Mazhuga, A. G. *Nanotechnol. Russ.* **2016,** *11,* 144–152. doi:10.1134/S1995078016020166
28. Angelakeris, M. *Biochim. Biophys. Acta, Gen. Subj.* **2017,** *1861,* 1642–1651. doi:10.1016/j.bbagen.2017.02.022
29. Liu, S.; Guo, S. J.; Sun, S.; You, X.-Z. *Nanoscale* **2015,** *7,* 4890–4893. doi:10.1039/C5NR00135H
30. Zhai, Y.; Jin, L.; Wang, P.; Dong, S. *Chem. Commun.* **2011,** *47,* 8268–8270. doi:10.1039/c1cc13149d
31. Salikhov, S. V.; Savchenko, A. G.; Grebennikov, I. S.; Yurtov, E. V. *Bull. Russ. Acad. Sci.: Phys.* **2015,** *79,* 1106–1112. doi:10.3103/S1062873815090166
32. Wang, C.; Yin, H.; Dai, S.; Sun, S. *Chem. Mater.* **2010,** *22,* 3277–3282. doi:10.1021/cm100603r
33. Sorenson, T. A.; Morton, S. A.; Waddill, G. D.; Switzer, J. A. *J. Am. Chem. Soc.* **2002,** *124,* 7604–7609. doi:10.1021/ja0201101
34. Verwey, E. J. W. *Nature* **1939,** *144,* 327–328. doi:10.1038/144327b0
35. Aragón, R. *Phys. Rev. B* **1992,** *46,* 5328–5333. doi:10.1103/PhysRevB.46.5328

36. Salazar, J. S.; Perez, L.; de Abril, O.; Lai Truong, P.; Ihiawakrim, D.; Vazquez, M.; Greneche, J.-M.; Begin-Colin, S.; Pourroy, G. *Chem. Mater.* **2011,** *23,* 1379–1386. doi:10.1021/cm103188a
37. Andrés Vergés, M.; Costo, R.; Roca, A. G.; Marco, J. F.; Goya, G. F.; Serna, C. J.; Morales, M. P. *J. Phys. D: Appl. Phys.* **2008,** *41,* 134003. doi:10.1088/0022-3727/41/13/134003
38. Witt, A.; Fabian, K.; Bleil, U. *Earth Planet. Sci. Lett.* **2005,** *233,* 311–324. doi:10.1016/j.epsl.2005.01.043
39. Fabian, K.; Kirchner, A.; Williams, W.; Heider, F.; Leibl, T.; Hubert, A. *Geophys. J. Int.* **1996,** *124,* 89–104. doi:10.1111/j.1365-246X.1996.tb06354.x
40. Goya, G. F.; Berquó, T. S.; Fonseca, F. C.; Morales, M. P. *J. Appl. Phys.* **2003,** *94,* 3520–3528. doi:10.1063/1.1599959
41. Park, J.; Lee, E.; Hwang, N.-M.; Kang, M.; Kim, S. C.; Hwang, Y.; Park, J.-G.; Noh, H. J.; Kini, J. Y.; Park, J. H.; Hyeon, T. *Angew. Chem., Int. Ed.* **2005,** *44,* 2872–2877. doi:10.1002/anie.200461665
42. Omelyanchik, A.; Levada, E.; Ding, J.; Lendinez, S.; Pearson, J.; Efremova, M.; Bessalova, V.; Karpenkov, D.; Semenova, E.; Khlusov, I.; Litvinova, L.; Abakumov, M.; Majouga, A.; Perov, N.; Novosad, V.; Rodionova, V. *IEEE Trans. Magn.* **2018,** *54,* 1–5. doi:10.1109/TMAG.2018.2819823
43. Demortiére, A.; Panissod, P.; Pichon, B. P.; Pourroy, G.; Guillon, D.; Donnio, B.; Bégin-Colin, S. *Nanoscale* **2011,** *3,* 225–232. doi:10.1039/C0NR00521E
44. Töpfer, J.; Angermann, A. *Mater. Chem. Phys.* **2011,** *129,* 337–342. doi:10.1016/j.matchemphys.2011.04.025
45. Wang, J.; Peng, Z.; Huang, Y.; Chen, Q. *J. Cryst. Growth* **2004,** *263,* 616–619. doi:10.1016/j.jcrysgro.2003.11.102
46. Berkowitz, A. E.; Schuele, W. J.; Flanders, P. J. *J. Appl. Phys.* **1968,** *39,* 1261. doi:10.1063/1.1656256
47. Sharrock, M. P. *J. Appl. Phys.* **1994,** *76,* 6413–6418. doi:10.1063/1.358282
48. Kuerbanjiang, B.; Wiedwald, U.; Haering, F.; Biskupek, J.; Kaiser, U.; Ziemann, P.; Herr, U. *Nanotechnology* **2013,** *24,* 455702. doi:10.1088/0957-4484/24/45/455702
49. Liébana-Viñas, S.; Wiedwald, U.; Elsukova, A.; Perl, J.; Zingsem, B.; Semisalova, A. S.; Salgueiriño, V.; Spasova, M.; Farle, M. *Chem. Mater.* **2015,** *27,* 4015–4022. doi:10.1021/acs.chemmater.5b00976
50. Wiedwald, U.; Han, L.; Biskupek, J.; Kaiser, U.; Ziemann, P. *Beilstein J. Nanotechnol.* **2010,** *1,* 24–47. doi:10.3762/bjnano.1.5
51. Massner, C.; Sigmund, F.; Pettinger, S.; Seeger, M.; Hartmann, C.; Ivleva, N. P.; Niessner, R.; Fuchs, H.; Hrabě de Angelis, M.; Stelzl, A.; Koonakampully, N. L.; Rolbieski, H.; Wiedwald, U.; Spasova, M.; Wurst, W.; Ntziachristos, V.; Winklhofer, M.; Westmeyer, G. G. *Adv. Funct. Mater.* **2018,** *28,* 1706793. doi:10.1002/adfm.201706793
52. Martínez, B.; Roig, A.; Obradors, X.; Molins, E.; Rouanet, A.; Monty, C. *J. Appl. Phys.* **1996,** *79,* 2580–2586. doi:10.1063/1.361125
53. Craik, D. J. *Magnetic Oxides;* Wiley & Sons: London, 1975.
54. Winklhofer, M.; Fabian, K.; Heider, F. *J. Geophys. Res.: Solid Earth* **1997,** *102,* 22695–22709. doi:10.1029/97JB01730
55. Liébana-Viñas, S.; Simeonidis, K.; Wiedwald, U.; Li, Z.-A.; Ma, Z.; Myrovali, E.; Makridis, A.; Sakellari, D.; Vourlias, G.; Spasova, M.; Farle, M.; Angelakeris, M. *RSC Adv.* **2016,** *6,* 72918–72925. doi:10.1039/C6RA17892H
56. Shao, H.; Yoon, T.-J.; Liong, M.; Weissleder, R.; Lee, H. *Beilstein J. Nanotechnol.* **2010,** *1,* 142–154. doi:10.3762/bjnano.1.17
57. Ni, D. L.; Bu, W. B.; Ehlerding, E. B.; Cai, W. B.; Shi, J. L. *Chem. Soc. Rev.* **2017,** *46,* 7438–7468. doi:10.1039/C7CS00316A
58. Lee, N.; Hyeon, T. *Chem. Soc. Rev.* **2012,** *41,* 2575–2589. doi:10.1039/C1CS15248C
59. Blanco-Andujar, C.; Walter, A.; Cotin, G.; Bordeianu, C.; Mertz, D.; Felder-Flesch, D.; Begin-Colin, S. *Nanomedicine (London, U. K.)* **2016,** *11,* 1889–1910. doi:10.2217/nnm-2016-5001
60. Laurent, S.; Forge, D.; Port, M.; Roch, A.; Robic, C.; Elst, L. V.; Muller, R. N. *Chem. Rev.* **2008,** *108,* 2064–2110. doi:10.1021/cr068445e
61. Poeselt, E.; Kloust, H.; Tromsdorf, U.; Janschel, M.; Hahn, C.; Masslo, C.; Weller, H. *ACS Nano* **2012,** *6,* 1619–1624. doi:10.1021/nn204591r
62. Jun, Y. W.; Huh, Y. M.; Choi, J. S.; Lee, J. H.; Song, H. T.; Kim, S.; Yoon, S.; Kim, K. S.; Shin, J. S.; Suh, J. S.; Cheon, J. *J. Am. Chem. Soc.* **2005,** *127,* 5732–5733. doi:10.1021/ja0422155
63. Paquet, C.; de Haan, H. W.; Leek, D. M.; Lin, H.-Y.; Xiang, B.; Tian, G.; Kell, A.; Simard, B. *ACS Nano* **2011,** *5,* 3104–3112. doi:10.1021/nn2002272
64. Huang, J.; Bu, L.; Xie, J.; Chen, K.; Cheng, Z.; Li, X.; Chen, X. *ACS Nano* **2010,** *4,* 7151–7160. doi:10.1021/nn101643u
65. Reguera, J.; Jiménez de Aberasturi,, D.; Henriksen-Lacey, M.; Langer, J.; Espinosa, A.; Szczupak, B.; Wilhelm, C.; Liz-Marzán, L. M. *Nanoscale* **2017,** *9,* 9467–9480. doi:10.1039/C7NR01406F
66. Vuong, Q. L.; Berret, J.-F.; Fresnais, J.; Gossuin, Y.; Sandre, O. *Adv. Healthcare Mater.* **2012,** *1,* 502–512. doi:10.1002/adhm.201200078
67. de la Presa, P.; Luengo, Y.; Multigner, M.; Costo, R.; Morales, M. P.; Rivero, G.; Hernando, A. *J. Phys. Chem. C* **2012,** *116,* 25602–25610. doi:10.1021/jp310771p
68. Chen, Z.-J.; Broaddus, W. C.; Viswanathan, R. R.; Raghavan, R.; Gillies, G. T. *IEEE Trans. Biomed. Eng.* **2002,** *49,* 85–96. doi:10.1109/10.979348
69. Salloum, M.; Ma, R. H.; Weeks, D.; Zhu, L. *Int. J. Hyperthermia* **2008,** *24,* 337–345. doi:10.1080/02656730801907937
70. Kim, D.; Yu, M. K.; Lee, T. S.; Park, J. J.; Jeong, Y. Y.; Jon, S. *Nanotechnology* **2011,** *22,* 155101. doi:10.1088/0957-4484/22/15/155101
71. Li, W.; Tutton, S.; Vu, A. T.; Pierchala, L.; Li, B. S. Y.; Lewis, J. M.; Prasad, P. V.; Edelman, R. R. *J. Magn. Reson. Imaging* **2005,** *21,* 46–52. doi:10.1002/jmri.20235
72. Choi, D.; Han, A.; Park, J. P.; Kim, J. K.; Lee, J. H.; Kim, T. H.; Kim, S.-W. *Small* **2009,** *5,* 571–573. doi:10.1002/smll.200801258
73. Hwang, L. P.; Freed, J. H. *J. Chem. Phys.* **1975,** *63,* 4017–4025. doi:10.1063/1.431841
74. Joshi, H. M.; Lin, Y. P.; Aslam, M.; Prasad, P. V.; Schultz-Sikma, E. A.; Edelman, R.; Meade, T.; Dravid, V. P. *J. Phys. Chem. C* **2009,** *113,* 17761–17767. doi:10.1021/jp905776g
75. Smolensky, E. D.; Park, H.-Y. E.; Zhou, Y.; Rolla, G. A.; Marjańska, M.; Botta, M.; Pierre, V. C. *J. Mater. Chem. B* **2013,** *1,* 2818–2828. doi:10.1039/c3tb00369h
76. Lee, N.; Choi, Y.; Lee, Y.; Park, M.; Moon, W. K.; Choi, S. H.; Hyeon, T. *Nano Lett.* **2012,** *12,* 3127–3131. doi:10.1021/nl3010308
77. Zhao, Z.; Zhou, Z.; Bao, J.; Wang, Z.; Hu, J.; Chi, X.; Ni, K.; Wang, R.; Chen, X.; Chen, Z.; Gao, J. *Nat. Commun.* **2013,** *4,* 2266. doi:10.1038/ncomms3266
78. Zhou, Z.; Zhao, Z.; Zhang, H.; Wang, Z.; Chen, X.; Wang, R.; Chen, Z.; Gao, J. *ACS Nano* **2014,** *8,* 7976–7985. doi:10.1021/nn5038652
79. Bakoglidis, K. D.; Simeonidis, K.; Sakellari, D.; Stefanou, G.; Angelakeris, M. *IEEE Trans. Magn.* **2012,** *48,* 1320–1323. doi:10.1109/TMAG.2011.2173474

80. Hergt, R.; Hiergeist, R.; Zeisberger, M.; Schüler, D.; Heyen, U.; Hilger, I.; Kaiser, W. A. *J. Magn. Magn. Mater.* **2005,** *293,* 80–86. doi:10.1016/j.jmmm.2005.01.047
81. Di Corato, R.; Espinosa, A.; Lartigue, L.; Tharaud, M.; Chat, S.; Pellegrino, T.; Ménager, C.; Gazeau, F.; Wilhelm, C. *Biomaterials* **2014,** *35,* 6400–6411. doi:10.1016/j.biomaterials.2014.04.036
82. Guardia, P.; Nitti, S.; Materia, M. E.; Pugliese, G.; Yaacoub, N.; Greneche, J.-M.; Lefevre, C.; Manna, L.; Pellegrino, T. *J. Mater. Chem. B* **2017,** *5,* 4587–4594. doi:10.1039/C7TB00968B
83. Simeonidis, K.; Martinez-Boubeta, C.; Balcells, L.; Monty, C.; Stavropoulos, G.; Mitrakas, M.; Matsakidou, A.; Vourlias, G.; Angelakeris, M. *J. Appl. Phys.* **2013,** *114,* 103904. doi:10.1063/1.4821020
84. Efremova, M. V.; Naumenko, V. A.; Spasova, M.; Garanina, A. S.; Abakumov, M. A.; Blokhina, A. D.; Melnikov, P. A.; Prelovskaya, A. O.; Heidelmann, M.; Li, Z.-A.; Ma, Z.; Shchetinin, I. V.; Golovin, Y. I.; Kireev, I. I.; Savchenko, A. G.; Chekhonin, V. P.; Klyachko, N. L.; Farle, M.; Majouga, A. G.; Wiedwald, U. *Sci. Rep.* **2018,** *8,* 11295. doi:10.1038/s41598-018-29618-w
85. Xu, C.; Xie, J.; Ho, D.; Wang, C.; Kohler, N.; Walsh, E. G.; Morgan, J. R.; Chin, Y. E.; Sun, S. *Angew. Chem., Int. Ed.* **2008,** *47,* 173–176. doi:10.1002/anie.200704392
86. Simon, H. U.; Haj-Yehia, A.; Levi-Schaffer, F. *Apoptosis* **2000,** *5,* 415–418. doi:10.1023/A:1009616228304
87. Circu, M. L.; Aw, T. Y. *Free Radical Biol. Med.* **2010,** *48,* 749–762. doi:10.1016/j.freeradbiomed.2009.12.022
88. Erofeev, A.; Gorelkin, P.; Garanina, A.; Alova, A.; Efremova, M.; Vorobyeva, N.; Edwards, C.; Korchev, Y.; Majouga, A. *Sci. Rep.* **2018,** *8,* 7462. doi:10.1038/s41598-018-25852-4
89. Soenen, S. J.; Rivera-Gil, P.; Montenegro, J.-M.; Parak, W. J.; De Smedt, S. C.; Braeckmans, K. *Nano Today* **2011,** *6,* 446–465. doi:10.1016/j.nantod.2011.08.001
90. Sadhukha, T.; Wiedmann, T. S.; Panyam, J. *Biomaterials* **2014,** *35,* 7860–7869. doi:10.1016/j.biomaterials.2014.05.085
91. Guardia, P.; Di Corato, R.; Lartigue, L.; Wilhelm, C.; Espinosa, A.; Garcia-Hernandez, M.; Gazeau, F.; Manna, L.; Pellegrino, T. *ACS Nano* **2012,** *6,* 3080–3091. doi:10.1021/nn2048137
92. Asín, L.; Ibarra, M. R.; Tres, A.; Goya, G. F. *Pharm. Res.* **2012,** *29,* 1319–1327. doi:10.1007/s11095-012-0710-z
93. Sanchez, C.; El Hajj Diab, D.; Connord, V.; Clerc, P.; Meunier, E.; Pipy, B.; Payré, B.; Tan, R. P.; Gougeon, M.; Carrey, J.; Gigoux, V.; Fourmy, D. *ACS Nano* **2014,** *8,* 1350–1363. doi:10.1021/nn404954s
94. Oh, Y.; Lee, N.; Kang, H. W.; Oh, J. *Nanotechnology* **2016,** *27,* 115101. doi:10.1088/0957-4484/27/11/115101
95. Estevanato, L. L. C.; Da Silva, J. R.; Falqueiro, A. M.; Mosiniewicz-Szablewska, E.; Suchocki, P.; Tedesco, A. C.; Morais, P. C.; Lacava, Z. G. M. *Int. J. Nanomed.* **2012,** *7,* 5287–5299. doi:10.2147/ijn.s35279
96. Sasikala, A. R. K.; Unnithan, A. R.; Park, C. H.; Kim, C. S. *J. Mater. Chem. B* **2016,** *4,* 785–792. doi:10.1039/C5TB02011E
97. Liu, X. O.; Atwater, M.; Wang, J. H.; Huo, Q. *Colloids Surf., B* **2007,** *58,* 3–7. doi:10.1016/j.colsurfb.2006.08.005
98. Yu, H.; Chen, M.; Rice, P. M.; Wang, S. X.; White, R. L.; Sun, S. H. *Nano Lett.* **2005,** *5,* 379–382. doi:10.1021/nl047955q
99. Wei, Y.; Klajn, R.; Pinchuk, A. O.; Grzybowski, B. A. *Small* **2008,** *4,* 1635–1639. doi:10.1002/smll.200800511
100. Jin, Y.; Jia, C.; Huang, S.-W.; O'Donnell, M.; Gao, X. H. *Nat. Commun.* **2010,** *1,* 41. doi:10.1038/ncomms1042

License and Terms

BEILSTEIN JOURNAL OF NANOTECHNOLOGY

Magnetic and luminescent coordination networks based on imidazolium salts and lanthanides for sensitive ratiometric thermometry

Pierre Farger[1,§], Cédric Leuvrey[1], Mathieu Gallart[1], Pierre Gilliot[1], Guillaume Rogez[1], João Rocha[2], Duarte Ananias[2], Pierre Rabu[*1] and Emilie Delahaye[*1]

Full Research Paper

Open Access

Address:
[1]Institut de Physique et Chimie des Matériaux de Strasbourg, Université de Strasbourg, CNRS UMR 7504, F-67034 Strasbourg Cedex 2, France and [2]Department of Chemistry, CICECO, University of Aveiro, 3810-193 Aveiro, Portugal

Email:
Pierre Rabu[*] - pierre.rabu@ipcms.unistra.fr; Emilie Delahaye[*] - emilie.delahaye@ipcms.unistra.fr

* Corresponding author
§ Current address: Laboratoire de Physique et Chimie des Nano-Objets, Institut National des Sciences Appliquées, 135 avenue de Rangueil, 31077 Toulouse Cedex 4, France

Keywords:
coordination network; imidazolium salt; lanthanides; magnetism; thermometry

Beilstein J. Nanotechnol. **2018,** *9,* 2775–2787.
doi:10.3762/bjnano.9.259

Received: 15 August 2018
Accepted: 11 October 2018
Published: 30 October 2018

This article is part of the thematic issue "Advanced hybrid nanomaterials".

Associate Editor: S. A. Claridge

Abstract

The synthesis and characterization of six new lanthanide networks [Ln(L)(ox)(H_2O)] with Ln = Eu^{3+}, Gd^{3+}, Tb^{3+}, Dy^{3+}, Ho^{3+} and Yb^{3+} is reported. They were synthesized by solvo-ionothermal reaction of lanthanide nitrate $Ln(NO_3)_3{\cdot}xH_2O$ with the 1,3-bis(carboxymethyl)imidazolium [HL] ligand and oxalic acid (H_2ox) in a water/ethanol solution. The crystal structure of these compounds has been solved on single crystals and the magnetic and luminescent properties have been investigated relying on intrinsic properties of the lanthanide ions. The synthetic strategy has been extended to mixed lanthanide networks leading to four isostructural networks of formula [$Tb_{1-x}Eu_x$(L)(ox)(H_2O)] with x = 0.01, 0.03, 0.05 and 0.10. These materials were assessed as luminescent ratiometric thermometers based on the emission intensities of ligand, Tb^{3+} and Eu^{3+}. The best sensitivities were obtained using the ratio between the emission intensities of Eu^{3+} ($^5D_0 \rightarrow {}^7F_2$ transition) and of the ligand as the thermometric parameter. [$Tb_{0.97}Eu_{0.03}$(L)(ox)(H_2O)] was found to be one of the best thermometers among lanthanide-bearing coordination polymers and metal-organic frameworks, operative in the physiological range with a maximum sensitivity of 1.38%·K^{-1} at 340 K.

Introduction

Metal-organic coordination networks have been the subject of considerable research in the last years as evidenced by the increasing number of papers published in the field [1]. Indeed, the possibility of combining different properties by judicious choice of the organic and inorganic moieties makes these systems good candidates for the elaboration of (multi)functional architectures

[2,3]. Among the various functionalities that can be envisioned for this class of hybrid compounds, the elaboration of luminescent networks is interesting in term of potential applications in lighting, display, sensing, biomedicine and for optical devices [4-12].

Luminescent coordination networks can be obtained either by the use of specific luminescent organic ligands or by the use of main-group elements, d^{10} transition metals or of trivalent lanthanide ions for the inorganic moiety [13,14]. The luminescent properties of the trivalent lanthanide ions are particularly interesting since they cover a large range of emission from the ultraviolet (Gd^{3+}) to near-infrared (Pr^{3+}, Nd^{3+}, Ho^{3+}, Er^{3+}, Yb^{3+}) through the visible domain (Pr^{3+}, Sm^{3+}, Eu^{3+}, Tb^{3+}, Dy^{3+}, Tm^{3+}). It confers to lanthanide-based networks a large tunability of emission properties, which is very useful for the elaboration of light-emitting devices or for biomedical applications [15]. Moreover, due to the narrowness and the hypersensitivity of their transitions, lanthanide-based networks can also find utility for the sensing of gases, vapors or small molecules [9,16]. In the case of mixed lanthanide coordination networks, the luminescent properties can be used to synthesize temperature probes with possible applications in the aerospace area, safety and health [17,18].

Beside luminescent properties, lanthanide ions exhibit large magnetic moment and strong magnetic anisotropy, which might have potential applications of lanthanide-based networks in information storage, quantum computing and spintronics [19-23].

Most of these lanthanide-based networks are obtained with neutral organic ligands such as benzene-1,4-dicarboxylate (1,4-bdc) [24], benzene-1,3,5-tricarboxylate (TMA) [25], pyridine-2,5-dicarboxylate (2,5-H_2pdc) [24] or 1*H*-2-propyl-4,5-imidazoledicarboxylate (pimda) [26]. Only few examples of lanthanide-based networks obtained with charged ligands are reported in the literature [27-30]. Following this last point, we have chosen to synthesize lanthanide-based networks from positively charged imidazolium dicarboxylate salts [31-34]. Contrarily to the classical imidazolium salts or ionic liquids used in ionothermal syntheses [35-40], the functionalization of imidazolium moieties with coordinating functions reduces the influence of the imidazolium salt on the ligand for a better rationalization of the synthesis [31-34].

We report in this paper the synthesis and the characterization of six new networks obtained from an imidazolium dicarboxylate salt, oxalic acid and lanthanide ions. The structure of these networks has been solved by single crystal X-ray diffraction and their physical properties (magnetism and luminescence) have been investigated. We establish that these networks show antiferromagnetic interactions. The study of the luminescent properties evidences the presence of well-defined transitions characteristic for the considered lanthanide. These results have prompted us to extend our strategy to the synthesis of mixed lanthanide networks with four different ratios Tb^{3+}/Eu^{3+}. The powder X-ray diffraction analysis indicates that these mixed lanthanide networks are isostructural to the parent homolanthanide compounds. The temperature-resolved photo-luminescent properties of the latter indicate possible applications in thermometry.

Results and Discussion

Synthesis

The 1,3-bis(carboxymethyl-)-imidazolium ligand [HL] was synthesized according to protocols published in the literature [41,42].

Single crystals and homogeneous powders of [Ln(L)(ox)(H_2O)] were obtained with Ln = Eu^{3+}, Gd^{3+}, Tb^{3+}, Dy^{3+}, Ho^{3+} and Yb^{3+} by reacting a water/ethanol solution of the lanthanide nitrate and oxalic acid (H_2ox) with [HL]. The mixture was sealed in a Teflon-lined stainless steel autoclave and heated at 393 K for 72 h. After cooling to room temperature, the autoclaves were opened and crystals were filtered and washed with ethanol. The yields of the reactions range from 36 to 59 %. Similar reactions were carried out with Nd^{3+} and Sm^{3+} ions leading to different structures [31]. In addition, in the case of Nd^{3+} and Sm^{3+}, various crystalline compounds were obtained depending on whether oxalic acid was added or not. When oxalic acid was not added in situ formation of the oxalate ligand has been observed. The peculiar behavior of these two ions compared to others can be explained by their place in the first part of the lanthanide series [43]. In the case of Eu^{3+}, Gd^{3+}, Tb^{3+}, Dy^{3+}, Ho^{3+} and Yb^{3+}, described in the present work, the direct reaction between lanthanide nitrate and [HL], without addition of oxalic acid, did not give crystalline compounds.

Characterization of the homolanthanide [Ln(L)(ox)(H_2O)] compounds with Ln = Eu^{3+}, Gd^{3+}, Tb^{3+}, Dy^{3+}, Ho^{3+} and Yb^{3+}

Single crystal X-ray analysis of the [Ln(L)(ox)(H_2O)] compounds with Ln = Eu^{3+}, Gd^{3+}, Tb^{3+}, Dy^{3+}, Ho^{3+} and Yb^{3+} reveal that the six compounds are isostructural. All compounds are obtained as colorless crystals and crystallize in the monoclinic space group $P2_1/a$ (no. 14). Crystal data for these series of compounds are collected in Table 1 and Table 2.

The asymmetric unit contains one Ln^{3+} ion, one $[L]^-$ ligand, two half-oxalate ligands and one coordinating water molecule (Figure 1). Ln^{3+} ions are surrounded by nine oxygens with four

Table 1: Crystallographic data for [Ln(L)(ox)(H_2O)] compounds with Ln = Eu^{3+}, Gd^{3+} and Tb^{3+}.[a]

	[Eu(L)(ox)(H_2O)]	[Gd(L)(ox)(H_2O)]	[Tb(L)(ox)(H_2O)]
chemical formula	$C_9H_9N_2O_9Eu$	$C_9H_9N_2O_9Gd$	$C_9H_9N_2O_9Tb$
molar mass [g·mol^{-1}]	441.14	446.43	448.10
crystal system	monoclinic	monoclinic	monoclinic
space group	$P2_1/a$	$P2_1/a$	$P2_1/a$
a [Å]	9.212(3)	9.224(4)	9.246(3)
b [Å]	13.228(4)	13.226(4)	13.219(9)
c [Å]	10.9893(17)	10.950(2)	10.904(3)
α [°]	90	90	90
β [°]	111.491(18)	111.48(2)	111.63(2)
γ [°]	90	90	90
Z	4	4	4
T [K]	293(2)	293(2)	293(2)
μ (Mo Kα) [mm^{-1}]	5.044	5.366	5.716
reflection collected	11538	6602	14582
independent reflections	2854	2825	2840
data/restraints/parameters	2854/3/196	2825/3/196	2840/3/196
R1, wR2 [$I > 2\sigma(I)$]	0.0358, 0.0690	0.0268, 0.0458	0.0427, 0.0769
R1, wR2 [all data]	0.0579, 0.0770	0.0430, 0.0501	0.0627, 0.0850
GOOF	1.063	1.092	1.094
largest diff. peak and hole (e·Å^{-3})	1.297, −1.365	0.681, −0.689	1.868, −1.838

[a]The relatively high values of the residual density can be explained by the difficulty to isolate single crystals. Indeed SEM images reveal the presence of relatively small and entangled crystals (see Figure S3, Supporting Information File 1).

Table 2: Crystallographic data for [Ln(L)(ox)(H_2O)] compounds with Ln = Dy^{3+}, Ho^{3+} and Yb^{3+}.[a]

	[Dy(L)(ox)(H_2O)]	[Ho(L)(ox)(H_2O)]	[Yb(L)(ox)(H_2O)]
chemical formula	$C_9H_9N_2O_9Dy$	$C_9H_9N_2O_9Ho$	$C_9H_9N_2O_9Yb$
molar mass [g·mol^{-1}]	451.68	454.11	462.22
crystal system	monoclinic	monoclinic	monoclinic
space group	$P2_1/a$	$P2_1/a$	$P2_1/a$
a [Å]	9.191(4)	9.228(10)	9.193(2)
b [Å]	13.188(4)	13.185(4)	13.097(3)
c [Å]	10.85(5)	10.862(8)	10.721(5)
α [°]	90	90	90
β [°]	111.63(3)	111.95(6)	112.19(3)
γ [°]	90	90	90
Z	4	4	4
T [K]	293(2)	293(2)	293(2)
μ (Mo Kα) [mm^{-1}]	6.137	6.479	7.843
reflection collected	13140	13992	7321
independent reflections	2802	2814	2735
data/restraints/parameters	2802/3/196	2814/3/196	2735/3/196
R1, wR2 [$I > 2\sigma(I)$]	0.0336, 0.0573	0.0494, 0.0751	0.0516, 0.1119
R1, wR2 [all data]	0.0517, 0.0624	0.0854, 0.0840	0.0914, 0.1319
GOOF	1.122	1.133	1.031
largest diff. peak and hole (e·Å^{-3})	0.742, −1.382	1.164, −1.034	2.751, −2.662

[a]The relatively high values of the residual density can be explained by the difficulty to isolate single crystals. Indeed SEM images reveal the presence of relatively small and entangled crystals (see Figure S3, Supporting Information File 1).

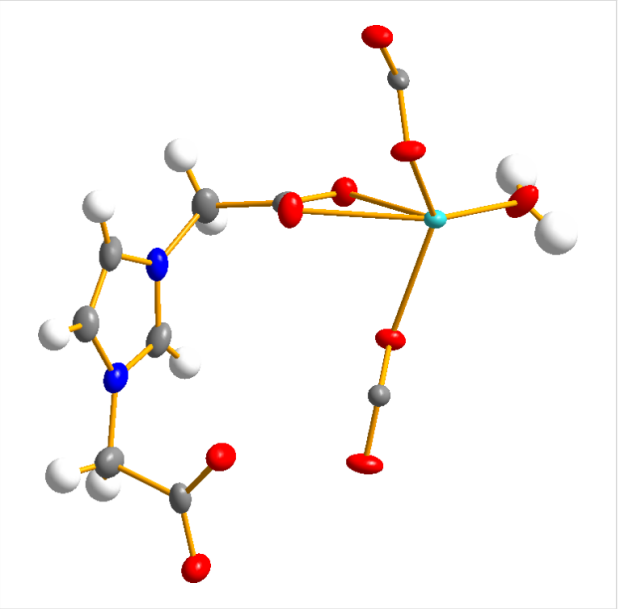

Figure 1: Ellipsoid view of the asymmetric unit of [Gd(L)(ox)(H_2O)] (Gd in green, C in grey, O in red, N in blue and H in white).

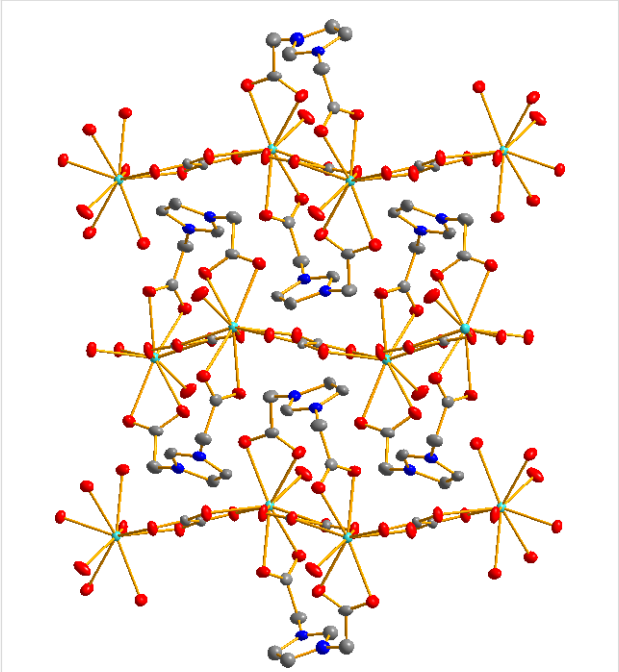

Figure 2: Selected packing view of the crystal structure of [Gd(L)(ox)(H_2O)] along the c-axis (Gd in green, C in grey, O in red, N in blue). H atoms have been omitted for clarity.

oxygen atoms coming from one and same carboxylate function of two different $[L]^-$ ligands, one from the water molecule and four from two different oxalate ligands. The coordination environment of Ln^{3+} ions is a tricapped trigonal prism (Figure S1, Supporting Information File 1) with Ln–O distances similar to those observed in structurally related compounds [44,45]. These distances decrease progressively with the size of the lanthanide ion in agreement with the lanthanide contraction effect (Table S1, Supporting Information File 1). The same tendency is observed with the shortest Ln–Ln distances, which correspond to two Ln^{3+} ions connected by an oxalate ligand (Table S1, Supporting Information File 1).

Two separate Ln^{3+} ions are connected through an oxalate ligand in a bis-bidentate bridging coordination mode forming undulating chains along the *a*-axis (Figure 2). The Ln^{3+} ions are connected to the carboxylate functions of the $[L]^-$ ligand in a bidentate chelate mode. The cohesion between these chains is realized through H bonding between H atoms of the coordinated water molecules and O atoms of the carboxylate functions.

Beside the single crystal analysis, the homogeneity of the six samples was checked by powder X-ray diffraction. As shown in Figure S2 (Supporting Information File 1), the experimental powder patterns fit well with the patterns calculated from the single crystal structure and show no additional phases.

In order to investigate the thermal stability, thermogravimetric analysis (TGA) was realized under air stream from 25 to 900 °C (Figure S4, Supporting Information File 1). The weight loss corresponding to the elimination of the coordinated water molecule occurs between 130 and 310 °C (step 1). The second weight loss between 310 and 750 °C (step 2) is associated to the combustion of the organic moieties (oxalate and $[L]^-$ ligands), concomitant with the formation of oxide (Ln_2O_3 was identified by powder X-ray diffraction in the final product). The total weight loss is in good agreement with the calculated values (Table S2, Supporting Information File 1).

The infrared spectra of the six compounds are similar (Figure S5, Supporting Information File 1). The broad band around 3250 cm^{-1} and the one at 1672 cm^{-1} are ascribed to the coordinated water (stretching and bending vibration modes, respectively). The vibration bands of the aromatic and aliphatic C–H bonds are observed in the range 3150–3050 cm^{-1} and 3050–2950 cm^{-1}, respectively. The characteristic frequencies of the coordinating carboxylate functions are observed at 1627 and 1571 cm^{-1} (antisymmetric vibration bands) and at 1411 and 1431 cm^{-1} (symmetric vibration bands). It leads to $\Delta\nu$ ($\Delta\nu = \nu_{antisym} - \nu_{sym}$) equal to 216 and 140 cm^{-1} in agreement with a bis-bidentate bridging coordination mode of the oxalate ligand and a bidentate chelate coordination mode of the carboxylate functions of the $[L]^-$ ligand, respectively [46,47].

Magnetic properties

The magnetic behavior of the six compounds [Ln(L)(ox)(H_2O)] have been studied in the temperature range of 1.8–300 K under

a 0.5 T dc magnetic field. The magnetic susceptibilities and products χT are presented as functions of the temperature in Figure 3.

At 300 K, the value of χT for the compound [Gd(L)(ox)(H_2O)] is 7.88 emu·K·mol^{-1}, which agrees well with the theoretical value for spin-only $S = 7/2$ Gd^{3+} ions. The χT product remains almost constant above 30 K and then decreases down to 6.7 emu·K·mol^{-1} at 1.8 K. This decrease suggests the occurrence of antiferromagnetic coupling between neighboring gadolinium centers. Since [Gd(L)(ox)(H_2O)] is constituted of linear chains of Gd^{3+} ions with large spin moment, $S = 7/2$, we evaluated the magnetic coupling, J, between neighboring Gd^{3+} ions by using the Fisher expression for classical spin chains [48,49]:

$$\chi = \frac{Ng^2\beta^2 S(S+1)}{3kT} \cdot \frac{1+\coth\left[\frac{JS(S+1)}{kT}\right] - \frac{kT}{JS(S+1)}}{1-\coth\left[\frac{JS(S+1)}{kT}\right] - \frac{kT}{JS(S+1)}}.$$

In the above expression, N is the Avogadro number, g is the Landé factor, β is the Bohr magneton, k is the Boltzmann constant, S is the spin moment, J is the magnetic coupling constant and T is the temperature. The simultaneous fitting of the susceptibility and the χT product with the Fischer expression above lead to refined values of $g = 2.00(1)$ and $J = -0.026$ cm^{-1}. The g value was left free during fitting and is in line with the tabulated g values for Gd ions [50]. The absolute value and the sign of J support the presence of weak antiferromagnetic interactions in [Gd(L)(ox)(H_2O)], in agreement with results reported in previous works [51-53]. The magnetic exchange coupling between lanthanide ions is usually weak, due to limited extension of the 4f orbitals.

For [Eu(L)(ox)(H_2O)], the χT product decreases continuously from 1.4 emu·K·mol^{-1} at 300 K to 0 emu·K·mol^{-1} at 1.8 K. This behavior is typical for Eu^{3+} ions for which the ^7F ground term is split in seven ^7F_J ($0 \le J \le 6$) states because of spin–orbit coupling [54,55]. The spin–orbit coupling constant, λ, can be evaluated considering isotropic isolated Eu^{3+} ions parametrized with the appropriate expression (E1 in Supporting Information File 1) for the isotropic susceptibility of Eu^{3+} ions [54,55].

A very good fit of the experimental susceptibility and the χT product of [Eu(L)(ox)(H_2O)] was obtained above 25 K giving the refined value of λ = 309.00(4) cm^{-1}. This value is consistent with the value determined from the luminescence measurements (see below) and confirms that considering only the isotropic component of the susceptibility is a good approximation to analyze the magnetic data [54].

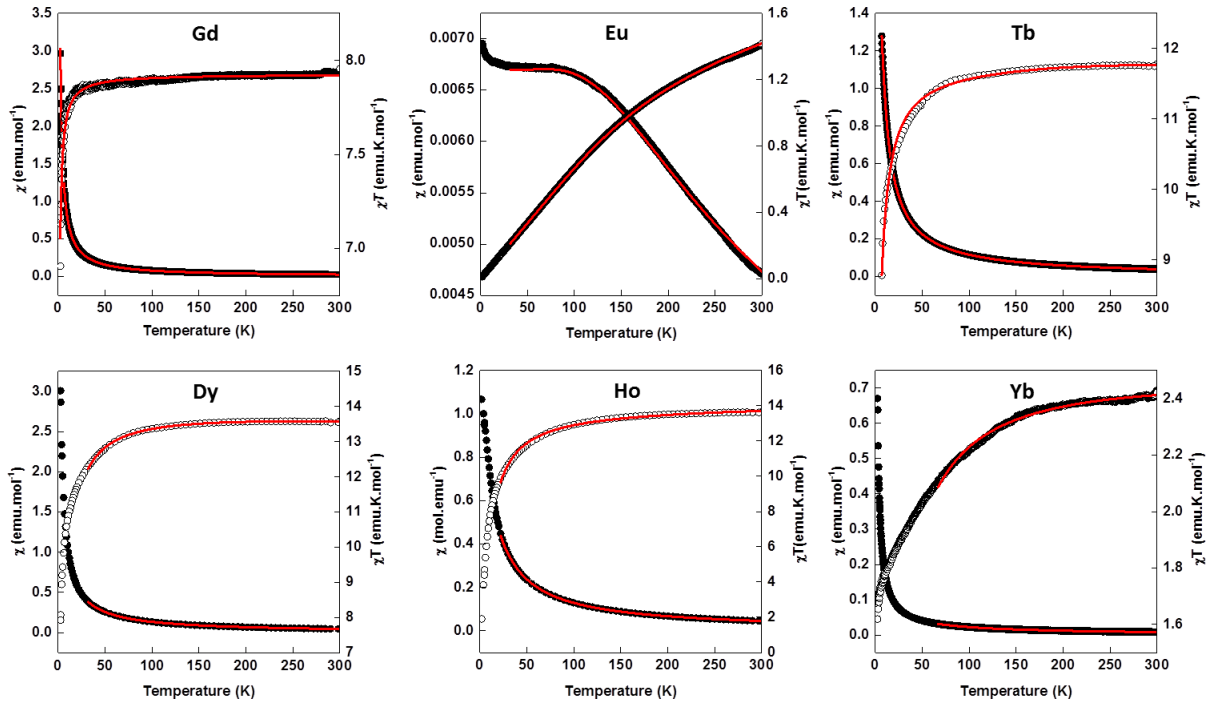

Figure 3: Plots of χ (closed circles) and χT (open circles) as functions of T for [Ln(L)$_2$(ox)(H_2O)] with Ln = Gd^{3+}, Eu^{3+}, Tb^{3+}, Dy^{3+}, Ho^{3+} and Yb^{3+}. The full lines correspond to the fit of the data using the expressions discussed in the text and given in Supporting Information File 1.

The behavior of [Tb(L)(ox)(H_2O)] is also typical for quasi-isolated Tb^{3+} ions with χT = 11.75 emu·K·mol^{-1} at 300 K (expected value: 11.82 emu·K·mol^{-1} with g = 1.5) [48,50]. When decreasing the temperature, the χT product remains constant until 100 K and then decreases to 4.50 emu·K·mol^{-1} at 1.8 K. This decay is due to the depopulation of the low-lying J states arising from the splitting of the ^{7}F ground term under spin–orbit coupling. In order to determine the spin–orbit coupling, λ, it was necessary to take into account an antiferromagnetic interaction between neighboring Tb^{3+} ions using a mean-field approach, in addition to the intrinsic behavior of isolated Tb^{3+} ions (E5 in Supporting Information File 1) [56].

Subsequently, a good fit of the magnetic data was obtained on the whole temperature range with λ = −303(75) cm^{-1} and zJ' = −0.106(1) cm^{-1}. The obtained λ value is consistent with other values reported in the literature for compounds containing isolated Tb^{3+} ions [57,58].

In the case of [Dy(L)(ox)(H_2O)], [Ho(L)(ox)(H_2O)] and [Yb(L)(ox)(H_2O)] the χT values at 300 K are 13.82, 13.61 and 2.48 emu·K·mol^{-1}, in line with the theoretical values for isolated Dy^{3+} ions (14.17 emu·K·mol^{-1} with g = 1.33) [50] Ho^{3+} ions (14.07 emu·K·mol^{-1} with g = 1.25) [50,59], and Yb^{3+} ions (theoretical value of 2.57 emu·K·mol^{-1} with g = 1.14) [48,50]. Upon cooling, the χT product of [Dy(L)(ox)(H_2O)] remains nearly constant until 170 K and then decreases to 9.90 emu·K·mol^{-1} at 1.8 K. For the Ho analogue [Ho(L)(ox)(H_2O)], the χT product decreases slowly between 300 and 100 K, and a steeper decrease is observed from 13.67 emu·K·mol^{-1} at 100 K to 2 emu·K·mol^{-1} at 1.8 K. Finally, for the Yb analogue [Yb(L)(ox)(H_2O)], the χT product decreases slowly as the temperature decreases to reach 1.61 emu·K·mol^{-1} at 1.8 K. This behavior is ascribed to the depopulation of the low lying states (m_J states) arising from the $^6H_{5/2}$ (Dy^{3+}), $^5I_8$ (Ho^{3+}) and $^2F_{7/2}$ (Yb^{3+}), ground states split through the action of the crystal field (for these ions, the ground state is well below the first excited J state). Using the free-ion approach and the isotropic (z) component of the susceptibility, the value of the zero-field splitting (ZFS), Δ, was evaluated for each ion using the expressions E2, E3 and E4 in Supporting Information File 1, leading to Δ = 0.169(3), 0.284(4) and 3.25(1) cm^{-1} for Dy, Ho and Yb, respectively. These values are in the range of those reported in the literature [51]. It can be noticed that the introduction of a zJ' term to fit the magnetic curves down to low temperatures for [Dy(L)(ox)(H_2O)], [Ho(L)(ox)(H_2O)] and [Yb(L)(ox)(H_2O)] compounds did not lead to better results.

Luminescence properties in the solid state

The excitation spectra of [Gd(L)(ox)(H_2O)], [Eu(L)(ox)(H_2O)] and [Tb(L)(ox)(H_2O)] were recorded at room temperature (ca. 297 K) and 12 K monitoring the ligand emission at 520 nm, and the strongest Eu^{3+} $^5D_0 \rightarrow {}^7F_2$ and Tb^{3+} $^5D_4 \rightarrow {}^7F_5$ transitions (Figure 4). The [Gd(L)(ox)(H_2O)] excitation spectra consist of three distinct broad UV bands, ranging from 230 to 400 nm, attributed to the $S_0 \rightarrow S_{3,2,1}$ excited transitions of the organic ligand. For [Eu(L)(ox)(H_2O)], these ligand transitions are

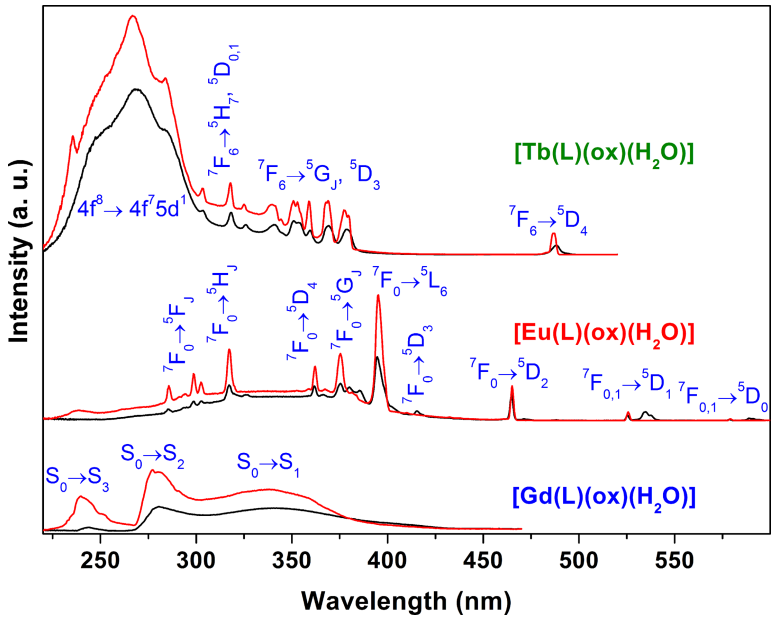

Figure 4: Excitation spectra of [Gd(L)(ox)(H_2O)] (λ_{Em} = 520 nm), [Eu(L)(ox)(H_2O)] (λ_{Em} = 619.6 nm) and [Tb(L)(ox)(H_2O)] (λ_{Em} = 542 nm) recorded at 297 K (black lines) and 12 K (red lines). The intensity is only comparable for the variation of the temperature in each compound.

partially superimposed with the intra-4f^6 $^7F_{0,1}\rightarrow{}^5D_{1\text{-}4}$, $^5L_6$, $^5G_{2\text{-}6}$, $^5H_{3\text{-}7}$ and $^5F_{1\text{-}5}$ transitions of Eu^{3+}, which dominate the corresponding excitation spectra. Finally, the [Tb(L)(ox)(H_2O)] excitation spectra feature a strong and broad UV band ranging from 220 to ca. 300 nm, with a maximum at 267 nm, which has no counterpart in the [Gd(L)(ox)(H_2O)] excitation spectra. Thus, this band is attributed to the inter-configurational spin-forbiden 4f$^8\rightarrow$4f^{7}5d^1 transition of Tb^{3+} because its energy is similar to the energy reported for layered Tb^{3+} silicates [60]. The additional sharp lines in the spectra of [Tb(L)(ox)(H_2O)] are ascribed to the intra-4f^8 $^7F_6\rightarrow{}^5D_{2\text{-}4}$, ^5G_J and $^5H_7$ transitions of Tb^{3+}. Although with a lower relevance, the excited states of the ligands also contribute to the entire excitation spectra of Tb^{3+}, as shown below.

The emission spectra of [Gd(L)(ox)(H_2O)], [Eu(L)(ox)(H_2O)] and [Tb(L)(ox)(H_2O)] recorded at 297 K and 12 K are given in Figure 5. [Gd(L)(ox)(H_2O)] displays two broad bands from 390 to ca. 650 nm attributed to the $S_1\rightarrow S_0$ (peaking at ca. 415 nm) fluorescence and $T_1\rightarrow S_0$ (peaking at 503 nm) ligand phosphorescence. This assignment is supported by the time-resolved emission spectra recorded at 12 K excited at 350 nm (Figure S6, Supporting Information File 1), which demonstrates a much faster time dependence of the $S_1\rightarrow S_0$ transition compared to the transition $T_1\rightarrow S_0$. Under 364 nm excitation, a relative minimum for the Eu^{3+} and Tb^{3+} auto-absorption, [Eu(L)(ox)(H_2O)] and [Tb(L)(ox)(H_2O)] show mainly the typical sharp Eu^{3+} and Tb^{3+} emission lines assigned to the $^5D_0\rightarrow{}^7F_{0\text{-}4}$ and $^5D_4\rightarrow{}^7F_{6\text{-}0}$ transitions, respectively. In addition, both compounds also exhibit a broad band from 400 to ca. 550 nm, particularly weak in the case of the former, attributed to the $S_1\rightarrow S_0$ transition of the ligand. Accordingly, as exemplified in Figure S7 (Supporting Information File 1) with the [Tb(L)(ox)(H_2O)] time-resolved 12 K emission spectra, the broad band has a very fast time dependence totally suppressed by a time delay of only 0.05 ms. The suppression of the low-energy $T_1\rightarrow S_0$ ligand emission denotes an energy transfer from the triplet excited state to the Eu^{3+} and Tb^{3+} excited levels. This energy transfer is more effective for the Eu^{3+} compound, which almost suppresses also the $S_1\rightarrow S_0$ emission. Under excitation at their corresponding maxima, 270 and 395 nm for Tb^{3+} and Eu^{3+}, respectively, both [Eu(L)(ox)(H_2O)] and [Tb(L)(ox)(H_2O)] show only the respective sharp emission lines (Figure S8; Supporting Information File 1).

The emission of Eu^{3+} is highly sensitive to slight changes in the first coordination sphere of the metal, and because of this it is widely used as a local probe [61]. For [Eu(L)(ox)(H_2O)], the

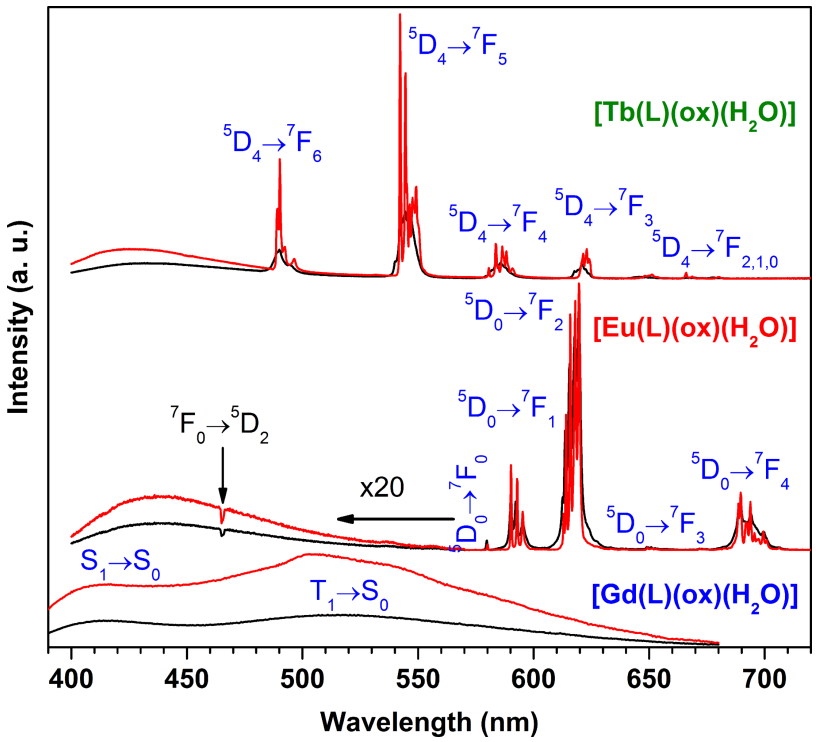

Figure 5: Emission spectra of [Gd(L)(ox)(H_2O)] (λ_{Exc} = 350 nm), [Eu(L)(ox)(H_2O)] (λ_{Exc} = 364 nm) and [Tb(L)(ox)(H_2O)] (λ_{Em} = 364 nm) recorded at 297 K (black lines) and 12 K (red lines). The intensity is only comparable for the variation of the temperature in each compound. For [Eu(L)(ox)(H_2O)], the negative peak at 465 nm is due to the Eu^{3+} auto-absorption from the $^7F_0\rightarrow{}^5D_2$ excited transition.

emission spectra recorded at 297 K and 12 K show i) a single $^5D_0 \rightarrow {}^7F_0$ transition and a local-field splitting of the $^7F_{1,2}$ levels into three and five Stark components, respectively; ii) and the predominance of the $^5D_0 \rightarrow {}^7F_2$ transition relatively to the $^5D_0 \rightarrow {}^7F_1$ one, witnessing the presence of a single low-symmetry Eu^{3+} environment, in accordance with the crystal structure. Additionally, the room-temperature Eu^{3+} $^5D_0$ and Tb^{3+} $^5D_4$ decay curves were well fitted by single exponential functions, yielding lifetimes of 0.60 ± 0.01 and 0.98 ± 0.01 ms for [Eu(L)(ox)(H_2O)] and [Tb(L)(ox)(H_2O)], respectively (Figure S9, Supporting Information File 1), corroborating the presence of a unique Ln^{3+} crystallographic site.

Consideration of these luminescence results prompted the study of isostructural mixed lanthanide networks. In particular, our interest was focused on networks bearing Tb^{3+} and Eu^{3+} in view of their potential application in optical thermometry [17,62]. Accordingly, four Tb^{3+}/Eu^{3+} mixed lanthanide networks of formula [$Tb_{1-x}Eu_x$(L)(ox)(H_2O)] with x = 0.01, 0.03, 0.05 and 0.10 have been synthesized using the same protocol but varying the molar ratio of $Tb(NO_3)_3{\cdot}6H_2O$ and $Eu(NO_3)_3{\cdot}6H_2O$. As expected, these mixed lanthanide networks are isostructural with the parent compound [Ln(L)(ox)(H_2O)] (Figure S10, Supporting Information File 1) and show the presence of Tb and Eu in the expected ratio and homogeneously distributed in the crystals (Figure S11, Supporting Information File 1).

Consider the emission spectra of the four Tb^{3+}/Eu^{3+} mixed lanthanide networks measured at room temperature (Figure S12, Supporting Information File 1). To maximize the relative poor ligand emission, 364 nm excitation was used since it corresponds to a maximum of the ligand excitation and to relative minima of both Eu^{3+} and Tb^{3+} auto-absorptions, as demonstrated by the selective 12 K excitation spectra of [$Tb_{0.90}Eu_{0.10}$(L)(ox)(H_2O)] (Figure S13, Supporting Information File 1). The room-temperature emission spectra of [$Tb_{0.90}Eu_{0.10}$(L)(ox)(H_2O)] under ambient pressure and after exposure to high vacuum (5×10^{-3} mbar, Figure S14, Supporting Information File 1) demonstrates the good stability of the emission of the sample against UV irradiation and pressure change.

Among the four mixed Tb^{3+}/Eu^{3+} mixed lanthanide networks, [$Tb_{0.97}Eu_{0.03}$(L)(ox)(H_2O)] presents at room temperature the best balance between the emissions of ligand, Tb^{3+} and Eu^{3+}. Based on the integrated areas of the ligand (I_L), Tb^{3+} $^5D_4 \rightarrow {}^7F_5$ (I_{Tb}) and Eu^{3+} $^5D_0 \rightarrow {}^7F_2$ (I_{Eu}) emissions, three distinct thermometric parameters may be defined, $\Delta_1 = I_{Tb}/I_{Eu}$, $\Delta_2 = I_{Tb}/I_L$ and $\Delta_3 = I_{Eu}/I_L$, allowing for the conversion of the emission intensities into absolute temperature values. The temperature dependence of the [$Tb_{0.97}Eu_{0.03}$(L)(ox)(H_2O)] emission in the range of 250–340 K is presented in Figure 6a. Four consecutive emission spectra were collected for each temperature and used to determine the average thermometric parameter, with the errors calculated from the corresponding standard deviation (95% confidence). I_L, I_{Tb} and I_{Eu} were determined by integrating the emission spectra in the ranges of 392–478 nm, 536–556 and 606–630 nm, respectively. Figure 6b depicts the temperature dependence of the three integrated emissions. The emission of the ligand decreases by 58% from 250 to 340 K, the Tb^{3+} and Eu^{3+} emissions decrease by 31% and by 20%, respectively.

The temperature dependence of the thermometric parameters Δ_1, Δ_2 and Δ_3 in the range of 250–340 K is shown in Figure 7a. The corresponding relative sensitivity, defined as $S_r = |\partial\Delta/\partial T|/\Delta$

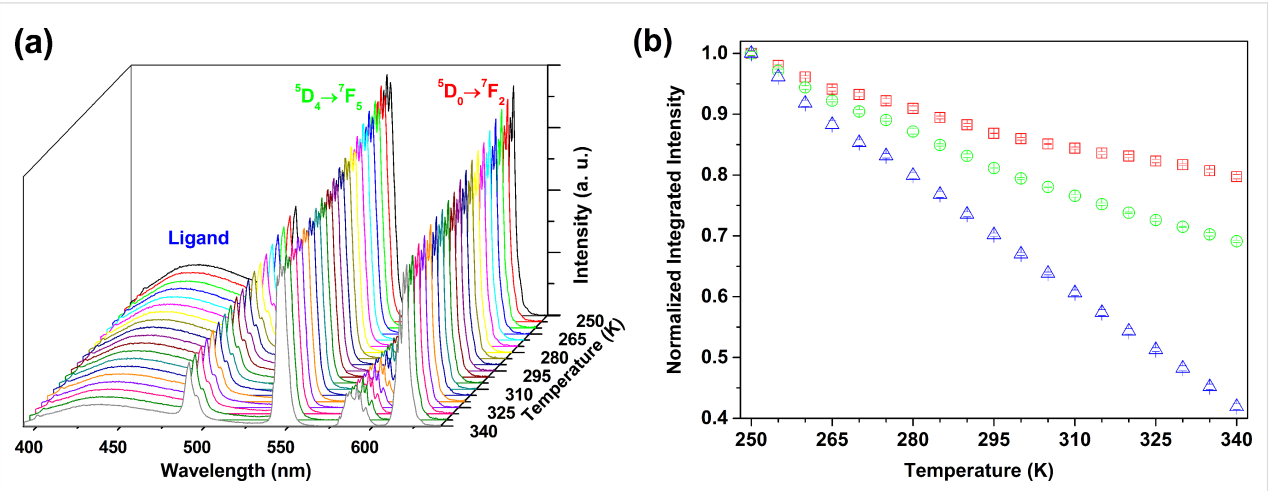

Figure 6: (a) Emission spectra of [$Tb_{0.97}Eu_{0.03}$(L)(ox)(H_2O)] in the range of 250–340 K with the excitation fixed at 364 nm, and (b) corresponding temperature dependence of I_L (blue), I_{Tb} (green) and I_{Eu} (red).

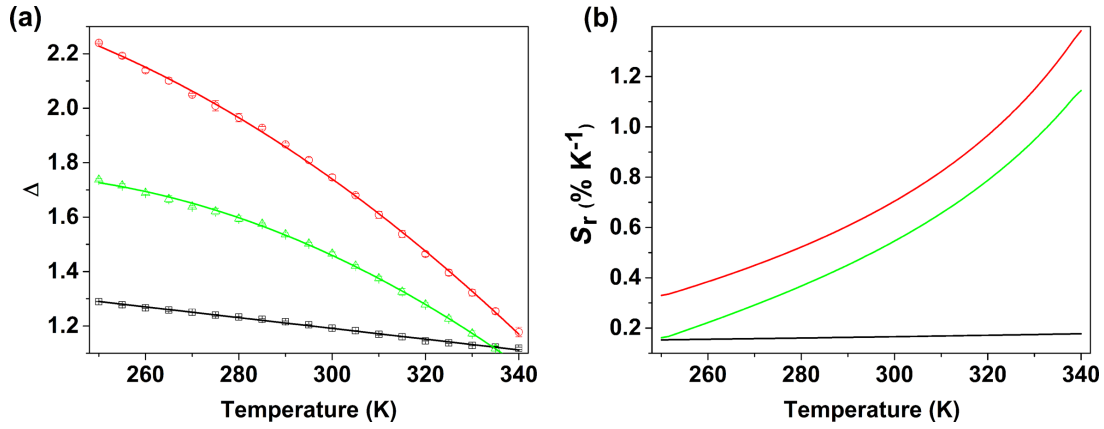

Figure 7: (a) Temperature dependence of Δ_1 (black), Δ_2 (green) and Δ_3 (red) in the range of 250–340 K for $[Tb_{0.97}Eu_{0.03}(L)(ox)(H_2O)]$. The solid lines are the calibration curves, resulting from the fit considering a linear function for Δ_1, $\Delta(T) = \Delta_0 + mT$ (r^2 = 0.998) and second-order polynomial functions, $\Delta(T) = \Delta_0 + a_1T + a_2T^2$, for Δ_2 (r^2 = 0.999) and Δ_3 (r^2 = 0.999). The bars depict the errors in the thermometric parameter resulting from the propagation of the errors determined for I_L, I_{Tb} and I_{Eu} and (b) corresponding relative thermal sensitivities in the same temperature range.

[63], a figure of merit used to compare the performance of ratiometric luminescent thermometers, is plotted in Figure 7b. Δ_2 and Δ_3 exhibit very good sensitivities in the range of 250–340 K with maximum relative sensitivities, S_m, of 1.14% and 1.38%·K^{-1} at 340 K, respectively. For Δ_1, S_m is only 0.18%·K^{-1}. The S_r values obtained for Δ_3, in particular, are among the highest reported for metal-organic frameworks or MOF-based luminescent thermometers operative in the physiological range. Indeed, to the best of our knowledge, only eight such visible luminescent ratiometric LnMOF thermometers have been reported [64-71], among which two outperform our material $[Tb_{0.97}Eu_{0.03}(L)(ox)(H_2O)]$: $Tb_{0.995}Eu_{0.005}$@In(OH)(2,2′-bipyridine-5,5′-dicarboxylate) with S_m = 4.47%·K^{-1} at 333 K [65] and Eu@UiO-(2,2′-bipyridine-5,5′-dicarboxylate) with S_m = 2.19%·K^{-1} at 293 K [67] (value recalculated and corrected using the published calibration curve). Two other thermometers have a performance similar to ours, $Eu_{0.089}Tb_{0.9911}$[2,6-di(2′,4′-dicarboxylphenyl)pyridine] with S_m = 1.39%·K^{-1} at 328 K [70] and $[(Eu_{0.231}Tb_{0.769}(adipate)_{0.5}(phthalate)(H_2O)_2]$ with S_m = 1.21%·K^{-1} at 303 K [71]. These systems are, thus, appealing for potential application as biological sensors [63,72]. The Tb^{3+}-to-Eu^{3+} energy transfer plays an important role in the higher sensitivity of Δ_3 (I_{Eu}/I_L). On the one hand, the Tb^{3+} lifetimes obtained for $[Tb_{0.97}Eu_{0.03}(L)(ox)(H_2O)]$ from single exponential functions (Figure S15, Supporting Information File 1) decrease from 0.98 ± 0.01 ms obtained for the Tb^{3+}-only sample at 297 K to 0.62 ± 0.01 ms (250 K) and 0.57 ± 0.01 ms (340 K). On the other hand, the Eu^{3+} lifetimes for the mixed compound (Figure S15, Supporting Information File 1), 0.86 ± 0.02 ms (250 K) and 0.78 ± 0.01 ms (340 K), increases relatively to the one obtained at 297 K for the Eu^{3+}-only compound (0.60 ± 0.01 ms). In addition, the Eu^{3+} decay curves also exhibit a rise, to 0.81 ± 0.08 ms (250 K) and 0.93±0.06 ms (340 K), most probably originating from the population of the Eu^{3+} $^5D_0$ emitting level trough the Tb^{3+} $^5D_4$ donor level.

Conclusion

Six novel coordination networks based on an imidazolium dicarboxylate 1,3-(biscarboxymethyl)imidazolium and Ln^{3+} ions (Ln = Eu^{3+}, Gd^{3+}, Tb^{3+}, Dy^{3+}, Ho^{3+} and Yb^{3+}) in the presence of oxalate have been obtained by solvothermal reaction and totally characterized. These coordination networks are isostructural and present a monoclinic structure (space group $P2_1/a$). They exhibit magnetic and luminescent properties that are characteristic for the considered lanthanide ions (except for compounds based on Gd^{3+} ions). The possibility to obtain Tb^{3+}/Eu^{3+} mixed lanthanide networks has been exploited for potential application in thermometry. Accordingly, four mixed lanthanide networks $[Tb_{1-x}Eu_x(L)(ox)(H_2O)]$ (x = 0.01, 0.03, 0.05 and 0.10) were synthesized with different Tb^{3+}/Eu^{3+} ratios. Using as the thermometric parameter the ratio between the Eu^{3+}, $^5D_0 \rightarrow {}^7F_2$ transition, and the ligand emissions, $[Tb_{0.97}Eu_{0.03}(L)_2(ox)(H_2O)]$ was found to be one of the best three luminescent ratiometric LnMOF thermometers, operative in the physiological range with a maximum sensitivity of 1.38%·K^{-1} at 340 K. The fact that the structure and properties of these coordination networks can be predicted by design constitutes a promising approach to new multifunctional materials, especially magnetic and luminescent, materials.

Experimental

Synthesis

Glycine, paraformaldehyde, oxalic acid, $Nd(NO_3)_3·6H_2O$, $Sm(NO_3)_3·6H_2O$, $Eu(NO_3)_3·6H_2O$, $Gd(NO_3)_3·6H_2O$,

$Tb(NO_3)_3{\cdot}6H_2O$, $Dy(NO_3)_3{\cdot}5H_2O$, $Ho(NO_3)_3{\cdot}5H_2O$ and $Yb(NO_3)_3{\cdot}xH_2O$ were purchased from Alfa Aesar and were used as received.

[HL] was synthesized according protocols published in the literature [41,42]. Synthesis method and characterizations (elemental analysis, ^1H and ^{13}C NMR) can be found in a previously published paper [31].

[Ln(L)(ox)(H_2O)] compounds with Ln = Eu^{3+}, Gd^{3+}, Tb^{3+}, Dy^{3+}, Ho^{3+} and Yb^{3+} were prepared by solvothermal reaction by mixing [HL] (0.5 mmol), lanthanide nitrate (0.5 mmol) and oxalic acid (0.25 mmol) in a water/ethanol solution (1.5 mL). The solution was sealed in a Teflon-line stainless steel bomb (6 mL) and heated at 393 K for 72 h. After cooling to room temperature, the bomb was opened and colorless crystals were filtered and washed with ethanol and dried at room temperature. Yields were between 41% and 59%. Elemental analysis confirmed the composition of each compounds. [Eu(L)(ox)(H_2O)]: Anal. calcd for $C_9H_9N_2O_9Eu$ (440.96 g·mol^{-1}): C, 24.49; H, 2.04; N, 6.35; found: C, 24.01; H, 2.06; N, 6.00; [Gd(L)(ox)(H_2O)]: anal. calcd for $C_9H_9N_2O_9Gd$ (446.25 g·mol^{-1}): C, 24.20; H, 2.02; N, 6.27; found: C, 23.96; H, 2.05; N, 6.24; [Tb(L)(ox)(H_2O)]: anal. calcd for $C_9H_9N_2O_9Tb$ (447.92 g·mol^{-1}): C, 24.11; H, 2.01; N, 6.25; found: C, 23.68; H, 2.07; N, 6.10; [Dy(L)(ox)(H_2O)]: anal. calcd for $C_9H_9N_2O_9Dy$ (451.50 g·mol^{-1}): C, 23.92; H, 1.99; N, 6.20; found: C, 23.47; H, 2.05; N, 6.15; [Ho(L)(ox)(H_2O)]: anal. calcd for $C_9H_9N_2O_9Ho$ (453.93 g·mol^{-1}): C, 23.79; H, 1.98; N, 6.17; found: C, 23.16; H, 2.03; N, 6.05; [Yb(L)(ox)(H_2O)]: anal. calcd for $C_9H_9N_2O_9Yb$ (462.04 g·mol^{-1}): C, 23.37; H, 1.95; N, 6.06; found: C, 23.08; H, 2.10; N 5.95.

[$Tb_{1-x}Eu_x$(L)(ox)(H_2O)] compounds with x = 0.01, 0.03, 0.05 and 0.10 were prepared in a similar manner but terbium nitrate and europium nitrate were introduced with the adapted stoichiometry. Yields were between 32% and 34%.

Physical measurements

Elemental analyses for C, H, N were carried out at the Service de Microanalyses of the Institut de Chimie de Strasbourg. The SEM images were obtained with a JEOL 6700F (scanning electron microscope (SEM) equipped with a field-emission gun (FEG), operating at 3 kV in the SEI mode instrument. FTIR spectra were collected on a Perkin Elmer Spectrum Two UATR-FTIR spectrometer. TGA-TDA experiments were performed using a TA instrument SDT Q600 (heating rates of 5 °C·min^{-1} under air stream). NMR spectra in solution were recorded using a Bruker AVANCE 300 (300 MHz) spectrometer. The emission and excitation spectra were recorded on a modular double grating excitation spectrofluorometer with a TRIAX 320 emission monochromator (Fluorolog-3, Horiba Scientific) coupled to a R928 or a H9170 Hamamatsu photomultiplier, for the detection on the visible and near-infrared spectral ranges, respectively, using the front-face acquisition mode. The excitation source was a 450 W Xe arc lamp. The emission spectra were corrected for detection and optical spectral response of the spectrofluorometer and the excitation spectra were corrected for the spectral distribution of the lamp intensity using a photodiode reference detector. Time-resolved measurements were carried out with the pulsed Xe–Hg lamp excitation, in front-face acquisition mode. The temperature was controlled with a helium closed-cycle cryostat with vacuum system (ca. 5×10^{-6} mbar) and a Lakeshore 330 auto-tuning temperature controller with a resistive heater. The temperature can be adjusted from ca. 12 to 450 K with a maximum accuracy of 0.1 K. The sample temperature was fixed to a particular value using the auto-tuning temperature controller; after waiting 5 min to thermalize the sample, four consecutive steady-state emission spectra were measured for each temperature; the maximum temperature difference detected during the acquisitions was 0.1 K, the temperature accuracy of the controller. Magnetic measurements were performed using a Quantum Design SQUID-VSM magnetometer. The static susceptibility measurements were performed in the temperature range of 1.8–300 K with an applied field of 0.5 T. Samples were blocked in eicosane to avoid orientation under magnetic field. Magnetization measurements at different fields and at given temperature confirm the absence of ferromagnetic impurities. Data were corrected for the sample holder and eicosane and diamagnetism was estimated from Pascal constants. The powder XRD patterns were collected with a Bruker D8 diffractometer (Cu Kα_1, λ = 1.540598 Å) operating at 40 kV and 40 mA equipped with a LynxEye detector. The X-ray diffraction data on single crystal were collected with graphite-monochromatized Mo Kα radiation (λ = 0.71073 Å) with a Kappa Nonius CCD diffractometer at room temperature. Intensity data were corrected for Lorenz-polarization and absorption factors. The structures were solved by direct methods using SIR92 [73], and refined against F^2 by full-matrix least-squares methods using SHELXL-2014 with anisotropic displacement parameters for all non-hydrogen atoms [74,75]. All calculations were performed by using the crystal structure crystallographic software package WINGX [76]. The structure was drawn using Mercury or Diamond [77,78]. Hydrogen atoms were located on a difference Fourier map and introduced into the calculations as a riding model with isotropic thermal parameters. Crystallographic data for the structures reported have been deposited in the Cambridge Crystallographic Data Centre with CCDC reference numbers 1541843, 1541844, 1541845, 1541846, 1541847, 1541848 for [Gd(L)(ox)(H_2O)], [Yb(L)(ox)(H_2O)], [Dy(L)(ox)(H_2O)], [Ho(L)(ox)(H_2O)], [Tb(L)(ox)(H_2O)], [Eu(L)(ox)(H_2O)].

Supporting Information

Supporting Information contains a representation of the coordination polyhedron, a table of selected bonds, a comparison of the experimental powder X-ray diffraction patterns of the different compounds and the simulated pattern from single crystals X-ray data, SEM analysis, TGA/TDA analysis, a summary of the weight loss values for the different compounds, infrared spectra, luminescence measurement and magnetic expression.

Supporting Information File 1

Additional experimental data.
[https://www.beilstein-journals.org/bjnano/content/supplementary/2190-4286-9-259-S1.pdf]

Acknowledgements

The authors thank the Centre National de la Recherche Scientifique (CNRS), the Université de Strasbourg (Idex), the Labex NIE (ANR-11-LABX-0058_NIE within the Investissement d'Avenir program ANR-10-IDEX-0002-02), the Agence Nationale de la Recherche (ANR contract no. ANR-15-CE08-0020-01) and the icFRC (http://www.icfrc.fr) for funding. Part of the present work comes from the thesis of Pierre Farger [32] and is part of the research activity supported by the European COST action MP1202: HINT (Rational design of hybrid organic–inorganic interfaces: the next step towards advanced functional materials. http://www.cost-hint.cnrs.fr). This work was also developed within the scope of the project CICECO-Aveiro Institute of Materials, POCI-01-0145-FEDER-007679 (Fundação para a Ciência e a Tecnologia, FCT, Ref. UID/CTM/50011/2013), financed by national funds through the FCT/MEC (Ministério da Educação e Ciência) and when appropriate co-financed by FEDER under the PT2020 Partnership Agreement. D.A. (SFRH/BPD/95032/2013) thanks FCT for a post-doctoral grant. The authors are grateful to Didier Burger for technical assistance.

ORCID® iDs

Guillaume Rogez - https://orcid.org/0000-0001-9006-7273
Duarte Ananias - https://orcid.org/0000-0003-4394-045X
Emilie Delahaye - https://orcid.org/0000-0001-9114-1682

References

1. Moghadam, P. Z.; Li, A.; Wiggin, S. B.; Tao, A.; Maloney, A. G. P.; Wood, P. A.; Ward, S. C.; Fairen-Jimenez, D. *Chem. Mater.* **2017,** *29,* 2618–2625. doi:10.1021/acs.chemmater.7b00441
2. Zhao, Y. *Chem. Mater.* **2016,** *28,* 8079–8081. doi:10.1021/acs.chemmater.6b04677
3. Li, S.; Huo, F. *Nanoscale* **2015,** *7,* 7482–7501. doi:10.1039/c5nr00518c
4. Pagis, C.; Ferbinteanu, M.; Rothenberg, G.; Tanase, S. *ACS Catal.* **2016,** *6,* 6063–6072. doi:10.1021/acscatal.6b01935
5. Yi, F.-Y.; Chen, D.; Wu, M.-K.; Han, L.; Jiang, H.-L. *ChemPlusChem* **2016,** *81,* 675–690. doi:10.1002/cplu.201600137
6. Yao, Q.; Bermejo Gómez, A.; Su, J.; Pascanu, V.; Yun, Y.; Zheng, H.; Chen, H.; Liu, L.; Abdelhamid, H. N.; Martín-Matute, B.; Zou, X. *Chem. Mater.* **2015,** *27,* 5332–5339. doi:10.1021/acs.chemmater.5b01711
7. Li, H.-Y.; Wei, Y.-L.; Dong, X.-Y.; Zang, S.-Q.; Mak, T. C. W. *Chem. Mater.* **2015,** *27,* 1327–1331. doi:10.1021/cm504350q
8. Li, B.; Wen, H.-M.; Cui, Y.; Qian, G.; Chen, B. *Prog. Polym. Sci.* **2015,** *48,* 40–84. doi:10.1016/j.progpolymsci.2015.04.008
9. Hu, Z.; Deibert, B. J.; Li, J. *Chem. Soc. Rev.* **2014,** *43,* 5815–5840. doi:10.1039/c4cs00010b
10. Cui, Y.; Chen, B.; Qian, G. *Coord. Chem. Rev.* **2014,** *273–274,* 76–86. doi:10.1016/j.ccr.2013.10.023
11. Cui, Y.; Yue, Y.; Qian, G.; Chen, B. *Chem. Rev.* **2012,** *112,* 1126–1162. doi:10.1021/cr200101d
12. Rocha, J.; Carlos, L. D.; Paz, F. A. A.; Ananias, D. *Chem. Soc. Rev.* **2011,** *40,* 926–940. doi:10.1039/c0cs00130a
13. Heine, J.; Müller-Buschbaum, K. *Chem. Soc. Rev.* **2013,** *42,* 9232. doi:10.1039/c3cs60232j
14. Allendorf, M. D.; Bauer, C. A.; Bhakta, R. K.; Houk, R. J. T. *Chem. Soc. Rev.* **2009,** *38,* 1330–1352. doi:10.1039/b802352m
15. Amghouz, Z.; García-Granda, S.; García, J. R.; Ferreira, R. A. S.; Mafra, L.; Carlos, L. D.; Rocha, J. *Inorg. Chem.* **2012,** *51,* 1703–1716. doi:10.1021/ic202020z
16. Fordham, S.; Wang, X.; Bosch, M.; Zhou, H.-C. Lanthanide Metal-Organic Frameworks: Syntheses, Properties, and Potential Applications. In *Lanthanide Metal-Organic Frameworks;* Cheng, P., Ed.; Structure and Bonding; Springer: Berlin, Germany, 2014; pp 1–27. doi:10.1007/430_2014_162
17. Rocha, J.; Brites, C. D. S.; Carlos, L. D. *Chem. – Eur. J.* **2016,** *22,* 14782–14795. doi:10.1002/chem.201600860
18. Wang, Z.; Ananias, D.; Carné-Sánchez, A.; Brites, C. D. S.; Imaz, I.; Maspoch, D.; Rocha, J.; Carlos, L. D. *Adv. Funct. Mater.* **2015,** *25,* 2824–2830. doi:10.1002/adfm.201500518
19. García-García, A.; Oyarzabal, I.; Cepeda, J.; Seco, J. M.; García-Valdivia, A. A.; Gómez-Ruiz, S.; Salinas-Castillo, A.; Choquesillo-Lazarte, D.; Rodríguez-Diéguez, A. *New J. Chem.* **2018,** *42,* 832–837. doi:10.1039/c7nj02935g
20. Oyarzabal, I.; Fernández, B.; Cepeda, J.; Gómez-Ruiz, S.; Calahorro, A. J.; Seco, J. M.; Rodríguez-Diéguez, A. *CrystEngComm* **2016,** *18,* 3055–3063. doi:10.1039/c6ce00318d
21. Seco, J. M.; Oyarzabal, I.; Pérez-Yáñez, S.; Cepeda, J.; Rodríguez-Diéguez, A. *Inorg. Chem.* **2016,** *55,* 11230–11248. doi:10.1021/acs.inorgchem.6b01845
22. Liu, K.; Li, H.; Zhang, X.; Shi, W.; Cheng, P. *Inorg. Chem.* **2015,** *54,* 10224–10231. doi:10.1021/acs.inorgchem.5b01356
23. Chen, M.; Sañudo, E. C.; Jiménez, E.; Fang, S.-M.; Liu, C.-S.; Du, M. *Inorg. Chem.* **2014,** *53,* 6708–6714. doi:10.1021/ic500490x
24. Decadt, R.; Van Hecke, K.; Depla, D.; Leus, K.; Weinberger, D.; Van Driessche, I.; Van Der Voort, P.; Van Deun, R. *Inorg. Chem.* **2012,** *51,* 11623–11634. doi:10.1021/ic301544q
25. Ma, R.; Chu, H.; Zhao, Y.; Wuren, Q.; Shan, M. *Spectrochim. Acta, Part A* **2010,** *77,* 419–423. doi:10.1016/j.saa.2010.06.005
26. Wang, P.; Fan, R.-Q.; Liu, X.-R.; Wang, L.-Y.; Yang, Y.-L.; Cao, W.-W.; Yang, B.; Hasi, W.; Su, Q.; Mu, Y. *CrystEngComm* **2013,** *15,* 1931–1949. doi:10.1039/c3ce26684b

27. Chai, X.-C.; Sun, Y.-Q.; Lei, R.; Chen, Y.-P.; Zhang, S.; Cao, Y.-N.; Zhang, H.-H. *Cryst. Growth Des.* **2010,** *10,* 658–668. doi:10.1021/cg901075r
28. Sequeira, G. M.; Tan, W. Y.; Moore, E. G. *Dalton Trans.* **2015,** *44,* 13378–13383. doi:10.1039/c5dt01875g
29. Abrahams, B. F.; Maynard-Casely, H. E.; Robson, R.; White, K. F. *CrystEngComm* **2013,** *15,* 9729–9737. doi:10.1039/c3ce41226a
30. Han, L.; Zhang, S.; Wang, Y.; Yan, X.; Lu, X. *Inorg. Chem.* **2009,** *48,* 786–788. doi:10.1021/ic800632r
31. Farger, P.; Leuvrey, C.; Gallart, M.; Gilliot, P.; Rogez, G.; Rabu, P.; Delahaye, E. *Magnetochemistry* **2017,** *3,* No. 1. doi:10.3390/magnetochemistry3010001
32. Farger, P. Synthèse Ionothermale de Réseaux Hybrides Multiferroïques. Ph.D. Thesis, Université de Strasbourg, Strasbourg, France, 2016.
33. Farger, P.; Guillot, R.; Leroux, F.; Parizel, N.; Gallart, M.; Gilliot, P.; Rogez, G.; Delahaye, E.; Rabu, P. *Eur. J. Inorg. Chem.* **2015,** 5342–5350. doi:10.1002/ejic.201500825
34. Martin, N. P.; Falaise, C.; Volkringer, C.; Henry, N.; Farger, P.; Falk, C.; Delahaye, E.; Rabu, P.; Loiseau, T. *Inorg. Chem.* **2016,** *55,* 8697–8705. doi:10.1021/acs.inorgchem.6b01232
35. Calderone, P. J.; Forster, P. M.; Borkowski, L. A.; Teat, S. J.; Feygenson, M.; Aronson, M. C.; Parise, J. B. *Inorg. Chem.* **2011,** *50,* 2159–2167. doi:10.1021/ic1015548
36. Ji, W.-J.; Zhai, Q.-G.; Li, S.-N.; Jiang, Y.-C.; Hu, M.-C. *Chem. Commun.* **2011,** *47,* 3834–3836. doi:10.1039/c0cc04890a
37. Morris, R. E. *Chem. Commun.* **2009,** 2990–2998. doi:10.1039/b902611h
38. Xu, L.; Yan, S.; Choi, E.-Y.; Lee, J. Y.; Kwon, Y.-U. *Chem. Commun.* **2009,** 3431–3433. doi:10.1039/b902223f
39. Zhang, J.; Chen, S.; Bu, X. *Angew. Chem., Int. Ed.* **2008,** *47,* 5434–5437. doi:10.1002/anie.200801838
40. Xu, L.; Choi, E.-Y.; Kwon, Y.-U. *Inorg. Chem.* **2007,** *46,* 10670–10680. doi:10.1021/ic701393w
41. Fei, Z.; Zhao, D.; Geldbach, T. J.; Scopelliti, R.; Dyson, P. J. *Chem. – Eur. J.* **2004,** *10,* 4886–4893. doi:10.1002/chem.200400145
42. Kühl, O.; Palm, G. *Tetrahedron: Asymmetry* **2010,** *21,* 393–397. doi:10.1016/j.tetasy.2010.02.015
43. Deng, Z.-P.; Kang, W.; Huo, L.-H.; Zhao, H.; Gao, S. *Dalton Trans.* **2010,** *39,* 6276–6284. doi:10.1039/c0dt00031k
44. Wang, X.-J.; Cen, Z.-M.; Ni, Q.-L.; Jiang, X.-F.; Lian, H.-C.; Gui, L.-C.; Zuo, H.-H.; Wang, Z.-Y. *Cryst. Growth Des.* **2010,** *10,* 2960–2968. doi:10.1021/cg1000045
45. Zhao, X.-Q.; Liu, X.-H.; Li, J.-J.; Zhao, B. *CrystEngComm* **2013,** *15,* 3308–3317. doi:10.1039/c2ce26695d
46. Dendrinou-Samara, C.; Tsotsou, G.; Ekateriniadou, L. V.; Kortsaris, A. H.; Raptopoulou, C. P.; Terzis, A.; Kyriakidis, D. A.; Kessissoglou, D. P. *J. Inorg. Biochem.* **1998,** *71,* 171–179. doi:10.1016/s0162-0134(98)10051-x
47. Deacon, G. B.; Phillips, R. J. *Coord. Chem. Rev.* **1980,** *33,* 227–250. doi:10.1016/s0010-8545(00)80455-5
48. Kahn, O. *Molecular Magnetism;* Wiley-VCH: Weinheim, Germany, 1993.
49. Fisher, M. E. *Am. J. Phys.* **1964,** *32,* 343–346. doi:10.1119/1.1970340
50. Benelli, C.; Gatteschi, D. *Chem. Rev.* **2002,** *102,* 2369–2388. doi:10.1021/cr010303r
51. Cepeda, J.; Balda, R.; Beobide, G.; Castillo, O.; Fernández, J.; Luque, A.; Pérez-Yáñez, S.; Román, P. *Inorg. Chem.* **2012,** *51,* 7875–7888. doi:10.1021/ic3009392
52. Cañadillas-Delgado, L.; Pasán, J.; Fabelo, O.; Hernández-Molina, M.; Lloret, F.; Julve, M.; Ruiz-Pérez, C. *Inorg. Chem.* **2006,** *45,* 10585–10594. doi:10.1021/ic061173d
53. Han, Z.-B.; Zhang, G.-X.; Zeng, M.-H.; Ge, C.-H.; Zou, X.-H.; Han, G.-X. *CrystEngComm* **2009,** *11,* 2629–2633. doi:10.1039/b905663g
54. Lhoste, J.; Pérez-Campos, A.; Henry, N.; Loiseau, T.; Rabu, P.; Abraham, F. *Dalton Trans.* **2011,** *40,* 9136–9144. doi:10.1039/c1dt10485c
55. Andruh, M.; Bakalbassis, E.; Kahn, O.; Trombe, J. C.; Porcher, P. *Inorg. Chem.* **1993,** *32,* 1616–1622. doi:10.1021/ic00061a017
56. Boča, R. *Theoretical Foundations of Molecular Magnetism;* Elsevier: Amsterdam, Netherlands, 1999.
57. Amar, N. B.; Hassairi, M. A.; Dammak, M. *J. Lumin.* **2016,** *173,* 223–230. doi:10.1016/j.jlumin.2016.01.023
58. Liu, G. K.; Carnall, W. T.; Jones, R. P.; Cone, R. L.; Huang, J. *J. Alloys Compd.* **1994,** *207–208,* 69–73. doi:10.1016/0925-8388(94)90179-1
59. Bernini, M. C.; Brusau, E. V.; Narda, G. E.; Echeverria, G. E.; Pozzi, C. G.; Punte, G.; Lehmann, C. W. *Eur. J. Inorg. Chem.* **2007,** 684–693. doi:10.1002/ejic.200600860
60. Ananias, D.; Kostova, M.; Almeida Paz, F. A.; Ferreira, A.; Carlos, L. D.; Klinowski, J.; Rocha, J. *J. Am. Chem. Soc.* **2004,** *126,* 10410–10417. doi:10.1021/ja047905n
61. Bünzli, J.-C. G.; Choppin, G. R. *Lanthanide Probes in Life, Chemical and Earth Sciences;* Elsevier: Amsterdam, Netherlands, 1989; pp 22 ff.
62. Cui, Y.; Xu, H.; Yue, Y.; Guo, Z.; Yu, J.; Chen, Z.; Gao, J.; Yang, Y.; Qian, G.; Chen, B. *J. Am. Chem. Soc.* **2012,** *134,* 3979–3982. doi:10.1021/ja2108036
63. Brites, C. D. S.; Lima, P. P.; Silva, N. J. O.; Millán, A.; Amaral, V. S.; Palacio, F.; Carlos, L. D. *Nanoscale* **2012,** *4,* 4799–4829. doi:10.1039/c2nr30663h
64. Cadiau, A.; Brites, C. D. S.; Costa, P. M. F. J.; Ferreira, R. A. S.; Rocha, J.; Carlos, L. D. *ACS Nano* **2013,** *7,* 7213–7218. doi:10.1021/nn402608w
65. Zhou, Y.; Yan, B.; Lei, F. *Chem. Commun.* **2014,** *50,* 15235–15238. doi:10.1039/c4cc07038k
66. Cui, Y.; Song, R.; Yu, J.; Liu, M.; Wang, Z.; Wu, C.; Yang, Y.; Wang, Z.; Chen, B.; Qian, G. *Adv. Mater.* **2015,** *27,* 1420–1425. doi:10.1002/adma.201404700
67. Zhou, Y.; Yan, B. *J. Mater. Chem. C* **2015,** *3,* 9353–9358. doi:10.1039/c5tc02004b
68. Zhao, D.; Rao, X.; Yu, J.; Cui, Y.; Yang, Y.; Qian, G. *Inorg. Chem.* **2015,** *54,* 11193–11199. doi:10.1021/acs.inorgchem.5b01623
69. Li, L.; Zhu, Y.; Zhou, X.; Brites, C. D. S.; Ananias, D.; Lin, Z.; Paz, F. A. A.; Rocha, J.; Huang, W.; Carlos, L. D. *Adv. Funct. Mater.* **2016,** *26,* 8677–8684. doi:10.1002/adfm.201603179
70. Yang, Y.; Chen, L.; Jiang, F.; Yu, M.; Wan, X.; Zhang, B.; Hong, M. *J. Mater. Chem. C* **2017,** *5,* 1981–1989. doi:10.1039/c6tc05316e
71. Chuasaard, T.; Ngamjarurojana, A.; Surinwong, S.; Konno, T.; Bureekaew, S.; Rujiwatra, A. *Inorg. Chem.* **2018,** *57,* 2620–2630. doi:10.1021/acs.inorgchem.7b03016
72. Yang, Z.; Cao, J.; He, Y.; Yang, J. H.; Kim, T.; Peng, X.; Kim, J. S. *Chem. Soc. Rev.* **2014,** *43,* 4563–4601. doi:10.1039/c4cs00051j
73. Altomare, A.; Cascarano, G.; Giacovazzo, C.; Guagliardi, A.; Burla, M. C.; Polidori, G.; Camalli, M. *J. Appl. Crystallogr.* **1994,** *27,* 435. doi:10.1107/s002188989400021x
74. Sheldrick, G. M. *Acta Crystallogr., Sect. A: Found. Crystallogr.* **2008,** *64,* 112–122. doi:10.1107/s0108767307043930

75. *SHELXS-97, Program for Crystal Structure Solution;* University of Göttingen: Göttingen, Germany, 1997.
76. Farrugia, L. J. *J. Appl. Crystallogr.* **1999,** *32,* 837–838. doi:10.1107/s0021889899006020
77. Macrae, C. F.; Edgington, P. R.; McCabe, P.; Pidcock, E.; Shields, G. P.; Taylor, R.; Towler, M.; van de Streek, J. *J. Appl. Crystallogr.* **2006,** *39,* 453–457. doi:10.1107/s002188980600731x
78. *DIAMOND;* Crystal Impact GbR: Bonn, Germany, 1999.

License and Terms

BEILSTEIN JOURNAL OF NANOTECHNOLOGY

Layered calcium phenylphosphonate: a hybrid material for a new generation of nanofillers

Kateřina Kopecká*[1,2,3], Ludvík Beneš[2], Klára Melánová[4], Vítězslav Zima[4], Petr Knotek[1] and Kateřina Zetková[3]

Full Research Paper

Open Access

Address:
[1]Department of General and Inorganic Chemistry, Faculty of Chemical Technology, University of Pardubice, Studentská 573, 532 10 Pardubice, Czech Republic, [2]Joint Laboratory of Solid State Chemistry, Faculty of Chemical Technology, University of Pardubice, Studentská 84, 532 10 Pardubice, Czech Republic, [3]SYNPO, akciová společnost, S. K. Neumanna 1316, 532 07 Pardubice, Czech Republic and [4]Institute of Macromolecular Chemistry of the Czech Academy of Sciences, Heyrovského nám. 2, 162 06 Prague 6, Czech Republic

Email:
Kateřina Kopecká* - katerina.kopecka@synpo.cz

* Corresponding author

Keywords:
exfoliation; layered phenylphosphonate; nanomaterial; nanofiller; polymer filler

Beilstein J. Nanotechnol. **2018,** *9,* 2906–2915.
doi:10.3762/bjnano.9.269

Received: 10 August 2018
Accepted: 25 October 2018
Published: 20 November 2018

This article is part of the thematic issue "Advanced hybrid nanomaterials".

Guest Editor: F. Leroux

Abstract

The use of nanosheets of layered calcium phenylphosphonate as a filler in a polymeric matrix was investigated. Layered calcium phenylphosphonate (CaPhP), with chemical formula $CaC_6H_5PO_3{\cdot}2H_2O$, is a hybrid organic–inorganic material that exhibits a hydrophobic character due to the presence of phenyl groups on the surface of the layers. In this paper, various CaPhP synthesis methods were studied with the aim of obtaining a product most suitable for its subsequent exfoliation. The liquid-based approach was used for the exfoliation. It was found that the most promising technique for the exfoliation of CaPhP in an amount sufficient for incorporation into polymers involved using propan-2-ol with a strong shear force generated in a high-shear disperser. The filler was tested both in its unexfoliated and exfoliated forms for the preparation of polymer composites, for which a low molecular weight epoxy resin based on bisphenol A was used as a polymer matrix. The prepared samples were characterized by powder X-ray diffraction, atomic force microscopy, optical and scanning electron microscopy, and dynamic mechanical analysis. Flammability and gas permeation tests were also performed. The addition of the nanofiller was found to influence the composite properties – the exfoliated particles were found to have a higher impact on the properties of the prepared composites than the unexfoliated particles of the same loading

Introduction

The idea to combine materials with different properties to create a composite that benefits from a synergistic effect and to gain better and novel materials by this way is a very old concept. The reinforcement of a polymer matrix with inorganic fillers with the aim to improve their stiffness, melt behavior, mechanical characteristic, durability and other properties of polymer

products is a well-known process and has been studied for decades. Platelets of clay minerals are suitable and widespread fillers. In addition, some clays can be exfoliated thanks to their layered structure and thus fillers formed from nanosheets can be obtained [1,2]. Convenient interactions among functional groups of the polymer chain and the surface groups of the filler are necessary to retain the nanoscale character of the filler and to protect it from the formation of agglomerates in order to achieve a homogenous distribution within the volume of the polymer matrix. This is a drawback for natural clays as they are usually hydrophilic, thus their application is more suitable for water-based systems. This limitation can be overcome by intercalation of organic molecules into the structure or by a surface modification [3,4] by grafting organophilic functional groups onto the clay surface, leading to the synthesis of hybrid organic–inorganic materials [5].

Layered metal organophosphonates are a class of materials which exhibit a hybrid character by their nature. They are generally defined as salts of phosphonic acids with the general formula RPO_3H_2 (R = alkyl or aryl group) with metals. They benefit from a well-defined inorganic structure in combination with organic moieties which can be functionalized and modified to obtain desired properties. Many different types of layered metal organophosphonates have been prepared. Well-known and well-studied are the organophosphonates of zirconium because of their good stability; however, it is also possible to prepare layered structures with divalent metals such as calcium, strontium or barium [6-9]. Although the properties of these compounds differ with the metal and organic group incorporated in their structure, the main characteristic remains the same: a strong in-plane bonding in combination with weak van der Waals interactions between the planes. This arrangement enables their use as a host material in intercalation chemistry and as a precursor for the preparation of nanosheets by exfoliation.

Exfoliation is a process whereby thin sheets of material are completely separated from the bulk. This happens when cohesive forces between the adjacent planes, which are usually caused by van der Waals interactions, are overcome. Mechanical or chemical action can be involved. Various exfoliation methods have been studied mainly for the exfoliation of graphite to produce graphene [10], but the main ideas and approaches are also applicable for other types of layered compounds. In this work a so-called liquid-based-exfoliation process was used [11-15], which is considered to be convenient for the production of larger quantities of material for further application. Briefly, particles are dispersed in a suitable liquid and then exfoliated by a force action; this can be done with or without adding further chemicals to weaken cohesive forces. The main advantage is that a ready-to-use dispersion of nanoplatelets is obtained, so the step of dispersing dry nanoparticles in a polymer matrix is avoided, which is usually challenging, and thus simplifies the preparation of the polymer composites.

In this work, layered calcium phenylphosphonate dihydrate with formula $CaC_6H_5PO_3{\cdot}2H_2O$ (CaPhP) was used both in exfoliated and unexfoliated forms to prepare a polymer composite with the intention to move towards applied science and find possible applications. The CaPhP layer can be imagined as a sheet consisting of three plies. The central ply comprises metal atoms coordinated by oxygen atoms of the phosphonate groups. The outer plies are formed by benzene rings connected to the central ply through phosphorus atoms of the phosphonate groups. The model of the CaPhP layer is depicted in Figure 1. Thanks to its structure, the surface of the CaPhP layer is formed by rather hydrophobic phenyl groups, which makes them a suitable material for incorporation into the hydrophobic polymer matrices. An epoxy resin was chosen as a polymer matrix because epoxy resins are widespread and useful in various industrial applications ranging from coatings, to adhesives, to the preparation of composites in automotive or aerospace industry [16,17]. The experiments were carried out with an unmodified low molecular weight epoxy resin based on bisphenol A, which is one of the basic ones.

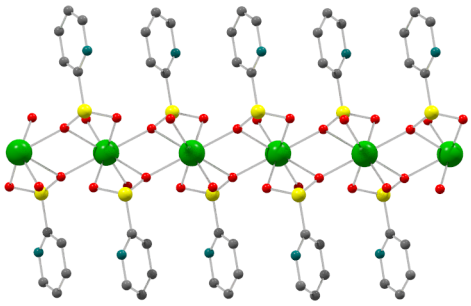

Figure 1: Model structure of the CaPhP layer. Calcium atoms are in green, phosphorus atoms in yellow and red and gray spheres correspond to oxygen and hydrogen, respectively.

Results and Discussion

Filler synthesis

The layered structure of calcium phenylphosphonate is formed at room temperature by a co-precipitation of starting compounds – phenylphosphonic acid and a soluble source of calcium (e.g., $CaCl_2$, as in our case) in a 1:1 molar ratio at pH > 9, as reported by Svoboda et al. [18] and described in the Experimental section. The previous work was focused on the material itself, characterization of its chemical composition, behavior under different pH and its intercalation chemistry. In this work, this material was studied from the point of its application

as a filler in a polymer matrix, which implies that possible ways for large-scale synthesis of this material were investigated. Therefore, the experimental procedure and its conditions were optimized with the aim to obtain a pure product on a large scale.

There are two points which need to be highlighted: First, the role of pH is crucial. To obtain the desired product, it is necessary to maintain a pH at around 9 all the times during the reaction process and in the whole reaction volume. If this condition is not fulfilled, an intermediate with formula $Ca_3(C_6H_5PO_3)_2(C_6H_5PO_3)_2{\cdot}4H_2O$ [18], which is formed near neutral pH, cannot be transformed into the desired CaPhP but remains present as an impurity in the final product. This intermediate can be identified as another layered phase in the XRD pattern with basal spacing around 15.2 Å. What is more important from the technological point of view, the reaction mixture tends to be denser, which causes problems with homogenous stirring. Over the course of the reaction, the pH decreases to about 8 during the first 15 minutes and then remains the same. Thus, it is recommended to start at pH 10 when working with higher volumes, even if it means a few more rounds of washing to remove ammonium in the final step. Second, it is appropriate and advantageous to add the whole volume of calcium chloride solution at once into the reaction mixture. Two methods, the "drop by drop" addition and addition in several portions, were tested in an effort to achieve larger but thinner particles as it is expected that the edges of already formed lamellas could act as nucleation centers; however, these methods were not successful. Although the shape of the particles differs minimally as they are rod-shaped in each case, the thickness of the individual lamellas differs significantly with the selected procedure, as was confirmed by the atomic force microscopy (AFM) analysis. The samples prepared by the “drop by drop” and “several portions” methods contained thinner particles in comparison those where the portion was all added at once. Nevertheless, as it can be seen in scanning electron microscopy (SEM) images (Figure 2) and as was also verified by AFM (Figure 3), in the first two mentioned cases, the lamellas tend to grow together into aggregates. A possible explanation is that the successive addition of the reactant causes preferential growth of new lamellas on the existing lamellas rather than being formed separately. Such formations are not so useful for application as a polymer filler where individual particles are more desirable. Thus, it was preferable to prepare thinner lamellas by exfoliation and not by varying the rate of the reactant addition.

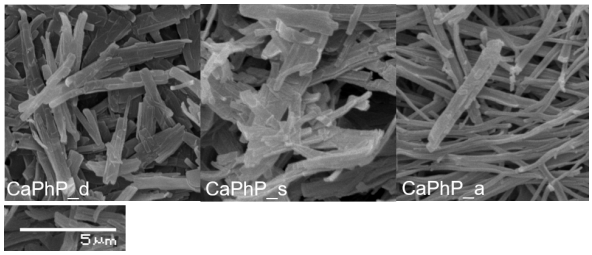

Figure 2: SEM pictures of calcium phenylphosphonate particles prepared by addition of chloride solution using the “drop by drop” (CaPhP_d) and “in several portions” methods (CaPhP_s) and “all at once” (CaPhP_a).

Preparation of the nanofiller – exfoliation

Exfoliation is a top-down approach that can be used to obtain nanostructures [12,13]. As was mentioned in the Introduction, calcium phenylphosphonate, by its layered nature, should be a good candidate for the delamination. As previously described by several research groups, solvent compatibility with exfoliated material is one of the key parameters for successful delamination [13,14]. If the solvent–material interaction is not favorable, delamination could likely be observed within a short time; however, the dispersion of the resulting nanosheets will not be stable enough for further application. There is the possibility to extend the duration of the nanosheet dispersion by adding surface-active agents but choosing an appropriate one is also not trivial. Based on this consideration, this work was focused on a selection of suitable solvents which produce stable dispersions without the addition of other chemicals. As described in the Ex-

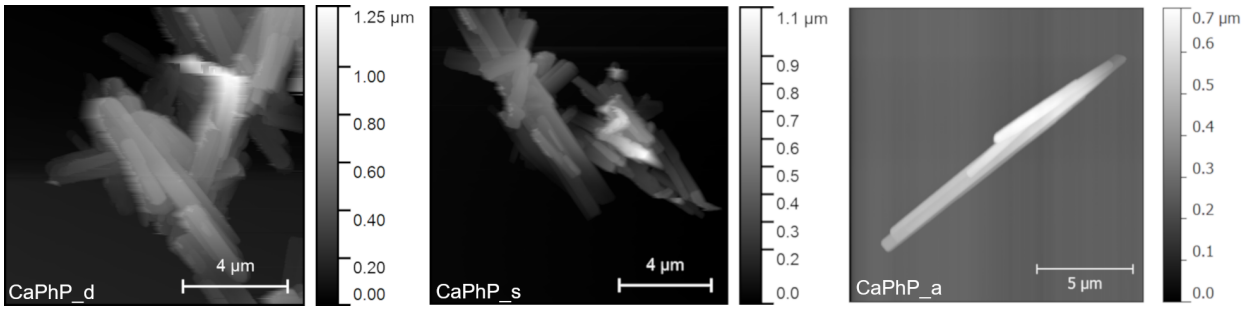

Figure 3: AFM images illustrating the topology of CaPhP particles prepared by addition of calcium chloride solution: “drop by drop” (CaPhP_d), “in several portions” (CaPhP_s) and “all at once” (CaPhP_a).

perimental section, an ultrasound treatment was applied to a combination of calcium phenylphosphonate with different solvents and then the dispersion stability was observed up to 24 hours after the ultrasound treatment. The presence of small particles in the dispersion was confirmed by Tyndall scattering of the green laser beam (see Figure 4).

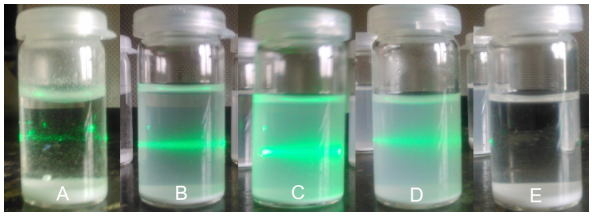

Figure 4: CaPhP nanoparticles in various solvents 24 hours after ultrasound treatment (A – distilled water, B – propan-2-ol, C – ethanol, D – butanol, E – acetone). The green line is Tyndall scattering by a green laser.

It is possible to conclude that this material is not compatible with water or acetone. Alcohols were shown to be the best solvents for this type of exfoliation, namely propan-2-ol and *n*-butanol. In fact, the stability of the dispersion in *n*-butanol was slightly better than in propan-2-ol; however, *n*-butanol is not so convenient for application in the composites due to its higher boiling point. Also, ethanol seems to be a promising solvent, however, ethanol is polar and thus less compatible with hydrophobic substances. Therefore, propan-2-ol was chosen, which is more appropriate for treatment with hydrophobic compounds and, in comparison to pure ethanol, less expensive.

The exfoliation of CaPhP in propan-2-ol was studied using various force actions starting with sonication, in addition to the combination with mild shear force, which is produced by pushing the particle dispersion through an injection needle by a peristaltic pump. Additionally, a strong shear force created by a high-shear disperser, where the velocity of dispersion was 5 m/s, was also applied. It was found out that the most suitable method for the exfoliation of calcium phenylphosphonate was the strong shear force applied by using the high-shear disperser.

These dispersion methods are primarily used for breaking down agglomerates; however, in the case of such layered compounds, as this material is, the force is strong enough to not only disperse but also to delaminate the particles. As can be seen in Figure 5A, one can get nanosheets that are 1.4 nm thin but with lateral dimensions of hundreds of nanometers. What is important is that there are also industrial-scale dispersion apparatus available, so this approach is not limited only to laboratory use.

However, there are also limits that need to be mentioned. From our experience, it is not possible (at least for CaPhP) to fully exfoliate all particles. The obtained dispersion is always a mixture of monolamellar and multilamellar entities (Figure 6).

It is possible to influence the exfoliation yield by the time applied and by the speed of the rotor but too long and too high speed (thus too strong force) lead to the complete destruction of the particles. A result of too long mixing is documented in Figure 5B. There are no visible particles with a lamellar structure or at least with a regular shape, therefore this product is not convenient for application as a nanofiller. The separation of fully exfoliated particles is possible by centrifugation but this also leads to a loss of the material, thus, it is more suitable for a small-scale sample preparation and not so convenient for large-scale production. Nevertheless, even exfoliation from hundreds

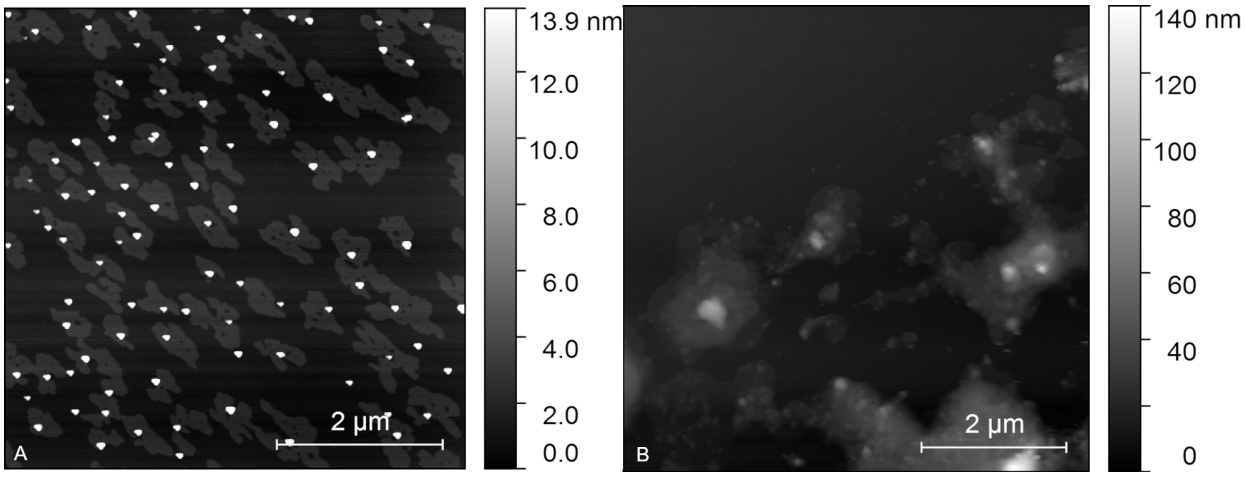

Figure 5: AFM pictures of exfoliated CaPhP: A) Particles successfully exfoliated into monolamellar sheets. B) Material destroyed by too long and too strong mixing.

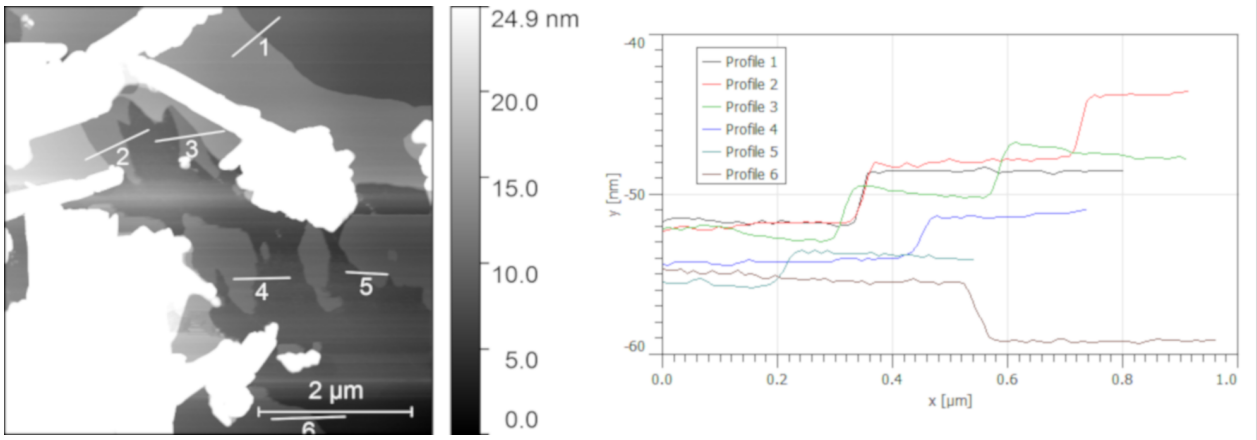

Figure 6: AFM topology scan of exfoliated CaPhP: monolamellar sheets (light gray areas), incompletely exfoliated particles (white areas) and line profiles (right) corresponding to the marked regions in the image to the left.

of layers to particles producing only 20–30 layers can significantly influence the behavior of the produced material when it is used as a polymer filler.

CaPhP as a filler in epoxy resin

Dispersion quality

To benefit from the filler properties, it is necessary to disperse the material well in the polymer matrix. The pristine calcium phenylphosphonate is able to form a stable and fine dispersion without visible agglomerates in the used CHS-EPOX 520 epoxy resin by a three roll milling, which is a standard polymer processing procedure in which high shear forces between rotating cylinders are used to break down the agglomerates. This dispersion is stable for months without sedimentation and visible changes. In the case of exfoliated lamellas, a nice dispersion without visible agglomerates was obtained even by mixing it with an ordinary dispersing disc. The particle distribution within the polymer matrix is homogenous and no large agglomerates are present. This is illustrated in pictures of the composite-free films obtained from the optical microscope and scanning electron microscope using a back-scattered electron detector to visualize the chemical contrast (Figure 7). This figure also reveals the difference between the unexfoliated filler (CaPhP_a) and the exfoliated nanoplatelets (CaPhP_exf). In both cases, the particles are homogenously dispersed in the whole volume of the matrix. However, in the case of the exfoliated filler (CaPhP_exf_0.5), significantly more individual particles can be detected than in the case of the unexfoliated filler (CaPhP_a_0.5).

This supports the idea that, in the case of the nanofiller, significantly less material is needed to produce the desired volume of filler. Of course, the nanoscale dimensions of the filler do not guarantee a proper particle distribution within the polymer matrix, and it is therefore also very important that the chemical nature of the particles and their compatibility with the polymer chains are also considered.

Interaction with the polymer blend components

Such good compatibility could be attributed to the hybrid character of the particles when the phenyl groups (as organic moieties) enhance interactions with the polymer chains in the polymer blend. As can be seen from the powder XRD patterns of the unexfoliated CaPhP particles in the free cured epoxy film (see Figure 8, CaPhP_a_5), the main reflection is shifted to smaller angles, which indicates an enlargement of the basal spacing up to 15.6 Å. To determine which component of the film influences the basal spacing of CaPhP, the X-ray diffraction patterns of CaPhP with amino groups containing curing and dispersing agents used in the preparation of the films were also measured. The amines used as curing agents (Jeffamines) enlarge the basal spacing from 15.05 Å to 15.45 Å (CaPhP_Jeff). The reaction of CaPhP with BYK 9076, which is used as a dispersing agent in the preparation of the composite film and is an alkyl ammonium salt of a high molecular weight copolymer, increases the basal spacing of CaPhP by 0.3 Å (CaPhP_BYK). On the contrary, the macromolecules of the epoxy resin alone do not cause enlargement of the basal spacing (CaPhP_epox). The values of the basal spacing are summarized in Table 1. The observed changes of the basal spacing in CaPhP_Jeff and CaPhP_BYK are small and most probably cannot be explained by penetration of the long-chain macromolecules of Jeffamines or BYK 9076 into the structure, as it was observed for short alkylamines in the previous studies [19,20]. More likely the macromolecules surround the particles and the present amine groups interact with the phenyl groups on the edge of the particles and prevent them from free movement. This leads to a slight rearrangement inside the layers and thus to

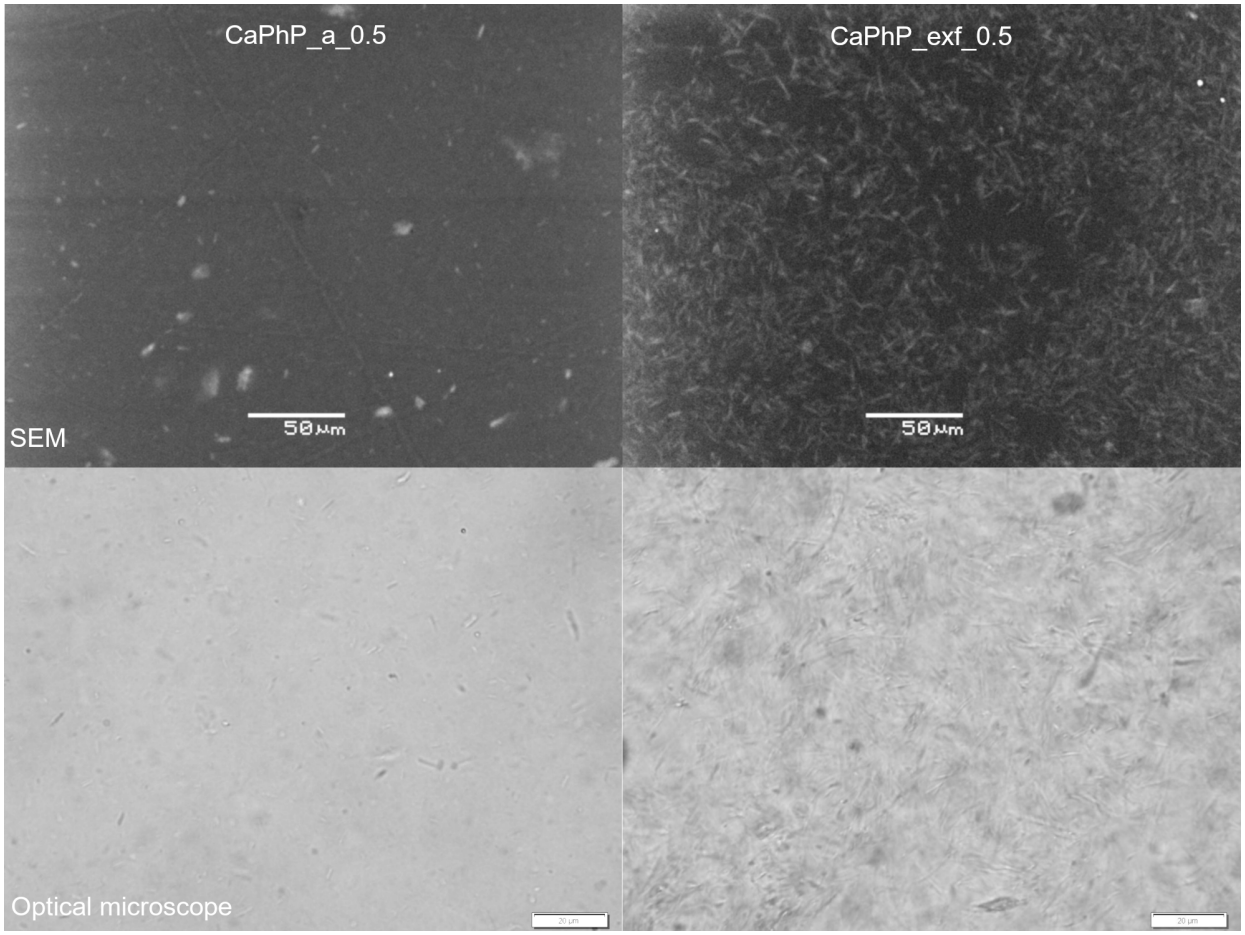

Figure 7: Pictures of the composite-free films with 0.5 wt % loading of the filler obtained from the scanning electron microscope and from the optical microscope. Scale bars in the optical microscope pictures are 20 µm.

a small increase of the basal spacing. The presence of the amino groups seems to be important because no change of the basal spacing was observed for the epoxy resin alone.

The filler particles in the films are highly preferably oriented, as follows from the much lower intensity of the main peak in the diffraction pattern measured in the transmission mode compared to that measured in the reflection mode. In the case of the exfoliated particles only a smaller enlargement was observed, if at all (for the XRD patterns of the exfoliated particles see Supporting Information File 1). As it was mentioned previously, the monolamellar particles form only a part of the filler after the exfoliation treatment, thus there are also incompletely exfoliated particles, containing up to 20 layers.

Dynamic mechanical properties

The effect of the exfoliation on the mechanical properties was studied by comparing the free films containing the same amount of the filler (0.5 wt %), both unexfoliated (CaPhP_a_0.5) and exfoliated (CaPhP_exf_0.5). In the temperature range from 0 °C to 45 °C the exfoliated particles increase the storage modulus compared to that of the pristine epoxy matrix, while the unexfoliated filler decreases it (see Figure 9). For the 0.5 wt % load, the glass transition temperature of the composite films is shifted to higher values compared to the pristine film. While the value of the loss modulus of the composite with unexfoliated CaPhP is roughly the same as for the pristine epoxy film, the loss modulus of the composite with exfoliated CaPhP is higher.

Barrier properties

The addition of thin but large particles can influence the barrier properties of polymer films. In the case of CaPhP, the permeability of the epoxy film with 5% CaPhP (CaPhP_ a_5) as a filler for H_2, CO_2, He and CH_4 was measured and the results were 21.02, 4.28, 13.55 and 4.85 Barrer, respectively (Table 2). This implies that the highest permeability was for H_2 and the smallest for CO_2. The addition of the filler increased the permeability for both these gases. In the case of hydrogen, it was

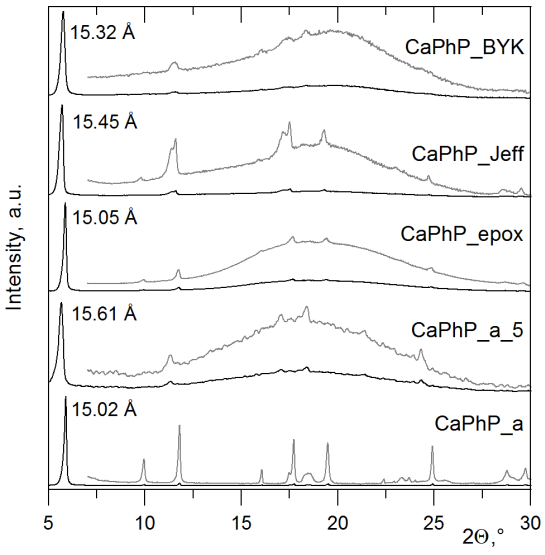

Figure 8: XRD patterns of original calcium phenylphosphonate (CaPhP_a), free film with 5 wt % of CaPhP as filler (CaPhP_a_5) and its blends with CHS-EPOX 520 (CaPhP_epox), curing agents Jeffamines (CaPhP_Jeff) and with dispersing agent BYK 9076 (CaPhP_BYK). The gray lines show the diffraction patterns with pronounced intensity of the peaks other than the (001) peak.

Table 1: Comparison of the basal spacings for calcium phenylphosphonate alone, as a filler in the free film and its mixtures with individual components of the polymer blend.

sample	basal spacing, Å
CaPhP_a	15.02
CaPhP_epox	15.05
CaPhP_Jeff	15.45
CaPhP_BYK	15.32
CaPhP_a_5	15.61

approximately four times higher and in the case of CO_2 even 5.6 times higher in comparison to the pristine epoxy film.

Flammability

Phosphorus containing compounds are used as flame retardant agents as an alternative to halogenated compound, which are effective but, on the other hand, they are considered to be hazardous for the environment and human health [21]. The structure of CaPhP contains a high amount of phosphorus as well as bound water molecules and seemed promising for this

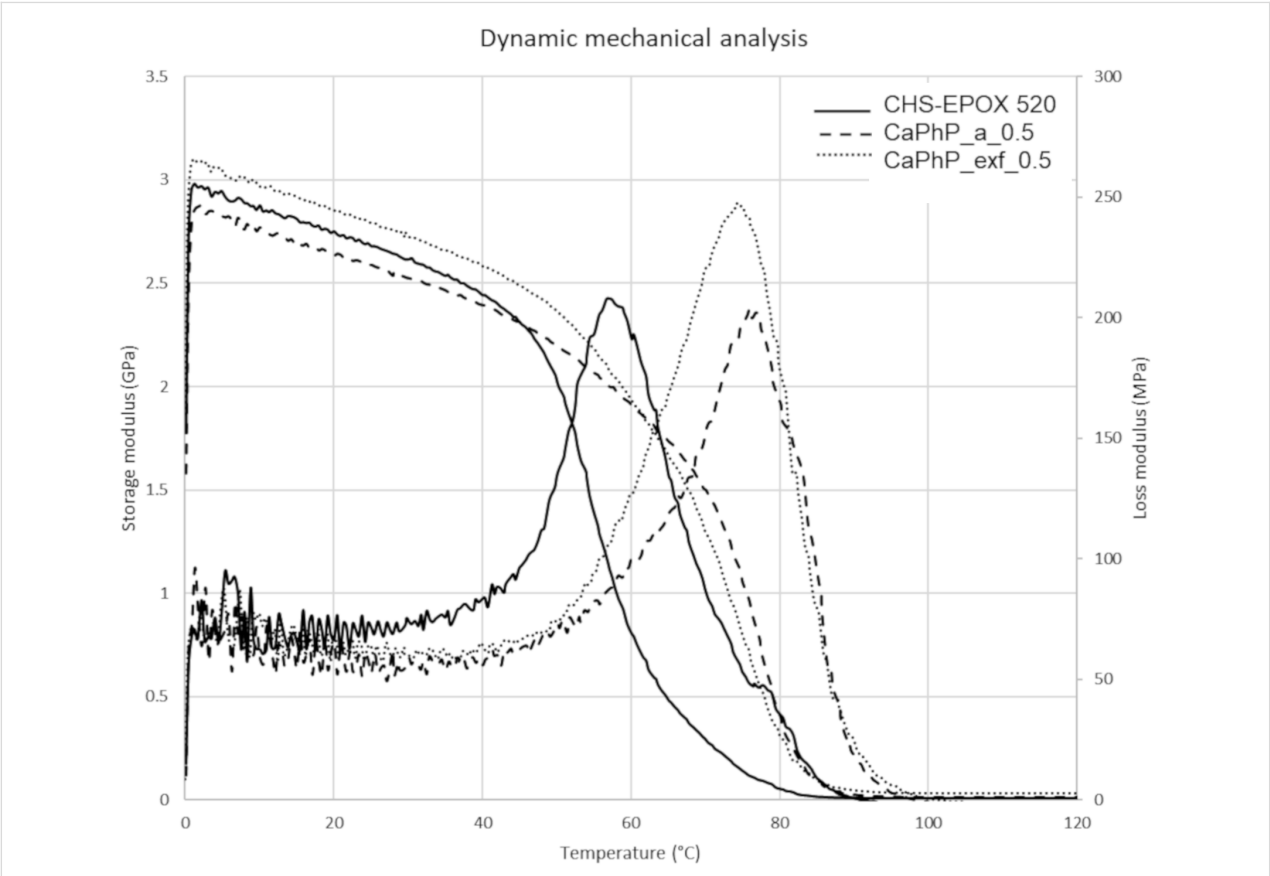

Figure 9: Storage and loss moduli measured by dynamic mechanical analysis for the pristine epoxy-free film (CHS-EPOX 520) and for free films loaded with 0.5 wt % of unexfoliated (CaPhP_a_0.5) and exfoliated (CaPhP_exf_0.5) filler.

Table 2: Results of gas permeability measurements. The permeability of pristine epoxy film for He and CH_4 were not measured.

	permeability (Barrer)			
sample	H_2	CO_2	He	CH_4
CaPhP_a_5	21.02	4.28	13.55	4.85
pristine epoxy film	5.01	0.76	–	–

kind of application. A composite containing 0.5 wt % of the filler was tested according to ISO 4589-2 and the limiting oxygen index was determined (LOI – the percentage of oxygen in atmosphere that the polymer specimen needs to burn). In the case of exfoliated particles, the system showed no improvement , whereas in the case of unexfoliated particles, there was a small increase in the LOI. Therefore, the system with 5 wt % of unexfoliated particles was tested. This amount of filler increased the LOI from 19 to 21. As 5% of the unexfoliated filler is usually the maximal content in order to maintain the mechanical properties of the polymer, it will not meet the criteria for the flame retardancy with CaPhP alone. However, even a small improvement could be useful in combination with other flame retardants. This feature will be further investigated.

Conclusion

The aim of this work was to study layered calcium phenylphosphonate, $CaC_6H_5PO_3{\cdot}2H_2O$, as a potential filler for an epoxy resin. This material was chosen as it can be incorporated into a polymer matrix not only as a bulk material but it can also be used as a precursor for the preparation of nanosheets by exfoliation and can thereby serve as a component of nanocomposites. The synthesis procedure was revised and the reaction conditions, under which this material can be prepared in a form suitable for exfoliation in a sufficient amount, were found. Furthermore, the conditions for the exfoliation of this compound were studied. The most suitable method for exfoliation was determined to be a treatment in alcohols, namely propan-2-ol, by an action of strong shear force generated by high-shear dispersers. It was found that this material is compatible with the epoxy resin used. The particle distribution in the polymer matrix was homogenous and CaPhP does not form agglomerates either in an unexfoliated or exfoliated form. It follows from the comparison of the composites with the same filler loading that the exfoliated particles have a higher impact on the composite properties, as determined by dynamic mechanical analysis. This is in agreement with the generally accepted idea that a higher surface-to-volume ratio leads to an enhanced interaction of nanoparticles with the surrounding polymer matrix. To conclude, this organic–inorganic hybrid material on its own is compatible with an epoxy resin and does not require any special treatment to be dispersed well in a polymer matrix. In the case of the exfoliated particles, the dispersion is even better. Thus, layered calcium phenylphosphonate can be considered as a promising nanofiller for polymer composites.

Experimental

Materials and methods

Phenylphosphonic acid (PhP), calcium chloride ($CaCl_2$), ammonia solution, propan-2-ol (all Sigma-Aldrich); CHS-EPOXY 520 (Spolchemie, a. s., Czech Republic) – a low molecular weight epoxy resin based on bisphenol A; Jeffamine D230 and Jeffamine D2000 (Huntsman International LLC) – polyether amines were used. BYK 9076 – an alkylammonium salt of a high molecular weight copolymer and BYK 066 and a solution of foam-destroying polysiloxanes (both BYK-CHEMIE GMBH, Germany) were also used. All chemicals were used as obtained.

The characterization of the samples was performed using the following techniques and devices. The topological profile of the particles was measured by AFM with a Dimension ICON instrument, Bruker, Germany, in peak force mode with a ScanAsyst tip. The dynamic mechanical properties were measured with a Discovery hybrid rheometer, DHR2, TA Instruments. The experiment was performed in tension mode with a deformation of 0.1% and frequency of 1 Hz. The heating rate was set to 3 °C/min. Pictures of the free films were obtained from an Olympus BX51 optical microscope equipped with a DP70 digital camera system in addition to a JEOL SEM JSM-55000 LV with an EDX detector (GRESHAM Sirius 10, JEOL, USA Inc.) with an acceleration voltage of 20 kV. Powder X-ray diffraction data were obtained with a D8-Advance diffractometer, Bruker, Germany, with a Bragg–Brentano θ–θ geometry and with an EMPYREAN diffractometer, PANalytical, Netherlands (in both cases using Cu Kα radiation). The barrier properties for gas permeation were measured at 25 °C for free film samples of area 2 cm^2. The limiting oxygen index was evaluated according to ISO 4589-2.

Synthesis of calcium phenylphosphonate (CaPhP)

First, phenylphosphonic acid (7.9 g, 5×10^{-2} mol) was dissolved in 100 mL and a pH of the obtained solution was adjusted to 9 by adding concentrated aqueous ammonia solution. Then, 50 mL of $CaCl_2$ solution (5.5 g, 5×10^{-2} mol) was added: a) at once (sample denoted as CaPhP_a); b) "drop by drop" (CaPhP_d); and c) in several portions (CaPhP_s). A white precipitate was formed immediately in all cases. Then, the reaction mixture was diluted by 50 mL of distilled water and stirred at medium speed (≈250 rpm) for 30 minutes. The precipitate

formed was collected by filtration, washed with water until neutral pH to remove the remaining ammonia, and dried at room temperature. To obtain a fine powder it was possible to grind dried material in a friction bowl.

Exfoliation of CaPhP

Solvent selection

A sample of CaPhP_a (10–13 mg) was put into a small glass vial to which 5 mL of a solvent (distilled water, propan-2-ol, ethanol, butanol, acetone) was added. The mixture was sonicated in an ultrasound bath (f = 37 kHz) for one hour and the temperature of the bath was cooled by adding ice. The quality and stability of the resulting dispersion was visually observed and photographs were taken immediately, 1 h, and 24 h after the ultrasound treatment. The presence of nanoparticles in dispersion after 24 h was confirmed by Tyndall scattering using a green laser (λ = 532 nm).

Preparation of stock dispersion of exfoliated particles

CaPhP_a (1.5 g, dry fine powder) was dispersed in 300 mL of propan-2-ol (c = 5 g/L). This dispersion was treated using an IKA T10 Standard Ultra-turrax® (a high-shear force disperser, IKA®-Werke GmbH & Co. KG, Germany) equipped with a dispergation tool (S 10 D-7 G-KS-65) for 5 minutes at 13,000 rpm. A mixture of fully and partly exfoliated particles was obtained and denoted as CaPhP_exf.

Preparation of polymer blends

Unexfoliated particles

First, 90 g of CHS-EPOXY 520 was heated to 80 °C and the dispersant BYK 9076 (9.5 g) was added and mixed with the polymer matrix using a dispersing disc. Then a fine powder of CaPhP_a (10 g) was added in small portions. The whole blend was mixed at 350 rpm 4 hours. After cooling down, the mixture was processed by a three-roll mill ten times with a 5 μm width of the slot between the rotating cylinders and rotation speed of 200 rpm. This polymer paste was used as a stock dispersion; from that, 10 g samples with a filler concentration of 0.5, 1, 3 and 5 wt % (denoted as CaPhP_a_0.5 to CaPhP_a_5, where the number indicates the amount of the filler added) were prepared by diluting with pristine CHS-EPOXY 520. Finally, a BYK 066 defoaming agent (0.05 g) was added under careful stirring with a glass stick into each sample.

Exfoliated particles

The dispersion of CaPhP_exf in an amount corresponding to 0.05, 0.1, 0.3 and 0.5 wt % was added to CHS-EPOXY 520 (10 g). The mixture was stirred with a dispersive disc and heated to 80 °C until most of the propan-2-ol was evaporated. Then the BYK 066 defoaming agent (0.05 g) was added into each sample under stirring with a glass stick. The samples were denoted as CaPhP_exf_0.05 to CaPhP_exf_0.5, where the number indicates the weight percentage of CaPhP_exf in the final product.

Preparation of free films

Prepared dispersions with the exfoliated and unexfoliated fillers were thoroughly mixed by hand with a mixture of curing agents (3.1 g of Jeffamine D230 and 0.78 g of Jeffamine D2000) and defoamed in a desiccator for a few minutes. Then the free films were prepared on polypropylene plates using a 150 μm gap applicator. The films were cured for one day at a room temperature and then for 1 h at 40 °C, 4 hours at 60 °C and finally 20 h at 80 °C. The cured films were collected from the supporting plates with the help of a razor blade.

Supporting Information

Supporting Information File 1

XRD patterns of exfoliated sample CaPhP_exf and XRD pattern of free film with exfoliated filler CaPhP_exf_0.5.
The XRD patterns of exfoliated sample CaPhP_exf prepared by spin coating on the glass support (A) and XRD pattern of free film with exfoliated filler CaPhP_exf_0.5 (B).
[https://www.beilstein-journals.org/bjnano/content/supplementary/2190-4286-9-269-S1.png]

Acknowledgements

This work was supported by the Technology Agency of the Czech Republic (project No. TH02020201).

ORCID® iDs

Vítězslav Zima - https://orcid.org/0000-0002-2456-2628
Petr Knotek - https://orcid.org/0000-0003-2407-4947

References

1. Pavlidou, S.; Papaspyrides, C. D. *Prog. Polym. Sci.* **2008,** *33,* 1119–1198. doi:10.1016/j.progpolymsci.2008.07.008
2. Paul, D. R.; Robeson, L. M. *Polymer* **2008,** *49,* 3187–3204. doi:10.1016/j.polymer.2008.04.017
3. He, H.; Tao, Q.; Zhu, J.; Yuan, P.; Shen, W.; Yang, S. *Appl. Clay Sci.* **2013,** *71,* 15–20. doi:10.1016/j.clay.2012.09.028
4. He, H.; Ma, L.; Zhu, J.; Frost, R. L.; Theng, B. K. G.; Bergaya, F. *Appl. Clay Sci.* **2014,** *100,* 22–28. doi:10.1016/j.clay.2014.02.008
5. Kotal, M.; Bhowmick, A. K. *Prog. Polym. Sci.* **2015,** *51,* 127–187. doi:10.1016/j.progpolymsci.2015.10.001
6. Cao, G.; Lee, H.; Lynch, V. M.; Mallouk, T. E. *Inorg. Chem.* **1988,** *27,* 2781–2785. doi:10.1021/ic00289a008
7. Mahmoudkhani, A. H.; Langer, V. *Solid State Sci.* **2001,** *3,* 519–525. doi:10.1016/s1293-2558(01)01161-x

8. Mahmoudkhani, A. H.; Langer, V.; Smrcok, L. *Solid State Sci.* **2002,** *4,* 873–878. doi:10.1016/s1293-2558(02)01294-3
9. Melánová, K.; Beneš, L.; Svoboda, J.; Zima, V.; Pospíšil, M.; Kovář, P. *Dalton Trans.* **2018,** *47,* 2867–2880. doi:10.1039/c7dt03728g
10. Yi, M.; Shen, Z. *J. Mater. Chem. A* **2015,** *3,* 11700–11715. doi:10.1039/c5ta00252d
11. Coleman, J. N. *Adv. Funct. Mater.* **2009,** *19,* 3680–3695. doi:10.1002/adfm.200901640
12. Nicolosi, V.; Chhowalla, M.; Kanatzidis, M. G.; Strano, M. S.; Coleman, J. N. *Science* **2013,** *340,* 1420–1439. doi:10.1126/science.1226419
13. Niu, L.; Coleman, J. N.; Zhang, H.; Shin, H.; Chhowalla, M.; Zheng, Z. *Small* **2016,** *12,* 272–293. doi:10.1002/smll.201502207
14. Coleman, J. N.; Lotya, M.; O'Neill, A.; Bergin, S. D.; King, P. J.; Khan, U.; Young, K.; Gaucher, A.; De, S.; Smith, R. J.; Shvets, I. V.; Arora, S. K.; Stanton, G.; Kim, H.-Y.; Lee, K.; Kim, G. T.; Duesberg, G. S.; Hallam, T.; Boland, J. J.; Wang, J. J.; Donegan, J. F.; Grunlan, J. C.; Moriarty, G.; Shmeliov, A.; Nicholls, R. J.; Perkins, J. M.; Grieveson, E. M.; Theuwissen, K.; McComb, D. W.; Nellist, P. D.; Nicolosi, V. *Science* **2011,** *331,* 568–571. doi:10.1126/science.1194975
15. Backes, C.; Higgins, T. M.; Kelly, A.; Boland, C.; Harvey, A.; Hanlon, D.; Coleman, J. N. *Chem. Mater.* **2016,** *29,* 243–255. doi:10.1021/acs.chemmater.6b03335
16. May, C. A. *Epoxy Resins Chemistry and Technology,* 2nd ed.; CRC Press, 1987.
17. Jin, F.-L.; Li, X.; Park, S.-J. *J. Ind. Eng. Chem.* **2015,** *29,* 1–11. doi:10.1016/j.jiec.2015.03.026
18. Svoboda, J.; Zima, V.; Beneš, L.; Melánová, K.; Vlček, M. *Inorg. Chem.* **2005,** *44,* 9968–9976. doi:10.1021/ic051606x
19. Beneš, L.; Melánová, K.; Svoboda, J.; Zima, V. *J. Inclusion Phenom. Macrocyclic Chem.* **2010,** *66,* 279–284. doi:10.1007/s10847-009-9614-x
20. Zima, V.; Svoboda, J.; Beneš, L.; Melánová, K.; Trchová, M. *Solid State Sci.* **2006,** *8,* 1380–1385. doi:10.1016/j.solidstatesciences.2006.07.009
21. Morgan, A. B.; Wilkie,, C. A. *The Non-halogenated Flame Retardant Handbook;* Wiley, 2014.

License and Terms

BEILSTEIN JOURNAL OF NANOTECHNOLOGY

Ternary nanocomposites of reduced graphene oxide, polyaniline and hexaniobate: hierarchical architecture and high polaron formation

Claudio H. B. Silva[*1,2,3], Maria Iliut[2], Christopher Muryn[4], Christian Berger[2], Zachary Coldrick[5], Vera R. L. Constantino[1], Marcia L. A. Temperini[1] and Aravind Vijayaraghavan[2]

Full Research Paper

Open Access

Address:
[1]Department of Fundamental Chemistry, Institute of Chemistry, University of São Paulo, Av. Prof. Lineu Prestes 748, São Paulo 05508-000, Brazil, [2]School of Materials and National Graphene Institute, The University of Manchester, Booth St E, Manchester M13 9PL, United Kingdom, [3]present address: Department of Physical Chemistry, Institute of Chemistry, Federal University of Bahia, Rua Barão de Jeremoabo, 147, Salvador 40170-115, Brazil, [4]School of Chemistry and Photon Science Institute, The University of Manchester, Alan Turing Building, Oxford Rd, Manchester M13 9PY, United Kingdom and [5]School of Electrical and Electronic Engineering, The University of Manchester, Sackville Street Building, Manchester M1 3BB, United Kingdom

Email:
Claudio H. B. Silva[*] - chbsilva@ufba.br

* Corresponding author

Keywords:
graphene oxide; hexaniobate; polyaniline; Raman spectroscopy; secondary doping

Beilstein J. Nanotechnol. **2018,** *9,* 2936–2946.
doi:10.3762/bjnano.9.272

Received: 16 August 2018
Accepted: 30 October 2018
Published: 26 November 2018

This article is part of the thematic issue "Advanced hybrid nanomaterials".

Guest Editor: F. Leroux

Abstract

Nanostructured systems, such as nanocomposites, are potential materials for usage in different fields since synergistic effects of their components at the nanoscale domain may improve physical/chemical properties when compared to individual phases. We report here the preparation and characterisation of a new nanocomposite composed of polyaniline (PANI), reduced graphene oxide (rGO) and hexaniobate (hexNb) nanoscrolls. Atomic force microscopy images show an interesting architecture of rGO flakes coated with PANI and decorated by hexNb. Such features are attributed to the high stability of the rGO flakes prepared at room temperature. Detailed characterisation by X-ray photoelectron and Raman spectroscopies indicates an intermediate reduction degree for the rGO component and high doping degree of the PANI chains compared to the neat polymer. The latter feature can be attributed to cooperative effects of PANI chains with rGO flakes and hexNb nanoscrolls, which promote conformational changes of the polymer backbone (secondary doping). Spectroscopic and electrochemistry data indicate a synergetic effect on the ternary nanocomposite, which is attributed to interactions between the components resulting from the morphological aspects. Therefore, the new

nanocomposite presents promising properties for development of new materials in the film form on substrates for sensing or corrosion protection for example.

Introduction

Nanostructured systems, such as nanocomposites, are potential materials for usage as electrochemical (bio)sensors for analytical purposes, electronics, energy storage devices and corrosion protection because the synergistic effects of their components at the nanoscale range may improve physical/chemical properties when compared to individual phases or enable new technological applications [1-3]. For instance, ternary nanocomposites (conducting polymers, metal oxides and carbon-based materials) exhibit improved energy and power densities, improved stabilities upon charge/discharge cycles [4], and higher electrocatalytic activity in the quantification of chemical species compared to the isolated components [5].

In earlier studies, some of us reported the preparation of binary nanocomposites of polyaniline (PANI) and hexaniobate (hexNb) nanoscrolls by layer-by-layer assembly and the characterisation by spectroscopic and cyclic voltammetry/spectroelectrochemical techniques [6]. The inorganic phase induces a secondary doping of the conductor polymer. In another work [7], Raman and EPR spectra also revealed that a PANI/hexNb nanocomposite prepared by the self-assembly approach exhibits a higher conversion of bipolaronic to polaronic segments compared to the neat polymer and a superior thermal stability (the doped form of PANI is observed even after heating at 150 °C for 90 min).

The literature has shown that PANI and reduced graphene oxide (rGO) show enhanced properties when combined at the nanoscale domain and applied, for instance, as supercapacitors, sensing materials, solar cells, electrochromic devices, anticorrosion coatings or as materials for carbon dioxide capture [8]. The layered inorganic phase offers a high surface area for PANI deposition and increases its thermal stability with regard to decomposition, which is assigned to strong interactions between the two components [8]. Besides, rGO presents defects and functional groups on its surfaces that are sites for catalysis or sorption of substrates [9]. Considering the confirmed synergistic effects of PANI/hexNb and PANI/rGO binary nanocomposites, materials comprising all three components can be expected to show improved properties.

Since its discovery in 2004, graphene has been proposed for a wide range of applications due to its supreme values of specific surface area, electronic mobility, thermal and electrical conductivities and elastic modulus [10,11]. Graphene oxide (GO) is a graphene derivative that has also attracted great scientific interest due to its better processability and scalable production in comparison with pristine graphene [12]. The great chemical versatility of GO is mostly attributed to its complex structure, composed of 2D carbon layers with several oxygen-containing groups, such as hydroxy, epoxy, carbonyl and carboxyl, as schematically shown in Figure 1a [12,13]. Moreover, stable aqueous dispersions containing large GO flakes (above 20 μm) can be prepared [14]. For some applications, the restoration of the hexagonal carbon lattice (removal of functional groups) may be required and this process is performed by thermal or chemical reduction of GO, resulting in reduced graphene oxide (rGO) in which some of the properties of graphene are almost recovered, such as mechanical resistance and thermal and electrical conductivities [15-17].

Polyaniline (PANI) is a conducting polymer that has shown promising properties for the development of materials for different fields such as chemical sensing [18,19], memory devices [20,21] and energy storage [22,23]. As schematically shown in Figure 1b, the conducting form of PANI, the emeraldine salt (PANI-ES) contains two species: unpaired spin segments, the polarons (also known as radical cations); and paired spin segments, the bipolarons (also known as dications) [24,25]. The combination of PANI and inorganic materials at the nanoscale has shown interesting results for the preparation of nanocomposites that exhibit improved electrochemical, mechanical or thermal behaviour [8,26,27].

Hexaniobate (hexNb) is a semiconducting metal oxide composed of negatively charged layers of $[NbO_6]$ octahedral units and interlayer cations, such as potassium ions (precursor form $K_4Nb_6O_{17}$) and protons (acidic form $H_2K_2Nb_6O_{17}$) [28,29]. Due to their high acidic surfaces, protonic niobates and titanoniobates have been reported as promising solid acid catalysts for various chemical reactions [30,31]. Moreover, hexaniobate can be exfoliated by treatment with a number of species such as *n*-alkylamines and tetra(*n*-alkyl)ammonium hydroxides, giving rise to colloidal dispersions of nanoparticles of different morphologies such as nanosheets and nanoscrolls [32,33]. As reported previously [6], the treatment of $H_2K_2Nb_6O_{17}$ with tetra(*n*-butyl)ammonium hydroxide (TBAOH) is an efficient method to produce dispersions of protonic hexNb nanoscrolls (schematised in Figure 1c). Moreover, strong interactions of PANI chains with acidic surfaces of $H_2K_2Nb_6O_{17}$ may dramati-

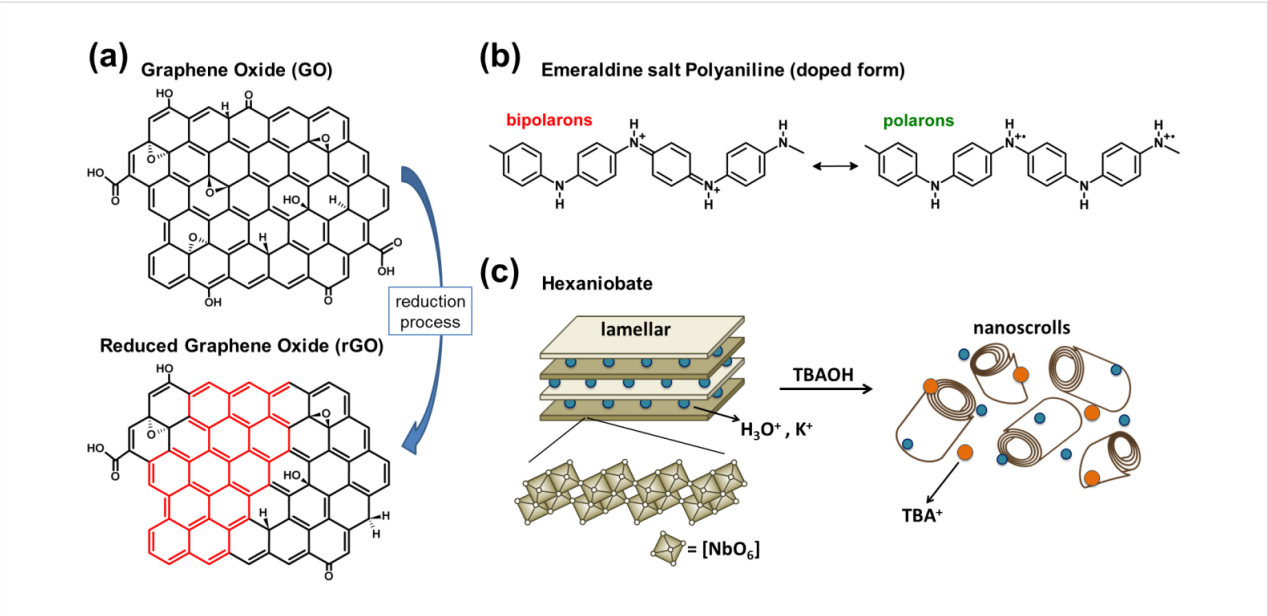

Figure 1: Schematic representation of (a) graphene oxide and reduced graphene oxide structures, (b) polaron and bipolaron segments of emeraldine salt polyaniline (doped form), and (c) hexaniobate in layered and nanoscroll morphologies. TBAOH: tetra(*n*-butyl)ammonium hydroxide, TBA^+: tetra(*n*-butyl)ammonium cation.

cally affect the doping state of the polymeric chains [6,7], which is an interesting feature regarding applications of PANI-based materials.

In this paper we report the development of a new nanocomposite, with interesting nanostructured features, composed of reduced graphene oxide, polyaniline and hexaniobate, as well as its spectroscopic and textural characterisation.

Results and Discussion

GO reduction at high temperatures (typically above 90 °C) results in the aggregation of the material due to restacking of the hydrophobic rGO layers [34,35]. This is a drawback in the preparation of rGO nanocomposites because phase segregation and/or composition heterogeneity will occur in the final materials. Although it is well known that high reaction temperatures are important for the degree of reduction of the resulting rGO, samples prepared at room temperature (25 °C) using longer reaction times (7 days) may present satisfactory properties for nanocomposites. To obtain stable mixture of the components and optimize the interaction between them, graphene oxide reduction was performed at diluted conditions with hydrazine at low temperature (see Experimental section). The resulting dispersions of rGO-25 and rGO/PANI nanocomposites are remarkably stable (see Supporting Information File 1), more so than sample rGO-80. This indicates that the nanocomposites may exhibit low compositional heterogeneity and possibly strong interactions (such as electrostatic and π–π interactions) between their components.

The morphological characterisation of rGO-25, rGO/PANI and rGO/PANI/hexNb samples was carried out by atomic force microscopy, as shown in Figure 2. AFM images of the rGO-25 sample show particles of well-defined edges and size ranging from 5 to 25 µm. The height profile (Figure 2, right column) shows thickness of ca. 1.0 nm and a surface roughness (RMS) of 0.24 nm for the rGO flake. These results clearly indicate the presence of smooth monolayer rGO particles, which are partially restacked when deposited on the Si/SiO_2 substrate. The AFM images of the rGO/PANI nanocomposite show similar flake dimensions (ca. 25 µm) as the rGO-25 sample, and no granular particles were observed, as reported for PANI aggregates [36]. On the other hand, this nanocomposite presents several creases and folds and, more interestingly, shows higher flake thickness and higher surface roughness (ca. 10 and ca. 4.0 nm, respectively). These results clearly indicate that the deposition of PANI on rGO flakes induces an increase of the surface heterogeneity. Analogously, the AFM images of rGO/PANI/hexNb also indicate the presence of large flakes in the nanocomposite and, as shown by the 5 µm scan-size image (and corresponding height profile), the flake thickness and surface roughness are ca. 19 and ca. 7.2 nm, respectively. These results clearly indicate that the surface heterogeneity of the ternary nanocomposite is even higher than that of rGO/PANI, probably due to the presence of hexaniobate nanoparticles (nanoscrolls) on the rGO/PANI flakes.

For further description of the rGO/PANI/hexNb nanocomposite morphology, Figure 3 presents the AFM image of the hybrid

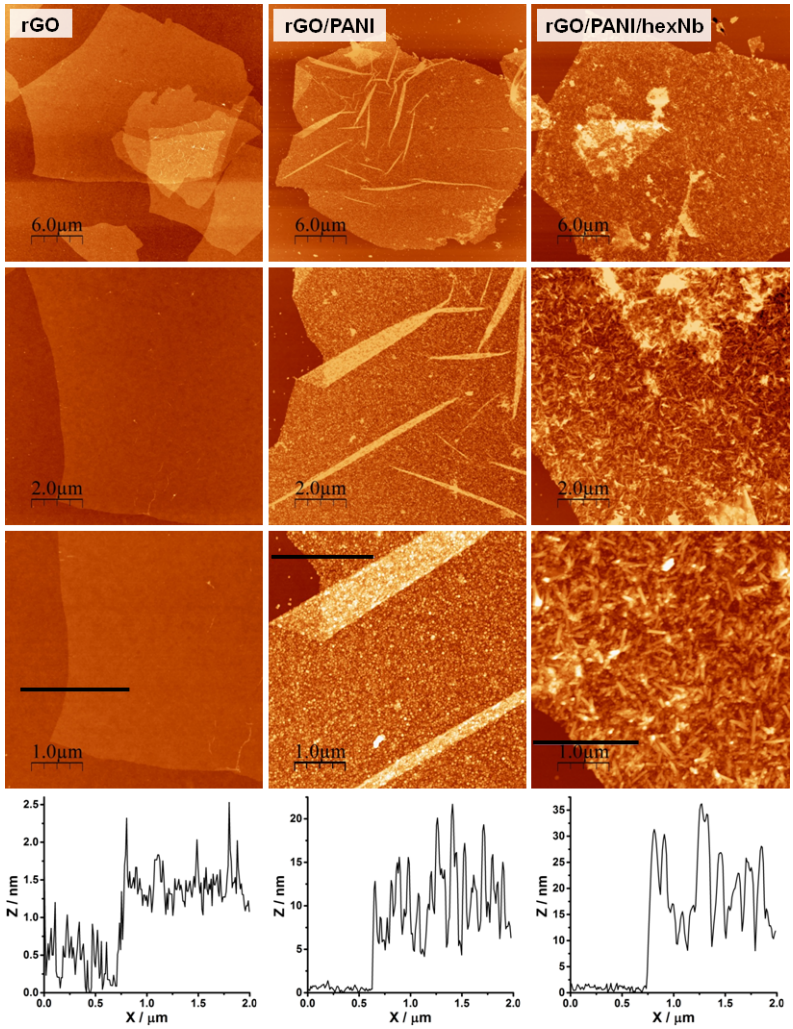

Figure 2: AFM images of rGO-25 sample, and rGO/PANI and rGO/PANI/hexNb nanocomposites at different scan sizes (30, 10 and 5 μm), and height profiles (for the 5 μm scan size images).

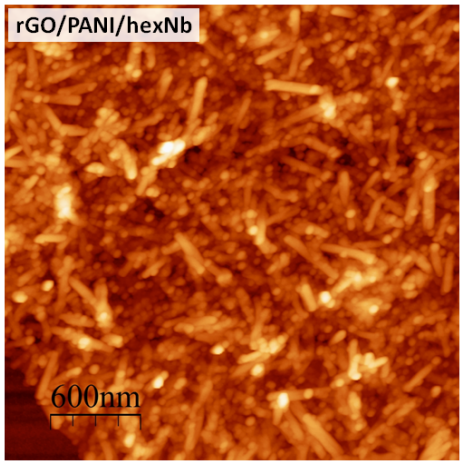

Figure 3: AFM images of rGO/PANI/hexNb nanocomposite at 3 μm scan size.

material at 3 μm scan size. Figure 3 shows that the particles on the surface of rGO/PANI/hexNb exhibit a scroll-like shape (high aspect ratio), which is very similar to well-described hexNb nanoscrolls [7,37,38]. These results show the interesting hierarchical architecture of the ternary nanocomposite of rGO flakes coated with PANI and decorated by hexNb nanoscrolls.

To analyse the reduction of graphene oxide under the present conditions, GO and rGO samples were characterised by XPS spectroscopy. High-resolution XPS spectra can also provide information on the reduction degree of GO, since C 1s core level photoelectrons present slightly different binding energies depending on the environment of the carbon atoms. Figure 4 shows the high-resolution XPS spectra at the C 1s core level for GO and rGO samples prepared by reactions at 25 °C for 7 days and at 80 °C for 3 h (rGO-25 and rGO-80, respectively). XPS spectra of GO and rGO-25 consist mainly of two asymmetric

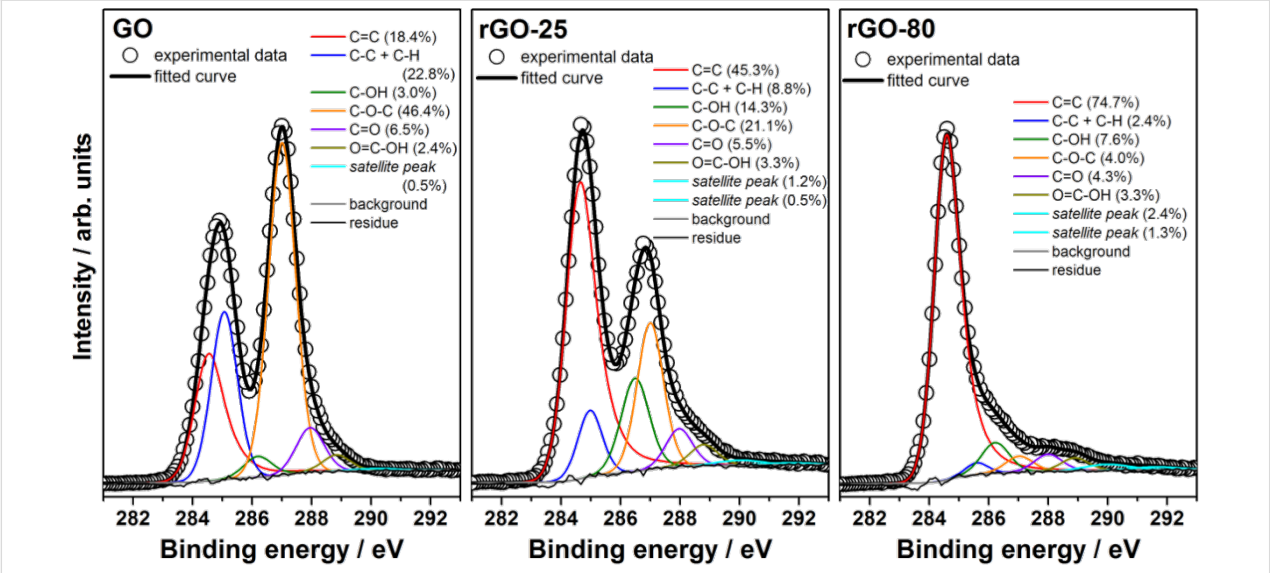

Figure 4: XPS spectra at the C 1s core level of GO and rGO samples prepared by reactions at 25 °C for 7 days or at 80 °C for 3 h (rGO-25 and rGO-80, respectively).

and highly overlapping peaks (maxima at ca. 285 and ca. 287 eV). The comparison of these spectra clearly shows the increase of relative intensity of the low-binding energy peak upon reduction. This is attributed to the partial recovery of the sp^2-hybridized carbons in the graphene structure, since pristine graphite presents only an asymmetric peak at ca. 284 eV (carbon atoms in sp^2 environment) [39-41]. The curve fitting of the C 1s spectra, also presented in Figure 4, can provide detailed information on the oxygen-containing groups, since these groups induce different environments for the carbon atoms and, consequently, their corresponding C 1s photoelectrons present slightly different binding energies [34,39,40,42-51]. The comparison of the curve fitting for GO and rGO-25 shows the increase of the contribution from sp^2 carbons (C=C) and hydroxy groups (C–OH) upon reduction, and the decrease of sp^3 carbons (C–C + C–H) and epoxy groups (C–O–C). These results are in good agreement with the literature and indicate the recovery of the sp^2 carbon atoms from the sp^3 carbon atoms and epoxy groups, and the conversion of some epoxy to hydroxy groups [28,45,46,48]. In contrast, rGO-80 presents a dramatic change in the C 1s spectral profile, evidenced by an intense peak at ca. 284 eV and a weak shoulder at 285–290 eV. The comparison of the curve fitting for this sample and rGO-25 shows a significant increase of the contribution from the sp^2 carbon atoms and decrease of the contribution from sp^3 carbon atoms, hydroxy and epoxy groups. These features are very similar to data reported in literature for chemically reduced GO [34,39,42-51] and indicate a high degree of reduction of the rGO-80 sample. This also points out the very important role of the temperature on the recovery of the sp^2 carbon network in graphene oxide.

Analogously to C 1s, XPS spectra at the N 1s core level can be discussed in detail and provide interesting structural information on the rGO/PANI and rGO/PANI/hexNb nanocomposites. In the present study, the N 1s peaks are mostly from nitrogen-containing groups of PANI, the amine, imine or charged nitrogen sites (from polarons or bipolarons) of the polymeric chains [52-55]. Therefore, XPS spectroscopy provides important information on the oxidation and doping states of the polymer in PANI-based materials. Figure 5 shows XPS spectra at the N 1s core level of PANI and rGO/PANI and rGO/PANI/hexNb nanocomposites, and the respective curve fitting results. The N 1s peak of PANI-based materials is dominated by an amine (–NH–)-related component at ca. 399 eV, but also shows components of quinone (=N–), polaron ($–N^{•+}H–$) and bipolaron ($=N^{+}H–$) groups at ca. 398, ca. 401 and ca. 402 eV, respectively. The comparison of spectral data for PANI and rGO/PANI in Figure 5 shows that the relative contributions of polarons and bipolarons are higher in the nanocomposite. These results indicate that PANI chains present a higher doping state in the presence of rGO flakes. XPS data for the rGO/PANI/hexNb nanocomposite clearly shows a significant increase in the relative intensity of the peak with higher biding energy, attributed to polarons and bipolarons. Fitting results show that relative contributions of polarons increase from 18.3% in PANI and 23.0% in rGO/PANI to 34.0% in the ternary nanocomposite. Also, relative contributions of bipolarons increase from 7.1% in PANI and 8.6% in rGO/PANI to 11.3% in the rGO/PANI/hexNb nanocomposite. These results clearly indicate that hexNb nanoparticles also play an important role to the increase of the doping state of PANI. More interestingly, fitting results indicate that the ratio between polarons and bipolarons is higher for

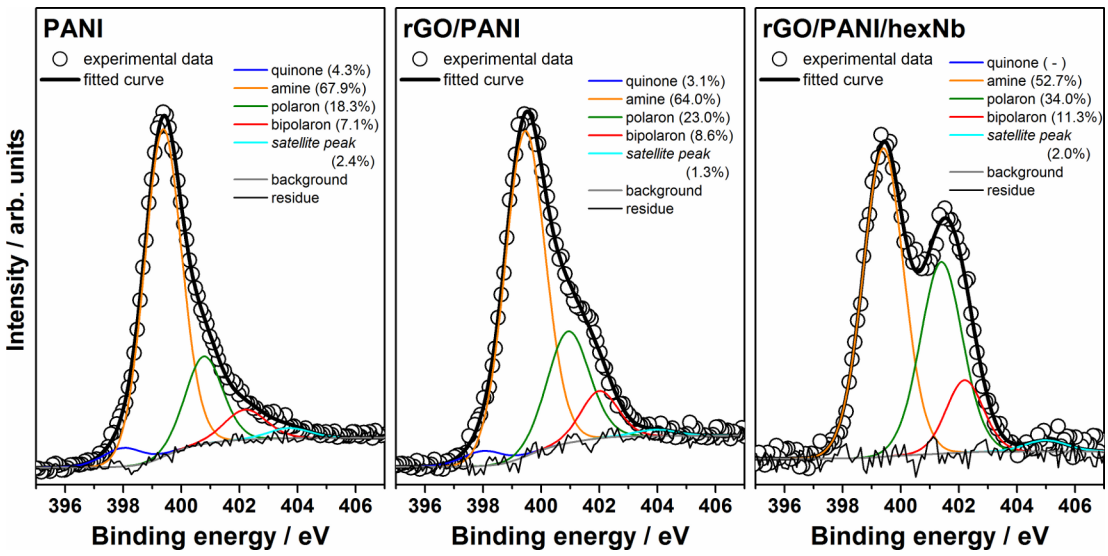

Figure 5: XPS spectra at N 1s core level of PANI and nanocomposites rGO/PANI and rGO/PANI/hexNb.

the ternary nanocomposite (polaron/bipolaron = 3.0), compared to PANI (2.6) and the binary nanocomposite (2.7). This indicates that the formation of polaron segments in the PANI chains is further induced by the interaction with rGO and hexNb components. This behaviour of high polaron formation induced by hexNb nanoparticles has been reported by us before [7]. The results of XPS spectra at N 1s core level are supported by resonance Raman spectroscopy, as shown below.

The structural characterisation of PANI in the nanocomposites was also performed by Raman spectroscopy, as presented in Figure 6. Raman bands in the spectra of rGO/PANI and rGO/PANI/hexNb at 632.8 nm excitation wavelength are mainly attributed to the polymer due to resonance effects with the polaronic/bipolaronic electronic transitions of PANI, and the high content of polymer in these materials [55-58]. The spectra presented in Figure 6a show the characteristic features of the emeraldine salt form (doped polymer) for all samples. However, comparing the spectra of the nanocomposites with the neat polymer (PANI), the bands at ca. 1336 and ca. 1600 cm^{-1} for the hybrid materials present higher relative intensities. These results can be attributed to the contribution of rGO bands [35,36,45,46,48,50,51,59,60], and changes in the doping state of the polymer due to interaction with the other components.

Figure 6b presents the curve fitting results in the range of 1450–1550 cm^{-1}. The component at lower wavenumber (red curve) is assigned to bipolaron segments, whereas the component at higher wavenumber (green curve) is assigned to polaron segments. The comparison of the results for PANI and rGO/PANI shows the increase of the relative intensity of the polaron

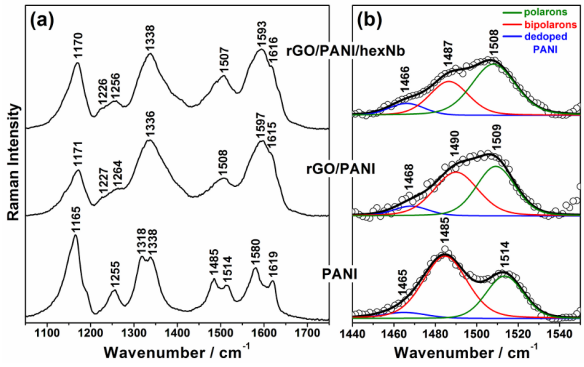

Figure 6: (a) Raman spectra (λ_0 = 632.8 nm) of PANI, rGO/PANI and rGO/PANI/hexNb in the range of 1050–1750 cm^{-1} and (b) curve fitting for bipolaron and polaron components in the range of 1440–1550 cm^{-1}.

component, which indicates a conversion of bipolarons to polarons in the presence of the rGO flakes. Moreover, Figure 6b shows that the relative contribution from the polaron segments is further increased for the rGO/PANI/hexNb sample, which suggests a higher formation of polarons induced by hexNb nanoparticles. These results are in agreement with XPS data previously discussed and reports of spectroscopic characterisation of PANI-based materials [6,7,26,61], which suggested a high doping level of PANI induced by conformational changes in the polymeric backbone.

Figure 7 presents the CV curves obtained for PANI, rGO, rGO/PANI, PANI/hexNb and rGO/PANI/hexNb in 1 $mol \cdot L^{-1}$

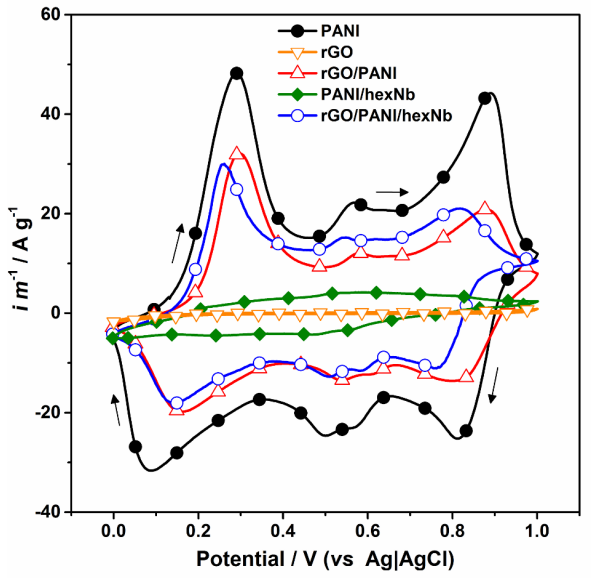

Figure 7: CV curves of PANI, rGO, rGO/PANI , PANI/hexNb and rGO/PANI/hexNb at 25 mV·s^{-1} scan rate. Electrolyte solution: 1 mol·L^{-1} sulfuric acid.

sulfuric acid solution. For PANI sample and nanocomposites, Figure 7 shows the characteristic redox peaks at ca. +0.30 V (+0.10 V), attributed to the oxidation (reduction) processes between leucoemeraldine and emeraldine salt states, and the peaks at potentials above +0.75 V attributed to the transitions between emeraldine salt and pernigraniline states [62-64]. The peaks at intermediate potentials (between +0.40 and +0.70 V) are attributed to oxidative electrochemical reactions initiated when PANI is cycled at higher potentials than +0.70 V. The CV curve for rGO sample confirms the absence of significant faradaic processes due to a very low current profile. For the PANI/hexNb reference sample, the CV curve presents less defined oxidation (reduction) peaks at +0.20 V (+0.25 V) and +0.80 V (+0.75 V), in addition to intermediate peaks in the range of +0.40–0.60 V. This low current potentiodynamic profile is attributed to the absence of faradaic processes in the hexaniobate component, which also affects polyaniline redox processes under the experimental conditions. The comparison of the curves of rGO/PANI and rGO/PANI/hexNb in Figure 7 indicates similar areas, although neat PANI still presents the highest current profile. The specific capacitances calculated for PANI, binary rGO/PANI and ternary rGO/PANI/hexNb are 880, 515 and 564 F·g^{-1}, respectively, whereas for the binary PANI/hexNb reference sample it is 87 F·g^{-1}. The difference between the specific capacitances of neat PANI and nanocomposites can be attributed to the presence of rGO. Surprisingly, the comparison of binary and ternary nanocomposites performances indicates that hexNb nanoparticles improve the electrochemical properties of the ternary material under the experimental conditions. Considering that PANI/hexNb sample presents a lower current profile, the observed improvement for rGO/PANI/hexNb indicates a synergetic effect, which is attributed to strong interactions between the components in the ternary nanocomposite. These results are in accordance with structural characterisation presented in this paper, which showed an enhancement of the polymer doping state, due to the secondary doping of the PANI backbone in the rGO/PANI/hexNb nanocomposite. The capacitances of the new nanocomposite presented in this work are comparable to other materials based on graphene oxide/polyaniline reported in literature, which present typical capacitances ranging from 350 to 800 F·g^{-1} [4,22,49,65]. Although this result does not stimulate studies focusing on the application of rGO/PANI/hexNb in energy-storage devices, the thin film obtained by dropcasting has potential to be explored for other purposes since the amount of charge carriers is increased in the ternary nanocomposite.

Conclusion

In this paper we reported the development a new nanocomposite composed of reduced graphene oxide (rGO), polyaniline (PANI) and hexaniobate (hexNb) prepared by mixing the colloidal dispersions of the components. Morphological characterisation showed an interesting architecture at the nanoscale range of rGO flakes coated with PANI and decorated with hexNb nanoparticles. Such organization was attributed to the good stability of the dispersion, which does not present major aggregation and phase separation. The dispersions of the ternary rGO/PANI/hexNb sample can be deposited on surfaces by spin-coating or dropcasting. Structural characterisation by XPS spectroscopy indicated an intermediate reduction degree for the rGO component, and a high doping degree of the PANI chains consistent with secondary doping of the polymer. Electrochemical studies by cyclic voltammetry showed that the capacitance of the ternary nanocomposite is higher compared to the binary composites. Such results are attributed to cooperative effects of PANI chains with rGO flakes and hexNb nanoscrolls promoted by the nanostructured architecture, resulting in a high doping degree of polymeric chains. The interesting chemical versatility and significant interactions between the components are attractive features for applications that require chemically functionalised materials in the film form, such as sensing or corrosion protection.

Experimental

Materials

Precursor graphite flakes (NGS Naturgraphit GmbH, 300 µm flake size) were used as received. Aniline (Merck) was distilled under reduced pressure prior to use. Niobium pentoxide

(Companhia Brasileira de Metalurgia e Mineração, CBMM) was used as received. All other chemicals (Sigma-Aldrich) were also used as received.

Preparation of graphene oxide and reduced graphene oxide

Graphene oxide was prepared by graphite oxidation according to a modified Hummers method [66,67]. The viscous gel-like dispersion of graphite oxide obtained after oxidation and purification (centrifugation and washing) was diluted with deionized water and the resulting dispersions were high-shear mixed at 7000 rpm for four times (15 min each). This procedure was used to avoid thermal degradation of the sample. The GO particles prepared by this method present flake sizes ranging from 5 to 30 μm [14,17], which are remarkably larger in comparison to GO reported in literature obtained by sonication (less than 10 μm) [34,35,42-44,67]. Reduced graphene oxide was prepared by chemical reduction of GO in 0.25 $mg \cdot mL^{-1}$ dispersions with hydrazine and ammonia solution at 25 °C for 7 days. The resulting rGO dispersion presents suitable stability for the preparation of the nanocomposites. This sample is labelled as "rGO-25" herein. A reference rGO sample was also prepared by GO reduction under similar conditions as rGO-25, but at 80 °C and 3 h of reaction. This sample is labelled as "rGO-80" herein. Detailed experimental procedures are available in Supporting Information File 1.

Preparation of polyaniline and hexaniobate precursor dispersions

Dispersions of polyaniline in water/*N*,*N*-dimethylacetamide (DMA) were prepared as described in the literature [6,50,68]. The concentration of PANI, the water/DMA volume ratio and the pH values of the dispersions were adjusted considering the procedure for the preparation of nanocomposites. Hexaniobate (hexNb) was prepared as reported previously [6], which results in colloidal dispersions of scrolled hexaniobate nanoparticles, called hexaniobate nanoscrolls. Detailed experimental procedures are available in Supporting Information File 1.

Preparation of the binary (rGO/PANI) and ternary (rGO/PANI/hexNb) nanocomposites

For preparation of the rGO/PANI nanocomposite, 35 mL of hydrochloric acid solution (pH 3) was slowly added to 25 mL of PANI solution in DMA (2.8 $mg \cdot mL^{-1}$), and the pH value of the resulting dispersion was carefully adjusted to 3 by adding 1 $mol \cdot L^{-1}$ HCl. Then, 70 mL of rGO-25 dispersion (0.25 $mg \cdot mL^{-1}$, pH 8.7) was slowly added to PANI dispersion along with 1 $mol \cdot L^{-1}$ HCl to maintain the pH value of the PANI/rGO mixture in a range of 2.7–3.0. After addition of rGO dispersion, the pH value was adjusted to 2.6 and the mixture was stirred for 5 days at 20 °C. The total volume of HCl solution used for the preparation of rGO/PANI was 8 mL. The rGO/PANI/hexNb nanocomposite was prepared by slowly adding 40 mL of hexNb dispersion (1.13 $mg \cdot mL^{-1}$, pH 6.8) to 45 mL of rGO/PANI mixture. After mixing hexNb and rGO/PANI dispersions, 1 $mol \cdot L^{-1}$ HCl solution was added to re-adjust the pH value to 2.6, and the rGO/PANI/hexNb mixture was stirred for 2 days at 20 °C. A PANI/hexNb reference sample was prepared with the same PANI/hexNb weight ratio as the ternary nanocomposite. rGO/PANI, rGO/PANI/hexNb and PANI/hexNb samples were further processed by centrifugation/washing cycles (14000 rpm, 20 min and HCl solution pH 2.6) to obtain dispersions of a total concentration of 1.0 $mg \cdot mL^{-1}$.

Characterization

The AFM images were recorded with a Bruker Dimension FastScan probe microscope, operating in tapping mode, with aluminium-coated Si tips (Bruker). Samples were prepared by spincoating the dispersions of rGO, rGO/PANI and rGO/PANI/hexNb (1.0 $mg \cdot mL^{-1}$ total concentration) on Si/SiO_2 substrates at 3000 rpm (300 $rpm \cdot s^{-1}$ acceleration, 90 s). In order to properly compare the AFM images, processing was performed with the aid of WSxM software (version 4.0 Beta 7.0) [69]. Height profiles were measured with the aid of WSxM software for the processed images and the surface roughness of the particles will be discussed by means of the root mean square (RMS) values calculated from the height profiles.

XPS spectra were acquired on a SPECS custom-built system composed of a Phobios 150 hemispherical electron analyser with 1D detector. The X-ray source was a microfocus monochromated Al Kα (1486.6 eV) source. Spectra were collected with pass energy of 20 eV, and the combined ultimate resolution is 0.5 eV with X-ray source and 20 eV pass, as measured from Ag 3d. The samples were prepared by dropcasting the dispersions (1.0 $mg \cdot mL^{-1}$ total concentration) on 1 cm^2 square Si substrates and drying under reduced pressure at room temperature. Data analysis was performed with the aid of CasaXPS software (version 2.3.16 PR 1.6). Peak fitting for high-resolution spectra (C 1s and N 1s core levels) was performed by applying tight constrains for binding energy range, full width at half maximum (FWHM) and shape of components, based on a comprehensive assessment of the literature [13,34,39,40,44-47]. Further details of the fitting parameters are presented in Supporting Information File 1.

Raman spectra were obtained on a Renishaw Raman imaging microscope (inVia) equipped with a Leica microscope and a CCD detector. Spectra were excited at 632.8 nm (RL633 Renishaw Class 3B HeNe laser, 12 mW) and samples were focused with a 50× lens. The laser power was kept below 50 μW to avoid thermal degradation of the samples. For better

comparison of the relative intensities, spectral baselines were subtracted.

The electrochemical performance of the samples was evaluated by cyclic voltammetry (CV) at 25 $mV \cdot s^{-1}$ scan rate using a μAutolabIII/FRA2 potentiostat/galvanostat (Metrohm Autolab). The measurements were performed with Ag/AgCl and Pt coil as reference and counter electrodes, respectively, and 1 $mol \cdot L^{-1}$ sulfuric acid as electrolyte solution. The working electrodes were prepared by dropcasting the samples on glass/Cr(5 nm)/Au(60 nm) substrates prepared by thermal evaporation.

Supporting Information

Supporting Information File 1

Additional experimental data.
[https://www.beilstein-journals.org/bjnano/content/supplementary/2190-4286-9-272-S1.pdf]

Acknowledgements

The authors acknowledge the Brazilian agencies FAPESP (projects 2014/05048-4, 2013/03013-6, 2012/13119-3 and 2011/50318-1) and CNPq (project 302792/2015-5) for fellowships and financial support. The authors are grateful for funding from the Bill & Melinda Gates Foundation Grand Challenge Explorations scheme and Engineering and Physical Sciences Research Council EPSRC (grant EP/G035954/1). They also thank Companhia Brasileira de Metalurgia e Mineração (CBMM) for providing Nb_2O_5 sample.

ORCID® iDs

Claudio H. B. Silva - https://orcid.org/0000-0003-4331-3755
Maria Iliut - https://orcid.org/0000-0003-0786-6408
Christopher Muryn - https://orcid.org/0000-0002-4281-9183
Christian Berger - https://orcid.org/0000-0001-5252-6328
Vera R. L. Constantino - https://orcid.org/0000-0001-9276-7329
Marcia L. A. Temperini - https://orcid.org/0000-0003-4655-6891
Aravind Vijayaraghavan - https://orcid.org/0000-0001-8289-2337

References

1. Zhang, Q.; Uchaker, E.; Candelaria, S. L.; Cao, G. *Chem. Soc. Rev.* **2013,** *42,* 3127–3171. doi:10.1039/c3cs00009e
2. Huang, X.; Qi, X.; Boey, F.; Zhang, H. *Chem. Soc. Rev.* **2012,** *41,* 666–686. doi:10.1039/c1cs15078b
3. Kim, S.; Le, T.-H.; Park, C. S.; Park, G.; Kim, K. H.; Kim, S.; Kwon, O. S.; Lim, G. T.; Yoon, H. *Sci. Rep.* **2017,** *7,* No. 15184. doi:10.1038/s41598-017-15552-w
4. Xia, X.; Hao, Q.; Lei, W.; Wang, W.; Wang, H.; Wang, X. *J. Mater. Chem.* **2012,** *22,* 8314–8320. doi:10.1039/c2jm16216d
5. Radhakrishnan, S.; Krishnamoorthy, K.; Sekar, C.; Wilson, J.; Kim, S. J. *Chem. Eng. J.* **2015,** *259,* 594–602. doi:10.1016/j.cej.2014.08.047
6. Silva, C. H. B.; Galiote, N. A.; Huguenin, F.; Teixeira-Neto, É.; Constantino, V. R. L.; Temperini, M. L. A. *J. Mater. Chem.* **2012,** *22,* 14052–14060. doi:10.1039/c2jm31531a
7. Silva, C. H. B.; Da Costa Ferreira, A. M.; Constantino, V. R. L.; Temperini, M. L. A. *J. Mater. Chem. A* **2014,** *2,* 8205–8214. doi:10.1039/c4ta00737a
8. Wang, L.; Lu, X.; Lei, S.; Song, Y. *J. Mater. Chem. A* **2014,** *2,* 4491–4509. doi:10.1039/c3ta13462h
9. Lei, W.; Si, W.; Xu, Y.; Gu, Z.; Hao, Q. *Microchim. Acta* **2014,** *181,* 707–722. doi:10.1007/s00604-014-1160-6
10. Geim, A. K.; Novoselov, K. S. *Nat. Mater.* **2007,** *6,* 183–191. doi:10.1038/nmat1849
11. Rao, C. N. R.; Sood, A. K.; Subrahmanyam, K. S.; Govindaraj, A. *Angew. Chem., Int. Ed.* **2009,** *48,* 7752–7777. doi:10.1002/anie.200901678
12. Dreyer, D. R.; Park, S.; Bielawski, C. W.; Ruoff, R. S. *Chem. Soc. Rev.* **2010,** *39,* 228–240. doi:10.1039/b917103g
13. Rourke, J. P.; Pandey, P. A.; Moore, J. J.; Bates, M.; Kinloch, I. A.; Young, R. J.; Wilson, N. R. *Angew. Chem., Int. Ed.* **2011,** *50,* 3173–3177. doi:10.1002/anie.201007520
14. Fiorillo, M.; Verre, A. F.; Iliut, M.; Peiris-Pagés, M.; Ozsvari, B.; Gandara, R.; Cappello, A. R.; Sotgia, F.; Vijayaraghavan, A.; Lisanti, M. P. *Oncotarget* **2015,** *6,* 3553–3562. doi:10.18632/oncotarget.3348
15. Lee, C.; Wei, X.; Kysar, J. W.; Hone, J. *Science* **2008,** *321,* 385–388. doi:10.1126/science.1157996
16. Iliut, M.; Silva, C.; Herrick, S.; McGlothlin, M.; Vijayaraghavan, A. *Carbon* **2016,** *106,* 228–232. doi:10.1016/j.carbon.2016.05.032
17. Garcia-Alegria, E.; Iliut, M.; Stefanska, M.; Silva, C.; Heeg, S.; Kimber, S. J.; Kouskoff, V.; Lacaud, G.; Vijayaraghavan, A.; Batta, K. *Sci. Rep.* **2016,** *6,* No. 25917. doi:10.1038/srep25917
18. Janata, J.; Josowicz, M. *Nat. Mater.* **2003,** *2,* 19–24. doi:10.1038/nmat768
19. Virji, S.; Huang, J.; Kaner, R. B.; Weiller, B. H. *Nano Lett.* **2004,** *4,* 491–496. doi:10.1021/nl035122e
20. Tseng, R. J.; Huang, J.; Ouyang, J.; Kaner, R. B.; Yang, Y. *Nano Lett.* **2005,** *5,* 1077–1080. doi:10.1021/nl050587l
21. Yang, Y.; Ouyang, J.; Ma, L.; Tseng, R. J.-H.; Chu, C.-W. *Adv. Funct. Mater.* **2006,** *16,* 1001–1014. doi:10.1002/adfm.200500429
22. Xu, Y.; Tao, Y.; Zheng, X.; Ma, H.; Luo, J.; Kang, F.; Yang, Q.-H. *Adv. Mater.* **2015,** *27,* 8082–8087. doi:10.1002/adma.201504151
23. Rego, L. S.; Antonio, J. L. S.; Silva, C. H. B.; Nobrega, M. M.; Temperini, M. L. A.; Torresi, R. M.; de Torresi, S. I. C. *J. Solid State Electrochem.* **2016,** *20,* 983–991. doi:10.1007/s10008-015-2952-2
24. Heeger, A. J. *Angew. Chem., Int. Ed.* **2001,** *40,* 2591–2611. doi:10.1002/1521-3773(20010716)40:14<2591::aid-anie2591>3.0.co;2-0
25. Stafström, S.; Brédas, J. L.; Epstein, A. J.; Woo, H. S.; Tanner, D. B.; Huan, W. S.; MacDiarmid, A. G. *Phys. Rev. Lett.* **1987,** *59,* 1464–1467. doi:10.1103/physrevlett.59.1464
26. Izumi, C. M. S.; Constantino, V. R. L.; Temperini, M. L. A. *J. Nanosci. Nanotechnol.* **2008,** *8,* 1782–1789.
27. Nobrega, M. M.; Martins, V. L.; Torresi, R. M.; Temperini, M. L. A. *J. Phys. Chem. C* **2014,** *118,* 4267–4274. doi:10.1021/jp4120755
28. Gasperin, M.; Le Bihan, M. T. *J. Solid State Chem.* **1982,** *43,* 346–353. doi:10.1016/0022-4596(82)90251-1
29. Bizeto, M. A.; Constantino, V. R. L. *Mater. Res. Bull.* **2004,** *39,* 1729–1736. doi:10.1016/j.materresbull.2004.05.001

30. Takagaki, A.; Sugisawa, M.; Lu, D.; Kondo, J. N.; Hara, M.; Domen, K.; Hayashi, S. *J. Am. Chem. Soc.* **2003,** *125,* 5479–5485. doi:10.1021/ja034085q
31. Dias, A. S.; Lima, S.; Carriazo, D.; Rives, V.; Pillinger, M.; Valente, A. A. *J. Catal.* **2006,** *244,* 230–237. doi:10.1016/j.jcat.2006.09.010
32. Bizeto, M. A.; Shiguihara, A. L.; Constantino, V. R. L. *J. Mater. Chem.* **2009,** *19,* 2512–2525. doi:10.1039/b821435b
33. Shiguihara, A. L.; Bizeto, M. A.; Constantino, V. R. L. *Colloids Surf., A* **2007,** *295,* 123–129. doi:10.1016/j.colsurfa.2006.08.040
34. Stankovich, S.; Dikin, D. A.; Piner, R. D.; Kohlhaas, K. A.; Kleinhammes, A.; Jia, Y.; Nguyen, S. T.; Ruoff, R. S. *Carbon* **2007,** *45,* 1558–1565. doi:10.1016/j.carbon.2007.02.034
35. Fernández-Merino, M. J.; Guardia, L.; Paredes, J. I.; Villar-Rodil, S.; Solis-Fernández, P.; Martínez-Alonso, A.; Tascón, J. M. D. *J. Phys. Chem. C* **2010,** *114,* 6426–6432. doi:10.1021/jp100603h
36. Huan, J. *Pure Appl. Chem.* **2006,** *78,* 15–27. doi:10.1351/pac200678010015
37. Bizeto, M. A.; Constantino, V. R. L. *Microporous Mesoporous Mater.* **2005,** *83,* 212–218. doi:10.1016/j.micromeso.2005.04.013
38. Saupe, G. B.; Waraksa, C. C.; Kim, H.-N.; Han, Y. J.; Kaschak, D. M.; Skinner, D. M.; Mallouk, T. E. *Chem. Mater.* **2000,** *12,* 1556–1562. doi:10.1021/cm981136n
39. Koinuma, M.; Tateishi, H.; Hatakeyama, K.; Miyamoto, S.; Ogata, C.; Funatsu, A.; Taniguchi, T.; Matsumoto, Y. *Chem. Lett.* **2013,** *42,* 924–926. doi:10.1246/cl.130152
40. Jeong, H.-K.; Lee, Y. P.; Lahaye, R. J. W. E.; Park, M.-H.; An, K. H.; Kim, I. J.; Yan, C.-W.; Park, C. Y.; Ruoff, R. S.; Lee, Y. H. *J. Am. Chem. Soc.* **2008,** *130,* 1362–1366. doi:10.1021/ja076473o
41. Leiro, J. A.; Heinonen, M. H.; Laiho, T.; Batirev, I. G. *J. Electron Spectrosc. Relat. Phenom.* **2003,** *128,* 205–213. doi:10.1016/s0368-2048(02)00284-0
42. Marcano, D. C.; Kosynkin, D. V.; Berlin, J. M.; Sinitskii, A.; Sun, Z.; Slesarev, A.; Alemany, L. B.; Lu, W.; Tour, J. M. *ACS Nano* **2010,** *4,* 4806–4814. doi:10.1021/nn1006368
43. Park, S.; An, J.; Piner, R. D.; Jung, I.; Yang, D.; Velamakanni, A.; Nguyen, S. T.; Ruoff, R. S. *Chem. Mater.* **2008,** *20,* 6592–6594. doi:10.1021/cm801932u
44. Rani, J. R.; Lim, J.; Oh, J.; Kim, J.-W.; Shin, H. S.; Kim, J. H.; Lee, S.; Jun, S. C. *J. Phys. Chem. C* **2012,** *116,* 19010–19017. doi:10.1021/jp3050302
45. Hsiao, M.-C.; Liao, S.-H.; Yen, M.-Y.; Teng, C.-C.; Lee, S.-H.; Pu, N.-W.; Wang, C.-A.; Sung, Y.; Ger, M.-D.; Ma, C.-C. M.; Hsiao, M.-H. *J. Mater. Chem.* **2010,** *20,* 8496–8505. doi:10.1039/c0jm01679a
46. Ren, P.-G.; Yan, D.-X.; Ji, X.; Chen, T.; Li, Z.-M. *Nanotechnology* **2011,** *22,* 055705. doi:10.1088/0957-4484/22/5/055705
47. Bagri, A.; Mattevi, C.; Acik, M.; Chabal, Y. J.; Chhowalla, M.; Shenoy, V. B. *Nat. Chem.* **2010,** *2,* 581–587. doi:10.1038/nchem.686
48. Krishnamoorthy, K.; Veerapandian, M.; Yun, K.; Kim, S.-J. *Carbon* **2013,** *53,* 38–49. doi:10.1016/j.carbon.2012.10.013
49. Jianhua, L.; Junwei, A.; Yecheng, Z.; Yuxiao, M.; Mengliu, L.; Mei, Y.; Songmei, L. *ACS Appl. Mater. Interfaces* **2012,** *4,* 2870–2876. doi:10.1021/am300640y
50. Yang, D.; Velamakanni, A.; Bozoklu, G.; Park, S.; Stoller, M.; Piner, R. D.; Stankovich, S.; Jung, I.; Field, D. A.; Ventrice, C. A., Jr.; Ruoff, R. S. *Carbon* **2009,** *47,* 145–152. doi:10.1016/j.carbon.2008.09.045
51. Bo, Z.; Shuai, X.; Mao, S.; Yang, H.; Qian, J.; Chen, J.; Yan, J.; Cen, K. *Sci. Rep.* **2014,** *4,* No. 4684. doi:10.1038/srep04684
52. Monkman, A. P.; Stevens, G. C.; Bloor, D. *J. Phys. D: Appl. Phys.* **1991,** *24,* 738–749. doi:10.1088/0022-3727/24/5/017
53. Tan, K. L.; Tan, B. T. G.; Kang, E. T.; Neoh, K. G. *J. Chem. Phys.* **1991,** *94,* 5382–5388. doi:10.1063/1.460524
54. Kang, E. T.; Neoh, K. G.; Tan, K. L. *Surf. Interface Anal.* **1993,** *20,* 833–840. doi:10.1002/sia.740201006
55. Zeng, X.-R.; Ko, T.-M. *Polymer* **1998,** *39,* 1187–1195. doi:10.1016/s0032-3861(97)00381-9
56. Furukawa, Y.; Ueda, F.; Hyodo, Y.; Harada, I.; Nakajima, T.; Kawagoe, T. *Macromolecules* **1988,** *21,* 1297–1305. doi:10.1021/ma00183a020
57. Louarn, G.; Lapkowski, M.; Quillard, S.; Pron, A.; Buisson, J. P.; Lefrant, S. *J. Phys. Chem.* **1996,** *100,* 6998–7006. doi:10.1021/jp953387e
58. Cochet, M.; Louarn, G.; Quillard, S.; Buisson, J. P.; Lefrant, S. *J. Raman Spectrosc.* **2000,** *31,* 1041–1049. doi:10.1002/1097-4555(200012)31:12<1041::aid-jrs641>3.0.co;2-r
59. Boyer, M. I.; Quillard, S.; Louarn, G.; Froyer, G.; Lefrant, S. *J. Phys. Chem. B* **2000,** *104,* 8952–8961. doi:10.1021/jp000946v
60. Eda, G.; Fanchini, G.; Chhowalla, M. *Nat. Nanotechnol.* **2008,** *3,* 270–274. doi:10.1038/nnano.2008.83
61. Iliut, M.; Leordean, C.; Canpean, V.; Teodorescu, C.-M.; Astilean, S. *J. Mater. Chem. C* **2013,** *1,* 4094–4104. doi:10.1039/c3tc30177j
62. da Silva, J. E. P.; Temperini, M. L. A.; de Torresi, S. I. C. *Electrochim. Acta* **1999,** *44,* 1887–1891. doi:10.1016/s0013-4686(98)00330-2
63. Huang, W. S.; Humphrey, B. D.; MacDiarmid, A. G. *J. Chem. Soc., Faraday Trans. 1* **1986,** *82,* 2385–2400. doi:10.1039/f19868202385
64. Geniès, E. M.; Lapkowski, M.; Penneau, J. F. *J. Electroanal. Chem. Interfacial Electrochem.* **1988,** *249,* 97–107. doi:10.1016/0022-0728(88)80351-6
65. Kobayashi, T.; Yoneyama, H.; Tamura, H. *J. Electroanal. Chem. Interfacial Electrochem.* **1984,** *161,* 419–423. doi:10.1016/s0022-0728(84)80201-6
66. Xiong, P.; Hu, C.; Fan, Y.; Zhang, W.; Zhu, J.; Wang, X. *J. Power Sources* **2014,** *266,* 384–392. doi:10.1016/j.jpowsour.2014.05.048
67. Hummers, W. S., Jr.; Offeman, R. E. *J. Am. Chem. Soc.* **1958,** *80,* 1339. doi:10.1021/ja01539a017
68. Cheung, J. H.; Stockton, W. B.; Rubner, M. F. *Macromolecules* **1997,** *30,* 2712–2716. doi:10.1021/ma970047d
69. Horcas, I.; Fernández, R.; Gómez-Rodríguez, J. M.; Colchero, J.; Gómez-Herrero, J.; Baro, A. M. *Rev. Sci. Instrum.* **2007,** *78,* No. 013705. doi:10.1063/1.2432410

BEILSTEIN JOURNAL OF NANOTECHNOLOGY

Hybrid Au@alendronate nanoparticles as dual chemo-photothermal agent for combined cancer treatment

Anouchka Plan Sangnier[1,2], Romain Aufaure[1], Laurence Motte[1], Claire Wilhelm[*,‡2], Erwann Guenin[*,‡1,3] and Yoann Lalatonne[*,‡1,4]

Letter

Open Access

Address:
[1]Inserm U1148, LVTS, Université Paris 13, Sorbonne Paris Cité, Bobigny, France, [2]Laboratoire Matière et Systèmes Complexes, CNRS and University Paris Diderot, Paris, France, [3]Sorbonne Universités, Université de Technologie de Compiègne, Integrated Transformations of Renewable Matter Laboratory (EA TIMR 4297 UTC-ESCOM), Compiègne, France and [4]Service de Médecine Nucléaire, Hôpital Avicenne Assistance Publique-Hôpitaux de Paris, Bobigny, France

Email:
Claire Wilhelm[*] - claire.wilhelm@univ-paris-diderot.fr; Erwann Guenin[*] - erwann.guenin@utc.fr; Yoann Lalatonne[*] - yoann.lalatonne@aphp.fr

* Corresponding author ‡ Equal contributors

Keywords:
alendronate; bisphosphonate; cancer treatment; gold nanoparticles; photothermia

Beilstein J. Nanotechnol. **2018,** *9,* 2947–2952.
doi:10.3762/bjnano.9.273

Received: 06 August 2018
Accepted: 26 October 2018
Published: 27 November 2018

This article is part of the thematic issue "Advanced hybrid nanomaterials".

Guest Editor: F. Leroux

Abstract

A gold therapeutic nanoplatform with the same molecule used as reductant, coating and therapeutic agent has been developed in a one-pot, one-phase process using alendronate, a drug from the bisphosphonate family known for its antitumor effects. In addition, the core made of gold nanoparticles (NPs) brings thermal functionalities under irradiation within the first biological window (650–900 nm). The Au@alendronate nanoplatform thus provided a combined antitumor activity through drug delivery and photothermal therapy. Au@alendronate NPs inhibited in vitro the proliferation of prostate cancer cells (PC3) in a dose-dependent manner, with an IC_{50} value of 100 µM. Under NIR irradiation a temperature increase was observed leading to a reduction of the IC_{50} value to 1 µM, with total tumor cell death at 100 µM.

Findings

Bisphosphonates (BPs) are used in the treatment of a variety of bone diseases, such as osteoporosis, solid tumor bone metastases and myeloma bone disease [1-4]. BPs contain two phosphonate groups linked by a common carbon atom (P–C–P) binding divalent metal ions (Ca^{2+}, Mg^{2+}, and Fe^{2+}) by coordination of the two phosphonate groups. The BP affinity for calcium is improved by adding a hydroxy (–OH) group, for instance in HMBP (hydroxylmethylene bisphosphonate), allowing for a tridentate coordination to Ca^{2+} ions (Supporting Information File 1, Figure S4) and leading to a high affinity to

bone (hydroxyapatite ($Ca_{10}(PO_4)_6(OH)_2$)) tissue [5,6]. We focus here on the antitumor activity of alendronate, a nitrogen-containing HMBP, clinically used as adjuvant (Fosamax®) in the treatment of prostate and breast metastatic cancers [7]. Nitrogen-containing HMBPs, such as alendronate, are inhibitors of the mevalonate pathway. They inhibit the prenylation of GTPase proteins, which affects cell morphology, replication and signalling that can cause cell death by apoptosis [8,9]. However, the in vivo therapeutic use of HMBPs is limited by low bioavailability. Once intravenously injected, free HMBPs are only slightly internalized by the cells and accumulates preferentially into bone tissue. Benyettou et al. showed that alendronate-coated magnetic NPs favour the intratumoral uptake and inhibit tumor growth [10].

HMBPs are also effective ligands to stabilize nanoparticles under biological conditions [11-15]. More recently, synthesis of gold and silver NPs have been developed using HMPB molecules [16-18]. For gold NPs, HMBPs act as both Au chelating and reducing agent comparable to citrates in the well-known Turkevich–Frens synthesis [19,20]. Besides, gold NPs exhibit a unique surface plasmonic resonance leading to strong enhancement of the absorption and scattering when exposed to electromagnetic radiation [21]. Due to this plasmonic absorption, light is converted to heat [22-26]. Photothermal therapy (PTT) is a powerful cancer-treatment technique. Gold NPs have to be activated within the biological transparency windows of 650–950 nm or 1000–1350 nm, to minimize light absorption by surrounding biological tissues [27]. The principal limitation of PTT is that it requires direct light irradiation, which reduces its effect against disseminated metastatic tumors. A promising strategy to increase the PTT efficiency is the combination with magnetic hyperthermia [28], or with chemotherapy [29,30].

Using a one-pot synthesis strategy, we developed Au@alendronate NPs for a combined application of the antitumor activity of alendronate and an efficient gold-mediated PTT. We further evaluated their combined chemo-photothermal antitumor activity.

Synthesis and characterization of Au@alendronate NPs

Gold NPs were synthesized in water by using alendronate both as reducing agent and chelating ligand. The gold solution is simply added to an alendronate solution at boiling temperature (see Supporting Information File 1). The excess of reactive species is eliminated by ultrafiltration. We thus obtained spherical NPs (Figure 1a, left) with an average diameter of

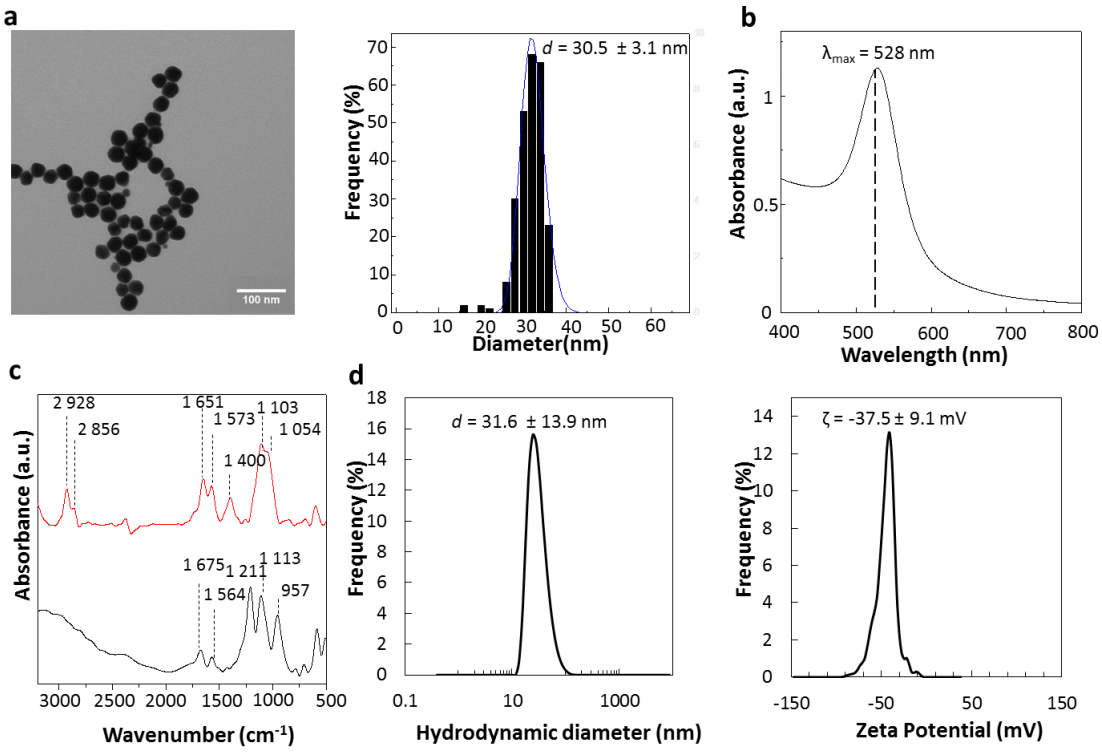

Figure 1: Au@alendronate NPs characterization: (a) transmission electron microscopy (TEM) image (left) and size distribution (right), (b) UV–vis spectrum, (c) FTIR spectra of Au@alendronate NPs (red curve) versus alendronate (black) curve, (d) Hydrodynamic diameter distribution (in volume, left) and zeta potential (right) of Au@alendronate NPs.

30.5 ± 3.0 nm (Figure 1a, right) and a plasmon band at 528 nm (Figure 1b).

Under similar synthesis conditions, gold NPs obtained with (1-hydroxy-1-phosphonopent-4-enyl)phosphonic acid (HMBPene), replacing alendronate were characterized by a smaller NPs size around 10 nm [16]. This indicates the influence of the reducing ligand on the crystal growth. Inductively coupled plasma atomic emission spectroscopy (ICP-AES) has been used to quantitatively determine the amount of alendronate per nanoparticles. 1.0 P atoms per 7.6 Au atoms was measured, which corresponds to 36,427 alendronate molecules per NP or a coating density of 12.5 alendronate molecules/nm^2 for a 30.5 nm spherical gold NP. Remarkably, the alendronate density is much higher than estimated values for other NPs coated with HMBP molecules (i.e., 3.4 HMBPene/nm^2) [18]. Indeed, alendronate is a zwitterion, capable of forming pairs of ions that generate multilayers around the gold NP.

The chemisorption of alendronate was qualitatively assessed (Figure 1c) by Fourier-transform infrared spectroscopy (FTIR) comparing the coated gold NPs (red curve) with free alendronate (black curve). Large modifications were observed within the PO region (900–1200 cm^{-1}). The free alendronate spectrum exhibits two sharp peaks at 1211 and 957 cm^{-1}, assigned to P=O and P–OH, respectively [31]. The broad band at 1113 cm^{-1} is characteristic for the vibrational mode for the PO_3 group [32]. For Au@alendronate NPs the strong tightening of P=O and P–O vibration bands around 1000 cm^{-1} (red curve), which is characteristic of the chelation of phosphorus species on a metallic surface [11,16,33], suggests a coordination of phosphonates as chelating groups. The –NH scissoring (1564 cm^{-1}) and bending vibration bands (1675 cm^{-1}) for alendronate were slightly shifted in the Au@alendronate NPs confirming the multilayer formation through anion/cation interactions due to the alendronate zwitterion form. These results suggest that alendronate was grafted onto the nanocrystal surface through the phosphonate groups and could be activated for further biocoupling [10].

The excellent coating density led to a good colloidal stability, as confirmed by dynamic light scattering (DLS) measurements at physiological pH values. A hydrodynamic diameter equal to 31.5 ± 13.9 nm (Figure 1d) was determined, which is sufficiently close to the TEM crystal size to testify to the absence of gold NP aggregates. Au@alendronate NPs were stable at pH > 4.7 and at least four months after synthesis (see Supporting Information File 1, Figure S1). The negative zeta potential, equal to −37.5 ± 9.1 mV confirms the presence of alendronate on the surface providing negative charges, which allow colloid stabilization despite the presence of ammonium cations.

Au@alendronate NPs as NIR photothermal nano-heater

Since gold NPs bring their own therapeutic asset, in the form of PTT, we first evaluated the specific photothermal properties of Au@alendronate NPs. In cancer therapy, it is desirable to use NPs that are active in the near-infrared (NIR) region to minimize light absorption of the laser radiation by surrounding tissues [27,34]. The plasmonic absorption band of Au@alendronate NPs is centered at 528 nm, but there is still absorption above 800 nm (Figure 1b). Here, a laser operating at 680 nm and 0.3 W/cm^2 (Supporting Information File 1, Figure S2) and 1.7 W/cm^2 (Figure 2) was used. As we recently reported, this 1.7 W/cm^2 laser power was efficient for inducing tumor growth

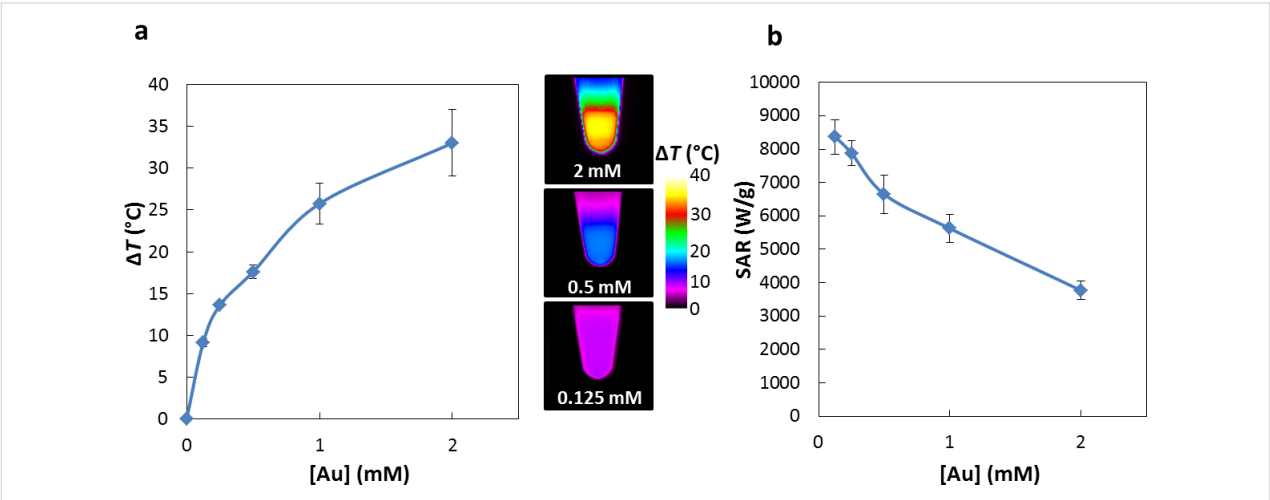

Figure 2: (a) Temperature increase and corresponding typical IR image and (b) SAR (W/g) as a function of the gold concentration under laser irradiation (1.7 W/cm^2, 680 nm).

inhibition in vivo without exhibit nonspecific phototoxicity [35]. In addition, this value is lower than the power used in many in vivo studies [36-38]. Figure 2 summarizes the heating characteristics of Au@alendronate NPs, measured in water as a function of the gold concentration. Figure 2 shows the plateau temperatures reached after 5 min of irradiation (Figure 2a), as well as the concentration-normalized heating efficiency expressed as the specific absorption rate (SAR) in watts per gram of Au (Figure 2b, see also Supporting Information File 1 for calculation details and Figure S2 for the temperature elevation at 0.3 W/cm^2).

The temperature elevation clearly increased with the gold concentration and reached ΔT = 30 °C at a gold concentration of 2 mM. A temperature increase of ΔT = 9 °C is observed at a low gold concentration of 0.125 mM. The SAR is above 4000 W/g at high concentrations, reaching very high values (over 8000 W/g) at low concentrations. These photothermal properties are in good agreement with those of other thermal agents [23] and show the applicability of Au@alendronate gold NPs as potential photothermal agents.

The colloidal stability of Au@alendronate NPs at physiological pH values and their photothermal properties within the NIR first biological window allowed us to further consider their study in a biological environment.

Au@alendronate NPs antitumor activity

PC3 human prostate adenocarcinoma cells were selected to explore the potential of Au@alendronate NPs as antitumor agents [9]. PC3 cells were first treated both with free alendronate and with Au@alendronate NPs (at various extracellular alendronate concentrations from 1 nM up to 0.1 M) for 48 h. Metabolic activity (Figure 3) was determined by Alamar Blue assay (see Supporting Information File 1). With this assay the half maximal inhibitory concentration (IC_{50} value) can be determined. This value is a good indicator of the effectiveness of a compound for inhibiting biological or biochemical functions. Free alendronate and Au@alendronate gold NPs reduced cell viability in a concentration-dependent manner (Figure 3a) with an IC_{50} equal to 100 µM for both systems whereas Au@HMBP-PEG NPs [39] do not exhibit any cytotoxicity (Supporting Information File 1, Figure S3). Under similar cell-treatment conditions, this IC_{50} value is consistent with values obtained for free alendronate with other cancer cell lines [10]. More importantly, it indicates that Au@alendronate NPs perfectly retained the antitumor activity of alendronate suggesting the alendronate release within the intracellular environment. However, at relevant concentrations, complete cell death was not achieved. Hence, we included photothermal treatment by using a 680 nm laser calibrated to illuminate cells at 1.7 W/cm^2. The metabolic activity on PC3 cells incubated with Au@alendronate NPs in presence or absence of laser irradiation is compared in Figure 3b.

At extracellular concentrations of alendronate below 1 µM, similar cell viability was observed in absence or presence of laser irradiation. This could be related to the low dose of internalized gold NPs and indicates that the laser power is sufficiently low to avoid nonspecific biological damage. At extracellular concentrations of alendronate over 1 µM, cell viability was considerably lowered in the presence of laser irradiation. The IC_{50} was reduced to 1 µM (instead of 100 µM), while at intermediate concentration of 100 µM, cell death was total. It clearly evidences the efficiency of the combined drug delivery and photothermal treatment of Au@alendronate NPs.

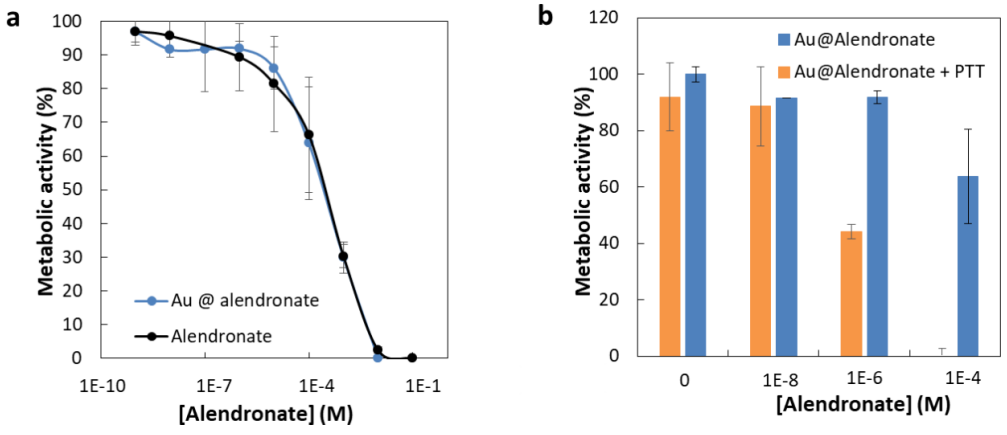

Figure 3: Metabolic activity of PC3 cells incubated (a) with free alendronate (black curve) and Au@alendronate NPs (blue curve), (b) with Au@alendronate NPs under the presence (orange column) or absence (blue column) of NIR irradiation (680 nm).

In summary, we developed a one-pot synthesis by simply mixing, in water, gold ions and alendronate molecules as reductant, coating and therapeutic agent. The synthesized Au@alendronate NPs maintain the alendronate antitumor activity, which is greatly improved under NIR laser radiation. These results pave the way for an efficient antitumor activity of Au@alendronate NPs through combining drug delivery in the form of a nanoplatform carrying alendronate and photothermal therapy. Indeed, Au@alendronate NPs will accumulate within cells because of the enhanced permeability retention effect: An enhanced permeability of blood vessels near the tumor allows for the penetration of nanoparticles into the tumor. The impaired lymphatic function within the tumor will not be able to clear those nanoparticles efficiently [40]. This proof-of-concept study will be completed by the intracellular behavior of Au@alendronate NPs with a special attention to alendronate release under photothermal activation.

Supporting Information

Supporting Information File 1

Materials and methods and supplementary figures.
[https://www.beilstein-journals.org/bjnano/content/supplementary/2190-4286-9-273-S1.pdf]

Acknowledgements

We thank the CNanoMat platform (University Paris 13) for physico-chemical characterization. We acknowledge financial support from Sorbonne Paris Cité (project CardioNanoStem). We acknowledge the ImagoSeine facility (Jacques Monod Institute, Paris, France), and the France BioImaging infrastructure supported by the French National Research Agency (ANR-10-INSB-04, «Investments fit the future». This research was also sponsored by the European Union, the Région Haut de France, the Ecole Supérieur de Chimie Organique et Minérale (ESCOM) and Université de Technologie de Compiègne (UTC) through FEDER funding of the chair: «Green Chemistry and Processes».

ORCID® iDs

Anouchka Plan Sangnier - https://orcid.org/0000-0002-4799-7149
Laurence Motte - https://orcid.org/0000-0001-6129-539X
Claire Wilhelm - https://orcid.org/0000-0001-7024-9627
Erwann Guenin - https://orcid.org/0000-0002-7125-9074
Yoann Lalatonne - https://orcid.org/0000-0003-2235-6561

References

1. Eriksen, E. F.; Díez-Pérez, A.; Boonen, S. *Bone* **2014,** *58,* 126–135. doi:10.1016/j.bone.2013.09.023
2. Abdelkarim, M.; Guenin, E.; Sainte-Catherine, O.; Vintonenko, N.; Peyri, N.; Perret, G. Y.; Crepin, M.; Khatib, A.-M.; Lecouvey, M.; Di Benedetto, M. *PLoS One* **2009,** *4,* e4685. doi:10.1371/journal.pone.0004685
3. Macedo, F.; Ladeira, K.; Pinho, F.; Saraiva, N.; Bonito, N.; Pinto, L.; Gonçalves, F. *Oncol. Rev.* **2017,** *11,* 321. doi:10.4081/oncol.2017.321
4. Polascik, T. J. *Drug Des., Dev. Ther.* **2009,** *3,* 27–40. doi:10.2147/dddt.s3169
5. Nancollas, G. H.; Tang, R.; Phipps, R. J.; Henneman, Z.; Gulde, S.; Wu, W.; Mangood, A.; Russell, R. G. G.; Ebetino, F. H. *Bone* **2006,** *38,* 617–627. doi:10.1016/j.bone.2005.05.003
6. Russell, R. G. G. *Bone* **2007,** *40,* S21–S25. doi:10.1016/j.bone.2007.03.002
7. Mundy, G. R. *Nat. Rev. Cancer* **2002,** *2,* 584–593. doi:10.1038/nrc867
8. Luckman, S. P.; Hughes, D. E.; Coxon, F. P.; Russell, R. G. G.; Rogers, M. J. *J. Bone Miner. Res.* **1998,** *13,* 581–589. doi:10.1359/jbmr.1998.13.4.581
9. Virtanen, S. S.; Väänänen, H. K.; Härkönen, P. L.; Lakkakorpi, P. T. *Cancer Res.* **2002,** *62,* 2708–2714.
10. Benyettou, F.; Lalatonne, Y.; Chebbi, I.; Benedetto, M. D.; Serfaty, J.-M.; Lecouvey, M.; Motte, L. *Phys. Chem. Chem. Phys.* **2011,** *13,* 10020–10027. doi:10.1039/c0cp02034f
11. Lalatonne, Y.; Paris, C.; Serfaty, J. M.; Weinmann, P.; Lecouvey, M.; Motte, L. *Chem. Commun.* **2008,** 2553–2555. doi:10.1039/b801911h
12. Giger, E. V.; Puigmartí-Luis, J.; Schlatter, R.; Castagner, B.; Dittrich, P. S.; Leroux, J.-C. *J. Controlled Release* **2011,** *150,* 87–93. doi:10.1016/j.jconrel.2010.11.012
13. Karimi, A.; Denizot, B.; Hindré, F.; Filmon, R.; Greneche, J.-M.; Laurent, S.; Daou, T. J.; Begin-Colin, S.; Le Jeune, J.-J. *J. Nanopart. Res.* **2010,** *12,* 1239–1248. doi:10.1007/s11051-009-9815-7
14. Torres Martin de Rosales, R.; Tavaré, R.; Paul, R. L.; Jauregui-Osoro, M.; Protti, A.; Glaria, A.; Varma, G.; Szanda, I.; Blower, P. J. *Angew. Chem., Int. Ed.* **2011,** *50,* 5509–5513. doi:10.1002/anie.201007894
15. Bolley, J.; Guenin, E.; Lievre, N.; Lecouvey, M.; Soussan, M.; Lalatonne, Y.; Motte, L. *Langmuir* **2013,** *29,* 14639–14647. doi:10.1021/la403245h
16. Aufaure, R.; Lalatonne, Y.; Lièvre, N.; Heintz, O.; Motte, L.; Guénin, E. *RSC Adv.* **2014,** *4,* 59315–59322. doi:10.1039/c4ra11847b
17. Benyettou, F.; Rezgui, R.; Ravaux, F.; Jaber, T.; Blumer, K.; Jouiad, M.; Motte, L.; Olsen, J.-C.; Platas-Iglesias, C.; Magzoub, M.; Trabolsi, A. *J. Mater. Chem. B* **2015,** *3,* 7237–7245. doi:10.1039/c5tb00994d
18. Aufaure, R.; Hardouin, J.; Millot, N.; Motte, L.; Lalatonne, Y.; Guénin, E. *Chem. – Eur. J.* **2016,** *22,* 16022–16027. doi:10.1002/chem.201602899
19. Turkevich, J.; Stevenson, P. C.; Hillier, J. *Discuss. Faraday Soc.* **1951,** *11,* 55–75. doi:10.1039/df9511100055
20. Frens, G. *Nature (London), Phys. Sci.* **1973,** *241,* 20–22. doi:10.1038/physci241020a0
21. Jain, P. K.; Lee, K. S.; El-Sayed, I. H.; El-Sayed, M. A. *J. Phys. Chem. B* **2006,** *110,* 7238–7248. doi:10.1021/jp057170o
22. Panikkanvalappil, S. R.; Hooshmand, N.; El-Sayed, M. A. *Bioconjugate Chem.* **2017,** *28,* 2452–2460. doi:10.1021/acs.bioconjchem.7b00427
23. Espinosa, A.; Kolosnjaj-Tabi, J.; Abou-Hassan, A.; Plan Sangnier, A.; Curcio, A.; Silva, A. K. A.; Di Corato, R.; Neveu, S.; Pellegrino, T.; Liz-Marzán, L. M.; Wilhelm, C. *Adv. Funct. Mater.* **2018,** *28,* 1803660. doi:10.1002/adfm.201803660

24. Lohse, S. E.; Murphy, C. J. *J. Am. Chem. Soc.* **2012,** *134,* 15607–15620. doi:10.1021/ja307589n
25. Dykman, L.; Khlebtsov, N. *Chem. Soc. Rev.* **2012,** *41,* 2256–2282. doi:10.1039/c1cs15166e
26. Espinosa, A.; Silva, A. K. A.; Sánchez-Iglesias, A.; Grzelczak, M.; Péchoux, C.; Desboeufs, K.; Liz-Marzán, L. M.; Wilhelm, C. *Adv. Healthcare Mater.* **2016,** *5,* 1112. doi:10.1002/adhm.201670046
27. Tsai, M.-F.; Chang, S.-H. G.; Cheng, F.-Y.; Shanmugam, V.; Cheng, Y.-S.; Su, C.-H.; Yeh, C.-S. *ACS Nano* **2013,** *7,* 5330–5342. doi:10.1021/nn401187c
28. Espinosa, A.; Bugnet, M.; Radtke, G.; Neveu, S.; Botton, G. A.; Wilhelm, C.; Abou-Hassan, A. *Nanoscale* **2015,** *7,* 18872–18877. doi:10.1039/c5nr06168g
29. Nam, J.; Son, S.; Ochyl, L. J.; Kuai, R.; Schwendeman, A.; Moon, J. J. *Nat. Commun.* **2018,** *9,* 1074. doi:10.1038/s41467-018-03473-9
30. Li, Y.; Liu, G.; Ma, J.; Lin, J.; Lin, H.; Su, G.; Chen, D.; Ye, S.; Chen, X.; Zhu, X.; Hou, Z. *J. Controlled Release* **2017,** *258,* 95–107. doi:10.1016/j.jconrel.2017.05.011
31. Podstawka, E.; Borszowska, R.; Grabowska, M.; Drąg, M.; Kafarski, P.; Proniewicz, L. M. *Surf. Sci.* **2005,** *599,* 207–220. doi:10.1016/j.susc.2005.09.048
32. Gao, W.; Dickinson, L.; Grozinger, C.; Morin, F. G.; Reven, L. *Langmuir* **1996,** *12,* 6429–6435. doi:10.1021/la9607621
33. Benyettou, F.; Guenin, E.; Lalatonne, Y.; Motte, L. *Nanotechnology* **2011,** *22,* 055102. doi:10.1088/0957-4484/22/5/055102
34. Weissleder, R. *Nat. Biotechnol.* **2001,** *19,* 316–317. doi:10.1038/86684
35. Plan Sangnier, A.; Preveral, S.; Curcio, A.; K. A. Silva, A.; Lefèvre, C. T.; Pignol, D.; Lalatonne, Y.; Wilhelm, C. *J. Controlled Release* **2018,** *279,* 271–281. doi:10.1016/j.jconrel.2018.04.036
36. von Maltzahn, G.; Park, J.-H.; Agrawal, A.; Bandaru, N. K.; Das, S. K.; Sailor, M. J.; Bhatia, S. N. *Cancer Res.* **2009,** *69,* 3892–3900. doi:10.1158/0008-5472.can-08-4242
37. Dickerson, E. B.; Dreaden, E. C.; Huang, X.; El-Sayed, I. H.; Chu, H.; Pushpanketh, S.; McDonald, J. F.; El-Sayed, M. A. *Cancer Lett.* **2008,** *269,* 57–66. doi:10.1016/j.canlet.2008.04.026
38. Zheng, X.; Zhou, F.; Wu, B.; Chen, W. R.; Xing, D. *Mol. Pharmaceutics* **2012,** *9,* 514–522. doi:10.1021/mp200526m
39. Aufaure, R.; Buendia, R.; Motte, L.; Hardouin, J.; Lalatonne, Y.; Guénin, E. *New J. Chem.* **2017,** *41,* 12153–12158. doi:10.1039/c7nj02773g
40. Greish, K. Enhanced Permeability and Retention (EPR) Effect for Anticancer Nanomedicine Drug Targeting. In *Cancer Nanotechnology;* Grobmyer, S. R.; Moudgil, B. M., Eds.; Methods in Molecular Biology; Humana Press: New York City, NY, U.S.A., 2010; pp 25–37. doi:10.1007/978-1-60761-609-2_3

License and Terms

BEILSTEIN JOURNAL OF NANOTECHNOLOGY

The nanoscaled metal-organic framework ICR-2 as a carrier of porphyrins for photodynamic therapy

Jan Hynek[1], Sebastian Jurík[2], Martina Koncošová[3], Jaroslav Zelenka[3], Ivana Křížová[4], Tomáš Ruml[3], Kaplan Kirakci[1], Ivo Jakubec[1], František Kovanda[2], Kamil Lang[1] and Jan Demel[*1]

Full Research Paper

Open Access

Address:
[1]Department of Materials Chemistry, Institute of Inorganic Chemistry of the Czech Academy of Sciences, Husinec-Řež 1001, 250 68 Řež, Czech Republic,, [2]Department of Solid State Chemistry, University of Chemistry and Technology, Technická 5, 166 28 Prague, Czech Republic,, [3]Department of Biochemistry and Microbiology, University of Chemistry and Technology, Technická 5, 166 28 Prague, Czech Republic, and [4]Department of Biotechnology, University of Chemistry and Technology, Technická 5, 166 28 Prague, Czech Republic

Email:
Jan Demel[*] - demel@iic.cas.cz

* Corresponding author

Keywords:
metal-organic framework; phosphinic acid based MOF; photodynamic therapy; porphyrin; singlet oxygen

Beilstein J. Nanotechnol. **2018,** *9,* 2960–2967.
doi:10.3762/bjnano.9.275

Received: 03 September 2018
Accepted: 06 November 2018
Published: 30 November 2018

This article is part of the thematic issue "Advanced hybrid nanomaterials".

Guest Editor: A. Taubert

Abstract

Nanosized porphyrin-containing metal-organic frameworks (MOFs) attract considerable attention as solid-state photosensitizers for biological applications. In this study, we have for the first time synthesised and characterised phosphinate-based MOF nanoparticles, nanoICR-2 (Inorganic Chemistry Rez). We demonstrate that nanoICR-2 can be decorated with anionic 5,10,15,20-tetrakis(4-R-phosphinatophenyl)porphyrins (R = methyl, isopropyl, phenyl) by utilizing unsaturated metal sites on the nanoparticle surface. The use of these porphyrins allows for superior loading of the nanoparticles when compared with commonly used 5,10,15,20-tetrakis(4-carboxyphenyl)porphyrin. The nanoICR-2/porphyrin composites retain part of the free porphyrins photophysical properties, while the photodynamic efficacy is strongly affected by the R substituent at the porphyrin phosphinate groups. Thus, phosphinatophenylporphyrin with phenyl substituents has the strongest photodynamic efficacy due to the most efficient cellular uptake.

Introduction

Metal-organic frameworks (MOFs) are a class of crystalline coordination polymers possessing potential voids. Their structures combine inorganic nodes, metal centres forming so-called secondary building units (SBU), with organic linkers. The diversity of possible SBUs coupled with organic linkers of variable geometry enables the preparation of a large number of structures with tuneable pore sizes, topologies, and chemical nature [1,2]. Among them, MOFs with photoactivatable proper-

ties such as luminescence and photosensitization of singlet oxygen, $O_2(^1\Delta_g)$, are particularly attractive [3-5]. Singlet oxygen is a short-lived, highly oxidative species with bactericidal and virucidal properties [6]. The cytotoxic effect can be intentionally employed in anticancer treatment in the form of photodynamic therapy (PDT) [7,8].

The most commonly utilised photosensitizers in PDT are porphyrins or related compounds since they offer high quantum yields of $O_2(^1\Delta_g)$, chemical and photochemical stability, and absorb light between 600 and 900 nm, the region in which tissue transmits light best [9]. However, porphyrins tend to form aggregates in which the photosensitizing properties are lost [10]. In order to avoid porphyrin aggregation various supramolecular structures have been designed [11-13]. In this context, porphyrin-based MOFs offer unique systems in which a regular arrangement prevents porphyrins from aggregation whereas the porosity enables fast diffusion of the ground state $O_2(^3\Sigma_g)$ to and the excited $O_2(^1\Delta_g)$ from the solid photosensitizer [14-16].

In our recent work we have shown that microcrystalline porphyrin containing MOFs are poor $O_2(^1\Delta_g)$ photosensitizers [17], due to the combined effect of the quenching of excited states in tightly stacked porphyrin units and strong light absorption at the surface of microcrystalline particles, which results in a small portion of the molecules actively taking place in the photosensitizing process. One of the successful strategies to overcome these effects is the use of MOFs as nanoparticles, which also provides easier internalisation by cells [18]. Moreover, the downsizing of MOFs also facilitates the diffusion of $O_2(^1\Delta_g)$, and makes interactions with bulky biomolecules inside the cells more effective.

This concept was successfully applied using the UiO-66 family of MOFs: nanoparticles made of Hf_6-based SBUs with dicarboxylic porphyrin or chlorin linkers [19,20], or using Zr_6-based SBUs with 5,10,15,20-tetrakis(4-carboxyphenyl)porphyrin (TCPP), named PCN-224 and PCN-222 [21,22]. Zeng et al. extended the π system of TCPP by employing tetracarboxyphenyl benzoporphyrin, which increased the absorption in the red region of visible light [23]. Alternatively, the antitumor activity of porphyrinic PCN-224 was increased by combining photodynamic and photothermal effects with chemotherapy; in this case the MOF was deposited onto gold nanorods and impregnated with a chemotherapeutic agent [24]. Strong phototoxic effects were reported in all of these studies. However, the drawback of zirconium-based MOFs is the degradation in the presence of phosphate buffer (Figure S1, Supporting Information File 1) and therefore the mode of action is highly disputable [15].

In this work, we employed metal-organic framework ICR-2 (ICR stands for Inorganic Chemistry Rez) constructed from Fe^{3+} and phenylene-1,4-bis(methylphosphinic acid) (PBPA) linkers [25]. ICR-2 in the microcrystalline form is stable in aqueous solutions even at high temperatures and partly retains its structure and porosity even after treatment with phosphate buffer saline (PBS) (Figure S1, Supporting Information File 1). We prepared ICR-2 nanoparticles (nanoICR-2) the surface of which we modified with three different anionic porphyrins forming stable colloids in absolute EtOH or *N*,*N*-dimethylformamide (DMF) (Figure 1). Importantly, the porphyrins on the nanoparticle surfaces retain their photophysical properties including $O_2(^1\Delta_g)$ generation. We demonstrate the photodynamic activity of these nanoICR-2/porphyrin composites on HeLa cells.

Results and Discussion

Preparation and characterisation

Various organic solvents and temperatures were screened for the successful preparation of nanoICR-2. The use of pure formamide (FA) or mixtures with DMF of more than 50 vol % FA at 100 °C led to the formation of nanoparticles with approx-

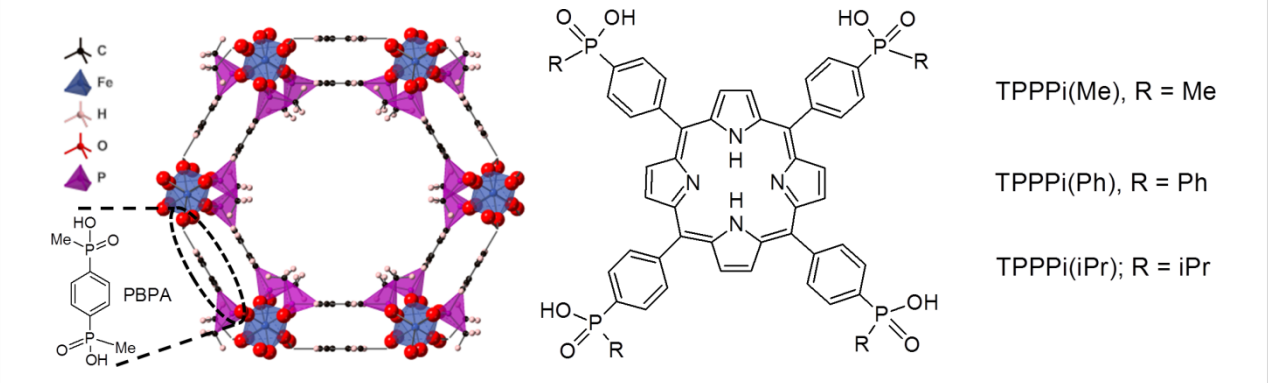

Figure 1: Structure of ICR-2 viewed along the *c* axis (left) and the structure of the modifying porphyrins (right). Colour coding: octahedrally coordinated iron atoms are blue and phosphinate tetrahedra are magenta, O (red), C (black), and H (white).

imately 30 nm in diameter. The origin of the nanoparticle formation is probably the suppression of the crystallization along the *c*-axis leading to a narrow particle size distribution (Figure 2 and Figure 3). Increasing the temperature to 120 °C resulted in the formation of longer nanoparticles (Figure S2, Supporting Information File 1). Unfortunately, all attempts to control the nanoparticle length failed and therefore we focused on the smaller nanoparticles. The best results were finally obtained in FA/DMF = 9:1 mixture at 100 °C for 96 h. The optimized synthesis was well reproducible and the size of the nanoparticles did not significantly differ from one batch to another.

To confirm the composition, nanoICR-2 was characterised by powder X-ray diffraction measurements (XRD), transmission electron microscopy (TEM), and dynamic light scattering (DLS). The powder XRD pattern depicted in Figure 4 clearly corresponds to the ICR-2 phase [25]. The size of the coherent diffraction domains of 29 nm was calculated from the broadening of the 110 and 020 diffractions using the Scherrer equation. The analysis of TEM images in Figure 2 (left) provides an average particle size of 28 nm, which is in good agreement with the results from the powder XRD analysis.

The dispersibility of nanoICR-2 in aqueous media and its surface charge potential were evaluated using dynamic light scattering (DLS, Figure S3A, Supporting Information File 1). In water, nanoICR-2 forms aggregates with a mean value of the size distribution of 87 ± 31 nm (by number, *Z*-average = 136 nm, PDI = 0.12). The zeta potential of nanoICR-2 in water is slightly positive with an average of 5 ± 5 mV (Figure S4A, Supporting Information File 1), evidencing that the prevailing terminal groups on the surface of nanoICR-2 are coordinatively unsaturated Fe cationic sites.

NanoICR-2 was modified with three anionic porphyrins: 5,10,15,20-tetrakis(4-methylphosphinatophenyl)porphyrin (TPPPi(Me)), 5,10,15,20-tetrakis(4-isopropylphosphinatophenyl)porphyrin (TPPPi(iPr)), and 5,10,15,20-tetrakis(4-phenylphosphinatophenyl)porphyrin (TPPPi(Ph)). We also tested commercially available 5,10,15,20-tetrakis(4-carboxyphenyl)porphyrin (TCPP). However, its binding was much weaker, which resulted in approximately 20-times lower porphyrin loading. This is probably due to weaker bond of the

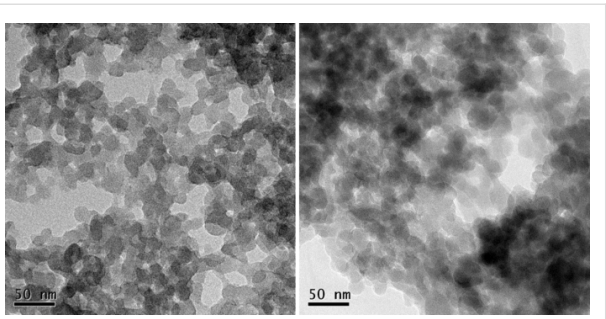

Figure 3: TEM images of parent nanoICR-2 (left) and nanoICR-2/TPPPi(Ph) (right). The scale bars represent 50 nm.

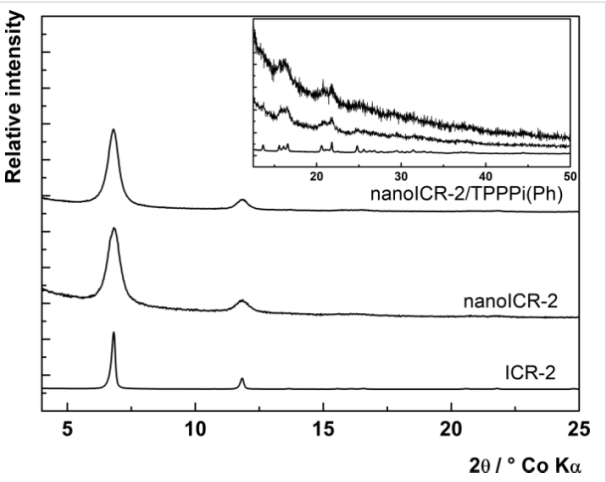

Figure 4: Powder XRD patterns of microcrystalline ICR-2 (bottom line), nanoICR-2 (middle line) and nanoICR-2/TPPPi(Ph) (top line), intensity of microcrystalline ICR-2 peaks were divided by 50.

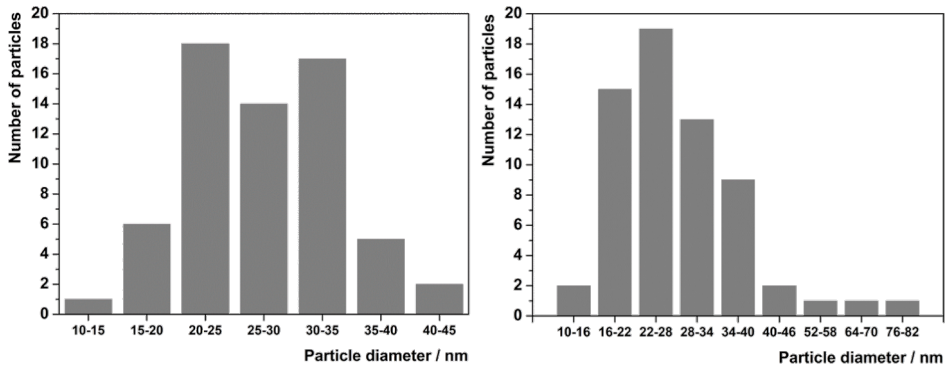

Figure 2: Particle size distributions of nanoICR-2 (left) and nanoICR-2/TPPPi(Ph) (right).

carboxylic group to Fe^{3+} in comparison with the phosphinic groups. The modification was done by shaking nanoICR-2 in DMF solution of the respective porphyrin. To achieve better biocompatibility, the modified nanoparticles were thoroughly washed with DMF and dispersed in absolute EtOH with a porphyrin concentration of 10^{-4} mol·L^{-1}. To investigate the effects of porphyrin loadings, we prepared two additional samples where 50% and 25% of the original amount of TPPPi(Ph) was used for the modification (denoted nanoICR-2/TPPPi(Ph)½ and nanoICR-2/TPPPi(Ph)¼). This resulted in lower amounts of attached porphyrin to the nanoparticles, i.e., 6×10^{-5} and 3×10^{-5} mol·L^{-1} for nanoICR-2/TPPPi(Ph)½ and nanoICR-2/TPPPi(Ph)¼, respectively.

The ideal structure of ICR-2 does not contain free binding sites for anions and therefore the anionic porphyrins can bind only to the terminal Fe atoms located on the surface of the nanoparticles. In addition, the porphyrin units are larger (over 10 Å) than the pore diameter of ICR-2 (9 Å) and thus they cannot enter the pores. This hypothesis was confirmed by the fact that non-anionic 5,10,15,20-tetraphenylporphyrin does not bind to nanoICR-2. Also, when larger ICR-2 nanoparticles (prepared at 120 °C, Figure S2, Supporting Information File 1) were used the TPPPi(Ph) loading was an order of magnitude lower than for nanoICR-2.

The porphyrin-modified nanoICR-2 particles (nanoICR-2/porphyrin) were characterised by powder XRD, TEM, DLS, and UV–vis and fluorescence spectroscopy. The powder XRD patterns of all composites, depicted in Figure 4 and Figure S5 (Supporting Information File 1), do not show significant changes in comparison with that of the parent nanoICR-2. Also, the coherent diffraction domain of 30 nm is virtually unchanged from the parent nanoparticles. The analysis of TEM data confirmed the preservation of the particle size (29 nm on average), only the particle size distribution was broader (Figure 2).

DLS experiments with aqueous dispersions of nanoICR-2/porphyrin revealed the formation of nanoparticle aggregates, with mean values of the size distribution of 91 ± 23 nm (by number, *Z*-average = 198 nm, PDI = 0.24), 195 ± 90 nm (by number, *Z*-average = 291 nm, PDI = 0.26), and 128 ± 53 nm (by number, *Z*-average = 193 nm, PDI = 0.16) for TPPPi(Me), TPPPi(iPr), and TPPPi(Ph), respectively (Figure S3, Supporting Information File 1). These values are somewhat bigger than the size of the parent nanoICR-2 aggregates in water (87 ± 31 nm). Importantly, the zeta potential of the nanoICR-2/porphyrin aggregates switched to negative values: −20 ± 4 mV, −25 ± 5 mV, and −28 ± 5 mV for TPPPi(Me), TPPPi(iPr), and TPPPi(Ph), respectively (Figure S4, Supporting Information File 1). These results are consistent with the binding of the porphyrin phosphinate groups to the coordinatively unsaturated Fe cationic sites at the surface of the nanoparticles. Because of the nearly square planar geometry of the porphyrins it is probable that only 1–2 phosphinate groups are bonded to nanoICR-2 and therefore some of the phosphinate groups remains unbound and induce the negative zeta potentials. In agreement with this assumption, the zeta potentials decrease with decreasing porphyrin loading to −22 ± 3 mV and −17 ± 4 mV for nanoICR-2/TPPPi(Ph)½ and nanoICR-2/TPPPi(Ph)¼, respectively.

We also tested the stability of nanoICR-2/porphyrin in PBS media. Even though ICR-2 can stand PBS treatment in its microcrystalline form, when nanoparticles of either nanoICR-2 or nanoICR-2/porphyrin were treated for 4 h in PBS it resulted in amorphisation of the ICR-2 nanoparticles, and in the case of nanoICR-2/porphyrin in partial dissolution of the porphyrin.

In order to ascertain the effects of the MOF structure on the porphyrin units, UV–vis absorption and fluorescence spectra were measured and compared with the corresponding spectra of the free porphyrins. The absorption spectra show characteristic absorption bands of metal-free porphyrins: the Soret band at 415 nm and four Q-bands in the region between 500 and 650 nm. The comparison of the absorption spectra of free TPPPi(Ph) and corresponding nanoICR-2/TPPPi(Ph) nanoparticles (Figure 5) demonstrates that the position and shape of the absorption bands do not change after binding of the porphyrin units onto the nanoparticles. The same observation is valid for both nanoICR-2/TPPPi(Ph)½ and nanoICR-2/TPPPi(Ph)¼ (Figure S6, Supporting Information File 1), indicating that the formation of porphyrin aggregates on the surface of the ICR-2

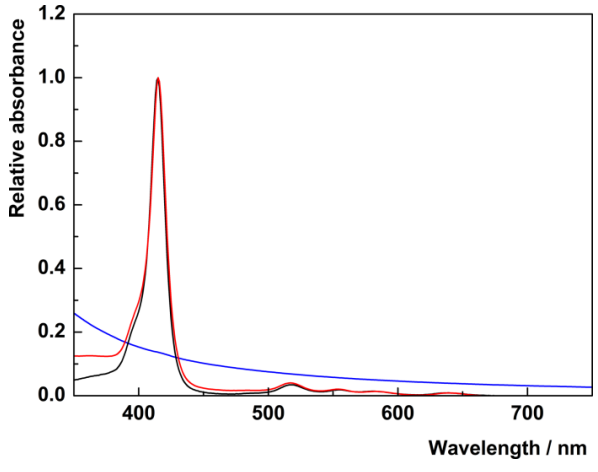

Figure 5: Normalized UV–vis spectra of nanoICR-2 (blue), TPPPi(Ph) (black), and nanoICR-2/TPPPi(Ph) (red) in EtOH solution.

nanoparticles is not controlled by the amount of bound porphyrins. On the other hand, the Soret bands of nanoICR-2/TPPPi(Me) and nanoICR-2/TPPPi(iPr) (Figure S7 and Figure S8, Supporting Information File 1) are broadened and red shifted because of partial porphyrin aggregation. The magnitude of aggregation is in the order TPPPi(Ph) < TPPPi(iPr) ≈ TPPPi(Me).

When excited at 415 nm, the dispersions of nanoICR-2/porphyrin in EtOH exhibit red fluorescence with two bands at 655 and 720 nm (Figure S9, Supporting Information File 1). The fluorescence quantum yields of approximately 0.01 are rather low, when compared with free porphyrins in the same solvent ($\Phi_f = 0.07$). The lower Φ_f values can be attributed to non-radiative quenching of the excited singlet states due to the partial aggregation of the porphyrins at the surface of nanoICR-2 and the proximity of iron atoms constituting the ICR-2 structure. It is worth noting that the porphyrin loading does not affect the fluorescence quantum yields.

Photobiological properties

Cellular uptake and intracellular localization

HeLa cells were treated with the nanoparticles in Eagle's Minimum Essential Medium (EMEM) without foetal bovine serum to avoid modification of the particle surface properties by nonspecific binding of serum albumin. The cellular uptake of the nanoparticles was quantified by flow-cytometry analysis of porphyrin fluorescence associated with the cells. Figure 6A shows the rate of internalization of the photosensitizers into the cells with different modifications of nanoICR-2. The highest cellular uptake was observed for nanoICR-2/TPPPi(Ph), followed by nanoICR-2/TPPPi(iPr) and nanoICR-2/TPPPi(Me). The most efficiently accumulating sample nanoICR-2/TPPPi(Ph) was therefore selected for determination of the uptake kinetic. As shown in Figure 6B, the incubation of the cells with a fixed amount of the nanoparticles for different time periods revealed significant uptake already after 30 min and the concentration increased gradually up to 4 h. For this reason, further photobiological experiments were performed after 4 h of incubation with the nanoparticles. The cellular uptake upon incubation with different concentrations of the nanoparticles yielded almost linear dose dependence (Figure 6C). Furthermore, the intracellular localization of nanoICR-2/TPPPi(Ph) was investigated using confocal microscopy. Figure 7 clearly shows that the nanoparticles accumulate in intracellular vesicles, which strongly co-localize with the fluorescent marker of lysosomes. This is similar to the results of a previous study performed with PCN-222 nanoparticles [22].

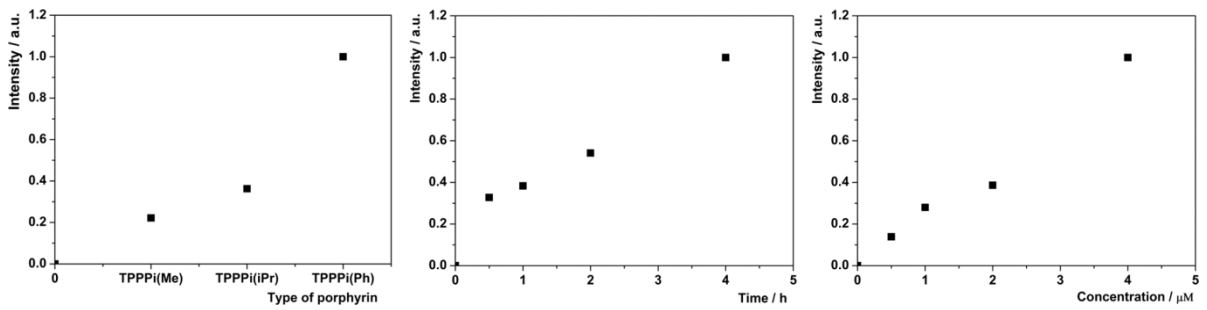

Figure 6: (A) Comparison of the cellular uptake of different types of nanoICR-2 with porphyrin concentration of 1 μM; (B) time dependence of the cellular uptake of nanoICR-2/TPPPi(Ph) with porphyrin concentration of 1 μM; (C) concentration dependence of the cellular uptake of nanoICR-2/TPPPi(Ph).

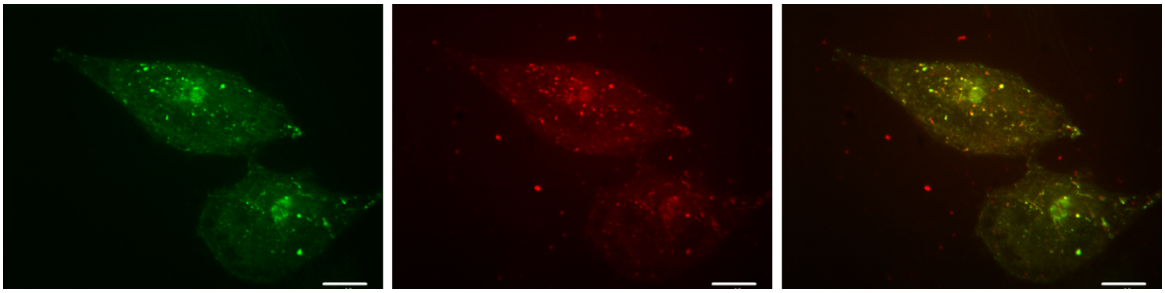

Figure 7: Confocal microscopy of HeLa cells incubated with 2 μM nanoICR-2/TPPPi(Ph) for 24 h: LysoTracker Green (left); nanoICR-2/TPPPi(Ph) (middle); overlay (right). The white scale bars correspond to 10 μm.

Toxicity and phototoxicity studies

Dark toxicity of the porphyrin-modified nanoICR-2 was investigated on HeLa cells in EMEM without serum in the presence of 0.5–4 μM nanoparticles (with respect to porphyrin) for 4 h followed by incubation in full culture medium without phenol red for 24 h. At concentrations used for the experiments, only limited suppression of cellular metabolic activity was observed for all three porphyrins (Figure 8A). On the other hand, when the cells were irradiated with a water-filtered halogen light, only nanoICR-2/TPPPi(Ph) exhibited a clear phototoxic effect. The IC_{50} value of this sample was 1.8 ± 0.5 μM. Interestingly, nanoICR-2/TPPPi(iPr) and nanoICR-2/TPPPi(Me) did not reveal any phototoxic effect (Figure 8B). The results of phototoxicity tests well correspond with the cellular uptake values, which were the highest for nanoICR-2/TPPPi(Ph). A comparison of PDT activity with other systems can be made only under identical conditions (e.g., irradiation wavelength, time, dose). We can compare the activity of nanoICR-2/TPPPi(Ph) with the activity of previously studied PCN-222 nanoparticles where both systems display comparable activity [22].

Conclusion

In the context of photodynamic therapy, we present composite materials based on nanoparticles of the ICR-2 metal-organic framework decorated with phosphinic acid-substituted porphyrins. These substituted porphyrins showed superior affinity towards the Fe-MOF ICR-2 in comparison with the well-known tetracarboxyphenyl porphyrin, and this feature allows for superior photosensitizer loading of the nanoparticles. The porphyrins retain part of their photophysical properties including production of singlet oxygen. Interestingly, the photodynamic activity on HeLa cells strongly depends on the R substituent at the P atom, i.e., only the phenyl substituent (TPPPi(Ph)) ensured high phototoxicity, comparable with the best MOF systems. This feature does not seem to arise from the differences in singlet oxygen photosensitizing ability [26], but can be assigned to the differences in the biological properties provided by the substituent of the unbounded phosphinic groups at the surface of the composite nanoparticles. Unfortunately, the elucidation of the structure–activity relationship is rendered difficult due to the instability of the nanoICR-2/porphyrin nanoparticles in PBS media, as also observed for Zr-based MOFs.

Experimental

Materials: *N*,*N*-dimethylformamide (DMF, Lach-Ner, Czech Republic), absolute ethanol (EtOH, Fischer Sci.), $FeCl_3 \cdot 6H_2O$, formamide, and phosphate-buffered saline suitable for cell culture (all Sigma-Aldrich) were used as purchased. Phenylene-1,4-bis(methylphosphinic acid) was prepared according to [25]. Phosphinic acid porphyrins 5,10,15,20-tetrakis(4-methylphosphinatophenyl)porphyrin (TPPPi(Me)), 5,10,15,20-tetrakis(4-isopropylphosphinatophenyl)porphyrin (TPPPi(iPr)), and 5,10,15,20-tetrakis(4-phenylphosphinatophenyl)porphyrin (TPPPi(Ph)) were prepared according to [26].

Synthesis of nanoICR-2: Into a 20mL vial (Wheaton) was added 5.4 mg (0.02 mmol) $FeCl_3 \cdot 6H_2O$, 9.4 mg (0.04 mmol) PBPA, 1 mL DMF, and 9 mL formamide. The vial was tightly closed and immersed into a programmable oven (Memmert UF30 Plus) for 96 h at 100 °C (heat ramp 1 h and cooling down 6 h). The resulting mixture was centrifuged (Hettich Rotina 380R, 11000 rpm for 5 min) and washed three times with distilled water and two times with absolute EtOH; dispersion of ICR-2 nanoparticles in EtOH (approximately 5 mL) was obtained.

Modification of nanoICR-2 with porphyrins: The whole batch of nanoICR-2 dispersion in EtOH prepared above was

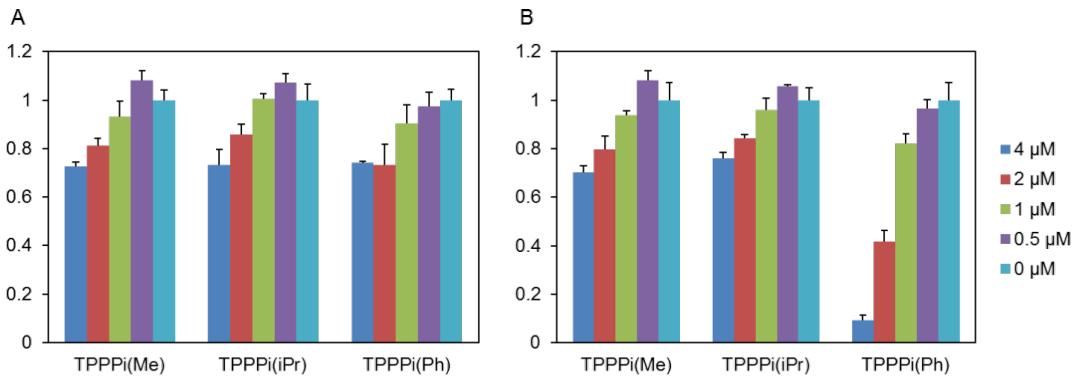

Figure 8: Relative viability of HeLa cells incubated for 4 h with specified concentrations of nanoICR-2/porphyrin in the dark (A) or irradiated with a halogen lamp for 15 min (B). Note: The results labelled 0 μM belong to the control experiments in which cells were irradiated in the absence of nanoICR-2/porphyrin.

centrifuged again (11000 rpm, 5 min), the solvent was decanted, and nanoICR-2 was dispersed in 5 mL of DMF. Separately, 2.5 mmol of each porphyrin was dissolved in 10 mL of DMF, the solution was added to the nanoICR-2 dispersion, and the mixture was shaken at RT overnight (16 h). Then, the mixture was centrifuged (11000 rpm, 5 min.) and washed three times with absolute EtOH to remove the excess of porphyrin. Finally, nanoICR-2/TPPPi(Me), nanoICR-2/ TPPPi(iPr), and nanoICR-2/TPPPi(Ph) were dispersed and stored in absolute EtOH (ca. 10 mL) at a concentration of 10^{-4} mol·L^{-1}. The samples with lower porphyrin loading were prepared analogously, only the amount of the TPPPi(Ph) in the DMF solution was 1.25 mmol (nanoICR-2/TPPPi(Ph)½) and 0.625 mmol (nanoICR-2/ TPPPi(Ph)¼). This led to lower porphyrin concentrations in the resulting colloids of 6×10^{-5} mol·L^{-1} and 3×10^{-5} mol·L^{-1} for nanoICR-2/TPPPi(Ph)½ and nanoICR-2/ TPPPi(Ph)¼, respectively.

Stability studies: NanoICR-2/TPPPi(Ph) in EtOH were centrifuged (11000 rpm, 5 min), redispersed in 10 mL of PBS, and shaken for 4 h at RT. The resulting mixture was centrifuged (11000 rpm, 5 min), washed three times with absolute EtOH, and air-dried before powder XRD measurement.

Instrumental methods: Powder X-ray diffraction (XRD) was measured using a PANalytical X'Pert PRO diffractometer in the reflexion setup equipped with a conventional Co X-ray tube (40 kV, 30 mA). Qualitative analysis was performed with the HighScorePlus software package (PANalytical, Almelo, The Netherlands, version 3.0) and the JCPDS PDF-2 database [27]. UV–vis absorption spectra of the dispersions were recorded on a Perkin Elmer Lambda 35 spectrometer. High-resolution transmission electron microscopy (TEM) was carried out on a JEOL JEM 3010 microscope operated at 300 kV (LaB_6 cathode, point resolution 1.7 Å) with an Oxford Instruments Energy Dispersive X-ray (EDX) detector. The particle size distributions and zeta potentials in water were determined by dynamic light scattering (DLS) using a particle size analyser Zetasizer Nano ZS (Malvern, UK). Fluorescence spectra and absolute fluorescence quantum yields, Φ_L, were measured using a Quantaurus QY C11347-1 spectrometer (Hamamatsu, Japan).

Cultivation of the cells: The human cervix carcinoma HeLa cell line was cultivated in the Eagle's Minimum Essential Medium (EMEM; Sigma-Aldrich) supplemented with 0.5 mM glutamine and 5% foetal bovine serum (full culture medium) at 37 °C in atmosphere containing 5% CO_2.

Phototoxicity and dark toxicity studies: The cells were seeded onto 96-well plates in full culture medium. Next day, the cells were exposed to 0.5–4 μM equivalent of the nanoparticles in the fresh medium without foetal bovine serum for 4 h. A final concentration of EtOH in the culture medium was less than 4 % v/v. After incubation, the medium was changed for full culture medium without phenol red and the cells were immediately irradiated by a 150 W halogen lamp (Thorlabs) with a water filter for 15 min (45 mW·cm^{-2}). After another 24 h, a viability of the cells was assayed by the resazurin assay (Sigma-Aldrich). Dark toxicity experiments were performed in the same way in the dark.

Confocal microscopy: HeLa cells were seeded onto dishes with a glass bottom (MatTek) in full culture medium. After 24 h, the cells received fresh medium without serum and phenol red, and were mixed with the nanoparticles of 2 μM total concentration. After 4 h, the cells were washed and stained with LysoTracker Green (Thermo Fisher Scientific) and inspected with a spinning disc confocal microscope (Revolution XD, Andor). The excitation wavelengths used for monitoring of nanoparticles and lysosomes were 405 nm and 488 nm, respectively. During the confocal microscopy, the cells were maintained at 37 °C and 5% CO_2 atmosphere.

Flow cytometry: The cells were plated onto 6-well plates in full culture medium. The next day, they were treated with indicated amount of nanoparticles for the indicated period of time in the fresh medium without serum. Then, the plates were washed with PBS and trypsinized. Uptake of MOFs was measured by flow cytometry analysis with excitation and emission recorded at 405 nm and 655–685 nm, respectively (BD FACSaria III).

Supporting Information

Supporting Information File 1

Additional experimental data.
[https://www.beilstein-journals.org/bjnano/content/supplementary/2190-4286-9-275-S1.pdf]

Acknowledgements

This work was supported by the Czech Science Foundation (project No. 16-02098S), the Operative Program Prague – Competitiveness (OPPC CZ.2.16/3.1.00/21537, OPPC CZ.2.16/3.1.00/24503), and by the National Program of Sustainability (NPU I LO1601). We thank Petr Bezdička for XRD measurements.

ORCID® iDs

Martina Koncošová - https://orcid.org/0000-0002-8951-1282
Jaroslav Zelenka - https://orcid.org/0000-0001-8145-8037
Kamil Lang - https://orcid.org/0000-0002-4151-8805
Jan Demel - https://orcid.org/0000-0001-7796-6338

References

1. Rosi, N. L.; Kim, J.; Eddaoudi, M.; Chen, B.; O'Keeffe, M.; Yaghi, O. M. *J. Am. Chem. Soc.* **2005,** *127,* 1504–1518. doi:10.1021/ja045123o
2. Férey, G. *Chem. Soc. Rev.* **2008,** *37,* 191–214. doi:10.1039/b618320b
3. Zhang, Y.; Yuan, S.; Day, G.; Wang, X.; Yang, X.; Zhou, H.-C. *Coord. Chem. Rev.* **2018,** *354,* 28–45. doi:10.1016/j.ccr.2017.06.007
4. Demel, J.; Kubát, P.; Millange, F.; Marrot, J.; Císařová, I.; Lang, K. *Inorg. Chem.* **2013,** *52,* 2779–2786. doi:10.1021/ic400182u
5. Medishetty, R.; Zaręba, J. K.; Mayer, D.; Samoć, M.; Fischer, R. A. *Chem. Soc. Rev.* **2017,** *46,* 4976–5004. doi:10.1039/c7cs00162b
6. Pellieux, C.; Dewilde, A.; Pierlot, C.; Aubry, J.-M. *Methods Enzymol.* **2000,** *319,* 197–207. doi:10.1016/s0076-6879(00)19020-2
7. Malatesti, N.; Munitic, I.; Jurak, I. *Biophys. Rev.* **2017,** *9,* 149–168. doi:10.1007/s12551-017-0257-7
8. Singh, S.; Aggarwal, A.; Bhupathiraju, N. V. S. D. K.; Arianna, G.; Tiwari, K.; Drain, C. M. *Chem. Rev.* **2015,** *115,* 10261–10306. doi:10.1021/acs.chemrev.5b00244
9. Habermeyer, B.; Guilard, R. *Photochem. Photobiol. Sci.* **2018,** *17,* 1675–1690. doi:10.1039/c8pp00222c
10. Lang, K.; Mosinger, J.; Wagnerová, D. M. *Coord. Chem. Rev.* **2004,** *248,* 321–350. doi:10.1016/j.ccr.2004.02.004
11. Demel, J.; Lang, K. *Eur. J. Inorg. Chem.* **2012,** 5154–5164. doi:10.1002/ejic.201200400
12. Hynek, J.; Zelenka, J.; Rathouský, J.; Kubát, P.; Ruml, T.; Demel, J.; Lang, K. *ACS Appl. Mater. Interfaces* **2018,** *10,* 8527–8535. doi:10.1021/acsami.7b19835
13. Mosinger, J.; Lang, K.; Plíštil, L.; Jesenská, S.; Hostomský, J.; Zelinger, Z.; Kubát, P. *Langmuir* **2010,** *26,* 10050–10056. doi:10.1021/la1001607
14. Zhou, J.; Tian, G.; Zeng, L.; Song, X.; Bian, X.-w. *Adv. Healthcare Mater.* **2018,** *7,* 1800022. doi:10.1002/adhm.201800022
15. Lismont, M.; Dreesen, L.; Wuttke, S. *Adv. Funct. Mater.* **2017,** *27,* 1606314. doi:10.1002/adfm.201606314
16. Lan, G.; Ni, K. *Coord. Chem. Rev.*, in press. doi:10.1016/j.ccr.2017.09.007
17. Hynek, J.; Rathouský, J.; Demel, J.; Lang, K. *RSC Adv.* **2016,** *6,* 44279–44287. doi:10.1039/c6ra04066g
18. Majewski, M. B.; Noh, H.; Islamoglu, T.; Farha, O. K. *J. Mater. Chem. A* **2018,** *6,* 7338–7350. doi:10.1039/c8ta02132e
19. Lu, K.; He, C.; Lin, W. *J. Am. Chem. Soc.* **2014,** *136,* 16712–16715. doi:10.1021/ja508679h
20. Lu, K.; He, C.; Lin, W. *J. Am. Chem. Soc.* **2015,** *137,* 7600–7603. doi:10.1021/jacs.5b04069
21. Park, J.; Jiang, Q.; Feng, D.; Mao, L.; Zhou, H.-C. *J. Am. Chem. Soc.* **2016,** *138,* 3518–3525. doi:10.1021/jacs.6b00007
22. Bůžek, D.; Zelenka, J.; Ulbrich, P.; Ruml, T.; Křížová, I.; Lang, J.; Kubát, P.; Demel, J.; Kirakci, K.; Lang, K. *J. Mater. Chem. B* **2017,** *5,* 1815–1821. doi:10.1039/c6tb03230c
23. Zeng, J.-Y.; Zou, M.-Z.; Zhang, M.; Wang, X.-S.; Zeng, X.; Cong, H.; Zhang, X.-Z. *ACS Nano* **2018,** *12,* 4630–4640. doi:10.1021/acsnano.8b01186
24. Zeng, J.-Y.; Zhang, M.-K.; Peng, M.-Y.; Gong, D.; Zhang, X.-Z. *Adv. Funct. Mater.* **2018,** *28,* 1705451. doi:10.1002/adfm.201705451
25. Hynek, J.; Brázda, P.; Rohlíček, J.; Londesborough, M. G. S.; Demel, J. *Angew. Chem., Int. Ed.* **2018,** *57,* 5016–5019. doi:10.1002/anie.201800884
26. Hynek, J.; Koncošová, M.; Zelenka, J.; Křížová, I.; Ruml, T.; Kubát, P.; Demel, J.; Lang, K. *Org. Biomol. Chem.* **2018,** *16,* 7274–7281. doi:10.1039/c8ob01984c
27. *JCPDS PDF-2 database,* Release 54; International Centre for Diffraction Data: Newtown Square, PA, U.S.A., 2004.

License and Terms

BEILSTEIN JOURNAL OF NANOTECHNOLOGY

Co-intercalated layered double hydroxides as thermal and photo-oxidation stabilizers for polypropylene

Qian Zhang[1], Qiyu Gu[1], Fabrice Leroux[2], Pinggui Tang[1], Dianqing Li[1] and Yongjun Feng[*1]

Full Research Paper

Open Access

Address:
[1]State Key Laboratory of Chemical Resource Engineering, Beijing Engineering Center for Hierarchical Catalysts, Beijing University of Chemical Technology, No. 15 Beisanhuan East Road, Beijing 100029, China and [2]Université Clermont Auvergne, Institut de Chimie de Clermont-Ferrand ICCF, UMR-CNRS 6296, F 63171 Aubière, France

Email:
Yongjun Feng[*] - yjfeng@mail.buct.edu.cn

* Corresponding author

Keywords:
co-intercalation; composites; layered double hydroxides; photo-oxidation stability; polypropylene; thermal stability

Beilstein J. Nanotechnol. **2018,** *9,* 2980–2988.
doi:10.3762/bjnano.9.277

Received: 22 July 2018
Accepted: 16 November 2018
Published: 05 December 2018

This article is part of the thematic issue "Advanced hybrid nanomaterials".

Associate Editor: C. T. Yavuz

Abstract

An elegant and efficient approach consisting in the co-intercalation of stabilizing molecular anions is described here. The thermal stabilizer calcium diethyl bis[[[3,5-bis(1,1-dimethylethyl)-4-hydroxyphenyl]methyl]phosphonate] (Irganox 1425, MP-Ca) and a photo-oxidation stabilizer (hindered amine light stabilizer, HALS) are co-intercalated into the interlayer regions of layered double hydroxides (LDH) in a one-step coprecipitation. These hybrid organic–inorganic materials are successively dispersed in polypropylene to form $H_nM_{n'}$-Ca_2Al/PP composite films (with H = HALS and M = MP) through a solvent casting method. The corresponding crystalline structure, chemical composition, morphology as well as the resistance against thermal aging and photo-oxidation are carefully investigated by various techniques. The results show that the powdered $H_nM_{n'}$-Ca_2Al-LDHs hybrid materials have a much higher thermal stability than MP-Ca and HALS before intercalation. In addition, the $H_nM_{n'}$-Ca_2Al/PP composites exhibit a higher overall resistance against thermal degradation and photo-oxidation compared to LDHs intercalated with only HALS or MP. This underlines the benefit of the co-intercalation. The co-intercalated LDH materials pave a new way in designing and fabricating high-performance multifunctional additives for polymers.

Introduction

Hindered phenols and hindered amines, containing the functional groups 2,6-di-*tert*-butylphenol and 2,2,6,6-tetramethylpiperidine, respectively, are widely used as functional additives in polymers to prolong the service life [1-3]. Generally, the anti-aging agents effectively inhibit the degradation in two ways: (1) through capturing generated free radicals and stopping auto-oxidation and (2) through decomposing and eliminating hydroperoxides [4,5]. However, anti-aging agents are often organic

chemicals that easily migrate and volatilize from the polymer, reducing the anti-aging efficiency and increasing environmental pollution [6]. Therefore, it is of interest to explore novel multifunctional additives for polymers with high anti-aging performance together with high migration resistance.

Recently, inorganic–organic hybrid functional additives have attracted increasing attention for their wide applications in polymers [7]. Organic anti-aging species have been immobilized onto inorganic supports (e.g., carbon nanotubes, SiO_2, graphene oxide) to produce inorganic–organic composites with higher migration resistance [8-10]. More recently, layered double hydroxides (LDHs), a layered host–guest material, have emerged as promising inorganic nanocontainers for functional organic active species to enhance the thermal and photo-oxidation stability of interleaved organic species as well as to endow the polymer/LDH composites with the desired properties [11-14]. In our previous work, a series of intercalated antioxidants and photo-oxidation stabilizers with a single active component have been prepared by coprecipitation. In these polymer/LDH compounds, the resistance against aging was significantly improved [15-17]. For example, the antioxidant Irganox 1425 (see Figure 1, abbreviated as MP-Ca) was intercalated into Ca_2Al-LDH through coprecipitation of MP-Ca and $Al(NO_3)_3$ at pH 10, to yield MP-Ca_2Al-LDH. Here, the MP-Ca was used the source of Ca for the host sheet and that of MP for the guest anions. Polypropylene (PP) protected with the prepared MP-Ca_2Al-LDH exhibited enhanced thermal stability and anti-migration behavior in comparison with MP-Ca/PP composites. Lately, some studies have demonstrated much better performance of multi-component intercalation compounds compared to the corresponding single-component intercalation compounds as well as to the physical mixtures of the components [18,19]. The benefit of the co-intercalation is attributed to synergistic effects between the different active species associated to a higher dispersion in the composites [20,21].

In this work, we designed and fabricated a series of novel co-intercalated thermal and photo-oxidation stabilizers ($H_nM_{n'}$-Ca_2Al) through straightforward co-precipitation of HALS and MP-Ca (Figure 1) [16,17], and examined the resistance of the $H_nM_{n'}$-Ca_2Al/PP composites against thermal degradation and photo-oxidation as a function of the molar ratio between HALS and MP in the interlayer regions.

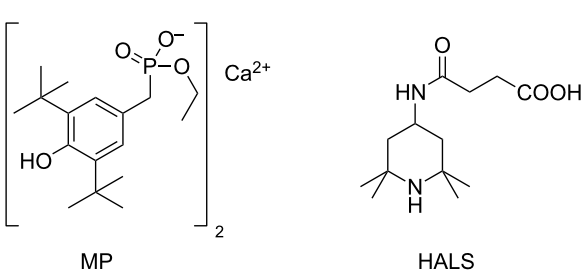

Figure 1: Molecular structures of Irganox 1425 (MP-Ca) and hindered amine light stabilizer (HALS).

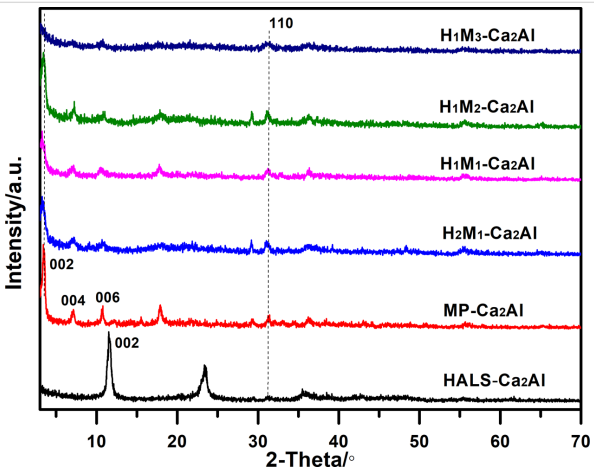

Figure 2: Powder X-ray diffraction patterns of different $H_nM_{n'}$-Ca_2Al-LDH samples.

Results and Discussion

Analysis of $H_nM_{n'}$-Ca_2Al-LDHs

Figure 2 displays powder XRD patterns of $H_nM_{n'}$-Ca_2Al-LDHs with sharp (002), (004) and (006) reflection peaks at low angles and the weaker (110) peak at a higher angle, corresponding to the layered structure and the intra-layer structure in the host sheet [22]. The (002) reflection peaks of HALS-Ca_2Al and MP-Ca_2Al are located at 11.5° (d_{002} = 0.77 nm) and 3.4° (d_{002} = 2.52 nm), respectively. Simultaneously, for LDHs co-intercalated with HALS and MP (H_2M_1-Ca_2Al, H_1M_1-Ca_2Al, H_1M_2-Ca_2Al, H_1M_3-Ca_2Al), the (002) reflection peaks appear at ca. 3.4°, corresponding to the *d*-spacing values of 2.55, 2.68, 2.55, and 2.75 nm, respectively. The enlarged *d*-spacing of $H_nM_{n'}$-Ca_2Al-LDHs suggests that HALS and MP anions were co-intercalated into the LDH, and the different ratios of HALS/MP result in a slightly different arrangement of guest anions leading to minor variations of the *d*-spacing values. The full width at half maximum values of the (002) reflection of all $H_nM_{n'}$-Ca_2Al compounds are smaller than those of HALS-Ca_2Al and MP-Ca_2Al, indicating that the number of stacked platelets was decreased due to the co-intercalation. The results show that co-precipitation yields Ca_2Al-LDHs free of $CaCO_3$ by-product [23].

Figure 3 shows FTIR spectra of all the $H_nM_{n'}$-Ca_2Al-LDHs. One can observe characteristic stretching-vibration bands of LDHs, for example, the broad band at ca. 3445 cm^{-1} associated to the OH groups of interlayer water molecules and brucite-like

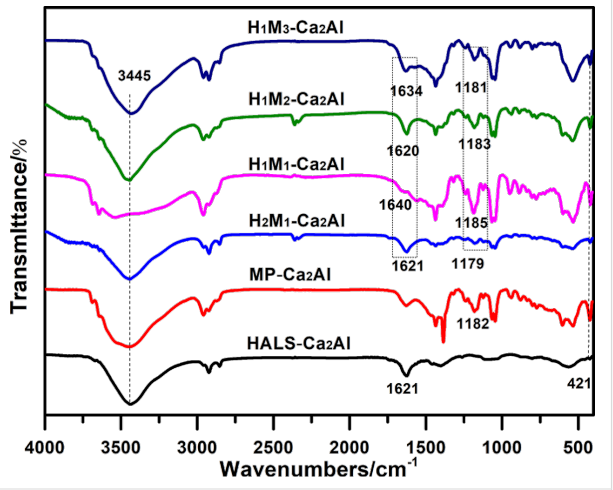

Figure 3: FTIR spectra of different $H_nM_{n'}$-Ca_2Al-LDH samples.

LDH layers. The band at 421 cm^{-1} is attributed to O–M–O lattice vibrations in LDH, which further proves the formation of a LDH platelet structure. Moreover, for HALS-Ca_2Al-LDH and MP-Ca_2Al-LDH, the characteristics stretching vibration bands of HALS and MP also occur, such as the carbonyl group of HALS at 1621 cm^{-1} (C=O) and the phosphate group of MP at 1181 cm^{-1} (P=O), 1050 cm^{-1} (P–O–C). Compared with 1645 cm^{-1} in HALS and 1164 cm^{-1} in MP-Ca, shifts of C=O and P=O are observed to 1621 cm^{-1} in HALS-Ca_2Al and 1182 cm^{-1} in MP-Ca_2Al, respectively, which probably results from the electrostatic interaction between the organic anions and the host sheets of Ca_2Al-LDH. After co-intercalation of HALS and MP, $H_nM_{n'}$-Ca_2Al samples demonstrate all of the characteristic absorption bands of the LDH host together with those of HALS and MP, suggesting the coexistence of active HALS and MP species within $H_nM_{n'}$-Ca_2Al-LDH.

Figure 4 presents SEM images of HALS-Ca_2Al, MP-Ca_2Al and $H_nM_{n'}$-Ca_2Al-LDHs. HALS-Ca_2Al and MP-Ca_2Al show typical platelet-like morphologies. In comparison with MP-Ca_2Al, HALS-Ca_2Al exhibits a flattened platelet-like structure and a larger average particle size. For the co-intercalated $H_nM_{n'}$-Ca_2Al, one observes a significant aggregation of LDH platelets leading to a porous flower-like morphology.

Figure 5 shows the TG and DTA curves of $H_nM_{n'}$-Ca_2Al-LDHs and Table 1 summarizes the corresponding data. In our previous work, the decomposition of HALS and Irganox 1425 molecular anions occurred with an exothermic DTA peak at 300 and 295 °C, respectively [16,17]. Here, three major stages of mass loss in the TG curve of $H_nM_{n'}$-Ca_2Al-LDH samples can be observed. The first mass loss up to 180 °C is assigned to the release of adsorbed water and crystal water; The second one in the range of 180–250 °C is attributed to the dehydroxylation of the metal-hydroxide layer. The third large mass loss stage corresponding to the decomposition of HALS and MP ions appears at 250–450 °C with endothermic peaks between 300 and 360 °C in the DTA curve. The thermal stability of $H_nM_{n'}$-Ca_2Al-LDHs was expressed through the temperatures associated to a certain weight loss (i.e., $T_{25\%}$ is the temperature at which the sample has lost 25 wt %) in Table 1. For intercalated Ca_2Al-LDHs, the thermal oxidative decomposition occurs at temperatures higher than those of HALS and Irganox 1425. Moreover, the co-intercalated $H_nM_{n'}$-Ca_2Al-LDHs exhibit a higher decomposition temperature than HALS-Ca_2Al and MP-Ca_2Al, especially H_1M_2-Ca_2Al (356 °C). For the co-intercalated $H_nM_{n'}$-Ca_2Al-LDHs, the $T_{25\%}$ values gradually increase from 257 °C for H_2M_1-Ca_2Al to 299 °C for H_1M_3-Ca_2Al with an increasing content of M. The above results illustrate that the thermal stability of HALS and MP anions are enhanced after the co-intercalation of both anions into the interlayer region of LDHs.

Table 1: TG/DTA results of $H_nM_{n'}$-Ca_2Al-LDH samples.

sample	$T_{25\%}$ (°C)	DTA peak (°C)	residual mass (wt %)
HALS-Ca_2Al	283	300	55
MP-Ca_2Al	303	308	51
H_2M_1-Ca_2Al	257	310	45
H_1M_1-Ca_2Al	286	312	49
H_1M_2-Ca_2Al	293	306, 356	52
H_1M_3-Ca_2Al	299	320	48

Table 2 lists the element analysis data and the calculated chemical compositions of $H_nM_{n'}$-Ca_2Al-LDHs analyzed by CHN elemental analysis for the organic moieties and ICP atomic emission spectrometry for metal cations. The content of interlayer water is determined from the mass loss between 100 and 200 °C in the TG curves (Figure 5a). The fractions of HALS and MP anions are calculated based on the content of Al and C taking into account the charge balance. The molar fractions of the guest anions are close to the feeding ratio, suggesting the ratio between HALS and MP can be adjusted as designed. These results also suggest that both of HALS and MP anions have been co-intercalated into Ca_2Al-LDH.

Analysis of $H_nM_{n'}$-Ca_2Al-LDHs/PP composites

Figure 6 shows XRD patterns of $H_nM_{n'}$-Ca_2Al-LDHs/PP composites. All samples show the characteristic Bragg reflections of α-PP at 12–30° for (110), (040), (130), (111) and (131)/(041) *d*-spacings. That is, the addition of $H_nM_{n'}$-Ca_2Al-LDHs has only insignificant influence on the crystallization behavior of PP [24]. For HALS-Ca_2Al/PP and MP-Ca_2Al/PP, the typical

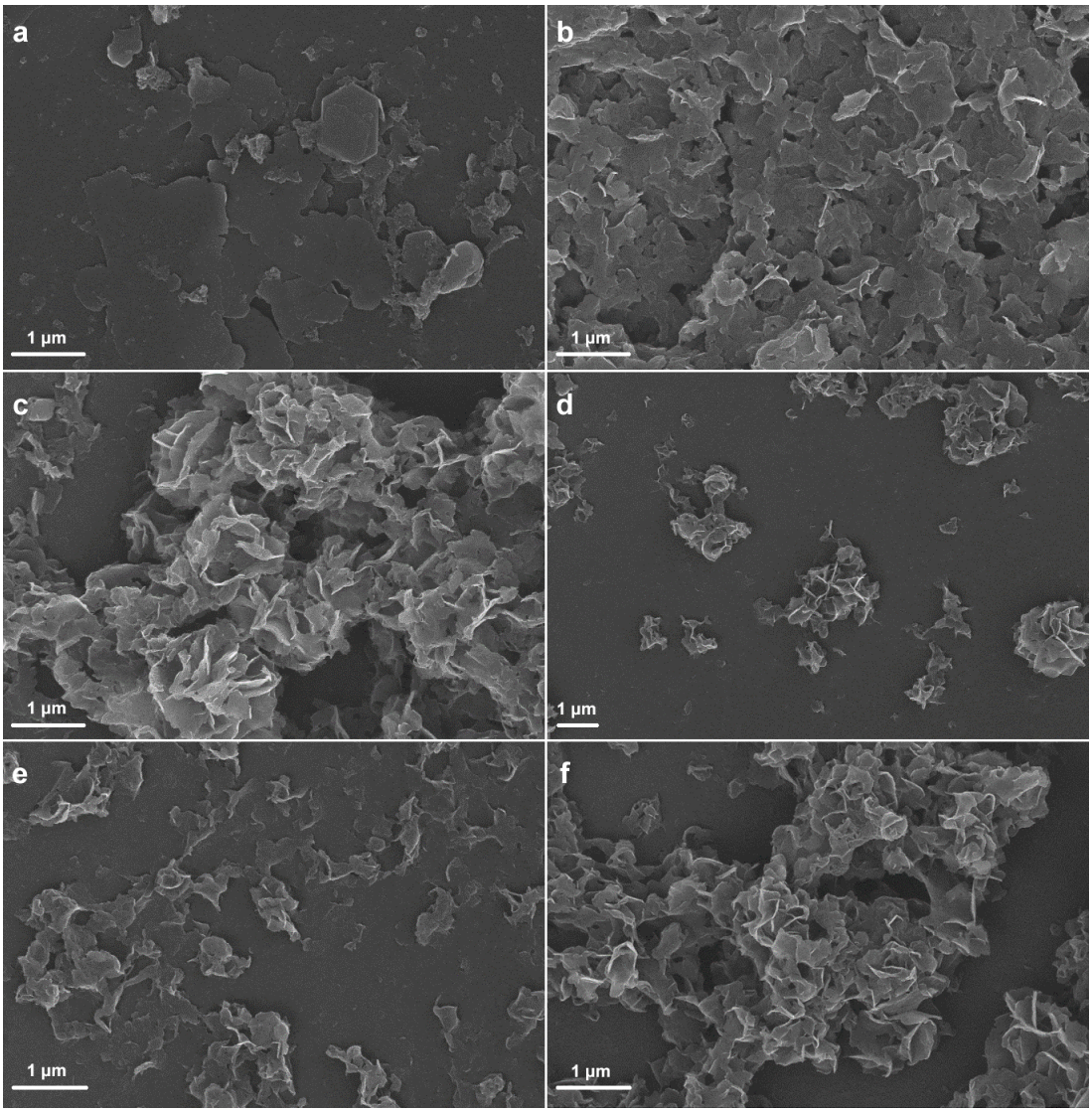

Figure 4: SEM images of (a) HALS-Ca_2Al, (b) MP-Ca_2Al and (c) H_2M_1-Ca_2Al, (d) H_1M_1-Ca_2Al, (e) H_1M_2-Ca_2Al, (f) H_1M_3-Ca_2Al.

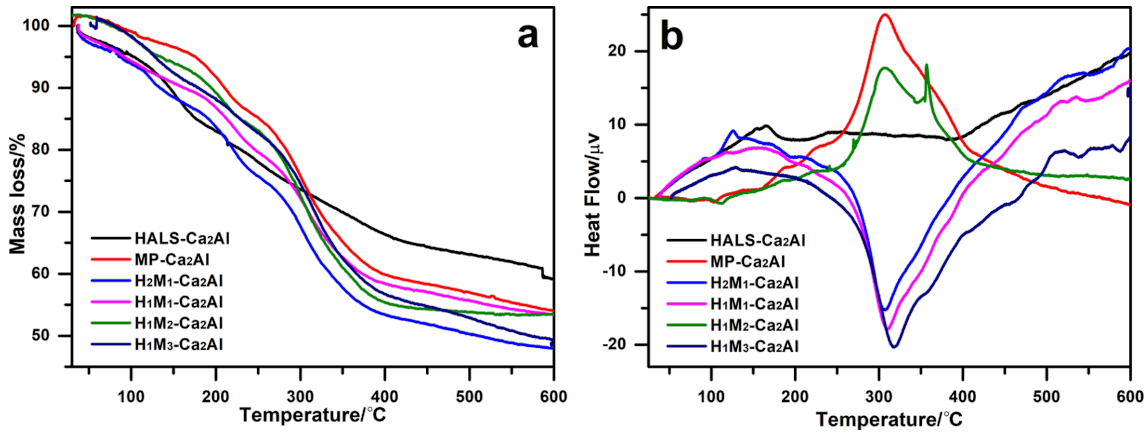

Figure 5: (a) TG and (b) DTA curves of Ca_2Al-LDHs: HALS-Ca_2Al, MP-Ca_2Al, H_2M_1-Ca_2Al, H_1M_1-Ca_2Al, H_1M_2-Ca_2Al, and H_1M_3-Ca_2Al.

Table 2: Chemical composition of $H_nM_{n'}$-Ca_2Al-LDH samples.

sample	Ca (wt %)	Al (wt %)	C (wt %)	Ca/Al	H_2O (wt %)	chemical composition
HALS-Ca_2Al	14.4	5.1	28.6	2.0	12.2	$Ca_{0.67}Al_{0.33}(OH)_2(HALS)_{0.33}\cdot 1.1H_2O$
MP-Ca_2Al	12.9	3.5	31.4	2.1	7.3	$Ca_{0.68}Al_{0.32}(OH)_2(MP)_{0.32}\cdot 0.85H_2O$
H_2M_1-Ca_2Al	15.8	3.8	29.1	2.3	8.4	$Ca_{0.7}Al_{0.3}(OH)_2(HALS)_{0.2}(MP)_{0.1}\cdot 0.68H_2O$
H_1M_1-Ca_2Al	14.5	3.7	30.2	2.2	7.5	$Ca_{0.69}Al_{0.31}(OH)_2(HALS)_{0.15}(MP)_{0.16}\cdot 0.72H_2O$
H_1M_2-Ca_2Al	14.9	3.3	31.6	2.3	9.4	$Ca_{0.7}Al_{0.3}(OH)_2(HALS)_{0.1}(MP)_{0.2}\cdot 0.83H_2O$
H_1M_3-Ca_2Al	16.5	3.9	29.5	2.5	8.0	$Ca_{0.72}Al_{0.28}(OH)_2(HALS)_{0.07}(MP)_{0.21}\cdot 0.66H_2O$

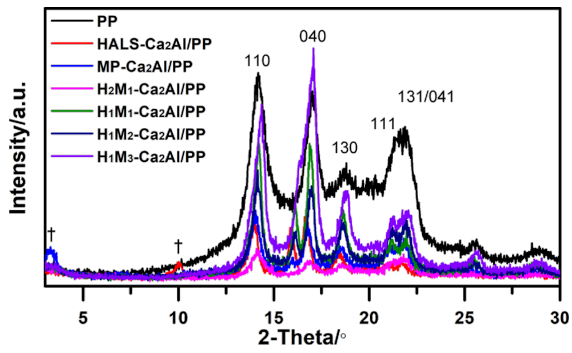

Figure 6: Powder X-ray diffraction pattern of $H_nM_{n'}$-Ca_2Al/PP composites. LDH reflection peaks were marked with "†".

reflection (002) peaks of HALS-Ca_2Al and MP-Ca_2Al clearly appear (marked with "†") with an increase in spacing from 0.77 to 0.88 nm for HALS-Ca_2Al and from 2.52 to 2.68 nm for MP-Ca_2Al. Probably, the PP chains were intercalated into the LDH gap structure to produce a polymer-intercalated nanocomposite [25]. Yet, none of the diffraction peaks of the co-intercalated $H_nM_{n'}$-Ca_2Al hybrid LDHs is observed in the resulting $H_nM_{n'}$-Ca_2Al/PP composites, suggesting a high dispersion of LDH nanoparticles in the composite.

Figure 7a depicts the FTIR spectra of $H_nM_{n'}$-Ca_2Al/PP composites in absorbance mode. Here, all composites present the characteristic bands of PP: 2950, 2915, 2868, 2837, 1454, and 1375 cm^{-1}. Some additional bands assigned to LDHs and guest

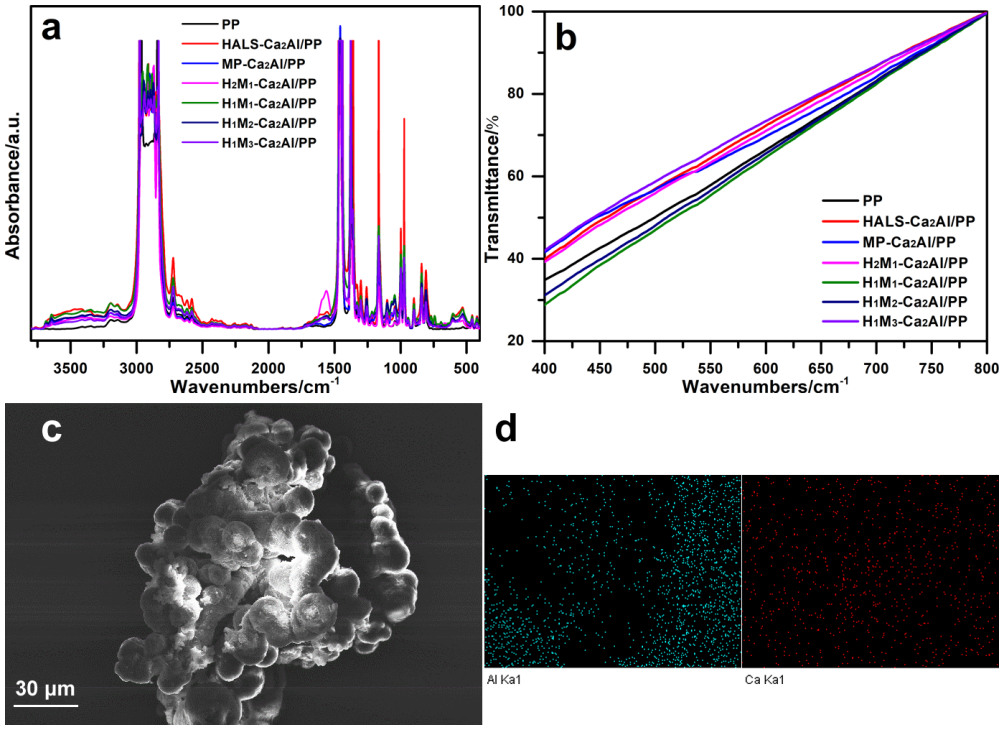

Figure 7: (a) FTIR spectra and (b) visible-light transmittance spectra of Ca_2Al/PP composites. (c) SEM image and (d) Al (left) and Ca (right) element mapping of the H_1M_1-Ca_2Al/PP composite.

anions are also observed after addition of $H_nM_{n'}$-Ca_2Al-LDHs. Figure 7b demonstrates the visible-light transmittance of $H_nM_{n'}$-Ca_2Al-LDH/PP composite films, which is one of crucial properties of the PP products. All the samples show a similar trend demonstrating that there is a good dispersion of Ca_2Al-LDHs in the PP matrix without affecting its visible-light transmission. Figure 7c,d displays the surface morphology and element distribution of H_1M_1-Ca_2Al/PP composites from SEM and element mapping. Consistent with PP free of filler, a spherical structure is observed for Ca_2Al/PP composites and Al (left) and Ca (right) elements are homogenously distributed in the H_1M_1-Ca_2Al/PP composite films. All results confirm that Ca_2Al-LDH particles are well dispersed in the PP matrix and have no negative effect on the structure and morphology.

Performance of $H_nM_{n'}$-Ca_2Al/PP composites

Figure 8a shows the thermal decomposition of $H_nM_{n'}$-Ca_2Al/PP composites measured by TG-DTA. The thermal decomposition observed for Ca_2Al/PP composites is comparable to that of PP free of filler, and the main decomposition process for all samples occurs between 250 and 450 °C. The incorporation of $H_nM_{n'}$-Ca_2Al-LDHs is found to increase the onset temperature (T_{onset}) of the initial degradation process. The onset values for co-intercalated $H_nM_{n'}$-Ca_2Al/PP composites are higher T_{onset} in the range of 336–367 °C than those of PP free of filler (265 °C), HALS-Ca_2Al/PP (335 °C) and MP-Ca_2Al/PP (333 °C). However, the onset temperature of co-intercalated $H_nM_{n'}$-Ca_2Al/PP does not increase with the percentage of M. H_2M_1-Ca_2Al/PP has the highest T_{onset} value. Moreover, with the addition of $H_nM_{n'}$-Ca_2Al-LDHs, the amount of residue is also increased, the promotion of the carbonization process leads to a better flame retardancy of Ca_2Al/PP composites. As a result, the thermal stability of $H_nM_{n'}$-Ca_2Al/PP composites is obviously improved.

Figure 8b shows the thermal degradation of $H_nM_{n'}$-Ca_2Al/PP composite films at 150 °C as a function of aging time, recorded by FTIR. With increasing thermal-aging time, the intensity of the carbonyl peak of the PP film (without filler) significantly increases in the range of 1810–1660 cm^{-1}, accompanied by

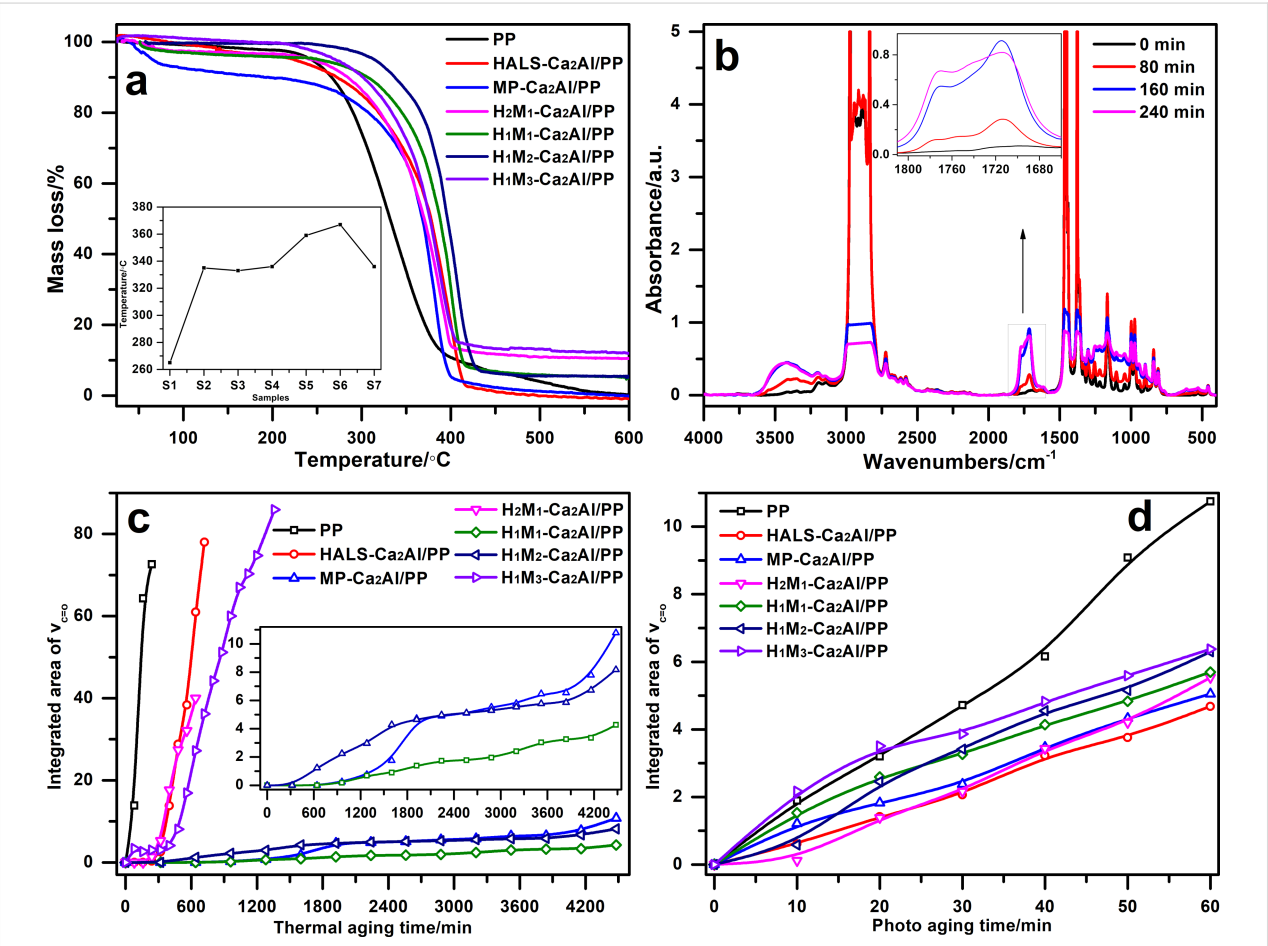

Figure 8: (a) TGA curves of $H_nM_{n'}$-Ca_2Al/PP composites. (b) FTIR spectra of PP after different periods of thermal aging. (c) Thermal aging and (d) photo-oxidation aging of $H_nM_{n'}$-Ca_2Al/PP films.

changes in shape and position. Here, the integrated area of the carbonyl band is measured to quantitatively analyze the degradation degree of $H_nM_{n'}$-Ca_2Al/PP composite films. Figure 8c shows the integrated area as a function of the aging time. Two things can be noted: (1) PP, HALS-Ca_2Al/PP, H_2M_1-Ca_2Al/PP and H_1M_3-Ca_2Al/PP films, during rapid thermal aging, completely break after less than 1600 min. (2) MP-Ca_2Al/PP, H_1M_1-Ca_2Al/PP and H_1M_2-Ca_2Al/PP films exhibit a good stability against thermal aging, and their appearance remains intact after 4500 min at 150 °C. The additive MP-Ca is an excellent protection against thermal degradation, while HALS is a photo-oxidation stabilizer. With the same amount of H and M, the composite H_1M_1-Ca_2Al/PP shows the best thermal stability among all intercalated Ca_2Al-LDHs. Also, the ratio between HALS and MP can be used to slightly tune the thermal properties of the LDH/PP composites.

Figure 8d displays the photo-oxidation degradation of $H_nM_{n'}$-Ca_2Al/PP composite films under UV irradiation. The integrated area in the range of 1810–1660 cm^{-1} for all samples becomes larger with increasing UV exposure time. In comparison with PP free of filler, the addition of $H_nM_{n'}$-Ca_2Al-LDHs enhances the photo-oxidation stability. The photo-oxidation stability is in the following order: HALS-Ca_2Al/PP > H_2M_1-Ca_2Al/PP > MP-Ca_2Al/PP > H_1M_1-Ca_2Al/PP > H_1M_2-Ca_2Al/PP > H_1M_3-Ca_2Al/PP. The different co-intercalated $H_nM_{n'}$-Ca_2Al-LDHs are found to enhance the thermal and photo-oxidation stability of $H_nM_{n'}$-Ca_2Al/PP composite films, and the co-intercalated LDH/PP composite films have better overall performances compared with the systems intercalated with HALS or MP only.

Conclusion

In this work, we have successfully co-intercalated a hindered amine light stabilizer (HALS) and a hindered phenolic antioxidant (MP) into the interlayer region of Ca_2Al-LDHs with different molar ratios through coprecipitation. The concomitant intercalation of HALS and MP significantly enhances the thermal stability of the powders due to the host–guest interactions between guest anions and the host LDH. Subsequently a series of $H_nM_{n'}$-Ca_2Al/PP composite films was prepared. The results show that the addition of $H_nM_{n'}$-Ca_2Al-LDH has no negative effect on the crystallization behavior of PP, while it improves significantly the stability of the composites against thermal degradation and photo-oxidation. Undoubtedly, the co-intercalation method for LDH framework will open a way to design and fabricate multifunctional additives for polymer composites.

Experimental

Chemicals

Succinic anhydride, tetramethylpiperidinamine, dioxane, ether, $Ca(NO_3)_2{\cdot}4H_2O$, $Al(NO_3)_3{\cdot}9H_2O$, NaOH, C_2H_5OH, CH_3COCH_3, xylene and hexane were directly used as received from Beijing Chemical Co. Limited. Deionized water was employed in all experiments. Polypropylene (PP1300, melting index: 1.5 g/10 min; melting point: 164–170 °C; density: 0.91 $g{\cdot}cm^{-3}$), and Irganox 1425 were supplied from Beijing Yanshan Petrochemical Co. Ltd., China.

Fabrication of HALS

The HALS was synthesized as reported [16]. Typically, succinic anhydride (15 mmol) was dissolved into 10 mL of dioxane at 80 °C under vigorous stirring, and tetramethylpiperidinamine (15 mmol) in 10 mL of dioxane was dropwise added. The solution was kept at 80 °C for 40 min. The product was washed three times using dioxane and ether. Finally, the powdered product HALS was collected after vacuum filtration.

Fabrication of $H_nM_{n'}$-Ca_2Al-LDHs

The HALS and MP co-intercalated LDHs ($H_nM_{n'}$-Ca_2Al-LDHs) were prepared through coprecipitation with different H/M molar ratios of 2:1, 1:1, 1:2, 1:3. For H_1M_1-Ca_2Al, HALS (3.072 g, 12 mmol) and Irganox 1425 (4.17 g, 6 mmol) were dissolved in 240 mL of ethanol/water (3:1, v/v). A solution containing 0.100 $mol{\cdot}L^{-1}$ $Al(NO_3)_3{\cdot}9H_2O$ and 1.40 $mol{\cdot}L^{-1}$ NaOH was added dropwise to the above HALS/MP-Ca solution at room temperature under vigorous stirring in nitrogen atmosphere. The pH value in the reaction system was maintained at pH 10 after finishing the addition, and the reaction was kept for another 12 h. The suspension was centrifuged and washed with 60% ethanol solution until pH 7. The resulting slurry was further washed twice with acetone with surface modification and then was used for the preparation of H_1M_1-Ca_2Al/PP composites. To obtain the H_1M_1-Ca_2Al powder, part of the slurry was dried in an oven at 80 °C for 24 h. Co-intercalated $H_nM_{n'}$-Ca_2Al with different molar ratios and MP-Ca_2Al were obtained through a similar process. Besides, HALS-Ca_2Al as the reference was prepared similarly with a metal solution of $Ca(NO_3)_2{\cdot}4H_2O$ and $Al(NO_3)_3{\cdot}9H_2O$.

Fabrication of $H_nM_{n'}$-Ca_2Al/PP composites

A series of $H_nM_{n'}$-Ca_2Al/PP composites was fabricated through solvent mixing with the same mass loading of 4.0 wt % compared with pure PP [26]. For the example of H_1M_1-Ca_2Al/PP, 6.36 g of H_1M_1-Ca_2Al slurry (solid content: 6.30 wt %) was dispersed in 100 mL xylene containing 10.0 g PP and the suspension was heated to 140 °C in an oil bath under vigorous stirring for 3 h. The resulting suspension was immediately transferred into 50 mL hexane solvent and then cooled down to 25 °C. Finally, the solid product was collected after drying to constant weight at 80 °C. For further analyses, the H_1M_1-

Ca_2Al/PP composite was pressed into a composite film by Teflon sheets at 170 °C and the thickness was controlled to be ca. 0.1 mm. Composites of other LDHs with PP (HALS-Ca_2Al/PP, MP-Ca_2Al/PP, H_2M_1-Ca_2Al/PP, H_1M_2-Ca_2Al/PP, H_1M_3-Ca_2Al/PP) were prepared following a similar process using the required amount of LDH slurry.

Characterization

Powder X-ray diffraction (XRD) measurements were performed on a Shimadzu XRD-6000 X-ray diffractometer with a wavelength of 0.154 nm at 40 kV and 30 mA in a 2θ range of 3–70° at 10°·min^{-1}. Fourier-transform infrared (FTIR) spectra were recorded on a Bruker Vector 22 infrared spectrophotometer with KBr pellets (sample/KBr of 1:100 by weight) or thin films. Thermogravimetry and differential thermal analysis (TG-DTA) was performed on a PCT-IA instrument in the range of 25 to 700 °C at 5 °C·min^{-1} under flowing air. Scanning electron microscopy (SEM) images were taken with a Zeiss scanning electron microscope by dropping dilute ethanol suspension at room temperature. Elemental analysis for metal elements (Ca and Al) was carried out on a Shimadzu ICPS-7500 inductively coupled plasma (ICP) atomic emission spectrometer. About 30 mg of the samples was dissolved in a few drops of concentrated nitric acid (65%) and diluted to 10 mL using water. CHN elemental analysis was carried out on a Vario EL III, Elementar instrument. The content of water in the samples was obtained by thermogravimetry. The UV–vis spectra in the range of 200 to 800 nm were collected by using a Shimadzu UV-2501PC spectrophotometer.

Stability evaluation of $H_nM_{n'}$-Ca_2Al/PP composites

Here, two methods were employed to evaluate the thermal stability of $H_nM_{n'}$-Ca_2Al/PP composites. One way was to examine the composite samples with TG-DTA, for example, ca. 7 mg of the samples was heated from 25 to 600 °C at 10 °C·min^{-1} in flowing air. The other was to perform an accelerated thermal aging test in an oven [15]. For this, $H_nM_{n'}$-Ca_2Al/PP composite films were tailored to a size of 20 × 20 × 0.1 mm and thermally aged at 150 °C. Every 80 min, the composition was monitored by FTIR. For the quantitative analysis of the degradation, the integrated area of peaks in the range of 1810–1660 cm^{-1}, assigned to carbonyl groups was used.

The photo stability of $H_nM_{n'}$-Ca_2Al/PP composites (20 × 20 × 0.1 mm) was examined in an accelerated photoaging instrument with an ultraviolet high-pressure mercury lamp (P = 100 W, λ_{max} = 360 nm) and the degradation degree was monitored every 5 min by FTIR [27]. The data processing method was the same as during the thermal aging.

Acknowledgements

This work is supported by the National Natural Science Foundation of China, the Fundamental Research Funds for the Central Universities (JD1716), and Program for Changjiang Scholars and Innovative Research Team in University (No. IRT1205). Prof. Feng would like to thank the guest-professor funding provided by the Université Clermont Auvergne.

ORCID® iDs

Fabrice Leroux - https://orcid.org/0000-0002-4671-9630
Yongjun Feng - https://orcid.org/0000-0001-9254-6219

References

1. Haidasz, E. A.; Meng, D.; Amorati, R.; Baschieri, A.; Ingold, K. U.; Valgimigli, L.; Pratt, D. A. *J. Am. Chem. Soc.* **2016,** *138,* 5290–5298. doi:10.1021/jacs.6b00677
2. Gryn'ova, G.; Ingold, K. U.; Coote, M. L. *J. Am. Chem. Soc.* **2012,** *134,* 12979–12988. doi:10.1021/ja3006379
3. Yousif, E.; Haddad, R. *SpringerPlus* **2013,** *2,* 398. doi:10.1186/2193-1801-2-398
4. Zhang, G.; Nam, C.; Chung, T. C. M.; Petersson, L.; Hillborg, H. *Macromolecules* **2017,** *50,* 7041–7051. doi:10.1021/acs.macromol.7b01235
5. Gijsman, P. *Polym. Degrad. Stab.* **2017,** *145,* 2–10. doi:10.1016/j.polymdegradstab.2017.05.012
6. Manteghi, A.; Ahmadi, S.; Arabi, H. *Polymer* **2016,** *104,* 31–39. doi:10.1016/j.polymer.2016.09.075
7. Sanchez, C.; Julián, B.; Belleville, P.; Popall, M. *J. Mater. Chem.* **2005,** *15,* 3559–3592. doi:10.1039/b509097k
8. Deligiannakis, Y.; Sotiriou, G. A.; Pratsinis, S. E. *ACS Appl. Mater. Interfaces* **2012,** *4,* 6609–6617. doi:10.1021/am301751s
9. Bu, J.; Huang, X.; Li, S.; Jiang, P. *Carbon* **2016,** *106,* 218–227. doi:10.1016/j.carbon.2016.05.020
10. Dintcheva, N. T.; Arrigo, R.; Gambarotti, C.; Carroccio, S.; Coiai, S.; Filippone, G. *J. Appl. Polym. Sci.* **2015,** *132,* 42420. doi:10.1002/app.42420
11. Wang, Q.; O'Hare, D. *Chem. Rev.* **2012,** *112,* 4124–4155. doi:10.1021/cr200434v
12. Taviot-Guého, C.; Prévot, V.; Forano, C.; Renaudin, G.; Mousty, C.; Leroux, F. *Adv. Funct. Mater.* **2018,** *28,* 1703868. doi:10.1002/adfm.201703868
13. Basu, D.; Das, A.; Stöckelhuber, K. W.; Wagenknecht, U.; Heinrich, G. *Prog. Polym. Sci.* **2014,** *39,* 594–626. doi:10.1016/j.progpolymsci.2013.07.011
14. Mao, N.; Zhou, C. H.; Tong, D. S.; Yu, W. H.; Cynthia Lin, C. X. *Appl. Clay Sci.* **2017,** *144,* 60–78. doi:10.1016/j.clay.2017.04.021
15. Feng, Y.; Jiang, Y.; Huang, Q.; Chen, S.; Zhang, F.; Tang, P.; Li, D. *Ind. Eng. Chem. Res.* **2014,** *53,* 2287–2292. doi:10.1021/ie403643v
16. Zhang, Q.; Jiao, Q.; Leroux, F.; Tang, P.; Li, D.; Feng, Y. *Polym. Degrad. Stab.* **2017,** *140,* 9–16. doi:10.1016/j.polymdegradstab.2017.04.012
17. Zhang, Q.; Leroux, F.; Tang, P.; Li, D.; Feng, Y. *Polym. Degrad. Stab.* **2018,** *154,* 55–61. doi:10.1016/j.polymdegradstab.2018.05.027

18. Beißmann, S.; Reisinger, M.; Grabmayer, K.; Wallner, G.; Nitsche, D.; Buchberger, W. *Polym. Degrad. Stab.* **2014,** *110,* 498–508. doi:10.1016/j.polymdegradstab.2014.09.020
19. Maringer, L.; Roiser, L.; Wallner, G.; Nitsche, D.; Buchberger, W. *Polym. Degrad. Stab.* **2016,** *131,* 91–97. doi:10.1016/j.polymdegradstab.2016.07.007
20. Kotal, M.; Bhowmick, A. K. *Prog. Polym. Sci.* **2015,** *51,* 127–187. doi:10.1016/j.progpolymsci.2015.10.001
21. Liu, M.; Jia, Z.; Jia, D.; Zhou, C. *Prog. Polym. Sci.* **2014,** *39,* 1498–1525. doi:10.1016/j.progpolymsci.2014.04.004
22. Tsai, T.-Y.; Bunekar, N. *RSC Adv.* **2016,** *6,* 65291–65298. doi:10.1039/c6ra15790d
23. Xu, S.; Zhang, B.; Chen, Z.; Yu, J.; Evans, D. G.; Zhang, F. *Ind. Eng. Chem. Res.* **2011,** *50,* 6567–6572. doi:10.1021/ie102135k
24. Lonkar, S. P.; Singh, R. P. *Thermochim. Acta* **2009,** *491,* 63–70. doi:10.1016/j.tca.2009.03.002
25. Zhang, Q.; Jiao, Q.; Leroux, F.; Tang, P.; Li, D.; Feng, Y. *New J. Chem.* **2017,** *41,* 2364–2371. doi:10.1039/c6nj03544b
26. Gao, Y.; Wu, J.; Zhang, Z.; Jin, R.; Zhang, X.; Yan, X.; Umar, A.; Guo, Z.; Wang, Q. *J. Mater. Chem. A* **2013,** *1,* 9928–9934. doi:10.1039/c3ta11695f
27. Li, D.; Qian, L.; Feng, Y.; Feng, J.; Tang, P.; Yang, L. *ACS Appl. Mater. Interfaces* **2014,** *6,* 20603–20611. doi:10.1021/am506696k

License and Terms

BEILSTEIN JOURNAL OF NANOTECHNOLOGY

Colloidal chemistry with patchy silica nanoparticles

Pierre-Etienne Rouet[1,2], Cyril Chomette[2], Laurent Adumeau[2], Etienne Duguet[2] and Serge Ravaine[*1]

Full Research Paper

Open Access

Address:
[1]CNRS, Univ. Bordeaux, CRPP, UMR 5031, 115, av. du Dr Albert Schweitzer 33600 Pessac, France and [2]CNRS, Univ. Bordeaux, ICMCB, UMR 5026, av. du Dr Albert Schweitzer 33600 Pessac, France

Email:
Serge Ravaine[*] - ravaine@crpp-bordeaux.cnrs.fr

* Corresponding author

Keywords:
colloidal molecules; covalent bonding; patchy nanoparticles; valence

Beilstein J. Nanotechnol. **2018,** *9,* 2989–2998.
doi:10.3762/bjnano.9.278

Received: 28 August 2018
Accepted: 15 November 2018
Published: 06 December 2018

This article is part of the thematic issue "Advanced hybrid nanomaterials".

Guest Editor: A. Taubert

Abstract

We report a new route to synthesize clusters, or so-called colloidal molecules (CMs), which mimic the symmetry of molecular structures made of one central atom. We couple site-specifically functionalized patchy nanoparticles, i.e., valence-endowed colloidal atoms (CAs), with complementary nanospheres through amide bonds. By analogy with the Gillespie formalism, we show that AX_4, AX_3E_1 and AX_2E_2 CMs can be obtained from tetravalent sp^3-like CAs when the relative amount of both building units is varied in a controlled manner. We obtain AX_2 CMs from divalent sp-like CAs. We also show that it is possible to covalently attach two different types of satellites to the same central patchy nanoparticle to create more complex CMs, opening the way to the fabrication of new multifunctional nanostructures with well-controlled shape and composition.

Introduction

The molecular world is essentially based on the covalent bonding of atoms displaying valences of 1, 2 (sp), 3 (sp^2), 4 (sp^3) and, to a lesser extent, 5 (sp^3d) and 6 (sp^3d^2). The molecules of water, ammonia and methane, in which the valence orbitals of the central atom adopt sp^3 hybridization and form equivalent bonds with two, three and four hydrogen atoms, respectively, well illustrate the great diversity of molecular structures that can be obtained. For the past two decades, this richness has been a great source of inspiration for designing colloidal analogues of molecular systems, the so-called "colloidal molecules" (CMs) [1]. Tremendous efforts have been devoted to the synthesis of particles with directional interactions to replicate bond schemes of molecular systems [2-5]. One efficient approach is to engineer particles with chemical anisotropy, that is, particles with heterogeneously surface regions in specific positions [6-12]. Bonding between particles occurs through patch–patch interactions so that the positioning of the patches can endow particles with valence. Patchy particles with various patch motifs were produced by taking benefit of the inherent directionality of colloidal clusters and by growing a matrix material onto the clusters [13,14]. By adjusting the matrix growth, it is possible to leave some zones of the clusters exposed to the outer medium, which further serve as patches with controlled size. The group of van Ravensteijn has also reported asymmetric dumbbell-like

particles, i.e., with two nodules of different chemical compositions, obtained through a phase separation process during the styrene emulsion polymerization seeded with cross-linked polystyrene (PS) particles coated with a thin layer of poly(vinylbenzyl chloride) [15]. Another way to get valence-endowed particles relies on shape recognition. Shape can indeed direct colloidal assembly as it was shown that linear supracolloidal polymers are obtained by self-assembly of cone-shaped particles in the presence of a depletant [16]. Similarly, microparticles with a specific number of dimples (i.e., entropic patches [17]) can act as "locks" and assemble with small spheres ("keys") via depletion interactions to give rise to well-defined CMs [18]. The valence of each lock particle is determined by the number of the cavities whereas their symmetry determines the bonding geometry. We have previously reported that the selective growth of the silica core of binary PS/silica CMs and the subsequent dissolution of the polymeric satellites [19] leads to silica particles with a precise number of dimples. The PS chains which are chemically grafted onto the silica surface remain at the bottom of the dimples after the dissolution stage and can be specifically chemically modified providing both enthalpic and entropic characteristics to the patches [20,21].

Here we report the use of these patchy silica nanoparticles with two or four dimples as sp- and sp^3-like colloidal atoms (CAs), respectively. We take benefit of the site-specific amination of PS residues remaining at the bottom of the dimples to form a variety of CMs through their covalent attachment with complementary spheres bearing activated carboxylic acid groups. By varying the relative amounts of both types of nanoparticles and the chemical composition of the spherical satellites, we demonstrate that a vast collection of CMs are accessible through assemblies that are analogous to chemical reactions (Figure 1).

Results and Discussion

Synthesis and surface modification of the precursors

The first type of precursors, i.e., well-calibrated silica nanospheres or core–shell nanoparticles, were obtained according to a seeded-growth protocol [22] and a method using methoxy poly(ethylene glycol)-thiol as a coupling agent [23], respectively. Their surface functionalization with carboxylic acid groups was performed by a two-step approach (Figure 2a). First, amine groups were grafted onto the silica surface by reaction with (3-aminopropyl)triethoxysilane (APTES). In a second step, the amine groups were subsequently treated with succinic anhydride in the presence of triethylamine (TEA) to convert amino groups into carboxylic acid groups. The grafting efficiency was evidenced by zeta potential measurements and diffuse reflectance infrared Fourier-transform (DRIFT) spectroscopy. Figure 2b shows that after treatment of the silica surface by APTES, the so-aminated nanoparticles display a quite high zeta potential value of about 23 mV at pH 7.0. The isoelectric point (IEP) at pH 8.4 is close to the pK_a value of the prima-

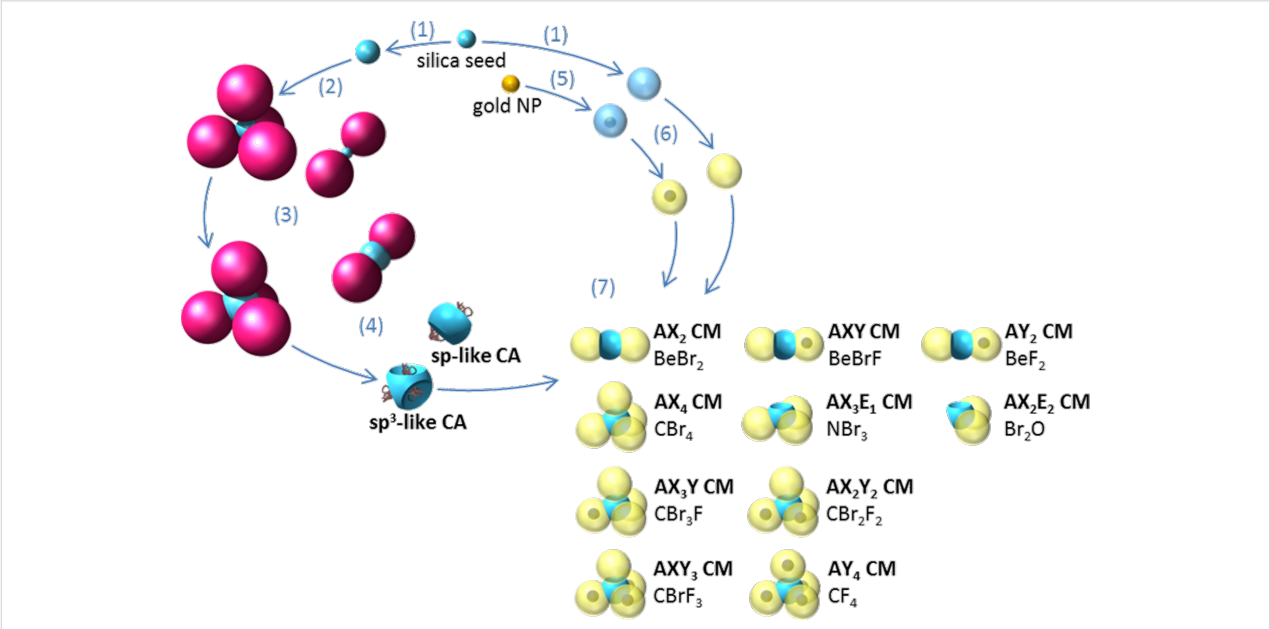

Figure 1: Synthesis of the CMs by covalent assembly of CAs: valence-endowed nanoparticles and nanospheres. (1) Growth of the silica seeds; (2) seeded-growth emulsion polymerization of styrene; (3) silica core regrowth; (4) dissolution of PS satellites for developing the dimples followed by the amination of the residual anchored PS chains at the bottom of the dimples; (5) growth of a silica shell around gold nanoparticles; (6) grafting of carboxylic acid groups at the silica surface of the nanospheres; (7) locking of carboxylated satellites within the aminated dimples through amide bonding.

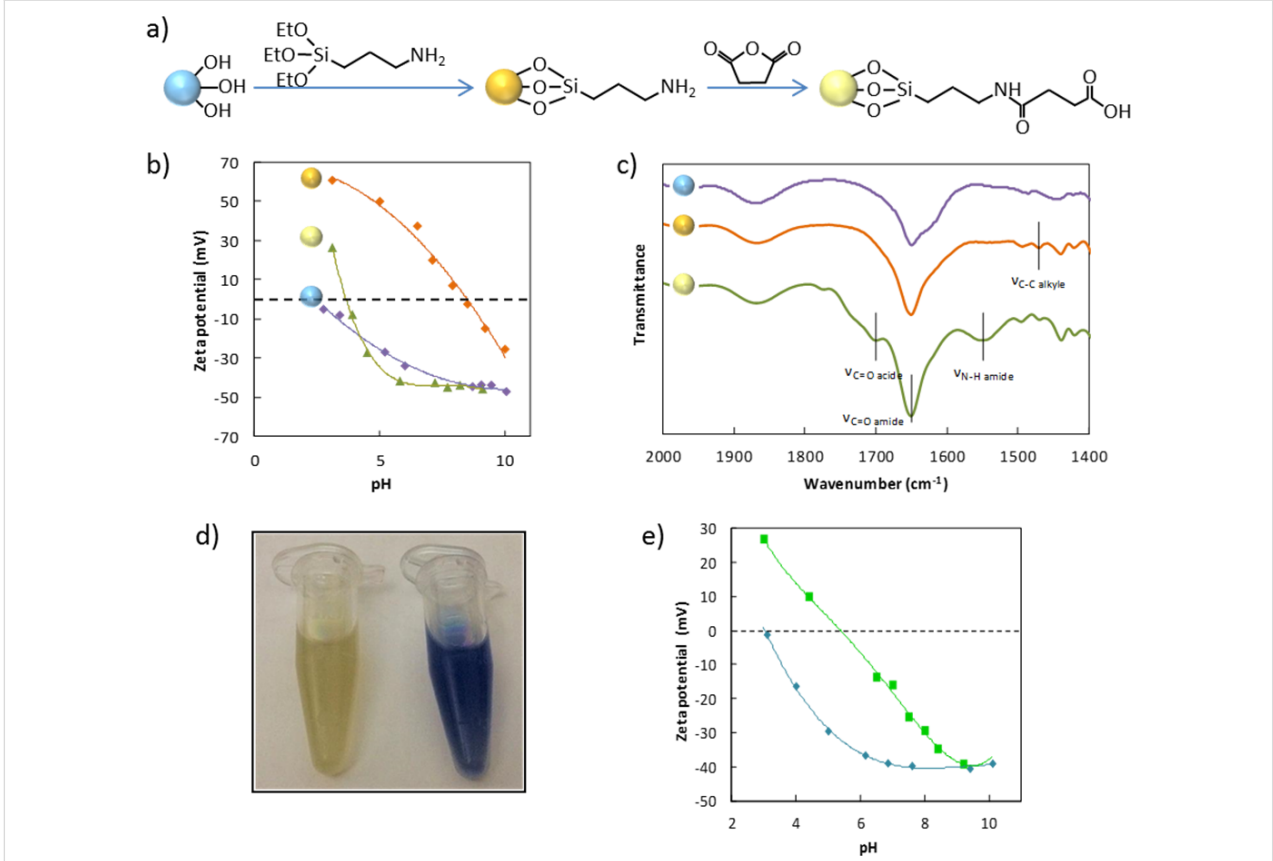

Figure 2: a) Silica surface modification with carboxylic acid groups, (b) zeta potential as a function of pH value, and (c) DRIFT spectra of bare (purple curve), aminated (orange curve) and carboxylated (green curve) silica particles; d) photograph of dimpled silica nanoparticles suspension before (left) and after (right) amination of the PS residues in the presence of ninhydrin; e) zeta potential as a function of pH value of silica particles with four dimples before (cyan curve) and after (green curve) chloromethylation and amination of the PS residues.

ry amine groups attesting to their efficient grafting and correct orientation on the silica surface. The carboxylated particles possess a zeta potential of about −43 mV at pH 7.0 and an isoelectric point shifted down to pH 3.8, attesting to the efficient grafting of the acid groups. Figure 2c shows that the IR spectrum of the aminated particles presents a characteristic band assigned to the C–C bond of the alkyl chain of APTES groups at 1473 cm^{-1}, while the IR spectrum of the carboxylated particles (Figure 2c) presents several characteristic bands such as the C=O stretching at 1712 cm^{-1} and the N–H stretching of the resulting amide at 1556 cm^{-1}.

The second type of precursors, i.e., the valence-endowed patchy nanoparticles, were fabricated according to the following protocol: Bipods or tetrapods made of a central silica core and two or four PS nodules were prepared by the seeded-growth emulsion polymerization of styrene, according to an already published procedure [24]. The regrowth of the silica cores of the multipods, the subsequent dissolution of the PS nodules to create dimpled particles and the amination of the PS residues at the bottom of the dimples were performed according to a method that we had also reported previously [20]. To evidence the success of the PS modification stages, we first performed a Kaiser test, which is based on the reaction of ninhydrin with primary amines and yields a characteristic dark blue color. Briefly, 1 mL of the aminated dimpled particles suspension in absolute ethanol and 5 mg of ninhydrin were mixed in an Eppendorf tube. After few minutes, the suspension turned blue, evidencing the presence of amine functions (Figure 2d). We also measured the zeta potential of the multipods before and after the chloromethylation/amination of the PS chains (Figure 2e). The comparison of the zeta potential curves shows that the modification stages of the PS residues induce a shift of the IEP to pH 5.3 attesting to the efficient grafting of amine groups.

Assembly of colloidal molecules

The binding of the aminated dimpled particles with the satellites is based on amide bonding, i.e., peptidic coupling, extensively studied in biochemistry for the modification of amino acids [25]. The carboxylic groups are not reactive enough toward amino groups, and a simple and well-known approach consists in converting them into more reactive groups such as

anhydrides. We chose to use TEA to deprotonate the carboxylic groups and ethyl chloroformate (ECF) to react with the resulting carboxylate groups to get mixed anhydrides [26]. The assemblies were performed in dry dimethylformamide (DMF) as it is a good solvent for the aminated PS macromolecules and thus favors their extension towards the external medium, which should optimize the formation of amide bonds with the carboxylated silica satellites. At this stage, any residual water must be carefully removed to avoid the deactivation of the anhydride groups by hydrolysis.

With our collection of dimpled particles and satellites, we can build colloidal assemblies that mimic both the chemistry and the geometry of molecules. We first performed a series of experiments by mixing 100 nm carboxylated silica nanospheres with particles with four aminated dimples in a number of dimples/number of satellites ratio equal to **1**/400 in order to maximize the filling of the dimples (the bold face of the number means that it concerns the number of dimples, knowing that the number of particles is this number divided by the valency of the particle). As shown in Figure 3a, AX_4-type CMs, the

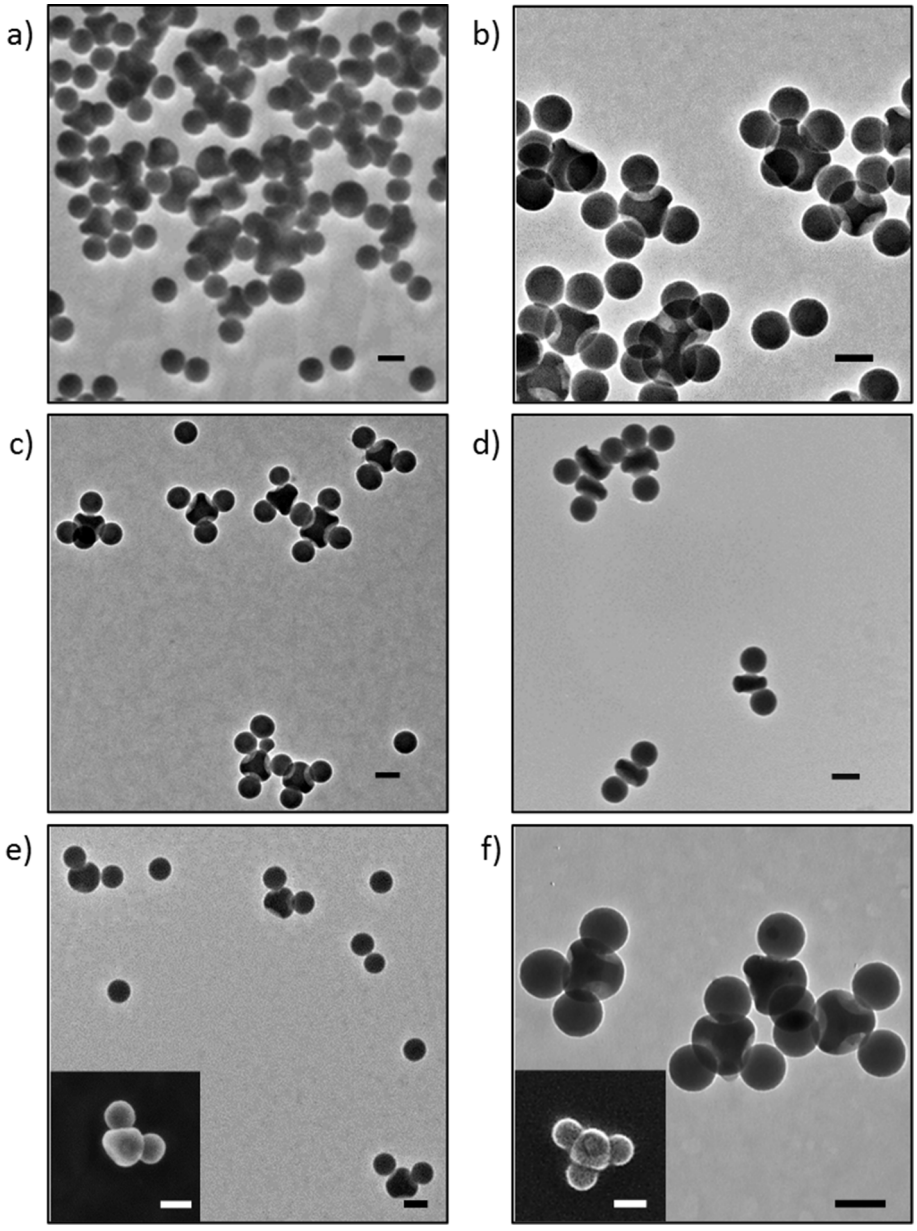

Figure 3: Top: TEM images of the CMs obtained from mixing particles with 4 aminated dimples with 100 nm silica nanospheres in a **1**/400 ratio before (a) and after (b) centrifugation. Middle: TEM images of the CMs obtained from mixing particles with 4 (c) and 2 (d) aminated dimples with 100 nm silica nanospheres in a **4**/4 and in a **2**/2 ratio, respectively. Bottom: TEM and SEM (inserts) images of the CMs obtained from mixing particles with 4 aminated dimples with 100 nm silica nanospheres in a **4**/2 (e) and in a **4**/3 (f) ratio. Scale bars: 100 nm.

colloidal analogues of molecules such as carbon tetrabromide (CBr_4), were obtained. One should note here that control experiments, which were carried out by mixing bare silica nanospheres with aminated dimpled CAs or carboxylated silica nanospheres with pristine dimpled CAs, both led to the observation of isolated silica nanospheres and individual CAs (not shown), evidencing that the CMs form through an amidation reaction. As expected, a large excess of free silica satellites could also be observed in Figure 3a, which was removed by centrifugation (Figure 3b). Nevertheless, the determination of the assembly yield by statistical analysis of the transmission electron microscopy (TEM) images was not possible, because CMs with a low amount of satellites could be removed with the excess of satellites during this purification step, leading distorted statistics. Therefore, we decided to perform another series of experiments dedicated to the assembly of the sp^3-like CAs with 100 nm silica nanospheres in a **4**/4 ratio. Figure 3c shows that colloidal analogues of CBr_4 molecules were mostly obtained, with a yield of 59% as determined by statistical analysis of TEM images (Table 1). Similarly, AX_2-type CMs, analogues of molecules like beryllium bromide ($BeBr_2$) were obtained (Figure 3d) , with a yield of 62% (Table 1) when sp-like CAs were mixed with 100 nm silica nanospheres in a **2**/2 ratio.

Table 1: Compositions of the batches[a] resulting from mixing the CAs with 100 nm nanospheres.

	sp^3-like CAs			sp-like CAs
number of dimples / number of nanospheres	**4**/4[b]	**4**/3[c]	**4**/2[d]	**2**/2[e]
% AX_4-type CMs	59	20	5	—
% AX_3E_1-type CMs	25	58	27	—
% AX_2E_2-type CMs	15	19	35	—
% AXE_3-type CMs	1	3	22	—
% AX_2-type CMs	—	—	—	62
% AX_1E_1-type CMs	—	—	—	29
% unreacted CAs	—	—	11	9

[a]Determined by statistical analysis of TEM images over [b]140, [c]200, [d]116, and [e]182 clusters.

Based on these results, we decided to extend our synthetic approach in order to first reproduce at the colloidal level the fact that a central atom can be surrounded by both bonded atoms and lone electron pairs. To do so, we decided to change the quantity ratio of both types of precursors. Hence, we mixed the sp^3-like CAs with 100 nm silica nanospheres in ratios of **4**/2 and **4**/3. Figure 3e,f show that AX_2E_2-type and AX_3E_1-type CMs, which are the colloidal analogues of molecules such as dibromine monoxide (Br_2O) and nitrogen tribromide (NBr_3), were obtained with a good yield (Table 1), respectively. In particular, the unfilled dimple(s) of the AX_2E_2- and AX_3E_1-type CMs can be clearly seen on the scanning electron microscopy (SEM) images shown as inserts of Figure 3e,f.

We also aimed to mimic at the colloidal scale the possible bonding of atoms of different natures to a same central atom, which is the source of the richness of the organic molecules. We focused on AX_nY_{4-n}-type and AX_nY_{2-n}-type CMs where $0 < n < 4$ and $0 < n < 2$, respectively. We used 90 nm core–shell nanoparticles as a second batch of satellites. This choice was motivated by two reasons. Firstly, we had to work with satellites with a slightly different diameter to mimic another type of atoms without modifying the valence of the dimpled particles. By doing so, we were sure to attach only one satellite per dimple, whatever its nature. Using much smaller satellites could induce the attachment of more than one satellite per dimple. In contrast, the dimples of the patchy particles must be big enough to allow one satellite to be linked to the aminated PS chains, which excludes to work with too large satellites. The second reason is related to the necessity to differentiate both types of satellites attached to a central dimpled particle by conventional TEM. Thanks to the high electron density of gold, core–shell nanoparticles can indeed be easily distinguished from silica nanospheres of similar size. We mixed the sp^3-like CAs with 100 nm nanospheres and 90 nm core–shell nanoparticles in a **4**/n/$(4 - n)$ ratio. Figure 4a–d shows that the colloidal analogues of molecules such as fluorotribromomethane ($CFBr_3$), difluorodibromomethane (CF_2Br_2), bromotrifluoromethane (CF_3Br), and carbon tetrafluoride (CF_4) are formed with a yield equal to 41%, 50%, 43% and 52 %, for n = 3, 2, 1 and 0, respectively. Similarly, the analogues of molecules such as beryllium fluoride bromide (BeFBr) and beryllium fluoride (BeF_2) were obtained from sp-like CAs in a **2**/1/1 and in a **2**/0/2 ratio, with a yield of 49% and 54%, respectively (Figure 4e,f).

Conclusion

In conclusion, colloidal molecules, which mimic the symmetry of molecular structures, have been synthesized through the covalent attachment of spherical satellites within the dimples of valence-endowed patchy nanoparticles. The synthetic route is highly versatile and can be extended to other precursors such as metallic or semiconductor nanoparticles, opening the way to the synthesis of a broad panel of (multi)functional nanomaterials with a controlled shape and composition. These new colloidal analogues of molecules could serve as building blocks for the assembly of the next generation (meta-)materials. For example, attaching four different satellites (such as one gold, one silver, one iron oxide and one semiconductor nanoparticle) around a central sp^3-like nanoparticle could lead to multifunctional chiral nanostructures, which may form novel two- or three-dimensional materials with unprecedented properties by self-assembly.

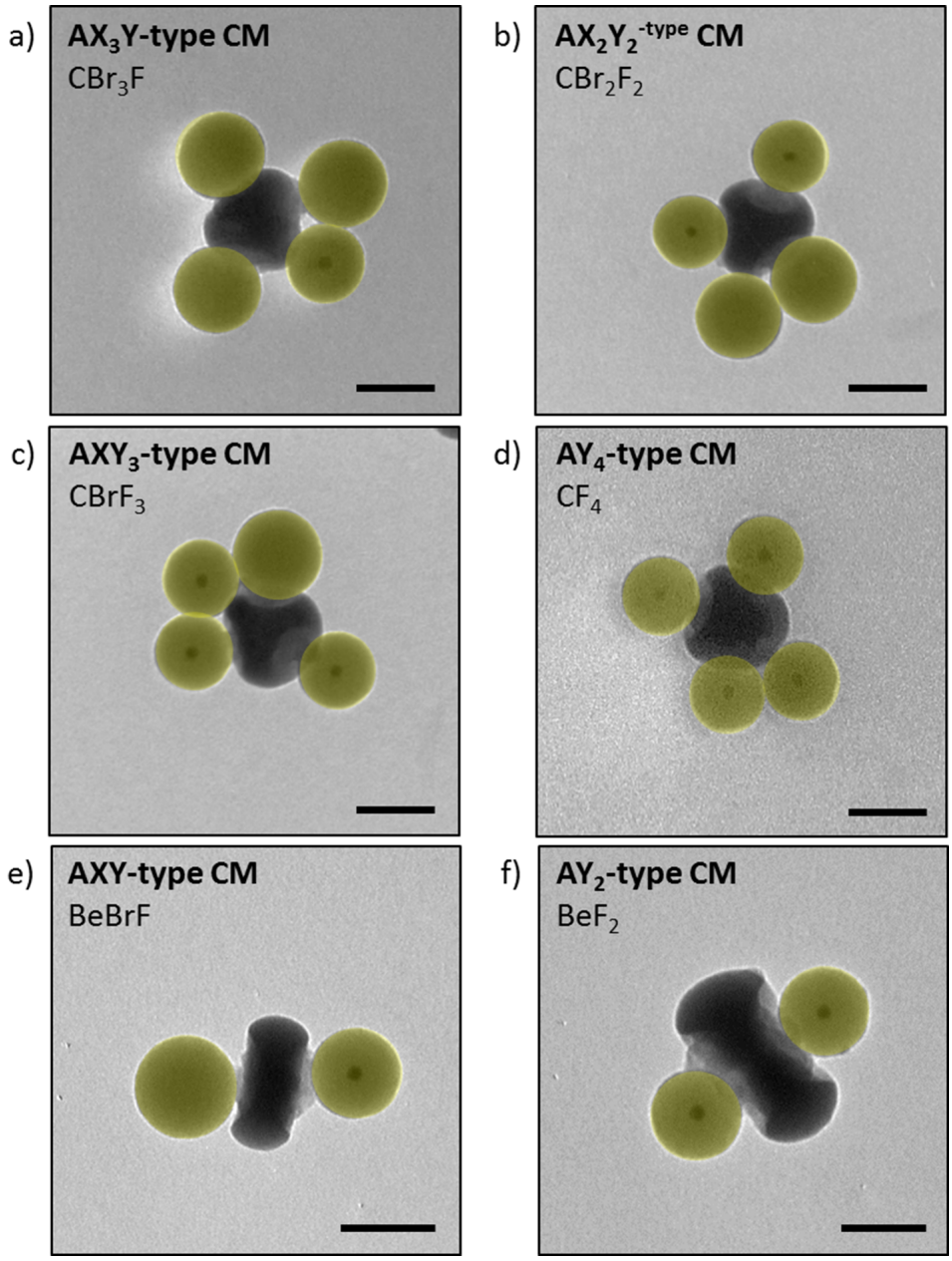

Figure 4: TEM images of the CMs obtained from mixing particles with four aminated dimples with 100 nm silica nanospheres and 90 nm core–shell nanoparticles in ratios of (a) **4**/3/1, (b) **4**/2/2, (c) **4**/1/3 and (d) **4**/0/4. TEM images of the CMs obtained from mixing particles with two aminated dimples with 100 nm silica nanospheres and 90 nm core–shell nanoparticles in ratios of (e) **2**/1/1 and (f) **2**/0/2 ratio; scale bars: 100 nm.

Experimental

Materials

We used styrene (Sigma-Aldrich, 99%), methacryloxymethyltriethoxysilane (MMS, ABCR, 98%), methacryloxypropylyltriethoxysilane (MPS, Aldrich, 98%), (3-aminopropyl)triethoxysilane (APTES, Aldrich, 99%), triethylamine (TEA, Sigma-Aldrich, 99%), sodium persulfate (Sigma-Aldrich, 99%), Symperonic® NP30 (Aldrich), sodium dodecylsulfate (SDS, Sigma-Aldrich, >90%), tetraethoxysilane (TEOS, Sigma-Aldrich, 99%), ammonia (30% in water, SDS), tin tetrachloride ($SnCl_4$, Sigma-Aldrich, >99%), hydrochloric acid (37%, Sigma-Aldrich), ethylenediamine (Fluka, 99.5%), gold(III) chloride trihydrate ($HAuCl_4 \cdot 3H_2O$, Sigma-Aldrich), trisodium citrate dihydrate (NaCit) ($Na_3C_6H_5O_7 \cdot 2H_2O$, Sigma-Aldrich, 99%), *O*-[2-(3-mercaptopropionylamino)ethyl]-O′-methylpoly(ethylene glycol) (PEG-SH, M_w = 5000) as we received them. We

systematically used ultrapure water at 25 °C obtained from a Milli-Q system (Millipore). We purchased tetrahydrofuran (THF), dimethylformamide (DMF) from Sigma-Aldrich and chloroform and absolute ethanol from VWR Chemicals. Butyl chloromethyl ether was synthesized according to a recipe already published [27].

Synthesis and surface modification of the spherical satellites

Synthesis of the "pre-seeds"

In a similar manner as described in [28], 100 mL of L-arginine aqueous solution (6 mM) were added into a 150 mL vial thermostated with hot water circulation at 60 °C and equipped with a reflux condenser and a 3 cm Teflon®-coated stirring bar. When a constant temperature of 60 °C was reached, 10 mL of TEOS were gently added in order to create a top organic phase. The stirring rate was adjusted in order to maintain the organic phase undisturbed and the aqueous phase efficiently mixed (ca. 150 rpm). The reaction was stopped after three days. Silica concentrations were determined by gravimetric analysis. In a given volume, the number of silica seeds was calculated from the silica concentration and the particle average diameter (ca. 23 nm) and assuming that the particles were spherical and their density was 2.2 $g \cdot cm^{-3}$.

Synthesis of the silica nanospheres

Regrowth stages were performed according to a previously reported protocol [28] at room temperature in a conventional glass flask where 455 mL of ethanol, 35 mL of ammonium hydroxide and 10 mL of the aqueous dispersion of silica "pre-seeds" were successively introduced. Then, a calculated amount of TEOS (Table 2) was added at the rate of 0.5 $mL \cdot h^{-1}$. The mixture was stirred until 2 h after the end of the TEOS addition.

Table 2: Experimental conditions of the silica particles synthesis and size measurement results of the silica particles obtained (as extracted from statistical analysis of TEM images).

TEOS/silica (weight ratio)	D_{silica} (nm)	PDI
28	48	1.042
33	53	1.035
218	103	1.027

The polydispersity index (PDI) given in Table 2 was calculated based on a minimum of 500 nanoparticles per batch using the following equation:

$$\mathrm{PDI} = \frac{\bar{D}_\mathrm{w}}{\bar{D}_n},$$

where

$$\bar{D}_n = \frac{\sum_i n_i D_i}{\sum_i n_i}$$

and

$$\bar{D}_\mathrm{w} = \frac{\sum_i n_i D_i^4}{\sum_i n_i D_i^3}$$

are the number-average and the weight-average diameter, respectively, and n_i is the number of particles of diameter D_i.

Synthesis of the Au@SiO_2 nanoparticles

Gold nanoparticles of 14 ± 2 nm were prepared by the citrate-reduction method reported by Turkevich [29]. SiO_2 coating was carried out after surface functionalization of the gold nanoparticles by using a PEG-SH (M_w = 5000) aqueous solution in a similar manner as described in [23]. The surface modification allowed for the replacement of the citrate molecules adsorbed onto the gold surface by PEG-SH. A ratio of four PEG molecules per square nanometer of available surface of the gold sol was fixed. The aqueous solution of PEG-SH was freshly prepared and added dropwise to the as-prepared gold nanoparticles under vigorous magnetic stirring. The mixture was left to react for 2 h, and was centrifuged at 9000 rpm for 30 min (twice) in order to eliminate undesired reactants. The AuNPs@PEG-SH nanoparticles were redispersed in absolute ethanol. To coat the gold nanoparticles with a silica shell, 15 mL of the Au nanoparticles dispersion were mixed under continuous magnetic stirring with a solution of deionized water and ammonia, at a volume ratio of 93.8/5/1.2 for absolute ethanol, water and ammonia, respectively. 18.3 µL of TEOS were added and the reaction mixture was stirred for 12 h at 20 ± 2 °C. Upon completion of the growth of silica shell, the core–shell particles were washed with absolute ethanol and water and redispersed in absolute ethanol.

Grafting of carboxylic acid groups onto the surface of the spherical satellites

We quickly added under vigorous stirring a pre-determined volume of APTES, corresponding to a nominal surface density of 20 functions per square nanometer, into the suspension of the as-prepared silica nanoparticles. The mixture was stirred at room temperature for 12 h to promote covalent bonding. The particle suspension was purified by three cycles of centrifugation/redispersion (10,000*g*; 20 min) in absolute ethanol. Then, a given volume of TEA corresponding to a nominal surface density of 50 functions square nanometer was added into the parti-

cle suspension. The mixture was stirred at 60 °C for 15 h before being centrifuged (10,000*g*; 20 min). The particles were redispersed in 30 mL of anhydrous DMF and a given volume of succinic anhydride corresponding to a nominal surface density of 50 functions square nanometer was added. The mixture was stirred at 60 °C for 15 h to promote covalent bonding. The particle dispersion was purified by two cycles of centrifugation (12,000*g*; 10 min)/redispersion in absolute ethanol followed by two cycles of centrifugation (12,000*g*; 10 min)/redispersion in anhydrous DMF.

Synthesis of the dimpled silica particles with aminated PS chains

Synthesis of the multipod-like PS/silica clusters

We prepared batches of bipods and tetrapods, consisting of a central silica core surrounded by two or four PS satellite nodules, by seeded-growth emulsion polymerization of styrene, according to a procedure we published previously [24]. We used two batches of silica seeds with diameters of 48 and 53 nm, respectively, previously surface-modified with MMS or MPS (0.5 molecules per square nanometer) and a surfactant mixture (3 $g \cdot L^{-1}$) of Symperonic® NP30 and SDS. The polymerization was performed at 70 °C for 6 h.

Regrowth of the silica core

We regrew the silica cores to create dimples using a method that we had reported previously [19]. We prepared a mixture of 227.5 mL ethanol and 17.5 mL ammonia (1 M) and added first 5 mL of the polymerization medium containing clusters and a given volume of TEOS at a rate of 1 $mL \cdot h^{-1}$. The experimental conditions and composition of the batches are described in Table 3. For dissolving the PS satellites, we added a volume of DMF corresponding to 10% of the total volume. Then, the dispersion was heated at 70 °C and partially evaporated under vacuum using a rotary evaporator. Then, the temperature was increased to 90 °C and the evaporation continued until the dispersion turns from white to almost transparent. The removal of the dissolved PS was performed by three cycles of centrifugation (10,000*g*; 10 min) and redispersion in THF.

Amination of the residual PS macromolecules at the bottom of the dimples

We used a recipe already reported [21]. Briefly, after transferring the as-prepared dimpled silica particles in chloroform, we added butyl chloromethyl ether in chloroform (3 M; 5 mL) and 0.3 mL $SnCl_4$. We set the temperature to 45 °C and then aged the mixture overnight. Finally we washed the nanoparticles by three cycles of centrifugation (5000*g*; 15 min) and redispersion in HCl aqueous solution (4 wt %) and then in water/ethanol (50/50 wt/wt) before redispersion in 20 mL DMF. We performed the amination stage by using 10^{13} chloromethylated patchy particles in DMF and 3 mL ethylenediamine, i.e., in large excess for minimizing cross-linking. We set the temperature at 90 °C and let the system react overnight under stirring. We washed the nanoparticles by two cycles of centrifugation (12,000*g*; 20 min) and redispersion in ethanol and two extra cycles in water. After having made the amino groups protonated using few drops of HCl, we centrifuged the dispersion and redispersed the nanoparticles in DMF.

Assembly of the aminated dimpled particles with the carboxylated silica spheres

The carboxylic acid functions at the surface of the silica spheres were transformed into carboxylic anhydrides through the addi-

Table 3: Experimental conditions and final compositions of the multipod-like silica/PS clusters used in this study and their geometrical features.

		bipod batch	tetrapod batch
experimental conditions for the seeded-growth emulsion polymerization of styrene	D_{silica} (nm)	48	53
	N_{silica} (10^{15} L^{-1})	18	18
	S_{silica} ($m^2 \cdot L^{-1}$)	130	159
	$[styrene]_0$ ($g \cdot L^{-1}$)	100	100
	coupling agent	MPS	MMS
	NP30/NP30 (%/%)	98/2	95/5
	styrene-to-PS conversion (%)	70	84
experimental conditions for the silica core regrowth	[clusters] (10^{14} $NPs \cdot L^{-1}$)	3.6	3.6
	added $V_{TEOS\ 10\ \%\ in\ ethanol}$ (mL)	5	5
	% bipods	86	4
	% tripods	11	19
	% tetrapods	1	76
	% others	2	1
	D_{silica} after regrowth (nm)	131	132

tion of ECF. To do so, 12 µL of TEA (which correspond to a surface density of 8 functions per square nanometer) were added into 5 mL of a suspension of particles in anhydrous DMF (at 46 $g \cdot L^{-1}$). After homogenization 4 µL of ECF were added. The suspension was stored at 4 °C. A given volume of the activated silica spheres was mixed with the aminated dimpled particles in an Eppendorf tube and the mixture was gently shaken for one week. The clusters were collected by three cycles of centrifugation (500*g*; 20 min) and redispersion in ethanol.

Characterization techniques

Transmission electron microscopy (TEM)

TEM experiments were performed using a Hitachi H600 microscope operating at an acceleration voltage of 75 kV and a JEOL JEM 1400 Plus microscope operating at 120 kV. We prepared the samples by depositing one drop of the colloidal dispersion on conventional carbon-coated copper grids. We let the liquid evaporate in the open air at room temperature and placed the grids in a box away from dust.

Scanning electron microscopy (SEM)

We performed high-resolution SEM experiments with a JSM 6700F microscope at the Plateforme de Caractérisation des Matériaux d'Aquitaine (PLACAMAT). One drop of the CMs suspension was deposited on a glass slide. It was then dried in the open air, metalized, and placed in a box away from dust.

Diffuse reflectance infrared Fourier-transform (DRIFT) spectroscopy

We evaporated solvent from the solution of PS or modified PS. To 9 mg of the dried sample we added 281 mg of desiccated KBr (spectroscopy grade). We ground the mixture in an agate mortar and deposited the powder on the sample holder. The sample was then introduced into the Bruker IFS Equinox 55 spectrometer and the measurements were performed in a Selector Graseby Specac reflection cell. After 30 min of degassing, the infrared spectrum was recorded by the acquisition of 120 measurements with a resolution of 2 cm^{-1}.

Zeta potential measurements

The nanoparticle dispersion was diluted to a concentration of about 10^{15} $NPs \cdot L^{-1}$. The pH value of the solution was adjusted by the addition of HCl (0.1 M) or NaOH (0.1 M). When the desired pH value was reached, a volume of 5 mL of the sample was collected. After equilibration of the pH value for 12 h, the pH value of the samples was measured once again and the zeta potential values were measured using the Malvern Zetasizer 3000 HS setup (Malvern Instruments). Each measurement was performed for 30 s, the dielectric constant of solvent (water) was set to 80.4 and the Smoluchowsky factor $f(\kappa a)$ was 1.5.

Acknowledgements

This work was supported by the Agence Nationale de la Recherche (ENLARgER project, ANR-15-CE09-0010), the LabEx AMADEus (ANR-10-LABX-42) and IdEx Bordeaux (ANR-10-IDEX-03-02), i.e., the Investissements d'Avenir programme of the French government managed by the Agence Nationale de la Recherche.

ORCID® iDs

Etienne Duguet - https://orcid.org/0000-0002-0675-5987
Serge Ravaine - https://orcid.org/0000-0002-6343-8793

References

1. v. Blaaderen, A. *Science* **2003,** *301,* 470–471. doi:10.1126/science.1087140
2. Cademartiri, L.; Bishop, K. J. M. *Nat. Mater.* **2015,** *14,* 2–9. doi:10.1038/nmat4184
3. Jones, M. R.; Mirkin, C. A. *Nature* **2012,** *491,* 42–43. doi:10.1038/491042a
4. Lee, K. J.; Yoon, J.; Lahann, J. *Curr. Opin. Colloid Interface Sci.* **2011,** *16,* 195–202. doi:10.1016/j.cocis.2010.11.004
5. Zhang, J.; Luijten, E.; Granick, S. *Annu. Rev. Phys. Chem.* **2015,** *66,* 581–600. doi:10.1146/annurev-physchem-040214-121241
6. Duguet, E.; Hubert, C.; Chomette, C.; Perro, A.; Ravaine, S. *C. R. Chim.* **2016,** *19,* 173–182. doi:10.1016/j.crci.2015.11.013
7. Ravaine, S.; Duguet, E. *Curr. Opin. Colloid Interface Sci.* **2017,** *30,* 45–53. doi:10.1016/j.cocis.2017.05.002
8. Yi, G.-R.; Pine, D. J.; Sacanna, S. *J. Phys.: Condens. Matter* **2013,** *25,* 193101. doi:10.1088/0953-8984/25/19/193101
9. Du, J.; O'Reilly, R. K. *Chem. Soc. Rev.* **2011,** *40,* 2402–2416. doi:10.1039/c0cs00216j
10. Pawar, A. B.; Kretzschmar, I. *Macromol. Rapid Commun.* **2010,** *31,* 150–168. doi:10.1002/marc.200900614
11. Rodríguez-Fernández, D.; Liz-Marzán, L. M. *Part. Part. Syst. Charact.* **2013,** *30,* 46–60. doi:10.1002/ppsc.201200057
12. Perro, A.; Reculusa, S.; Ravaine, S.; Bourgeat-Lami, E.; Duguet, E. *J. Mater. Chem.* **2005,** *15,* 3745–3760. doi:10.1039/b505099e
13. Wang, Y.; Hollingsworth, A. D.; Yang, S. K.; Patel, S.; Pine, D. J.; Weck, M. *J. Am. Chem. Soc.* **2013,** *135,* 14064–14067. doi:10.1021/ja4075979
14. Wang, Y.; Wang, Y.; Breed, D. R.; Manoharan, V. N.; Feng, L.; Hollingsworth, A. D.; Weck, M.; Pine, D. J. *Nature* **2012,** *491,* 51–55. doi:10.1038/nature11564
15. van Ravensteijn, B. G. P.; Kamp, M.; van Blaaderen, A.; Kegel, W. K. *Chem. Mater.* **2013,** *25,* 4348–4353. doi:10.1021/cm4025606
16. Tigges, T.; Walther, A. *Angew. Chem., Int. Ed.* **2016,** *55,* 11261–11265. doi:10.1002/anie.201604553
17. van Anders, G.; Ahmed, N. K.; Smith, R.; Engel, M.; Glotzer, S. C. *ACS Nano* **2014,** *8,* 931–940. doi:10.1021/nn4057353
18. Wang, Y.; Wang, Y.; Zheng, X.; Yi, G.-R.; Sacanna, S.; Pine, D. J.; Weck, M. *J. Am. Chem. Soc.* **2014,** *136,* 6866–6869. doi:10.1021/ja502699p
19. Désert, A.; Hubert, C.; Fu, Z.; Moulet, L.; Majimel, J.; Barboteau, P.; Thill, A.; Lansalot, M.; Bourgeat-Lami, E.; Duguet, E.; Ravaine, S. *Angew. Chem., Int. Ed.* **2013,** *52,* 11068–11072. doi:10.1002/anie.201304273

20. Hubert, C.; Chomette, C.; Désert, A.; Sun, M.; Treguer-Delapierre, M.; Mornet, S.; Perro, A.; Duguet, E.; Ravaine, S. *Faraday Discuss.* **2015,** *181,* 139–146. doi:10.1039/c4fd00241e
21. Chomette, C.; Duguet, E.; Mornet, S.; Yammine, E.; Manoharan, V. N.; Schade, N. B.; Hubert, C.; Ravaine, S.; Perro, A.; Tréguer-Delapierre, M. *Faraday Discuss.* **2016,** *191,* 105–116. doi:10.1039/c6fd00022c
22. Le Beulze, A.; Gomez-Graña, S.; Gehan, H.; Mornet, S.; Ravaine, S.; Correa-Duarte, M.; Guerrini, L.; Alvarez-Puebla, R. A.; Duguet, E.; Pertreux, E.; Crut, A.; Maioli, P.; Vallée, F.; Del Fatti, N.; Ersen, O.; Treguer-Delapierre, M. *Nanoscale* **2017,** *9,* 5725–5736. doi:10.1039/c7nr00969k
23. Fernandes, B. D.; Vilar-Vidal, N.; Baida, H.; Massé, P.; Oberlé, J.; Ravaine, S.; Treguer-Delapierre, M.; Saviot, L.; Langot, P.; Burgin, J. *J. Phys. Chem. C* **2018,** *122,* 9127–9133. doi:10.1021/acs.jpcc.7b12559
24. Perro, A.; Duguet, E.; Lambert, O.; Taveau, J.-C.; Bourgeat-Lami, E.; Ravaine, S. *Angew. Chem., Int. Ed.* **2009,** *121,* 367–371. doi:10.1002/ange.200802562
25. Valeur, E.; Bradley, M. *Chem. Soc. Rev.* **2009,** *38,* 606–631. doi:10.1039/b701677h
26. Rho, H. S.; Baek, H. S.; Kim, D. H.; Chang, I. S. *Bull. Korean Chem. Soc.* **2006,** *27,* 584–586. doi:10.5012/bkcs.2006.27.4.584
27. Warshawsky, A.; Deshe, A. *J. Polym. Sci., Polym. Chem. Ed.* **1985,** *23,* 1839–1841. doi:10.1002/pol.1985.170230623
28. Désert, A.; Morele, J.; Taveau, J.-C.; Lambert, O.; Lansalot, M.; Bourgeat-Lami, E.; Thill, A.; Spalla, O.; Belloni, L.; Ravaine, S.; Duguet, E. *Nanoscale* **2016,** *8,* 5454–5469. doi:10.1039/c5nr07613g
29. Turkevich, J.; Stevenson, P. C.; Hillier, J. *Discuss. Faraday Soc.* **1951,** *11,* 55–75. doi:10.1039/df9511100055

License and Terms

BEILSTEIN JOURNAL OF NANOTECHNOLOGY

New micro/mesoporous nanocomposite material from low-cost sources for the efficient removal of aromatic and pathogenic pollutants from water

Emmanuel I. Unuabonah[*1,2,3,4], Robert Nöske[3], Jens Weber[5], Christina Günter[6] and Andreas Taubert[3]

Full Research Paper

Open Access

Address:
[1]Environmental and Chemical Processes Research Laboratory, Centre for Chemical and Biochemical Research, Redeemer's University, PMB 230, Ede, Osun State, Nigeria, [2]Department of Chemical Sciences, Redeemer's University, PMB 230, Ede, Osun State, Nigeria, [3]Institute of Chemistry, University of Potsdam, 14476 Potsdam, Germany, [4]State Key Laboratory of Catalysis, Dalian Institute of Chemical Physics, Chinese Academy of Sciences, Dalian, 116023, China, [5]Department of Chemistry, Hochschule Zittau/Görlitz (University of Applied Science), Theodor-Körner-Allee 16, 02763 Zittau, Germany and [6]Department of Earth and Environmental Science, University of Potsdam, 14476 Potsdam, Germany

Email:
Emmanuel I. Unuabonah[*] - unuabonahe@run.edu.ng

* Corresponding author

Keywords:
4-nitrophenol; *Carica papaya* seeds; clay; *E. coli*; micro/mesoporous; nanocomposite; water remediation

Beilstein J. Nanotechnol. **2019,** *10,* 119–131.
doi:10.3762/bjnano.10.11

Received: 13 April 2018
Accepted: 19 December 2018
Published: 09 January 2019

This article is part of the thematic issue "Advanced hybrid nanomaterials".

Associate Editor: B. Bhushan

Abstract

A new micro/mesoporous hybrid clay nanocomposite prepared from kaolinite clay, *Carica papaya* seeds, and $ZnCl_2$ via calcination in an inert atmosphere is presented. Regardless of the synthesis temperature, the specific surface area of the nanocomposite material is between ≈150 and 300 m^2/g. The material contains both micro- and mesopores in roughly equal amounts. X-ray diffraction, infrared spectroscopy, and solid-state nuclear magnetic resonance spectroscopy suggest the formation of several new bonds in the materials upon reaction of the precursors, thus confirming the formation of a new hybrid material. Thermogravimetric analysis/differential thermal analysis and elemental analysis confirm the presence of carbonaceous matter. The new composite is stable up to 900 °C and is an efficient adsorbent for the removal of a water micropollutant, 4-nitrophenol, and a pathogen, *E. coli,* from an aqueous medium, suggesting applications in water remediation are feasible.

Introduction

Porous carbon-based materials and carbon/inorganic hybrid materials have extensively been used for the adsorption of pollutants, such as heavy metals or aromatic hydrocarbons, from water in developing countries [1-4]. The removal of such contaminants is a necessity for public health in many developing countries because these pollutants can negatively alter important biochemical processes and thus are a critical threat to the health of plants, animals, and humans [5]. In addition to chemical contaminants, the removal of biological pollutants from water is a key issue in water treatment and public health. According to the World Health Organization, increasing discharges of untreated sewage, in addition to agricultural runoff and wastewater from industry, have drastically reduced the quality of water around the world. The problem is expected to persist in the coming decades if not quickly addressed [6]. For example, the *Escherichia coli* (*E. coli*) O157:H7 strain causes diarrhea, hemorrhagic colitis, and hemolytic uremic syndrome [7] with serious consequences for the infected individuals.

Unfortunately, many pathogens have developed multiple resistances over the years. Moreover, as bacteria also have a spore or vegetative phase, biological pathogens can persist for a very long time in the environment and withstand common disinfection methods [7,8]. Thus, there is a real need for advanced water treatment processes that overcome these issues.

When water remediation in developing countries is considered, the price of the materials and not their performance is unfortunately the key aspect to take into account. Current technologies such as activated carbon or silica-based materials are still too expensive for these situations. As a result, cheap yet highly efficient materials that can be used for the purification of very large volumes of water are therefore highly sought after [4]. This approach applies to all subgroups of contaminants – heavy metals, organic pollutants, and biological contaminants.

One approach to reduce cost while maintaining the functionality of the material is the use of kaolinite as a cheap yet functional component. Indeed, kaolinite-based materials are efficient materials for the desulphurization of crude oil and heavy metal removal from aqueous media [9-14].

Although effective, the preparation of these materials still often involves metakaolinization, dealumination, ageing, and autoclave heating for several days [15,16]. In some cases, silica, alumina, and structure-directing agents have to be added to the metakaolin to tune the properties of the resulting materials [13,14]. These approaches are less expensive than the use of all-synthetic reagents, such as highly developed silica materials, but they are tedious and still rely on autoclave technology, which is not generally available to the countries in need of these materials. Thus, there is a need for cheap, high volume, and low-tech processes towards materials for water treatment. This is particularly important for developing countries, but with sustainability becoming one of the world's core issues, interest in such materials and processes has also soared in highly industrialized countries.

Indeed, there are reports of the use of clay/carbon materials for the removal of toxic micropollutants from water. In some cases, sugars have been used as starting compounds [17,18], while in other cases, dyes and other organic molecules have been loaded into the clay interlayer and calcined together with the clay to produce hybrid carbon/inorganic adsorbents [19,20].

We have previously described the synthesis and performance of a new hybrid material based on kaolinite and *Carica papaya* seeds for water treatment [1]. The material has several advantages over conventional processes: (i) it can be made from local raw materials, (ii) the raw materials are either waste or very cheap, (iii) the process does not require a complex technical setup, (iv) the process can be adapted to local requirements, such as exchanging the papaya seeds with other organic components that are available locally, and (v) the material performs very well (according to the World Health Organization limits) for Cd(II) and Pb(II) removal from water. However, recent experiments in our laboratories (unpublished) show that the material performs very poorly when attempting to remove anionic pollutants from water.

In response to this observation, we have modified the synthesis strategy using microwave irradiation rather than thermal treatment during synthesis. The resulting materials have been successfully used for the removal of phosphates and gram-negative bacteria from aqueous media [21,22].

Unfortunately, these materials are not effective in the removal of nitrophenol (anionic) pollutants from water. The materials are only able to disinfect water by adsorption without killing the pathogens [22]. The current study shows that these limitations are, however, surmounted by a further modification of the base materials via an improved materials synthesis procedure.

The current study describes the synthesis of a new porous nanocomposite material. Unlike earlier versions of these materials prepared with alkali activation [1,22], the resulting micro/mesoporous carbon–clay nanocomposite in this study shows a high efficiency for the removal of anionic organic and pathogenic pollutants from water. As in the previous study [1], the starting

materials are purified raw kaolinite clay (one of the most abundant materials on earth), *Carica papaya* seeds, and $ZnCl_2$. The synthesis protocol is very simple and thus is amenable to upscaling and fabrication in less developed regions of the world. No high pressure nor additional (expensive) and environmentally harmful template is necessary.

Materials and Methods

Materials

$ZnCl_2$, $MgCl_2$ (≥98%) and HNO_3 (>90%) were purchased from Sigma-Aldrich. *Carica papaya* seeds were obtained from the local market in Benin City, Nigeria and sun-dried until all fleshy parts of the fruits were dried off the seeds. The dry seeds were collected into an airtight container. Kaolinite clay was collected from Redeemer's University, Redemption City, Nigeria, and purified according to the method described by Adebowale et al. [23].

Methods

Synthesis. Hybrid clay (HYCA) materials were prepared by vigorously mixing $MgCl_2$ or $ZnCl_2$, kaolinite clay, and papaya seeds (in specific ratios as described in the section "Sample nomenclature" below, 10 g of material in total) in 100 mL of Millipore water in a beaker yielding a turbid paste. These pastes were allowed to stand open to the air for 24 h, after which they were dried in an oven at 70 °C. The dried samples were heated to between 450 and 900 °C in a Carbolite furnace in N_2 for 2 h. Subsequently, the samples were washed with 3 M HNO_3 for 30 min with intermittent stirring, filtered, and dried in an oven at 70 °C.

Sample nomenclature. The samples prepared with $ZnCl_2$ in a 1:1:1 ($ZnCl_2$:papaya seeds:kaolinite clay, 10 g total mass) weight ratio were labelled 1Z-HYCA, and samples with a 2:1:1 weight ratio were labelled 2Z-HYCA. Samples prepared with $MgCl_2$ were labelled following the same concept but using the prefix M instead of Z. The total mass of all components combined was always 10 g.

Physicochemical characterization

X-ray powder diffraction analysis

The X-ray diffraction analysis data were collected on a PANalytical Empyrean powder X-ray diffractometer in a Bragg–Brentano geometry. This instrument was equipped with a PIXcel1D detector using Cu Kα radiation (λ = 1.5419 Å) operating at 40 kV and 40 mA. The θ/θ scans were run in a 2θ range of 4–70° with a step size of 0.0131° and a sample rotation time of 1 s. The diffractometer was equipped with a programmable divergence and antiscatter slit and a large Nibeta filter. The detector was set to continuous mode with an active length of 3.0061°.

Scanning electron microscopy (SEM) and specific surface area analysis

SEM analysis was performed on a Japan Electron Optics Laboratory JSM 6510 with an energy dispersive X-ray spectrometer (Oxford INCAx-act SN detector) to determine the morphology of particles prepared in this study. The porosity analysis and specific surface area determination were performed using Autosorb-1MP and Quadrasorb-MP machines (both Quantachrome Instruments). The samples were degassed under high vacuum at 150 °C for 20 h prior to analysis. The surface areas were calculated either by the single-point or multipoint Brunauer–Emmett–Teller (BET) method [24]. The pore size distributions were calculated using the quenched solid density functional theory (QSDFT) methodology (part of the QuadraWin 5.05 Software package of Quantachrome Instruments). The QSDFT analysis was obtained from the adsorption branch of the isotherms assuming slit-like micropores and cylindrical mesopores.

Spectroscopy analysis

Fourier transform infrared spectra (FT-IR) were obtained from transmission measurements (Shimadzu 8400S FTIR, 4000–400 cm^{-1}, 40 Scans) using KBr pellets prepared with a Shimadzu MHP-1 mini hand press. The background correction was performed with a pure KBr pellet, and the samples were measured at 10% in 90% KBr. UV–vis spectroscopy was performed on a Shimadzu 1650pc UV–vis spectrophotometer for analysis of 4-nitrophenol. Cross-polarized magic angle spinning nuclear magnetic resonance ^{27}Al (104.1 MHz), ^{13}C (100.5 MHz), and ^{29}Si (79.4 MHz) spectra of the 2Z-HYCA@650 °C nanocomposite were recorded on a Bruker DRX-400 spectrometer with a magic angle spin probe and 4 mm ZrO_2 rotor ^{27}Al signals were referenced to a 0.5 M aqueous solution of aluminum nitrate. ^{13}C and ^{29}Si signals were referenced to tetramethylsilane (TMS).

Other analysis

Thermogravimetric /differential thermal analysis was performed on a Netzsch STA 449F3 from 25 to 1000 °C at 5 °C/min under N_2. The point of zero charge (pH_{pzc}) analysis meant to determine the surface charge of samples prepared was carried out using the salt addition method, as described by Unuabonah et al. [22]. Elemental analysis to determine the amount of C, H, and N in the samples was performed with an Elementar Vario EL III elemental analyzer.

Adsorption of 4-nitrophenol

For each measurement, 0.7 g of 2Z-HYCA was added to a Salamander tubular reactor (Cambridge Reactor Design Ltd, UK) operating at 30 °C. The fixed bed reactor (length of 3.625 cm, diameter of 6 mm) was flushed with 20 mL of deionized water

to wash the 2Z-HYCA material. With the column delivering clean and clear deionized water and with the deionized water allowed to run out completely, a 1 mg/L solution of 4-nitrophenol was allowed to flow through the reactor bed in upward flow mode at a flow rate of 10 mL/min. Effluents from the column were collected at selected time intervals. An analysis of 4-nitrophenol was performed according to Al-Asheh et al. [25] using a 0.5 mol/L sodium carbonate solution, and measurements of the absorption of the solutions at 400 nm vs distilled water were carried out. Kyplot 2.0 software was used to model the experimental data against the Thomas model [26] by minimizing the sum of squared differences between the experimental and predicted values of the dependent variable using the quasi-Newton least squares algorithm.

Pathogenic pollutant removal

To evaluate the efficiency of 2Z-HYCA for pathogen removal from water in a real application, commercial Eva® drinking water was used for the removal experiments. Freshly purchased Eva® water does not contain *E. coli* and was therefore used as the reference. *E. coli* ATCC 25922 cultures were grown in nutrient broth at 37 °C for 24 h to yield a cell count of approximately 10^9 cfu/mL. The tip of a sterile inoculation loop was then used to spike 1 L of the water six times, which yielded approximately 10^3 cfu/mL as measured using the optical density method that utilized a UV–vis spectrophotometer at an absorption maximum of 600 nm. This step was repeated twice, and the average optical density readings were determined.

A sample of 0.5 g of 2Z-HYCA was pretreated with 10 mL of ethanol and then dried in an oven. Subsequently, the sample was placed in an autoclave-sterilized fixed bed column (8 mm internal diameter and length 28 cm) and flushed with warm sterile water. The *E. coli*-spiked water was then passed through the bed of the 2Z-HYCA adsorbent, and effluent samples were collected at specified time intervals. To test for the presence of *E. coli* in the effluent, 1 mL of the effluent solution samples were inoculated in eosin methylene blue (EMB) agar plates, incubated at 37 °C for 24 h, and *E. coli* colonies (as indicated by a metallic sheen on the plates) were counted with a colony counter. This test was conducted in duplicate.

Results and Discussion

Physicochemical analysis

Specific surface area analysis

To evaluate the effect of the type of metal salt on the efficiency of the resulting materials to remove 4-nitrophenol and *E. coli* bacteria, we prepared an initial set of materials with $MgCl_2$ and $ZnCl_2$ at a reaction temperature of 500 °C. Figure 1a shows the nitrogen sorption isotherms of 1M-HYCA, 1Z-HYCA, and 2Z-HYCA (see experimental part for sample labels). The shape of the isotherms suggests the presence of micro- and mesopores in 1Z- and 2Z-HYCA, while 1M-HYCA only shows a low nitrogen uptake. Its specific surface area, S_{BET}, is only 20 m^2/g, while the S_{BET} of 1Z-HYCA is 162 m^2/g and the S_{BET} of 2Z-HYCA is 228 m^2/g (Figure 1A). As a result, M-HYCA was not considered any further because high surface areas are a prerequisite for successful water treatment.

In contrast, both Zn-containing samples show adsorption–desorption isotherms indicative of porous materials. The isotherm shape is, however, rather ill-defined and can be understood as a mixture of different isotherm types. A significant uptake is observed at low relative pressure (p/p_0), which is indicative of some microporosity. A monotonic increase in the adsorbed gas amount is observed at intermediate relative pressures, followed by a steeper volume increase at high relative pressures. The increase can be related to the condensation of N_2 in the intersti-

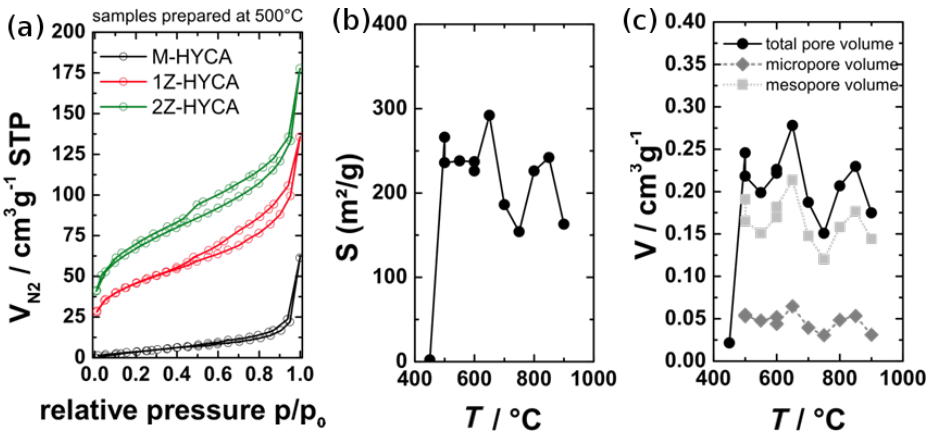

Figure 1: (A) N_2 adsorption/desorption isotherms (77.4 K) for the HYCA materials prepared at 500 °C. (B) BET surface area of the 2Z-HYCA materials vs calcination temperature. (C) Pore volumes of the 2Z-HYCA nanocomposite materials vs calcination temperature.

tial voids among the particles. A very modest hysteresis is observed, which closes at approximately $p/p_0 = 0.45$. This result is indicative of a few mesopores with restricted access within the material, which are emptied by cavitation [27].

Furthermore, analysis of 2Z-HYCA vs the synthesis temperature indicates that significant porosity in the materials is generated at approximately 500 °C. Indeed, 2Z-HYCA prepared at 450 °C does not show any porosity, while materials prepared at 500 °C and higher show surface areas that remain roughly constant until a preparation temperature of 900 °C. No clear trend of the specific surface areas or the pore volume is observed with increasing temperature. The specific surface areas are scattered at approximately 230 m^2/g (Figure 1b), and the total pore volume scatters at approximately 0.23 cm^3/g (Figure 1c).

Pore size distributions (PSDs) were determined from the adsorption branches of the isotherms using a commercialized QSDFT methodology [28]. A rather constant micropore content was observed (Figure 1c) along with mesopores. The ratio of the mesopore surface area to micropore surface area is approximately 1. The pore volume of mesopores is accordingly significantly higher than the pore volume of the micropores (Table S1, Supporting Information File 1). The size distribution of the mesopores is broad (Figure S1, Supporting Information File 1) with the main fraction of pores between 2 and 8 nm. Similar to the total surface area, the PSD is independent of the synthesis temperature.

Overall, nitrogen sorption analysis indicates that the porosity does not directly correlate with the synthesis conditions as soon as the threshold temperature of 500 °C is passed.

As stated above, a high surface area is a key requirement for a material to work in water treatment. The remainder of the article will therefore focus on 2Z-HYCA nanocomposite materials which had the highest surface area.

Influence of synthesis temperature

Figure 2A shows the isolated yields of 2Z-HYCA after the reaction at different temperatures. The data clearly show that the yield decreases as the reaction temperature increases.

In light of the need for a (reasonably) sustainable and efficient process with good yields, the reaction temperature should thus be as low as possible to provide the highest mass possible. In spite of this, the reaction temperature must be high enough to provide a high surface area and substantial transformation into the desired high surface area 2Z-HYCA nanocomposite materials. As a result, a reaction temperature of approximately 500 °C appears the most suitable for the synthesis of 2Z-HYCA nanocomposite because it is high enough to produce a material with a high surface area, yet low enough to produce substantial yields. A reaction temperature of 500 °C is even more attractive if the aspect of reduced energy cost for reactions at lower temperatures (500 vs 700 or even 900 °C) is considered. Specifically, the lower the reaction temperature is, the lower the energy cost for producing the material is.

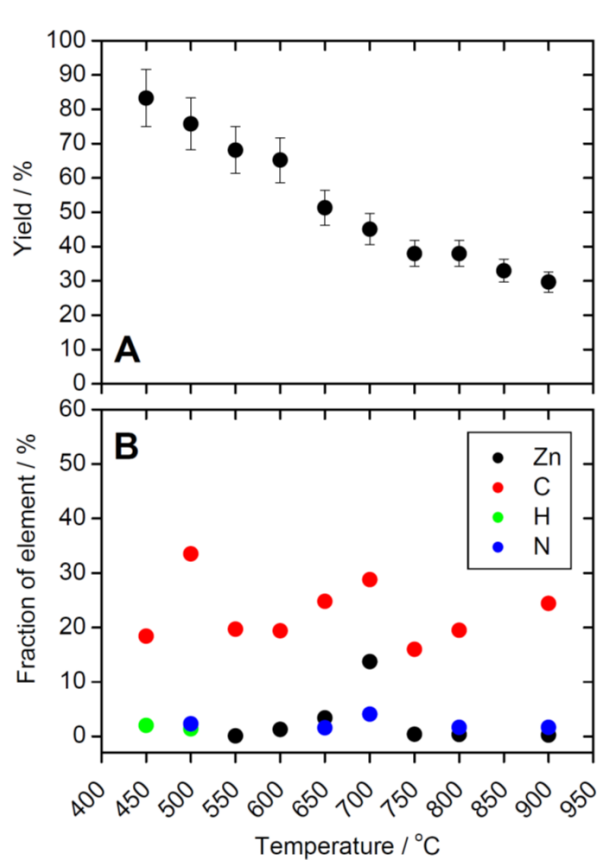

Figure 2: (A) Yield vs reaction temperature. (B) Chemical composition data from elemental analysis (EA) and energy dispersive X-ray spectroscopy (EDXS): Zn, C, H, and N fractions vs temperature. No symbol in (B) indicates that the concentrations of the respective elements are below the limit of detection of the respective instrument (EA = 0.3%, EDXS = 0.1%).

Elemental analysis

The 2Z-HYCA nanocomposite samples were further analyzed with energy dispersive X-ray spectroscopy (EDXS) and elemental analysis (EA) to determine the elemental make-up of the nanocomposite and to specifically determine if it was successfully Zn doped. Figure 2B shows the fractions of Zn, C, H, and N vs sample treatment. The EA shows that increasing the reaction temperature eliminates hydrogen from the samples. This finding is consistent with previous work showing that activation using $ZnCl_2$ induces the loss of hydrogen and oxygen atoms from carbon materials in the form of water, rather than as

hydrocarbons or as oxygenated organic compounds [29]. The hydrogen loss could have led to aromatization of the carbon skeleton, and the formation of pores. Some authors suggest that $ZnCl_2$ is very mobile above its melting point (283 °C) which inhibits the formation of volatile matter (devolatization) and thus allows for the development of a microporous structure [30,31].

The amount of Zn (obtained from EDXS) is shown to increase in 2Z-HYCA nanocomposites prepared at temperatures below 700 °C and reaches a maximum at this temperature. It then decreases sharply above 700 °C while remaining practically constant at very low levels in all samples prepared at 750 °C or higher (Figure 2B). We speculate that the tendency to incorporate Zn into the final material is maximized at temperatures of 650 and 700 °C but is greatly reduced at temperatures above the boiling point of $ZnCl_2$ (732 °C) due to the evaporation of $ZnCl_2$ [30].

Analysis of chemical functionalities

Figure 3 shows selected FTIR spectra of 2Z-HYCA prepared at different temperatures. The signals are indicative of surface octahedral –OH groups at 3697, 3670, and 3649 cm^{-1}, which are observed in the spectra of the raw kaolinite, and are no longer visible in the spectra of the 2Z-HYCA samples. This result is similar to our previous HYCA materials prepared with NaOH in air at 300 °C [1].

The broad band at approximately 3426 cm^{-1} in raw kaolinite clay is an –OH stretching vibration that is present in all 2Z-HYCA micro/mesoporous nanocomposite materials. The –OH bending vibration from adsorbed water at ≈1600 cm^{-1} decreases in intensity and shifts from 1624 to 1585 cm^{-1} with increasing reaction temperature.

The bands observed in the spectra of raw kaolinite between 1000–1200 cm^{-1} significantly change upon heating. The spectra of samples produced at 450 °C exhibit new bands at 1067 and 459 cm^{-1}, which become sharper in 2Z-HYCA nanocomposite materials prepared above 450 °C. These new well-defined peaks suggest a mixed phase of Si–O and SiO_4 tetrahedra [32]. The new distinct peak at 459 cm^{-1} is associated with the presence of Si–O [33].The –OH bending vibration from absorbed water in raw kaolinite clay (1630 cm^{-1}) shifts to lower wave numbers in 2Z-HYCA (between 1615 and 1599 cm^{-1}) with increasing temperature. The band at approximately 1700 cm^{-1} is attributed to the C=O stretching vibrations of carbonyl groups present in the organic fraction in the 2Z-HYCA composites. There appears to be a doublet peak at 2352 and 2356 cm^{-1} which signifies the presence of the –C–N stretching mode [34]. The Al–O absorption peak at 917 cm^{-1} decreases in intensity as the temperature increases. As a result, IR spectroscopy demonstrates that the 2Z-HYCA nanocomposite material is a complex hybrid material containing Si–O, Si–O, Al–O, –OH, –C–N, and C=O.

X-ray diffraction analysis

Figure 4a shows the powder X-ray diffraction (PXRD) diagrams of raw kaolinite (RK) and 2Z-HYCA prepared at different temperatures. After heating, dehydroxylation of kaolinite

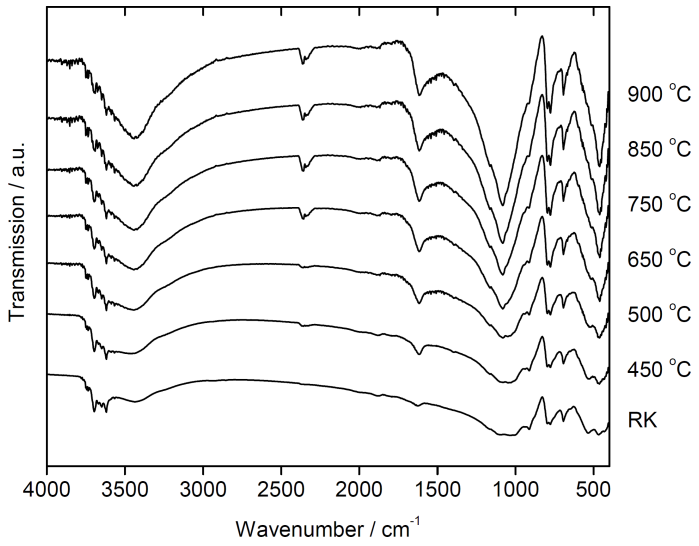

Figure 3: Fourier transform infrared spectra of the 2Z-HYCA nanocomposites obtained at various temperatures. “RK” indicates the spectrum of the raw kaolinite mentioned in the text.

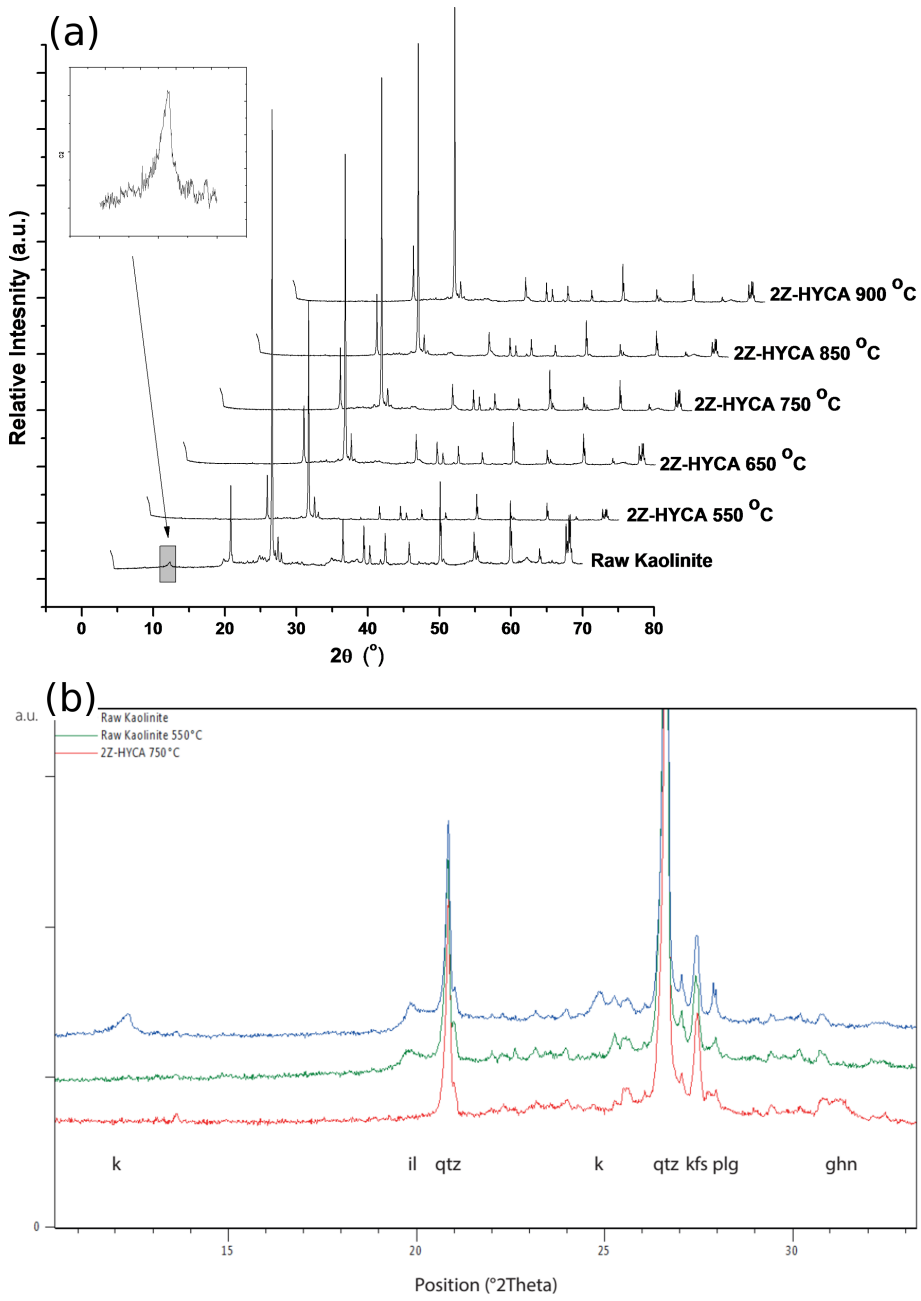

Figure 4: (a) XRD patterns of raw kaolinite clay and 2Z-HYCA composite materials obtained at various temperatures. (b) Powder X-ray diffraction (PXRD) diagrams of raw kaolinite (RK), raw kaolinite heated at 550 °C and 2Z-HYCA prepared at 750 °C. k = K-feldspat (microcline), il = illite, qtz = quartz, plg = plagioclase, ghn = gahnite.

occurs, which causes the reflections of kaolinite to disappear (for example, at 12.35° and 20.34°, 2θ, JCPDF 98-008-7771). In the absence of the reflections of kaolinite, the remaining reflections of quartz (JCPDF 98-008-9277 at 2θ values of 20.83°, 26.61°, 36.49°, 39.43°, 50.08°, etc.), K-feldspar (microcline, JCPDF 98-020-2423 at 2θ values of 21.04°, 27.07° and 27.45°) and plagioclase (JCPDF 98-003-4917 at 2θ values of 22.01° and 27.95°) occur more clearly.

Figure 4b shows the comparison of the PXRD diagrams of raw kaolinite, raw kaolinite heated at 550 °C and 2Z-HYCA heated at 750 °C for one hour. The originally used raw kaolinite is composed of kaolinite (k), quartz (qtz) and feldspar (microcline (kfs) and plagioclase (plg)) and small amounts of illite (il, JCPDF 98-009-0144) and anatase (TiO_2, JCPDF 98-009-6946, at 2θ values of 25.29°). As already mentioned, the kaolinite reflections disappear for all heated samples. Additionally, the

illite reflection (see Figure 4b at 2θ 19.82°) decreases, probably due to the dehydroxylation illite, which begins at temperatures >550 °C. Additionally, above 650 °C, the heated 2Z-HYCA diagrams show broad reflections (see Figure 4a at 2θ values of 31.25, 36.82°, 55.62°, 59.32° and 65.19°), which can be assigned to a new Al_2ZnO_4-phase (ghn, gahnite-type JCPDF 98-007-5098).

Interestingly, the new materials prepared in this study exhibit no ZnO phase, as seen from the FTIR or XRD spectra, unlike in our previous studies [21]. This behavior is because a standard solution of NaOH used in the previous preparation of the materials (which, when reacted with $ZnCl_2$, will yield ZnO) was omitted in the preparation of the nanocomposites in this study.

Nuclear magnetic resonance spectroscopy analysis

To further evaluate the composition and structure of 2Z-HYCA, a sample calcined at 650 °C was investigated with solid-state cross-polarized magic angle spinning nuclear magnetic resonance (CP-MAS-NMR) spectroscopy. The corresponding ^{29}Si, ^{27}Al, and ^{13}C CP-MAS-NMR spectra are shown in Figure 5.

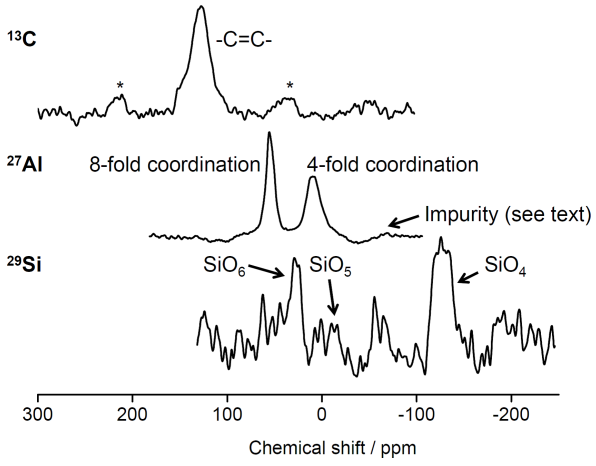

Figure 5: ^{29}Si, ^{27}Al and ^{13}C CP-MAS-NMR spectra of 2Z-HYCA calcined at 650 °C. *Rotation side bands of ethylene carbon.

The ^{13}C spectrum only shows a prominent peak at 128 ppm, indicating the presence of sp^2-bonded carbon environments, specifically $CH{=}CH_2$ moieties [35]. The weak bands at ≈215 and ≈35 ppm are rotation sidebands [36].

The ^{29}Si MAS-NMR spectrum shows a set of low-resolution signals. The bands at −89, −100 and −126 ppm correspond to Q^3 (1Al) [37], isolated silanol [SiO_3(OH)] [38] and Q^4 (0Al) [37] silicon sites of metakaolin, respectively. These peaks are common to kaolinite heated between 550–850 °C [38]. The presence of these peaks suggests that 2Z-HYCA is an organic–inorganic hybrid material.

The ^{27}Al MAS-NMR spectrum shows two distinct peaks at 55 and 10 ppm, characteristic of tetrahedrally (T) and octahedrally (O) coordinated aluminum centers, respectively, in metakaolin [39,40]. The T/O ratio suggests that the fraction of T-coordinated Al is almost twice that of O-coordinated Al. A broader resonance with low intensity is observed at ≈−68 ppm, perhaps resulting from an amorphous or less crystalline (impurity) phase [41].

Overall the XRD and solid-state NMR data support the FTIR spectroscopy spectra in that all methods detect some chemical changes in the zinc-based HYCA materials compared to the starting materials, thus confirming the formation of a real hybrid material. This result is also confirmed by SEM.

Scanning electron microscopy analysis

Figure 6 shows representative SEM images of all samples. Although the morphologies of the materials synthesized at different temperatures are quite similar, some differences can be observed. In all cases, roughly spherical primary particles are observed, but the materials produced at lower temperatures appear to consist of smaller particles (approximate diameter between ≈50 and 150 nm), while the samples produced at higher temperatures contain larger particles with approximate diameters of 200 to 300 nm. Moreover, the samples made at 750 °C and higher also contain plate-like or fiber-like features.

Thermogravimetric and differential thermal analysis

Figure 7 shows representative thermogravimetric analysis/differential thermal analysis (TGA/DTA) data obtained from measurements in nitrogen. Consistent with the data shown above, there are clear differences between samples produced at reaction temperatures up to 450 °C and the samples obtained at higher temperatures. The samples made between 500 and 900 °C only show a weak and very gradual weight loss of ≈5–6% of the total mass at the end of the TGA/DTA experiment. This finding indicates that most of the volatiles have already been eliminated during the synthesis of the materials.

In contrast, the samples produced at lower temperatures are much less stable and lose up to 45% of their original mass. Here, the weight losses can be separated in three (although strongly overlapping) steps between 25 and 100 °C, 110 and ≈450 °C, and finally ≈450 to 900 °C [42]. The first loss can be assigned to the desorption of water adsorbed in the pores of the hybrid clay materials. The second loss is attributed to the predehydration process as a result of a reorganization in the octahedral layers in kaolinite associated with condensation and water elimination [43,44]. The third loss is assigned to the dehydroxylation of kaolinite (and formation of metakaolinite), which is supported by an exothermic peak in the thermogravimetric anal-

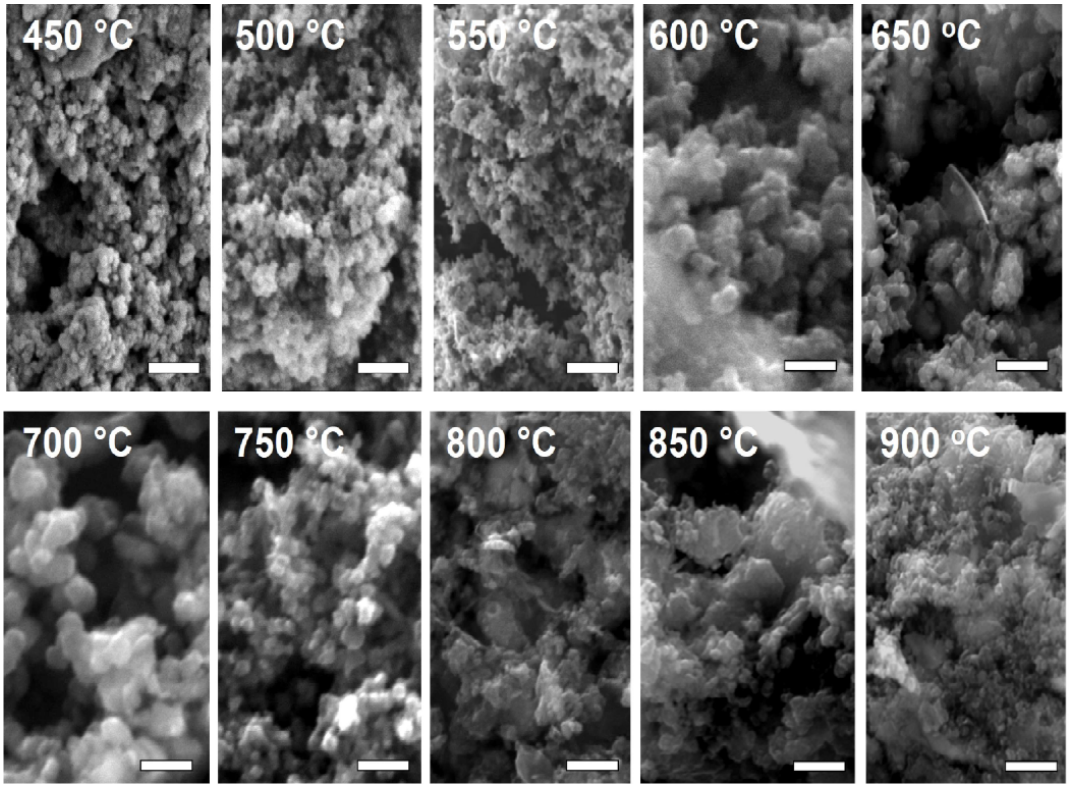

Figure 6: SEM images showing the growth pattern of 2Z-HYCA nanocomposite particles with increasing temperature after acid washing. All scale bars = 1 µm.

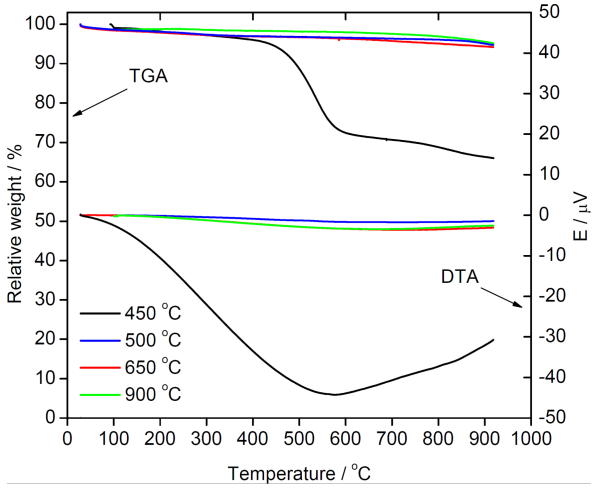

Figure 7: TGA and DTA curves for 2Z-HYCA nanocomposites prepared at various temperatures.

ysis (DTA) [42]. This explains the loss of the inner hydroxyl related to kaolinites initially observed from our FTIR analysis in this study. Moreover, some fraction of the weight losses at higher temperatures may also be assigned to condensation reactions in the inorganic components and concurrent water elimination, but these individual processes cannot be separated here. TGA/DTA data analysis therefore indicates that the reaction temperature is indeed a key parameter to obtain a stable material that will resist rapid attrition during use. Comparison with the nitrogen sorption data suggests that a reaction temperature of ≈500 °C is interesting both from stability and surface area aspects.

Pollutant removal from aqueous solutions

Removal of 4-nitrophenol

We have previously reported that a first-generation HYCA material prepared via a low-temperature calcination process in air very efficiently adsorbs cationic pollutants such as Pb^{2+}, Cd^{2+}, Ni^{2+} [1], and methylene blue [4] from an aqueous solution. However, this material fails when attempting to remove anionic pollutants such as 4-nitrophenol (with a pK_a of 7.2 [45]), methyl orange dye, or phosphate.

The data demonstrate that the 2Z-HYCA nanocomposite is able to overcome the limitations of the highly negatively charged original HYCA material [1] and provides sites for the adsorption of anionic pollutants, such as 4-nitrophenol.While used as a model compound here, 4-nitrophenol is an organic anionic pollutant of high interest because acute exposure to 4-nitrophenol causes blood disorders or liver and kidney damage [46,47].

Figure 8 shows a representative dataset obtained from a setup with 0.7 g of 2Z-HYCA@650 °C (the material with the highest surface area) in a fixed bed reactor. 2Z-HYCA@650 °C reduces the concentration of 4-nitrophenol to below the detection limit after 80 min when aqueous solutions with 4-nitrophenol concentrations of 1 mg/L were used. Moreover, a 50% breakthrough was reached at ≈900 min after treating 9 L of the same solution, and the 2Z-HYCA@650 °C was 100% spent after 28 h 40 min. This result demonstrates that 2Z-HYCA is a highly effective adsorbent for 4-nitrophenol, especially when considering the very short empty bed contact time (the time a treated solution is in contact with 2Z-HYCA@650 °C nanocomposite material) of 8.6 s, as determined from the AdDesignS™ software [48]. The rate constant obtained by fitting the data with the Thomas model (Figure 8) is 3.69 mL/min·g, and the adsorption capacity is 3.61 mg/g.

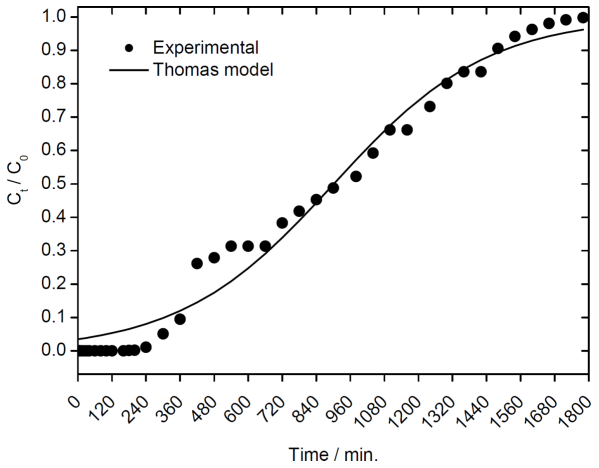

Figure 8: Experimental breakthrough curve for the adsorption of 4-nitrophenol onto 2Z-HYCA@650 °C (C_o = Concentration of 4-nitrophenol at time 0; C_t = Concentration of 4-nitrophenol at time *t*).

The data obtained were modelled against the pore and surface diffusion model (PSDM) and the constant pattern homogeneous surface diffusion model (CPHSDM) using the AdDesignS™ software and making various inputs (parameters given in Table 1).

The results suggest that data obtained for the adsorption of 4-nitrophenol onto 2Z-HYCA@650 °C nanocomposite is mainly by a pore and diffusion mechanism as supported by the good fit to PSDM (Figure 9A) rather than a surface reaction that is supported by the CPHSDM that showed a very poor fit with the data (Figure 9B).

The PSDM predicted that 1 kg of 2Z-HYCA@650 °C micro/mesoporous nanocomposite material can reduce a concentration of 1 mg/L of 4-nitrophenol (single solute solution) in 290 L of aqueous solution below 50 µg/L in 346 min (5 h 46 min). To maintain this same concentration of 4-nitrophenol in aqueous solution below the World Health Organization's drinking water equivalent level (DWEL) of 0.3 mg/L [49], 1 kg of 2Z-HYCA@650 °C will be required for ≈10 h 20 min and will treat 2.49 m^3 of water per day.

Table 1: Input data for pore and surface diffusion model (PSDM) and constant pattern homogeneous surface diffusion model (CPHSDM) modelling using AdDesignS software.

Input data for CPHSDM	
chemical	
molecular weight of 4-NP	139 g/moL
initial concentration	1 mg/L
bed data	
bed length	5.075×10^{-2} m
bed diameter	6.000×10^{-3} m
weight of HYCA	0.7 g
inlet flow rate	10 mL/min
temperature	30 °C
water density	30 °C = 0.9957 g/cm^3
water viscosity	8.15×10^{-3} g/cm·s
input data PSDM	
chemical	
molecular weight of 4-NP	139 g/moL
initial concentration	1 mg/L
bed data	
bed length	5.075×10^{-2} m
bed diameter	6.000×10^{-3} m
weight of HYCA	0.7 g
inlet flow rate	10 mL/min
temperature	30 °C
water density	30 °C = 0.9957 g/cm^3
adsorbent properties	
name	2Z-HYCA
apparent density	2.42 g/cm^3
particle radius	0.030000 cm
porosity	1.000

Removal of *Escherichia coli*

Figure 10A shows that 0.5 g of 2Z-HYCA@650 °C essentially eliminates *Escherichia coli* (*E. coli*) completely from water, which was initially spiked with *E. coli* (at 10^3 cfu/mL), within 75 min.

After 75 min, the amount of *E. coli* in the treated water increased with time. In contrast, the regular HYCA material [1] can also remove *E. coli* from the same solutions but with a much lower efficiency. This finding suggests that the presence of Zn^{2+} in the composite material directly affects *E. coli*

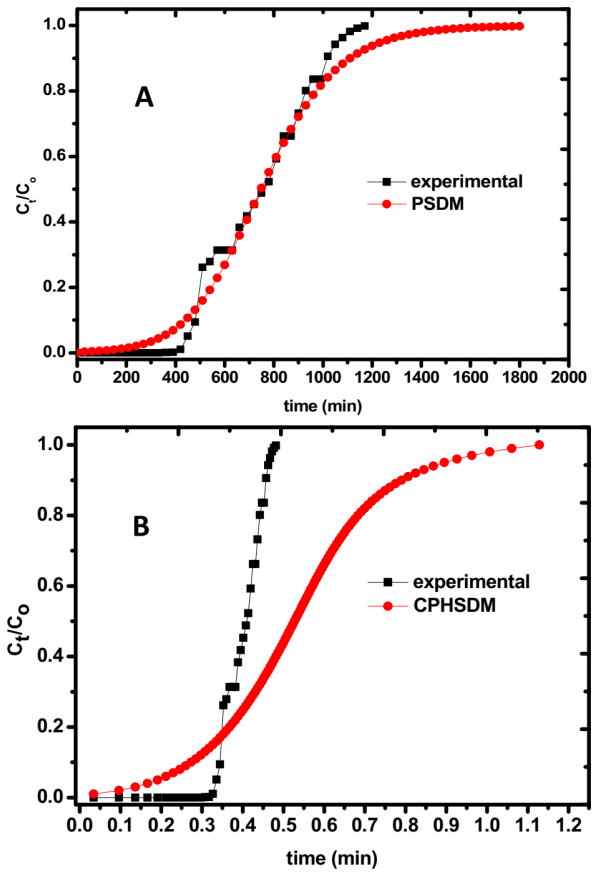

Figure 9: (A) Pore and surface diffusion model (PSDM) plot for the removal of 4-nitrophenol from aqueous solution by 2Z-HYCA@650 °C loaded into a fixed-bed reactor (C_o = initial concentration of 4-nitrophenol at time 0 and C_t = concentration of 4-nitrophenol at time *t*). (B): Constant pattern homogeneous surface diffusion model (CPHSDM) plot for the removal of 4-nitrophenol from aqueous solution by 2Z-HYCA@650 °C loaded into a fixed-bed reactor (C_o = initial concentration of 4-nitrophenol at time 0 and C_t = concentration of 4-nitrophenol at time *t*).

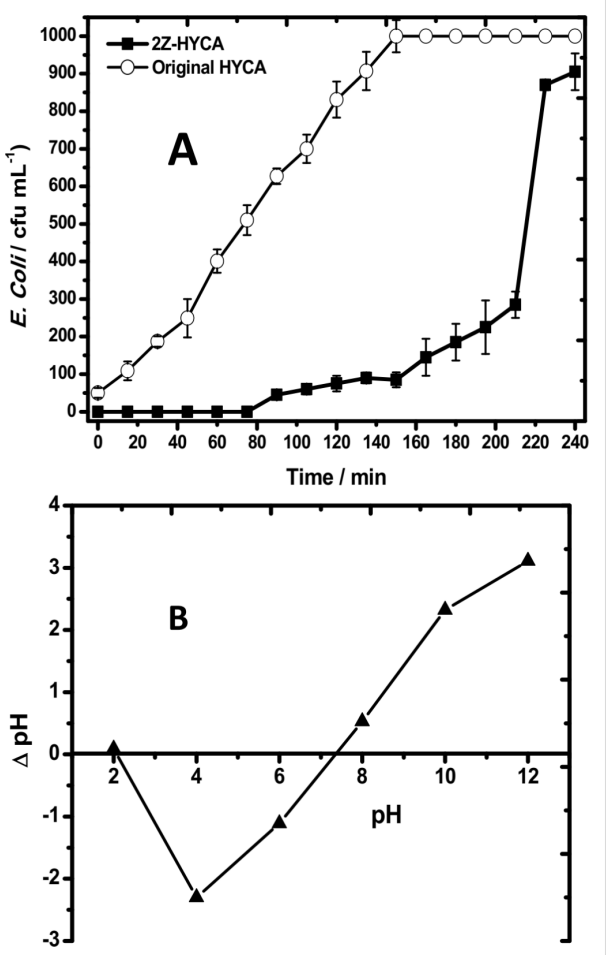

Figure 10: (A) Bacterial load (*E. coli*) vs treatment time measured in water treated with a fixed bed process for both the original HYCA material and the new 2Z-HYCA@650 °C material. The initial *E. coli* concentration was 10^3 cfu/mL; (B): The pH_{pzc} plot for 2Z-HYCA@650 °C.

removal from solution, likely because zinc has antibacterial properties. Although the precise functional mechanism is unknown, it has been suggested that Zn-doped materials deactivate bacteria by damaging its cell membrane and DNA [50]. It is known that electrostatic adsorbent–adsorbate interactions do occur in solution at pH values either above or below the pH_{pzc} of the adsorbent [51]. Based on the latter, it is believed that the composite adsorbent material in this study does become positively charged below its pH_{pzc} of 7.4 (Figure 10B) in an aqueous mixture of bacteria (whose pH was measured to be 6.36) since a mixture of bacteria solution and nanocomposite will reduce the pH to below 7.4. This will aid electrostatic interaction between the negatively charged bacteria and the positively charged 2Z-HYCA@650 °C. This behavior also explains, in part, the mechanism for the uptake of 4-NP by 2Z-HYCA nanocomposite material, as it is expected that 4-nitrophenol will ionize in water at pH 6.3 to yield some 4-nitrophenoxide anions that will be electrostatically held onto the positive sites on the surface of the material.

Even after 3 h of run time, the level of *E. coli* in the treated solution was still below the alert/action levels of 500 cfu/mL in drinking water for *E. coli* [52], as shown in Figure 10. This suggests the potential of the 2Z-HYCA@650 °C as a water disinfectant for the future. However, more studies still need to be conducted to ascertain this.

Conclusion

This study introduces the newest generation of the HYCA material, namely, 2Z-HYCA, two low-cost precursor sources, kaolinite clay and *Carica papaya* seeds, synthesized without the need for alkali activation. The preparation is simple, and the resulting nanocomposite material is micro/mesoporous, unlike the initial hybrid clay material prepared in our previous study [1]. The new micro/mesoporous material is efficient for the removal

of 4-nitrophenol and *E. coli* from drinking water. Zinc may not be desirable from a heavy metal pollution point of view; however, the introduction of zinc significantly enhances the performance of the original HYCA materials for remediation of these pollutants in water. As such, and because the Zinc concentration leached into treated water from the 2Z-HYCA nanocomposite material is very low [22], it is thus the belief of the authors that the dual functionality of this new material in efficiently removing a recalcitrant anionic organic pollutant (4-nitrophenol) and bacteria (*E. coli*) from water compensates for the cost of N_2 and high temperature employed in its preparation, even in developing countries. As a result, the current approach opens a new door towards cheap and sustainable materials development with exciting performance in one of the key areas of today's world, the treatment of water in developing countries.

Supporting Information

The Supporting Information contains additional information on the specific surface area analysis using the quenched solid density functional theory, the raw data for elemental and specific surface area analyses.

Supporting Information File 1

Additional experimental results.
[https://www.beilstein-journals.org/bjnano/content/supplementary/2190-4286-10-11-S1.pdf]

Acknowledgements

We acknowledge Ms. Y. Mai-Linde (University of Potsdam) for help with the elemental analysis and Prof. C. Li and Prof. Q. Yang (State Key Laboratory for Catalysis, Dalian Institute of Chemical Physics, Chinese Academy of Sciences) for support with the NMR experiments. E.I.U. acknowledges a Georg Forster Fellowship (Alexander von Humboldt Foundation) and a TWAS-UNESCO Associate Research Fellowship that enabled some analysis to be conducted. The Max Planck Institute of Colloids and Interfaces, University of Potsdam, Alexander von Humboldt Foundation, and Chinese Academy of Sciences are also appreciated for financial support.

ORCID® iDs

Emmanuel I. Unuabonah - https://orcid.org/0000-0001-9854-3924
Christina Günter - https://orcid.org/0000-0001-8955-7849

References

1. Unuabonah, E. I.; Günter, C.; Weber, J.; Lubahn, S.; Taubert, A. *ACS Sustainable Chem. Eng.* **2013,** *1,* 966–973. doi:10.1021/sc400051y
2. Sankar, M. U.; Aigal, S.; Maliyekkal, S. M.; Chaudhary, A.; Anshup; Kumar, A. A.; Chaudhari, K.; Pradeep, T. *Proc. Natl. Acad. Sci. U. S. A.* **2013,** *110,* 8459–8464. doi:10.1073/pnas.1220222110
3. Das, S. K.; Khan, M. M. R.; Parandhaman, T.; Laffir, F.; Guha, A. K.; Sekaran, G.; Mandal, A. B. *Nanoscale* **2013,** *5,* 5549–5560. doi:10.1039/c3nr00856h
4. Unuabonah, E. I.; Taubert, A. *Appl. Clay Sci.* **2014,** *99,* 83–92. doi:10.1016/j.clay.2014.06.016
5. Das, S.; Raj, R.; Mangwani, N.; Dash, H. R.; Chakraborty, J. Heavy Metals and Hydrocarbons. *Microbial Biodegradation and Bioremediation;* Elsevier: Amsterdam, Netherlands, 2014; pp 23–54. doi:10.1016/b978-0-12-800021-2.00002-9
6. Connor, R.; Renata, A.; Ortigara, C.; Koncagül, E.; Uhlenbrook, S.; Qadir, M.; Kjellén, M.; Sjödin, J. *The United Nations World Water Development Report 2017. Wastewater: The Untapped Resource;* United Nations Educational, Scientific and Cultural Organization: Paris, France, 2017; p 180.
7. Zhu, P.; Shelton, D. R.; Li, S.; Adams, D. L.; Karns, J. S.; Amstutz, P.; Tang, C.-M. *Biosens. Bioelectron.* **2011,** *30,* 337–341. doi:10.1016/j.bios.2011.09.029
8. Mohmood, I.; Lopes, C. B.; Lopes, I.; Ahmad, I.; Duarte, A. C.; Pereira, E. *Environ. Sci. Pollut. Res.* **2013,** *20,* 1239–1260. doi:10.1007/s11356-012-1415-x
9. Murat, M.; Amokrane, A.; Bastide, J. P.; Montanaro, L. *Clay Miner.* **1992,** *27,* 119–130. doi:10.1180/claymin.1992.027.1.12
10. Akolekar, D.; Chaffee, A.; Howe, R. F. *Zeolites* **1997,** *19,* 359–365. doi:10.1016/s0144-2449(97)00132-2
11. Belver, C.; Vicente, M. A. *J. Chem. Educ.* **2006,** *83,* 1541. doi:10.1021/ed083p1541
12. Ibrahim, H. S.; Jamil, T. S.; Hegazy, E. Z. *J. Hazard. Mater.* **2010,** *182,* 842–847. doi:10.1016/j.jhazmat.2010.06.118
13. Duan, A.; Wan, G.; Zhang, Y.; Zhao, Z.; Jiang, G.; Liu, J. *Catal. Today* **2011,** *175,* 485–493. doi:10.1016/j.cattod.2011.03.044
14. Holmes, S. M.; Khoo, S. H.; Kovo, A. S. *Green Chem.* **2011,** *13,* 1152–1154. doi:10.1039/c1gc15099e
15. Caballero, I.; Colina, F. G.; Costa, J. *Ind. Eng. Chem. Res.* **2007,** *46,* 1029–1038. doi:10.1021/ie060367y
16. Kovo, A. S.; Hernandez, O.; Holmes, S. M. *J. Mater. Chem.* **2009,** *19,* 6207–6212. doi:10.1039/b907554b
17. Chen, L.-F.; Liang, H.-W.; Lu, Y.; Cui, C.-H.; Yu, S.-H. *Langmuir* **2011,** *27,* 8998–9004. doi:10.1021/la2017165
18. Zhu, K.; Jia, H.; Wang, F.; Zhu, Y.; Wang, C.; Ma, C. *J. Chem. Eng. Data* **2017,** *62,* 333–340. doi:10.1021/acs.jced.6b00676
19. Martínez Martínez, V.; López Arbeloa, F.; Bañuelos Prieto, J.; López Arbeloa, I. *J. Phys. Chem. B* **2005,** *109,* 7443–7450. doi:10.1021/jp050440i
20. Khireddine, O.; Berredjem, Y.; Hailaimia, F.; Nouacer, S.; Djellaibi, R.; Bensid, N.; Boulmokh, A. *Sens. Lett.* **2016,** *14,* 258–265. doi:10.1166/sl.2016.3647
21. Unuabonah, E. I.; Agunbiade, F. O.; Alfred, M. O.; Adewumi, T. A.; Okoli, C. P.; Omorogie, M. O.; Akanbi, M. O.; Ofomaja, A. E.; Taubert, A. *J. Cleaner Prod.* **2017,** *164,* 652–663. doi:10.1016/j.jclepro.2017.06.160
22. Unuabonah, E. I.; Kolawole, M. O.; Agunbiade, F. O.; Omorogie, M. O.; Koko, D. T.; Ugwuja, C. G.; Ugege, L. E.; Oyejide, N. E.; Günter, C.; Taubert, A. *J. Environ. Chem. Eng.* **2017,** *5,* 2128–2141. doi:10.1016/j.jece.2017.04.017
23. Adebowale, K. O.; Unuabonah, I. E.; Olu-Owolabi, B. I. *Appl. Clay Sci.* **2005,** *29,* 145–148. doi:10.1016/j.clay.2004.10.003

24. Polarz, S.; Smarsly, B. *J. Nanosci. Nanotechnol.* **2002,** *2,* 581–612. doi:10.1166/jnn.2002.151
25. Al-Asheh, S.; Banat, F.; Masad, A. *Environ. Geol. (Heidelberg, Ger.)* **2004,** *45,* 1109–1117. doi:10.1007/s00254-004-0969-4
26. Thomas, H. C. *J. Am. Chem. Soc.* **1944,** *66,* 1664–1666. doi:10.1021/ja01238a017
27. Landers, J.; Gor, G. Y.; Neimark, A. V. *Colloids Surf., A* **2013,** *437,* 3–32. doi:10.1016/j.colsurfa.2013.01.007
28. Gor, G. Y.; Thommes, M.; Cychosz, K. A.; Neimark, A. V. *Carbon* **2012,** *50,* 1583–1590. doi:10.1016/j.carbon.2011.11.037
29. Kim, J.-W.; Sohn, M.-H.; Kim, D.-S.; Sohn, S.-M.; Kwon, Y.-S. *J. Hazard. Mater.* **2001,** *85,* 301–315. doi:10.1016/s0304-3894(01)00239-4
30. Hu, Z.; Vansant, E. F. *J. Colloid Interface Sci.* **1995,** *176,* 422–431. doi:10.1006/jcis.1995.9949
31. Viswanathan, B.; Varadarajan, T. *Methods of activation and specific applications of carbon materials;* National Centre for Catalysis Research: Chennai, India, 2009.
32. Manocha, L. M.; Yasuda, E.; Tanabe, Y.; Manocha, S.; Vashistha, D. *Bull. Mater. Sci.* **2000,** *23,* 1–4. doi:10.1007/bf02708602
33. Frost, R. L. *Clays Clay Miner.* **1995,** *43,* 191–195. doi:10.1346/ccmn.1995.0430206
34. Eigner, A. A.; Rohde, J. A.; Knutson, C. C.; Phillips, J. A. *J. Phys. Chem. B* **2007,** *111,* 1402–1407. doi:10.1021/jp0656375
35. Zhang, L.; Abbenhuis, H. C. L.; Yang, Q.; Wang, Y.-M.; Magusin, P. C. M. M.; Mezari, B.; van Santen, R. A.; Li, C. *Angew. Chem.* **2007,** *119,* 5091–5094. doi:10.1002/ange.200700640
36. Zhai, S.-R.; Kim, I.; Ha, C.-S. *J. Solid State Chem.* **2008,** *181,* 67–74. doi:10.1016/j.jssc.2007.11.011
37. Jackson, S. D.; Hargreaves, J. S. J., Eds. *Metal Oxide Catalysis;* Wiley-VCH Verlag GmbH: Weinheim, Germany, 2008. doi:10.1002/9783527626113
38. Bendjeriou-Sedjerari, A.; Pelletier, J. D. A.; Abou-hamad, E.; Emsley, L.; Basset, J.-M. *Chem. Commun.* **2012,** *48,* 3067–3069. doi:10.1039/c2cc00143h
39. Yang, Q.; Yang, J.; Feng, Z.; Li, Y. *J. Mater. Chem.* **2005,** *15,* 4268–4274. doi:10.1039/b507437a
40. McManus, J.; Ashbrook, S. E.; MacKenzie, K. J. D.; Wimperis, S. *J. Non-Cryst. Solids* **2001,** *282,* 278–290. doi:10.1016/s0022-3093(01)00313-1
41. Seymour, V. R.; Eschenroeder, E. C. V.; Castro, M.; Wright, P. A.; Ashbrook, S. E. *CrystEngComm* **2013,** *15,* 8668. doi:10.1039/c3ce40965a
42. Ilić, B. R.; Mitrović, A. A.; Miličić, L. R. *Hem. Ind.* **2010,** *64,* 351–356. doi:10.2298/hemind100322014i
43. Ece, O. I.; Nakagawa, Z.-E.; Schroeder, P. *Clays Clay Miner.* **2003,** *51,* 675–688. doi:10.1346/ccmn.2003.0510610
44. Karamanova, E.; Avdeev, G.; Karamanov, A. *J. Eur. Ceram. Soc.* **2011,** *31,* 989–998. doi:10.1016/j.jeurceramsoc.2011.01.006
45. Woods, B. L.; Walker, R. A. *J. Phys. Chem. A* **2013,** *117,* 6224–6233. doi:10.1021/jp400482v
46. Yao, Y.-X.; Li, H.-B.; Liu, J.-Y.; Tan, X.-L.; Yu, J.-G.; Peng, Z.-G. *J. Nanomater.* **2014,** *2014,* 84. doi:10.1155/2014/571745
47. Hamidouche, S.; Bouras, O.; Zermane, F.; Cheknane, B.; Houari, M.; Debord, J.; Harel, M.; Bollinger, J.-C.; Baudu, M. *Chem. Eng. J.* **2015,** *279,* 964–972. doi:10.1016/j.cej.2015.05.012
48. Gobin, F.; Gobin, F.; Hand, D. W.; Hokanson, D. R.; Crittenden, J. C. *Manual: Adsorption Design Software for Windows, AdDesignSTM;* Michigan Technological University: Houghton, MI, U.S.A., 1999.
49. Eckenfelder, W. W. *Industrial Water Pollution Control;* McGraw-Hill Science: New York, NY, U.S.A., 1999.
50. Baruah, S.; Pal, S.; Dutta, J. *Nanosci. Nanotechnol.–Asia* **2012,** *2,* 90–102. doi:10.2174/2210681211202020090
51. Gulicovski, J. J.; Čerović, L. S.; Milonjić, S. K. *Mater. Manuf. Processes* **2008,** *23,* 615–619. doi:10.1080/10426910802160668
52. Penna, V. T. C.; Martins, S. A. M.; Mazzola, P. G. *BMC Public Health* **2002,** *2,* 13. doi:10.1186/1471-2458-2-13

License and Terms

BEILSTEIN JOURNAL OF NANOTECHNOLOGY

pH-mediated control over the mesostructure of ordered mesoporous materials templated by polyion complex micelles

Emilie Molina[1], Mélody Mathonnat[1,2], Jason Richard[1], Patrick Lacroix-Desmazes[1], Martin In[2], Philippe Dieudonné[2], Thomas Cacciaguerra[1], Corine Gérardin[*1] and Nathalie Marcotte[*1]

Full Research Paper

Open Access

Address:
[1]ICGM UMR 5253 CNRS – Université de Montpellier - ENSCM, ENSCM 240 Av Pr E. Jeanbrau, 34296 Montpellier cedex 5, France, and [2]Laboratoire Charles Coulomb, UMR 5221 CNRS – Université de Montpellier, 34095 Montpellier, France

Email:
Corine Gérardin[*] - corine.gerardin@enscm.fr; Nathalie Marcotte[*] - nathalie.marcotte@enscm.fr

* Corresponding author

Keywords:
double-hydrophilic block copolymer; hybrid organic–inorganic interface; mesoporous materials; nanostructured materials; polyion complex micelles; polyion electrostatic complexation

Beilstein J. Nanotechnol. **2019,** *10,* 144–156.
doi:10.3762/bjnano.10.14

Received: 11 September 2018
Accepted: 27 December 2018
Published: 11 January 2019

This article is part of the thematic issue "Advanced hybrid nanomaterials".

Guest Editor: A. Taubert

Abstract

Ordered mesoporous silica materials were prepared under different pH conditions by using a silicon alkoxide as a silica source and polyion complex (PIC) micelles as the structure-directing agents. PIC micelles were formed by complexation between a weak polyacid-containing double-hydrophilic block copolymer, poly(ethylene oxide)-*b*-poly(acrylic acid) (PEO-*b*-PAA), and a weak polybase, oligochitosan-type polyamine. As both the micellization process and the rate of silica condensation are highly dependent on pH, the properties of silica mesostructures can be modulated by changing the pH of the reaction medium. Varying the materials synthesis pH from 4.5 to 7.9 led to 2D-hexagonal, wormlike or lamellar mesostructures, with a varying degree of order. The chemical composition of the as-synthesized hybrid organic/inorganic materials was also found to vary with pH. The structure variations were discussed based on the extent of electrostatic complexing bonds between acrylate and amino functions and on the silica condensation rate as a function of pH.

Introduction

Due to their unique physicochemical properties originating from their uniform pore size and periodically arranged network at the mesoscale, silica-based ordered mesoporous materials (OMMs) have attracted considerable attention in various fields such as adsorption, separation and catalysis. The formation of these mesostructures relies on a supramolecular assembly process between silicic species and surfactants or amphiphilic block copolymers acting as structure directing agents (SDAs) of silica. The assembly process can occur following two different interaction pathways: one is based on an electrostatic charge-

matching mechanism between the SDA (cationic S^+, anionic S^- or protonated neutral S^0 denoted as S^0H^+) and inorganic species (I^+ or I^-) interacting either directly or through a mediator species (halide anion X^- or alkaline cation M^+),[1] while the other one proceeds through an electrically neutral route involving hydrogen bond interactions between neutral amine (S^0) [2] or poly(ethylene oxide) (N^0) [3] based SDA and neutral inorganic species (I^0). Concerning the poly(ethylene oxide) based SDA, it is believed that the nature of the attractive interaction is hydrogen bonding between the silanol groups and the ether oxygen in the PEO block [4,5], as it is the case when PEO adsorbs on a silica surface [6]. It should be noted that the charge-matching pathway requires extreme pH conditions to produce OMMs, as for the synthesis of the well-known SBA (Santa Barbara Amorphous) and M41S (from Mobil Corporation) materials families, which proceed at pH < 1 and pH > 9, respectively. On the contrary, the neutral route necessitates less severe pH conditions, which are much more appropriate for a large-scale material production with controlled environmental, health and safety risks. Among the SDA materials that have been employed, non-ionic block copolymers such as poly(alkylene oxide) triblock copolymers have attracted more attention due to the formation of thermally and mechanically stable materials with larger pore sizes and thicker walls than those obtained with surfactants. This opens up the possibility of easily functionalizing them and tailoring the mesopore arrangement into various ordered mesostructures [7]. This is especially true as long as the material synthesis is conducted under strongly acidic conditions (charge-matching pathway $(S^0H^+)(X^-I^+)$) [4,8]. In contrast, the first attempts to synthesize materials in quasi neutral solution (pH > 2) using non-ionic block copolymers, which involve weaker interactions between the PEO chains and neutral silicic species, resulted in more disordered framework structures with worm-like mesopore channels of uniform diameter [3], designed as MSU-*X*. It should be mentioned that the reported synthesis protocols made use of synchronous reaction steps involving co-assembly of the template and the inorganic precursor and hydrolysis and condensation of the silica precursor. Bearing this in mind, the lack of a well-defined periodic structure of MSU-*X* may be imputed to the type of silica precursor generally used, namely alkoxysilanes like tetraethoxysilane (TEOS), whose rate of hydrolysis and condensation varies inversely as a function of pH [9]. Thus, synthesis at pH values above the isoelectric point of silica promotes condensation reactions that occur between silica species, which are only partially hydrolyzed, whereas fully hydrolyzed monomeric silica species would be desired for producing mesostructures with optimal structural order. As a matter of fact, using a rapid hydrolyzing alkoxysilane such as tetramethoxysilane (TMOS) that hydrolyses faster than TEOS, Kim et al. evidenced the possibility to produce hexagonally ordered structures from Pluronic P123 up to pH 4. The structural order can even be further extended up to pH 9 in the presence of fluoride ions due to their catalytic activity in hydrolysis reactions [10].

Several synthesis approaches aiming at separating the hydrolysis and the condensation steps were subsequently proposed to produce ordered mesostructured silica materials under mild pH conditions. Among them the use of sodium silicate as a silica source instead of silicon alkoxide judiciously discards the hydrolysis reactions. Adding silicate directly to a non-ionic block copolymer solution made of acid [11,12] or buffer [13-16] media allowed materials with ordered mesopores to be obtained up to pH 6.5. Interestingly, this relatively inexpensive silica precursor and the rather environmentally friendly synthesis route employed (neutral pH conditions, low temperature, short synthesis and aging times) open up new opportunities for batch and continuous mode large-scale production of ordered mesoporous silica materials [17,18]. Alternatively, the hydrolysis and condensation steps of the more popular silicon alkoxide precursors can be separated following a two-step approach in which the hydrolysis of the alkoxysilane is first performed in acidic medium and the silica condensation step is triggered with the aid of sodium fluoride and/or pH adjustment [19]. Separating the hydrolysis of TEOS from the condensation step enabled highly ordered 2D hexagonal SBA-15-type [20] and cubic [21,22] SBA-16-type materials to be obtained up to pH 5 and pH 4–4.5, respectively.

Since 2008, we have been developing an original route for the synthesis of ordered mesoporous materials based on the use of non-conventional structure-directing agents. Ordered mesoporous silica and organosilica materials were prepared under mild acidic conditions by using polyion complex (PIC) micelles as versatile pH-sensitive structure-directing agents [23,24]. This route relies on the use of a weak polyacid double hydrophilic block copolymer (DHBC) able to form polyion complex micelles upon interaction with a weak polybase. We reported that DHBCs such as poly(ethylene oxide)-*b*-poly(acrylic acid) (PEO-*b*-PAA) or poly(ethylene oxide)-*b*-poly(methacrylic acid) (PEO-*b*-PMAA) copolymers, are able to form polyion complex (PIC) micelles upon interaction with weak polybases such as oligochitosan (OC) [25], poly-L-lysine (PLL) [26,27] and aminoglycoside antibiotics [28]. PIC micelles present a core–corona structure, whose core is formed by electrostatic interactions between the two charged blocks (i.e., the PAA and the weak polybase) and the corona is constituted by the neutral PEO block of the DHBC, which ensures the steric stabilization of the assembly in water. In the presence of silica precursors, the hybrid organic–inorganic interface, which is necessary for directing the macroscopic precipitation of the hybrid material,

can form through an interaction between the PEO neutral block and silicic species via the N^0/I^0 pathway, as in the case of SBA-type materials synthesized under acidic conditions, as long as no competing interactions involving silicic species exist. In a previous study, we had shown that when the strength of the organic–inorganic interaction is kept constant (by synthesizing hybrid materials at a fixed pH), the material mesostructure can be controlled by varying parameters that alter interactions between the different constituents of the system, such as the molar ratio between the complexing units, the molar ratio between ethylene oxide (EO) units and silica species, and the mass concentration of the reactants in the synthesis medium [26]. In the present paper, we investigate how a simple synthesis parameter, such as the pH of the reaction medium, which governs not only the extent of the polyion electrostatic complexation but also the silica condensation rate, influences the macrophase separation of the hybrid material and the nature of the mesostructures which are obtained. The variations of the mesostructures and the chemical composition of the corresponding hybrid materials as a function of pH are reported and discussed.

Experimental

Materials

Poly(ethylene oxide)-*b*-poly(acrylic acid) (PEO-*b*-PAA, M_{PEO} = 5000 g·mol^{-1}, M_{PAA} = 1420 g·mol^{-1}) was synthesized by atom transfer radical polymerization (ATRP) according to published procedures [29]. All reactions were carried out in the absence of air using standard Schlenk techniques and vacuum-line manipulation. All the chemicals used for the reaction (tert-butyl acrylate 98%, α-methoxy-ω-hydroxy-poly(ethylene oxide) with M_n = 5000 g·mol^{-1}, CuBr 98%, 1,1,1,7,10,10-hexamethyltriethylenetetramine 97%, trifluoroacetic acid 99%, triethylamine 99%, 2-bromoisobutyryl bromide 98%, absolute ethanol, toluene 99.8%, THF 99.9%, acetone 99.5%, diethyl ether 99.5%, glacial acetic acid, dichloromethane, pentane, sodium chloride, DOWEX MSC-H resin, neutral alumina 50–200 μm) were purchased from Sigma-Aldrich and purified when necessary (α-methoxy-ω-hydroxy-poly(ethylene oxide), tert-butyl acrylate, toluene, THF, acetone); the solvents were dried and distilled by routine procedures. Oligochitosan lactate (OC, M < 5000 g·mol^{-1}), tetraethoxysilane (TEOS), nitric acid (HNO_3) and sodium hydroxide (NaOH) were purchased from Aldrich and used as received.

Chemical composition of the oligochitosan

A detailed characterization of the commercial oligochitosan (OC) was undertaken in order to determine the chemical composition of the repetitive unit necessary to fix the quantity of nitrogen per acrylic acid (N/AA ratio) used in the materials synthesis. The deacetylation degree (DD = 83 ± 5%) was determined by solid state ^{15}N NMR using a Varian VNMRS 600 spectrometer operating at 5 kHz using cross-polarization magic-angle spinning conditions [30]. The DD was calculated from the integration of the amide (δ = 101 ppm) and amine (10 ppm) peaks using the following formula:

$$\%DD = \frac{I_{\text{N-amine}}}{I_{\text{N-amine}} + I_{\text{N-amide}}} * 100. \quad (1)$$

Note that a similar DD was obtained from liquid ^{1}H NMR data recorded on a Bruker 400 MHz spectrometer using the method reported by Trombotto et al. [30].

The quantity of lactate/lactic acid present in the sample was calculated from the liquid ^{1}H NMR spectrum recorded in D_2O. The amount of water was deduced from elemental analysis. The molar composition of the repetitive unit constituting the oligochitosan was then: H-$(C_6H_{11}O_4N)_{0.83}(C_8H_{13}O_5N)_{0.17}$-OH, $1.31(C_3H_6O_3)$, $0.09(H_2O)$, where $C_6H_{11}O_4N$ represents the deacetylated unit, $C_8H_{13}O_5N$ the acetylated unit and $C_3H_6O_3$ the lactate ion.

Preparation of mesostructured silica materials

Mesostructured hybrid silica materials were prepared following a one-pot synthesis approach. The concentration of OC and TEOS were fixed with respect to the number of acrylic acid (AA) and ethylene oxide (EO) units of the PEO-*b*-PAA, using a molar ratio of 0.8 nitrogen per AA (N/AA = 0.8) and 1 silicon per EO (EO/Si = 1). The final concentration of the reaction medium was set at 3.9 wt % of PEO-*b*-PAA, unless otherwise specified. Typically, TEOS (0.397 mL) was added into a homogeneous aqueous solution (2.0 mL) containing PEO-*b*-PAA (100 mg) and OC (77.5 mg) and the pH of the reaction medium was adjusted to 2 using HNO_3 (2 mol·L^{-1}). After completion of TEOS hydrolysis (about 40 min under vigorous magnetic stirring), the pH was rapidly increased to a fixed and well-defined value (ranging from 4 to 7.9) by adding a small amount of an aqueous NaOH solution (3 mol·L^{-1}). This results in macroscopic precipitation, which occurs more or less rapidly according to the pH value (3 min at pH 5 and 0.5 min at pH 7.9). The mixture was stirred slowly for 24 additional hours at 30 °C. The precipitate was then recovered by centrifugation and air-dried at 40 °C for 48 hours. For characterization purposes, the as-synthesized hybrid materials were calcined under air flow from room temperature to 550 °C at a heating rate of 2 °C·min^{-1} and then maintained at 550 °C for 8 hours.

Characterization techniques

The formation of polyion complex (PIC) micelles as a function of pH (3 < pH < 10) was studied by dynamic light scattering (DLS) experiments at 25 ± 1°C using a Malvern 4800 spectrogoniometer (Malvern Instruments, UK) equipped with a 50 mW

laser operating at 532 nm. The scattered light was collected at an angle of 90°. The static scattered light intensities were corrected from the pinhole size and normalized with respect to a Rayleigh scattered reference (toluene). The intensity autocorrelation function was fitted using the CONTIN algorithm for the determination of the volume-averaged hydrodynamic diameters (D_{hv}); the polydispersity index (PDI) values were obtained from the cumulant method.

The chemical composition of the hybrid materials was calculated by combining thermogravimetric analysis (TGA), which allows quantifying the silica content, and N and C elemental analyses (EA), which allow determining the quantity of OC and PEO-*b*-PAA in the material. The results were expressed as N/AA and EO/Si ratios given with ±5% relative error. TGA was performed on a Perkin Elmer STA 6000 instrument at a heating rate of 10 °C·min^{-1} under an air flow (20 mL·min^{-1}) up to 900 °C. The mass percentage of silica (% mass(SiO_2)) was calculated from the residual mass at 900 °C. The EA of the hybrid materials was performed on an Interscience Flash EA 1112 series (Thermo Finnigan) instrument. The value of the mass percentage of OC (% mass (OC)) in the hybrid materials, %N, which in turn was used to calculate the DHBC weight percentage (% mass (DHBC)), %C, can be calculated according to the following equations:

$$\%\mathrm{N} = \%\ \mathrm{mass(OC)} \times \%\ \mathrm{mass(N/OC)} \quad (2)$$

$$\%\mathrm{C} = \left(\%\ \mathrm{mass(OC)} \times \%\ \mathrm{mass(C/OC)}\right) + \left(\%\ \mathrm{mass(DHBC)} \times \%\ \mathrm{mass(C/DHBC)}\right) \quad (3)$$

where % mass (N/OC), % mass (C/OC) and % mass (C/DHBC), respectively stand for the mass content of N and C in OC and of C in the DHBC.

The degree of condensation (D) of the as-synthesized silica network was determined by ^{29}Si MAS-NMR spectroscopy using a Varian VNMRS 300MHz spectrometer. The typical Q_4, Q_3 and Q_2 signals appearing respectively at −110 ppm (SiO_2), −100 ppm ($SiO_{3/2}$) and −90 ppm ($SiO(OH)_2$) were deconvoluted, and the areas were used for calculating D.

The textural properties of the materials were determined from the nitrogen sorption isotherms recorded at 77 K using a Micrometics Tristar 3000 apparatus. Prior to analysis, the samples were outgassed for 14 h under vacuum (0.08 mbar) at 250 °C for calcined materials and at 45 °C for hybrid materials. The surface area (S_{BET}) was determined from the Brunauer–Emmett–Teller (BET) analysis in the relative pressure range corresponding to $p/p^0 < 0.4$ and assuming a surface coverage of 13.5 Å^2 per nitrogen molecule [31,32]. The mesopore volume was calculated using the α_S method; the diameter of cylindrical pores was determined from the adsorption branch using the nonlocal density functional theory (NLDFT) model [32] and the width of slit-shaped pores was estimated from the desorption branch using the method of Broekhoff and de Boer [33].

The structural properties were studied by small angle X-ray scattering (SAXS) and electron microscopy. SAXS measurements were performed in transmission mode on an in-house setup at the Laboratoire Charles Coulomb (Université Montpellier, France) using a high brightness, low power X-ray tube (λ = 1.5418 Å). All the intensities were corrected from transmission and empty capillary. Transmission electron microscopy (TEM) images were acquired on microtomed samples (slices of ≈70 nm thickness) with a JEOL 1200 EX II instrument operating at 120 kV. Material characterization by scanning electron microscopy (SEM) was done on a HITACHI S4800 (FEG-HR) apparatus operating at 5 kV.

Results and Discussion

Formation of polyion complex micelles

The double hydrophilic block copolymer (DHBC) used in this study is a poly(ethylene oxide)-*b*-poly(acrylic acid) copolymer (PEO-*b*-PAA, M_{PEO} = 5000 g·mol^{-1}, M_{PAA} = 1420 g·mol^{-1}) able to complex oligochitosan (OC) via electrostatic interactions in a suitable pH range where both the DHBC and OC are charged. The formation of polyion complex (PIC) micelles is evidenced by an increase of the scattered light intensity due to the formation of macromolecular assemblies. Figure 1 shows the variation of the scattered light intensity of mixtures of PEO-*b*-PAA and OC as a function of pH (2 < pH < 10). PEO-*b*-PAA/OC PIC micelles are obtained in the 4.5–7.2 pH range and are characterized by a mean hydrodynamic diameter (D_{hv}) of ≈25 nm.

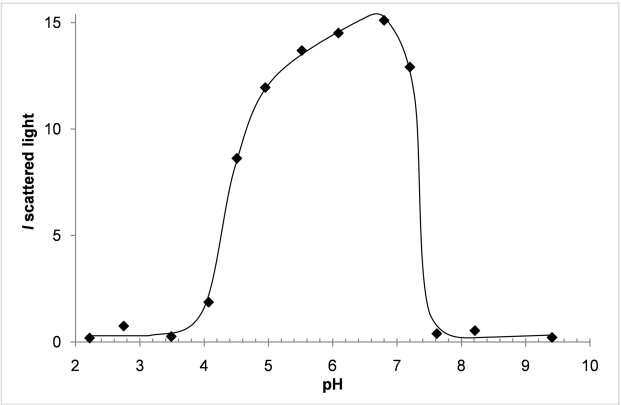

Figure 1: Variation of the scattered light intensity of PEO-*b*-PAA/OC mixtures ([AA] = 0.01 mol·L^{-1}, N/AA = 0.8) as a function of pH.

Structure characterization of the calcined materials

Hybrid organic–inorganic materials were synthesized following a two-step approach. First, the reactants (TEOS, PEO-*b*-PAA and OC) were mixed together at low pH (pH 2) until a homogeneous solution of hydrolyzed silicic species, PEO-*b*-PAA and OC was obtained. Note that at pH 2 the silica structure-directing agent (SDA) constituted of PEO-*b*-PAA/OC PIC micelles is not formed (see Figure 1) due to the lack of favorable electrostatic interactions, whereas the organic–inorganic interface is thought to be formed by the N^0/I^0 pathway. Then the pH of the reaction medium was increased in order to promote both formation of PIC micelles and condensation of silica oligomers, inducing sudden macroscopic precipitation in less than 3 min. Two different mass concentrations of the reaction medium, expressed by the wt % of DHBC, were used. The 3.9 wt % concentration was aimed at evaluating the influence of the pH on the texture, structure and chemical composition of the obtained materials by carefully screening the 4–7.9 pH domain, whereas the 1.9 wt % concentration was used at only two strategic pH values (pH 4.5 and 6.5, see thereafter) with the aim of confirming the general effects observed at 3.9 wt %. After calcination (8 h at 550 °C), the materials synthesized under the various pH conditions presented an organization at the mesoscale as clearly evidenced on the TEM images of Figure 2a and Figure S1 in Supporting Information File 1, except in the

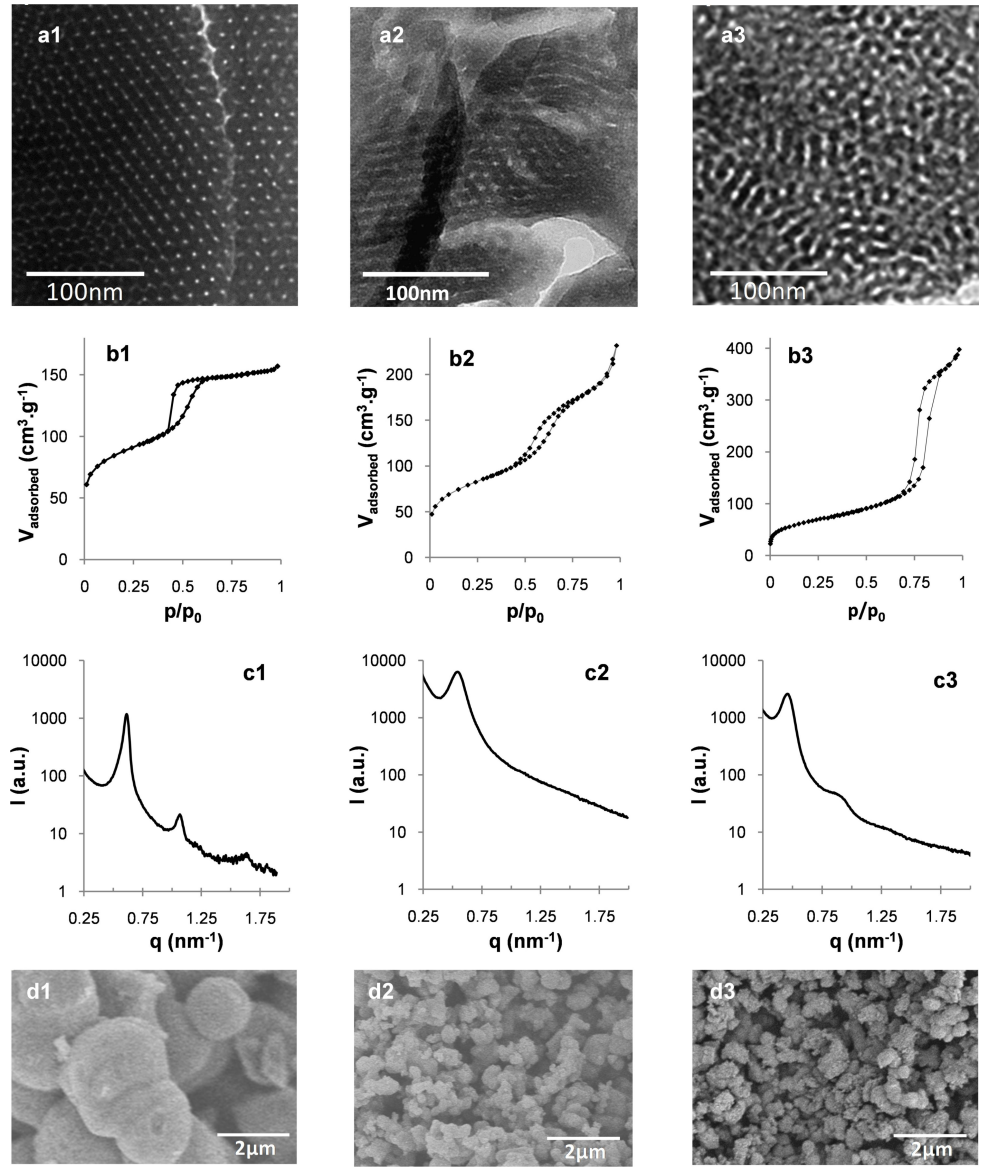

Figure 2: TEM micrographs (a), N_2 adsorption/desorption isotherms (b), SAXS patterns (c) and SEM images (d) of the calcined materials synthesized with 3.9 wt % DHBC at pH 4.5 (d1), 6.5 (d2) and 7.9 (d3).

case of pH 4 where a moderately porous silica material (V_{meso} = 0.11 g·cm^3) with non-ordered small mesopores (d_{pore} = 3.9 nm) was obtained (see TEM in Figure S1, Supporting Information File 1). At pH 4, only very few PIC micelles were formed, as evidenced by the very low light scattered intensity (Figure 1); it is then obvious that the silicic species induced precipitation of a long range organized hybrid PIC-based mesostructure, which requires a sufficient amount of micelles, cannot occur. Interestingly, at the highest pH values (pH 7.4 and 7.9), ordered mesostructures were obtained. This could appear as a surprising result since these two pH values are outside of the micellization pH range (Figure 1), as determined in the absence of silica precursors. The formation of mesostructures at a pH above pH 7 can be understood by considering (1) the fact that the adjustment of pH at its final value is done by a progressive addition of a base solution up to the final pH, going inevitably through the micellization pH range where the structure-directing agent forms, and (2) the fact that the silica condensation rate regularly increases above pH 2 favoring the formation of the hybrid structure. These two features lead to the precipitation of the hybrid mesostructures at a pH well below the final targeted synthesis pH. These considerations will be further developed when discussing the silica material structuring below. At intermediate pH, but within the pH domain where micelles formed (Figure 1), the structure of the mesopores is 2D-hexagonal in the 4.5–5.5 pH range and a mixture of wormlike/lamellar at pH 5.5–6.9 (Figure S1, Supporting Information File 1). The mesopore volume increases from V_{meso} = 0.17 cm^3·g^{-1} at pH 4.5 to 0.32 cm^3·g^{-1} at pH 6.9, in accordance with the pore diameter change (d_{pore} = 5.0 nm at pH 4.5 and 6.4 nm at pH 6.9, see Table 1). Similarly, the lattice spacing value, d_0, of the calcined materials shows a slight tendency to increase (Table 1). The d_{pore}/d_0 ratio is then almost constant ($d_{pore}/d_0 \approx 0.50$), indicating that the mesostructure formation mechanism is similar within that pH range. Figure 3 helps to highlight the changes in the mesoporous volume (Figure 3a) and pore diameter (Figure 3b) observed upon synthesis of the materials on the whole pH range studied ($4.5 \leq pH < 7.9$). It evidences three main pH domains ($4.5 \leq pH < 5.5$, $5.5 \leq pH \leq 6.9$ and $7.4 \leq pH \leq 7.9$), for which the porous properties exhibit

Table 1: Textural and structural properties of the calcined materials synthesized at 3.9 wt % DHBC: lattice parameter (d_0), pore diameter (d_{pore}), full width at half maximum of the pore size distribution ($\Delta d_{1/2}$), mesoporous volume (V_{meso}), external surface area (S_{ext}) of the particles and particle size ($d_{particle}$).

pH	4.5	4.9	5.3	5.5	6.0	6.5	6.9	7.4	7.9
d_0 (nm)	10.2	11.1	10.6	11.6	11.9	11.5	11.3	13.5	13.8
d_{pore} (nm)	5.0	5.4	5.4	5.7	5.7	5.9[a]	6.4[a]	9.2	10.2
$\Delta d_{1/2}$ (nm)	1.0	1.0	1.2	1.6	1.7	1.7	2.3	3.0	2.9
V_{meso} (cm^3·g^{-1})	0.17	0.19	0.19	0.17	0.23	0.25	0.32	0.53	0.55
S_{ext} (m^2·g^{-1})	13	15	27	39	73	125	123	124	130
$d_{particle}$ (nm)	2300	1200	900	700	600	290	380	310	220

[a]mean pore diameter.

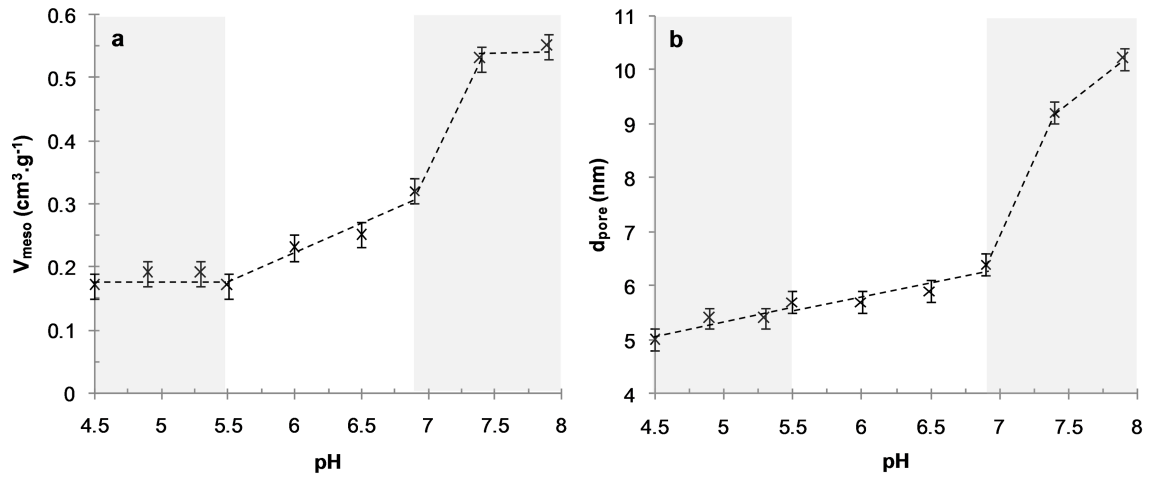

Figure 3: Mesopore volume (a) and pore diameter (b) of the calcined materials synthesized at 3.9 wt % DHBC at various values of pH.

some common features together with the typical mesostructures of the materials illustrated on Figure 2a, which evolved from long-range ordered 2D-hexagonal (4.5 ≤ pH < 5.5) to a less-ordered worm-like/lamellar mixture (5.5 ≤ pH ≤ 6.9) to a short-range ordered honeycomb-like arrangement of cylindrical mesopores. For the sake of clarity, in the following, the influence of the synthesis pH on the material formation will be discussed by distinguishing these three main pH domains.

In the most acidic domain (4.5 ≤ pH < 5.5), agglomerated spherical particles with a well-defined 2D hexagonal ordered mesostructure were obtained, as evidenced by TEM images (Figure 2a and Figure S1 in Supporting Information File 1). This mesostructure is confirmed by SAXS profiles (Figure 2c and Figure S2a in Supporting Information File 1), which exhibit up to four distinct scattering peaks whose relative positions respective to the first one appear at a ratio of 1:√3:√4:√7, corresponding to the (100), (110), (200) and (210) diffraction planes of long-range ordered hexagonally packed cylindrical structures (Table S1a, Supporting Information File 1). It should also be mentioned that the N_2 sorption isotherms (Figure S3 in Supporting Information File 1) exhibited the typical type-IV shape of mesoporous materials with H1-like hysteresis loop (IUPAC classification [34]) showing capillary condensation at a relative pressure p/p_0 ranging from 0.42 to 0.70. This indicates that the structural mesoporosity presents a cylindrical pore geometry with a high degree of pore size uniformity. This is confirmed by the narrow pore size distribution (PSD) calculated from the adsorption branch by the NLDFT method (Figure S3 in Supporting Information File 1). Within that pH range, the mean pore diameter (d_{pore}) and mesopore volume (V_{meso}) slightly increase with pH (Table 1). When the synthesis was performed at 1.9 wt % of DHBC and pH 4.5, a material with a mixed mesostructure consisting of lamellar domains coexisting with some 2D-hexagonal domains was obtained, as evidenced both by TEM images (Figure 4a) and SAXS profiles (Figure S2d in Supporting Information File 1), which exhibit two major diffraction peaks ascribed to the (100), and (200) planes of the lamellar/hexagonal structure and a weaker peak that could correspond to the (110) plane of the hexagonal structure. The nitrogen sorption isotherm (Figure 4b) exhibits a very low adsorption step, in good agreement with this mixture of mesostructures.

When further increasing the pH (5.5 ≤ pH ≤ 6.9), the well-ordered hexagonal mesostructure progressively evolved towards less-ordered structures containing domains with wormhole-like mesopores coexisting with domains of slit-shaped pores resem-

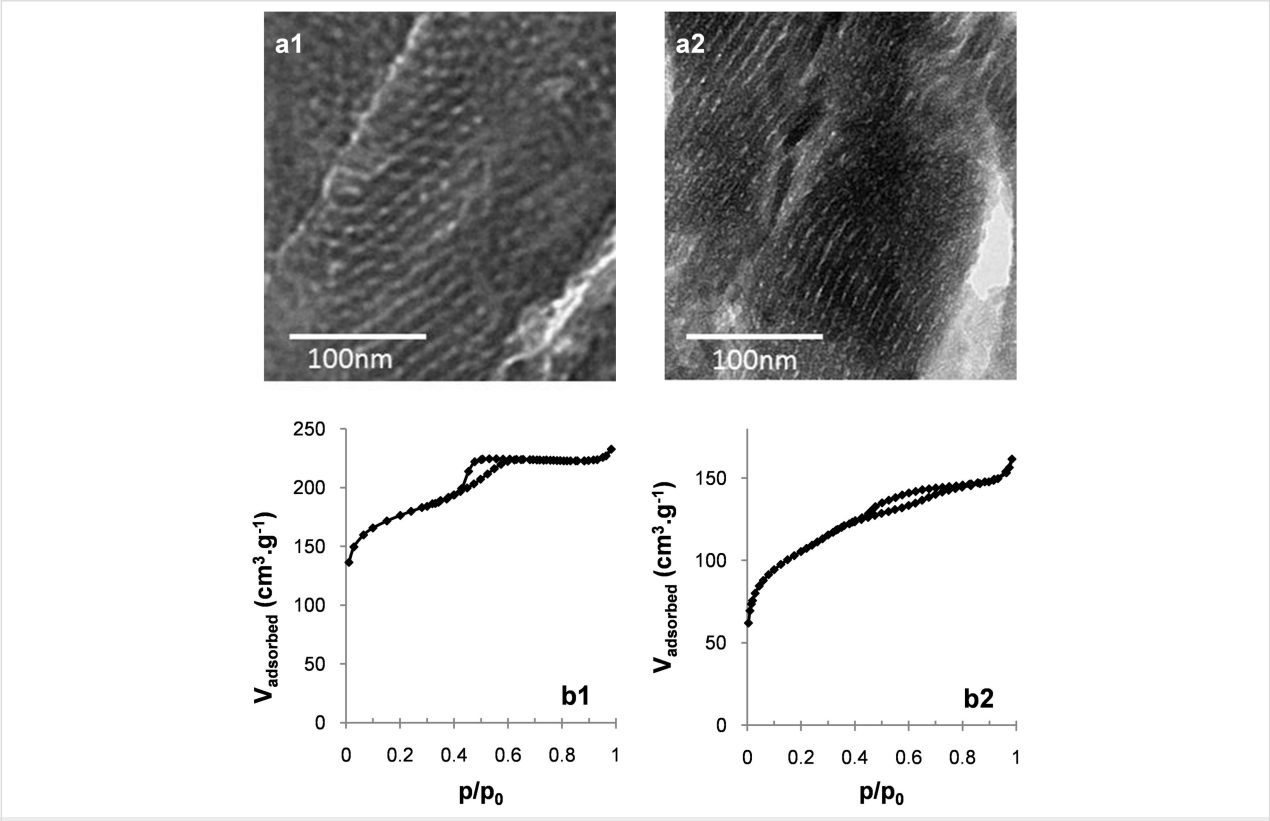

Figure 4: TEM micrographs (a) and N_2 adsorption/desorption isotherms (b) of the calcined materials prepared at 1.9 wt % DHBC at pH 4.5 (b1) and 6.5 (b2).

bling short-range lamellar structure. Such lamellar domains appeared first (from pH 5.5) on the edge of the particles (see TEM images on Figure S1 in Supporting Information File 1). At pH 6.9, almost no hexagonal mesostructure was visible on TEM images. Moreover, the correlation peaks of the SAXS patterns broadened upon pH increase and their number decreased until a single peak was observed for materials synthesized at pH 6.9 (Table S1a and Figure S2 in Supporting Information File 1). This is in accordance with the loss of long range-ordered hexagonal structure, as observed in TEM images. In the sorption isotherms, the sharp adsorption step assigned to mesopore filling in the hexagonal materials becomes less pronounced, and the hysteresis loop extends on a wider partial pressure range, in agreement with the presence of lamellar domains coexisting with wormhole pore morphologies. The increase of pH from 5.5 to 6.9 resulted in a size pore increase with broadening PSD until pH 6 (Table 1), then to the appearance of a bimodal distribution with d_{pore} = 5.7 and 7.2 nm, with the fraction of the larger mesopores increasing with pH (from 12% to 48%). Accordingly, the mesopore volume increased within that pH range. Such observations reveal an increase of the mean radius of curvature of the mesostructure as a function of pH up to 6.9. Such an influence of the solution pH on the variation of mesostructure and mesopore size has also been reported with non-ionic surfactants/copolymers [11,20,35,36] and ionic cetyltrimethylammonium. [37] The up-curvature observed at $p/p^0 > 0.85$ on the $5.5 \leq pH \leq 6.9$ isotherms (Figure S3 in Supporting Information File 1) revealed an interparticle porosity, which is consistent with the small size of the silica particles as observed on SEM images (Figure S4 in Supporting Information File 1). As reported in Table 1, the mean particle size decreases from about 700 to 380 nm in the considered pH range. When the material synthesis was performed at a lower mass concentration (1.9 wt % of DHBC) and at pH 6.5, the material presented a well-defined lamellar mesostructure, which survived the removal of the SDA by calcination, as revealed by the TEM image of Figure 4a. The N_2 sorption isotherm (Figure 4b) exhibited the classical H3-like hysteresis loop expected for such a mesostructure, with a mesoporous volume of 0.17 $cm^3 \cdot g^{-1}$. A pore thickness of 3 nm was calculated using the Broekhof and De Boer method from the relative pressure at which complete capillary condensation took place. [33].

The materials prepared at higher pH (pH 7.4 and 7.9) exhibited a relatively well-ordered pore arrangement, whose mesostructure was however difficult to identify (Figure 2a and Figure S1 in Supporting Information File 1). Nonetheless, some insights can be gathered from TEM, SAXS profiles and N_2-adsorption/desorption data. Up to three scattering peaks with interplanar spacing ratios of 1:2:3 were revealed by SAXS for the material synthesized at pH 7.9 (Figure 2c and Table S1a in Supporting Information File 1), corresponding either to a lamellar structure or to a hexagonal one with some of the diffraction planes masked under broaden peaks. Let us add that the sorption isotherm did not exhibit the characteristic H3 hysteresis loops of mesoporous structures with slit-like pores, but rather the typical H1 type of cylindrical pore geometry. We thus propose that the mesostructures obtained at pH > 7 correspond to an hexagonal arrangement of cylindrical pores organized on very short distances that would account both for the TEM observation and SAXS data. Note that the pores of those materials are particularly large (d_{pore} = 9.2 and 10.2 nm at pH 7.4 and 7.9, respectively) compared to the mesopores obtained at lower pH. At pH 7.9, the pore diameter is about twice that of the material obtained at pH 4.5 (d_{pore} = 5.0 nm). This pore diameter increase is accompanied by a significant increase of the d-spacing value (d_0 = 13.8 nm at pH 7.9, Table 1), compared to the almost constant value obtained between pH 4.5 and pH 6.9 (d_0 = 11.3 ± 0.7 nm).

The pH increase also affected the size of the obtained primary spherical particles (see SEM images on Figure 2d and Figure S4 in Supporting Information File 1), which gradually decreased from several micrometers at low pH (2300 nm at pH 4.5) to a few hundred nanometers above pH 7 (220 nm at pH 7.9, Table 1). The external surface area of the particles, as measured by BET analysis, consistently increases within that pH range (Table 1). Similar particle size reduction upon pH increase was reported using polyethylene oxide based surfactants [38,39] as SDA of silica; it was ascribed to an increase of the polycondensation rate of silicic species with pH favoring fast nucleation of small flocs of surfactant and silica [40]. As emphasized by Berggren and Palmqvist [35], these small flocs further grow until reaching a final size that depends on the electrostatic stabilization provided by the pH-dependent negative charge of silica.

Chemical composition of the hybrid materials and formation mechanism of mesostructures

The chemical composition of the as-synthesized hybrid materials was determined in order to understand how the pH of the reaction medium influences the interactions between the various constituents of the system and the subsequent mesostructures. The three main interactions to be considered are: the electrostatic interaction involved in the polyion complex formation between amine units (related to N atoms in OC) and acrylic acid units (AA in the DHBC), the hydrogen bond interaction ensuring the formation of the hybrid organic–inorganic interface between the ether oxygen (EO) of the PEO and the silica species (Si), and the self-condensation of silica species. The two molar ratios N/AA and EO/Si, respectively indicative of the extent of electrostatic complexation and hydrogen bonding, were determined from the chemical mass compositions of

DHBC (wt % DHBC), oligochitosan (OC) (wt % OC) and silica (wt % SiO_2) obtained by elemental analysis and thermogravimetric data after drying of the hybrid materials. The silica condensation degree (*D*) was quantified by ^{29}Si MAS NMR spectroscopy. Table 2 gathers the data related to the compositions of the materials expressed in weight percentages and mg (organics) per gram of SiO_2. Figure 5 shows the N/AA and EO/Si ratio variations in the materials as a function of pH.

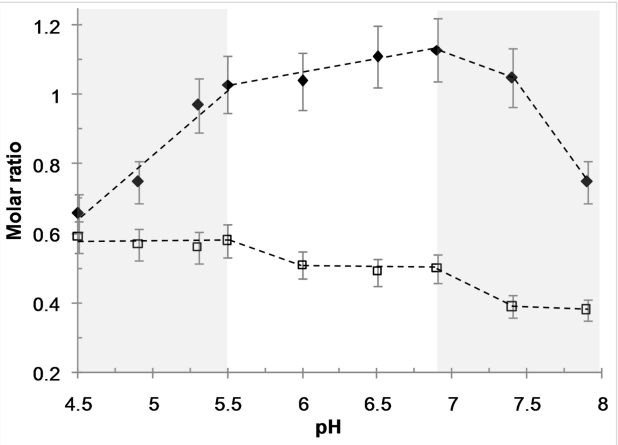

Figure 5: Molar ratio N/AA (filled triangles) and EO/Si (open squares) of the hybrid materials synthesized at 3.9 wt % DHBC as a function of pH.

For all pH values of the reaction medium, the materials present a high silica content (SiO_2 wt % > 50%, associated with high silica yield above 80%) and a highly condensed inorganic network (*D* > 86%). As the pH increased, the degree of condensation rose (from *D* = 86% at pH 4.5 to 91.5% at pH 7.4), in agreement with the pH-dependent condensation rate of silica. The amount of PEO-*b*-PAA incorporated in the materials was relatively high and the variation depends on the pH domain already discussed above. At 4.5 ≤ pH < 5.5, the DHBC content was almost constant (average 540 ± 15 mg·g_{SiO2}^{-1}), and it slightly decreased between pH 5.5 and 6.9 (468 mg·g_{SiO2}^{-1} at pH 6.9) and decreased to a higher extent above pH 7.4 where it reached a plateau (average 365 ± 5 mg·g_{SiO2}^{-1} for pH ≥ 7.4). The OC content in the materials was much smaller than the DHBC amounts. The OC content relative to silica varies non-monotonically with pH: it increases from pH 4.5 to pH 5.3 (from 211 to 299 mg·g_{SiO2}^{-1}, respectively), and remained constant up to pH 6.9, and decreased strongly in the highest pH range to reach 157 mg·g_{SiO2}^{-1} at pH = 7.9. The changes of N/AA and EO/Si ratios reported on Figure 5 reflect those organic content variations.

In the most acidic domain range (4.5 ≤ pH < 5.5), in which 2D hexagonal mesostructures were obtained, the N/AA increase (from about 0.65 up to a value of ≈1) accounts for the rise of the ionization degree of the acrylate functions expected for this weak polyacid (pKa_{AA} 4.8). The number of negative charges on the PAA increases with pH what favors the interaction with OC in the formation of polyion complex (see Figure 1), and allows more OC to be integrated in the material. This is consistent with the increase of the pore diameter of the calcined materials from 5 to 5.7 nm (Table 1 and Figure 3b). The EO/Si ratio is almost constant (EO/Si ≈0.6), which highlights the favorable hydrogen bond interactions between the ethylene oxide groups of PEO blocks and hydrolyzed silicic species (Si–OH) in this pH range.

At an intermediate pH (5.5 < pH ≤ 6.9), the N/AA increase may reflect not only the decrease of the charge density of oligochitosan (pKa_{OC} 6.7) but also the increase of the PAA charge density, leading to an increase of the OC content relative to the DHBC in order to compensate the PAA charge in the PIC nanophase. Let us note that the fact that the amount of OC integrated in the material (OC/SiO_2) remained constant within that pH range could be due either to the formation of a polyion complex richer in OC or to the development of favorable interactions between negatively charged silica species and OC species, which could also favor OC incorporation. Even if this last interaction cannot be totally ruled out, the increase of the mean pore diameter in the calcined materials synthesized at 3.9 wt % of DHBC (Table 1) argues in favor of an OC-richer polyion complex. In such conditions, a looser polyion complex rich in OC is expected to form, in accordance with the increased mesopore volume. The EO/Si decrease reflects the weaker hydrogen bond interactions between EO and silica species, which are expected due to the pH-dependence of the charge density of silica species [40]. This decreased EO/SiOH interaction with pH is in good accordance with the well-admitted mechanism of formation of Pluronic-templated mesostructured silica [5,41-43], in which

Table 2: Chemical composition of the as-synthesized hybrid materials synthesized at 3.9 wt % DHBC.

pH	4.5	4.9	5.3	5.5	6.0	6.5	6.9	7.4	7.9
wt % SiO_2	51.8	53.1	50.4	49.0	52.0	53.1	51.8	58.5	60.4
DHBC (mg·g_{SiO2}^{-1})	553	536	528	545	480	456	468	370	361
OC (mg·g_{SiO2}^{-1})	211	233	299	325	290	294	306	225	157
D (%)	86	86	87	88	87	88	88	91	90

the primary step for a good mesostructure to be obtained is entropy driven by hydrogen bonding between the silica oligomers and PEO chains [5]. Variations in the respective sizes of the two nanodomains of the system, (1) the polyion electrostatic complex core and (2) the PEO/inorganic corona, as a function of pH, lead to changes of the interfacial curvature of the system that controls the mesostructure of the material. At 3.9 wt % of DHBC, the well-ordered 2D-hexagonal mesostructure of the pH 4.5–5.3 domain, presenting purely cylindrical mesopores, thus evolves towards a mixture of less-ordered worm-like/lamellar structures with larger pore diameter and the subsequent appearance of a bimodal distribution of mesopores at higher pH. It is noted that from pH 4.5 to 6.9, the pH increase leads to a decrease of the mean curvature of the mesostructure, as revealed by the increase of the pore diameter and/or the tendency to form domains of lamellar structures at the expense of 2D hexagonal structure domains. Let us add that these variations can be related to the increase in OC content in the PIC nanodomains.

At the highest pH values (pH 7.4 and 7.9), the N/AA ratio sharply drops whereas EO/Si further decreases. The low value of N/AA is quite surprising since the charge density of OC decreases strongly above pH 6.5, and then even higher values of N/AA could be expected as a result of the necessary charge compensation in the PIC nanophase. Let us note that the low value of N/AA is associated with a significant porosity of the as-synthesized hybrid materials (see Figure S5 in Supporting Information File 1). Large mesopore volumes (V_{meso} = 0.39 and 0.29 $cm^3 \cdot g^{-1}$ at pH 7.4 and 7.9, respectively) and large pore diameters (d_{pore} = 9.1 and 10.2 nm at pH 7.4 and 7.9, respectively) in the hybrid materials were obtained; they are close to the ones obtained on the calcined materials (Table 1). Those combined observations suggest that part of the oligochitosan molecules would be eluted from the material while the reaction medium is maintained for hours at pH above 7, as it can be expected when considering the micellization pH range (Figure 1) The occurrence of mesoporosity in the dried hybrid materials is currently under investigation and will be discussed further in a forthcoming paper. The very low value of the EO/Si ratio indicates a decay of the extent of the SiOH/EO hydrogen bond interaction compared to the syntheses performed at lower pH. Mesopore volumes (above 0.5 cm^3/g) and pore diameters (about 10 nm) observed on the calcined materials (Figure 3 and Table 1) are much higher than at pH below 7, suggesting that the PEO block was not trapped into silica walls of the materials but rather acted as a porogen agent contributing to the mesopore volume once the materials were calcined. Such an occurrence is reminiscent of the size increase of the structural mesopores of SBA-15 materials observed at temperature of synthesis higher than 80 °C, which reduces the solvation of the PEO chains and thus weakens the interaction between PEO and silica [44]. A similar effect was observed with the present PIC structure directing agent when performing a material synthesis at pH 6.5 at 80 °C for 24 hours: the mesopore diameter of the calcined material increased from 5.9 to 12 nm and the mesopore volume from 0.25 to 0.95 $cm^3 \cdot g^{-1}$ (Figure S6 in Supporting Information File 1). The material contained a lower amount of DHBC (EO/Si 0.4 and 315 $mg \cdot g_{SiO2}^{-1}$ instead of EO/Si 0.5 and 456 $mg \cdot g_{SiO2}^{-1}$ at 30 °C) as it is the case for the synthesis performed at high pH, and it is also slightly poorer in OC (N/AA 1.07 and 239 mg/g_{SiO2}^{-1} instead of N/AA 1.1 and 294 mg/g_{SiO2}^{-1} at 30 °C). Interestingly, the mesostructure observed on the TEM image (Figure S7 in Supporting Information File 1) of such a temperature-treated sample is similar to the short-range ordered cylindrical mesopores presenting honeycomb-like arrangement of the materials synthesized at pH 7.4 and 7.9, thus supporting the role of the weaker interaction between PEO and silica at those pH. It is worth noting that the involvement of mediating cations ensuring the interface neutrality through a $N^0Na^+I^-$ pathway (in our case Na^+ coming from the sodium hydroxide solution used to adjust the pH) that has been proposed in some studies [4] does not hold in this high pH material synthesis, since the Na/Si molar ratio obtained from EDX measurements was too low (Na/Si ≈0.04) to support such an assembly.

The pH-dependent mesoproperties of the PEO-*b*-PAA/OC PIC structuring agent can be depicted by defining an induced amphiphilic unit that determines the nature of the mesophase. This amphiphilic unit can be described as a ternary system constituted of OC, PEO-*b*-PAA and silica species. The core of the amphiphilic system is constituted by a polyion electrostatic complex of OC/PAA and the corona by the H-bonded assembly of PEO block and silica species. As the pH of the synthesis medium is increased (from pH 4.5 to 6.5), the extent of the electrostatic interactions increases and the hydrogen bond interaction with silica species weakens, whereas the condensation rate of silica increases. Figure 6 schematically depicts the different interactions involved in the formation of the hybrid precipitate, and how they vary with pH, allowing us to tune the relative sizes of the electrostatic complex core and the PEO/inorganic corona of the amphiphilic unit. The pH sensitivity of the various interactions provided by this peculiar amphiphilic system allows tuning the mesostructure of the material from hexagonal to worm-like/lamellar simply by varying the pH of the reaction medium at 3.9 wt % of DHBC. At a lower DHBC concentration (1.9 wt %), the mesostructure transformed from lamellar/hexagonal at pH 4.5 to purely lamellar at pH 6.5. Interestingly, the hybrid materials prepared in more dilute conditions exhibited N/AA (0.62 and 1.24 at pH 4.5 and 6.5, respectively) and EO/Si (0.56 and 0.48 at pH 4.5 and 6.5, respectively) ratios sim-

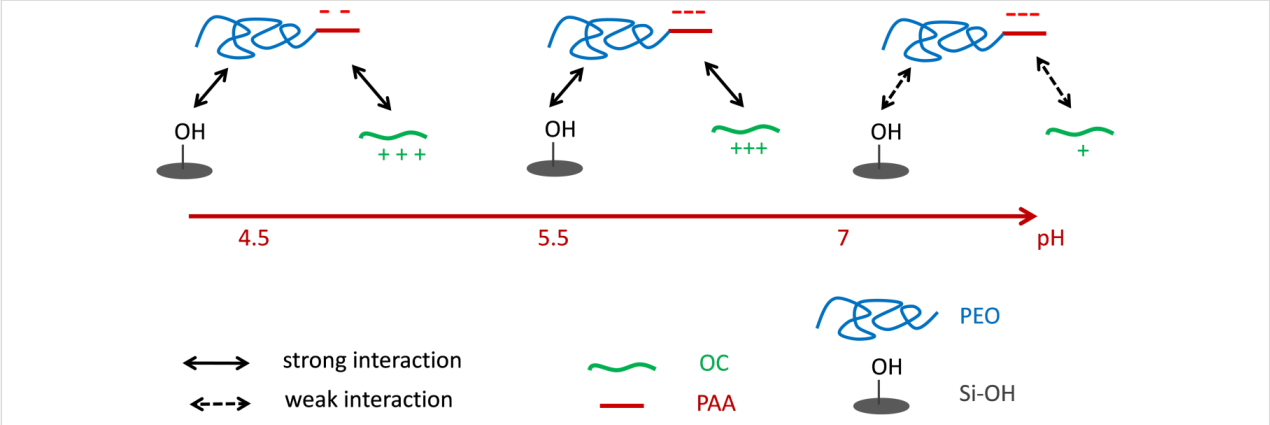

Figure 6: Schematic representation of the interactions between silicic species and PEO, OC and PAA entities as a function of pH.

ilar to those obtained at 3.9 wt % whereas the mesostructures were found to be rather different from those obtained at 3.9 wt %. Several factors may be involved in the difference in mesostructures between the two concentrations of the reaction medium (hexagonal vs lamellar/hexagonal mixture at pH 4.5 and short-range ordered worm-like/lamellar mixture vs purely lamellar at pH 6.5): the different silica condensation rates, the different quantities of ethanol released upon TEOS hydrolysis and their influence on the polymer solubility, and the amounts of water contained in both the hydrophilic PEO shell and the PIC core, which may swell differently the two different compartments.

Conclusion

In conclusion, mesoporous materials of various structures including 2D hexagonal, worm-like, and lamellar structures were formed by using polyion complex micelles as structure-directing agents under different pH conditions of material synthesis. As a weak polyacid-containing DHBC and a weak polybase were chosen as constituents of the polyion complexes, micelle formation occurs on a restricted pH domain between about 4.5 and 7. The silica framework is obtained by condensation of silicic species, which are formed by hydrolysis of the silicon alkoxide at pH 2. Due to the pH dependence of the PIC micelle properties, of the silica condensation rate, and of the PEO-silanol interactions, the variation of the pH of the reaction medium from 4.5 to about 8 led to considerable changes in the structural, textural and compositional properties of the materials.

After hydrolysis of TEOS in the presence of the polymers, the increase of the pH of the aqueous mixture between 4.5 and 7.9 leads to the formation of a macroscopic hybrid organic–inorganic precipitate. When the materials were synthesized in the pH 4.5–5.5 range, long-range ordered 2D hexagonal structures exhibiting pore diameters which regularly increase with pH were obtained. In the pH 5.7–6.5 range, a mixture of short-range ordered worm-like and lamellar structures was obtained; it appears to be a pure long-range ordered lamellar phase when the reaction medium was twice less concentrated. When the pH of the material synthesis exceeds pH 7, cylindrical pore morphologies were obtained, exhibiting some short-range ordered 2D hexagonal arrangement. In the pH range 4.5–6.9, pore diameters were shown to increase progressively with pH up to 5.7 nm, whereas they dramatically increase above pH 7 exceeding 10 nm. The variations of the structural and porous properties of the materials were shown to be related to variations of the compositions. Mesostructures with larger pore diameters or with a higher radius of curvature were obtained in the pH range 4.5–6.9, in relation with increased content of the polybase (oligochitosan) in the PIC nanodomain (increased ratio between amine and acrylate functions).

In summary, the pH of the reaction medium appears to be a key parameter in the determination of the structural and textural characteristics of mesoporous materials whose synthesis is directed by polyion complex micelles. This is due to the variation of three essential properties as a function of pH: the extent of the electrostatic bonding between the weak polyelectrolytes, the extent of the hydrogen bond interaction between silanol and PEO ether groups, and finally, the silica condensation rate. As a complementary investigation, the influence of other synthesis parameters, which were identified to play a role in the structure determination, including the concentration of the reaction medium and the temperature, is currently under study.

Supporting Information

Supporting Information File 1

Additional experimental data.
[https://www.beilstein-journals.org/bjnano/content/supplementary/2190-4286-10-14-S1.pdf]

Acknowledgements

The authors would like to acknowledge Philippe Gaveau (Institut Charles Gerhardt Montpellier) for his help in NMR experiments, the "Laboratoire de Mesures Physiques de l'Université de Montpellier" for elemental analyses. The authors are also thankful to the MENRT (Ministry of National Education, Research and Technology), the ANR for ANR MESOPIC Project ANR-15-CE07-0005 and the Chemisyst Labex of Montpellier for financial support.

ORCID® iDs

Emilie Molina - https://orcid.org/0000-0002-0967-9836
Patrick Lacroix-Desmazes - https://orcid.org/0000-0002-0197-7062
Martin In - https://orcid.org/0000-0001-8074-180X

References

1. Huo, Q.; Margolese, D. I.; Ciesla, U.; Demuth, D. G.; Feng, P.; Gier, T. E.; Sieger, P.; Firouzi, A.; Chmelka, B. F.; Schüth, F.; Stucky, G. D. *Chem. Mater.* **1994,** *6,* 1176–1191. doi:10.1021/cm00044a016
2. Tanev, P. T.; Pinnavaia, T. J. *Science* **1995,** *267,* 865–867. doi:10.1126/science.267.5199.865
3. Bagshaw, S. A.; Prouzet, E.; Pinnavaia, T. J. *Science* **1995,** *269,* 1242–1244. doi:10.1126/science.269.5228.1242
4. Zhao, D.; Huo, Q.; Feng, J.; Chmelka, B. F.; Stucky, G. D. *J. Am. Chem. Soc.* **1998,** *120,* 6024–6036. doi:10.1021/ja974025i
5. Sundblom, A.; Oliveira, C. L. P.; Pedersen, J. S.; Palmqvist, A. E. C. *J. Phys. Chem. C* **2010,** *114,* 3483–3492. doi:10.1021/jp100087z
6. Rubio, J.; Kitchener, J. A. *J. Colloid Interface Sci.* **1976,** *57,* 132–142. doi:10.1016/0021-9797(76)90182-x
7. Chaudhary, V.; Sharma, S. *J. Porous Mater.* **2017,** *24,* 741–749. doi:10.1007/s10934-016-0311-z
8. Zhao, D.; Feng, J.; Huo, Q.; Melosh, N.; Fredrickson, G. H.; Chmelka, B. F.; Stucky, G. D. *Science* **1998,** *279,* 548–552. doi:10.1126/science.279.5350.548
9. Brinker, C. J.; Scherer, G. W. *Sol–Gel Science. The Physics and Chemistry of Sol–Gel Processing;* Academic Press, 1990. doi:10.1016/c2009-0-22386-5
10. Kim, J. M.; Han, Y.-J.; Stucky, G. D.; Chmelka, B. F. *Chem. Commun.* **2000,** 2437–2438. doi:10.1039/b005608l
11. Kim, S.-S.; Karkamkar, A.; Pinnavaia, T. J.; Kruk, M.; Jaroniec, M. *J. Phys. Chem. B* **2001,** *105,* 7663–7670. doi:10.1021/jp010773p
12. Kim, S.-S.; Pauly, T. R.; Pinnavaia, T. J. *Chem. Commun.* **2000,** *17,* 1661–1662. doi:10.1039/b002856h
13. Jammaer, J.; Aerts, A.; D'Haen, J.; Seo, J. W.; Martens, J. A. *J. Mater. Chem.* **2009,** *19,* 8290–8293. doi:10.1039/b915273c
14. Martens, J. A.; Jammaer, J.; Bajpe, S.; Aerts, A.; Lorgouilloux, Y.; Kirschhock, C. E. A. *Microporous Mesoporous Mater.* **2011,** *140,* 2–8. doi:10.1016/j.micromeso.2010.09.018
15. Kerkhofs, S.; Willhammar, T.; Van Den Noortgate, H.; Kirschhock, C. E. A.; Breynaert, E.; Van Tendeloo, G.; Bals, S.; Martens, J. A. *Chem. Mater.* **2015,** *27,* 5161–5169. doi:10.1021/acs.chemmater.5b01772
16. Wang, Y.-Q.; Zheng, C.-M.; Liu, Z.-J.; Guo, M.-L. *New J. Chem.* **2015,** *39,* 7763–7767. doi:10.1039/c5nj01632k
17. Colmenares, M. G.; Simon, U.; Cruz, O.; Thomas, A.; Goerke, O.; Gurlo, A. *Microporous Mesoporous Mater.* **2018,** *256,* 102–110. doi:10.1016/j.micromeso.2017.08.002
18. Jammaer, J.; van Erp, T. S.; Aerts, A.; Kirschhock, C. E. A.; Martens, J. A. *J. Am. Chem. Soc.* **2011,** *133,* 13737–13745. doi:10.1021/ja205627t
19. Boissière, C.; Larbot, A.; van der Lee, A.; Kooyman, P. J.; Prouzet, E. *Chem. Mater.* **2000,** *12,* 2902–2913. doi:10.1021/cm991188s
20. Cui, X.; Zin, W.-C.; Cho, W.-J.; Ha, C.-S. *Mater. Lett.* **2005,** *59,* 2257–2261. doi:10.1016/j.matlet.2005.02.073
21. Jin, Z.; Wang, X.; Cui, X. *J. Colloid Interface Sci.* **2007,** *307,* 158–165. doi:10.1016/j.jcis.2006.11.006
22. Jin, Z.; Wang, X.; Cui, X. *Microporous Mesoporous Mater.* **2008,** *108,* 183–192. doi:10.1016/j.micromeso.2007.03.042
23. Baccile, N.; Reboul, J.; Blanc, B.; Coq, B.; Lacroix-Desmazes, P.; In, M.; Gérardin, C. *Angew. Chem., Int. Ed.* **2008,** *47,* 8433–8437. doi:10.1002/anie.200802431
24. Birault, A.; Molina, E.; Carcel, C.; Bartlett, J.; Marcotte, N.; Toquer, G.; Lacroix-Desmazes, P.; Gerardin, C.; Wong Chi Man, M. *J. Sol-Gel Sci. Technol.* **2018,** 4667. doi:10.1007/s10971-018-4667-1
25. Warnant, J.; Marcotte, N.; Reboul, J.; Layrac, G.; Aqil, A.; Jerôme, C.; Lerner, D. A.; Gérardin, C. *Anal. Bioanal. Chem.* **2012,** *403,* 1395–1404. doi:10.1007/s00216-012-5947-1
26. Houssein, D.; Warnant, J.; Molina, E.; Cacciaguerra, T.; Gérardin, C.; Marcotte, N. *Microporous Mesoporous Mater.* **2017,** *239,* 244–252. doi:10.1016/j.micromeso.2016.10.013
27. Mebarek, N.; Aubert-Pouëssel, A.; Gérardin, C.; Vicente, R.; Devoisselle, J.-M.; Bégu, S. *Int. J. Pharm.* **2013,** *454,* 611–620. doi:10.1016/j.ijpharm.2013.06.014
28. Molina, E.; Warnant, J.; Mathonnat, M.; Bathfield, M.; In, M.; Laurencin, D.; Jérôme, C.; Lacroix-Desmazes, P.; Marcotte, N.; Gérardin, C. *Langmuir* **2015,** *31,* 12839–12844. doi:10.1021/acs.langmuir.5b03221
29. Reboul, J.; Nugay, T.; Anik, N.; Cottet, H.; Ponsinet, V.; In, M.; Lacroix-Desmazes, P.; Gérardin, C. *Soft Matter* **2011,** *7,* 5836–5846. doi:10.1039/c1sm05230f
30. Trombotto, S.; Ladavière, C.; Delolme, F.; Domard, A. *Biomacromolecules* **2008,** *9,* 1731–1738. doi:10.1021/bm800157x
31. Brunauer, S.; Emmett, P. H.; Teller, E. *J. Am. Chem. Soc.* **1938,** *60,* 309–319. doi:10.1021/ja01269a023
32. Neimark, A. V.; Ravikovitch, P. I. *Microporous Mesoporous Mater.* **2001,** *44–45,* 697–707. doi:10.1016/s1387-1811(01)00251-7
33. Broekhoff, J. C. P.; de Boer, J. H. *J. Catal.* **1968,** *10,* 391–400. doi:10.1016/0021-9517(68)90154-1
34. Thommes, M.; Kaneko, K.; Neimark, A. V.; Olivier, J. P.; Rodriguez-Reinoso, F.; Rouquerol, J.; Sing, K. S. W. *Pure Appl. Chem.* **2015,** *87,* 1051–1069. doi:10.1515/pac-2014-1117
35. Berggren, A.; Palmqvist, A. E. C. *J. Phys. Chem. C* **2008,** *112,* 732–737. doi:10.1021/jp0766858
36. Léonard, A.; Blin, J. L.; Jacobs, P. A.; Grange, P.; Su, B. L. *Microporous Mesoporous Mater.* **2003,** *63,* 59–73. doi:10.1016/s1387-1811(03)00432-3
37. Muto, S.; Imai, H. *Microporous Mesoporous Mater.* **2006,** *95,* 200–205. doi:10.1016/j.micromeso.2006.05.023
38. Sierra, L.; Guth, J.-L. *Microporous Mesoporous Mater.* **1999,** *27,* 243–253. doi:10.1016/s1387-1811(98)00258-3
39. Sierra, L.; Lopez, B.; Guth, J.-L. *Microporous Mesoporous Mater.* **2000,** *39,* 519–527. doi:10.1016/s1387-1811(00)00227-4

40. Iler, R. K. *The Chemistry of Silica: Solubility, Polymerization, Colloid and Surface Properties, and Biochemistry;* Wiley: New York, NY, U.S.A., 1979.
41. Ruthstein, S.; Frydman, V.; Goldfarb, D. *J. Phys. Chem. B* **2004,** *108,* 9016–9022. doi:10.1021/jp049133n
42. Blin, J. L.; Impéror-Clerc, M. *Chem. Soc. Rev.* **2013,** *42,* 4071–4082. doi:10.1039/c2cs35362h
43. Sundblom, A.; Palmqvist, A. E. C.; Holmberg, K. *Langmuir* **2010,** *26,* 1983–1990. doi:10.1021/la902144h
44. Galarneau, A.; Cambon, H.; Di Renzo, F.; Ryoo, R.; Choi, M.; Fajula, F. *New J. Chem.* **2003,** *27,* 73–79. doi:10.1039/b207378c

License and Terms

BEILSTEIN JOURNAL OF NANOTECHNOLOGY

Targeting strategies for improving the efficacy of nanomedicine in oncology

Gonzalo Villaverde[1] and Alejandro Baeza[*2]

Review

Open Access

Address:
[1]Dpto. Química Inorgánica y Bioinorgánica, Universidad Complutense de Madrid, Instituto de Investigación Sanitaria, Hospital 12 de Octubre i+12, Plaza Ramón y Cajal s/n, 28040 Madrid, Spain; CIBER de Bioingeniería, Biomateriales y Nanomedicina, CIBER-BBN, Madrid, Spain and [2]Dpto. Materiales y Producción Aeroespacial, ETSI Aeronáutica y del Espacio, Universidad Politécnica de Madrid, 28040-Madrid, Spain

Email:
Alejandro Baeza[*] - alejandro.baeza@upm.es

* Corresponding author

Keywords:
antitumoral therapy; nanomedicine; smart nanocarriers; targeted nanoparticles

Beilstein J. Nanotechnol. **2019,** *10,* 168–181.
doi:10.3762/bjnano.10.16

Received: 11 August 2018
Accepted: 19 December 2018
Published: 14 January 2019

This article is part of the thematic issue "Advanced hybrid nanomaterials".

Guest Editor: V. de Zea Bermudez

Abstract

The use of nanoparticles as drug carriers has provided a powerful weapon in the fight against cancer. These nanocarriers are able to transport drugs that exhibit very different nature such as lipophilic or hydrophilic drugs and big macromolecules as proteins or RNA. Moreover, the external surface of these carriers can be decorated with different moieties with high affinity for specific membrane receptors of the tumoral cells to direct their action specifically to the malignant cells. The selectivity improvement yielded by these nanocarriers provided a significative enhancement in the efficacy of the transported drug, while the apparition of side effects in the host was reduced. Additionally, it is possible to incorporate targeting moieties selective for organelles of the cell, which improves even more the effect of the transported agents. In the last years, more sophisticated strategies such as the use of switchable, hierarchical or double targeting strategies have been proposed for overcoming some of the limitations of conventional targeting strategies. In this review, recent advances in the development of targeted nanoparticles will be described with the aim to present the current state of the art of this technology and its huge potential in the oncological field.

Introduction

Nanotechnology has become a powerful weapon in the search of novel strategies for addressing unmet clinical challenges, from the treatment of complex diseases as cancer or neurological disorders, to the early diagnosis of these pathologies that could allow for eliminating them before the appearance of any symptoms. Nanoparticles can interact with cells, bacteria and viruses in a very intimate and efficient way because they present a similar size than these biological entities [1]. This close interaction has been exploited for achieving important abilities such as the selective transport of drugs directly to

diseased cells and tissues [2], the precise recognition of extremely low concentrations of important biomarkers indicative of pathological processes that are present in complex environments (e.g., urine, blood, saliva) [3] or the creation of smart nanorobots able to perform precision surgery inside the body [4]. One of the applications in which the nanoparticles have found an interesting niche is oncology. The conventional treatment of cancer is based on three strategies: surgery, radiotherapy and chemotherapy. These approaches exhibit a lack of selectivity affecting also the surrounding healthy tissues, in the case of surgery and radiotherapy, and/or to the whole organism, in the case of chemotherapy. This last strategy could be visualized as carpet bombing with the aim of destroying an enemy army that is hidden in a populated city. In many cases, the effect on the malignant "soldiers" is scarce but the number of "civilian casualties" is unbearable. Nanomedicine has provided a promising alternative to these strategies through the development of engineered nanocarriers capable to deliver therapeutic agents specifically to tumoral cells without affecting healthy tissue. These nanoparticles are able to load great amounts of drugs, to transport them in the blood stream and finally, to recognize the tumoral tissue and release their cargo inside the tumoral cells. The idea to use nanoparticles as drug carriers in oncology arose in 1986, when two Japanese researchers reported that nanoparticles present a passive tendency to be accumulated into tumoral tissues [5]. This passive accumulation, also known as passive or primary targeting, is called "enhanced permeation and retention (EPR)" effect and is one of the keystones of tumour treatment with the help of nanocarriers [6]. Moreover, the external surface of these nanocarriers can be decorated with different bioorganic moieties (targeting groups) that bind specifically to receptors located on the membrane of tumoral cells in order to enhance the particle uptake in the malignant cells. This strategy is the so-called "cellular or secondary targeting", because it is generally based on a ligand–receptor-mediated endocytosis, triggered by the strong interaction of the targeting group with the membrane receptor of the tumoral cell. It improves the selectivity of the treatment achieving a drastic reduction of the side effects caused by the transported drugs and also reduces the drug resistance developed through the high doses in conventional treatments [7]. Finally, it is also possible to place additional targeting moieties on the particle surface that do not bind to receptors located on the external membrane of the cells but recognize internal organelles. This approach is known as tertiary targeting and it has been widely exploited for the transportation of potent cytotoxic compounds or genetic materials (i.e., silencing RNA) that present an improved effect when they are released close to specific organelles such as mitochondria or the nucleus. In this review, some of the recent advances of the different targeting approaches investigated in the last years will be presented. Additionally, the development of sophisticated strategies that allow for the sequential targeting of cells and organelles, or tissues and cells, as well as the employ of hierarchical targeting will also be described to provide an insight about the great potency of targeted nanomedicines in antitumoral therapy.

Review

Passive targeting based on the EPR effect

As mentioned above, the use of nanoparticles in oncology was proposed for the first time by Maeda and Matsumura, who reported the selective accumulation of nanometric entities in tumoral tissue [5]. The reason of this passive accumulation lies in the unique architecture of the blood vessels that irrigate the solid tumour. The accelerated growth of a solid tumour must be sustained by the continuous construction of blood vessels in order to transport nutrients and oxygen to the malignant cells spreading through the tissue. The creation of completely functional blood vessels requires a fine balance between pro- and anti-angiogenic factors. These factors are unbalanced in the tumoral tissue with the amount of pro-angiogenic factors being higher [8]. As a consequence of this, the newly formed blood vessels have an aberrant and tortuous structure with pores and fenestrations of a few hundreds of nanometres. Therefore, when the nanoparticles reach the tumoral blood vessels, they can leak from the vessels through these pores into the malignant tissue. Moreover, the accelerated growth of the tumoral mass usually compresses the lymphatic vessels that are on charge of the elimination of wastes products and liquids from the tissue and thus, the extravasated nanoparticles cannot leave the tissue resulting in accumulation over long periods of time. These two characteristics, the high permeability of tumoral blood vessels and the lack of an efficient drainage system are responsible for the accumulation of the nanoparticles into neoplastic tissues. Unfortunately, the EPR effect is not as universal as originally thought. It highly depends of the type of tumour and even of the state of disease progression [9]. Despite the fact that the EPR effect is really pronounced in mice models, this effect is not general in humans. There are tumours with a very pronounced EPR effect, such as Kaposi sarcoma and multiple myeloma, while other tumours barely exhibit this effect, as pancreatic cancer. Therefore, it is required to design strategies able to increase the nanoparticle accumulation in tumoral tissues where the EPR effect is weak [10]. Additionally, even in the case where the EPR effect is present, there are other barriers that compromise the efficacy of nanoparticle-based therapies. One of these barriers is the elevated interstitial fluid pressure (IFP) present in the interstitial space of solid tumours, which approaches or even surmounts the intravascular pressure [11]. This effect strongly compromises the diffusion of the nanoparticles into the tumour tissues. Some authors have proposed the previous normalization of the tumoral vasculature by the administration of anti-

angiogenic factors in order to reduce the IFP and therefore, to enhance the nanoparticle diffusion into the tumour [12]. Another strong barrier that hampers the efficacy of nanomedicines is the dense extracellular matrix (ECM), which is usually present in many solid tumours. ECM is commonly denser in solid tumours than in healthy tissues due to a higher content in collagen and other structural proteins. This fact hinders the penetration of the nanoparticles into tumoral tissues restraining their effect to the periphery of the neoplasia. In order to overcome this limitation, diverse alternatives have been proposed, from the application of ultrasounds for propelling the nanoparticles inside the tissue [13] to the previous administration of proteolytic enzymes that digest the ECM [14]. As an example, Villegas et al. have reported the use of pH-sensitive polymeric nanocapsules that are able to release collagenase once they arrive at the tumoral tissue due to the mild acidic conditions present there [15]. These nanocapsules were anchored on the surface of mesoporous silica nanoparticles (MSN) coated with a lipid bilayer (protocells) enhancing their penetration into 3D tumoral tissue models, which yielded a significant enhancement of the therapeutic efficacy of these nanodevices (Figure 1) [16].

Active targeting: from cellular to organelle vectorization

Once the nanoparticle reaches the tumoral area, it faces a complex scenario. Tumoral masses are not composed by an homogeneous tumoral cell distribution but they are formed by a myriad of different cell populations, from tumoral cells to immune, supportive and healthy cells of the original tissue [17]. Therefore, nanoparticles should possess the capacity to recognize the malignant cells and focus the effect onto them in order to achieve an efficient therapeutic effect. This ability can be incorporated in the nanodevice by anchoring targeting moieties on the particle surface [1,18]. These targeting moieties are molecules or macromolecules that bind to specific receptors located on the surface of the tumoral cells. In many cases, these cellular receptors are also present in healthy cells, e.g., for the widely employed targeting moieties folic acid [19], transferrin [20] or sugars [21]. But their number is significantly higher in tumoral than in healthy cells due to their stronger nutrient demand. Thus, this receptor overexpression can be exploited for the selective delivery of therapeutic drugs to tumoral cells. Another possibility consists in the development of synthetic targeting moieties that bind to certain receptors in a more selective and efficient manner [22]. Villaverde et al. have reported the synthesis of *meta*-aminobenzylguanidine (MABG) and its anchorage to the surface of MSN in order to guide these particles specifically to neuroblastoma cells [23]. About 90% of neuroblastoma cells overexpress the norepinephrine receptor (NET) on their surface. *Meta*-iodobenzylguanidine is a synthetic analogue of norepinephrine that, with a radioactive iodine substituent (^{131}I), has been widely employed for the diagnosis of neuroblastoma due to its strong affinity for NET. The replacement of the iodine by an amino group in MABG did not reduce the ability to bind to NET while it provided a reactive group that allowed for grafting this molecule to the surface of MSN employing a bifunctionalized polyethylene glycol (PEG) molecule as spacer between the MSN surface and MABG. MSN decorated with these moieties were engulfed by neuroblastoma

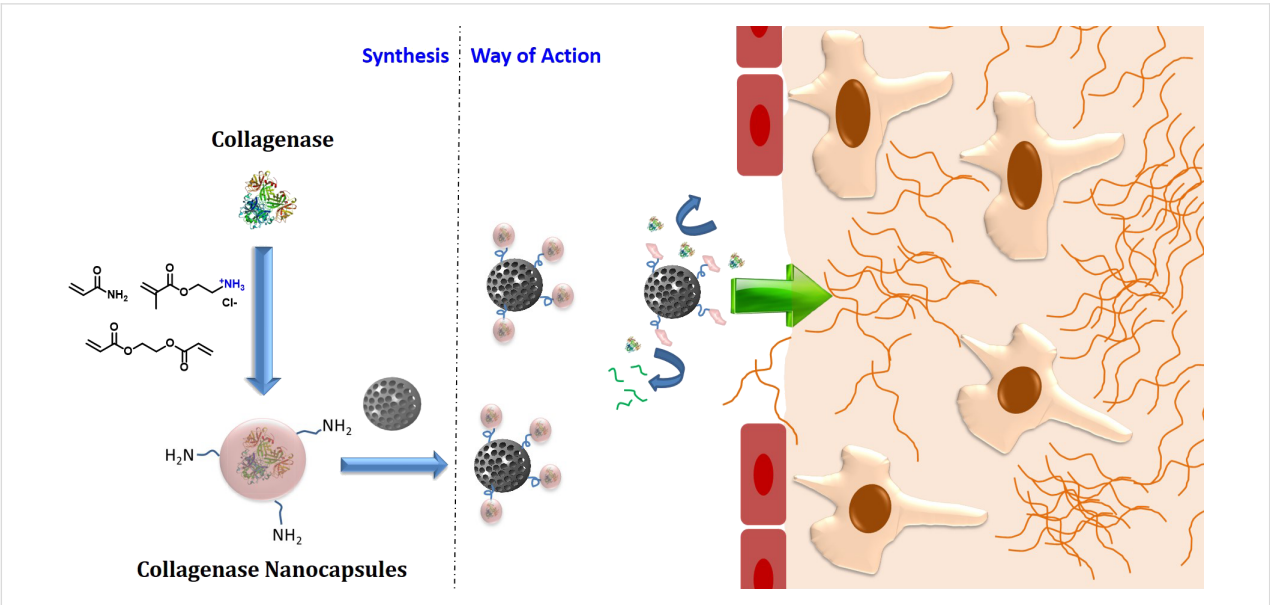

Figure 1: Highly penetrating nanosystems based on the incorporation of pH-responsive collagenase nanocapsules. This image has been adapted from [15], copyright 2015 American Chemical Society.

cells up to four times more than non-targeted MSN. The in vivo evaluation in neuroblastoma xenograft model showed strong accumulation of the targeted system and high retention in the tumoral zone over a period of more than 72 h. Non-targeted nanoparticles were rapidly cleared. Interestingly, MSN decorated with the same type of PEG but without MABG at the end failed to be accumulated in the tumoral area, but they showed slight accumulation in the liver of the animal, probably due to the increase in the circulation time of the particles caused by the presence of the PEG chains (Figure 2) [23].

The small size of these synthetic molecules allows for the grafting of multiple copies of them, or even combinations of two different molecules on the surface of the nanoparticles [24]. This fact can induce a significant enhancement of the particle uptake due to multiple binding processes with tumoral receptors through a multivalence effect [25]. Nature usually employs antibodies for the recognition of cells and pathogenic bodies. Antibodies are large proteins that present a characteristic Y-shaped structure in which the recognition event takes place in a very specific manner through the interaction between the antigen located on the diseased cell and the two ends of the Y-shaped protein. Thus, many different antibodies have been attached on the surface of multiple types of nanoparticles to induce selectivity against specific cell populations. As example, Herceptin is an antibody that recognizes the human epidermal growth factor receptor 2 (HER2) overexpressed in breast cancer cells (HER2+). This antibody has been attached on the surface of poly(D,L-lactic-*co*-glycolic acid) (PLGA) nanoparticles loaded with the potent estrogen receptor modulator tamoxifen [26]. These nanoparticles were capable to induce a significant in vivo tumour growth inhibition due to the enhanced nanoparticle uptake within the tumoral cells owing to the strong interaction between the antibody and HER2. Another interesting possibility is to employ antibodies for the recognition of the tumoral blood vessels instead of the tumoral cells. Endoglin, or CD105, is a glycoprotein usually overexpressed on the surface of the endothelial cells which compose the tumoral vessels. TRC105 is a human/murine chimeric antibody which recognizes CD105 with high specificity and due to this property it has been incorporated on the surface of MSN labelled with ^{64}Cu in order to perform imaging by positron emission tomography (PET) [27]. The injection of these particles into the blood stream of mice bearing breast tumour allowed for the visualization of the tumoral mass thanks to the enhanced accumulation of the particles. One of the problems associated with the use of antibodies for targeting is the partial loss of the binding capacity of the attached antibody during the anchoring process, which is usually carried out by non-specific chemical techniques as carbodiimide coupling chemistry [28]. An alternative is the introduction of certain functional groups on specific positions of the antibody, which allows the utilization of bio-orthogonal chemical strategies, such as azide-strained alkyne or thiol–maleimide reaction, for carrying out the antibody attachment with a high precision level [29]. Another interesting strategy is the attachment of protein A on the nanoparticle surface prior to the incorporation of the antibody [30]. Protein A is a membrane protein produced by *Staphylococcus aureus* in order to complex the immunoglobulins by the complement region (Fc) deactivating the immune attack of the host. Thus, antibodies can be anchored to the surface of a nanoparticle decorated with protein A thanks to the strong affinity between the protein and the Fc region, which is not involved in the recognition process and therefore, this process occurs without any loss of the antibody binding capacity. Unfortunately, the use of antibodies as targeting moieties has an important drawback, which is the possibility to trigger immune responses due to the uncontrolled exposition of immunogenic regions (as Fc) on the particle surface. Peptides

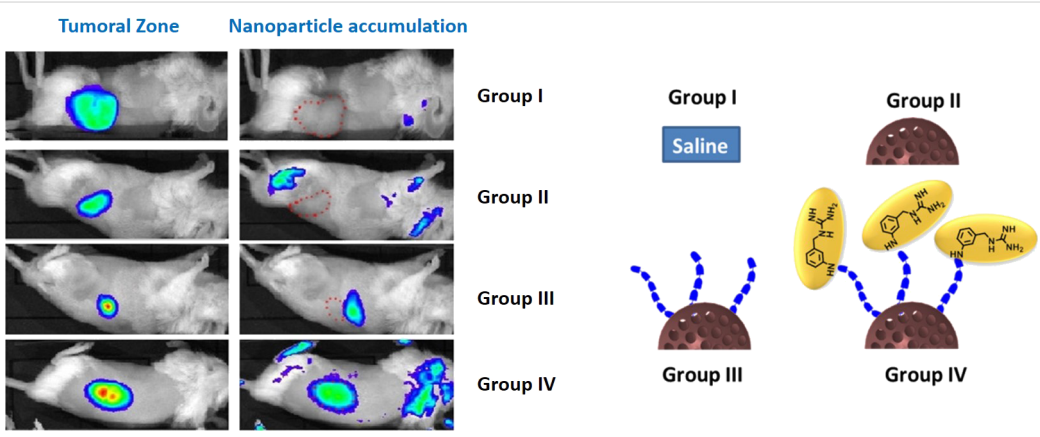

Figure 2: Left: tumoral zone monitored by bioluminescence and nanoparticle accumulation detected by IVIS® Spectrum in vivo imaging system. Group IV exhibited strong particle accumulation in the tumour, whereas group III only showed slight accumulation in the liver. Right: images of each group of particles that were injected in mice. This image has been adapted from [23], copyright 2015 Royal Society of Chemistry.

are versatile alternatives to antibodies for targeting purposes. The use of relatively short peptide chains provides some important advantages, such as i) only little alteration of the hydrodynamic diameter of the nanoparticles, ii) multigram production with high purity, iii) possibility to attach multiple copies of them on the nanoparticle surface which enhances the uptake, iv) possibility to use non-natural aminoacids improving the versatility and v) low immunogenicity [31]. The tripeptide Arg–Gly–Asp (RGD) is probably one of the most employed peptide in the targeting design of nanoparticles. RGD binds specifically to αβ-integrin, which is usually upregulated in many different tumoral cell lines such as breast, lung or fibroblast cancer cells, and also by the epithelial cells of the tumoral blood vessels [32,33]. Ruoshlati et al. have reported that the cyclic version of RGD, CRGDKGPDC (called iRGD), which is cyclized by the disulfide bridge between both terminal cysteines, exhibits significantly a higher tumour specificity than linear RGD [34]. iRGD works in a sequential manner, first it binds to αβ-integrin by the RGD sequence encrypted within the cyclic structure and then, the peptide is broken by the action of a cell surface-associated protease exposing the RGD, which then binds to neuropilin-1 triggering the particle endocytosis. Another cell-penetrating peptide (or CPP, which is the usual name of the peptides used for targeting purposes in nanomedicine) closely related to RGD is the tripeptide Asn–Gly–Arg (NGR). The asparagine present in this peptide sequence experiences spontaneous deamidation producing a mimetic of the RGD peptide (iso-DGR), which presents similar targeting capacities. Additionally, this sequence also binds to tumoral blood vessels [35]. Thus, this peptide has been anchored to different nanoparticles for enhancing their uptake into tumoral cells or for binding to tumour vessels. As an example, cyclic NGR, which binds to the aminopeptidase receptor (CD13), was grafted on the surface of temperature-sensitive liposomes loaded with doxorubicin (Dox) for the selective destruction of CD13+ cancer cells as human fibrosarcoma cells (HT-1080) [36]. These liposomes released more than 75% of their payload when the temperature reached 41.3 °C whereas they maintained the Dox within their hydrophilic core at physiological temperature. Other systems widely employed for targeting purposes are aptamers. Aptamers are oligonucleotide chains that exhibit a characteristic three-dimensional structure capable to bind to specific membrane cell receptors overproduced by the tumoral cells. The aptamer that specifically binds to a certain protein is usually selected by the technique named systematic evolution of ligands by exponential enrichment (SELEX) [37]. Through this technique it is possible to obtain oligonucleotide sequences selective for many different membrane proteins. These macromolecules have been widely employed both alone and conjugated with drugs or nanoparticles [38]. Aptamers specifically designed for binding to the epidermal growth factor receptors (EGFR) have been anchored on the surface of hollow gold nanospheres [39]. The thiolated version of these aptamers was anchored on the gold surface through the thiol groups producing an average anchorage yield of 250 aptamers per particle. The biodistribution of these particles was evaluated in vivo by micro-single-photon emission computed tomography/computed tomography (micro-SPECT/CT) employing particles labelled with ^{111}In, showing an excellent tumour-homing capacity of these particles. AS1411 aptamers have been widely employed for cell targeting in tumoral cell lines that overexpress nucleolin [40].

The use of targeting moieties provides not only the capacity to the nanoparticles to be selectively engulfed by tumoral cells. It also allows for the localization of the nanocarriers in specific intracellular localizations or organelles, such as nucleus or mitochondria [41,42]. This enables the precise delivery of therapeutics to key organelles of the cells, which could significantly increase their cytotoxic effect. Mitochondria are the energetic plants of the cells. In addition, they carry out other important functions such as the control of the intracellular calcium concentration or the removing of the oxidative species, which could damage the cell. Therefore, the specific delivery of toxic species to these key organelles compromises the function of the entire cell causing its destruction. Yoong et al. have decorated the external surface of multiwalled carbon nanotubes (MWCNTs) with rhodamine-110 to localize them close to the mitochondria membrane [43]. The positive charge provided by rhodamine-110 provokes the electrostatic binding with the highly negative mitochondria membrane (−180 mV to −160 mV). These MWCNTs were loaded with a platinum(IV) pro-drug that released active cisplatin(II) in the reductive environment of the intracellular space. Another targeting moiety that has been employed for delivering therapeutics to mitochondria is triphenylphosphine [44]. This positively charged group also binds to the mitochondria membrane by electrostatic interactions. The nucleus contains practically all the genetic information (except for the mitochondrial DNA) and is of paramount importance for the correct function of the entire cell. Targeting nuclei has received huge attention regarding the delivery of cytotoxic species that act on DNA or the direct delivery of genes to their place of action. Viruses are one of the inspiration sources for strategies to reach the inner nuclear space. They contain on their membrane small peptide sequences with nuclear translocation capacity such as the KKKRKV peptide in simian vacuolating virus 40 (SV40), GRKKRRQRRRPQ in the TAT peptide present in human immunodeficiency virus (HIV), or KRPAATKKAGQAKKKKL in the case of nucleoplasmin [45]. These peptides have been anchored on the surface of different nanocarriers providing excellent results [46]. The aptamer AS1411 selective for nucleolin, a protein present on the nuclear

membrane, has also been widely employed for the selective release of therapeutic compounds to the nucleus [47,48]. Shiga and cholera toxins exhibit the ability to target Golgi and endoplasmic compartments and they have been conjugated with drugs for their selective delivery to these organelles [49]. The peptide Lys–Asp–Glu–Leu (KDEL) has been anchored on gold nanoparticles loaded with siRNA for the selective delivery of the genetic material into the endoplasmic reticulum [50].

The main mechanism for the internalization of nanoparticles within mammalian cells is endocytosis [51]. Usually, the nanocarriers enter into the cells into endosomes, which evolve into lysosomes, which can lead to the degradation of the transported cargo, especially in the case of sensitive agents such as genes or siRNA. Therefore, it is necessary to design mechanisms to induce the endosomal escape to reach the cytosol. Multiple strategies for overcoming the endosomal entrapment have been designed [52]. One of the most widely employed is the incorporation of polycationic groups on the particle surface such as poly(ethyleneimine), cationic dendrimers or poly(histidine) chains [53]. Tertiary amino groups in these polymers bring protons into the endosomes producing osmotic alterations that provoke endosomal rupture (proton sponge effect) [54]. The incorporation of peptides such as the GALA peptide (WEAALAEALAEALAEHLAEALAEALEALAA) capable to fuse with the endosomal/liposomal membrane is another mechanism for inducing endosomal escape of nanomedicines [55]. Finally, the incorporation of photosensitizers able to produce radical oxidative species (ROS) upon exposure to certain wavelengths of light induces the controlled endosomal disruption under light exposure [56].

Double targeting solutions, a real alternative?

Active targeting is already one of the most used strategies for bringing nanoformulations into tumoral cells. Although usually great results were achieved in vitro, the in vivo assays have shown smaller effects regarding cell internalization. There has been no real enhancement in the treatment efficacy compared to the passive vectorization effect provided by EPR [57]. Physical and also biological barriers disrupt, to a high extent, the desired selective interactions between the targeting ligands and their receptors. Effects such as off-targeting towards common cell receptors expressed in tumoral but also in healthy cells, and the rapid uptake by the reticuloendothelial system, macrophages and supportive cells such as fibroblasts the decrease the nanocarrier concentration in the blood stream. Also, the poor penetration capacity into the tumoral mass due to strong interactions between cell receptors and targeting agent in the first layers of cells of the tumoral tissues, to so-called binding-site barrier effect, reduces the efficacy of the nanomedicine to an outside stratum of the tumoral zone. In contrast, good results for imaging have been achieved to improve diagnosis in early stages of the disease. Thus, active targeting is still widely studied not only for nanomedicine but also for conjugate drugs [58,59].

As was mentioned above, there are three levels of active targeting: tissular targeting, cellular targeting and intracellular or organelle targeting. A combination of them in single system providing new functionalities and capacities may allow the system to overcome the natural barriers of the nanomedicine approaches. The improvement of the EPR effect in order to increase the nanomedicine accumulation, retention and even penetration into the diseased tissue is one of the main goals [10]. Usually, fast growing tumours such as carcinoma exhibit a highly vascularized tumour mass, while slow growing tumours as sarcoma are poorly irrigated [60]. There are three main strategies for improving the accumulation and retention in tumour tissue: i) the modification of physical conditions of the tumor mass; ii) the selectively targeting of the payload towards tumoral stroma or vasculature tissue and iii) to kill the cancer cells that belong to the external shell of the tumour primary layers [61]. All of them and their combinations need active tissular or cellular targeting systems for a better performance. The strategies for providing multiple targeting abilities within one single nanocarrier will be discussed in the following section.

Simultaneous targeting of tissue and cells

Double vectorization has been proposed in the last years as an approach to overcome some of the physical barriers in nanomedicine. The combination of tissular and cellular targeting agents in a unique nanocarrier may improve accumulation and/or the uptake in cancer cells without affecting healthy cells.

Firstly, the simplest approach is to randomly attach both tissular and cellular targeting moieties on the nanocarrier surface. Through tissular targeting the nanocarrier would be directed to the diseased cells improving its accumulation. Once there, the presence of the cellular targeting moieties would enhance the cellular uptake into the tumoral cells. In several types of cancers and depending on the location of the malignant tissue, the EPR is not effective at all. Combining tissular and celluar agents is a powerful tool in such cases making that active tissular targeting ligands even more important. In 2014, Yang et al. [62] described a peptide dual targeting system with drug-loaded liposomes for glioblastoma treatment. Glioblastoma, localized in the brain, represents one of the major challenges in drug delivery due to the necessity to pass the blood brain barrier (BBB). BBB inhibits the passage of 98% of the medicines administered through the systemic route and constitutes a formidable barrier for tissue targeting not only in nanomedicine but

also in common drug delivery [63]. In this case, liposomes were modified with Angiopep-2 and tLyP-1 homing and penetrating peptides for the simultaneous delivery of siRNA and (docetaxel) DTX. Angiopep-2 showed affinity to the lipoprotein receptor (LPR) typically overexpressed in glioma and in BBB cells [62] and therefore, it shows excellent capabilities for the penetration into the brain through the transcytosis pathway. The peptide tLyP-1 also exhibits both tissue penetration ability through the neurophilin-1-dependent C-end rule and affinity to glioma cells for LPR interaction. The exposed dual peptide cation enables the possible accumulation into gliomas via the combination of EPR effect and active targeting for an antiangiogenic and apoptotic treatment. In vitro assays showed improved internalization only when the liposomes have both targeting systems exposed, demonstrating the synergy of the two peptides in the assisted internalization (Figure 3). In vivo experiments showed an amazing reduction in subcutaneous induced glioma tumours in mice by intratumoral but also by systemic administration. This example represents the collaboration of two targeting agents to improve the vectorization of the system on tissular and cellular levels.

Another representative example of cooperation of multiple tissular and cellular targeting systems is the use of albumin-based systems [64]. Their accumulation properties in tissue are based on two effects: the EPR due to their size and active targeting provided by the glycoprotein gp60 interaction. The protein gp60 is overexpressed in the endothelial cell surface and allows the albumin-based systems to extravasate to the tumour mass through caveola formation and transcytosis. After this, albumin may also bind to the "secreted protein, acidic and rich in cysteine" (SPARC) present in the extracellular matrix, facilitating the approximation to tumoral cells. This is the postulated mechanism of action of Abraxane®, one of the most commonly administered nanomedicines based on albumin today (Figure 4).

Another commonly employed strategy to improve the transportation efficiency of nanosystems is the combination of an unspecific cell penetrating peptide (CPP) with a selective targeting ligand. With this strategy, the nanocarrier combines the selectivity of the receptor–ligand interaction with the power of the CPP for an effective internalization and an endosomal escape to the cytosol (Figure 5). This methodology has been applied by using a combination of RGD-type or NGR-type peptide specific for neovascular tissues with R8 (eight units of arginine) or R4 (four units of arginine) CPP peptides [65,66].

Hierarchical and encrypted sequential targeting – novel strategies for dual targeting

All targeting methodologies described above are obviously of limited clinical use. The coexistence of two active vectorization ligands at the same time and close to each other may lead to unwanted interactions not only between them, but also with the physiological environment during circulation. Furthermore, the existence of positively or negatively charged moieties or active targeting groups on the nanocarrier surface could reduce the circulation time of the systems by off-target accumulation or accelerated clearance by the reticuloendothelial system (RES). This leads to a reduced accumulation of the nanocarriers in the diseased tissue. The concept of spatiotemporally modulated

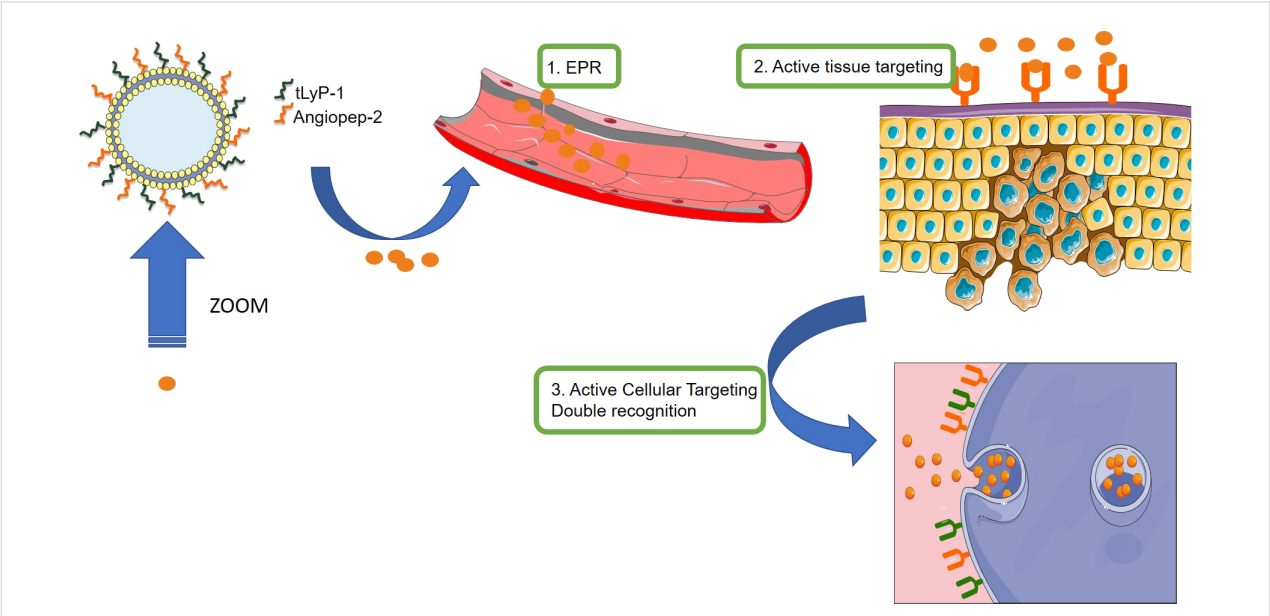

Figure 3: EPR and active targeting working together for glioma tissue accumulation and preferential glioma cells internalization.

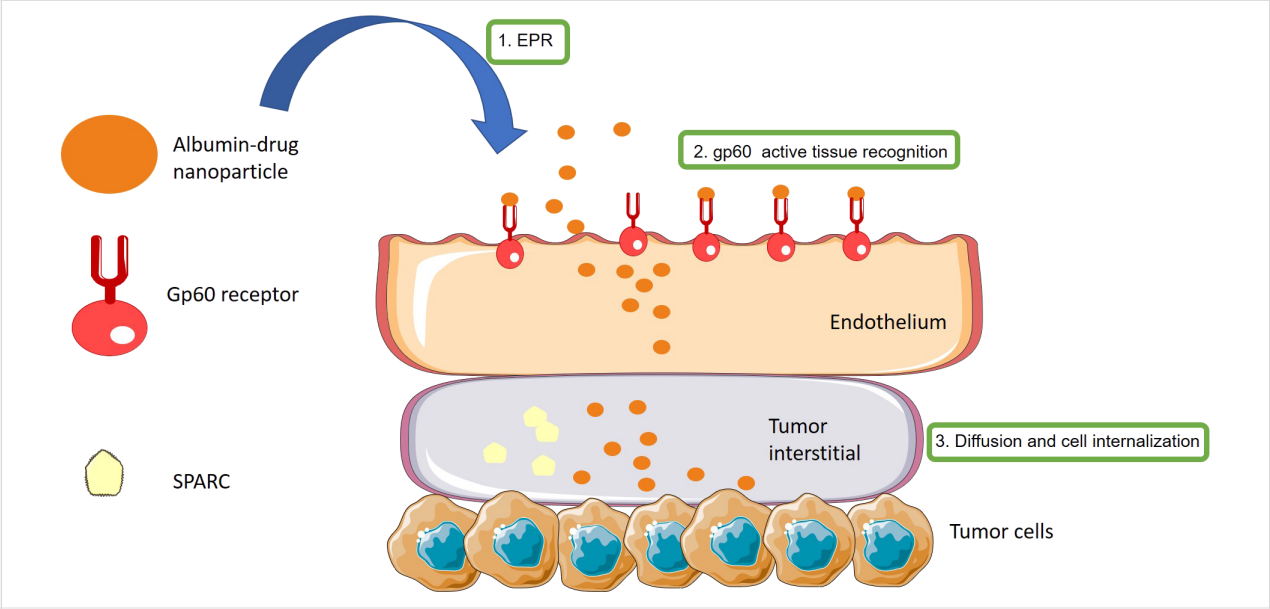

Figure 4: Mechanism of retention and accumulation of Abraxane in tumoral tissue. The authors' own generalized depiction of the scheme proposed previously in [64].

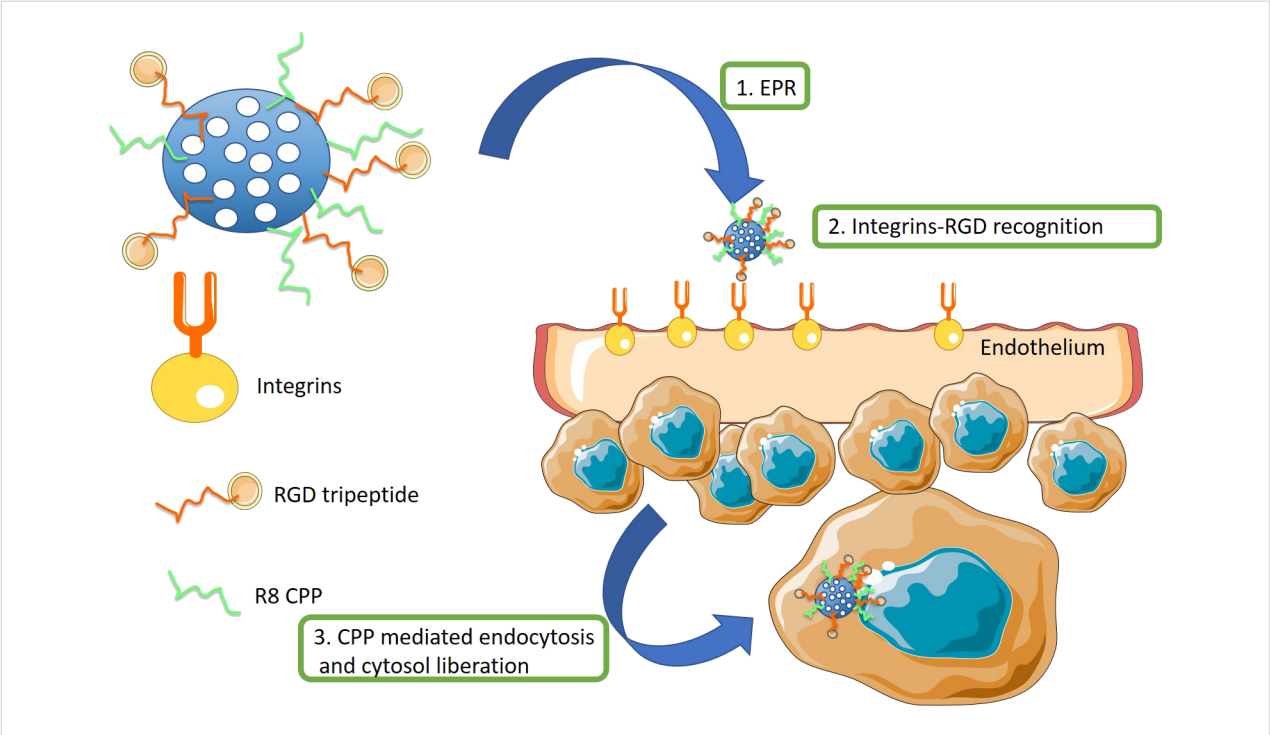

Figure 5: Combination of unspecific CPP and endothelial specific ligands for tissue recognition and efficient internalization on cells.

dual-targeting systems has been introduced lately as a response to these undesired interactions between two targeting motives [67]. With the aim to control and tune the targeting properties depending on time and the localization of the nanocarrier, hierarchical targeting has been recently proposed as a novel strategy [68]. This strategy is based on hiding the targeting moieties and only activating them in the appropriate scenario. Hierarchical targeting systems incorporate stimuli-responsive strategies in such a way that the targeting groups are hidden during the circulation of the carrier through the body and, therefore, the tissular accumulation occurs mainly through the EPR effect. Once the carrier reaches the tumoral tissue, the specific condi-

tions there (e.g., low pH values or the presence of certain enzymes) or the application of an external stimuli (e.g., light, magnetic fields or ultrasound) triggers the targeting inducing the particle uptake into the diseased cells [69-71]. Thus, the targeting is only activated in the malignant tissue, which would significantly reduce the off-target accumulation and the RES clearance. The hierarchical systems can be classified according to the targeting activation mechanism and include changeable particle sizes, switchable surface charges and activatable surface ligands (Figure 6).

There are numerous active vectorization motifs that are capable of being tagged for their deactivation, from small molecules such as folic acid to penetrating (CPP) or homing peptides (RGD-type). The tagged agents may be activated once the system is accumulated in the tumoral tissue by EPR through both internal or external stimuli [72-74]. The tagging motive should be designed specifically for each type of active targeting. To solve this limiting problem of scope, one of the main strategies followed lately is the use of shielding molecules with high molecular weight such as PEG for simply sterically hindering the active vectorization agents. Usually, PEG chains are functionalized through a responsive group over the nanocarrier surface. Thus, PEG plays a dual role. It acts as shield that keeps the targeting agent hidden and it prevents the opsonisation of the nanocarrier, which would be the first step required for a capture by macrophages. When the system reaches the tumoral tissue, the PEG chain is cleaved leaving exposed the targeting ligand for tumoral cell recognition and internalization. In the recent years, several works reported that the use of PEG could induce immunogenic reactions in the host due to the production of anti-PEG antibodies. More research is required to clarify this question [75,76].

The use of shielded targeting agents renders the EPR effect [77,78] the sole reason for nanocarrier accumulation in tumoral tissues [79]. Sometimes this is not effective at all. Double sequential targeting strategies have been proposed as important alternatives. In these systems, there are two targeting agents: a primary moiety selective to the tumour tissue and a secondary moiety selective to tumoral cells but only active when the system reaches the tumoral mass. In 2017, Villaverde et al. [80] described a double sequential encrypted targeting system focused on bone tumour. Bone is usually poorly irrigated and nanoparticles have serious difficulties to reach this tissue. The system is based on a hybrid peptide/polymeric chain that contains a bisphosphonate (BP) group at the end. BP acts as tissular targeting motif, due to its high affinity for the exposed mineral part of bones (hydroxyapatite). An RGD sequence conjugated with a peptide sequence cleavable by the action of cathepsin-K (CK) was incorporated within the hybrid chain. CK is a proteolytic enzyme, which is usually typically overproduced in osteosarcoma tumours. Thus, the complete targeting moiety, which can be conjugated with drugs or nanoparticles, induced the accumulation in diseased bone tissue in which the mineral part is more exposed than in healthy bones due to the disruption of the bone architecture caused by the tumour. When the bone tissue presents a malignancy, the local overexpression

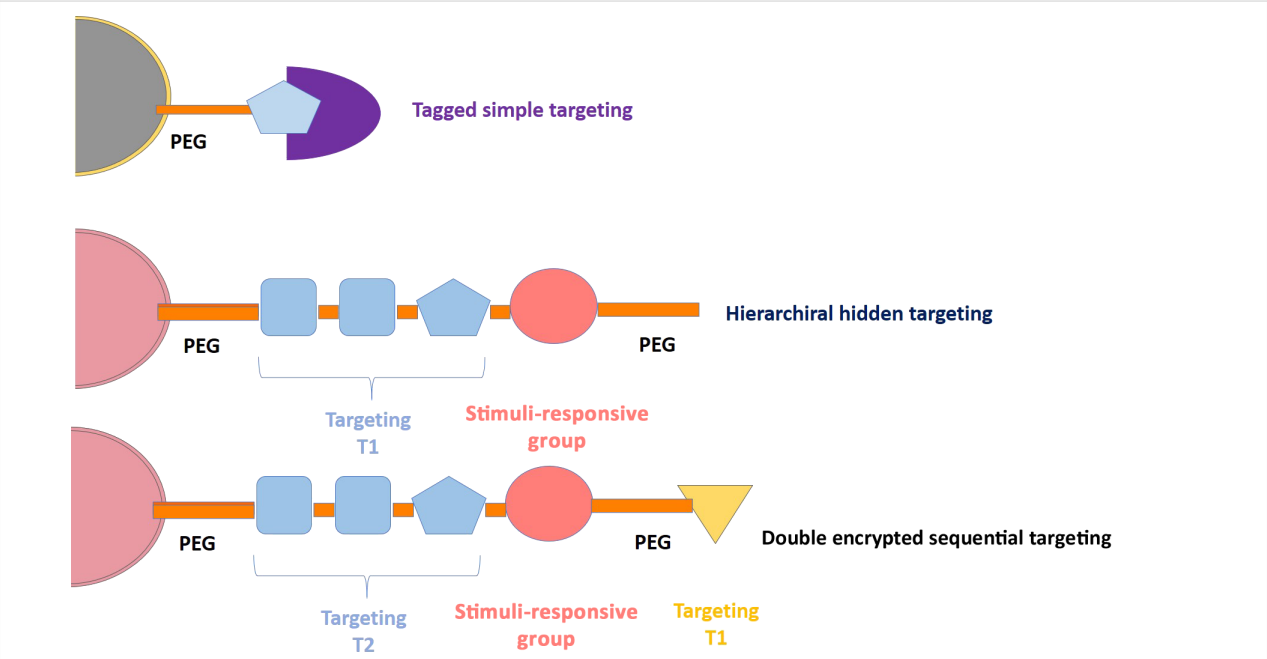

Figure 6: Different strategies for the construction of hierarchical targeting ligands.

of cathepsin-K leads to the detachment of the cargo with a simultaneous exposition of the RGD pattern inducing the internalization of the transported drugs into the tumoral cells.

Double targeting cellular–intracellular trafficking

Besides tissue accumulation, the preferential internalization in tumoral cells is the main goal to improve the efficacy of a drug. Endosomal scape and nanocarrier vectorization to one specific organelle may be essential for improving the therapeutic effect at low concentrations, as has been described above. The combination of subcellular targeting agents that allow for endosomal scape and regulate the intracellular trafficking and a targeting agent directed to cell membrane receptors is a promising strategy for increasing the efficacy of treatments. The presence of both an intracellular and extracellular targeting agent would drive the drug nanotransporter directly to the desired organelle. Many systems use the combination of two different targeting agents to carry out the multi-vectorization process. In other cases, the intracellular and extracellular targeting effects come from the structural properties of the nanocarriers [81]. Usually, the aim of the intracellular vectorization is oriented to nucleus or mitochondria to improve the efficacy of the transported drug for cancer treatments. Fortunately, there are intracellular vectorization motives for almost all subcellular localizations [42,82].

There are many cytotoxic drugs, such as doxorubicin, that induce cell apoptosis through intercalation with nuclear DNA. Further, gene silencing therapies based on an effective delivery of short hairpin RNA (shRNA) bearing genes for small interfering RNA (siRNA) need nuclear vectorization for enhancing the cell growth inhibition. In these cases, the goal is to drive the payload to the nucleus after selective internalization in the cytoplasm. Nuclear delivery with the HIV trans-activator of transcription (TAT) peptoid in combination with the vasculature and tumor cell membrane targeting RGD tripeptide is a novel strategy recently described. Both vectorization agents were grafted on mesoporous silicananoparticles in a random manner [72]. RGD act as tissular and cellular targeting ligand, while TAT act as CPP mediating the endosomal escape and driving the payload to the nucleus. This example reflects how the combination of two targeting agents works on three levels of vectorization, namely tissular, cellular and subcellular targeting.

As mentioned above, there are unwanted interaction effects between two agents, especially in the case of random decoration. Janus systems have become a great alternative for including double functional targeting agents to a nanocarrier. Villegas et al. [83] recently described mesoporous Janus nanoparticles for dual targeting of tumour cells and mitochondria (Figure 7). There are multiple “mitochondriotoxic” drugs that act on mitochondria inducing cell apoptosis, such as gamitrinibs and

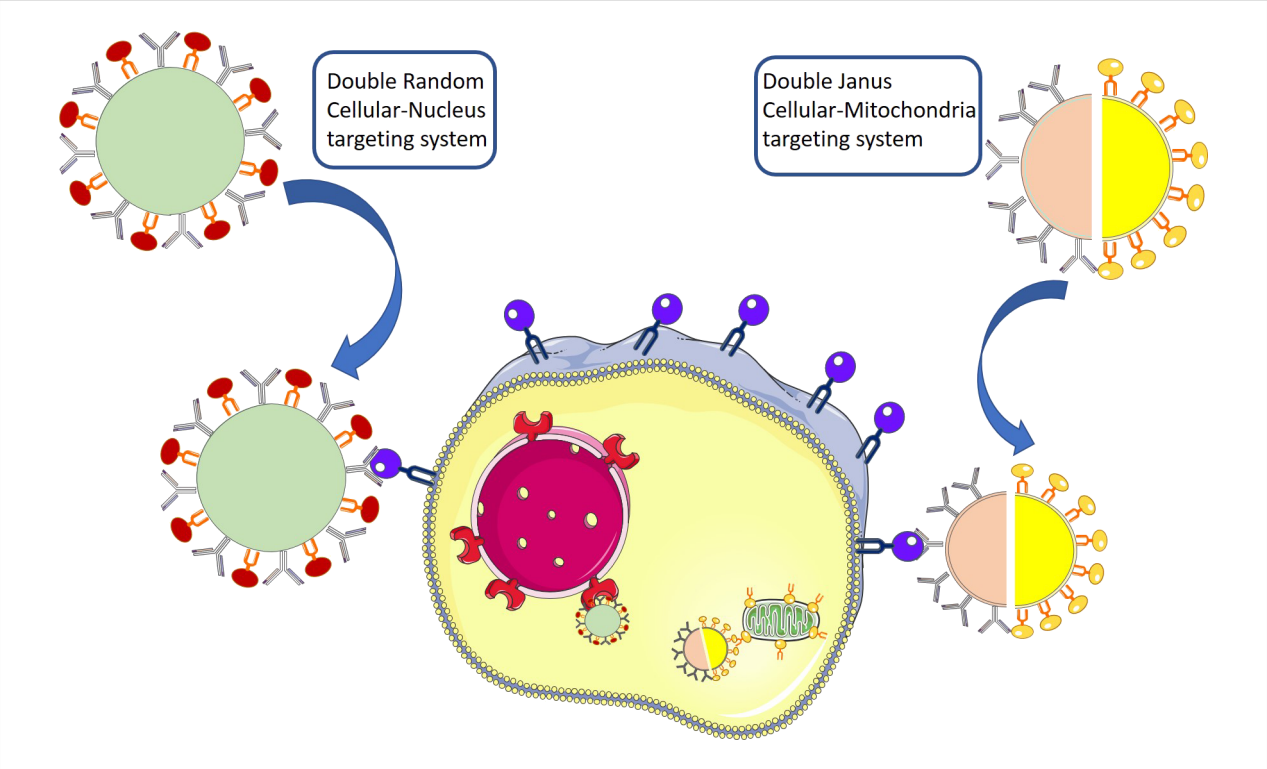

Figure 7: Double cell–organelle targeting strategies.

cisplatin [84]. One of the best ways to bring molecules or nanocarriers to mitochondria is by using positively charged groups. These motives are able to escape from the early endosome and reach to the mitochondria [85,86]. One of the most commonly used cationic groups as mitochondrial targeting agent is the triphenylphosphonium cation (TTP) [87]. The vectorization agents are anchored separately on each of the hemispheres of the nanocarrier through an asymmetrisation process. One hemisphere is functionalized with folic acid as cell membrane targeting ligand and the other hemisphere is functionalized with a TPP analogue, which allows for endosomal escape and drives the nanocarrier to the mitochondria surroundings. This strategy turned out to be successful for the transportation of topotecan to the mitochondrial environment resulting in a highly efficient in vitro treatment of human prostate cancer cells. The excellent performance could be explained by the multivalence effect. The fact of having the same ligand interacting with the same receptor simultaneously without any other non-specific interaction from the other ligand maximized the interactions enhancing the particle uptake.

Double targeting with the same motive: multivalence effect

The design of double targeting agents with the same motive in a single system is nowadays an alternative to inefficient vectorization in the cases in which the single ligand–receptor recognition is not strong enough to induce an enhancement of the cell internalization. Jin et al. [88] developed a double linear RGD-type ligand that was evaluated in comparison to the single counterpart with regard to binding affinity and specificity to integrins in vitro and in vivo. Further, Rosca et al. [89] described effective single, double and triple systems decorated with dodecapeptide with affinity to integrins overexpressed in glioma cells. The effect of multiplying the motives in the structure sharpens the contrast of binding between cancer and healthy cells. The work demonstrated an improvement in terms of selectivity and retention in tumoral tissues overexpressing integrins. Nature uses these types of double interaction moieties as secure systems, the double interaction between ligand and receptor is present in recognition processes of, e.g., DNA and antibodies [90]. The structural flexibility and the distance between the motives yield the desired interaction with the receptor and allow for strongest interactions compared to nonspecific interactions (Figure 8).

Conclusion

The last few decades have witnessed the emergence of nanomedicine in the oncological field. The use of nanoparticles as drug delivery systems provided unique advantages such as the possibility to transport highly lipophilic drugs and to improve the pharmacokinetic profile of these drugs, enhancing their accumulation both in the tumoral tissue and within the malignant cells. Moreover, it is even possible to control the drug release process through the incorporation of stimuli-responsive mechanisms that regulate the drug release from the nanocarrier. The incorporation of targeting moieties on the carrier surface produces a significative increase in the particle accumulation inside tumoral cells, which could improve the efficacy of the therapy due to the high amount of drug that is possible to deliver into the diseased cells, and by the reduction of side effects. Despite the encouraging results there is much work left to be done until these targeted nanocarriers fulfill the high expectations. Many of these systems have been tested employing in vitro assays, or xenograft in vivo models in the best cases. The fact that excellent results are observed with these assays does not guarantee the same behaviour in clinical trials due to the huge complexity of real tumours. It is compulsory to evaluate the real efficacy of the targeted nanodevices in more

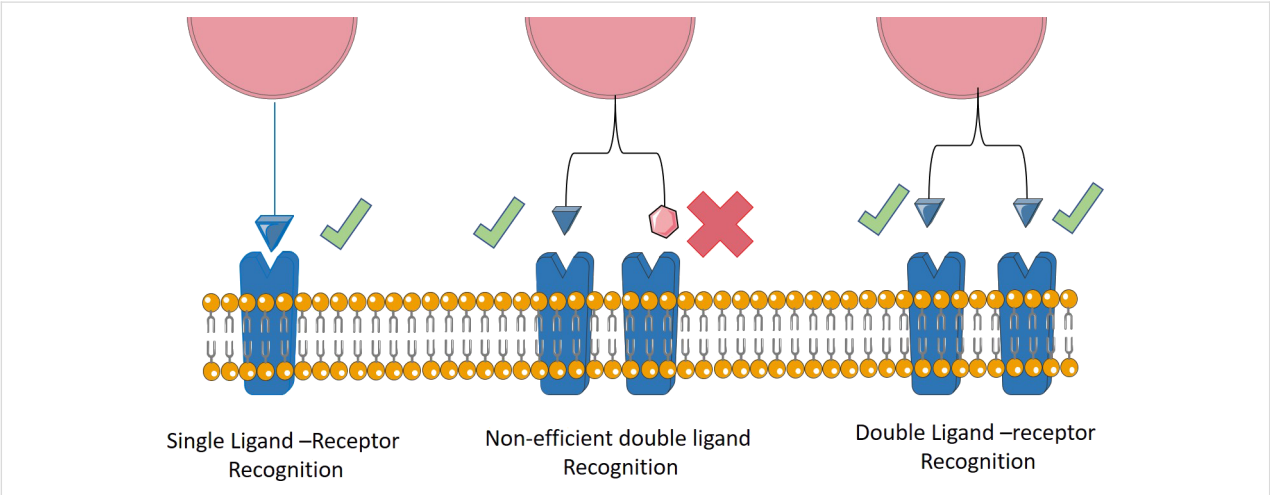

Figure 8: Multivalence effect in multiple targeting systems.

realistic scenarios such as the utilization of orthotopic animal models in which the tumour growths in its natural environment. Additionally, the efficacy of these systems should be studied employing immunocompetent animal models to study how a fully operative immune system reacts to the administered nanocarriers. In any case, we are at the beginning of nanomedicine. The excellent results obtained until now paved the way for the development of novel and more functional targeted nanocarriers that would eradicate devastating diseases in the coming future.

Acknowledgements

The authors would like to acknowledge the financial support that the Spanish Government have provided during the last decade which allow us to carry out our research in form of scholarships: F.P.U (AB) and F.P.I (GV) grant from Ministerio de Educación y Ciencia and research projects in different calls. We hope that the commitment of Spanish government with the formation of new scientists and the development of cutting-edge research will be increased even more in the coming years.

ORCID® iDs

Alejandro Baeza - https://orcid.org/0000-0002-9042-8865

References

1. Tong, R.; Langer, R. *Cancer J.* **2015,** *21,* 314–321. doi:10.1097/ppo.0000000000000123
2. Tibbitt, M. W.; Dahlman, J. E.; Langer, R. *J. Am. Chem. Soc.* **2016,** *138,* 704–717. doi:10.1021/jacs.5b09974
3. Howes, P. D.; Chandrawati, R.; Stevens, M. M. *Science* **2014,** *346,* 1247390. doi:10.1126/science.1247390
4. Sánchez, S.; Soler, L.; Katuri, J. *Angew. Chem., Int. Ed.* **2015,** *54,* 1414–1444. doi:10.1002/anie.201406096
5. Matsumura, Y.; Maeda, H. *Cancer Res.* **1986,** *46,* 6387–6392.
6. Maeda, H.; Nakamura, H.; Fang, J. *Adv. Drug Delivery Rev.* **2013,** *65,* 71–79. doi:10.1016/j.addr.2012.10.002
7. Bar-Zeev, M.; Livney, Y. D.; Assaraf, Y. G. *Drug Resist. Updates* **2017,** *31,* 15–30. doi:10.1016/j.drup.2017.05.002
8. Jain, R. K.; Stylianopoulos, T. *Nat. Rev. Clin. Oncol.* **2010,** *7,* 653–664. doi:10.1038/nrclinonc.2010.139
9. Nichols, J. W.; Bae, Y. H. *J. Controlled Release* **2014,** *190,* 451–464. doi:10.1016/j.jconrel.2014.03.057
10. Nehoff, H.; Parayath, N. N.; Domanovitch, L.; Taurin, S.; Greish, K. *Int. J. Nanomed.* **2014,** *9,* 2539–2555. doi:10.2147/ijn.s47129
11. Netti, P. A.; Baxter, L. T.; Boucher, Y.; Skalak, R.; Jam, R. K. *Cancer Res.* **1995,** *55,* 5451–5458.
12. Khawar, I. A.; Kim, J. H.; Kuh, H.-J. *J. Controlled Release* **2015,** *201,* 78–89. doi:10.1016/j.jconrel.2014.12.018
13. Paris, J. L.; Mannaris, C.; Cabañas, M. V.; Carlisle, R.; Manzano, M.; Vallet-Regí, M.; Coussios, C. C. *Chem. Eng. J.* **2018,** *340,* 2–8. doi:10.1016/j.cej.2017.12.051
14. McKee, T. D.; Grandi, P.; Mok, W.; Alexandrakis, G.; Insin, N.; Zimmer, J. P.; Bawendi, M. G.; Boucher, Y.; Breakefield, X. O.; Jain, R. K. *Cancer Res.* **2006,** *66,* 2509–2513. doi:10.1158/0008-5472.can-05-2242
15. Villegas, M. R.; Baeza, A.; Vallet-Regí, M. *ACS Appl. Mater. Interfaces* **2015,** *7,* 24075–24081. doi:10.1021/acsami.5b07116
16. Villegas, M. R.; Baeza, A.; Noureddine, A.; Durfee, P. N.; Butler, K. S.; Agola, J. O.; Brinker, C. J.; Vallet-Regí, M. *Chem. Mater.* **2018,** *30,* 112–120. doi:10.1021/acs.chemmater.7b03128
17. Egeblad, M.; Nakasone, E. S.; Werb, Z. *Dev. Cell* **2010,** *18,* 884–901. doi:10.1016/j.devcel.2010.05.012
18. Ediriwickrema, A.; Saltzman, W. M. *ACS Biomater. Sci. Eng.* **2015,** *1,* 64–78. doi:10.1021/ab500084g
19. Lee, K. Y.; Seow, E.; Zhang, Y.; Lim, Y. C. *Biomaterials* **2013,** *34,* 4860–4871. doi:10.1016/j.biomaterials.2013.03.029
20. Martínez-Carmona, M.; Baeza, A.; Rodriguez-Milla, M. A.; García-Castro, J.; Vallet-Regí, M. *J. Mater. Chem. B* **2015,** *3,* 5746–5752. doi:10.1039/c5tb00304k
21. Vaillant, O.; El Cheikh, K.; Warther, D.; Brevet, D.; Maynadier, M.; Bouffard, E.; Salgues, F.; Jeanjean, A.; Puche, P.; Mazerolles, C.; Maillard, P.; Mongin, O.; Blanchard-Desce, M.; Raehm, L.; Rebillard, X.; Durand, J. O.; Gary-Bobo, M.; Morere, A.; García, M. *Angew. Chem., Int. Ed.* **2015,** *54,* 5952–5956. doi:10.1002/anie.201500286
22. Yang, K. S.; Budin, G.; Tassa, C.; Kister, O.; Weissleder, R. *Angew. Chem., Int. Ed.* **2013,** *52,* 10593–10597. doi:10.1002/anie.201304096
23. Villaverde, G.; Baeza, A.; Melen, G. J.; Alfranca, A.; Ramirez, M.; Vallet-Regí, M. *J. Mater. Chem. B* **2015,** *3,* 4831–4842. doi:10.1039/c5tb00287g
24. Feng, G.; Qin, W.; Hu, Q.; Tang, B. Z.; Liu, B. *Adv. Healthcare Mater.* **2015,** *4,* 2667–2676. doi:10.1002/adhm.201500431
25. Weissleder, R.; Kelly, K.; Sun, E. Y.; Shtatland, T.; Josephson, L. *Nat. Biotechnol.* **2005,** *23,* 1418–1423. doi:10.1038/nbt1159
26. Vivek, R.; Thangam, R.; NipunBabu, V.; Rejeeth, C.; Sivasubramanian, S.; Gunasekaran, P.; Muthuchelian, K.; Kannan, S. *ACS Appl. Mater. Interfaces* **2014,** *6,* 6469–6480. doi:10.1021/am406012g
27. Chen, F.; Hong, H.; Zhang, Y.; Valdovinos, H. F.; Shi, S.; Kwon, G. S.; Theuer, C. P.; Barnhart, T. E.; Cai, W. *ACS Nano* **2013,** *7,* 9027–9039. doi:10.1021/nn403617j
28. Yu, M. K.; Park, J.; Jon, S. *Theranostics* **2012,** *2,* 3–44. doi:10.7150/thno.3463
29. Agarwal, P.; Bertozzi, C. R. *Bioconjugate Chem.* **2015,** *26,* 176–192. doi:10.1021/bc5004982
30. Mazzucchelli, S.; Colombo, M.; De Palma, C.; Salvadè, A.; Verderio, P.; Coghi, M. D.; Clementi, E.; Tortora, P.; Corsi, F.; Prosperi, D. *ACS Nano* **2010,** *4,* 5693–5702. doi:10.1021/nn101307r
31. Field, L. D.; Delehanty, J. B.; Chen, Y.; Medintz, I. L. *Acc. Chem. Res.* **2015,** *48,* 1380–1390. doi:10.1021/ar500449v
32. Lin, R.-Y.; Dayananda, K.; Chen, T.-J.; Chen, C.-Y.; Liu, G.-C.; Lin, K.-L.; Wang, Y.-M. *Contrast Media Mol. Imaging* **2012,** *7,* 7–18. doi:10.1002/cmmi.457
33. Chen, W.; Jarzyna, P. A.; van Tilborg, G. A. F.; Nguyen, V. A.; Cormode, D. P.; Klink, A.; Griffioen, A. W.; Randolph, G. J.; Fisher, E. A.; Mulder, W. J. M.; Fayad, Z. A. *FASEB J.* **2010,** *24,* 1689–1699. doi:10.1096/fj.09-139865
34. Sugahara, K. N.; Teesalu, T.; Karmali, P. P.; Kotamraju, V. R.; Agemy, L.; Girard, O. M.; Hanahan, D.; Mattrey, R. F.; Ruoslahti, E. *Cancer Cell* **2009,** *16,* 510–520. doi:10.1016/j.ccr.2009.10.013
35. Alberici, L.; Roth, L.; Sugahara, K. N.; Agemy, L.; Kotamraju, V. R.; Teesalu, T.; Bordignon, C.; Traversari, C.; Rizzardi, G.-P.; Ruoslahti, E. *Cancer Res.* **2013,** *73,* 804–812. doi:10.1158/0008-5472.can-12-1668

36. Negussie, A. H.; Miller, J. L.; Reddy, G.; Drake, S. K.; Wood, B. J.; Dreher, M. R. *J. Controlled Release* **2010,** *143,* 265–273. doi:10.1016/j.jconrel.2009.12.031
37. Darmostuk, M.; Rimpelova, S.; Gbelcova, H.; Ruml, T. *Biotechnol. Adv.* **2015,** *33,* 1141–1161. doi:10.1016/j.biotechadv.2015.02.008
38. Keefe, A. D.; Pai, S.; Ellington, A. *Nat. Rev. Drug Discovery* **2010,** *9,* 537–550. doi:10.1038/nrd3141
39. Melancon, M. P.; Zhou, M.; Zhang, R.; Xiong, C.; Allen, P.; Wen, X.; Huang, Q.; Wallace, M.; Myers, J. N.; Stafford, R. J.; Liang, D.; Ellington, A. D.; Li, C. *ACS Nano* **2014,** *8,* 4530–4538. doi:10.1021/nn406632u
40. Bates, P. J.; Laber, D. A.; Miller, D. M.; Thomas, S. D.; Trent, J. O. *Exp. Mol. Pathol.* **2009,** *86,* 151–164. doi:10.1016/j.yexmp.2009.01.004
41. Ma, X.; Gong, N.; Zhong, L.; Sun, J.; Liang, X.-J. *Biomaterials* **2016,** *97,* 10–21. doi:10.1016/j.biomaterials.2016.04.026
42. Rajendran, L.; Knölker, H.-J.; Simons, K. *Nat. Rev. Drug Discovery* **2010,** *9,* 29–42. doi:10.1038/nrd2897
43. Yoong, S. L.; Wong, B. S.; Zhou, Q. L.; Chin, C. F.; Li, J.; Venkatesan, T.; Ho, H. K.; Yu, V.; Ang, W. H.; Pastorin, G. *Biomaterials* **2014,** *35,* 748–759. doi:10.1016/j.biomaterials.2013.09.036
44. Smith, R. A. J.; Porteous, C. M.; Gane, A. M.; Murphy, M. P. *Proc. Natl. Acad. Sci. U. S. A.* **2003,** *100,* 5407–5412. doi:10.1073/pnas.0931245100
45. Sakhrani, N. M.; Padh, H. *Drug Des., Dev. Ther.* **2013,** *7,* 585. doi:10.2147/dddt.s45614
46. D'Souza, G. G.; Weissig, V. *Expert Opin. Drug Delivery* **2009,** *6,* 1135–1148. doi:10.1517/17425240903236101
47. Li, L.; Hou, J.; Liu, X.; Guo, Y.; Wu, Y.; Zhang, L.; Yang, Z. *Biomaterials* **2014,** *35,* 3840–3850. doi:10.1016/j.biomaterials.2014.01.019
48. Kotula, J. W.; Pratico, E. D.; Ming, X.; Nakagawa, O.; Juliano, R. L.; Sullenger, B. A. *Nucleic Acid Ther.* **2012,** *22,* 187–195. doi:10.1089/nat.2012.0347
49. Sandvig, K.; van Deurs, B. *Annu. Rev. Cell Dev. Biol.* **2002,** *18,* 1–24. doi:10.1146/annurev.cellbio.18.011502.142107
50. Acharya, S.; Hill, R. A. *Nanomedicine (N. Y., NY, U. S.)* **2014,** *10,* 329–337. doi:10.1016/j.nano.2013.07.015
51. Sahay, G.; Alakhova, D. Y.; Kabanov, A. V. *J. Controlled Release* **2010,** *145,* 182–195. doi:10.1016/j.jconrel.2010.01.036
52. Varkouhi, A. K.; Scholte, M.; Storm, G.; Haisma, H. J. *J. Controlled Release* **2011,** *151,* 220–228. doi:10.1016/j.jconrel.2010.11.004
53. Moreira, C.; Oliveira, H.; Pires, L. R.; Simões, S.; Barbosa, M. A.; Pêgo, A. P. *Acta Biomater.* **2009,** *5,* 2995–3006. doi:10.1016/j.actbio.2009.04.021
54. Miller, D. K.; Griffiths, E.; Lenard, J.; Firestone, R. A. *J. Cell Biol.* **1983,** *97,* 1841–1851. doi:10.1083/jcb.97.6.1841
55. Hatakeyama, H.; Ito, E.; Akita, H.; Oishi, M.; Nagasaki, Y.; Futaki, S.; Harashima, H. *J. Controlled Release* **2009,** *139,* 127–132. doi:10.1016/j.jconrel.2009.06.008
56. Schloßbauer, A.; Sauer, A. M.; Cauda, V.; Schmidt, A.; Engelke, H.; Rothbauer, U.; Zolghadr, K.; Leonhardt, H.; Bräuchle, C.; Bein, T. *Adv. Healthcare Mater.* **2012,** *1,* 316–320. doi:10.1002/adhm.201100033
57. Dai, Q.; Wilhelm, S.; Ding, D.; Syed, A. M.; Sindhwani, S.; Zhang, Y.; Chen, Y. Y.; MacMillan, P.; Chan, W. C. W. *ACS Nano* **2018,** *12,* 8423–8435. doi:10.1021/acsnano.8b03900
58. Wu, X.; Chen, J.; Wu, M.; Zhao, J. X. *Theranostics* **2015,** *5,* 322–344. doi:10.7150/thno.10257
59. Kydd, J.; Jadia, R.; Velpurisiva, P.; Gad, A.; Paliwal, S.; Rai, P. *Pharmaceutics* **2017,** *9,* 46. doi:10.3390/pharmaceutics9040046
60. Wang, A. Z. *Sci. Transl. Med.* **2015,** *7,* 294ec112. doi:10.1126/scitranslmed.aac8108
61. Kobayashi, H.; Watanabe, R.; Choyke, P. L. *Theranostics* **2014,** *4,* 81–89. doi:10.7150/thno.7193
62. Yang, Z.-Z.; Li, J.-Q.; Wang, Z.-Z.; Dong, D.-W.; Qi, X.-R. *Biomaterials* **2014,** *35,* 5226–5239. doi:10.1016/j.biomaterials.2014.03.017
63. Pardridge, W. M. *Drug Discovery Today* **2007,** *12,* 54–61. doi:10.1016/j.drudis.2006.10.013
64. Elsadek, B.; Kratz, F. *J. Controlled Release* **2012,** *157,* 4–28. doi:10.1016/j.jconrel.2011.09.069
65. Takara, K.; Hatakeyama, H.; Ohga, N.; Hida, K.; Harashima, H. *Int. J. Pharm.* **2010,** *396,* 143–148. doi:10.1016/j.ijpharm.2010.05.002
66. Kibria, G.; Hatakeyama, H.; Ohga, N.; Hida, K.; Harashima, H. *J. Controlled Release* **2011,** *153,* 141–148. doi:10.1016/j.jconrel.2011.03.012
67. Doolittle, E.; Peiris, P. M.; Doron, G.; Goldberg, A.; Tucci, S.; Rao, S.; Shah, S.; Sylvestre, M.; Govender, P.; Turan, O.; Lee, Z.; Schiemann, W. P.; Karathanasis, E. *ACS Nano* **2015,** *9,* 8012–8021. doi:10.1021/acsnano.5b01552
68. Wang, S.; Huang, P.; Chen, X. *Adv. Mater.* **2016,** *28,* 7340–7364. doi:10.1002/adma.201601498
69. Wang, Y.; Kohane, D. S. *Nat. Rev. Mater.* **2017,** *2,* 17020. doi:10.1038/natrevmats.2017.20
70. Paris, J. L.; Manzano, M.; Cabañas, M. V.; Vallet-Regí, M. *Nanoscale* **2018,** *10,* 6402–6408. doi:10.1039/c8nr00693h
71. Wang, J.; Wang, F.; Li, F.; Zhang, W.; Shen, Y.; Zhou, D.; Guo, S. *J. Mater. Chem. B* **2016,** *4,* 2954–2962. doi:10.1039/c5tb02450a
72. Xiao, D.; Jia, H.-Z.; Zhang, J.; Liu, C.-W.; Zhuo, R.-X.; Zhang, X.-Z. *Small* **2014,** *10,* 591–598. doi:10.1002/smll.201301926
73. Zhao, D.; Yi, X.; Yuan, G.; Zhuo, R.; Li, F. *Macromol. Biosci.* **2017,** *17,* 1700150. doi:10.1002/mabi.201700150
74. Li, J.; Liu, F.; Shao, Q.; Min, Y.; Costa, M.; Yeow, E. K. L.; Xing, B. *Adv. Healthcare Mater.* **2014,** *3,* 1230–1239. doi:10.1002/adhm.201300613
75. Schellekens, H.; Hennink, W. E.; Brinks, V. *Pharm. Res.* **2013,** *30,* 1729–1734. doi:10.1007/s11095-013-1067-7
76. Yang, Q.; Lai, S. K. *Wiley Interdiscip. Rev.: Nanomed. Nanobiotechnol.* **2015,** *7,* 655–677. doi:10.1002/wnan.1339
77. Fang, J.; Nakamura, H.; Maeda, H. *Adv. Drug Delivery Rev.* **2011,** *63,* 136–151. doi:10.1016/j.addr.2010.04.009
78. Nakamura, H.; Jun, F.; Maeda, H. *Expert Opin. Drug Delivery* **2015,** *12,* 53–64. doi:10.1517/17425247.2014.955011
79. Zhang, J.; Yuan, Z.-F.; Wang, Y.; Chen, W.-H.; Luo, G.-F.; Cheng, S.-X.; Zhuo, R.-X.; Zhang, X.-Z. *J. Am. Chem. Soc.* **2013,** *135,* 5068–5073. doi:10.1021/ja312004m
80. Villaverde, G.; Nairi, V.; Baeza, A.; Vallet-Regí, M. *Chem. – Eur. J.* **2017,** *23,* 7174–7179. doi:10.1002/chem.201605947
81. He, W.; Yan, J.; Sui, F.; Wang, S.; Su, X.; Qu, Y.; Yang, Q.; Guo, H.; Ji, M.; Lu, W.; Shao, Y.; Hou, P. *ACS Nano* **2018,** *12,* 11664–11677. doi:10.1021/acsnano.8b07079
82. Sakhrani, N. M.; Padh, H. *Drug Des., Dev. Ther.* **2013,** *7,* 585. doi:10.2147/dddt.s45614
83. López, V.; Villegas, M. R.; Rodríguez, V.; Villaverde, G.; Lozano, D.; Baeza, A.; Vallet-Regí, M. *ACS Appl. Mater. Interfaces* **2017,** *9,* 26697–26706. doi:10.1021/acsami.7b06906
84. Kang, B. H.; Plescia, J.; Song, H. Y.; Meli, M.; Colombo, G.; Beebe, K.; Scroggins, B.; Neckers, L.; Altieri, D. C. *J. Clin. Invest.* **2009,** *119,* 454–464. doi:10.1172/jci37613

85. Hickey, J. L.; Ruhayel, R. A.; Barnard, P. J.; Baker, M. V.; Berners-Price, S. J.; Filipovska, A. *J. Am. Chem. Soc.* **2008,** *130,* 12570–12571. doi:10.1021/ja804027j
86. Chen, M.; Bhattarai, N.; Cong, M.; Pérez, R. L.; McDonough, K. C.; Warner, I. M. *RSC Adv.* **2018,** *8,* 31700–31709. doi:10.1039/c8ra05484c
87. Luo, G. F.; Chen, W. H.; Liu, Y.; Lei, Q.; Zhuo, R.-X.; Zhang, X.-Z. *Sci. Rep.* **2014,** *4,* 6064. doi:10.1038/srep06064
88. Jin, Z.-H.; Furukawa, T.; Waki, A.; Akaji, K.; Coll, J.-L.; Saga, T.; Fujibayashi, Y. *Biol. Pharm. Bull.* **2010,** *33,* 370–378. doi:10.1248/bpb.33.370
89. Rosca, E. V.; Stukel, J. M.; Gillies, R. J.; Vagner, J.; Caplan, M. R. *Biomacromolecules* **2007,** *8,* 3830–3835. doi:10.1021/bm700791a
90. Nguyen, T. Q. N.; Lim, K. W.; Phan, A. T. *Sci. Rep.* **2017,** *7,* 11969. doi:10.1038/s41598-017-10583-9

License and Terms

BEILSTEIN JOURNAL OF NANOTECHNOLOGY

Mechanism of silica–lysozyme composite formation unravelled by in situ fast SAXS

Tomasz M. Stawski*[1], Daniela B. van den Heuvel[2,3], Rogier Besselink[1,4], Dominique J. Tobler[5] and Liane G. Benning[1,2,6]

Full Research Paper

Open Access

Address:
[1]German Research Centre for Geosciences, GFZ, Interface Geochemistry, Telegrafenberg, 14473, Potsdam, Germany, [2]School of Earth and Environment, University of Leeds, Woodhouse Lane, LS2 9 JT, Leeds, UK, [3]Rock-Water Interaction Group, Institute of Geological Sciences, University of Bern, Baltzerstrasse 3, 3012, Bern, Switzerland, [4]Université Grenoble Alpes, Université Savoie Mont Blanc, CNRS, IRD, IFSTTAR, ISTerre, 38000 Grenoble, France, [5]Nano-Science Center, Department of Chemistry, University of Copenhagen, Universitetsparken 5, 2100, Copenhagen, Denmark and [6]Department of Earth Sciences, Free University of Berlin, Malteserstr. 74–100 / Building A, 12249, Berlin, Germany

Email:
Tomasz M. Stawski* - stawski@gfz-potsdam.de

* Corresponding author

Keywords:
composite; lysozyme; scattering; silica; small-angle X-ray scattering (SAXS)

Beilstein J. Nanotechnol. **2019,** *10,* 182–197.
doi:10.3762/bjnano.10.17

Received: 09 August 2018
Accepted: 11 December 2018
Published: 14 January 2019

This article is part of the thematic issue "Advanced hybrid nanomaterials".

Guest Editor: V. de Zea Bermudez

Abstract

A quantitative understanding of aggregation mechanisms leading to the formation of composites of inorganic nanoparticles (NPs) and proteins in aqueous media is of paramount interest for colloid chemistry. In particular, the interactions between silica (SiO_2) NPs and lysozyme (LZM) have attracted attention, because LZM is well-known to adsorb strongly to silica NPs, while at the same time preserving its enzymatic activity. The inherent nature of the aggregation processes leading to NP–LZM composites involves structural changes at length scales from few to at least hundreds of nanometres but also time scales much smaller than one second. To unravel these we used in situ synchrotron-based small-angle X-ray scattering (SAXS) and followed the subtle interparticle interactions in solution at a time resolution of 50 ms/frame (20 fps). We show that if the size of silica NPs (ca. 5 nm diameter) is matched by the dimensions of LZM, the evolving scattering patterns contain a unique structure-factor contribution originating from the presence of LZM. We developed a scattering model and applied it to analyse this structure function, which allowed us to extract structural information on the deformation of lysozyme molecules during aggregation, as well as to derive the mechanisms of composite formation.

Introduction

A mechanistic understanding of aggregation in aqueous media leading to the formation of composites of inorganic nanoparticles and proteins is of paramount interest for colloid chemistry, Earth sciences, or the design of protein-sensitized biomedical devices and sensors [1-6]. In a broader perspective, many processes involving the assembly of nanoparticles to higher-level hierarchical structures are known to be directed by small organic molecules and macromolecules [7-10]. Such fundamental interactions are the key to understand the crystallisation of biominerals in living organisms (e.g., in bone formation), and to manufacture better functional materials [11-15].

In particular, composites of amorphous silica (SiO_2) nanoparticles (NPs) and lysozyme (LZM) have attracted attention because silica NPs readily form in many Earth surface environments (e.g., oceans, hot springs) where biological activity dominates (e.g., diatom formation) but they are also key components in numerous technological applications from electronics to paint production. In turn, lysozyme adsorbs strongly to silica NPs [16-18], while at the same time preserving its enzymatic activity, most notably antibacterial properties [19]. Over a wide range of pH values (2 to ca. 10), the surface of silica NPs is negatively charged, whereas the LZM molecule is positively charged [20,21]. This way LZM can act as a bridge between silica NPs, leading to aggregation and flocculation and thus to large silica NP–LZM composites. In the SiO_2–LZM model system, a number of studies investigating the relationship between silica NP sizes, and adsorption modes of lysozyme revealed a correlation between composite properties and the folding/structure of the protein, its enzymatic activity and the exact protein localization with respect to the silica NPs inside flocculated composites [16,17,19,21-24]. The inherent nature of the aggregation processes leading to silica–lysozyme composites, involves structural changes at length scales from a few to hundreds of nanometres, which makes this system well-suited to be characterized by scattering methods. In particular, recent advances [25,26] in detector technology for synchrotron-based in situ and time-resolved small-angle X-ray scattering (SAXS), now allow one to follow all steps in the formation of SiO_2–LZM composites from the individual components. Nevertheless, although such scattering data will reflect the in situ state of a system during measurement, the quantitative information related to any changes in structural properties of the particles/species of interest can only be accessed by developing, testing and validating relevant models and bespoke data analysis methods.

In this study we show step-by-step how a scattering model was developed, verified and applied to time-resolved synchrotron-based SAXS data in which we followed in situ the lysozyme-induced aggregation of silica NPs (ca. 5 nm in diameter) at a time resolution of 50 ms. It is important to note that at typical NPs sizes and concentrations [17,24] and protein concentrations [27] usually employed to make such SiO_2–LZM composites, the relative X-ray scattering contrast/intensity of lysozyme, in the presence of silica, is insufficient to determine the protein contribution to the overall scattering pattern (ratio of ca. 1:100 between LZM and NPs), and only the NP component can directly be followed. However, through this study we demonstrate that if the size of the silica NPs is matched with the dimensions of lysozyme (ellipsoidal molecule [28] $3 \times 3 \times 4.5$ nm^3), the evolving scattering patterns contain a unique structure-factor contribution originating from the presence of lysozyme, and this way this important contribution can be assessed. The analysis of this structure function through the derived model then allowed us to extract detailed structural information on the deformation of the LZM molecules upon aggregation, and to determine the mechanisms of the formation of SiO_2–LZM composites.

Results and Discussion

This section of the manuscript is organised in the following way: (1) data presentation and a discussion of general trends; (2) derivation of a self-consistent mathematical model to fit the timer-resolved scattering curves; (3) presentation of the quantitative results from the model fits; (4) discussion of the quantitative trends.

Evolution of SAXS patterns and derived aggregation stages

Upon mixing of the silica NPs and the LZM solution we observed very fast flocculation, which indicated the formation of the composites. In Figure 1 we show an overview of these formation processes based on SAXS data collected at a time resolution of 50 ms and spanning ca. 300 s.

In a contour plot of the time-resolved scattering patterns (Figure 1A), one can distinguish four characteristic time periods (I–IV) and one region of interest (ROI V), which spanned through periods II to IV. Period I corresponds to the initial ca. 24 s of the scattering patterns of silica NPs before the injection of lysozyme. Based on this data we determined the initial form factor (size distribution) of the silica NPs prior to mixing with lysozyme (Figure 1B). The scattering pattern in a log–log representation prominently flattens out at low q (i.e., $I(q) \propto q^0$). This shows that the initial silica NPs were not aggregated and well-suspended. We derived a discrete size distribution (histogram in the inset of Figure 1B) for the NPs from the Monte Carlo fit implemented [29,30] in MCSAS under the a priori assumption that the NPs were spherical in shape [31] (physicochemical parameters of amorphous silica given in Table S1, Supporting Information File 1). The as-obtained histogram indi-

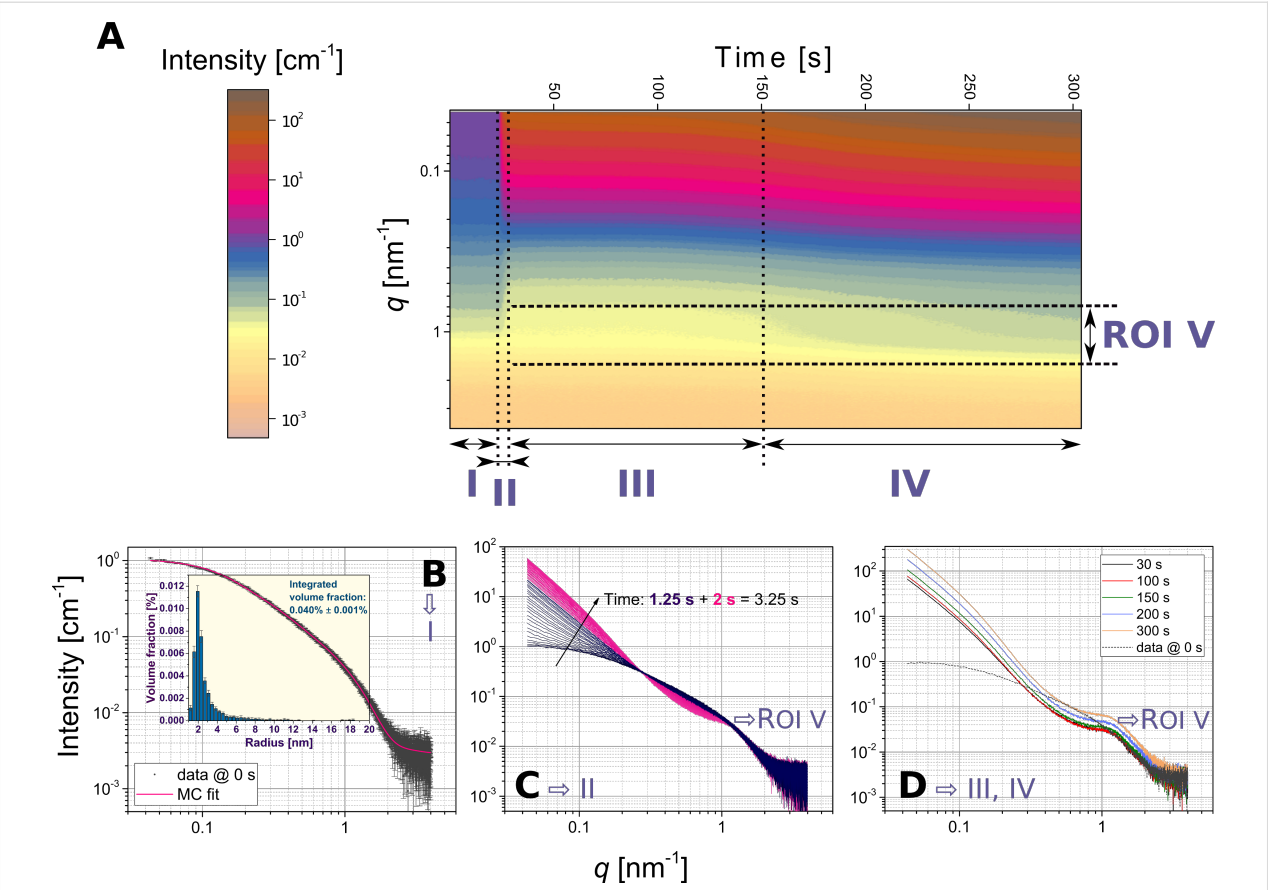

Figure 1: Time-resolved and in situ SAXS patterns documenting the formation of silica–lysozyme aggregates from an experiment where data was recorded at a rate of 50 ms/pattern (20 fps); A) contour plot depicting the scattering intensity as a function of q and time. The changes in the data reveal four distinct time periods; I – scattering from pure silica NPs, II – the moment of lysozyme injection, III – the growth of the aggregates/composites with the original form factor of the silica NPs preserved, and IV – further growth of aggregates and a change in the original silica NPs. We further identified a q-range as a region of interest "ROI V" indicating a local maximum due to interparticle correlations; B) the initial silica NP form factor with a Monte Carlo (MC) fit and the derived discrete particle size distribution (inset); C) the scattering data for period II showing the time frames spanning the injection of the LZM solution between 24.25 s and 27.50 s of the experiment, with the first 1.25 s (blue) dominated by the formation of large aggregates, followed by ca. 2 s (pink) during which the local maximum related to the interparticle interactions (ROI V) clearly developed; D) selected patterns spanning periods III and IV highlighting the differences in the form factor of the silica particles (q > 1.5 nm^{-1}). In C) and D) the data uncertainties are not shown for clarity.

cated that the size distribution was relatively narrow with a mean radius of 2.53 ± 0.01 nm (distribution statistics given in Table S2, Supporting Information File 1). The total integrated volume fraction for the NPs obtained from the fit, was 0.040% ± 0.001%, which matches very closely the expected value of 0.041% calculated for silica NP precipitated from a 1000 ppm SiO_2 solution at pH 7.5 and 21 °C (Table S1, Supporting Information File 1, calculated with PHREEQC [32]).

Period II (ca. 25–30 s) in Figure 1A represents scattering patterns during and soon after the injection of the LZM solution and its mixing with the silica NPs. Period II is hence preceded by a dead-time period of 500 ms (see Experimental section). Period II (Figure 1C) can be divided into multiple steps. The first 1.25 s were primarily characterized by a rapid and significant (ca. 11-fold) increase in intensity at low q (q < 0.3 nm^{-1}). During the following 2 s, the low-q part still kept increasing (to ca. 15-times of the initial intensity) but less rapidly, and at $q \approx 1$ nm^{-1} a characteristic local maximum developed (ROI V in Figure 1A). The intensity increase at low q originated from the formation of large aggregates constituting the composites, with sizes outside the minimum q-range, whereas the local maximum (the correlation peak $q \approx 1$ nm^{-1}) indicated the presence of interparticle correlations within those aggregates.

The intensity increase at low q associated with the aggregation continued throughout period III (between ca. 30 and 150 s), yet the correlation peak in ROI V did not change significantly (Figure 1D). Note that up to 150 s (periods I–III) the high-q part of the data (q > 1.5 nm^{-1}, Figure 1C,D) did not change, indicating that the original form factor of silica NPs remained the same

after the injection of lysozyme. Therefore, as a first approximation the observed electron-density scattering contrast in these periods (I–III) can be interpreted to originate solely from the silica NPs and not from the combination of silica and lysozyme (Figure S1, Supporting Information File 1). Hence, we could treat the system as a system with two different electron densities (silica NPs and solvent matrix). However, because our silica nanoparticles were smaller (ca. 5 nm) compared to silica NPs in previous scattering studies (ca. 20 nm) on silica–protein composite formation [16,17,23,24] and because the lysozyme addition dramatically changed the silica aggregation state, the contributions of the lysozyme scattering can be accounted for indirectly from the interparticle correlations observed in ROI V. This is key here, because it allows us to extract the changes in lysozyme structural properties as the composites evolve over time, without deriving circumstantial models for a system with three electron densities (silica, lysozyme, and the solvent matrix).

In period IV (150–300 s, Figure 1A and Figure 1D), we observed a further intensity increase at low q (three-times higher at 300 s than at 150 s), which indicated a continuous increase in aggregate size from periods II and III. In time period IV the intensity of ROI V (Figure 1A) started to increase together with the silica form factor at high q ($q > 1.5$ nm^{-1}, Figure 1D). This suggests that as aggregation continued between 150 and 300 s, the silica NPs themselves started to grow, e.g., due the coalescence of NPs or similar processes (under an assumption that the particles remained spherical in shape).

Scattering model

In the considered silica–LZM composites, the scattering contrast originating from the lysozyme itself can be mostly disregarded (see Figure S1, Supporting Information File 1). Hence, the scattering contrast of the primary silica particles, $(\Delta\rho_p)^2$, – expressed as the difference in scattering length density, SLD – is equal to the squared difference in the SLDs of silica and the surrounding water matrix (Table S1, Supporting Information File 1). Consequently, using such an approximation allows us to deal with a two-electron-density system, where the scattering intensity, $I(q)$ is a product of the scattering contrast, $(\Delta\rho_p)^2$, the form factor of the silica NPs, $P_p(q)$, weighted by a volume fraction of silica NPs, ϕ_p, and their volume, V_p, together with an effective structure-factor function describing the spatial arrangement of silica NPs within the aggregates, $S_{eff}(q)$ (Equation 1). We use subscript "p" to emphasize that the parameters and functions concern the primary silica NPs.

$$I(q) = (\Delta\rho_p)^2 \cdot \phi_p \cdot V_p \cdot P_p(q) \cdot S_{eff,\,p}(q). \quad (1)$$

Equation 1 is valid only for a system of ideally monodisperse particles (i.e., the distribution is a delta function), which is actually not the case for the silica NPs used here (Figure 1B). This is an important consideration when including the interparticle interactions from the structure factor. There are several approaches to consider the polydispersity of particles together with a structure factor [33], but because the fitted size distribution (histogram in Figure 1B) is discrete with a finite number of n bins a local monodisperse approximation (LMA) [34] is used in our models:

$$I(q) = (\Delta\rho_p)^2 \sum_{i=1}^{n} \left(\phi_{p,i}(r_i) \cdot V_p(r_i) \cdot P_p(q, r_i) \cdot S_{eff,\,p}(q, r_i)\right), \quad (2)$$

where $P_p(q,r_i)$ is the form factor of a sphere of radius r_i.

The discrete size distribution (Figure 1B) has the form of Equation 3, where for each size contribution (r_i) the corresponding volume fractions, ϕ_i, are known:

$$D(r_i) = \sum_{i=1}^{n} \phi_{p,i}(r_i). \quad (3)$$

Since the partial i-th structure factor, $S_{eff}(q,r_i)$, includes the interparticle correlations between silica NPs and lysozyme (the local maximum at $q_{max} \approx 1$ nm^{-1}, ROI V in Figure 1), it is also dependent on r_i of the primary silica NPs. Additionally, the structure factor expression has to account for the aggregation of the silica NPs to large objects (the low-q increase), yet the size of these aggregates, in turn, does not necessarily depend on the size of the primary silica NPs.

The interparticle correlations and the local maximum

Under the considered physicochemical conditions the inorganic silica NPs and the protein molecules are oppositely charged [21], and hence they interact through the attractive potential. This, in turn, leads to the formation of aggregates/composites in which NPs behave closely to adhesive hard spheres. The aforementioned interactions and the arrangement of particles in space lead to the occurrence of a broad maximum in the scattering pattern (Figure 1, ROI V). We simulate these effects by implementing the adhesive hard-sphere structure factor, $S_{SHS}(q)$ [35-37]. The interaction between particles at the distance x is approximated by the following potential $U(x)$:

$$\frac{U(x)}{k_B T} = \begin{cases} \infty \Rightarrow 0 < x < 2R_{HS} \\ \ln\left[12\tau\Delta/(2R_{HS}+\Delta)\right] \Rightarrow 2R_{HS} < x < 2R_{HS}+\Delta \\ 0 \Rightarrow x > 2R_{HS}+\Delta \end{cases}, \quad (4)$$

where R_{HS} is a hard sphere radius of particles, Δ is the width of a potential well, and τ is a stickiness parameter. The structure factor expression, $S_{SHS}(q)$, is defined through the following set of equations (Equations 5–14). The structure factor is a function of four parameters in Equation 5, whereas the remaining variables and the associated expressions in Equations 6–14 are merely auxiliary by convention, so that we avoid writing a very long single expression. They should be consequently substituted into each other where suitable to obtain the final expression.

$$S_{\mathrm{SHS}}\left(q,R_{\mathrm{HS}},\nu,\tau\right)=\frac{1}{1-C\left(q\right)} \tag{5}$$

$$\kappa = 2qR_{\mathrm{HS}} \tag{6}$$

$$\eta = \nu\left(\frac{2R_{\mathrm{HS}}+\Delta}{2R_{\mathrm{HS}}}\right)^3 \tag{7}$$

$$\varepsilon = \tau+\frac{\eta}{1-\eta} \tag{8}$$

$$\gamma = \nu\frac{1+\eta/2}{3\left(1-\eta\right)^2} \tag{9}$$

$$\lambda = \frac{6}{\eta}\left(\varepsilon-\sqrt{\varepsilon^2-\gamma}\right) \tag{10}$$

$$\mu = \lambda\eta\left(1-\eta\right) \tag{11}$$

$$\alpha = \frac{\left(1+2\eta-\mu\right)^2}{\left(1-\eta\right)^4} \tag{12}$$

$$\beta = -\frac{3\eta\left(2+\eta\right)^2-2\mu\left(1+7\eta+\eta^2\right)+\mu^2\left(2+\eta\right)}{2\left(1-\eta\right)^4} \tag{13}$$

In this study, the stickiness τ is calculated from Equation 4, based on the literature data for silica–LZM composites synthesized under similar physicochemical conditions [24]: $U(2R_{HS} < x < 2R_{HS} + \Delta) = -2.5\ k_BT$; $\Delta = 0.1\cdot(2R_{HS})$ under the restriction that $\Delta_{min} \geq 0.15$ nm (i.e., the average H-bond length). The value of U in our study may slightly differ from literature values, because for constant pH value and salinity, the surface charge of NPs increases with decreasing size [38]. However, it is unlikely that $U > -3k_BT$, and within the considered range, the value of U will not affect our fitting results. ν is a local packing parameter, i.e., a local volume fraction within the aggregate, and for the random packing of polydisperse spheres it does not exceed 0.65 [39-42]. Figure 2 shows the scattering patterns at 0 and 100 s (Figure 1D) together with simulated curves based on Equation 2, in which the contributions of the silica NPs were taken from the Monte Carlo-fitted form factor (Figure 1B), while the contribution of $S_{eff}(q,r_i)$ was included from Equation 5 (and Equations 6–14).

The simulations show the important effects that polydispersity has on the structure factor and the position of the correlation peak in ROI V. Typically, for correlations originating from (sticky) hard-sphere interactions, one considers the following dependence, for the approximated position of the peak at q_{max}:

$$2R_{\mathrm{HS}} \approx \frac{2\pi}{q_{\mathrm{max}}}. \tag{15}$$

Equation 15 infers that the expected average hard-sphere radius, R_{HS}, would be equal to the mean radius of a silica particle $\langle r\rangle \approx 2.5$ nm (Figure 1B, Table S2, Supporting Information File 1). This, in turn, suggests that silica NPs on average touch each other without any LZM molecules in between, or that the protein molecules, if present within the aggregates and among individual silica NPs, are very strongly deformed, likely to a point that they barely contribute to the determined R_{HS}. Nevertheless, the simulation in Figure 2A clearly shows that if the size distribution of silica NPs is actually correctly accounted for, then in order to fit the peak position accurately, an additional "spacer", aR_{eHS} (additional effective hard sphere radius) has to be included in Equation 2 and Equations 5–14:

$$R_{\mathrm{HS},i} = r_i + aR_{\mathrm{eHS}}. \tag{16}$$

$$\begin{aligned} C\left(q\right) = {} & 2\frac{\eta\lambda}{\kappa}\sin\kappa-2\frac{\eta^2\lambda^2}{\kappa^2}\left(1-\cos\kappa\right) \\ & -\Big[\alpha\kappa^3\left(\sin\kappa-\kappa\cos\kappa\right)+\beta\kappa^2\left(2\kappa\sin\kappa-\left(\kappa^2-2\right)\cos\kappa-2\right) \\ & +\frac{\eta\alpha}{2}\left(\left(4\kappa^3-24\kappa\right)\sin\kappa-\left(\kappa^4-12\kappa^2+24\right)\cos\kappa+24\right)\Big]\cdot 24\frac{\eta}{\kappa^6} \end{aligned} \tag{14}$$

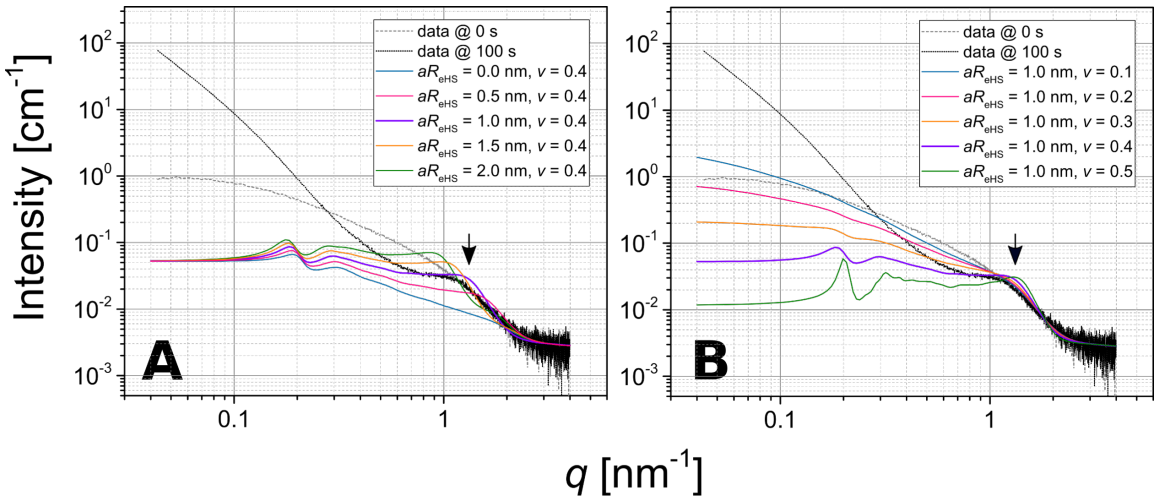

Figure 2: Comparison of the measured (black) and simulated (coloured) scattering patterns to illustrate the contribution of $S_{SHS}(q)$ from Equations 5–14, plugged into Equation 2 as the only structure-factor expression. It was the aim to represent the correlation peak at $q \approx 1$ nm^{-1}, whereas the effects at low q are further discussed in the text and in Figure 3. A) The position of the correlation peak at $q \approx 1$ nm^{-1} (arrow) is reproduced more accurately by $S_{SHS}(q)$ for the polydisperse silica NPs (Figure 1B), only if one considers an additional effective hard sphere radius, aR_{eHS} (Equation 16); B) the effect of the local volume fraction v onto the intensity of the correlation peak (arrow). The data uncertainties are not shown for clarity.

By setting merely $r_i = R_{HS,i}$ (i.e., $aR_{eHS} = 0$) the position of the simulated peak visibly shifts towards higher q values with respect to the measured peak. Here, aR_{eHS} is associated with the presence of a single LZM molecule located in between individual silica NPs with the diameter of the LZM molecule represented by $2aR_{eHS}$. The simulation in Figure 2B also shows that the packing factor ν within the aggregates, which directly correlates with the intensity of the broad peak around $q \approx 1$ nm^{-1}, has to be relatively high (ν above ca. 0.4) in order to be able to simulate the intensity profile at $q \approx 1$ nm^{-1} in the later stages (ca. 100 s).

Low-q intensity increase, aggregation, and the structure factor expression of aggregates with internal correlations

The structure factor from Equations 5–14 does not reproduce the observed intensity increase at low q (Figure 1 and Figure 2A), because the sticky hard-sphere structure factor is derived under the assumption that the interactions extend to an infinite length scale, with respect to the probed volume. However, in our experiments, we initially have a finite number of "loose" silica NPs that are then rearranged to large aggregates upon mixing with lysozyme. Hence, microscopically such aggregates must have a finite size, even if their size (radii of gyration) cannot be determined directly from our scattering data, due to the used q range (see Experimental section). However, ultimately, to obtain a good fit an expression for $S_{eff}(q)$ (Equation 2) has to account for both the fine structure within the aggregates causing the interparticle correlations (as in Equations 5–14) and also the low-q intensity increase due to the presence of the interface between the aggregates/composites and the solvent matrix.

A general expression for such an effective structure factor for particles within an aggregate/droplet was proposed originally by Hashimoto and co-workers [43]. Several variations and applications of this concept are furthermore known [37,44]. For the purpose of the analysis of our data, we further extended the expressions originating from Hashimoto et al. as we show below in a final form. In the Appendix section the complete derivation and the rationale are presented. Our derivation is essential here, because it allowed us to quantify indirectly the changes in the size of the aggregates, although the direct measurement of their radii of gyration was not possible. The so-derived general expression for $S_{eff}(q,r_i)$ (Equation 17) is expressed as the sum between the structure function of an aggregate ("template"), $S_{agg}(q)$, and the structure factor of the internal arrangement of the aggregate, $S_{int}(q)$, which in our case becomes subsisted by $S_{SHS}(q)$ (Equations 5–14):

$$\begin{aligned} S_{\text{eff}}\left(q,r_i\right) &= S_{\text{int}}\left(q\right) + S_{\text{agg}}\left(q\right) \\ &= S_{\text{SHS}}\left(q,R_{\text{HS},i},\nu,\tau\right) + A\cdot q^{-D}, \end{aligned} \tag{17}$$

where D is a fractal dimension describing the arrangement of primary particles within the composites, and A is a single collective fitting parameter in our model, which is proportional to the number density of aggregates, N_{agg}, and their specific surface area, SSA_{agg}. Hence, it expresses indirectly the size/

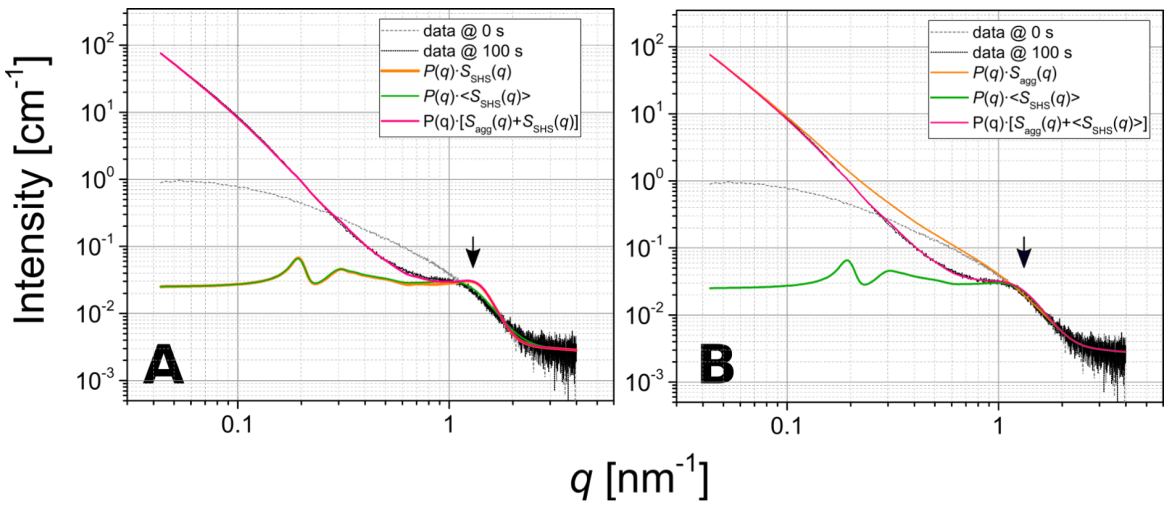

Figure 3: Fitting of the structure-factor contributions to a scattering curve measured at 100 s during the composite-formation processes. A) Comparison between the effect of the unsmeared (monodisperse aR_{eHS}, red line) $S_{SHS}(q)$ from Equations 5–14 and the smeared (polydisperse, green line) $\langle S_{SHS}(q)\rangle$ from Equation 18. Fits yielded ν = 0.454 ± 0.008, aR_{eHS} = 0.979 ± 0.036 nm, $\langle aR_{eHS}\rangle$ = 0.930 ± 0.000 nm, and σ = 0.533 ± 0.050 nm; the complete structure factor fit (pink line), which includes the unsmeared $S_{SHS}(q)$, illustrates that the form of the function affects only the correlation peak at $q \approx 1$ nm^{-1} (arrow), and not the low-q scattering intensity of the aggregates; B) the final fit to the data (pink line) with each structure-factor contribution plotted separately (green and orange lines). Parameters for $\langle S_{SHS}(q)\rangle$ are the same as in panel A, whereas for the $S_{agg}(q)$ from Equation 17, we obtained A = 0.0437 ± 0.0001 and D = 2.37 ± 0.00. The data uncertainties are not shown for clarity.

extent of the aggregates. In Figure 3, we show that the fits with the introduced expressions for the partial structure-factor contributions indeed represent the structural features present in the selected scattering pattern (example @ 100 s).

However, as is evident from Figure 3A, the $S_{SHS}(q)$ from Equations 6–14 has to be further improved, because in Figure 3A the correlation peak is relatively broad ("smeared out"), yet still intense. Typically one would expect such a broadened shape if the local volume-fraction parameter, ν, was smaller than derived from the best fit (i.e., below ca. 0.4). However, this would also inevitably yield a smaller relative intensity of this peak (see Figure 2B). Hence, in order to explain this contradiction, one has to remember that the position of the maximum and its shape are predominantly related to aR_{eHS}. The shape of the peak can be modelled substantially better if one allows for a distribution of this parameter in the fitting routine. The need for such mathematical treatment is in fact a manifestation of the actual physical effects, if we consider that aR_{eHS} represents a radius of a LZM molecule. A LZM molecule can become, at least partially, heterogeneously deformed (on average, in a global sense) within an aggregate, e.g., due to the variation of local forces, which, in turn, is a consequence of polydispersity of the silica NPs and the random character of the packing of the silica NPs. More importantly, since lysozyme is a small prolate ellipsoidal protein, with its principal semi-axes being 1.5 nm × 1.5 nm × 2.25 nm, the polydispersity in aR_{eHS} may account for the fact that the protein molecules can be differently orientated during adsorption to the NPs. Yet, so far we tried to represent their contribution through a (hard) spherical model. To overcome this, we used a Gaussian distribution to define the average structure factor $\langle S_{SHS,i}(q)\rangle$ in Equation 18. The application of this structure factor ultimately leads to smearing of the maximum at a constant value of ν and hence yields significantly improved fits (Figure 3B):

$$\left\langle S_{\mathrm{SHS},i}\left(q, r_i + \left\langle aR_{\mathrm{eHS}}\right\rangle, \sigma, \nu, \tau\right)\right\rangle = \\ = \frac{\int_0^{\langle aR_{\mathrm{eHS}}\rangle+8\sigma} D_{\mathrm{G}}\left(\left\langle aR_{\mathrm{eHS}}\right\rangle, \sigma, R\right)\cdot S_{\mathrm{SHS},i}\left(q, r_i + R, \nu, \tau\right)\mathrm{d}R}{\int_0^{\langle aR_{\mathrm{eHS}}\rangle+8\sigma} D_{\mathrm{G}}\left(\left\langle aR_{\mathrm{eHS}}\right\rangle, \sigma, R\right)\mathrm{d}R}, \quad (18)$$

$$D_{\mathrm{G}}\left(\left\langle aR_{\mathrm{eHS}}\right\rangle, \sigma, R\right) = \frac{1}{\sqrt{2\pi\sigma^2}}\exp\left(-\frac{\left(R - \left\langle aR_{\mathrm{eHS}}\right\rangle\right)^2}{2\sigma^2}\right). \quad (19)$$

In Equation 18, the mean of the distribution (Equation 19) is $\langle aR_{eHS}\rangle$, whereas σ denotes the standard deviation. This is the final expression used to represent $S_{int}(q)$ in Equation 17 and to fit all the scattering curves from regions II and III in Figure 1. The numerical integration was performed for each i-th bin of the discrete size distribution characterizing the form factor (Figure 1B). The complete source code and selected data sets are deposited at GitHub.com [45].

Application of the scattering model

We used the above described scattering model to fit the time-resolved data set and to derive the fitting parameters as a function of the time (Figure 1, Period II, III and beginning of IV, 3010 curves). Figure 4 shows the time dependence of the five model parameters obtained by fitting the scattering data between 24.5 and 175 s.

During the first ca. 5 s after mixing, the values of $\langle aR_{eHS}\rangle$ and σ lie way outside reasonable error margins (Figure 4A,B). This is to be expected, because the corresponding local volume fraction, ν, is very low (well below 0.1, Figure 4C) at the beginning of the composite-formation process (i.e., the beginning of period II in Figure 1). Consequently, the contribution of $\langle S_{SHS}(q)\rangle$ to the structure factor during this period is mostly

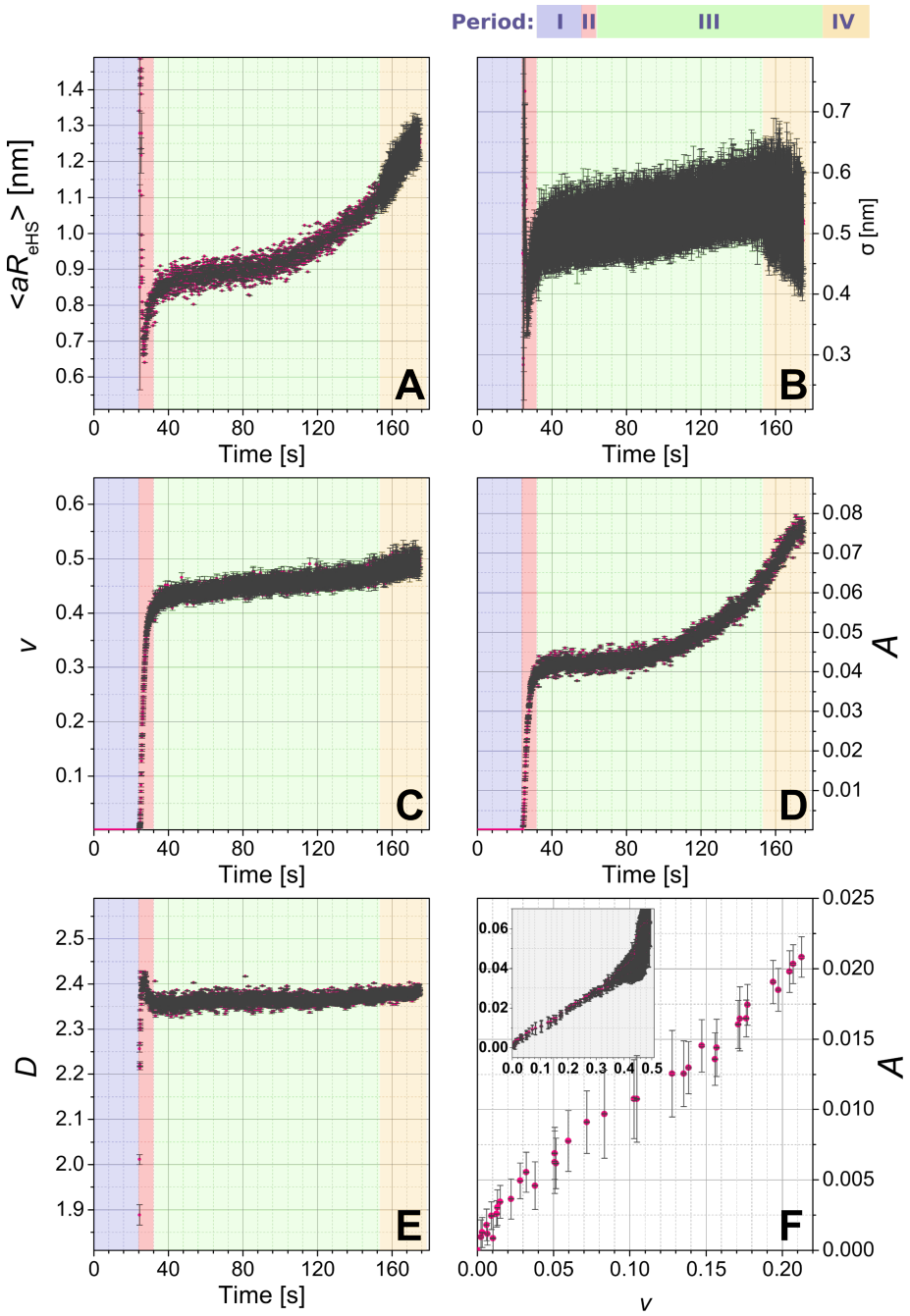

Figure 4: Evolution in the crucial parameters of the fitting model plotted as a function of the time. A) Mean additional hard sphere radius $\langle aR_{eHS}\rangle$; B) the corresponding standard deviation σ; C) local volume fraction ν; parameters characterising $\langle S_{agg}(q)\rangle$: D) *A*, relative product of the number density of the aggregates N_{agg} and their specific surface area SAA_{agg}; E) dimensionality of the aggregate *D*; F) correlation *A* vs ν, with inset showing the same as the main Figure 4F, but for a wider range; axes legends in the inset correspond to those in the main figure.

negligible with respect to $S_{agg}(q)$. As ν reaches ca. 0.1 after about 30 s (transition between regions II and III in Figure 1) the actual evolution of $<aR_{eHS}>$ and σ begin: $<aR_{eHS}>$ starts at a value of ca. 0.7 nm and rapidly increases to ca. 0.9 nm after 50 s and then more gradually to ca. 1.1 nm after 150 s (period III in Figure 1). The associated standard deviation σ follows a similar trend as $<aR_{eHS}>$, growing from 0.35 to 0.5 nm after 50 s, and then levels off at ca. 0.5 nm after 150 s (end of period III in Figure 1A) within the fitting uncertainty. These initial rapid changes after up to 50 s are also reflected in the evolution of parameter ν (Figure 4C), where the parameter rapidly increases to ca. 0.45 and then remains constant within the fitting uncertainty after up to 150 s. Because $<aR_{eHS}>$ directly relates to the size of lysozyme within the silica aggregate, we can link the changes in $<aR_{eHS}>$ to possible changes in the structure/folding/shape of the protein. Between ca. 30 and ca. 50 s, where the LZM molecules rapidly induce the aggregation of the silica NPs, the LZM molecules appear to undergo a deformation (compression). However, as this process approaches equilibrium, through the internal densification of the aggregates, the molecules gradually return to their native dimensions. This result is in agreement with findings concerning the activity of lysozyme within composites with silica, showing that smaller silica NPs (as those used for our experiments) promote higher enzymatic activity of lysozyme, and that this, in turn, depends on the preservation of the native shape of the molecule upon composite formation [22].

Furthermore, the formation of the silica–LZM composite is dominated, from the very moment of mixing for the initial 20 s, by a rapid, 4.5-fold increase of parameter A (Figure 4D). This is best explained by the increasing number density of the aggregates, N_{agg}, and the associated increasing specific surface area, SSA_{agg} (see Equation 17 and Equation 29 in the Appendix). After $t = 40$ s, parameter A further increased, albeit at a slower rate. The concurrent evolution of the fractal dimension (parameter D; Figure 4E) suggests that initially (up to 50 s), the aggregates have a relatively open morphology with $D < 2.4$ and characterized by a limited contribution of $<S_{SHS}(q)>$ due to $\nu < 0.1$ (Figure 4C). Afterwards (after more than 50 s), the aggregates reached an internally denser state, as reflected by the steadying of both values for D (ca. 2.4) and ν (ca. 0.45). In other words, since these two parameters, D and ν, reflect the internal structure of the aggregates from the perspective of the two structure-factor contributions (Equation 17), their evolution clearly indicates no further internal changes in the aggregates between 50 and 150 s. If such an internal densification processes had occurred, one would expect that it would have contributed to the decrease of the specific surface area of the aggregates, SSA_{agg}. Interestingly, however, parameter A (Figure 4D) keeps increasing after 50 s, i.e., after the internal dense structure is established, meaning that the product of number density of the aggregates and their specific surface area actually increased. This is possibly a result of secondary processes involving the "breakup" of larger aggregates into smaller units. Indeed, if we correlate the changes in A and ν (Figure 4F), we observe three stages of such secondary processes. In the first stage for $\nu < 0.1$ (up to 25.5 s), A grows as a function of ν in a bound exponential mode, which translates into an increasing number of low-dimensional aggregates with hardly any internal correlations, forming an extended network of particles of low dimensionality D (Figure 4E). In the second stage, as ν increases from 0.1 to ca. 0.45 (25.5 to 70 s), A as a function of ν (Figure 4F) shows a linear dependence, indicating that as the number density of aggregates increases they also gradually densify, and that the growth of the aggregates occurs at the same rate as their internal densification. Finally, in the third stage, once ν remains relatively constant at ca. 0.45 (after 70 s), the product of the number density and the specific surface area of the aggregates continues to increase as documented by the increasing value of A, yet without any further dramatic changes to the internal structure/arrangement (i.e., constant values of D and ν), implying the aforementioned breakup of the larger aggregates into smaller units. These processes can be best explained as the initial rapid flocculation/clumping of NPs and LZM together into an extensive network just after mixing as the system is out of equilibrium, followed by the gradual evolution towards a steady state, in which smaller aggregates are more favourable.

During period IV (after more than 150 s), the time evolution of the three parameters ($<aR_{eHS}>$, ν and σ; Figure 4A–C) exhibited a characteristic discontinuity from the trends observed during periods II and III. This is because at times greater than 150 s, the scattering intensity at high q (which corresponds to the form factor, Figure 1D) changed significantly, so that the original form factor of pre-mixing silica NPs from Figure 1B was not representative for silica particles after 150 s. Thus, we could no longer use the fitted size distribution in our model, and any trends of these three parameters (Figure 4A–C) were not valid any more after 150 s. On the other hand, due to the fact that the low-q part of the data by definition is practically independent from the form factor, in fact the evolution of parameters A and D (trends in Figure 4D,E), even after 150 s are representative for the processes at the length scales corresponding to entire aggregates. However, due to the fact that in period IV our scattering model is no longer self-consistent, we did not analyse those trends.

Implications

The analysis of the evolution of the fitting parameters (Figure 4) draws a clear image of the four-step sequence of events during

aggregation induced by the interaction between the protein LZM and amorphous silica NPs (Figure 5).

Immediately upon mixing, aggregation is induced due to the opposing surface charge of the silica NPs and the protein. An infinitely extensive and open (D = 1.8–2.2) aggregate network, from the point of view of the SAXS measurement, forms within ca. four data frames (ca. 200 ms). The so-formed network initially has no internal correlations, as is expected for a classical mass fractal [46]. However soon after (ca. 1 s), areas of correlated NPs–LZM domains start forming within the network and the increase in the internal volume fraction, ν, indicates an internal densification and ordering. This is also reflected by the fact that parameter D reaches a stable and relatively high value of ca. 2.4, which is characteristic for denser mass fractals. Such a fractal dimension for silica–lysozyme aggregates was previously reported [16,23] and can be associated with the diffusion-limited particle–cluster aggregation (DLPCA) mechanism [47-52]. The DLPCA growth mode is also evidenced not only by the plateau value of D, but also through the fact that the value of D increases with the size/extent of the aggregates [47,49] expressed indirectly by the parameter A (see region II in Figure 4D–E). This means that aggregates grow through the accretion of individual primary particles to larger aggregates [52], where aggregates as such become denser as their size increases, which in consequence favours the eventual occurrence of the correlated domains (which are the ultimate dense regions in the aggregate composed of smaller particles).

The parameters characterizing the interparticle correlation effects carry information about the size of the LZM molecules bridging the silica NPs. From Figure 4A–B it is clear that in this network the dimensions of the protein molecules are considerably smaller than the native dimensions of lysozyme in any possible orientation. Hence, this suggests that initially the binding of silica NPs by lysozyme involves a severe deformation/unfolding of the protein molecules, followed in time by a relaxation and increase in the protein dimensions towards a (more) native state (Figure 5). The final value of the radius of 1.1 ± 0.5 nm for the protein, which is reached before 150 s, is close to a radius of the protein in a side-on orientation (ca. 1.5 nm), rather than in the end-on orientation (ca. 2.25 nm). Our ex situ analysis of the dried composite samples (see Experimental section) showed that at 1000 ppm lysozyme, 32.7 wt % of the protein was incorporated into the composites. This means that for silica NPs precipitated at the concentration of 0.8737 g/L (calculated from the volume distribution in the SAXS patterns), the concentration of lysozyme in the composite was 0.4245 g/L. This is valid under the assumption that all available silica NPs were bound in aggregates with lysozyme.

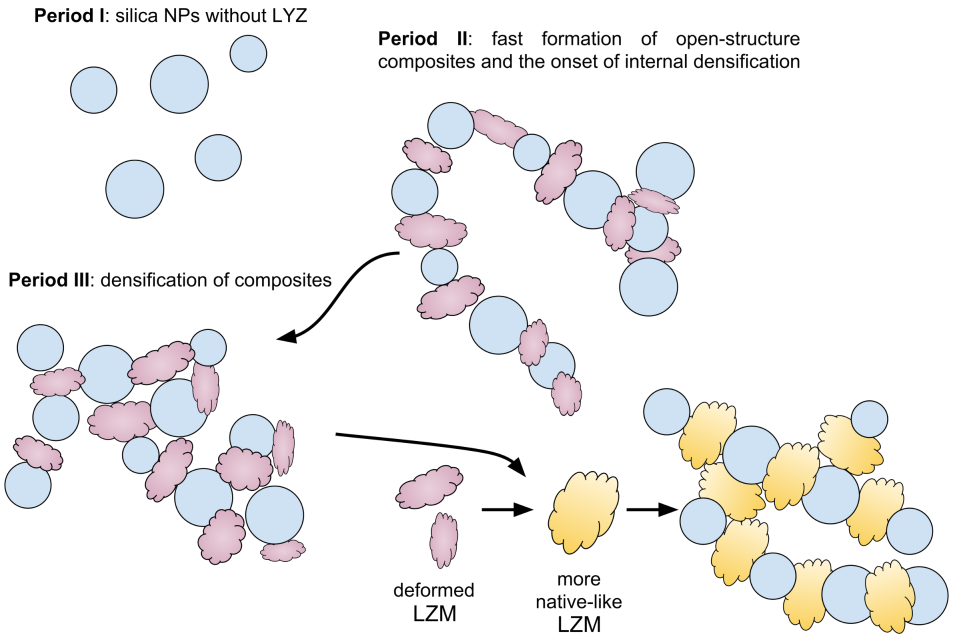

Figure 5: Schematic of the selected steps in the formation of silica–LZM composites as derived from the fast in situ and time-resolved SAXS data. Period I – unaggregated silica NPs (spherical in shape blue objects) before LZM addition. Following the LZM addition (cloud-like purple and yellow objects) occurs period II – fast aggregation to low-dimensionality fractal networks constituting the internal structure of large composite particles (primarily $S_{agg}(q)$ contribution); period III – internal densification of the network in the process of which the interparticle correlations develop (evolution of $<S_{SHS}(q)>$ and $S_{agg}(q)$). At the early stages of densification the lysozyme molecules are strongly deformed within the aggregates; during further densification the protein molecules appear to relax to a more native structure.

Hence, the number density of the protein molecules was $N_{LZM} \approx 1.8 \cdot 10^{19}$ L^{-1}, and for silica $N_{NP} \approx 1.8 \cdot 10^{19}$ L^{-1} (from SAXS by converting the volume distribution to a number distribution). This directly suggests that the silica–lysozyme aggregates are near almost stoichiometric, with one protein molecule associated with one silica NP. Such a stoichiometric relationship is actually expected for small silica particles of the size close to that of the protein molecule [22,53]. Su et al. [54] found that at small surface coverage the lysozyme attaches to silica NPs in a side on orientation, and recently the molecular dynamics simulations by Hildebrand et al. [55] also further confirmed that the side-on orientation of lysozyme with respect to silica constitutes the configuration of the highest attraction. This together with the relatively low dipole moment and the positive surface charge of the protein surface, potentially accounts for the bridging of the NPs by the LZM molecules, as the protein does not show a favoured orientation of the opposite active sites in the side-on orientation (i.e., both active sites show similar binding properties). In such a case one should indeed expect the DLPCA mode of aggregation, with the binding of the protein to the silica NP surfaces taking place through specific amino acids at the opposite sides of the molecule [24,55-57]. The densification of the internal structure of the aggregates reaches a steady point, when the LZM molecules relax to their native-like dimensions. Yet, at the same time the actual network constituting the composite, appears to break up into smaller aggregate units. The morphological changes of the composites further continue beyond 150 s. This is documented through the change in the form factor of the silica NPs that appear to grow in size, compared to the pre-mixed initial NPs. Although we cannot use our model to explain this last stage, we can speculate that the observed change is caused by a partial coalescence or Ostwald ripening of NPs inside of the aggregates. It is well documented that silica NPs synthesized from monosilicic acid are internally highly disordered and hydrated at their surfaces [31]. Previous studies found that the initially formed NPs if aggregated continued their growth, resulting in some cases in larger homogeneous silica spheres [31,58,59], and this may explain why silica is such a persistent scaling material in hydrothermal systems.

Conclusion

The analysis of in situ scattering data collected at 20 fps from the formation of silica–lysozyme composites showed that the processes included the formation of large aggregated structures in which individual silica NPs were bridged by LZM molecules. We developed and applied a new scattering model to underpin the changes of the morphology of the composites as a function of time. This model allowed us to unravel that the formation follows a diffusion limited particle–cluster aggregation (DLPCA) mechanism, which results in relatively densely packed mass-fractal-like aggregates within which non-fractal correlated domains of particles evolve. Furthermore, we used the scattering model to link the evolution in the measured structure factor to the lysozyme molecule, and we found that the aggregation processes involve severe deformation of the protein molecules, which is then followed by the relaxation towards the original dimensions.

Appendix

Derivation of Equation 17

The contribution of $S_{int}(q)$ in Equation 17 has a rather simple form. However, the actual meaning of the parameter A extends beyond this short representation. Below, we present the derivation of the equation and we indicate the approximations we make on the way to the final form of the equation.

First we consider a structure factor function describing an arrangement of primary particles of a certain scattering length density (SLD), ρ_p, within an aggregate. The SLD of the space between the particles within the aggregate (the "template") is ρ_t, while the SLD of the surrounding ("solvent") is ρ_s. The average scattering contrast of the aggregate, $\Delta\rho_{agg}$, is then:

$$\Delta\rho_{agg} = \nu\left(\rho_p - \rho_s\right) + (1-\nu)\left(\rho_t - \rho_s\right), \tag{20}$$

where ν is a local volume fraction of particles within the aggregate (as in Equation 5). We also define any contrast fluctuation within an aggregate as:

$$\Delta\eta = \rho_p - \rho_t. \tag{21}$$

If we write the structure function of an aggregate ("template") as $S_{agg}(q)$ and the internal arrangement within this aggregate as $S_{int}(q)$, then similar to Hashimoto et al. [43] and Lin et al. [44], we can express the scattering intensity by the generalized Equation 22, in which "⊗" denotes a convolution operation of the functions:

$$\begin{aligned} S_{eff}(q) &= S_{agg}(q) + \frac{V_p \cdot \phi_p \cdot \Delta\eta^2}{V_{agg} \cdot \phi_{agg} \cdot \Delta\rho_{agg}^2} S_{agg}(q) \otimes S_{int}(q) \\ &\approx S_{agg}(q) + \frac{V_p \cdot \phi_p \cdot \Delta\eta^2}{V_{agg} \cdot \phi_{agg} \cdot \Delta\rho_{agg}^2} S_{int}(q), \end{aligned} \tag{22}$$

where V_{agg} and ϕ_{agg} represent the volume and the volume fraction of aggregates in the solution, respectively. Here, $S_{int}(q) = S_{SHS}(q)$ from Equations 5–14, whereas the $S_{agg}(q)$ contributes to the increase in intensity at low q in the course of the

formation of aggregates. The approximation in Equation 22 is valid when the overall radii of the aggregates, ξ, are significantly larger that the interparticle correlation distance from Equations 5–14 ($\xi >> R_{HS}$). Furthermore, we must re-normalize $S_{eff}(q)$ in a different way than Hashimoto et al. and Lin et al. in order to combine it with the form factor defined in Equation 1 as for our scattering data the intensity for $q \to 0$ in a log–log representation does not level off to a finite value (Figure 2 and Figure 3). Consequently, it is impossible to determine V_{agg}. On the other hand the radii of the primary particles and, consequently, their volume, V_p, are known, and therefore it is reasonable to normalize $S_{eff}(q)$ with respect to the primary particle volume rather than the aggregate volume:

$$S_{\text{eff}}(q) = S_{\text{int}}(q) + \frac{V_{\text{agg}} \cdot \phi_{\text{agg}} \cdot \Delta\rho_{\text{agg}}^2}{V_{\text{p}} \cdot \phi_{\text{p}} \cdot \Delta\eta^2} S_{\text{agg}}(q). \quad (23)$$

Now let us assume that the aggregates follow mass-fractal behaviour and that the correlation function of mass fractals is described [60,61] by Equation 24:

$$g_{\text{agg}}(r) = K \cdot r^{D-d}, \quad (24)$$

where D is a fractal dimension, d is the Euclidean dimension ($d = 3$) and K is a normalization constant that is proportional to the mass and surface area of an aggregate. We do not include a cut-off function since in our case the intensity did not level off at low q as mentioned above. For the sake of simplicity let us assume again that the electron density of the aggregates is homogeneously distributed and its corresponding correlation function only involves a two-phase system. In this case the specific surface area of aggregates (SSA_{agg}) is proportional to the derivative of the correlation function at the near-zero length scale $r \to 0$:

$$\text{SSA}_{\text{agg}} = -4 \cdot \phi_{\text{agg}} \left(1 - \phi_{\text{agg}}\right) \cdot \lim_{r \to 0} \frac{\mathrm{d}g_{\text{agg}}(r)}{\mathrm{d}r}. \quad (25)$$

This is valid for the considered small volume fractions ($1 - \phi_{agg} \approx 1$). The limit in Equation 25 exists essentially only for $D = 4$, and since $D < 4$, SSA_{agg} becomes increasingly larger for decreasing length scales, yielding an infinite surface area at an infinitely small length scale r. However, since the aggregates are composed of primary particles with a typical radius, R_{HS}, we can say that the aggregate does not contain smaller features than those primary particles (i.e., $r \geq R_{HS}$). Therefore, we find a finite specific surface area for mass fractal aggregates for $\lim(r \to R_{HS})$:

$$\begin{aligned} \text{SSA}_{\text{agg}} &= 4 \cdot (3 - D) \cdot \phi_{\text{agg}} \cdot K \cdot R_{\text{HS}}^{D-4} \\ \Rightarrow K &= \frac{\text{SSA}_{\text{agg}} \cdot R_{\text{HS}}^{4-D}}{4 \cdot (3 - D) \cdot \phi_{\text{agg}}}. \end{aligned} \quad (26)$$

This way this newly derived K constant in Equation 26 substitutes the K constant from Equation 24 and thus, we can use the correlation function from Equation 24 to calculate the structure factor. Please note the Hashimoto et al. described the structure factor in such a way that it is normalized as a form factor, i.e., it is normalized by the total volume. This is in line with the structure factor of mass-fractal aggregates as described by Sorensen and Wang [60], yet it is different from a better-known derivation by Teixeira [62]. Both Sorensen and Wang's and Teixeira's approaches are valid as long as one considers normalizations explicitly. The structure factor is described by the rotation-averaged Fourier transform:

$$\begin{aligned} S_{\text{agg}}(q) &= \frac{N_{\text{agg}}}{V_{\text{agg}}} \int_0^\infty g_{\text{agg}}(r) \cdot 4\pi r^2 \frac{\sin(qr)}{qr} \mathrm{d}r \\ &= \frac{\pi \cdot \Gamma(D-1) \cdot N_{\text{agg}} \cdot \text{SSA}_{\text{agg}} \cdot R_{\text{HS}}^{4-D}}{V_{\text{agg}} \cdot \phi_{\text{agg}} \cdot (3 - D)} \\ &\quad \cdot \sin\left(\frac{(D-1)\pi}{2}\right) \cdot q^{-D}, \end{aligned} \quad (27)$$

where N_{agg} is the number density of aggregates and SSA_{agg} is their specific surface area. By substitution of Equation 27 into Equation 23, we obtain:

$$\begin{aligned} S_{\text{eff}}(q) &= S_{\text{int}}(q) + \frac{\Delta\rho_{\text{agg}}^2}{\Delta\eta^2} \cdot \frac{\pi \cdot \Gamma(D-1)}{(3-D)} \\ &\quad \cdot \frac{N_{\text{agg}} \cdot \text{SSA}_{\text{agg}} \cdot R_{\text{HS}}^{4-D}}{V_{\text{p}} \cdot \phi_{\text{p}}} \cdot \sin\left(\frac{(D-1)\pi}{2}\right) \cdot q^{-D}. \end{aligned} \quad (28)$$

For spherical primary particles V_p is known and a final form of the equation for the effective structure factor could be derived:

$$\begin{aligned} S_{\text{eff}}(q) &= S_{\text{int}}(q) + \frac{\Delta\rho_{\text{agg}}^2}{\Delta\eta^2} \cdot \frac{\Gamma(D-1)}{(3-D)} \cdot \frac{3N_{\text{agg}} \cdot \text{SSA}_{\text{agg}}}{4\phi_{\text{p}} \cdot R_{\text{HS}}^{D-1}} \\ &\quad \cdot \sin\left(\frac{(D-1)\pi}{2}\right) \cdot q^{-D} \\ &= S_{\text{int}}(q) + A \cdot q^{-D}. \end{aligned} \quad (29)$$

In Equation 29 we introduced several simplifications. Firstly, N_{agg}, SSA_{agg}, $\Delta\eta$ and $\Delta\rho_{agg}$ are essentially unknown, and it is impossible to determine any one of these parameters independently. They have to be combined into a collective parameter.

This is necessary as Equation 29 was derived for a system characterized by a monodisperse particle distribution with only a single value of ϕ_p for a given R_{HS} and the resulting N_{agg}. For a polydisperse distribution, as in our study, although a population of primary particles is described by $D(r_i)$ (Equation 2), the resulting distribution of aggregate sizes will be totally independent from this initial distribution, and it will also be unpredictable. Secondly, the ${R_{HS}}^{1-D}$ component in Equation 29 could be important, since it determines the high-q cut-off at which the contribution of the structure to the intensity lessens, and the form factor dominates. In Equation 29 this very transition point is dominated by a $S_{int}(q)$ contribution and its strong correlation peak. Hence, we assume that ${R_{HS}}^{1-D} \approx 1$. Thirdly, the remaining part of the expression depending on parameter D is practically constant at a value of ca. 1.2, and although we could introduce it explicitly in the model it does not affect the final trends. Hence, as a result of the above approximations, we use A as a single collective fitting parameter in our model. Changes in A therefore should be interpreted primarily as the average change of the product of the number density of aggregates and their specific surface area, and these two physical parameters are related to the size (or "extent") of the aggregates.

Experimental

Synthesis of amorphous silica–lysozyme composites

Sodium metasilicate ($Na_2SiO_3 \cdot 5H_2O$, technical grade), hen egg-white lysozyme (crystalline, powdered, >90% pure, residual sodium acetate and chloride) and HCl (37%, analytical grade) were purchased from Sigma-Aldrich. Separate stock solutions of dissolved silica (SiO_2 = 1000 ppm, pH 12.5) and lysozyme (5 wt %, pH 3.5) were prepared by dissolving the required amount of sodium metasilicate or lysozyme in ultrapure deionised water (18.2 MΩ·cm). Silica NPs were prepared in a 500 mL plastic reactor by neutralizing the silica stock solution through titration with HCl until pH 7.5 was reached. This neutralized solution was left to polymerize and age for 16 h. Silica–protein composites were obtained by mixing the silica NP solution with a pre-measured amount of the lysozyme stock solution under rapid stirring (500 rpm) to yield a SiO_2 NPs solution with 1000 ppm lysozyme (final pH 6.9, salinity 20 mM).

Scattering experiments

The formation process and the development of the structure of the silica–LZM composites was studied in situ and in a time-resolved manner by using synchrotron-based small-angle X-ray scattering (SAXS) at the BioSAXS beamline [63] P12 of the EMBL at PETRA III (DESY, Germany) using a monochromatic X-ray beam at 10 keV. Two-dimensional scattered intensities were collected at small angles with a Dectris Pilatus 2M (2D large-area pixel array detector) using an acquisition time of 50 ms per frame. Transmission was measured by means of a photodiode installed in the beam stop of the SAXS detector. A sample-to-detector distance of ca. 3 m allowed for a usable q-range of $0.04 < q < 4.5$ nm^{-1}. The scattering-range at small angles was calibrated against silver behenate, and the intensity was calibrated to absolute units against water. For the in situ experiment, first, the starting silica NP solution was continuously circulated between the reactor (where the suspension was stirred at 500 rpm) and the flow-through cell with embedded quartz capillary (ID 1.7 mm, wall thickness 50 µm; aligned with the X-ray beam) using a peristaltic pump (Gilson MiniPuls 3, flow ca. 500 mL/min; tubing: ID 2 mm, total length 2 m; reactor-to-cell-distance: 0.7 m of tubing). All experiments were conducted at 21 °C. Once a SAXS baseline for the silica NP solution was recorded, the pre-measured amount of lysozyme stock solution was pumped into the reactor at a fast rate. This injection was done remotely from the operator hutch via a 10 m long PTFE tube (ID 4 mm) that was routed into the reactor located in the experimental hutch. The tube was filled in such a way that the LZM solution was located in the last ca. 40 cm of the tube on the reactor side. The other end of the tube in the operator room was equipped with a 50 mL syringe filled with air. Thus the experiment started with recording of 24 s (480 × 50 ms) SAXS patterns of the silica NP solution circulating through the capillary, prior to the fast injection of the entire content of the tube containing the lysozyme with a single rapid push of the syringe plunger that lasted ca. 200–400 ms. This fast injection rate in combination with the fast stirring in the reactor (500 rpm), pumping (500 mL/min) and fast data acquisition (50 ms per SAXS pattern) provided the best possible conditions for the characterisation of all the steps leading to the formation of the silica–LZM composites. The used experimental set up introduced an unavoidable dead-time of ca. 500 ms between the injection moment and the first actual measurement of the mixed solution, i.e., the time required for the mixed solution to reach the capillary where the SAXS pattern was recorded. In order to be able to analyse and model the silica–LZM composite scattering patterns we also acquired a series of backgrounds and reference samples including an empty capillary and a capillary filled with water, silica stock solution, LZM solutions at different concentrations. The initial SAXS data processing and reduction included a series of automatic post-data-collection steps including masking of undesired pixels, normalizations and correction for transmission, instrumental background subtraction and data integration of the collected 2D data to 1D. Further data processing and water background subtraction, model fitting, validation and analysis, were performed through a custom-made script developed in GNU Octave [64,65]. The script we developed as well as all the documentation and the selected scattering curves are available at [45]: https://github.com/

tomaszstawski/SilicaLysozymeSAXS. In a first instance for the model, we obtained the size distribution of the initial silica NPs from a Monte Carlo fitting implemented [29,30] in MCSAS under the assumption that the silica NPs particles were spherical [31].

Characterization of dry samples

To cross-correlate the in situ SAXS data, the silica–lysozyme suspensions were dried in an oven at 40 °C for ca. 48 h. The resulting powders were washed five times with MilliQ water to remove excess lysozyme and salts followed by a 2nd drying step at 40 °C. The amount of lysozyme associated with the composites was quantified by determining the total carbon content in solids by mass spectrometry (DELTAplusXL ThermoFisher) with a Carlo-Erba NC2500. From these analyses the lysozyme content was calculated using the molecular formula $C_{613}H_{959}N_{193}O_{185}S_{10}$ and the molecular weight of 14313 g/mol for lysozyme [66] (ProtParam based on UniProtKB entry P00698).

Supporting Information

Supporting Information File 1

Additional experimental data.
[https://www.beilstein-journals.org/bjnano/content/supplementary/2190-4286-10-17-S1.pdf]

Acknowledgements

This research was made possible by two Marie Curie grants from the European Commission: the NanoSiAl Individual Fellowship, Project No. 703015 and the MINSC Initial Training Research network, Project No. 290040. We also acknowledge the financial support of the Helmholtz Recruiting Initiative grant No. I-044-16-01 and we thank EMBL Hamburg for granting us beamtime at BioSAXS beamline P12 at the PETRA III storage ring (DESY, Hamburg, Germany).

.

ORCID® iDs

Tomasz M. Stawski - https://orcid.org/0000-0002-0881-5808
Liane G. Benning - https://orcid.org/0000-0001-9972-5578

References

1. Patwardhan, S. V. *Chem. Commun.* **2011,** *47,* 7567. doi:10.1039/c0cc05648k
2. Shemetov, A. A.; Nabiev, I.; Sukhanova, A. *ACS Nano* **2012,** *6,* 4585–4602. doi:10.1021/nn300415x
3. Coradin, T.; Lopez, P. J. *ChemBioChem* **2003,** *4,* 251–259. doi:10.1002/cbic.200390044
4. Belton, D. J.; Deschaume, O.; Perry, C. C. *FEBS J.* **2012,** *279,* 1710–1720. doi:10.1111/j.1742-4658.2012.08531.x
5. Franzmann, E.; Khalil, F.; Weidmann, C.; Schröder, M.; Rohnke, M.; Janek, J.; Smarsly, B. M.; Maison, W. *Chem. – Eur. J.* **2011,** *17,* 8596–8603. doi:10.1002/chem.201100715
6. Frasca, S.; Richter, C.; von Graberg, T.; Smarsly, B. M.; Wollenberger, U. *Eng. Life Sci.* **2011,** *11,* 554–558. doi:10.1002/elsc.201100079
7. Rao, A.; Drechsler, M.; Schiller, S.; Scheffner, M.; Gebauer, D.; Cölfen, H. *Adv. Funct. Mater.* **2018,** *28,* 1802063. doi:10.1002/adfm.201802063
8. Rao, A.; Cölfen, H. Mineralization Schemes in the Living World: Mesocrystals. *New Perspectives on Mineral Nucleation and Growth;* Springer: Berlin, Germany, 2017; pp 155–183. doi:10.1007/978-3-319-45669-0_8
9. Tobler, D. J.; Rodriguez-Blanco, J. D.; Dideriksen, K.; Bovet, N.; Sand, K. K.; Stipp, S. L. S. *Adv. Funct. Mater.* **2015,** *25,* 3081–3090. doi:10.1002/adfm.201500400
10. De Yoreo, J. J.; Gilbert, P. U. P. A.; Sommerdijk, N. A. J. M.; Penn, R. L.; Whitelam, S.; Joester, D.; Zhang, H.; Rimer, J. D.; Navrotsky, A.; Banfield, J. F.; Wallace, A. F.; Michel, F. M.; Meldrum, F. C.; Colfen, H.; Dove, P. M. *Science* **2015,** *349,* aaa6760. doi:10.1126/science.aaa6760
11. Helminger, M.; Wu, B.; Kollmann, T.; Benke, D.; Schwahn, D.; Pipich, V.; Faivre, D.; Zahn, D.; Cölfen, H. *Adv. Funct. Mater.* **2014,** *24,* 3187–3196. doi:10.1002/adfm.201303547
12. Gebauer, D.; Kellermeier, M.; Gale, J. D.; Bergström, L.; Cölfen, H. *Chem. Soc. Rev.* **2014,** *43,* 2348–2371. doi:10.1039/c3cs60451a
13. Cölfen, H.; Antonietti, M. *Langmuir* **1998,** *14,* 582–589. doi:10.1021/la970765t
14. Mann, S.; Ozin, G. A. *Nature* **1996,** *382,* 313–318. doi:10.1038/382313a0
15. Fratzl, P. *J. Stat. Phys.* **1994,** *77,* 125–143. doi:10.1007/bf02186835
16. Kumar, S.; Aswal, V. K.; Callow, P. *Langmuir* **2014,** *30,* 1588–1598. doi:10.1021/la403896h
17. Bharti, B.; Meissner, J.; Klapp, S. H. L.; Findenegg, G. H. *Soft Matter* **2014,** *10,* 718–728. doi:10.1039/c3sm52401a
18. Cardoso, M. B.; Luckarift, H. R.; Urban, V. S.; O'Neill, H.; Johnson, G. R. *Adv. Funct. Mater.* **2010,** *20,* 3031–3038. doi:10.1002/adfm.201000144
19. Luckarift, H. R.; Dickerson, M. B.; Sandhage, K. H.; Spain, J. C. *Small* **2006,** *2,* 640–643. doi:10.1002/smll.200500376
20. Parks, G. A. *Chem. Rev.* **1965,** *65,* 177–198. doi:10.1021/cr60234a002
21. van den Heuvel, D. B.; Stawski, T. M.; Tobler, D. J.; Wirth, R.; Peacock, C. L.; Benning, L. G. *Front. Mater.* **2018,** *5,* 19. doi:10.3389/fmats.2018.00019
22. Vertegel, A. A.; Siegel, R. W.; Dordick, J. S. *Langmuir* **2004,** *20,* 6800–6807. doi:10.1021/la0497200
23. Kumar, S.; Aswal, V. K.; Kohlbrecher, J. *Langmuir* **2011,** *27,* 10167–10173. doi:10.1021/la201291k
24. Bharti, B.; Meissner, J.; Findenegg, G. H. *Langmuir* **2011,** *27,* 9823–9833. doi:10.1021/la201898v
25. Stawski, T. M.; Benning, L. G. *Methods Enzymol.* **2013,** *532,* 95–127. doi:10.1016/b978-0-12-416617-2.00005-9
26. ten Elshof, J. E.; Besselink, R.; Stawski, T. M.; Castricum, H. L. Time-Resolved Small-Angle X-Ray Scattering. *The Sol-Gel Handbook;* Wiley-VCH Verlag GmbH: Weinheim, Germany, 2015; pp 673–712. doi:10.1002/9783527670819.ch21

27. Shukla, A.; Mylonas, E.; Di Cola, E.; Finet, S.; Timmins, P.; Narayanan, T.; Svergun, D. I. *Proc. Natl. Acad. Sci. U. S. A.* **2008,** *105,* 5075–5080. doi:10.1073/pnas.0711928105
28. Blake, C. C. F.; Koenig, D. F.; Mair, G. A.; North, A. C. T.; Phillips, D. C.; Sarma, V. R. *Nature* **1965,** *206,* 757–761. doi:10.1038/206757a0
29. Pauw, B. R.; Pedersen, J. S.; Tardif, S.; Takata, M.; Iversen, B. B. *J. Appl. Crystallogr.* **2013,** *46,* 365–371. doi:10.1107/s0021889813001295
30. Bressler, I.; Pauw, B. R.; Thünemann, A. F. *J. Appl. Crystallogr.* **2015,** *48,* 962–969. doi:10.1107/s1600576715007347
31. Tobler, D. J.; Shaw, S.; Benning, L. G. *Geochim. Cosmochim. Acta* **2009,** *73,* 5377–5393. doi:10.1016/j.gca.2009.06.002
32. Parkhurst, D. L.; Appelo, C. A. J. *Description of input and examples for PHREEQC version 3: a computer program for speciation, batch-reaction, one-dimensional transport, and inverse geochemical calculations;* Techniques and Methods; US Geological Survey, 2013. doi:10.3133/tm6a43
33. Kotlarchyk, M.; Chen, S.-H. *J. Chem. Phys.* **1983,** *79,* 2461–2469. doi:10.1063/1.446055
34. Pedersen, J. S. *J. Appl. Crystallogr.* **1994,** *27,* 595–608. doi:10.1107/s0021889893013810
35. Baxter, R. J. *J. Chem. Phys.* **1968,** *49,* 2770–2774. doi:10.1063/1.1670482
36. Menon, S. V. G.; Manohar, C.; Rao, K. S. *J. Chem. Phys.* **1991,** *95,* 9186–9190. doi:10.1063/1.461199
37. Sztucki, M.; Narayanan, T.; Belina, G.; Moussaïd, A.; Pignon, F.; Hoekstra, H. *Phys. Rev. E* **2006,** *74,* 051504. doi:10.1103/physreve.74.051504
38. Barisik, M.; Atalay, S.; Beskok, A.; Qian, S. *J. Phys. Chem. C* **2014,** *118,* 1836–1842. doi:10.1021/jp410536n
39. Hansen, J. P.; McDonald, I. R. *Theory of Simple Liquids;* Elsevier: Amsterdam, Netherlands, 2006.
40. Baranau, V.; Tallarek, U. *Soft Matter* **2014,** *10,* 3826. doi:10.1039/c3sm52959b
41. Farr, R. S.; Groot, R. D. *J. Chem. Phys.* **2009,** *131,* 244104. doi:10.1063/1.3276799
42. Al-Raoush, R.; Alsaleh, M. *Powder Technol.* **2007,** *176,* 47–55. doi:10.1016/j.powtec.2007.02.007
43. Hashimoto, T.; Tanaka, H.; Koizumi, S.; Naka, K.; Chujo, Y. *J. Appl. Crystallogr.* **2007,** *40* (Suppl. 1), s73–s77. doi:10.1107/s0021889807003445
44. Lin, Y.-C. C.; Chen, C.-Y. Y.; Chen, H.-L. L.; Hashimoto, T.; Chen, S.-A. A.; Li, Y.-C. C. *J. Chem. Phys.* **2015,** *142,* 214905. doi:10.1063/1.4921567
45. Stawski, T. M. SilicaLysozymeSAXS. https://github.com/tomaszstawski/SilicaLysozymeSAXS (accessed Aug 8, 2018).
46. Besselink, R.; Stawski, T. M.; Van Driessche, A. E. S.; Benning, L. G. *J. Chem. Phys.* **2016,** *145,* 211908. doi:10.1063/1.4960953
47. Mandelbrot, B. B. *Phys. A (Amsterdam, Neth.)* **1992,** *191,* 95–107. doi:10.1016/0378-4371(92)90511-n
48. Lin, M. Y.; Lindsay, H. M.; Weitz, D. A.; Klein, R.; Ball, R. C.; Meakin, P. *J. Phys.: Condens. Matter* **1990,** *2,* 3093–3113. doi:10.1088/0953-8984/2/13/019
49. Gmachowski, L. *Colloids Surf., A* **2002,** *211,* 197–203. doi:10.1016/s0927-7757(02)00278-9
50. Lin, M. Y.; Lindsay, H. M.; Weitz, D. A.; Ball, R. C.; Klein, R.; Meakin, P. *Nature* **1989,** *339,* 360–362. doi:10.1038/339360a0
51. Ball, R. C.; Weitz, D. A.; Witten, T. A.; Leyvraz, F. *Phys. Rev. Lett.* **1987,** *58,* 274–277. doi:10.1103/physrevlett.58.274
52. Ball, R. C.; Witten, T. A. *J. Stat. Phys.* **1984,** *36,* 873–879. doi:10.1007/bf01012946
53. Malmsten, M. *Colloids Surf., B* **1995,** *3,* 297–308. doi:10.1016/0927-7765(94)01139-v
54. Su, T. J.; Lu, J. R.; Thomas, R. K.; Cui, Z. F.; Penfold, J. *J. Colloid Interface Sci.* **1998,** *203,* 419–429. doi:10.1006/jcis.1998.5545
55. Hildebrand, N.; Köppen, S.; Derr, L.; Li, K.; Koleini, M.; Rezwan, K.; Colombi Ciacchi, L. *J. Phys. Chem. C* **2015,** *119,* 7295–7307. doi:10.1021/acs.jpcc.5b00560
56. Kubiak-Ossowska, K.; Mulheran, P. A. *Langmuir* **2010,** *26,* 15954–15965. doi:10.1021/la102960m
57. Kubiak-Ossowska, K.; Mulheran, P. A. *Langmuir* **2010,** *26,* 7690–7694. doi:10.1021/la101276v
58. Tobler, D. J.; Stefánsson, A.; Benning, L. G. *Geobiology* **2008,** *6,* 481–502. doi:10.1111/j.1472-4669.2008.00179.x
59. van den Heuvel, D. B.; Gunnlaugsson, E.; Gunnarsson, I.; Stawski, T. M.; Peacock, C. L.; Benning, L. G. *Geothermics* **2018,** *76,* 231–241. doi:10.1016/j.geothermics.2018.07.006
60. Sorensen, C. M.; Wang, G. M. *Phys. Rev. E* **1999,** *60,* 7143–7148. doi:10.1103/physreve.60.7143
61. Sinha, S. K.; Freltoft, T.; Kjems, J. *Observation of Power-Law Correlations in Silica-Particle Aggregates by Small Angle Neutron Scattering;* Elsevier: Amsterdam, Netherlands, 1984. doi:10.1016/b978-0-444-86912-8.50026-2
62. Teixeira, J. *J. Appl. Crystallogr.* **1988,** *21,* 781–785. doi:10.1107/s0021889888000263
63. Blanchet, C. E.; Spilotros, A.; Schwemmer, F.; Graewert, M. A.; Kikhney, A.; Jeffries, C. M.; Franke, D.; Mark, D.; Zengerle, R.; Cipriani, F.; Fiedler, S.; Roessle, M.; Svergun, D. I. *J. Appl. Crystallogr.* **2015,** *48,* 431–443. doi:10.1107/s160057671500254x
64. Eaton, J. W. *J. Process Control* **2012,** *22,* 1433–1438. doi:10.1016/j.jprocont.2012.04.006
65. Eaton, J. W.; Bateman, D.; Hauberg, S.; Wehbring, R. *GNU Octave Version 4.2.1 Manual: A High-Level Interactive Language for Numerical Computations;;* 2017.
66. Gasteiger, E.; Hoogland, C.; Gattiker, A.; Duvaud, S.; Wilkins, M. R.; Appel, R. D.; Bairoch, A. Protein Identification and Analysis Tools on the ExPASy Server. *The Proteomics Protocols Handbook;* Humana Press: Totowa, NJ, U.S.A., 2005; pp 571–607. doi:10.1385/1-59259-890-0:571

BEILSTEIN JOURNAL OF NANOTECHNOLOGY

Thermal control of the defunctionalization of supported $Au_{25}(glutathione)_{18}$ catalysts for benzyl alcohol oxidation

Zahraa Shahin[1], Hyewon Ji[1], Rodica Chiriac[2], Nadine Essayem[1], Franck Rataboul[1] and Aude Demessence[*1]

Full Research Paper

Open Access

Address:
[1]Univ Lyon, Université Claude Bernard Lyon 1, CNRS, Institut de Recherches sur la Catalyse et l'Environnement de Lyon (IRCELYON), Villeurbanne, France and [2]Univ Lyon, Université Claude Bernard Lyon 1, CNRS, Laboratoire des Multimatériaux et Interfaces (LMI), Villeurbanne, France

Email:
Aude Demessence[*] - aude.demessence@ircelyon.univ-lyon1.fr

* Corresponding author

Keywords:
benzyl alcohol oxidation; glutathione; gold nanoclusters; partial defunctionalization; supported catalyst; zirconium oxide nanoparticles

Beilstein J. Nanotechnol. **2019,** *10,* 228–237.
doi:10.3762/bjnano.10.21

Received: 08 October 2018
Accepted: 28 December 2018
Published: 18 January 2019

This article is part of the thematic issue "Advanced hybrid nanomaterials".

Guest Editor: A. Taubert

Abstract

$Au_{25}(SG)_{18}$ (SG – glutathione) clusters deposited on ZrO_2 nanoparticles have been used as a catalyst for benzyl alcohol oxidation. Calcination was performed at different temperatures to study the ligand and particle size effect on the catalytic activity. In contrast to most gold nanoclusters which have to be completely defunctionalized for maximum catalytic activity, the partially defunctionalized $Au_{25}(SG)_{18}@ZrO_2$ catalyst, thermally treated at 300 °C, exhibits full conversion of benzyl alcohol within 15 h under atmospheric pressure with 94% selectivity towards benzaldehyde.

Introduction

Since Haruta's discovery of the catalytic activity of gold nanoparticles (GNPs), GNPs have been of great interest in chemistry, dispersed on metal oxides and in CO oxidation reaction [1]. Today, GNPs of diameter less than 10 nm are known to be a remarkable, heterogeneous catalyst, capable of catalyzing a wide range of reactions including hydrocarbon combustion [2], direct synthesis of hydrogen peroxide by the hydrogenation of O_2 [3], ozone decomposition [4], selective oxidation reactions [5-8] and so on. However, a debate regarding the particle size effect on the catalytic activity and the concerns related to the synthesis and stabilization of monodisperse GNPs is still ongoing [9,10].

Gold thiolate nanoclusters (GNCs) hold promise due to (i) their atomically well-defined structure with a precise formula, $Au_n(SR)_m$, in the range of $n = 10$ [11] to 279 [12], i.e., from 1 to 2.2 nm and (ii) for some of them their crystallographically solved structures [13-15]. The $Au_{25}(SR)_{18}$ gold thiolate cluster, the captain of the gold nanoclusters ship, is a thermodynamically stable cluster consisting of 25 gold atoms and protected by 18 thiolate ligands [16]. This gold thiolate cluster has been widely studied for its high potential in different domains of chemical sensing, bioimaging, biotherapy and catalysis. As a catalyst, GNCs, and mostly $Au_{25}(SR)_{18}$ gold thiolate clusters, have shown high activity for different reactions such as liquid or gas

phase oxidation, hydrogenation, C–C coupling and electro/photocatalysis [13].

Based on different studies, it is has been shown that the presence or absence of the thiolate ligand affects the catalytic activity and selectivity of gold thiolate clusters [17,18]. For example, high activity in the aerobic epoxidation of *trans*-stilbene was observed using non-calcined $Au_{25}(SPhNH_2)_{17}$@SBA-15, whereas upon calcination, its activity decreased [19]. In contrast, fully defunctionalized clusters are essential for CO [20], alcohol [17,21], cyclohexane [22] and styrene [23,24] oxidation, as well as nitrobenzene hydrogenation [24]. Recently, a partially calcined Au_{38}(2-phenylethanethiolate)$_{24}$ cluster supported on activated carbon (AC) exhibited high efficiency in glucose oxidation [25]. The full defunctionalization at higher temperature usually induces an increase in particle size and decrease of the catalytic activity [26].

Benzyl alcohol oxidation is a model reaction generally used to test the catalytic activity of gold-based materials [27-31]. In the literature, different gold thiolate clusters grafted on different supports were used to selectively oxidize benzyl alcohol. Thus, Au_{25}(6-mercaptohexanoic)acid$_{18}$@HAP (HAP – hydroxyapatite) was defunctionalized either by using *tert*-butyl hydroperoxide or by calcination at 300 °C and showed, in both cases, incomplete conversion of the alcohol (46%) under 5 bar of O_2, at 30 °C and in the presence of a base [32]. Another heterogeneous catalyst, Au_{25}(dodecanethiolate)$_{18}$ deposited on porous carbon nanosheets, has been thermally treated at 500 °C for 4 h and showed full conversion of benzyl alcohol into mostly benzoic acid, under 1 atm of O_2 at 30 °C using a base [17]. In a previous study by our group, $Au_{25}(SPhNH_2)_{17}$@SBA-15, calcined at 400 °C to fully remove the ligands, induced the full conversion of benzyl alcohol after a couple of hours in toluene at 80 °C with a base and under atmospheric conditions [21]. Using O_2 as an oxidant under atmospheric conditions is a limitless and inexpensive oxidizing agent and allows for a sustainable transformation. Nevertheless, in the last example, the mesoporous silica support exhibits low stability in basic media.

In the context of using atmospheric conditions for the oxidation of benzyl alcohol and a stable support, we present in this work the catalytic activity of a new composite material: $Au_{25}(SG)_{18}$ clusters (SG – glutathione) supported on ZrO_2 nanoparticles. The interest in using ZrO_2 comes from its high physical and chemical stability, along with its ability to form nanoparticles for high dispersion of the gold nanoclusters [24]. In this work, we synthesized $Au_{25}(SG)_{18}$@ZrO_2 (A), a composite material, and studied the calcination effect to control the defunctionalization of the clusters on the activity and selectivity of the heterogeneously catalyzed benzyl alcohol oxidation.

Results and Discussion

Catalyst characterization

A $Au_{25}(SG)_{18}$@ZrO_2 composite material (A), with a theoretical gold loading of 1 wt % Au, was prepared by depositing $Au_{25}(SG)_{18}$ gold clusters on ZrO_2 nanoparticles.

Zirconium hydroxide, $Zr(OH)_4$, was used as a precursor for the ZrO_2 nanoparticles. $Zr(OH)_4$ was calcined at 550 °C for 12 h under air at a rate of 2 °C/min. The powder X-ray diffraction (PXRD) pattern of the obtained powder indicated the presence of two crystallographic phases of ZrO_2, monoclinic and tetragonal (Figure S1, Supporting Information File 1). The transmission electron microscopy (TEM) image shows that the ZrO_2 particles have a diameter of around 50 nm.

$Au_{25}(SG)_{18}$ was synthesized according to a reported method [33]. The characterization of the clusters by UV–vis spectroscopy shows two absorption peaks centered at 450 and 650 nm, which correspond to the electronic transitions typical of this molecular composition (Figure S2, Supporting Information File 1) [34,35]. The PXRD of the clusters exhibited an intense reflection at 5.01°, corresponding to a center-to-center distance between two clusters of 1.76 nm, by applying Bragg's law (Figure S3, Supporting Information File 1) [36]. This distance is in good agreement with the expected size of $Au_{25}(SG)_{18}$ including the ligands. In addition, the broad peak at 37° corresponds to the ultra-small Au_{25} gold core and confirms the absence of large gold nanoparticles or bulk gold.

Impregnation of the clusters on ZrO_2 nanoparticles was done by adding ZrO_2 powder to an aqueous solution of $Au_{25}(SG)_{18}$, stirred for 15 min and then centrifuged to collect the powder without further washing. The composite material $Au_{25}(SG)_{18}$@ZrO_2 comprised of 0.7% Au was calcined at different temperatures (200, 300 and 400 °C) to gradually remove the ligands. This calcination process induces a change in color from beige for $Au_{25}(SG)_{18}$@ZrO_2 to pink for the calcined samples. Before and after each calcination step, the PXRD patterns of the obtained materials showed no change from the ZrO_2 diagrams and no indication of reflection of bulk gold (Figure S4, Supporting Information File 1). These observations mean that there is no modification of the support and that the quantity of gold is too small to be detected.

Thermal studies of the materials were done by thermogravimetric analysis (TGA) under air on pure $Au_{25}(SG)_{18}$ gold clusters, gold clusters deposited on ZrO_2 and ZrO_2 alone. From the TGA curve of the clusters, a first gradual weight loss of 6.5% is observed before 200 °C, corresponding to the evaporation of the solvent (Figure 1a). Then a second gradual weight loss of 46.2% happens up to 500 °C and the remaining gold is 47.3%.

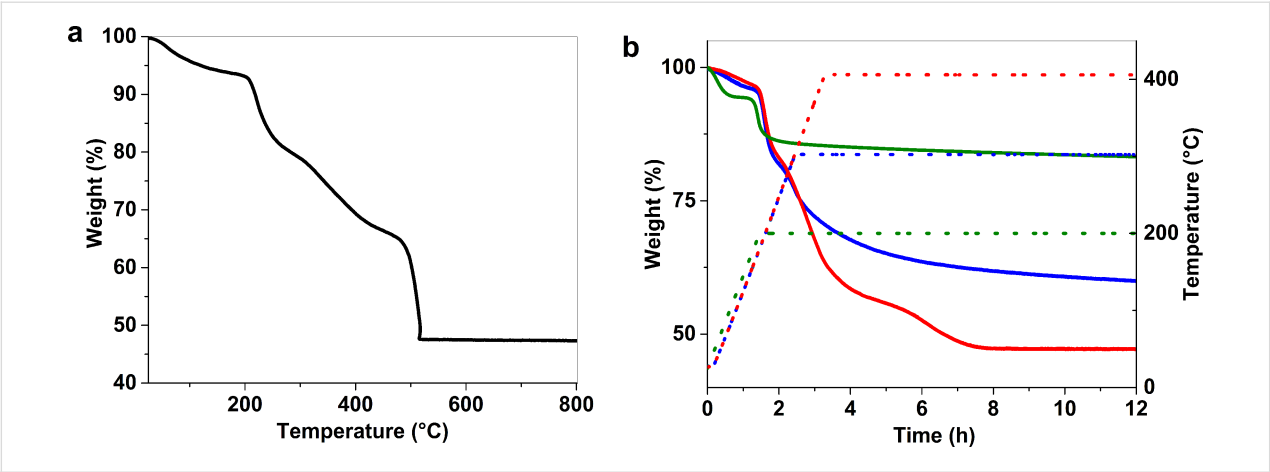

Figure 1: (a) TGA experiment on $Au_{25}(SG)_{18}$ under air at 10 °C/min. (b) Isotherm experiments on $Au_{25}(SG)_{18}$ under air at 200 °C (green), 300 °C (blue) and 400 °C (red) for 12 h. Solid lines represent the weight (%) and dotted lines represent the heating ramp.

The actual percentage of glutathione (49.4%) is a little less than the calculated value (53.0%). This difference in thiolate ligand may be due to the early decomposition of the molecules before 200 °C or to the presence of impurities such as bigger clusters [37]. Isotherm analysis was performed at 200 °C, 300 °C, and 400 °C, with the temperatures kept constant for 12 hours under air, in order to simulate the calcination procedures. For the isotherm analysis at 200 °C, 300 °C, and 400 °C, the final loss reached 17.0%, 40.8% and 52.9%, respectively, corresponding to a partial calcination of 36.5% at 300 °C and to a complete removal of the ligand (77.1%) at 400 °C (Figure 1b). It is interesting to note that the complete calcination of the ligands at 400 °C is reached after almost 8 h of heating, suggesting that a heating ramp of at least 8 hours is required to completely remove the glutathione molecules from the gold surface. For the TGA of the ZrO_2 support, 2.4% weight loss was observed at low temperature that corresponds to trace water (Figure 2). After the deposition of 1 wt % Au using $Au_{25}(SG)_{18}$ on ZrO_2, a first weight loss of 2.4% is observed and a second weight loss of 1.3% from 250 °C is also seen and fits well with the decomposition of the glutathione molecules (Figure 2).

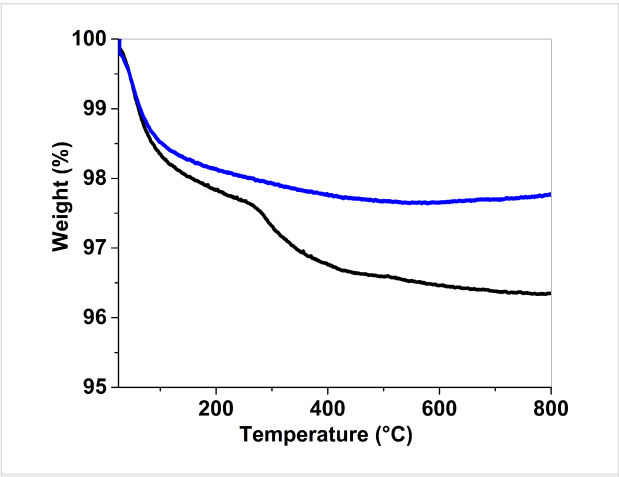

Figure 2: TGA experiments on $Au_{25}(SG)_{18}$ deposited on ZrO_2 (black) and ZrO_2 alone (blue) carried out under air at 10 °C/min.

The influence of calcination temperature on the particle size of the clusters deposited on ZrO_2 was evaluated from the TEM images and size distribution analysis (Figure 3). The composite material $Au_{25}(SG)_{18}@ZrO_2$ is named (A) and (A_{200}), (A_{300}) and (A_{400}) after calcination under air at 200 and 300 °C for 4 h and 400 °C for 12 h, respectively. Sample (A) exhibits homogeneous clusters of size 1.6 ± 0.3 nm (Figure 3a,e), being close to the expected Au_{25} diameter estimated from the crystal structure (1 nm) [38]. For (A_{200}) the mean particle size is 1.6 ± 0.7 nm and approximately the same for (A_{300}) at 1.7 ± 0.5 nm (Figure 3b,c,e). For (A_{400}), the particle size increased to 2.0 ± 0.7 nm, which may be due to the sintering of the bare Au_{25} gold cores (Figure 3d,e). In general, supported gold thiolate clusters are known to grow when calcined at high temperature [24], except when they are inserted in a porous material, such as SBA-15 [21], or loaded with a very small quantity of clusters [22]. Here we note that the gold clusters maintain a diameter of around 2 nm or below, with a narrow size distribution, upon calcination at temperatures up to 400 °C with 0.7 wt % Au loading.

Catalytic performance

The catalytic activity of $Au_{25}(SG)_{18}@ZrO_2$, calcined at different temperatures, was studied for the oxidative dehydrogenation of benzyl alcohol to benzaldehyde in the presence of an excess of base (Cs_2CO_3, 3 eq.) at 80 °C and under atmospheric conditions (Scheme 1). Before observing the influence of calcination of thiolates on the activity of the gold catalysts, a blank and the support alone were run to confirm the catalytic activity

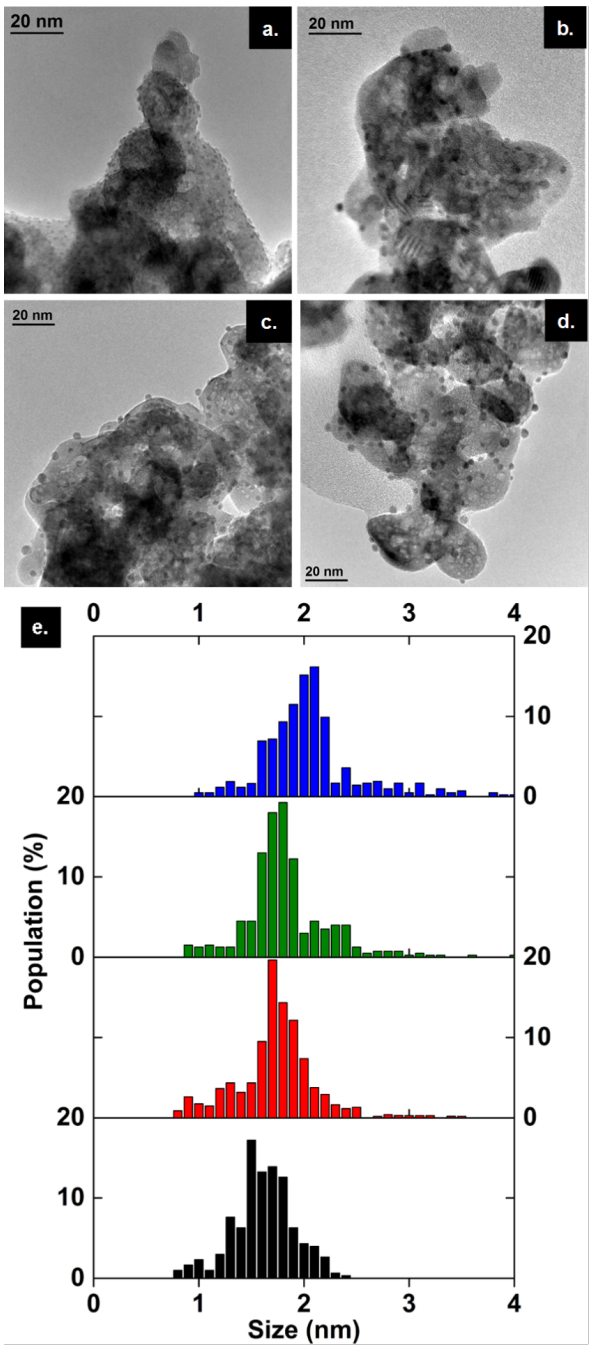

Figure 3: TEM images of $Au_{25}(SG)_{18}@ZrO_2$ (Au 0.7 wt %) (a) before calcination, sample (A), (b) calcined at 200 °C for 4 hours under air, sample (A_{200}), (c) calcined at 300 °C for 4 hours under air, sample (A_{300}), and (d) calcined at 400 °C for 12 hours under air, sample (A_{400}), and (e) the size distribution of the composites – (A) in black, (A_{200}) in red, (A_{300}) in green and (A_{400}) in blue.

of the gold catalyst. Since there was no benzyl alcohol conversion and no formation of benzaldehyde in both cases, it was deduced that the reaction conditions, such as temperature or atmospheric O_2 did not have any catalytic role in the oxidation reaction.

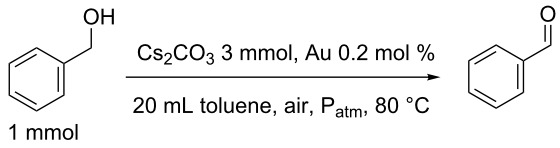

Scheme 1: Benzyl alcohol oxidative dehydrogenation under standard conditions.

Influence of the calcination temperature

$Au_{25}(SG)_{18}@ZrO_2$ (A) was inactive and unable to oxidize benzyl alcohol to benzaldehyde. Despite the well-dispersed, homogenously small-sized gold particles, as seen from the TEM image (Figure 3a) and the size distribution graph (Figure 3e), their catalytic activity was likely to be affected by the presence of the thiolate ligands. The same behavior was observed for the untreated $Au_{25}(SPhNH_2)_{17}@SBA\text{-}15$, which did not show any activity for benzyl alcohol oxidation [21]. For (A_{200}), 64.2% of the thiolate ligands remained, and benzyl alcohol conversion reached 50% after 12 h with an initial turn over frequency (TOF) of 10 h^{-1}, which was very low compared to that of (A_{300}). The latter had 46.5% of the thiolate ligands remaining and only 1.5 h were needed to reach 50% conversion with a TOF = 261 h^{-1}, showing that the partial calcination had improved the catalyst activity. For (A_{400}), for which no thiolate ligands remained, 2.4 h were needed to reach 50% conversion with a TOF = 123 h^{-1} (Figure 4 and Table 1).

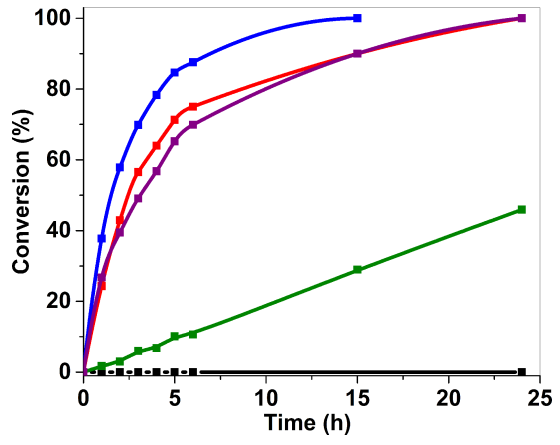

Figure 4: Monitoring over time of benzyl alcohol oxidative dehydrogenation conversion with $Au_{25}(SG)_{18}@ZrO_2$ before calcination (black), after calcination at 200 °C for 4 hours under air, (A_{200}) (green), at 300 °C for 4 hours under air, (A_{300}) (blue), at 400 °C for 12 hours under air, (A_{400}) (red) and compared to $AuNP@ZrO_2$ (purple).

The increase in catalytic activity from (A) to (A_{200}) and the highest TOF (261 h^{-1}) in the case of (A_{300}), is explained by the increase of defunctionalization of the supported thiolate clus-

Table 1: Catalytic performance of $Au_{25}(SG)_{18}@ZrO_2$ based catalysts (2 μmol Au) in the oxidative dehydrogenation of benzyl alcohol in toluene at 80 °C (1 atm of air): 25%, 50% and 90% conversion times (*t*), benzaldehyde selectivity at half conversion (Sel 50%), turn over frequency (TOF) and gold particle size measured by TEM before the catalytic test. ND: Not determined.

Sample	Catalyst	$t_{25\%}$ (h)	$t_{50\%}$ (h)	$t_{90\%}$ (h)	$Sel_{50\%}$ (%)	TOF (h^{-1})	Average AuNP diameter (nm)
(A)	$Au_{25}(SG)_{18}@ZrO_2$	ND	ND	ND	ND	–	1.6 ± 0.3
(A_{200})	(A) calcined at 200 °C	6	12	21.6	80	10	1.6 ± 0.7
(A_{300})	(A) calcined at 300 °C	0.6	1.5	6.8	94	261	1.7 ± 0.5
(A_{400})	(A) calcined at 400 °C	1	2.4	15	100	123	2.0 ± 0.7
(B)	$AuNP@ZrO_2$	1	3	15	100	144	2.7 ± 1.5

ters, which triggered the catalytic activity. However, the decrease in catalytic activity of (A_{400}), with a lower TOF value (123 h^{-1}), though it was fully defunctionalized, is related to the sintering of the gold nanoparticles, where bigger 2.0 ± 0.7 nm particles were observed on the TEM images. This means that both the defunctionalization and the particle size affect the catalytic activity of the composite material. A balance between both is required to have maximum activity, as in (A_{300}), where 46.5% of the thiolate ligands remained, triggering gold activity and keeping small sized particles at 1.7± 0.5 nm. Therefore, partially calcined clusters did not inhibit high catalytic activity, in contrast, it was enhanced, which was similar to a recent reported work [25].

The catalyst performance was compared to a catalyst synthesized by the deposition-precipitation method of gold nanoparticles on ZrO_2 nanoparticles, compound (B). The average particle size of (B), measured by TEM images, is 2.7 ± 1.5 nm, higher than that of the gold particles obtained in (A_{400}) after full calcination (Figure 5). Compound (B) showed 50% conversion of benzyl alcohol in 3 h, a value close to that obtained with (A_{400}), having slightly higher initial TOF (144 h^{-1}). They both reached 90% conversion after 15 h. This shows that when gold nanoparticles have a diameter more than 2 nm, they act in a similar catalytic manner, but still have slower catalytic activity compared to the partially calcined composite material (A_{300}) (Table 1).

At the selectivity level of 50% ($Sel_{50\%}$) conversion toward benzaldehyde, an increase with the increase of calcination temperature was observed for compound (A). The $Sel_{50\%}$ for (A_{200}) was 80%, less than that of (A_{300}), at 94%, which was also lower than the $Sel_{50\%}$ of (A_{400}) and (B) at 100% (Table 1). This means that having pure gold without any organic linker is necessary to have high selectivity toward benzaldehyde, but still the partially calcined composite material (A_{300}), with comparable selectivity of 94%, to (A_{400}) and (B), resulted in the best activity with highest TOF = 261 h^{-1}.

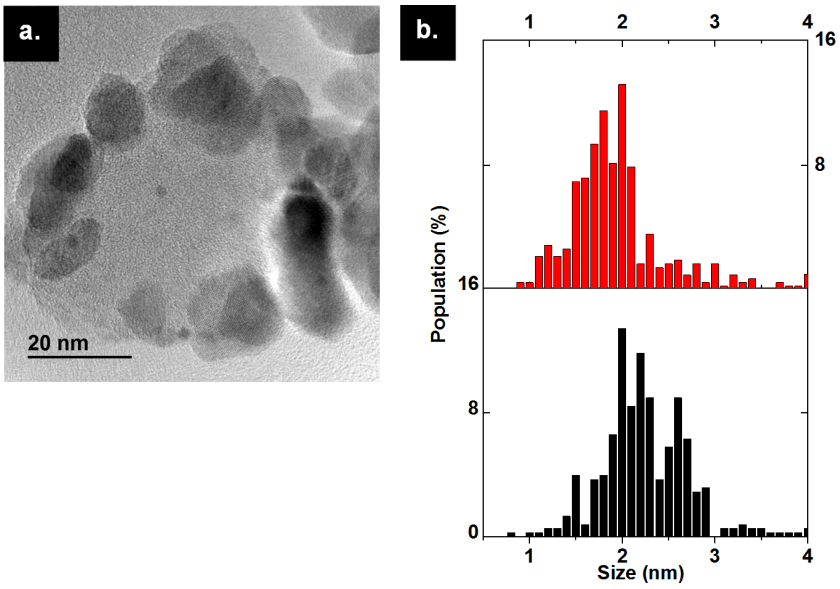

Figure 5: (a) TEM image of $AuNP@ZrO_2$ prepared by the deposition-precipitation method (B). (b) Comparison of size distribution of $Au_{25}(SG)_{18}@ZrO_2$ calcined at 400 °C for 12 hours under air (A_{400}) in red and $AuNps@ZrO_2$ (B) in black.

Compared to previous studies, $Au_{25}(SC_{12}H_{25})_{18}$ supported on hierarchically porous carbon nanosheets [17] and $Au_{25}(SPhNH_2)_{17}$ supported on SBA-15 [21], both calcined at 400 °C, showed 67% and 68% of selectivity for benzaldehyde, respectively. Thus, the 100% selectivity for benzaldehyde of $Au_{25}(SG)_{18}$ over ZrO_2 when calcined at 400 °C may result from the different compositions of the clusters or the effect of the type of support that can be involved in the oxidation mechanism or their different morphologies, as porous materials for the carbon nanosheets and the silica, and nanoparticles for ZrO_2.

Effect of the reaction temperature

In general, the oxidation of benzyl alcohol is performed under harsh conditions of temperature and pressure without a catalyst [39]. Gold-based catalysts perform this oxidation under milder conditions [31]. The reaction using (A_{300}) as a catalyst, was performed at two different temperatures, 60 °C and 80 °C, with all other experimental conditions being the same. Such relatively low temperatures showed no thermal conversion of benzyl alcohol without catalyst. The conversion curves clearly showed that the increase of the temperature of 20 °C favors the benzyl alcohol conversion (Figure 6). At 60 °C, the time necessary to reach 50% conversion is 3 h, whereas it is 1.5 h at 80 °C. Besides, the $Sel_{50\%}$ increased from 75% to 94% with temperature, suggesting that the faster the reaction rate, the higher the benzaldehyde selectivity (Table 2).

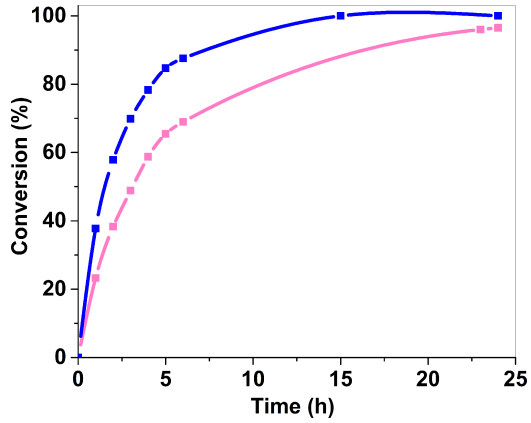

Figure 6: Monitoring over time of benzyl alcohol oxidative reaction with $Au_{25}(SG)_{18}@ZrO_2$ calcined at 300 °C for 4 hours under air (A_{300}) at 60 °C (pink), and at 80 °C (blue).

Recyclability of the catalyst

The recyclability of (A_{300}), the catalyst that showed the highest TOF value in the oxidative dehydrogenation of benzyl alcohol, was tested by adding a new portion of benzyl alcohol to the reaction mixture after each cycle. It was observed that after each run, the catalytic stability decreased, giving full conversion in the first cycle $(A_{300})^1$, 86.6% conversion in the second cycle $(A_{300})^2$ and 70.3% in the third cycle $(A_{300})^3$, after 24 h of reaction (Figure 7). This decrease in the catalytic activity is explained by particle aggregation and sintering with time. The particle size after the third cycle in $(A_{300})^3$ was 2.8 ± 0.8 nm (Figure 8).

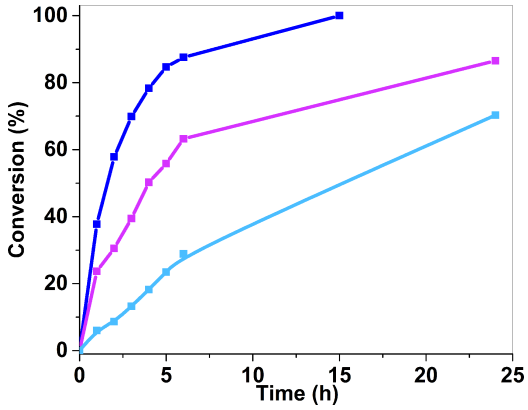

Figure 7: Monitoring over time of benzyl alcohol oxidative dehydrogenation conversion for successive additions of 1 mmol BnOH in the reaction medium (each reaction was carried out during 24 h) using (A_{300}) as a catalyst. $(A_{300})^1$ represents the conversion (%) while using the catalyst for the first cycle (blue), $(A_{300})^2$ for the second cycle (pink) and $(A_{300})^3$ for the third cycle (cyan).

Conclusion

Successfully supported $Au_{25}(SG)_{18}$ clusters on ZrO_2 nanoparticles was used as a catalyst, after activation, in the oxidative dehydrogenation of benzyl alcohol to benzaldehyde. The effect of the calcination temperature was studied by subsequent calcination steps under different conditions. For partial defunctionalization, activation at 200 °C and 300 °C for 4 h was done under air, whereas the treatment at 400 °C for 12 hours resulted in the complete removal of the thiolate ligands. The influence of the presence of thiolate ligands and the size of the particles was clearly observed during benzyl alcohol conversion, where the

Table 2: Catalytic performance of (A_{300}) catalyst (2 µmol Au) in the oxidative reaction of benzyl alcohol in toluene at 80 °C and 60 °C (1 atm of air): 25%, 50% and 90% conversion time (t), benzaldehyde selectivity at half conversion (Sel 50%) and turn over frequency (TOF).

	Reaction temperature (°C)	$t_{25\%}$ (h)	$t_{50\%}$ (h)	$t_{90\%}$ (h)	$Sel_{50\%}$ (%)	TOF (h^{-1})
(A_{300})	80	0.6	1.5	6.8	94	261
(A_{300})	60	1.2	3	16	75	101

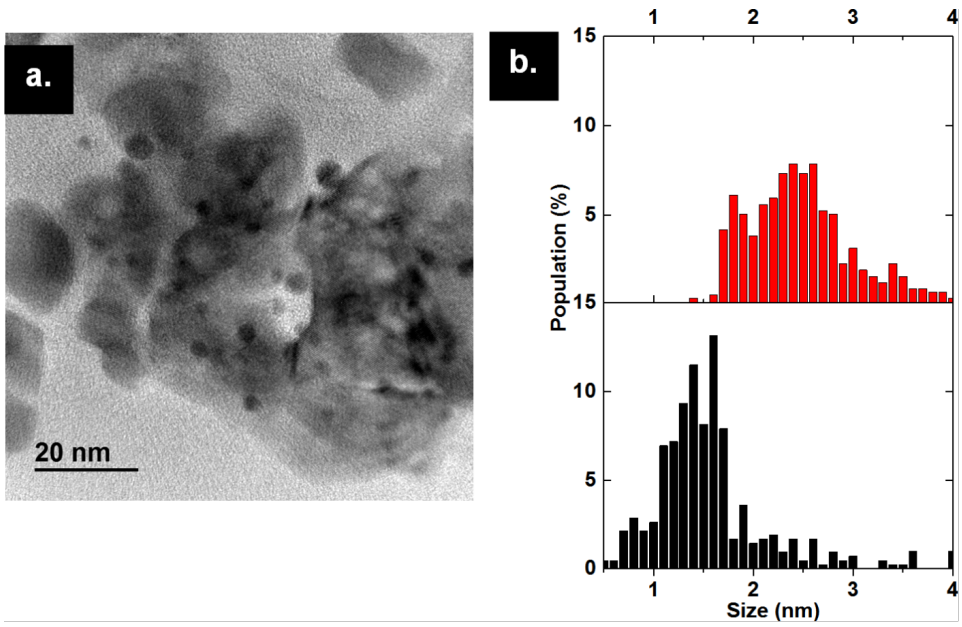

Figure 8: (a) TEM image of $(A_{300})^3$ after the third catalytic cycle. (b) Comparison of the size distribution of $(A_{300})^3$ in red and (A_{300}) before the catalytic test in black.

full conversion was observed after 15 h with the catalyst partially defunctionalized at 300 °C under air for 4 hours with particle of 1.7 ± 0.5 nm diameter. This study confirmed that the activity and selectivity of supported $Au_{25}(SG)_{18}$ clusters are highly efficient for oxidation reactions carried out under mild conditions of ambient atmosphere and temperature (80 °C), and most importantly do not require the complete removal of the thiolate ligands.

Experimental

Chemicals

Tetrachloroauric acid trihydrate ($HAuCl_4{\cdot}3H_2O$, ≥99.9% trace metal basis), sodium borohydride ($NaBH_4$, ≥98.0%), benzyl alcohol and dodecane (≥99%) were purchased from Sigma-Aldrich. L-glutathione (HSG, +98%) and cesium carbonate (99%, metal basis) were obtained from Alfa Aesar, Methanol (HPLC grade) from VWR International, and toluene from Emsure. Zirconium oxide (ZrO_2) was prepared from $Zr(OH)_4$ calcined at 550 °C for 12 hours under air flow at a rate of 2 °C/min. All chemicals were used without further purification. All glassware were washed with aqua regia and rinsed with ethanol. Ultrapure water (18 MΩ) was used in all experiments.

Characterization techniques

Powder X-ray diffraction (PXRD) was carried out on a Bruker D8 Advance A25 diffractometer using Cu Kα radiation. Small-angle X-ray scattering was recorded between 0.45° and 7° (2θ) with 0.01° steps and 2 s per step. Standard acquisition was recorded between 4° and 80° (2θ) with 0.02° steps and 0.5 s per step.

Thermogravimetric analysis (TGA) was performed with a TGA STARE system from Mettler Toledo Thermobalance MX1. Around 2 mg of sample was heated from 25 °C to 800 °C at a rate of 10 °C/min in a 70 µL alumina crucible, under air.

For isothermal TGA, the samples were heated at a rate of 2 °C/min from 25 °C to the final targeted temperature (200 °C, 300 °C, and 400 °C) in a 70 µL alumina crucible, under air. The final temperature was maintained for 12 hours.

Transmission electron microscopy (TEM) was carried out on a JEOL 2010 LaB_6 microscope operating at 200 kV. The samples were prepared on a copper grid for analysis. The measurement of the diameter of the particles was done by using the TEM images, where the diameter of each particle was measured by hand by using Image J software. A minimum number of particles of 300 was measured to get a distribution.

Gas chromatography was carried out on a Shimadzu GC-2010 device using a 30 m × 0.25 mm × 0.25 µm column programmed from 30 °C to 180 °C, injector and FID detector set at 220 °C, and using N_2 as carrier gas. External calibration was carried out by injecting distinct standard solutions of benzyl alcohol and benzaldehyde with dodecane.

UV–visible spectroscopy was performed with Agilent UV 8453 UV–visible spectrometer, with a deuterium discharge lamp as the radiation source for ultraviolet wavelength region and a tungsten lamp for the visible and short wave near-infrared wavelength region. Water was used as the blank.

Synthesis of $Au_{25}(SG)_{18}$

$Au_{25}(SG)_{18}$ clusters were synthesized following a previously reported synthesis procedure with some modifications [33]. In a 100 mL round-bottom flask, 0.25 mmol $HAuCl_4{\cdot}3H_2O$ was dissolved in 50 mL methanol under stirring at 1500 rpm in an ice bath. Then, 1 mmol glutathione was rapidly added to the flask, and the mixed solution was left stirring for 30 minutes. The color of the mixed solution gradually changed from clear yellow to transparent. Meanwhile, the $NaBH_4$ solution was prepared by dissolving 2.5 mmol $NaBH_4$ in 12.5 mL ice-cold water, which was rapidly added to the mixed solution. An obvious color change to dark brown was observed after the addition of $NaBH_4$. The reaction was allowed to proceed under stirring at 1500 rpm in an ice bath for 1 hour, and UV–vis spectra were collected at 45 minutes into the reaction. The product was purified by repeated centrifugation (10000 rpm, 15 minutes) and was washed several times with methanol (5000 rpm, 15 minutes). The obtained product was dried under vacuum at room temperature, and was kept in the refrigerator until the second part. In the second part of the synthesis, the product was dissolved in 12.5 mL water and 0.5 mmol glutathione was added. The mixture was left stirring at 60 rpm and heated with an oil bath at 55 °C for 4 hours. The final product $Au_{25}(SG)_{18}$ was filtered, isolated by precipitation with methanol and centrifuged (10000 rpm for 15 minutes), washed several times with methanol (5000 rpm, 15 minutes), and was air-dried.

Synthesis of the composite material $Au_{25}(SG)_{18}@ZrO_2$

Gold cluster deposition

$Au_{25}(SG)_{18}$ cluster deposition was performed using a wet impregnation method. Gold clusters, with a mass of 10 mg corresponding to a theoretical loading of 1 wt % Au, and 500 mg of support (ZrO_2) were dispersed in 5 mL of water, swirled, and left for 15 minutes. The prepared catalyst (A) was recovered by centrifugation (4000 rpm, 10 minutes) after the addition of small amounts of ethanol, and was followed by drying under air.

Calcination

Calcination was performed on $Au_{25}(SG)_{18}@ZrO_2$. Around 100 mg of compounds were heated at 200 °C for 4 hours under air, 300 °C for 4 hours under air, and 400 °C for 12 hours under air, with a rate of 2 °C/min.

Synthesis of $AuNP@ZrO_2$ by deposition-precipitation

The synthesis of $AuNP@ZrO_2$ was done according to a reported protocol [40]. An aqueous solution of tetrachloroauric acid trihydrate (1.5% by mass, in 10 mL H_2O) was added dropwise to ZrO_2 (1 g) dispersed in 30 mL H_2O while stirring at 400 rpm at room temperature. A yellow solution was obtained. NaOH (0.5 M) was used to adjust the pH at 9, where the solution then turned transparent. The mixture was kept stirring at 400 rpm for 1 h at room temperature. The temperature was then increased up to 80 °C and left stirring for 2 h while keeping pH 9. The reaction was set back at room temperature and left overnight. The product was filtered, dried at 110 °C for 30 minutes, calcined at 350 °C for 4 h under air, then reduced under H_2 flow at 350 °C for 2 h. The final powder had dark pink-purple color and named (B).

Benzyl alcohol oxidation

Catalytic evaluation was carried out following a previously reported procedure [21]. In a two-neck 100 mL round-bottom flask equipped with a condenser and a magnetic stirrer, benzyl alcohol (BnOH, substrate, 1 mmol), cesium carbonate (Cs_2CO_3, base, 3 mmol), toluene (solvent, 20 mL) and gold-based catalyst (2 μmol Au) were stirred at 400 rpm at 80 °C under atmospheric air pressure, while connecting the flask to a reflux.

The reactions were monitored by regular samplings (0.2 mL) that were diluted 2 times in the standard dodecane solution (1 wt % in toluene) and were analyzed immediately by gas chromatography. Benzyl alcohol (BnOH) conversion was calculated from the ratio of the number of moles of BnOH converted over the initial quantity of BnOH introduced at the beginning of the reaction. The benzaldehyde (BnAld) yield was calculated from the ratio of the number of moles of BnAld produced over the initial quantity of BnOH introduced at the beginning of the reaction. The selectivity was defined as the ratio of the BnAld yield over BnOH conversion. The given TOF (h^{-1}) are the initial TOF, calculated from the ratio of the converted moles of benzyl alcohol over the total moles of the gold content in the catalyst per unit of time.

$$\mathrm{TOF}(h^{-1}) = \frac{\text{moles of converted benzylalcohol}}{\text{moles of total Au content in the catalyst} \times \text{time}}$$

Supporting Information

Supporting Information File 1

Additional experimental results.
[https://www.beilstein-journals.org/bjnano/content/supplementary/2190-4286-10-21-S1.pdf]

Acknowledgements

The authors would like to thank L. Burel, F. Simonet, F. Bosselet and Y. Aizac, from IRCELYON, for their help and F. Toche, from LMI, for his assistance with the TGA experiments. Z. S. would like to acknowledge Lyon 1 University for her Ph.D. grant.

ORCID® iDs

Zahraa Shahin - https://orcid.org/0000-0002-4210-2801
Hyewon Ji - https://orcid.org/0000-0001-8690-1253
Franck Rataboul - https://orcid.org/0000-0002-4299-5937
Aude Demessence - https://orcid.org/0000-0002-8690-5489

References

1. Haruta, M.; Kobayashi, T.; Sano, H.; Yamada, N. *Chem. Lett.* **1987,** *16,* 405–408. doi:10.1246/cl.1987.405
2. Miao, S.; Deng, Y. *Appl. Catal., B* **2001,** *31,* L1–L4. doi:10.1016/s0926-3373(01)00122-9
3. Landon, P.; Collier, P. J.; Papworth, A. J.; Kiely, C. J.; Hutchings, G. J. *Chem. Commun.* **2002,** 2058–2059. doi:10.1039/b205248m
4. Hao, Z.; Cheng, D.; Guo, Y.; Liang, Y. *Appl. Catal., B* **2001,** *33,* 217–222. doi:10.1016/s0926-3373(01)00172-2
5. Prati, L.; Porta, F. *Appl. Catal., A* **2005,** *291,* 199–203. doi:10.1016/j.apcata.2004.11.050
6. Biradar, A. V.; Asefa, T. *Appl. Catal., A* **2012,** *435–436,* 19–26. doi:10.1016/j.apcata.2012.05.029
7. Hughes, M. D.; Xu, Y.-J.; Jenkins, P.; McMorn, P.; Landon, P.; Enache, D. I.; Carley, A. F.; Attard, G. A.; Hutchings, G. J.; King, F.; Stitt, E. H.; Johnston, P.; Griffin, K.; Kiely, C. J. *Nature* **2005,** *437,* 1132–1135. doi:10.1038/nature04190
8. Lignier, P.; Morfin, F.; Mangematin, S.; Massin, L.; Rousset, J.-L.; Caps, V. *Chem. Commun.* **2007,** 186–188. doi:10.1039/b610546g
9. Roldan Cuenya, B.; Behafarid, F. *Surf. Sci. Rep.* **2015,** *70,* 135–187. doi:10.1016/j.surfrep.2015.01.001
10. Zanella, R.; Giorgio, S.; Henry, C. R.; Louis, C. *J. Phys. Chem. B* **2002,** *106,* 7634–7642. doi:10.1021/jp0144810
11. Lavenn, C.; Albrieux, F.; Tuel, A.; Demessence, A. *J. Colloid Interface Sci.* **2014,** *418,* 234–239. doi:10.1016/j.jcis.2013.12.021
12. Sakthivel, N. A.; Theivendran, S.; Ganeshraj, V.; Oliver, A. G.; Dass, A. *J. Am. Chem. Soc.* **2017,** *139,* 15450–15459. doi:10.1021/jacs.7b08651
13. Jin, R.; Zeng, C.; Zhou, M.; Chen, Y. *Chem. Rev.* **2016,** *116,* 10346–10413. doi:10.1021/acs.chemrev.5b00703
14. Kurashige, W.; Niihori, Y.; Sharma, S.; Negishi, Y. *Coord. Chem. Rev.* **2016,** *320–321,* 238–250. doi:10.1016/j.ccr.2016.02.013
15. Sakthivel, N. A.; Dass, A. *Acc. Chem. Res.* **2018,** *51,* 1774–1783. doi:10.1021/acs.accounts.8b00150
16. Kang, X.; Chong, H.; Zhu, M. *Nanoscale* **2018,** *10,* 10758–10834. doi:10.1039/c8nr02973c
17. Yoskamtorn, T.; Yamazoe, S.; Takahata, R.; Nishigaki, J.-i.; Thivasasith, A.; Limtrakul, J.; Tsukuda, T. *ACS Catal.* **2014,** *4,* 3696–3700. doi:10.1021/cs501010x
18. Nasaruddin, R. R.; Chen, T.; Yan, N.; Xie, J. *Coord. Chem. Rev.* **2018,** *368,* 60–79. doi:10.1016/j.ccr.2018.04.016
19. Lavenn, C.; Demessence, A.; Tuel, A. *Catal. Today* **2014,** *235,* 72–78. doi:10.1016/j.cattod.2014.02.045
20. Wu, Z.; Jiang, D.-e.; Mann, A. K. P.; Mullins, D. R.; Qiao, Z.-A.; Allard, L. F.; Zeng, C.; Jin, R.; Overbury, S. H. *J. Am. Chem. Soc.* **2014,** *136,* 6111–6122. doi:10.1021/ja5018706
21. Lavenn, C.; Demessence, A.; Tuel, A. *J. Catal.* **2015,** *322,* 130–138. doi:10.1016/j.jcat.2014.12.002
22. Liu, Y.; Tsunoyama, H.; Akita, T.; Xie, S.; Tsukuda, T. *ACS Catal.* **2011,** *1,* 2–6. doi:10.1021/cs100043j
23. Huang, P.; Chen, G.; Jiang, Z.; Jin, R.; Zhu, Y.; Sun, Y. *Nanoscale* **2013,** *5,* 3668. doi:10.1039/c3nr00144j
24. Fang, J.; Li, J.; Zhang, B.; Yuan, X.; Asakura, H.; Tanaka, T.; Teramura, K.; Xie, J.; Yan, N. *Nanoscale* **2015,** *7,* 6325–6333. doi:10.1039/c5nr00549c
25. Liu, C.; Zhang, J.; Huang, J.; Zhang, C.; Hong, F.; Zhou, Y.; Li, G.; Haruta, M. *ChemSusChem* **2017,** *10,* 1976–1980. doi:10.1002/cssc.201700407
26. Moulijn, J. A.; van Diepen, A. E.; Kapteijn, F. *Appl. Catal., A* **2001,** *212,* 3–16. doi:10.1016/s0926-860x(00)00842-5
27. Wang, Z.; Xu, C.; Wang, H. *Catal. Lett.* **2014,** *144,* 1919–1929. doi:10.1007/s10562-014-1344-z
28. Pina, C. D.; Falletta, E.; Rossi, M. *Chem. Soc. Rev.* **2012,** *41,* 350–369. doi:10.1039/c1cs15089h
29. Della Pina, C.; Falletta, E. *Catal. Sci. Technol.* **2011,** *1,* 1564. doi:10.1039/c1cy00283j
30. Davis, S. E.; Ide, M. S.; Davis, R. J. *Green Chem.* **2013,** *15,* 17–45. doi:10.1039/c2gc36441g
31. Sharma, A. S.; Kaur, H.; Shah, D. *RSC Adv.* **2016,** *6,* 28688–28727. doi:10.1039/c5ra25646a
32. Zhang, B.; Fang, J.; Li, J.; Lau, J. J.; Mattia, D.; Zhong, Z.; Xie, J.; Yan, N. *Chem. – Asian J.* **2016,** *11,* 532–539. doi:10.1002/asia.201501074
33. Liu, X.; Wu, Y.; Li, S.; Zhao, Y.; Yuan, C.; Jia, M.; Luo, Z.; Fu, H.; Yao, J. *RSC Adv.* **2015,** *5,* 30610–30616. doi:10.1039/c4ra17239f
34. Zhu, M.; Qian, H.; Jin, R. *J. Am. Chem. Soc.* **2009,** *131,* 7220–7221. doi:10.1021/ja902208h
35. Qian, H.; Zhu, M.; Andersen, U. N.; Jin, R. *J. Phys. Chem. A* **2009,** *113,* 4281–4284. doi:10.1021/jp810893w
36. Lavenn, C.; Albrieux, F.; Bergeret, G.; Chiriac, R.; Delichère, P.; Tuel, A.; Demessence, A. *Nanoscale* **2012,** *4,* 7334. doi:10.1039/c2nr32367b
37. Shibu, E. S.; Muhammed, M. A. H.; Tsukuda, T.; Pradeep, T. *J. Phys. Chem. C* **2008,** *112,* 12168–12176. doi:10.1021/jp800508d
38. Heaven, M. W.; Dass, A.; White, P. S.; Holt, K. M.; Murray, R. W. *J. Am. Chem. Soc.* **2008,** *130,* 3754–3755. doi:10.1021/ja800561b
39. Sheldon, R. A.; Arends, I. W. C. E.; ten Brink, G.-J.; Dijksman, A. *Acc. Chem. Res.* **2002,** *35,* 774–781. doi:10.1021/ar010075n
40. Schade, O. R.; Kalz, K. F.; Neukum, D.; Kleist, W.; Grunwaldt, J.-D. *Green Chem.* **2018,** *20,* 3530–3541. doi:10.1039/c8gc01340c

BEILSTEIN JOURNAL OF NANOTECHNOLOGY

Removal of toxic heavy metals from river water samples using a porous silica surface modified with a new β-ketoenolic host

Said Tighadouini[1], Smaail Radi[*1,2], Abderrahman Elidrissi[1], Khadija Haboubi[3], Maryse Bacquet[4], Stéphanie Degoutin[4], Mustapha Zaghrioui[5] and Yann Garcia[*6]

Full Research Paper

Open Access

Address:
[1]Laboratoire de Chimie Appliquée et Environnement (LCAE), Faculté des Sciences, Université Mohamed I, 60 000 Oujda, Morocco, [2]Centre de l'Oriental des Sciences et Technologies de l'Eau (COSTE), Université Med I, 60 000 Oujda, Morocco, [3]Group of material sciences, energy and environnement, ENSAH, Alhoceima, Morocco, [4]Unité Matériaux et Transformations UMR8207 (UMET), Equipe Ingénierie des Systèmes Polymères, Université des Sciences et Technologies de Lille, Bâtiment C6 salle 119-59655 Villeneuve d'Ascq, France, [5]Laboratoire GREMAN CNRS-UMR 7347 IUT de BLOIS, Université François-Rabelais de Tours, 15 Rue de la Chocolaterie, 41029 Blois, France and [6]Institute of Condensed Matter and Nanosciences, Université catholique de Louvain, Place Louis Pasteur 1, 1348 Louvain-la-Neuve, Belgium

Email:
Smaail Radi* - s.radi@ump.ac.ma; Yann Garcia* - yann.garcia@uclouvain.be

* Corresponding author

Keywords:
heavy metals; hybrid materials; β-ketoenol–pyridine–furan ligands; polluted media; porous silica; remediation

Beilstein J. Nanotechnol. **2019,** *10,* 262–273.
doi:10.3762/bjnano.10.25

Received: 13 September 2018
Accepted: 28 November 2018
Published: 23 January 2019

This article is part of the thematic issue "Advanced hybrid nanomaterials".

Guest Editor: A. Taubert

Abstract

A new hybrid adsorbent material for the efficient removal of heavy metals from natural real water solutions (Moroccan river water samples) was prepared by the immobilization of a new conjugated β-ketoenol–pyridine–furan ligand onto a silica matrix. The thermodynamical properties including pH, adsorption isotherms, competitive adsorption, selectivity and regeneration were studied to investigate the effect of ketoenol–pyridine–furan–silica (SiNL) on the removal of Zn(II), Pb(II), Cd(II) and Cu(II) from aqueous solutions. An increase in adsorption as a function of pH and fast adsorption was reached within 25 min. The maximum sorption capacities for Zn(II), Pb(II), Cd(II) and Cu(II) were 96.17, 47.07, 48.30 and 32.15 $mg \cdot g^{-1}$, respectively. Furthermore, the material proved to be very stable – its adsorption capacity remained greater than 98% even after five cycles of adsorption/desorption. Compared to literature results, this material can be considered a high-performing remediation adsorbent for the extraction of Zn(II) from natural real water solution.

Introduction

Nowadays, pollution by a large number of heavy metals in water sources is commonly observed due the constant economical growth of our modern society. This environmental issue is being seriously considered by different circles [1,2], given that heavy metal ions are known to cause health problems even at low concentrations in living systems [3-5]. Among these toxic metals included on the US Environmental Protection Agency's (EPA's) list of priority pollutants, zinc, lead, cadmium and copper are considered as the most hazardous.

Solutions to remove heavy metals from polluted media have been thus proposed. These include several well-known analytical chemistry methods [6-16] as well as adsorption materials able to extract metal ions from aqueous solutions [17-23]. However, this latter solution presents numerous drawbacks [24,25].

A new generation of hybrid organic–inorganic silica adsorbents displaying superior properties have been recently proposed [26-33]. Our group has been active in this field with the preparation of a large set of chemically modified silica [34-36]. We could show, for instance, that their adsorption behavior is mainly dependent on the presence of donor atoms within the incorporated organic moieties [37-40].

In this context, β-ketoenol receptors, which are very important organic molecules, are also known for their potential to form stable coordination complexes with most transition metals [41,42]. The incorporation at the surface silica of a β-ketoenol group thus affords these hybrids the capacity to retain heavy metal ions. The group of C. Sanchez has prepared some mesoporous thin films functionalized with silylated β-ketoenol compounds as fast uranyl species sensors with high selectivity and sensitivity [43]. Our group has also recently prepared several β-ketoenols derivatives incorporated at the surface silica as effective and stable adsorbents for selective removal of toxic metals from water [44-48].

In the present work, we present the synthesis of a highly selective adsorbent material via covalent immobilization of a mixed ligand (β-ketoenol–pyridine–furan) onto silica particles (Scheme 1). The engineered system is low-cost, solid, chemically and mechanically stable as well as recyclable. It exhibited a high affinity and adsorption capacity for toxic heavy metal detection with less equilibrium time, a discovery that has significant environmental issues. Parameters that may improve the retention effectiveness of the metal ions have also been studied. The system was used for the confinement of lead, cadmium, zinc and copper metal ions from aqueous solutions as well as in natural water samples.

Experimental

Synthesis

Solvents and chemicals, used without further purification, were of analytical grade (Aldrich, 99.5% purity). Silica gel (particle size of 70–230 mesh, median pore diameter of 60 Å) (E. Merck) was activated before use by heating at 120 °C. The silylating agent (3-aminopropyltrimethoxysilane: Janssen Chimica) was used without purification.

(*Z*)-1-(Furan-2-yl)-3-hydroxy-3-(pyridin-2-yl)prop-2-en-1-one (**L_1**). To a mixture of sodium (0.4 g, 17.39 mmol) and ethyl picolinate (2 g, 13.23 mmol) in 50 mL of toluene 1-(furan-2-

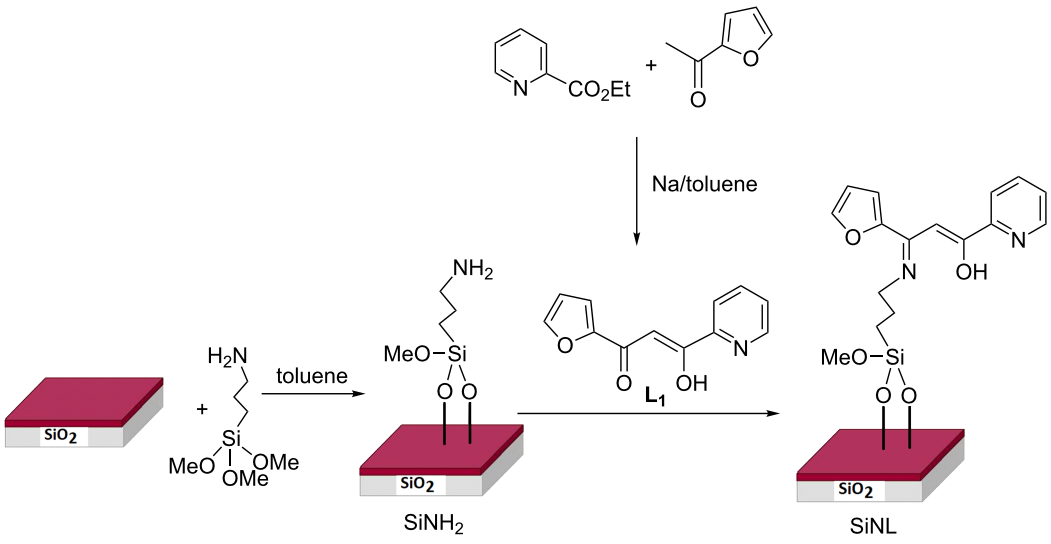

Scheme 1: Synthetic route of our modified chelating material.

yl)ethanone (1.91 g, 17.39 mmol) was added at 0 °C. The resulting solution was kept under stirring, at room temperature, for two days. The resulting precipitate was filtered, washed with the reaction solvent, dissolved in water and neutralized with acetic acid to pH 5. The organic layer, extracted with CH_2Cl_2, was dried and concentrated in vacuo. The resulting residue was chromatographed using silica and dichloromethane as eluent. Final product characteristic: yellow powder; yield: 30%; mp 102 °C; R_f: 0.6 (CH_2Cl_2/MeOH 9:1)/silica. ^{1}H NMR (DMSO-d_6) 3.48 (s, 0.1H, keto, CH_2); 7.29 (t, 1H, Fu-Hβ); 7.37 (s, 0.9H, enol, C–H); 7.42 (m, 1H, Fu-Hγ); 7.62 (m, 1H, Py-Hβ); 7.84 (t, 1H, Py-Hγ); 8.09 (d, 1H, Fu-Hα) 8.68 (d, 2H, Py-Hα). ^{13}C NMR (DMSO-d_6) 48.52 (1C, keto, CH_2); 93.81 (1C, enol, C–H), 112.78 (1C, Fu-Cβ), 116.66 (1C, Fu-Hγ), 122.00 (1C, Py-Cδ), 126.32 (1C, Py-Cβ), 127.65 (1C, Py-Cγ), 137.14 (1C, Fu-Cα), 149.54 (1C,Py-Cα), 151.17 (1C, Py-Cε), 151.95 (1C, Fu-Cε), 178.71 (1C, C=O), 179.57 (1C; C–OH); IR (KBr, cm^{-1}): ν (OH) = 3428; ν (C=O) = 1625; ν (enolic C=C) = 1515; MS *m*/*z:* 216 $[M + H]^+$.

3-Aminopropylsilica ($SiNH_2$). $SiNH_2$ was prepared according to our published procedure [37].

Pyridine-enol-imine-furan-substituted silica (SiNL). After having refluxed 5 g of $SiNH_2$ with **L_1** in dry methanol (50 mL) for 24 h, the resulting hybrid was filtered, and Soxhlet was extracted with several organic solvents for 12 h and finally dried at 70 °C for 24 h. The material was characterized by elemental analysis, Fourier transform infrared spectroscopy (FTIR), scanning electron microscopy (SEM) images, thermogravimetric analysis (TGA) and nitrogen adsorption–desorption isotherms.

Physical methods. Atomic adsorption measurements were performed on a Varian A.A. 400 spectrophotometer. pH determinations were carried out with a pH 2006, J. P. Selecta s. a. pH meter. Microanalysis was performed at the Microanalysis Centre Service (CNRS). FTIR spectra were recorded on a Perkin Elmer System 2000 device. SEM imaging was run on a FEI-Quanta 200 microscope. TG/DTA were performed on a Perkin Elmer Diamond under a 90:10 oxygen/nitrogen atmosphere at 10 °C·min^{-1}. The specific area was determined by using the BET equation. Nitrogen adsorption–desorption isotherm plots were obtained on a Thermoquest Sorpsomatic 1990 analyzer after the materials had been purged in a stream of dry nitrogen.

Batch experiments. The batch experiments were performed according to our published procedure [37]. Residual metal content was determined by atomic adsorption, using the following equations to determine the amount of adsorbed metal:

$$Q_M = (C_0 - C_e) \times V/W \quad (1)$$

$$Q_W = Q_M \times M \quad (2)$$

where Q_M (mmol·g^{-1}) and Q_W (mg·g^{-1}) are the amount of the metal ion on the adsorbent. The aqueous solution volume, the weight of the adsorbent, the initial concentration of metal ion, the equilibrium metal ion concentration and the atomic weight for metals are designated by: V (L), W (g), C_0 (mmol·L^{-1}), C_e (mmol·L^{-1}) and M (g·mol^{-1}), respectively. The average data from duplicate analyzes were reported for each sample.

The performance of SiNL adsorption of Zn(II), Pb(II), Cd(II) and Cu(II) was carried out by stirring 10 mg of adsorbent with 10 mL of a solution of metal ions a concentration of 10–250 mg·L^{-1} at room temperature. The pH values were adjusted with dilute HCl and NaOH solution.

Selectivity. The selectivity sorption of Zn(II) ion was studied using solution containing: Zn(II), Pb(II), Cd(II) and Cu(II) ions (100 mg·L^{-1} of each, pH 6). Then, 10 mg of SiNL was added into 10 mL of the metal solution at room temperature for 60 min. The atomic adsorption measurements is used to measure the concentration of Zn(II), Pb(II), Cd(II) and Cu(II) before and after adsorption.

Reusability. Following the adsorption tests, 10 mg of SiNL was separated from the residue solution by filtration. The fractions containing unretained metal ions were examined by atomic absorption spectrometry. The sorbents were then rinsed once with acetonitrile (2 mL) and twice with distilled water (10 mL). The material was regenerated using 10 mL of HCl (6 M), and the reconditioned SiNL used in sequential experiments was used to repeat the adsorption procedure to achieve five cycles.

Results and Discussion

Materials and methods

The synthetic procedure of the adsorption material is given in Scheme 1. The first step refers to the synthesis of the target (*Z*)-1-(furan-2-yl)-3-hydroxy-3-(pyridin-2-yl)prop-2-en-1-one (**L_1**) ligand in its stable conjugated enol tautomeric form. The reaction was carried out from ethyl pyridine-2-carboxylate and 2-acetylfuran via in situ Claisen condensation reaction [49]. The reaction of the activated silica gel with (3-aminopropyl)trimethoxysilane in toluene afforded amino groups onto the silica surface ($SiNH_2$), which were then reacted with L_1 under gentle conditions (reflux, 24 h) to form the newly chelating adsorbent SiNL (Scheme 1).

Characterization of the adsorbent material

Elemental analysis was carried out for $SiNH_2$ (C: 4.46% and N: 1.66%) showing that the amount of (3-aminopropyl)trimethoxysilane grafted on the surface of silica SiG is 0.92 mmol·g^{-1} whereas for SiNL (C: 6.54% and N: 1.71%) the amount of the ligand $\mathbf{L_1}$ on the surface of $SiNH_2$ is 0.14 mmol·g^{-1}. The high carbon concentration in $SiNH_2$ supports the anchoring of the silylating agent. The observed increase in both N and C content for SiNL indicates that the reaction with (*Z*)-1-(furan-2-yl)-3-hydroxy-3-(pyridin-2-yl)prop-2-en-1-one was successful.

FTIR spectra of original silica gel (SiG), $SiNH_2$ and SiNL are shown in Figure 1. The characteristics of the precursor materials (SiG, $SiNH_2$) are consistent with literature [44-48]. In the SiNL spectrum, the stretching vibration of O–H band of material surface was obtained at 3351 cm^{-1} and the peak observed at 1050 cm^{-1} corresponds to Si–O–Si band, the strong bands observed at 2943 cm^{-1} are attributed to the stretching vibration of aliphatic C–H bands. The new ν(C=C) and ν(C=N) vibrations detected at 1459 cm^{-1} and 1531 cm^{-1}, respectively, demonstrate the modification of $SiNH_2$ with $\mathbf{L_1}$. Compared to the blank silica, the surface of the new material (SiNL) shown by SEM (Figure 2) became rough, which confirms the success of organic moieties filling the surface.

The thermal stability of SiG, $SiNH_2$ and SiNL was evaluated by TGA (Figure 3). SiG presents a mass loss of 3.15% from 25 °C to 110 °C, which can be attributed to the release of water molecules [50]. A second mass loss of 5.85% from 110 °C up to 800 °C was detected, which presumably results from the release of silanol groups from the surface of the silica gel [48]. Similar to SiG, $SiNH_2$ and SiNL also present two thermal steps. The first mass loss of 2.72% was assigned to the evaporation of adsorbed water. The second mass loss of 6.19% and 9.07% from 110 °C to 800 °C was attributed to $SiNH_2$ and SiNL, respectively. This mass loss is attributed to the pyrolysis of the

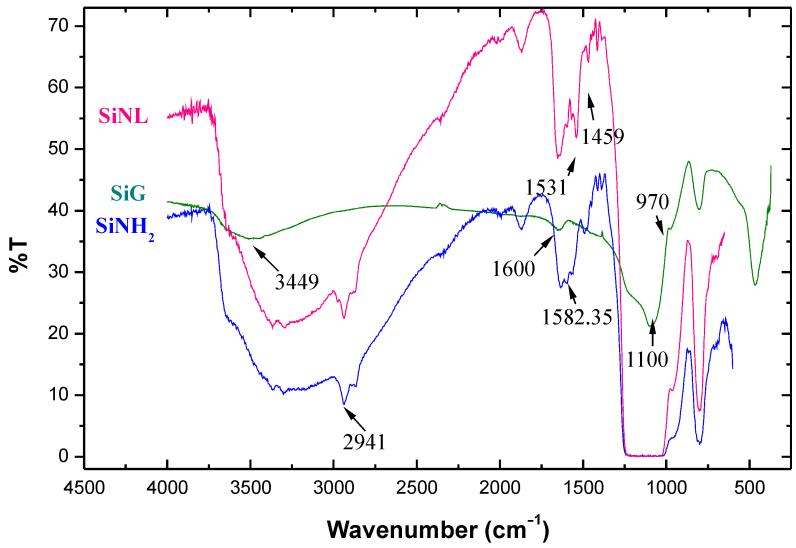

Figure 1: FTIR spectra of SiG, $SiNH_2$ and SiNL.

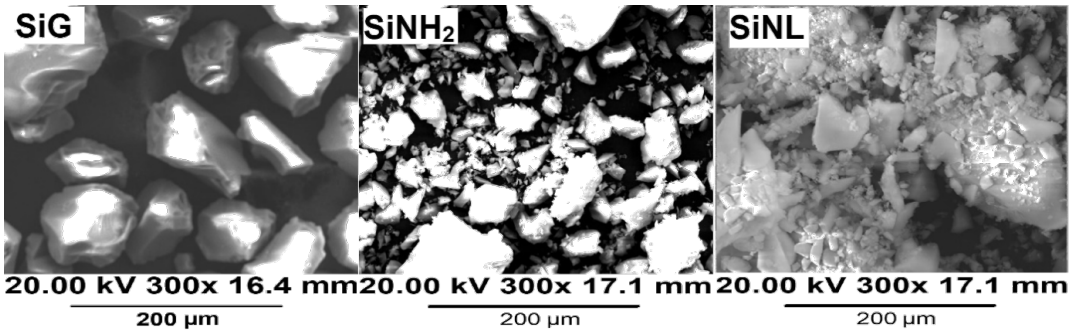

Figure 2: SEM images of free silica (SiG), $SiNH_2$ and SiNL.

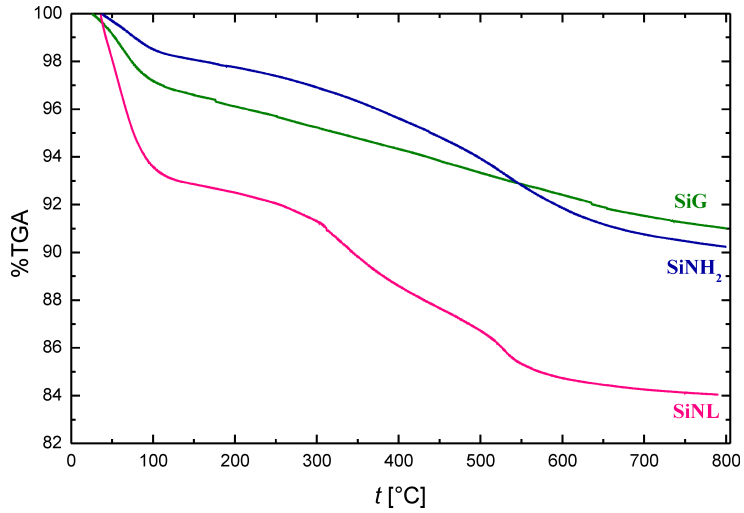

Figure 3: Thermogravimetric profiles of free silica SiG, $SiNH_2$ and SiNL.

organic entities decorating the silica surface as well as to the condensation of the unreacted silanol groups [51-53]. These results prove that the SiNL system has been successfully fabricated and is thermally stable.

The specific surface area (S_{BET}) of SiG, $SiNH_2$ and SiNL was obtained by nitrogen adsorption at several pressures [54] and is shown in Figure 4. A clear decrease is observed after grafting. This is obviously due to the obstruction of $N_{2(g)}$ access by organic moieties anchored onto the silica matrix, thus reducing its surface area [55].

The observed decrease of the initial specific surface area, S_{BET}, from 305.21 ± 0.79 $m^2 \cdot g^{-1}$ to 283.08 ± 0.77 $m^2 \cdot g^{-1}$ and pore volume from 0.77 ± 0.002 $cm^3 \cdot g^{-1}$ to 0.69 ± 0.002 $cm^3 \cdot g^{-1}$ from free silica to $SiNH_2$ results from the immobilization of organic moieties which can block the access of $N_{2(g)}$ to the silica base. Further immobilization decreases the pore volume to 0.62 ± 0.01 $cm^3 \cdot g^{-1}$ for SiNL. The increase of S_{BET} to 339.84 ± 2.01 $m^2 \cdot g^{-1}$ for SiNL is presumably due to the increasing surface roughness, as noticed by SEM imaging (Figure 2), or due to the pore plugging of the support by the ligand.

Solid–liquid adsorption of metal ions by SiNL

Effect of pH. The speciation of metal ions in solution and the surface charge of the adsorbents can be influenced by the pH of a solution [56]. Donor groups attached to the adsorbents may be

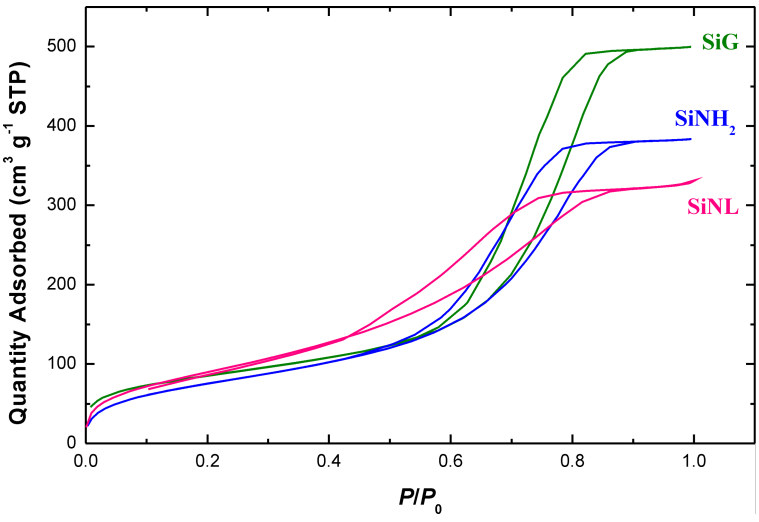

Figure 4: Nitrogen adsorption–desorption isotherm plots of SiG, $SiNH_2$ and SiNL.

easily protonated or deprotonated to form different surface charges in solution at different pH values [40]. The effect of the pH on Zn(II), Pb(II), Cd(II) and Cu(II) sorption onto SiNL was investigated in the range of pH 1–7 using the batch method as shown in Figure 5.

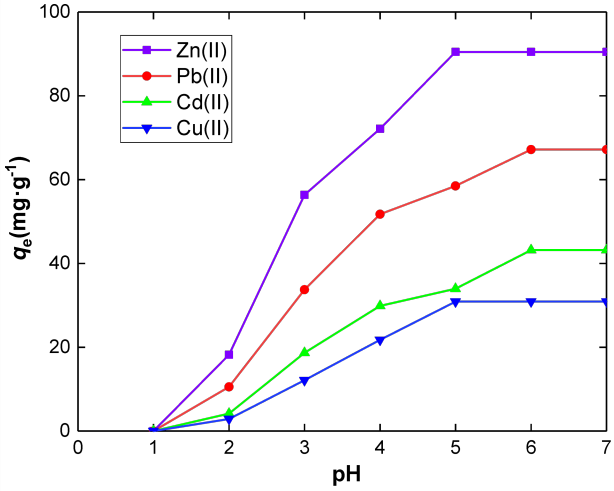

Figure 5: Effect of pH on the adsorption of metal ions on SiNL, Adsorption dose: V = 10 mL, m = 10 mg of SiNL at optimum concentration (100 ppm in each case), t = 35 min and 25 °C, Δq_e = 0.3 (mg·g^{-1}). (The optimum concentration means the initial concentration of metal ions required to reach a plateau shape).

The absorption of the metal ions increases with pH. When the pH is low, the retention of metal ions by SiNL is negligible. This is presumably due to the total protonation of the active chelation sites. As the pH rises, the protonation decreases, which tends to improve the chelation and therefore the adsorption of the metal ions. At pH > 8, the metal ion concentration decreases because of their hydrolysis. Actually, the adequate pH for the maximum adsorption of Zn(II) and Cu(II) was found at pH ≥ 5, and at 6 for Pb(II) and Cd(II). The best adsorption properties were identified for Zn(II) (Figure 5), which is presumably due to the higher stability of the formed Zn-ligand complex compared to other complexes formed with other metal ions. This can be indeed explained by the different binding affinity towards the adsorbent [57,58].

Effect of contact time and adsorption kinetics. The effect of contact time on the removal efficiency of Zn(II), Pb(II), Cd(II) and Cu(II) using SiNL was investigated (Figure 6). The adsorbed amount of metal increases sharply up to 5 min, after which a very gradual increase is observed to reach saturation after 25 min. The high amount of active sites of SiNL as well as the high solute gradient of concentration favors this behavior [59]. A contact time of 25 min was thus considered for all equilibrium adsorption studies.

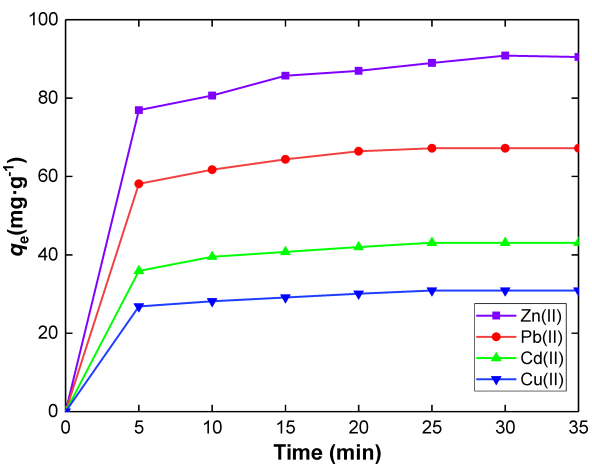

Figure 6: Effect of contact time on the adsorption capacity of Zn(II), Pb(II), Cd(II) and Cu(II) ions. Adsorption dose: V = 10 mL, m = 10 mg of SiNL at optimum concentration (100 ppm in each case), at pH 6 and 25 °C, Δq_e = 0.3 (mg·g^{-1}).

First or second order kinetic models can be applied to evaluate the efficiency of the adsorption processes, and are therefore of the utmost importance to understand adsorption mechanisms [60]. The nonlinear equation for the pseudo-first-order model is recalled below:

$$q_t = q_e\left[1 - e^{-k_1 t}\right], \quad (3)$$

where q_e and q_t are the amounts of metal ions adsorbed on the adsorbent (mg·g^{-1}) at equilibrium and at time t, respectively, and k_1 is the rate constant of the first-order adsorption in min^{-1}. The nonlinear equation for the pseudo-second-order can be written as follows:

$$q_t = \left(k_2 q_e^2 t\right) \Big/ \left(1 + k_2 q_e t\right), \quad (4)$$

where k_2 (g·mg^{-1}·min^{-1}) is the pseudo-second-order adsorption rate constant.

The kinetic rate constants for the adsorption of Zn(II), Pb(II), Cd(II) and Cu(II) by SiNL were determined by regression analysis (Figure 7). The data were best fitted by the pseudo second-order model (Table 1), which suggests that the adsorption of heavy metals in water proceeds by chemisorption [61-63], a phenomenon which could be attributed to the complexation reaction.

Effect of initial concentration in metal and isotherm modeling. A detailed concentration study was conducted, and isotherm studies were carried out to interpret the metal reten-

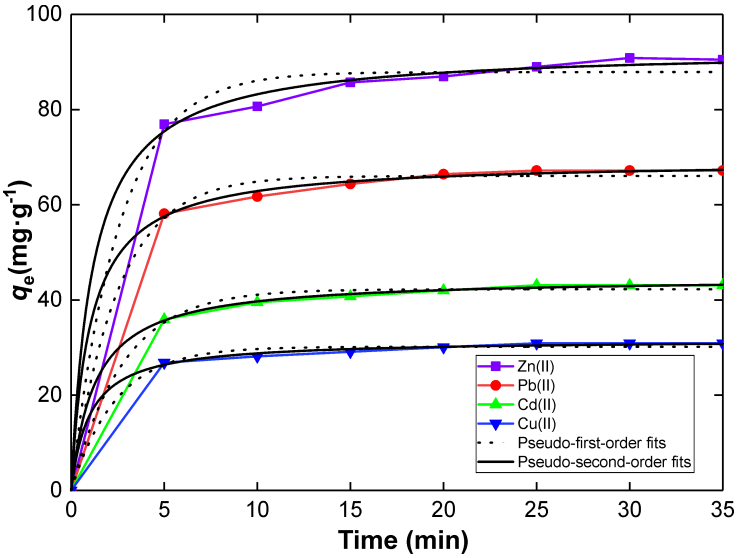

Figure 7: Pseudo-first-order and pseudo-second-order models fits for the adsorption of Zn(II), Pb(II), Cd(II) and Cu(II) ions by SiNL. Adsorption dose: V = 10 mL, m = 10 mg of SiNL using optimum pH (pH 6), optimum concentration (100 ppm in each case), and at 25 °C, Δq_e = 0.3 (mg·g^{-1}).

Table 1: Kinetics of heavy metal removal onto SiNL.

Parameters	Metal			
	Zn(II)	Pb(II)	Cd(II)	Cu(II)
$q_{e(exp)}$ (mg/g)	90.48 ± 0.30	67.18 ± 0.30	43.10 ± 0.30	30.91 ± 0.30
1st-order				
q_e (mg/g)	87.87 ± 1.29	66.04 ± 0.72	42.25 ± 0.46	30.17 ± 0.39
k_1 (min^{-1})	0.38 ± 0.05	0.40 ± 0.04	0.36 ± 0.03	0.41 ± 0.05
R^2	0.991	0.995	0.995	0.993
2nd-order				
q_e (mg/g)	92.79 ± 1.05	69.30 ± 0.47	92.79 ± 1.05	92.79 ± 1.05
k_2 (g/mg min)	(9.36 ± 1.3) × 10^{-3}	(14.13 ± 1.3) × 10^{-3}	(17.59 ± 1.1) × 10^{-3}	(31.61 ± 4.5) × 10^{-3}
R^2	0.998	0.999	0.999	0.998

tion by our system. Figure 8 highlights the increase in the retention capacity as a function of the increase in the initial concentration of Zn(II), Pb(II), Cd(II) and Cu(II) metals. The maximum adsorption was achieved gradually after an initial concentration of each metal of about 40 mg·L^{-1}.

The adsorption isotherms allow the metal uptake per unit of adsorbent to be determined at equilibrium. The Langmuir isotherm model, which considers all adsorbent sites to be at equal energy with no adsorbent/adsorbate interactions, is one of the most popular.

The non-linearized form of the Langmuir isotherm equation is given below [64,65]:

$$q_e = \left(qK_L C_e\right)/\left(1+K_L C_e\right), \quad (5)$$

Where q_e is the amount of solute sorbed on the surface of the sorbent (mg·g^{-1}), C_e is the equilibrium ion concentration in the solution (mg·L^{-1}), q is the saturated adsorption capacity (mg·g^{-1}) and K_L is the Langmuir adsorption constant (L·mg^{-1}).

Another popular isotherm model is the Freundlich model which has been described by the multilayer sorption for the sorption on heterogeneous surfaces. The non-linearized Freundlich isotherm equation is recalled below [66]:

$$q_e = K_F C_e^{1/n}, \quad (6)$$

where q_e is the adsorption capacity (mg·g^{-1}), C_e is the equilibrium concentration of the solute (mg·L^{-1}), n is Freundlich constant and K_F is the binding energy constant reflecting the affinity of the adsorbents to metal ions (mg·g^{-1}).

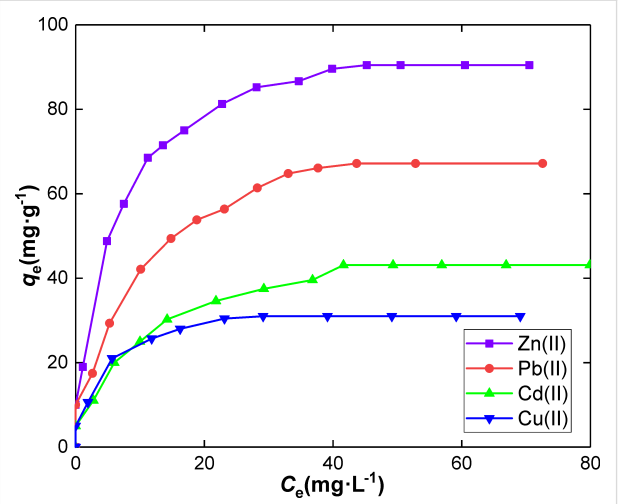

Figure 8: Effect of concentration on metal ion adsorption onto SiNL. Adsorption dose: 10 mg, V = 10 mL, at 25 °C and pH 6 for Zn(II), Pb(II), Cd(II) and Cu(II) ions, Δq_e = 0.3 (mg·g^{-1}).

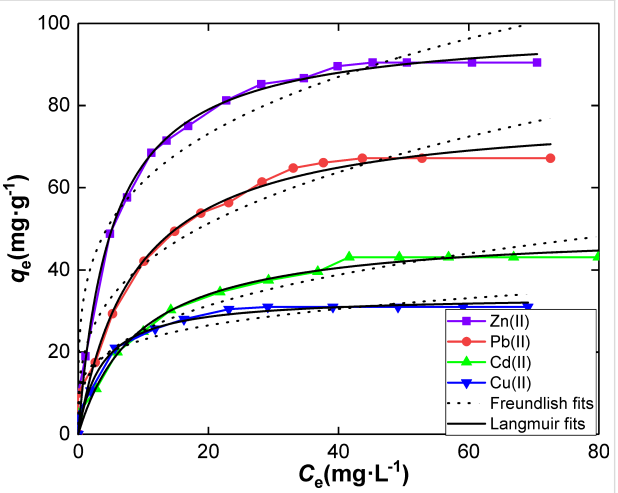

Figure 9: Langmuir and Freundlich adsorption models fits of Zn(II), Pb(II), Cd(II) and Cu(II)) on SiNL.

The adsorption parameters resulting from both isotherm models applied in this work to a selection of toxic metal ions on SiNL are listed in Table 2. Clearly, the best fits were obtained with the Langmuir model (Figure 9). This indicates that the adsorption of metal ions occurs by a monolayer formation in the same limited number of adsorption sites on a homogeneous adsorbent surface.

Thermodynamic modeling. The influence of temperature on the adsorption of Zn(II), Pb(II), Cd(II) and Cu(II) ions onto SiNL was evaluated too. The adsorption thermodynamic parameters (Table 3) were calculated with the van 't Hoff equation [67] which is recalled below:

$$K_d = \frac{C_0 - C_e}{C_e}\frac{V}{m}, \quad (7)$$

$$\ln K_d = \frac{\Delta S^0}{R} - \frac{\Delta H^0}{RT}, \quad (8)$$

where C_0 (mg/L) is the initial concentration of metal solution, C_e (mg/L) is the equilibrium concentration, V (mL) is the volume of solution and m (g) is the dosage of sorbents. The ΔH^0 and ΔS^0 values were derived from the slop and intercept of ln K_d vs 1/T as shown in Figure 10.

A value of $\Delta G^0 < 0$ at all temperatures indicates a spontaneous reaction whereas $\Delta H^0 > 0$ indicates an exothermic adsorption

Table 3: Thermodynamical parameters.

Metal	ΔH^0 (kJ·mol^{-1})	ΔS^0 (J·K^{-1}·mol^{-1})	T (K)	ΔG^0 (kJ·mol^{-1})
Zn(II)	0.68	24.78	299.15	−06.72
			309.15	−06.97
			319.15	−07.22
Pb(II)	1.48	44.74	299.15	−11.90
			309.15	−12.35
			319.15	−12.79
Cd(II)	2.50	69.76	299.15	−18.36
			309.15	−19.06
			319.15	−19.76
Cu(II)	1.21	34.18	299.15	−09.01
			309.15	−09.34
			319.15	−09.69

Table 2: Adsorption isotherm parameters of heavy metals onto SiNL.

Metal	Langmuir isotherm model			Freundlich isotherm model		
	q (mg·g^{-1})	K_L (L·mg^{-1})	R^2	K_F (mg·g^{-1})	N	R^2
Zn(II)	99.23 ± 1.77	0.19 ± 0.01	0.991	34.53 ± 3.61	3.99 ± 0.48	0.949
Pb(II)	79.11 ± 2.88	0.11 ± 0.01	0.982	20.00 ± 2.96	3.18 ± 0.42	0.943
Cd(II)	49.94 ± 1.37	0.10 ± 0.01	0.988	12.39 ± 1.66	3.23 ± 0.38	0.957
Cu(II)	33.70 ± 1.05	0.278 ± 0.05	0.978	14.41 ± 2.12	4.92 ± 1.02	0.929

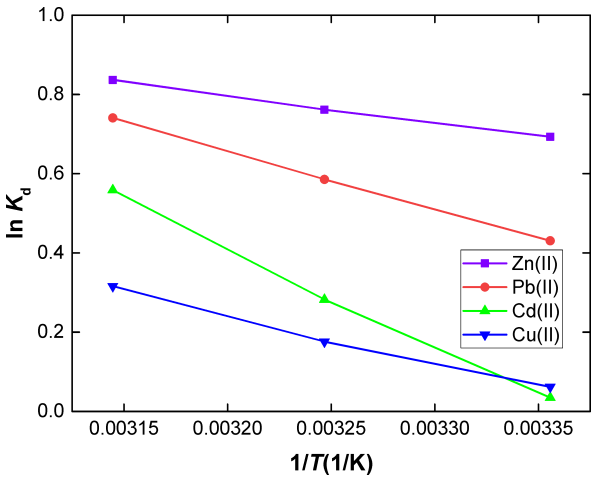

Figure 10: Effect of temperature for the sorption of metal ions onto SiNL (shaking time 60 min, pH 6, adsorption dose: V = 10 mL, m = 10 mg of SiNL at optimum concentration: 100 ppm of each metal).

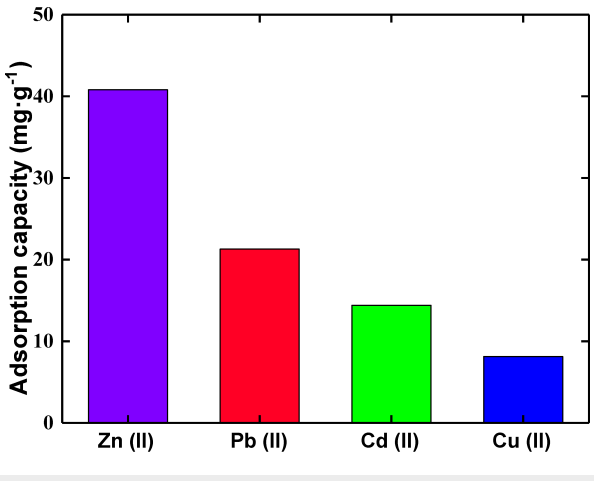

Figure 11: Effect of metal ions on the extraction of Zn(II) with SiNL. (shaking time: 25 min, pH 6, T = 25 °C. Adsorption dose: V = 10 mL, m = 10 mg of SiNL at optimum concentrations: 100 ppm of each studied metal, Pb(II), Cu(II), Zn(II), and Cd(II).

process, which is more favored at low temperatures. $\Delta S^0 > 0$ suggests a higher randomness at the solid solution interface during the adsorption of Zn(II), Pb(II), Cd(II) and Cu(II) onto SiNL.

Selectivity of SiNL. A remarkable selectivity of SiNL towards Zn(II) (at optimum conditions) compared to other metal ions is shown in Figure 11. The adsorption capacity of SiNL to the metal ions studied is in the order Zn(II) > Pb(II) > Cd(II) > Cu(II). This result is interesting because of the negative influence of zinc on rivers. For example, in Norway, zinc has been found in salmon [68] at concentrations that can kill fish and alter their physiology [69]. Since salmon is a common dish consumed by humans, body damage from consumption can be expected, including cerebral, prostatic, respiratory and gastric abnormalities [70]. Soil contaminated with zinc is also well documented [71]. Many factors can be thought to explain the observed selectivity of SiNL, such as the properties of the metal ions (size, charge, nature), the properties of the grafted ligand (its concentration, its chelating force), and also the properties of the material (its specific surface, nature of the pores). It is therefore quite normal to obtain different adsorption affinities of the same material towards different metals.

Stability and reusability of the adsorbent. Our hybrid material can be reused more than five times without significant loss in adsorption efficiency (Table 4). This can be explained by the high stability of organic groups onto SiNL which was confirmed by TGA, showing no distinct changes in the sorbent material after five cycles of use. This suggests that SiNL has excellent chemical stability as a highly efficient adsorbent for the recovery of Zn(II), Pb(II), Cd(II) and Cu(II) ions.

Table 4: Adsorption/regeneration of hybrid material towards Zn(II).

Cycle number	Zn(II) (mg·g^{-1})
1	90.48
2	90.16
3	90.06
4	89.76
5	89.12

Extraction of heavy metal in natural real water samples. The mesoporous SiNL adsorbent was also used for in-field metal ion removal. Two samples were selected from Morocco rivers: (i) Ghiss (Al Hoceima), (ii) Touissit-bou-bekker (Jerada-Oujda). All samples were collected with a polyethylene bottle and used without storage. The river water was filtered through a 0.45 µm nylon membrane. The ability of SiNL for the sorption of heavy metal was studied by using the batch method by a mixture of 10 mg of adsorbent with 10 mL of river water and 0.5 mL of 1% HNO_3 at room temperature for 60 min.

The removal efficiency was investigated under optimal conditions. As shown in Table 5, Zn(II) and Cd(II) were successfully removed from environmental water samples using this adsorbent. Of particular interest, is the Touissit River near Oujda, which crosses a mining site of the oriental region of Morocco. This site is well known to be polluted by As, Zn, Pb, Cu and Cd [72]. As a matter of fact, this heavily polluted water was better purified by our hybrid solid (Table 5) compared to Ghiss water.

Comparison with alternative materials. Table 6 shows the adsorption efficiency of SiNL towards Zn(II), Pb(II), Cd(II) and

Table 5: Extraction of heavy metal in natural real water samples.

Water samples	Metal ion	C_{found} (mg·L^{-1})	Adsorption capacity (mg·g^{-1})
Ghiss river (Al Hoceima-Morocco)	Zn(II)	1.15	0.43
	Cd(II)	1.45	0.52
	Cu(II)	not detectable	–
	Pb(II)	not detectable	–
Touissit-Boubeker river (Jerada-Morocco)	Zn(II)	12.05	6.89
	Cd(II)	2.25	0.53
	Cu(II)	not detectable	–
	Pb(II)	not detectable	–

Table 6: Comparison of adsorption capacity of SiNL with selected reported sorbents.

Support: silica gel/ligand	Ref.	Metal ion (mg·g^{-1})			
		Zn(II)	Pb(II)	Cd(II)	Cu(II)
this work	–	90.48	67.18	43.10	30.91
bipyrazole	[58]	86.51	35.26	26.96	20.24
gallic acid	[73]	–	12.63	6.09	15.38
1,2,4-triazol-2-ylaminopropyl	[74]	09.15	–	–	13.34
C,*N*-pyridylpyrazole	[75]	0.0	9.5	1.4	1.8
resacetophenone	[76]	12.49	13.79	06.49	11.80
acid red 88	[77]	0.79	03.35	01.31	0.76
dithizone	[78]	02.32	08.28	03.93	06.07
1,8-dihydroxyanthraquinone	[79,80]	11.79	15.83	07.89	14.39

Cu(II), compared to literature results. Considering the adsorbed mass quantity, the adsorption capacity values and the affinity for effective adsorption of metal cations under study, our material shows better performance.

Conclusion

A novel hybrid material based on a silica surface covalently anchored to a new highly chelating β-ketoenol–pyridine–furan receptor was prepared. Interestingly, the best adsorption properties were identified for Zn(II), presumably due to the higher stability of the formed Zn–ligand complex compared to other complexes formed with other metal ions. The SiNL adsorbent could remove Zn(II) (90.48 mg·g^{-1}) and, to a lesser extent, Pb(II) (67.18 mg·g^{-1}) and Cd(II) (43.10 mg·g^{-1}) ions, in addition to a relatively small amount of Cu(II) (43.10 mg·g^{-1}) ions. This material showed the strongest selectivity for Zn(II) (40.8 mg·g^{-1}), followed by Pb(II) (21.28 mg·g^{-1}), Cd(II) (14.4 mg·g^{-1}), and Cu(II) (8.12 mg·g^{-1}) at optimum adsorption conditions. The hybrid material has a high tolerance limit in natural water. The regeneration of the material was studied for several cycles of adsorption–desorption and showed very low loss of its extraction capacity (−1.36 mg·g^{-1}). All of these results suggest that SiNL, which showed superior performance for Zn(II), is a suitable material for the removal of heavy metals from real aqueous solutions – a topic which bears enormous importance in environmental remediation.

Acknowledgements

The authors extend their appreciation to the WBI-Morocco project (COP 22 Program 2018-2022). They also warmly thank the PPR2-MESRSFC-CNRST-P10 project (Morocco) and the Fonds National de la Recherche Scientifique (FNRS) (PDR T.01202.15).

ORCID® iDs

Smaail Radi - https://orcid.org/0000-0002-5062-6904
Mustapha Zaghrioui - https://orcid.org/0000-0001-9297-0503
Yann Garcia - https://orcid.org/0000-0002-3105-0735

References

1. Kılıç, M.; Kırbıyık, Ç.; Çepelioğullar, Ö.; Pütün, A. E. *Appl. Surf. Sci.* **2013,** *283,* 856–862. doi:10.1016/j.apsusc.2013.07.033
2. Yang, W.; Ding, P.; Zhou, L.; Yu, J.; Chen, X.; Jiao, F. *Appl. Surf. Sci.* **2013,** *282,* 38–45. doi:10.1016/j.apsusc.2013.05.028
3. Huang, X.; Chang, X.; He, Q.; Cui, Y.; Zhai, Y.; Jiang, N. *J. Hazard. Mater.* **2008,** *157,* 154–160. doi:10.1016/j.jhazmat.2007.12.113
4. Li, M.; Li, M.-y.; Feng, C.-g.; Zeng, Q.-x. *Appl. Surf. Sci.* **2014,** *314,* 1063–1069. doi:10.1016/j.apsusc.2014.06.038

5. Najafi, M.; Yousefi, Y.; Rafati, A. A. *Sep. Purif. Technol.* **2012,** *85,* 193–205. doi:10.1016/j.seppur.2011.10.011
6. Dabrowski, A.; Hubicki, Z.; Podkościelny, P.; Robens, E. *Chemosphere* **2004,** *56,* 91–106. doi:10.1016/j.chemosphere.2004.03.006
7. Fernane, F.; Mecherri, M. O.; Sharrock, P.; Hadioui, M.; Lounici, H.; Fedoroff, M. *Mater. Charact.* **2008,** *59,* 554–559. doi:10.1016/j.matchar.2007.04.009
8. Misra, R. K.; Jain, S. K.; Khatri, P. K. *J. Hazard. Mater.* **2011,** *185,* 1508–1512. doi:10.1016/j.jhazmat.2010.10.077
9. Chan, B. K. C.; Dudeney, A. W. L. *Miner. Eng.* **2008,** *21,* 272–278. doi:10.1016/j.mineng.2007.10.003
10. Mohsen-Nia, M.; Montazeri, P.; Modarress, H. *Desalination* **2007,** *217,* 276–281. doi:10.1016/j.desal.2006.01.043
11. Afkhami, A.; Saber-Tehrani, M.; Bagheri, H. *J. Hazard. Mater.* **2010,** *181,* 836–844. doi:10.1016/j.jhazmat.2010.05.089
12. Wan Ngah, W. S.; Teong, L. C.; Hanafiah, M. A. K. M. *Carbohydr. Polym.* **2011,** *83,* 1446–1456. doi:10.1016/j.carbpol.2010.11.004
13. Sakai, H.; Matsuoka, S.; Zinchenko, A. A.; Murata, S. *Colloids Surf., A* **2009,** *347,* 210–214. doi:10.1016/j.colsurfa.2009.04.031
14. Silva, R.; Cadorin, L.; Rubio, J. *Miner. Eng.* **2010,** *23,* 1220–1226. doi:10.1016/j.mineng.2010.08.016
15. Nataraj, S. K.; Hosamani, K. M.; Aminabhavi, T. M. *Desalination* **2009,** *249,* 12–17. doi:10.1016/j.desal.2009.06.008
16. Wu, Z.; He, M.; Guo, X.; Zhou, R. *Sep. Purif. Technol.* **2010,** *76,* 184–190. doi:10.1016/j.seppur.2010.10.006
17. Jha, V. K.; Nagae, M.; Matsuda, M.; Miyake, M. *J. Environ. Manage.* **2009,** *90,* 2507–2514. doi:10.1016/j.jenvman.2009.01.009
18. Abu-Eishah, S. I. *Appl. Clay Sci.* **2008,** *42,* 201–205. doi:10.1016/j.clay.2008.02.003
19. Ahn, C. K.; Park, D.; Woo, S. H.; Park, J. M. *J. Hazard. Mater.* **2009,** *164,* 1130–1136. doi:10.1016/j.jhazmat.2008.09.036
20. Mohan, S.; Gandhimathi, R. *J. Hazard. Mater.* **2009,** *169,* 351–359. doi:10.1016/j.jhazmat.2009.03.104
21. Brown, P. A.; Gill, S. A.; Allen, S. J. *Water Res.* **2000,** *34,* 3907–3916. doi:10.1016/s0043-1354(00)00152-4
22. Ahluwalia, S. S.; Goyal, D. *Bioresour. Technol.* **2007,** *98,* 2243–2257. doi:10.1016/j.biortech.2005.12.006
23. Sud, D.; Mahajan, G.; Kaur, M. *Bioresour. Technol.* **2008,** *99,* 6017–6027. doi:10.1016/j.biortech.2007.11.064
24. Pérez-Quintanilla, D.; del Hierro, I.; Fajardo, M.; Sierra, I. *Microporous Mesoporous Mater.* **2006,** *89,* 58–68. doi:10.1016/j.micromeso.2005.10.012
25. Wang, M.; Qu, R.; Sun, C.; Yin, P.; Chen, H. *Chem. Eng. J.* **2013,** *221,* 264–274. doi:10.1016/j.cej.2013.02.036
26. Zhao, J.; Niu, Y.; Ren, B.; Chen, H.; Zhang, S.; Jin, J.; Zhang, Y. *Chem. Eng. J.* **2018,** *347,* 574–584. doi:10.1016/j.cej.2018.04.151
27. Ge, S.; Geng, W.; He, X.; Zhao, J.; Zhou, B.; Duan, L.; Wu, Y.; Zhang, Q. *Colloids Surf., A* **2018,** *539,* 154–162. doi:10.1016/j.colsurfa.2017.12.016
28. Cashin, V. B.; Eldridge, D. S.; Yu, A.; Zhao, D. *Environ. Sci.: Water Res. Technol.* **2018,** *4,* 110–128. doi:10.1039/c7ew00322f
29. Zhang, A.; Chen, C.; Ji, Y.; Liu, S.; Guo, S. *J. Chem. Eng. Data* **2018,** *63,* 1578–1587. doi:10.1021/acs.jced.7b01092
30. Zhang, P.; Niu, Y.; Qiao, W.; Xue, Z.; Bai, L.; Chen, H. *J. Mol. Liq.* **2018,** *263,* 390–398. doi:10.1016/j.molliq.2018.05.023
31. Nurhajawarsi, N.; Rafi, M.; Syafitri, U. D.; Rohaeti, E. *J. Pure Appl. Chem. Res.* **2018,** *7,* 198–208. doi:10.21776/ub.jpacr.2018.007.02.402
32. Biesuz, R.; Santos, M. A.; Nurchi, V. M.; Alberti, G. *New J. Chem.* **2018,** *42,* 15237–15244. doi:10.1039/c8nj00869h
33. Mohammedi, H.; Miloudi, H.; Tayeb, A.; Bertagnolli, C.; Boos, A. *Sep. Purif. Technol.* **2019,** *209,* 359–367. doi:10.1016/j.seppur.2018.07.035
34. Radi, S.; El Abiad, C.; Carvalho, A. P.; Santos, S. M.; Faustino, M. A. F.; Neves, M. G. P. M. S.; Moura, N. M. M. *J. Mater. Chem. A* **2018,** *6,* 13096–13109. doi:10.1039/c8ta02560f
35. Radi, S.; El Abiad, C.; Moura, N. M. M.; Faustino, M. A. F.; Neves, M. G. P. M. S. *J. Hazard. Mater.* **2017,** in press. doi:10.1016/j.jhazmat.2017.10.058
36. Tighadouini, S.; Radi, S.; Anannaz, M.; Bacquet, M.; Degoutin, S.; Tillard, M.; Eddike, D.; Amhamdi, H.; Garcia, Y. *New J. Chem.* **2018,** *42,* 13229–13240. doi:10.1039/c8nj01918e
37. Radi, S.; Tighadouini, S.; Bacquet, M.; Degoutin, S.; Janus, L.; Mabkhot, Y. N. *RSC Adv.* **2016,** *6,* 82505–82514. doi:10.1039/c6ra14349k
38. Radi, S.; Tighadouini, S.; Toubi, Y.; Bacquet, M. *J. Hazard. Mater.* **2011,** *185,* 494–501. doi:10.1016/j.jhazmat.2010.09.016
39. Tighadouini, S.; Radi, S.; Bacquet, M.; Dacquin, J.-P.; Mabkhot, Y. N.; Jodeh, S.; Warad, I.; Zaghrioui, M. *Sep. Sci. Technol.* **2015,** *50,* 710–717. doi:10.1080/01496395.2014.959134
40. Radi, S.; Toubi, Y.; Bacquet, M.; Degoutin, S.; Mabkhot, Y. N.; Garcia, Y. *RSC Adv.* **2016,** *6,* 34212–34218. doi:10.1039/c6ra05138c
41. Hui, Y.-Y.; Shu, H.-M.; Hu, H.-M.; Song, J.; Yao, H.-L.; Yang, X.-L.; Wu, Q.-R.; Yang, M.-L.; Xue, G.-L. *Inorg. Chim. Acta* **2010,** *363,* 3238–3243. doi:10.1016/j.ica.2010.06.002
42. Verma, P.; Juneja, H. *Int. J. ChemTech Res.* **2012,** *4,* 1000–1006.
43. Nicole, L.; Boissière, C.; Grosso, D.; Hesemann, P.; Moreau, J.; Sanchez, C. *Chem. Commun.* **2004,** 2312–2313. doi:10.1039/b408869g
44. Tighadouini, S.; Radi, S.; Bacquet, M.; Degoutin, S.; Zaghrioui, M.; Jodeh, S.; Warad, I. *Sep. Sci. Technol.* **2017,** *52,* 608–621. doi:10.1080/01496395.2016.1262874
45. Radi, S.; Tighadouini, S.; Bacquet, M.; Degoutin, S.; Garcia, Y. *Anal. Methods* **2016,** *8,* 6923–6931. doi:10.1039/c6ay01825d
46. Radi, S.; Tighadouini, S.; Bacquet, M.; Degoutin, S.; Dacquin, J.-P.; Eddike, D.; Tillard, M.; Mabkhot, Y. *Molecules* **2016,** *21,* 888–900. doi:10.3390/molecules21070888
47. Radi, S.; Tighadouini, S.; Bacquet, M.; Degoutin, S.; Revel, B.; Zaghrioui, M. *J. Environ. Chem. Eng.* **2015,** *3,* 1769–1778. doi:10.1016/j.jece.2015.06.016
48. Radi, S.; Tighadouini, S.; El Massaoudi, M.; Bacquet, M.; Degoutin, S.; Revel, B.; Mabkhot, Y. N. *J. Chem. Eng. Data* **2015,** *60,* 2915–2925. doi:10.1021/acs.jced.5b00281
49. Radi, S.; Tighadouini, S.; Feron, O.; Riant, O.; Bouakka, M.; Benabbes, R.; Mabkhot, Y. *Molecules* **2015,** *20,* 20186–20194. doi:10.3390/molecules201119684
50. Arakaki, L. N. H.; Filha, V. L. S. A.; Germano, A. F. S.; Santos, S. S. G.; Fonseca, M. G.; Sousa, K. S.; Espínola, J. G. P.; Arakaki, T. *Thermochim. Acta* **2013,** *556,* 34–40. doi:10.1016/j.tca.2013.01.024
51. Dai, B.; Cao, M.; Fang, G.; Liu, B.; Dong, X.; Pan, M.; Wang, S. *J. Hazard. Mater.* **2012,** *219–220,* 103–110. doi:10.1016/j.jhazmat.2012.03.065
52. Pérez-Quintanilla, D.; Hierro, I. d.; Fajardo, M.; Sierra, I. *J. Hazard. Mater.* **2006,** *134,* 245–256. doi:10.1016/j.jhazmat.2005.11.004

53. Yin, P.; Tian, Y.; Wang, Z.; Qu, R.; Liu, X.; Xu, Q.; Tang, Q. *Mater. Chem. Phys.* **2011,** *129,* 168–175. doi:10.1016/j.matchemphys.2011.03.067
54. Brunauer, S.; Emmett, P. H.; Teller, E. *J. Am. Chem. Soc.* **1938,** *60,* 309–319. doi:10.1021/ja01269a023
55. Sharma, R. K.; Pandey, A.; Gulati, S.; Adholeya, A. *J. Hazard. Mater.* **2012,** *209–210,* 285–292. doi:10.1016/j.jhazmat.2012.01.022
56. Iqbal, S.; Yun, J.-I. *Microporous Mesoporous Mater.* **2017,** *248,* 149–157. doi:10.1016/j.micromeso.2017.04.028
57. Banerjee, I. A.; Yu, L.; Matsui, H. *Proc. Natl. Acad. Sci. U. S. A.* **2003,** *100,* 14678–14682. doi:10.1073/pnas.2433456100
58. Radi, S.; El Massaoudi, M.; Bacquet, M.; Degoutin, S.; Adarsh, N. N.; Robeyns, K.; Garcia, Y. *Inorg. Chem. Front.* **2017,** *4,* 1821–1831. doi:10.1039/c7qi00322f
59. Vojoudi, H.; Badiei, A.; Bahar, S.; Mohammadi Ziarani, G.; Faridbod, F.; Ganjali, M. R. *J. Magn. Magn. Mater.* **2017,** *441,* 193–203. doi:10.1016/j.jmmm.2017.05.065
60. Largitte, L.; Pasquier, R. *Chem. Eng. Res. Des.* **2016,** *109,* 495–504. doi:10.1016/j.cherd.2016.02.006
61. Gündoğan, R.; Acemioğlu, B.; Alma, M. H. *J. Colloid Interface Sci.* **2004,** *269,* 303–309. doi:10.1016/s0021-9797(03)00762-8
62. Ho, Y. S.; McKay, G. *Process Biochem. (Oxford, U. K.)* **1999,** *34,* 451–465. doi:10.1016/s0032-9592(98)00112-5
63. Zheng, H.; Liu, D.; Zheng, Y.; Liang, S.; Liu, Z. *J. Hazard. Mater.* **2009,** *167,* 141–147. doi:10.1016/j.jhazmat.2008.12.093
64. Foo, K. Y.; Hameed, B. H. *Chem. Eng. J.* **2010,** *156,* 2–10. doi:10.1016/j.cej.2009.09.013
65. Krishni, R. R.; Foo, K. Y.; Hameed, B. H. *Desalin. Water Treat.* **2014,** *52,* 6712–6719. doi:10.1080/19443994.2013.827818
66. Limousin, G.; Gaudet, J.-P.; Charlet, L.; Szenknect, S.; Barthès, V.; Krimissa, M. *Appl. Geochem.* **2007,** *22,* 249–275. doi:10.1016/j.apgeochem.2006.09.010
67. Cui, L.; Wang, Y.; Gao, L.; Hu, L.; Yan, L.; Wei, Q.; Du, B. *Chem. Eng. J.* **2015,** *281,* 1–10. doi:10.1016/j.cej.2015.06.043
68. United nation for Food and Agriculture, **1977.** Rapport sur l'effet de la pollution par le zinc et le cuivre sur les pécheries de salmonidés dans un système fluviolacustre du centre de la Norvège.
69. Giardina, A.; Larson, S. F.; Wisner, B.; Wheeler, J.; Chao, M. *Environ. Toxicol. Chem.* **2009,** *28,* 287–295. doi:10.1897/07-461.1
70. Plum, L. M.; Rink, L.; Haase, H. *Int. J. Environ. Res. Public Health* **2010,** *7,* 1342–1365. doi:10.3390/ijerph7041342
71. Dumoulin, D.; Billon, G.; Proix, N.; Frérot, H.; Pauwels, M.; Saumitou-Laprade, P. *J. Geochem. Explor.* **2017,** *172,* 142–150. doi:10.1016/j.gexplo.2016.10.005
72. Smouni, A.; Ater, M.; Auguy, F.; Laplaze, L.; El Mzibri, M.; Berhada, F.; Filali-Maltouf, A.; Doumas, P. *Cah. Agric.* **2010,** *19,* 273–279. doi:10.1684/agr.2010.0413
73. Xie, F.; Lin, X.; Wu, X.; Xie, Z. *Talanta* **2008,** *74,* 836–843. doi:10.1016/j.talanta.2007.07.018
74. Dias Filho, N. L.; Costa, R. M.; Marangoni, F. *Colloids Surf., A* **2008,** *317,* 625–635. doi:10.1016/j.colsurfa.2007.11.050
75. Radi, S.; Attayibat, A.; Lekchiri, Y.; Ramdani, A.; Bacquet, M. *Mater. Chem. Phys.* **2008,** *111,* 296–300. doi:10.1016/j.matchemphys.2008.04.011
76. Goswami, A.; Singh, A. K. *Anal. Chim. Acta* **2002,** *454,* 229–240. doi:10.1016/s0003-2670(01)01552-5
77. Kocjan, R. *Microchim. Acta* **1999,** *131,* 153–158. doi:10.1007/s006040050021
78. Zaporozhets, O.; Petruniock, N.; Sukhan, V. *Talanta* **1999,** *50,* 865–873. doi:10.1016/s0039-9140(99)00172-1
79. Goswami, A.; Singh, A. K. *Anal. Bioanal. Chem.* **2002,** *374,* 554–560. doi:10.1007/s00216-002-1524-3
80. Goswami, A.; Singh, A. K. *Talanta* **2002,** *58,* 669–678. doi:10.1016/s0039-9140(02)00374-0

License and Terms

The definitive version of this article is the electronic one which can be found at:
doi:10.3762/bjnano.10.25

BEILSTEIN JOURNAL OF NANOTECHNOLOGY

One-step nonhydrolytic sol–gel synthesis of mesoporous TiO_2 phosphonate hybrid materials

Yanhui Wang, P. Hubert Mutin* and Johan G. Alauzun*

Full Research Paper

Open Access

Address:
Institut Charles Gerhardt Montpellier, UMR 5253, Université de Montpellier, CC 1701, Place Eugène Bataillon, 34095 Montpellier Cedex 5, France

Email:
P. Hubert Mutin* - hubert.mutin@umontpellier.fr; Johan G. Alauzun* - johan.alauzun@umontpellier.fr

* Corresponding author

Keywords:
anatase; mesoporous; nonaqueous sol–gel; phosphonate

Beilstein J. Nanotechnol. **2019,** *10,* 356–362.
doi:10.3762/bjnano.10.35

Received: 25 October 2018
Accepted: 17 January 2019
Published: 05 February 2019

This article is part of the thematic issue "Advanced hybrid nanomaterials".

Guest Editor: A. Taubert

Abstract

Mesoporous TiO_2–octylphosphonate hybrid materials were prepared in one step by a nonhydrolytic sol–gel method involving the reaction of $Ti(OiPr)_4$, acetophenone (2 equiv) and diethyl octylphosphonate (from 0 to 0.2 equiv) at 200 °C for 12 hours, in toluene. The different samples were characterized by ^{31}P magic angle spinning nuclear magnetic resonance, Fourier transform infrared spectroscopy, Raman spectroscopy, X-ray diffraction, and nitrogen physisorption. For P/Ti ratios up to 0.1, the hybrid materials can be described as aggregated, roughly spherical, crystalline anatase nanoparticles grafted by octylphosphonate groups via Ti–O–P bonds. The crystallite size decreases with the P/Ti ratio, leading to an increase of the specific surface area and a decrease of the pore size of the hybrid samples. For a P/Ti ratio of 0.2, the volume fraction of organic octyl groups exceeds 50%. The hybrid material becomes nonporous and can be described as amorphous TiO_2 clusters modified by octylphosphonate units, where the octyl chains form an organic continuous matrix.

Introduction

The development of porous hybrid organic–inorganic materials has been a major goal for materials scientists for more than 25 years [1-3]. Combining inorganic and organic moieties at the nanoscale allows the design of tailor-made functional materials with enhanced or new properties, adapted to a wide range of advanced applications [4-7]. In Class I hybrid materials, the inorganic and organic parts are linked through weak bonds (e.g., van der Waals or hydrogen bonds), while in Class II hybrid materials, they are linked by stronger ionocovalent or covalent bonds [8].

The majority of Class II hybrid materials utilize the stability of the Si–C bond and are based on organosilsesquioxane ($R–SiO_{1.5}$) or bridged organosilsesquioxane ($O_{1.5}Si–R–O_{1.5}$). These hybrids are usually prepared by conventional sol–gel processing, i.e., by hydrolysis and condensation of alkoxysilane

precursors, which offers an excellent control over composition and homogeneity, while texture can be tuned using various templating approaches [9].

In the case of metals, as M–C bonds are (in most cases) quite unstable, the organic groups can be linked to the metal oxide network via carboxylate or β-diketonate ligands [5,10,11]. Organophosphorus ligands such as phosphonates appear quite promising as they form strong ionocovalent M–O–P bonds with many metals, as shown by the numerous examples of metal phosphonates reported in the literature [12-14]. However, in the case of monophosphonate groups, metal phosphonates usually form semicrystalline layered materials with no interlayer porosity. A way to avoid the formation of a layered material is to use an excess of metal precursor in order to form a metal oxide–phosphonate hybrid material. There are very few examples of the preparation of such materials by sol–gel methods [15,16], and the texture of these materials has not been reported. Actually, most metal oxide–phosphonate-based porous hybrids are obtained in two steps, by surface modification of a porous metal oxide support [17-19].

Nonhydrolytic (or nonaqueous) sol–gel (NHSG) chemistry has provided simple and powerful routes to synthesize oxides or mixed oxides with different morphologies (e.g., nanoparticles) or textures (e.g., mesoporous materials) [20-24]. Several NHSG routes have also been used to prepare Class II hybrids. For instance the alkyl elimination route was applied to the synthesis of organosilsesquioxanes, organosilsesquioxane–metal oxide hybrids [25-27], silica–titania modified by organosilicon groups [28,29], and metal phosphonates [30]. More recently, hybrid silicophosphate xerogels have been produced by reaction of acetoxysilanes with trimethylsilyl esters of phosphoric or phosphonic acids [31], and porous organosilicate covalent polymers have been synthesized by reaction of silicon acetate with 1,3,5-trihydroxybenzene [32].

The reaction of alkoxides in acetophenone (used as a solvent and an oxygen donor) has already been described for the synthesis of TiO_2 [33] and $BaTiO_3$ [34] nanoparticles, but it has never been used to prepare mesoporous oxides or hybrid materials.

In the present work, we present an original one-step NHSG synthesis of mesoporous TiO_2–octylphosphonate hybrid materials, using a nonhydrolytic sol–gel method involving the reaction of titanium tetraisopropoxide and diethyl octylphosphonate precursors at 200 °C in the presence of acetophenone as an oxygen donor.

Results

A series of TiO_2–octylphosphonate hybrids was synthesized by reaction of $Ti(OiPr)_4$ (1 equiv) with different amounts of diethyl octylphosphonate (0.02, 0.05, 0.1 and 0.2 equiv) and acetophenone (2 equiv) at 200 °C. It must be mentioned that, in the absence of acetophenone, diethyl octylphosphonate did not react with titanium tetraisopropoxide under the same conditions. All four materials are referred to as TiP_x where x is the P/Ti ratio. For comparison, a TiO_2 sample was prepared under the exact same conditions but without diethyl octylphosphonate.

Elemental analysis by energy dispersive X-ray spectroscopy (EDX) of these materials showed that in all cases the measured P/Ti ratios were close to the nominal ones, indicating that all the octylphosphonate units were incorporated in the materials (Table 1).

The ^{31}P solid-state NMR spectra of the hybrid materials (Figure 1) display a very broad signal in the 10 to 35 ppm range. Similar broad resonances have been reported for TiO_2–phenylphosphonate hybrid materials prepared in a two-step sol–gel process from $Ti(OiPr)_4$ and $PhPO_3H_2$ [15], whereas the hybrid materials obtained by surface modification of ana-

Table 1: Elemental analysis, crystallite size and textural data for TiO_2–octylphosphonate hybrids and TiO_2.

Sample	P/Ti ratio[a]	Cryst. size[b] (nm)	S_{BET}[c] ($m^2\ g^{-1}$)	V_p[d] ($cm^3\ g^{-1}$)	D_p[e] (nm)
TiO_2	NA	9	120	0.35	9.7
$TiP_{0.02}$	0.023	16	120	0.29	8.0
$TiP_{0.05}$	0.054	11	160	0.23	4.5
$TiP_{0.1}$	0.096	6	240	0.17	3.1
$TiP_{0.2}$	0.192	NA	<10	<0.01	NA

[a]P/Ti ratio determined by EDX; [b]crystallite size determined by the Scherrer equation for the (101) reflection; [c]specific surface area, Brunauer–Emmett–Teller (BET) method; [d]total pore volume at P/P_0 = 0.990; [e]Barrett–Joyner–Halenda (BJH) average pore diameter calculated from the desorption branch. NA: not applicable. ^{31}P solid-state nuclear magnetic resonance (NMR) spectroscopy is a useful tool for studying phosphonate-based hybrid materials: it gives information on the presence of phosphonate units bonded to the oxide nework, on the presence of a metal phosphonate phase or of "free" phosphonate precursor (e.g., excess precursor, physisorbed or trapped molecules), but it is not possible to ascribe the different components found in the ^{31}P NMR spectrum to the different bonding modes (mono-, bi-, and tridentate phosphonate units) [35].

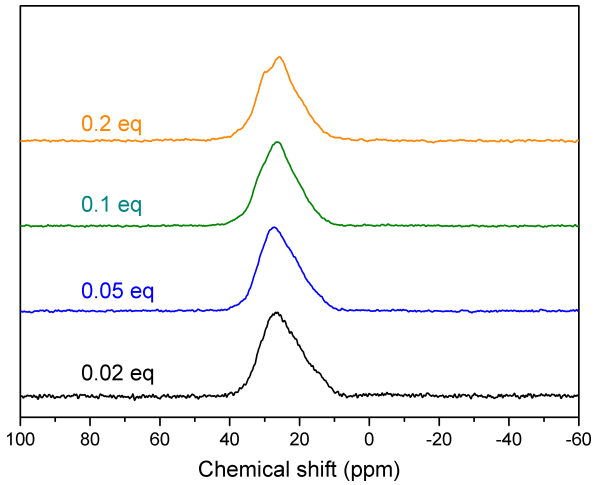

Figure 1: ^{31}P CP magic angle spinning solid-state NMR spectra of the hybrid materials produced by the reaction of octylphosphonate, $Ti(OiPr)_4$ and acetophenone (TiO_2-octylphosphonate hybrids).

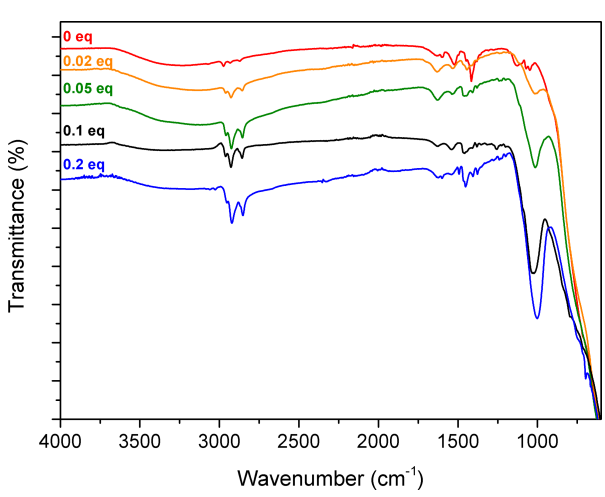

Figure 2: ATR-FTIR spectra of the TiO_2–octylphosphonate hybrid materials.

tase supports usually show narrower resonances [36]. These spectra confirm the presence of phosphonate species linked to the TiO_2 network through Ti–O–P bonds, and show the absence of a layered titanium octylphosphonate phase, which would lead to a sharp resonance at 7 ppm. In the case of the $TiP_{0.2}$ sample, the shoulder at 31 ppm suggests the presence of a small amount of noncondensed diethyl octylphosphonate precursor, possibly molecules trapped in the network of this nonporous sample (see below).

The attenuated total reflection (ATR)-Fourier transform infrared (FTIR) spectra of the TiO_2–octylphosphonate hybrid materials (Figure 2) showed a single broad vibration between 900 and 1200 cm^{-1} arising from vibration modes of the CPO_3 tetrahedra. The intensity of this band increases with the P/Ti ratio. The absence of bands at ≈1220 cm^{-1} (P=O stretching vibration) and ≈950 cm^{-1} (P–OC stretching vibrations) [36] suggests that most of the phosphonate groups are in the same tridentate environment as in layered titanium phosphonates, that is, bonded to three Ti atoms in $CP(OTi)_3$ sites, as previously reported for sol–gel TiO_2–phenylphosphonate hybrid materials [15]. The vibrations in the 1400–1500 cm^{-1} range can be ascribed to CH_3 and CH_2 deformations of groups in residual surface moieties (e.g., Ti–O^{i}Pr, Ti–O–CMePhOiPr), and to CH_3, CH_2 and P–CH_2 deformations in the octylphosphonate groups. The three bands between 2800 and 3000 cm^{-1} are ascribed to the C–H symmetric and asymmetric stretching vibrations of bonds in CH_2 and CH_3, mostly in the octyl groups, as shown by the intensity of these bands which is directly related to the P/Ti ratio. The weak, broad band between 3000 and 3800 cm^{-1} is characteristic of O–H stretching vibrations. This band indicates the presence of a low amount of adsorbed water (confirmed by the vibration at 1620 cm^{-1} assigned to a deformation mode of adsorbed water), and also of surface hydroxyl groups resulting from the hydrolysis of residual surface groups during washing or manipulation under air.

The X-ray diffraction (XRD) patterns of TiO_2 and of the hybrid samples are presented in Figure 3. The patterns of $TiP_{0.02}$ and $TiP_{0.05}$ showed the presence of well-crystallized anatase nanocrystals (JCPDS 21-1272), as in the TiO_2 sample. There was no evidence of rutile. The $TiP_{0.1}$ sample appeared partially crystallized, while the $TiP_{0.2}$ sample was amorphous in XRD experiments. The crystallite size (Table 1) of the hybrid samples decreased with the P/Ti ratio from 16 to 6 nm. The lower intensity of the (004) reflection compared to the (200) reflection indi-

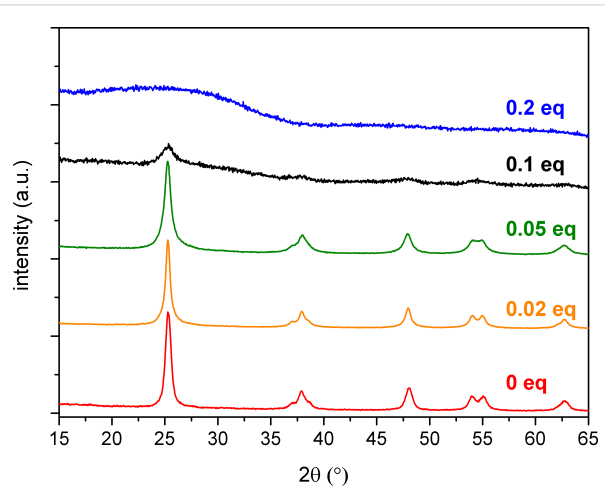

Figure 3: Powder XRD patterns of the TiO_2–octylphosphonate hybrid materials.

cated that the crystallites are not elongated and have a roughly spherical morphology.

Raman spectroscopy (Figure 4) confirmed the XRD results. For P/Ti ratios between 0 and 0.05, the spectra showed a strong peak at 145 cm^{-1} and smaller peaks at 195, 400, 515 and 640 cm^{-1} indicating the presence of anatase. The spectrum of $TiP_{0.1}$ showed broader and weaker bands, and the first band was shifted to 148 cm^{-1}. Under the same conditions, no bands could be observed in the spectrum of $TiP_{0.2}$, indicating highly disordered TiO_2 domains.

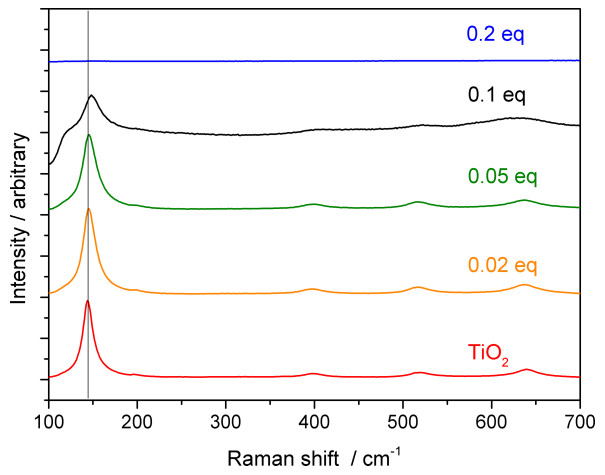

Figure 4: Raman spectra of TiO_2–octylphosphonate hybrid materials and TiO_2.

Scanning electron microscopy (SEM) images of the TiO_2 sample and of the TiO_2–octylphosphonate hybrid materials are displayed in Figure 5. The morphology of the samples did not significantly depend on the P/Ti ratio: all samples appeared to be formed of densely aggregated, roughly spherical, nanoparticles. For P/Ti ratios of 0.1 and 0.2, the particles were smaller and formed denser aggregates than for lower P/Ti ratios.

The nitrogen adsorption–desorption isotherms of the different samples are displayed in Figure 6, except for the $TiP_{0.2}$ sample which was nonporous with a negligible specific surface area. All other samples showed significant porosity. Their specific surface area increased with the P/Ti ratio, from 120 $m^2\ g^{-1}$ for $TiP_{0.02}$ to 240 $m^2\ g^{-1}$ for $TiP_{0.1}$, while their pore volume decreased, from 0.29 to 0.17 $cm^3\ g^{-1}$ (Table 1). Interestingly, the Brunauer–Emmett–Teller (BET) C constant, which is related to the adsorption enthalpy, decreased with the P/Ti ratio (42 for $TiP_{0.02}$, 36 for $TiP_{0.05}$, 28 for $TiP_{0.1}$), as previously reported for nanoparticles grafted by octylphosphonic acid [37]. According to the recent IUPAC classification, the isotherms of TiO_2 and of the hybrid samples are mainly of type IVa, characteristic of mesoporous adsorbents, with an H2 hysteresis loop indicating complex pore structures [38]. The $TiP_{0.02}$ and $TiP_{0.05}$ isotherms also showed Type II features (lack of plateau at high relative pressure) suggesting the presence of some macropores. As SEM images do not show the presence of macropores in $TiP_{0.05}$ and $TiP_{0.02}$ samples, these macropores likely correspond to pores between relatively small aggregates resulting from the grinding of the samples. The pore size distribution

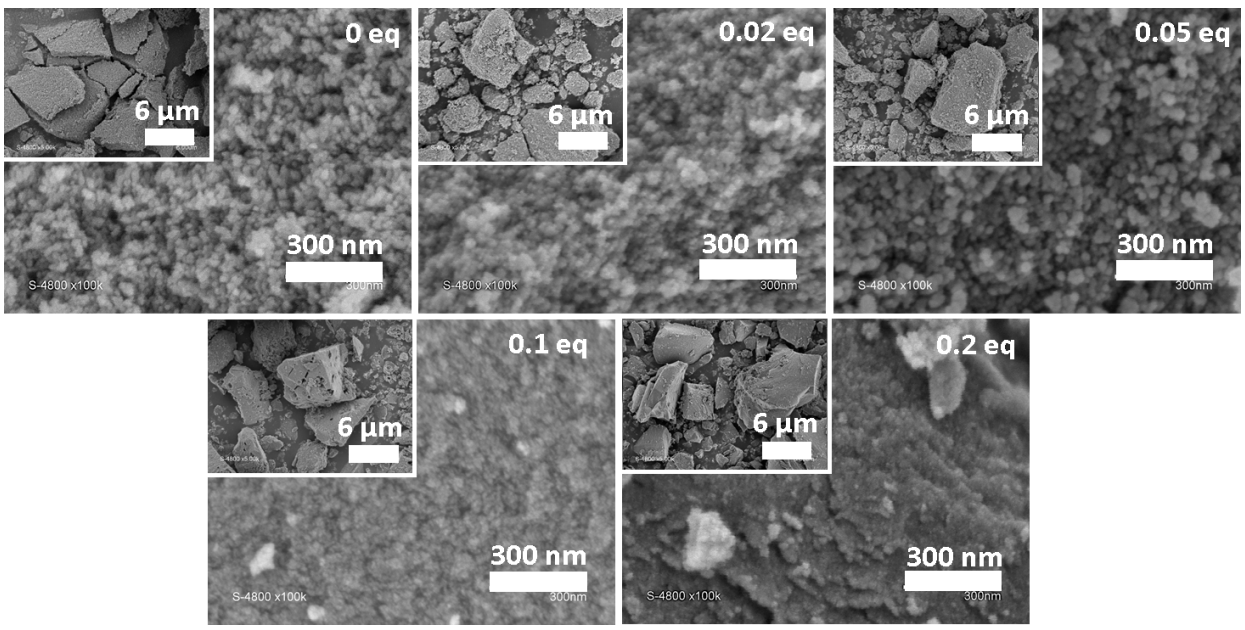

Figure 5: SEM images of TiO_2–octylphosphonate hybrid materials and TiO_2.

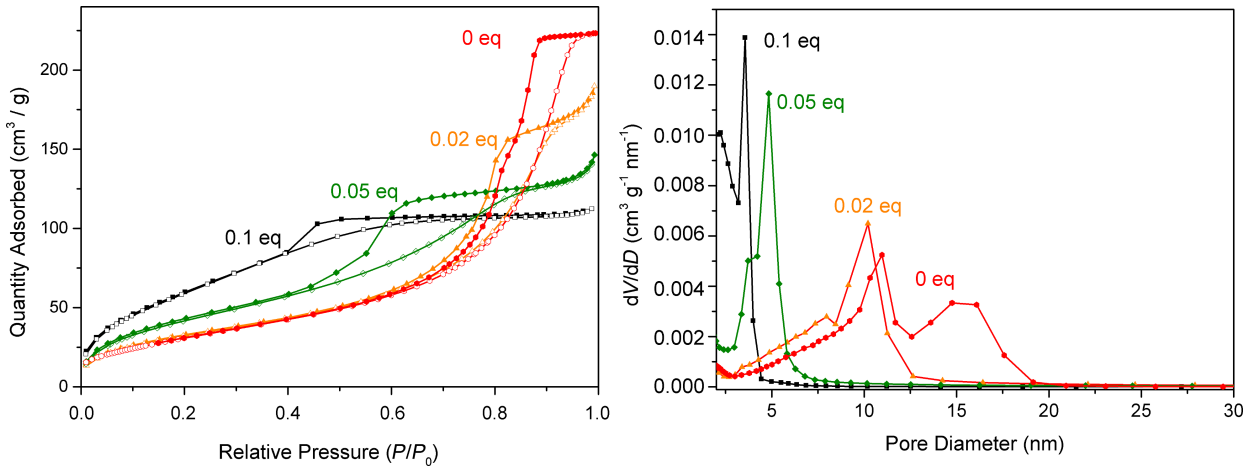

Figure 6: N_2 physisorption isotherms at 77 K (left) and Barrett–Joyner–Halenda (BJH) mesopore size distribution (desorption branch, right) of TiO_2–octylphosphonate hybrid materials and TiO_2. Open and filled symbols in the isotherms refer to adsorption and desorption, respectively.

results confirmed the presence of mesopores in all samples (except the nonporous $TiP_{0.2}$ sample). The sharp peak found in the distribution for $TiP_{0.1}$ at ≈4 nm is a well-known artefact related to the instability of the meniscus at relative pressures lower than 0.42; it simply indicates the presence of small pores of diameter <4 nm. The average mesopore diameter decreased when the P/Ti ratio increased, from 8.0 nm for $TiP_{0.02}$ to 3.1 nm for $TiP_{0.1}$ (Table 1).

Discussion and Conclusion

The reaction at 200 °C of diethyl octylphosphonate and $Ti(OiPr)_4$ in the presence of acetophenone provides a simple and original method to prepare TiO_2–octylphosphonate hybrid materials in one step (Scheme 1).

The different characterization methods allow us to better understand the structure of these hybrid materials. The presence of even a relatively small amount of phosphonate units strongly influences the size and crystallinity of the TiO_2 domains.

For P/Ti ratios up to 0.1, the hybrid materials can be described as rounded anatase nanoparticles grafted by octylphosphonate groups via Ti–O–P bonds. This is a major advantage of the present nonhydrolytic sol-gel method: previous attempts to

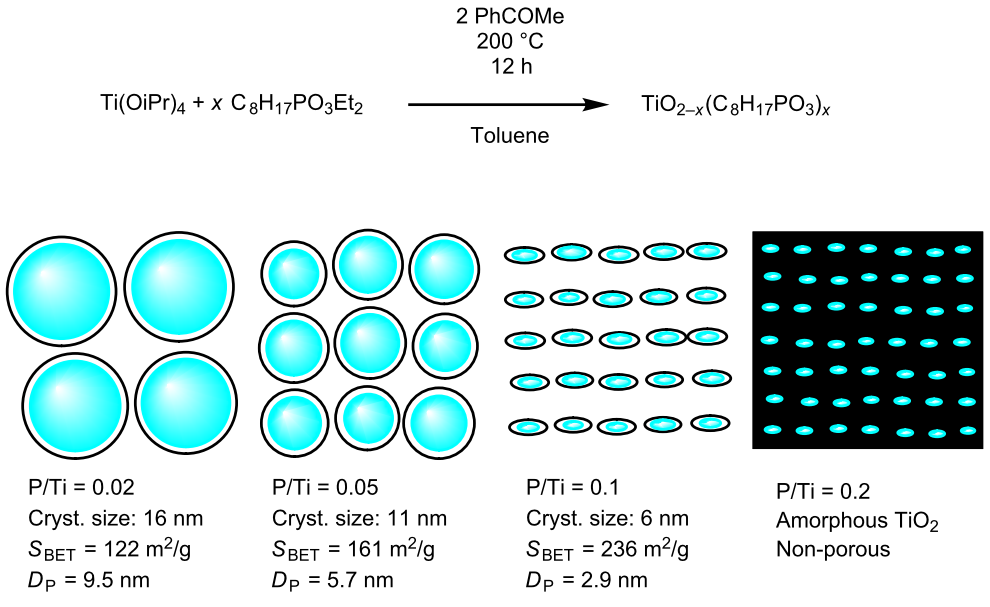

Scheme 1: Ideal reaction scheme and hypothetical structures of the obtained hybrid materials.

prepare such TiO_2–phosphonate hybrids by hydrolytic sol–gel routes led to amorphous TiO_2 domains [15,39].

The low values found for the BET C constant (from 42 for $TiP_{0.02}$ to 28 for $TiP_{0.1}$) confirm that the surface of the anatase nanoparticles is capped by apolar octyl groups. C values of 47 and 34 have been reported for oxide nanoparticles post-modified by octylphosphonic acid with grafting densities of 1.4 and 4.1 P/nm^2, respectively [37]. In our hybrid materials, the anatase particle size decreases with the P/Ti ratio, leading to an increase of the specific surface area of the crystallites. The density of grafting, estimated from the composition and from the diameter of the crystallites (assuming a spherical shape and a density of 3.8), increases with the P/Ti ratio from 1.5 P/nm^2 for $TiP_{0.02}$ to 2.9 P/nm^2 for $TiP_{0.1}$. These values suggest the formation of monolayers with low to moderate density (grafting densities of up to 4 to 5 P/nm^2 have been reported for well-ordered self-assembled monolayers). The mesoporosity of the hybrid materials with P/Ti ratios up to 0.1 stems from the aggregation of the grafted nanoparticles (interparticle porosity). The smaller the size of the particles, the higher the specific surface area and the lower the pore volume (Scheme 1).

For a P/Ti ratio of 0.2, the TiO_2 domains are completely amorphous, probably because they involve very few Ti atoms. In this case the volume fraction of the octyl groups exceeds 50%. The diameter of the TiO_2 domains and the length of octyl chains are in the same order of magnitude, and the lack of porosity of this sample likely results from the interdigitation or mixing of the alkyl chains.

These mesoporous metal oxide–phosphonate materials can be seen as a low-cost alternative to periodic mesoporous organosilicas (PMOs) and metal–organic frameworks (MOFs) for applications in the field of heterogeneous catalysis or selective adsorption. Their high hydrolytic stability over a wide range of pH [15] and the possibility to functionalize them with a variety of functional groups makes them particularly promising for applications in aqueous phase catalysis (e.g., for biomass conversion) and in aqueous wastewater treatment.

Experimental

Titanium(IV) isopropoxide ($Ti(OiPr)_4$, 97 %), and acetophenone (99%) were obtained from Sigma-Aldrich. Diethyl 1-octylphosphonate ($C_8H_{17}PO_3Et_2$, 98%) was purchased from Sikémia. Toluene was dried over a Pure-Solve MD5 solvent purification system (H_2O <10 ppm, controlled with a Karl Fischer coulometer). All other chemicals were used without further purification. All manipulations were carried out in a glove box under argon atmosphere (<5 ppm of water and O_2).

Synthesis of TiO_2–octylphosphonate hybrids

In a typical preparation, $Ti(OiPr)_4$ (1.72 g, 6.00 mmol), acetophenone (1.44 g, 12.00 mmol), $C_8H_{17}PO_3Et_2$ (0 mmol, 0.24 mmol, 0.60 mmol, 1.20 mmol, or 2.40 mmol) and toluene (8.0 mL) were mixed in a stainless steel digestion vessel with a PTFE lining (23 mL). The sealed autoclave was heated in an oven at 200 °C for 12 h under autogenous pressure. After reaction, the resulting monoliths were thoroughly washed with acetone (5 times, 30 mL). Then, they were dried under reduced pressure (5.10^{-2} mbar) at room temperature and ground into a fine powder.

Characterization

FTIR spectra were collected in ATR mode on a Spectrum II spectrometer (Perkin-Elmer). The powder XRD patterns were collected with a PANalytical X'Pert Pro MPD diffractometer (Cu $K\alpha_1$ = 0.1540598 nm). The SEM images were obtained with a Hitachi S-4800 electron microscope. EDX was done on an Oxford Instruments X-Max^N SDD instrument. Nitrogen adsorption and desorption isotherms were measured at 77 K with a Micrometrics TriStar 3000 apparatus; the specific surface area was determined by the BET method in the 0.05–0.25 P/P_0 range. The mesopore volume and pore size distribution were obtained by the Barrett–Joyner–Halenda (BJH) method from the desorption branch.

Solid-state ^{31}P magic angle spinning (MAS) NMR experiments were performed on a Varian VNMRS 400 MHz (9.4 T) spectrometer using a 3.2 mm Varian T3 HXY MAS probe. Single pulse experiments were carried out with a spinning rate of 20 kHz, a 90° excitation pulse of 3 μs, a recycle delay of 30 s and 100 kHz spinal-64 ^1H decoupling. 200 transients were recorded. The ^{31}P chemical shift was determined using an external reference, hydroxyapatite $Ca_{10}(PO_4)_6(OH)_2$, at 2.8 ppm (with respect to H_3PO_4, 85 wt % in water).

Acknowledgements

The authors acknowledge the Agence Nationale pour la Recherche (project ANR-16-CE08-0015 SYNCOPE), the University of Montpellier and CNRS for financial support.

ORCID® iDs

P. Hubert Mutin - https://orcid.org/0000-0002-6031-6467
Johan G. Alauzun - https://orcid.org/0000-0002-6531-0750

References

1. Sanchez, C.; Ribot, F. *New J. Chem.* **1994,** *18,* 1007–1047.
2. Sanchez, C.; Shea, K. J.; Kitagawa, S. *Chem. Soc. Rev.* **2011,** *40,* 471–472. doi:10.1039/c1cs90001c

3. Kickelbick, G. *Introduction to Hybrid Materials;* Wiley-VCH Verlag GmbH & Co: Weinheim, Germany, 2007. doi:10.1002/9783527610495.ch1
4. Drisko, G. L.; Sanchez, C. *Eur. J. Inorg. Chem.* **2012,** 5097–5105. doi:10.1002/ejic.201201216
5. Nicole, L.; Laberty-Robert, C.; Rozes, L.; Sanchez, C. *Nanoscale* **2014,** *6,* 6267–6292. doi:10.1039/c4nr01788a
6. Parola, S.; Julián-López, B.; Carlos, L. D.; Sanchez, C. *Adv. Funct. Mater.* **2016,** *26,* 6506–6544. doi:10.1002/adfm.201602730
7. Santos, L. D.; Maréchal, M.; Guillermo, A.; Lyonnard, S.; Moldovan, S.; Ersen, O.; Sel, O.; Perrot, H.; Laberty-Robert, C. *Adv. Funct. Mater.* **2016,** *26,* 594–604. doi:10.1002/adfm.201504076
8. Judeinstein, P.; Sanchez, C. *J. Mater. Chem.* **1996,** *6,* 511–525. doi:10.1039/jm9960600511
9. Hoffmann, F.; Cornelius, M.; Morell, J.; Fröba, M. *Angew. Chem., Int. Ed.* **2006,** *45,* 3216–3251. doi:10.1002/anie.200503075
10. Schubert, U. *J. Mater. Chem.* **2005,** *15,* 3701–3715. doi:10.1039/b504269k
11. Schubert, U. *Acc. Chem. Res.* **2007,** *40,* 730–737. doi:10.1021/ar600036x
12. Clearfield, A. *Curr. Opin. Solid State Mater. Sci.* **2002,** *6,* 495–506. doi:10.1016/s1359-0286(02)00151-1
13. Gagnon, K. J.; Perry, H. P.; Clearfield, A. *Chem. Rev.* **2012,** *112,* 1034–1054. doi:10.1021/cr2002257
14. Clearfield, A. The early history and growth of metal phosphonate chemistry. In *Metal Phosphonate Chemistry: From Synthesis to Applications;* Clearfield, A.; Demadis, K., Eds.; Royal Society of Chemistry: Cambridge, United Kingdom, 2011; pp 1–44. doi:10.1039/9781849733571-00001
15. Guerrero, G.; Mutin, P. H.; Vioux, A. *Chem. Mater.* **2000,** *12,* 1268–1272. doi:10.1021/cm991125+
16. Maillet, C.; Janvier, P.; Bertrand, M.-J.; Praveen, T.; Bujoli, B. *Eur. J. Org. Chem.* **2002,** 1685–1689. doi:10.1002/1099-0690(200205)2002:10<1685::aid-ejoc1685>3.0.co;2-i
17. Mutin, P. H.; Guerrero, G.; Vioux, A. *J. Mater. Chem.* **2005,** *15,* 3761–3768. doi:10.1039/b505422b
18. Guerrero, G.; Alauzun, J. G.; Granier, M.; Laurencin, D.; Mutin, P. H. *Dalton Trans.* **2013,** *42,* 12569–12585. doi:10.1039/c3dt51193f
19. Queffélec, C.; Petit, M.; Janvier, P.; Knight, D. A.; Bujoli, B. *Chem. Rev.* **2012,** *112,* 3777–3807. doi:10.1021/cr2004212
20. Mutin, P. H.; Vioux, A. *Chem. Mater.* **2009,** *21,* 582–596. doi:10.1021/cm802348c
21. Debecker, D. P.; Hulea, V.; Mutin, P. H. *Appl. Catal., A* **2013,** *451,* 192–206. doi:10.1016/j.apcata.2012.11.002
22. Pinna, N.; Niederberger, M. *Angew. Chem., Int. Ed.* **2008,** *47,* 5292–5304. doi:10.1002/anie.200704541
23. Deshmukh, R.; Niederberger, M. *Chem. – Eur. J.* **2017,** *23,* 8542–8570. doi:10.1002/chem.201605957
24. Styskalik, A.; Skoda, D.; Barnes, C.; Pinkas, J. *Catalysts* **2017,** *7,* 168. doi:10.3390/catal7060168
25. Bourget, L.; Leclercq, D.; Vioux, A. *J. Sol-Gel Sci. Technol.* **1999,** *14,* 137–147. doi:10.1023/a:1008729832145
26. Crouzet, L.; Leclercq, D.; Mutin, P. H.; Vioux, A. *Chem. Mater.* **2003,** *15,* 1530–1534. doi:10.1021/cm020985e
27. Hay, J. N.; Raval, H. M. *Chem. Mater.* **2001,** *13,* 3396–3403. doi:10.1021/cm011024n
28. Smeets, V.; Ben Mustapha, L.; Schnee, J.; Gaigneaux, E. M.; Debecker, D. P. *Mol. Catal.* **2018,** *452,* 123–128. doi:10.1016/j.mcat.2018.04.011
29. Lorret, O.; Lafond, V.; Mutin, P. H.; Vioux, A. *Chem. Mater.* **2006,** *18,* 4707–4709. doi:10.1021/cm061478q
30. Corriu, R. J. P.; Leclercq, D.; Mutin, P. H.; Sarlin, L.; Vioux, A. *J. Mater. Chem.* **1998,** *8,* 1827–1833. doi:10.1039/a803755h
31. Styskalik, A.; Skoda, D.; Moravec, Z.; Babiak, M.; Barnes, C. E.; Pinkas, J. *J. Mater. Chem. A* **2015,** *3,* 7477–7487. doi:10.1039/c4ta06823h
32. Kejik, M.; Moravec, Z.; Barnes, C. E.; Pinkas, J. *Microporous Mesoporous Mater.* **2017,** *240,* 205–215. doi:10.1016/j.micromeso.2016.11.012
33. Garnweitner, G.; Antonietti, M.; Niederberger, M. *Chem. Commun.* **2005,** 397–399. doi:10.1039/b414510k
34. Pazik, R.; Tekoriute, R.; Håkansson, S.; Wiglusz, R.; Strek, W.; Seisenbaeva, G. A.; Gun'ko, Y. K.; Kessler, V. G. *Chem. – Eur. J.* **2009,** *15,* 6820–6826. doi:10.1002/chem.200900836
35. Brodard-Severac, F.; Guerrero, G.; Maquet, J.; Florian, P.; Gervais, C.; Mutin, P. H. *Chem. Mater.* **2008,** *20,* 5191–5196. doi:10.1021/cm8012683
36. Guerrero, G.; Mutin, P. H.; Vioux, A. *Chem. Mater.* **2001,** *13,* 4367–4373. doi:10.1021/cm001253u
37. Lassiaz, S.; Labarre, D.; Galarneau, A.; Brunel, D.; Mutin, P. H. *J. Mater. Chem.* **2011,** *21,* 8199–8205. doi:10.1039/c1jm10128e
38. Thommes, M.; Kaneko, K.; Neimark, A. V.; Olivier, J. P.; Rodriguez-Reinoso, F.; Rouquerol, J.; Sing, K. S. W. *Pure Appl. Chem.* **2015,** *87,* 1051. doi:10.1515/pac-2014-1117
39. Maillet, C.; Janvier, P.; Pipelier, M.; Praveen, T.; Andres, Y.; Bujoli, B. *Chem. Mater.* **2001,** *13,* 2879–2884. doi:10.1021/cm010123y

License and Terms

BEILSTEIN JOURNAL OF NANOTECHNOLOGY

Nanocomposite–parylene C thin films with high dielectric constant and low losses for future organic electronic devices

Marwa Mokni[1], Gianluigi Maggioni[2,3], Abdelkader Kahouli[1], Sara M. Carturan[2,3], Walter Raniero[3] and Alain Sylvestre[*1]

Full Research Paper

Open Access

Address:
[1]Univ. Grenoble Alpes, CNRS, Grenoble INP, G2Elab, 38000 Grenoble, France, [2]Dipartimento di Fisica e Astronomia "G. Galilei", Università di Padova, Via Marzolo 8, 35121 Padova (PD), Italy and [3]Istituto Nazionale di Fisica Nucleare, Laboratori Nazionali di Legnaro, Viale dell'Università 2, 35020 Legnaro (PD), Italy

Email:
Alain Sylvestre[*] - alain.sylvestre@g2elab.grenoble-inp.fr

* Corresponding author

Keywords:
dielectric; nanocomposite polymer; organic field-effect transistor; parylene C; silver-containing nanoparticle

Beilstein J. Nanotechnol. **2019,** *10,* 428–441.
doi:10.3762/bjnano.10.42

Received: 12 August 2018
Accepted: 07 January 2019
Published: 12 February 2019

This article is part of the thematic issue "Advanced hybrid nanomaterials".

Guest Editor: V. de Zea Bermudez

Abstract

Nanocomposite–parylene C (NCPC) thin films were deposited with a new technique based on the combination of chemical vapor deposition (CVD) for parylene C deposition and RF-magnetron sputtering for silver deposition. This method yields good dispersion of Ag-containing nanoparticles inside the parylene C polymer matrix. Film composition and structure were studied by using several techniques. It was found that the plasma generated by the RF-magnetron reactor modifies the film density as well as the degree of crystallinity and the size of parylene C crystallites. Moreover, silver is incorporated in the parylene matrix as an oxide phase. The average size of the Ag oxide nanoparticles is lower than 20 nm and influences the roughness of the NCPC films. Samples with various contents and sizes of silver-oxide nanoparticles were investigated by broadband dielectric spectroscopy (BDS) in view of their final application. It was found that both the content and the size of the nanoparticles influence the value of the dielectric constant and the frequency-dependence of the permittivity. In particular, β-relaxation is affected by the addition of nanoparticles as well as the dissipation factor, which is even improved. A dielectric constant of 5 ± 1 with a dissipation factor of less than 0.045 in the range from 0.1 Hz to 1 MHz is obtained for a 2.7 µm thick NCPC with 3.8% Ag content. This study provides guidance for future NCPC materials for insulating gates in organic field-effect transistors (OFETs) and advanced electronic applications.

Introduction

Increasing the dielectric constant of gate dielectrics for oxide thin-film transistors (TFTs) improves the performance of such devices. Challenges are in the processing of these high-*k* dielectrics and various approaches were tested over time. Among them, low-cost and innovative methods were recently proposed for low operating voltages of TFTs [1,2]. By using water-in-

ducement, scandium oxide was succesfully integrated as gate dielectric in both InZnO and CuO TFTs [1]. Using a sol–gel approach, high-*k* ink hybrid AlOOH nanocomposites demonstrated low leakage currents suitable for low operating voltages of TFTs [2]. Unfortunately these approaches can not be used when parylene C (PPXC) is chosen as gate dielectric as the only proven process for producing high-quality PPXC layers is chemical vapor deposition (CVD). Parylene C has emerged as a particularly interesting material for organic electronic devices as a gate dielectric, coating insulator film, or flexible substrate [3-5] due to its numerous advantageous properties. PPXC films are biocompatible and environmentally friendly [6-9]. Its deposition process makes it accessible as a coating for many semiconductor polymers [10] for organic field-effect transistors (OFETs) [11], organic light-emitting diodes (OLEDs) [12,13], and flexible organic electronic devices (FEDs) [14,15]. It presents an easy deposition process at low temperatures with a conformal and uniform layer [16]. Parylene C is a well-controlled material when used as gate dielectric, which is a crucial requirement for the performance of the OFETs and for the device reliability. Charge-carrier mobility is improved in the presence of this polymer [17]. PPXC is also an appropriate hydroxyl-free gate dielectric and prevents trapping of electrons at the semiconductor–dielectric interface in contrast to polymers containing hydroxyl groups such as poly(vinyl phenol) and polyimides (due to residual COOH groups) [18-20]. The stability of the devices, which is impacted by this charge trapping at the interfaces, is improved when parylene C is integrated in the device [21,22]. Parylene C is highly corrosion resistant on metallic surfaces and possesses outstanding electrical insulation with high tensile strength, moderate dielectric losses [16,23] and low permeability to gases [24,25]. Hydrophobicity [26] and physical stability [27] of parylene C make it a good candidate as a coating dielectric material to protect the sensitive organic layer from oxygen and water vapor [28], which are among the greatest degradation mechanisms contributing to the electrical instability of OFETs [29-32] and oxide TFTs [33].

It is inferred that parylene C presents a broad applicability and a versatile role in the technology of OFETs and organic compounds [3]. However, parylene C, as the vast majority of polymers, exhibits a low dielectric constant (3.15 at 1 kHz [34]) thus limiting its performance in specific applications in OFETs and electronic devices.

Using nanocomposite polymers as gate dielectrics presents several advantages for the improvement of the electronic device properties such as higher dielectric constant [35] and dielectric strength [36], reduced threshold voltage [37], increased charge mobility and reduced leakage current [38]. Compared to pure parylene C and other pure materials such as SiO_2, polyimide, polyethylene, alumina (Al_2O_3), benzocyclobutenes (BCB) and SiO_2/poly(methyl methacrylate) (PMMA), nanocomposite parylene C (NCPC) exhibits some interesting properties [39-47]. As an example, parylene C/Silica nanocomposites show greatly improved mechanical properties and thermal stability in comparison to pure PPXC films [48]. In a recent study, these properties, and especially thermal and UV stability, were further improved by combining nanosilica/titania particles with parylene C [49]. As shown in other works [50,51], parylene C/Al_2O_3 bilayers applied to medical devices exhibit a longer-term reliability in comparison to pure PPXC.

The goal of this study is to improve the electrical properties of parylene C used in advanced electronic devices [52-54] as a gate dielectric or an insulation coating. The challenge is to increase the dielectric constant of NCPC without degrading its dielectric losses. In this context, this work presents a new strategy to synthesize nanocomposite parylene C materials by a combination of two processes, CVD and RF-magnetron sputtering. The NCPC properties are analyzed in detail by different experimental techniques. Particularly, in order to evaluate the effect of the Ag-containing nanofiller charges regarding a possible integration as gate insulating material for OFETs, broadband dielectric spectroscopy (BDS) is carried out on NCPCs with different content of silver-containing nanoparticles. As a final result, a gain in the gate insulation capacitance is expected for OFETs with the addition of conductive particles inside the native parylene C insulating gate.

Results and Discussion

Silver-PPXC co-deposition: film composition and structure

Table 1 gives the experimental parameters of deposited pure parylene C and NCPCs. Apart from sample O, which was produced by keeping the sputtering source off, all the samples were deposited with the plasma switched on but with different numbers of rotations with the shutter open (i.e., changing the amount of Ag atoms incorporated inside the film). Therefore, the number of rotations increases from 0 (sample K) to 6 (sample F). Samples from A to F are multilayers (three layers), consisting of a pure parylene C layer (PPXC, 1st layer) followed by an Ag-containing parylene C layer (PPXC+Ag, 2nd layer) and then by another pure parylene C layer (PPXC, 3rd layer). The thickness of each single layer (either with or without Ag) was measured by RBS in monomeric units·cm^{-2}. As highlighted in the Experimental section (see below), the parylene C amount deposited on the substrate (in monomeric units·cm^{-2}) is directly obtained from the Cl RBS atomic dose, since each monomeric unit contains one Cl atom. In the case of three-layered samples (from A to F), the SIM simulation

Table 1: Experimental parameters of pure parylene C and NCPCs deposited by combined CVD and RF sputtering at room temperature. The layer sequence starts from the sample surface. The single layer thickness is measured in 10^{17} monomeric units·cm^{-2}. The total Ag content has been calculated by dividing the Ag dose (in atoms·cm^{-2}) by the total parylene amount (in monomeric units·cm^{-2}). The total thickness (in μm, last column) was measured by a mechanical profilometer.

sample	RF power to Ag target (W)	layer sequence from surface: 1. 1st layer 2. 2nd layer 3. 3rd layer	thickness of each single layer (10^{17} monomeric units·cm^{-2})	total Ag content (%)	total thickness (μm)
O	NO	PPXC	4.4	—	0.75 ± 0.05
K	60	PPXC	6.4	—	1.32 ± 0.06
A	120	1. PPXC 2. PPXC+Ag (1 rotation) 3. PPXC	1. 3.4 2. 0.75 3. 4.3	1.0	1.72 ± 0.03
B	120	1. PPXC 2. PPXC+Ag (1 rotation) 3. PPXC	1. 4.4 2. 0.75 3. 3.6	1.8	1.76 ± 0.04
C	120	1. PPXC 2. PPXC+Ag (2 rotations) 3. PPXC	1. 4.6 2. 2.2 3. 5.0	3.8	2.68 ± 0.14
D	120	1. PPXC 2. PPXC+Ag (3 rotations) 3. PPXC	1. 5.2 2. 2.8 3. 2.7	2.6	2.07 ± 0.07
E	120	1. PPXC 2. PPXC+Ag (4 rotations) 3. PPXC	1. 4.0 2. 4.8 3. 3.3	2.5	2.49 ± 0.05
F	120	1. PPXC 2. PPXC+Ag (6 rotations) 3. PPXC	1. 5.5 2. 6.0 3. 0.20	4.45	2.30 ± 0.04

package in the RUMP software [55] was used to simulate the experimental spectra and to determine the thickness of each layer (in monomeric units·cm^{-2}).

Figure 1 (left) shows the corresponding Ag dose incorporated in these samples as a function of the number of rotations. If the samples B and C are neglected, one finds that the dose increases almost linearly as could be expected. Ag dose incorporated during a single rotation is 8.3×10^{15} atoms·cm^{-2}. The reason of the anomalous behavior of samples B and C, the dose of which is higher than expected, is not completely clear, but it is thought to lie mainly in the very peculiar nature of the parylene deposition process, which is controlled by setting the pressure inside the chamber. This control method gives rise to hysteresis loops in the chamber pressure and then in the crucible temperature, which can last for several minutes. The loops can then produce an oscillation in the parylene sublimation rate during the film deposition. If the Ag deposition coincides with a

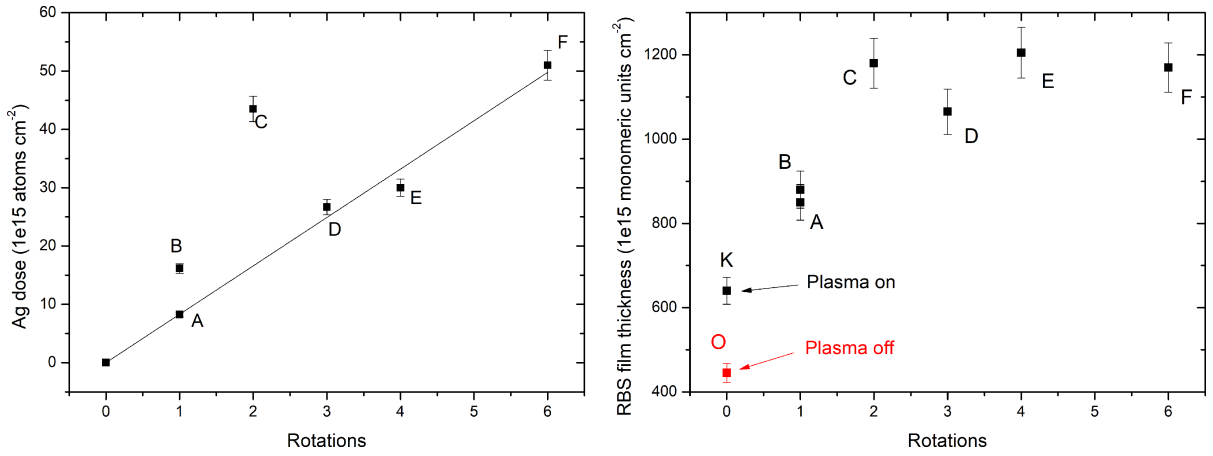

Figure 1: Ag dose (left) and film thickness (right) versus rotations.

low parylene deposition rate, the parylene deposition on the Ag target surface will be lower and then the Ag sputtering yield will increase together with the Ag content incorporated in the film. The Ag incorporation will be further enhanced, if one considers that the lower the parylene deposition rate, the lower the pressure in the chamber, the higher the number of Ag atoms reaching the substrates. The anomalous behavior of samples B and C highlights the complexity of this new deposition method, which arises from coupling two different processes (CVD and sputtering) for the first time. This process complexity is also responsible for the very different thickness of 1st and 3rd layers in some of the NCPCs (see, e.g., samples F and D). In order to solve this problem, a process control based on setting a direct parameter (such as, e.g., parylene deposition rate) instead of the total pressure in the chamber would be more effective.

Figure 1 (right) shows the film thickness measured in monomeric units·cm^{-2} (by RBS) of the samples O, K and from A to F as a function of the number of rotations. The first important feature to be noted is the effect of plasma on the deposition rate of parylene. When the plasma is switched on (sample K), we observe an increase of the amount of parylene deposited on the substrate compared to when the plasma is switched off (sample O). This increase is thought to be due to an increase of the turbulent motions inside the chamber, which perturb the flow of monomer molecules, resulting in an increase of the parylene residence time, as already observed in the case of co-deposition of UV absorber and parylene [56]. When the shutter is open, the deposition rate further increases (samples A, B and C) showing that the plasma effect on the monomer flow is more pronounced. The deposition rate reaches a plateau for the remaining samples (see samples C to F).

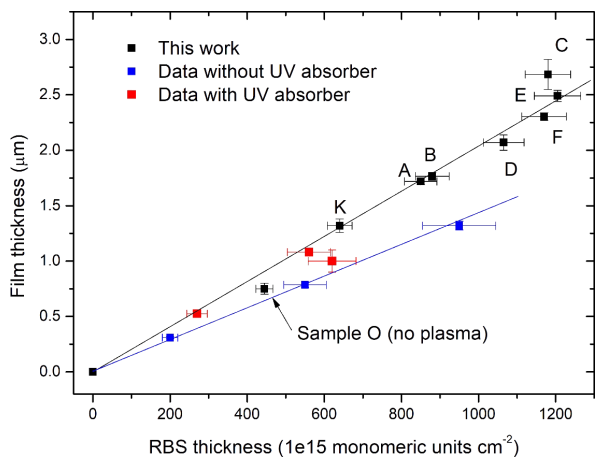

Figure 2: Film thickness versus RBS thickness (see text for details). Blue and red squares data are drawn from [56]. The two lines are guides for the eye.

The plasma-induced increase of the deposition rate affects the film density, as shown by the data in Figure 2, where the film thickness measured in micrometers (by the profilometer) is plotted as a function of the thickness measured in monomeric units·cm^{-2} (by RBS). In Figure 2 the data for our set of samples (black squares) are compared with those of parylene samples deposited without plasma (blue squares, from [56]) and those without plasma but with co-deposition of UV-absorber (red squares, from [56]). Figure 2 highlights the good linear correlation between film thickness measured by profilometer and RBS for both sets of samples with and without plasma (black and blue squares, respectively) up to a value of about 1.0×10^{18} monomeric units·cm^{-2}, as highlighted by the two straight lines. Moreover, the different slopes for these two data sets imply that, for the same RBS thickness, the samples deposited with plasma have a higher physical thickness. This means that the plasma gives rise to a decrease of the film density, as already found in the case of samples obtained by co-deposition of parylene and UV-absorber (red squares), the thickness of which is closer to that of plasma-deposited samples.

The decrease of film density matches the change of structural order in the film matrix, as shown by GIXRD results (Figure 3). Spectrum of film deposited when plasma is off (sample O) shows only the characteristic reflection at $2\theta = 13.85°$ ((020) plane of a monoclinic unit cell with dimensions: $a = 5.96$ Å, $b = 12.69$ Å, $c = 6.66$ Å, $\beta = 135.28°$ [57]), thus highlighting the strong preferred orientation of the parylene nanocrystalline domains in this sample. When the plasma is switched on, we observe that the (020) peak becomes less intense in spite of the higher parylene amount and shifts to $2\theta = 14.00$–$14.05°$. The average parylene nanocrystallite size, as determined through the Scherrer equation [58] applied to this peak, slightly increases from around 9 nm for sample O to 12–16 nm for the plasma-deposited samples (see Table 2 for the FWHM values of the (020) peak used for the calculation of the average size). Moreover, another peak at $2\theta = 22.33°$, assigned to the (110) parylene reflection, appears, even if very weakly in samples C to F. All these features hint at a different structural arrangement of the parylene matrix in the plasma-deposited samples, consisting in a lower preferred orientation and a higher amount of randomly oriented nanocrystalline domains. It is inferred that this evolution is mainly an effect of the plasma, while Ag incorporation plays only a minor role.

When silver deposition is enabled (open shutter), peaks of Ag-containing nanocrystallites appear and are clearly visible in the spectrum of sample C at $2\theta = 27.8°$, $32.3°$, $46.3°$, $54.9°$ and $57.6°$. All these peaks can be referred to silver-oxide phases, i.e., Ag_2O [59], Ag_3O_4 [60], AgO [61], Ag_2O_2 [62] and Ag_2O_3 [63]. It is noteworthy that there is no peak that can be ascribed

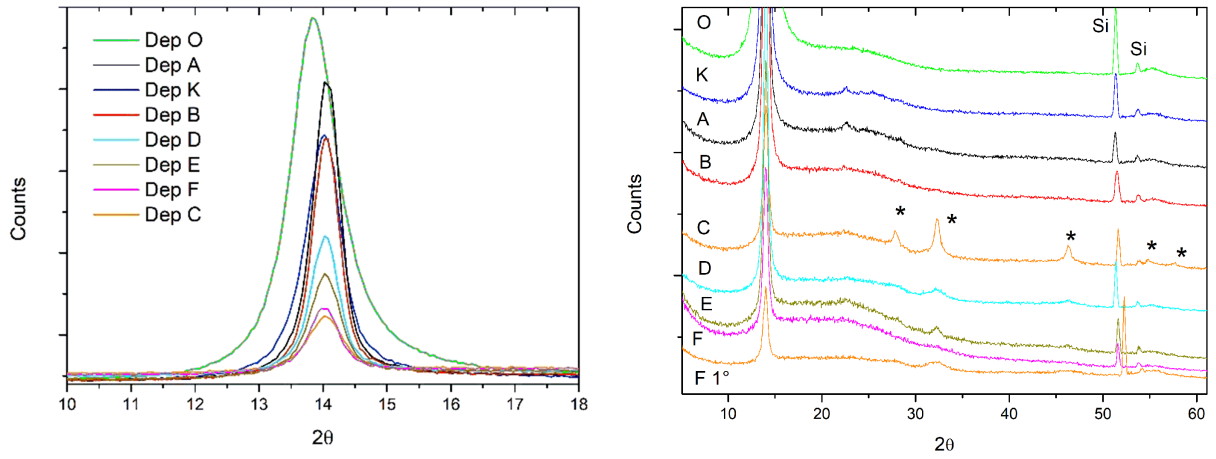

Figure 3: GIXRD spectra of pure and NCPC samples: left) the 2θ region of the main parylene peak; right) the entire 2θ range, which shows the effect of Ag incorporation on the structure of the films. The spectrum of sample F at 1° incidence angle is also shown. Asterisks indicate the peaks of Ag oxides. Si peaks coming from the substrate are also highlighted.

to metal Ag phases. Taking into account that Ag is sputtered from the target surface as metal atoms, it is thought that the silver oxidation occurs mostly during the film growth owing to the relatively high residual pressure (2–3 Pa) in the deposition chamber, which promotes the adsorption and incorporation of oxygen-containing species (such as oxygen and water vapor molecules) in the growing film. On the other hand, post-deposition silver oxidation in the external environment can not be completely ruled out, because the lower density of plasma-deposited films can decrease the well-known gas barrier properties of parylene C and then promote the diffusion of oxygen-containing species inside the films. In order to decrease the oxidation, the residual pressure in the chamber should be drastically reduced (e.g., using a high-vacuum pump). Concerning the silver-oxide peaks, the reason why they are much more visible in the spectrum of sample C than in the spectra of the other samples can be easily understood if one considers the properties of these samples. In sample C, the Ag dose is very high (see Figure 1, left) and concentrated in a thin parylene layer (2.2×10^{17} monomeric units·cm^{-2}, see Table 1). Hence, the formation of nanocrystallites with higher average size is promoted (the size is around 13–14 nm, as determined through the Scherrer equation applied to the most intense peak at 32.3°; see Table 2 for the FWHM values used in the size calculation). On the other hand, weaker peaks are visible in samples D and E because Ag dose is lower than that of sample C and is distributed in a thicker layer (2.8×10^{17} and 4.8×10^{17} monomeric units·cm^{-2}, respectively) so that smaller nanocrystallites grow (average sizes of 6–7 nm and 10–11 nm, respectively).

For samples A and B, which do not show any peaks, we had to increase the acquisition time due to the low total Ag dose in these samples and then an average size of 6–7 nm was found for both samples. In the case of sample F, which has the highest Ag dose, the Ag-containing layer is buried below a thick parylene layer (see Table 1) so that we had to increase the X-ray incidence angle to 1.0° in order to probe all the film thickness and highlight the Ag oxides crystalline peaks (see Figure 3 right). The broadness of these peaks indicates that the average nanocrystallite size is small (≤5 nm), as could be expected taking into account that silver is distributed in an even thicker layer (6.0×10^{17} monomeric units·cm^{-2}) as compared to the other samples. As a general remark, the small average size of Ag-containing nanoparticles (less than 20 nm for all the samples)

Table 2: XRD data and AFM roughness of NCPC samples: effect of Ag incorporation on the peak width (FWHM) and roughness (Ra, Rq) of the films.

sample	O	K	A	B	C	D	E	F
FWHM of parylene peak	0.89	0.67	0.52	0.51	0.64	0.53	0.57	0.57
FWHM of AgO_x peak	—	—	1.35	1.20	0.61	1.30	0.77	1.9
Ra (nm)	10	10	20	24	161	25	84	58
Rq (nm)	14	13	30	36	201	35	106	75

confirms their fine dispersion in the parylene matrix, already highlighted in a previous work [64].

The roughness of different NCPC samples was measured by AFM and displayed in Table 2. In the case of pure parylene films (samples K and O), the surface is relatively smooth and the roughness is around 10 nm. It has to be noted that the plasma-induced increase of the deposition rate does not change the film roughness. When Ag is incorporated in the parylene matrix, the films become increasingly rough with increasing Ag amount, the roughness increasing from 20–25 nm for samples A, B and D to more than 50 nm for samples C, E and F. Even if it has been previously shown that an increase in parylene C thickness produces an increase in roughness [65], the increase for the pure parylene C samples in [65] is much less pronounced as compared to our samples, as can be appreciated in Figure 4, which shows the trend of the two sets of data. Therefore, the thickness does not appear to be the main criterion explaining the roughness in our NCPC samples. It is inferred that maybe there is also an effect of nanoparticle size because the highest roughness is found in samples E and C, which have also the greatest average nanoparticle size (10–11 nm and 13–14 nm, respectively).

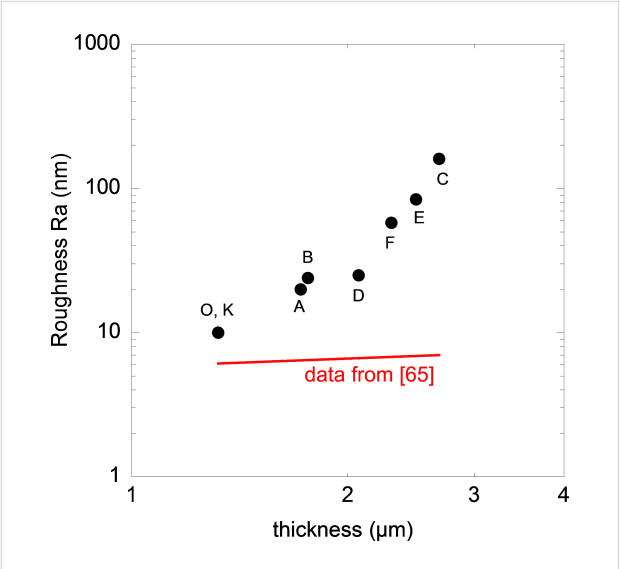

Figure 4: Roughness (Ra) as a function of the thickness. The red curve is the trend for pure parylene C films obtained in [65].

The total Ag content appears to play a minor role as compared to the nanoparticle size, as shown by the samples F and E. The former has the highest Ag content and the lowest nanoparticle size and ultimately exhibits a lower roughness than the samples E and C. The latter, with an Ag content equivalent to that of sample D, has a greater roughness than sample D maybe due to a larger nanoparticle size. To summarize, film thickness, AgO_x nanoparticle size and, to a lesser extent, Ag content concur to affect the roughness of the NCPC samples.

FTIR analysis

According to the FTIR analysis (Figure 5), the main spectral features of parylene C appear in all NCPC samples regardless of Ag content and AgO_x nanoparticle size. Compared to sample O (pure PPXC), neither shift or disappearance of the most intense parylene C peaks nor appearance of new peaks is found in the spectra of sample K and of all the NCPC samples. Only a slight broadening of some specific peaks occurs, especially of the peaks at 3020 cm^{-1} (aromatic C–H stretching), 2950, 2926 and 2861 cm^{-1} (C–H aliphatic stretching of methylene groups $–CH_2$), 1452 cm^{-1} (C–H bending), 877 cm^{-1} (one adjacent C–H bending on benzene ring) and 825 cm^{-1} (two adjacent C–H bending on benzene ring) [60]. Moreover, the intensity of some minor peaks slightly changes. It increases for peaks at 1608 cm^{-1} (aromatic C–C ring stretching [57]) and 455 cm^{-1} (out-of-plane ring bending [66]), whereas it decreases for the

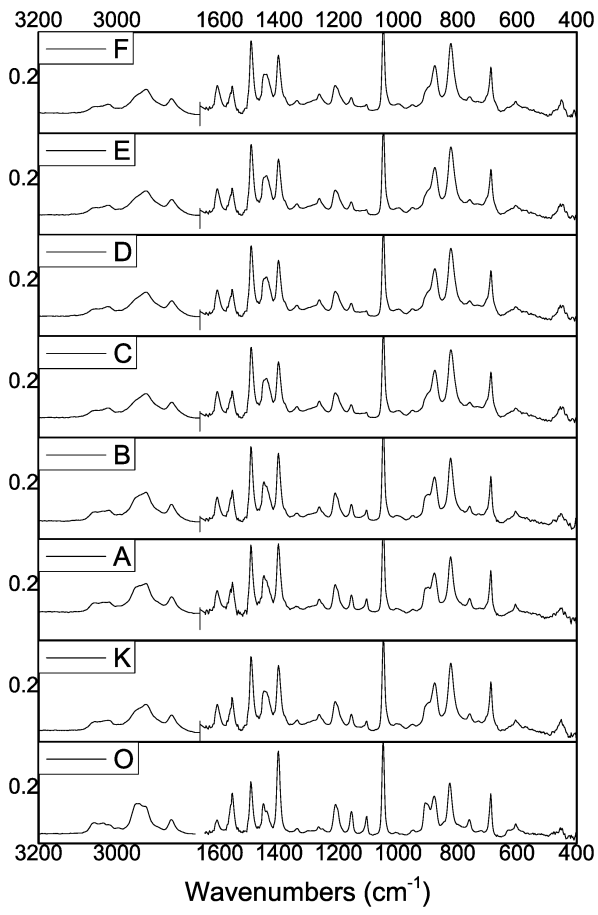

Figure 5: FTIR spectra of pure parylene C (samples O and K) and NCPCs (samples A to F).

peaks at 1157, 1106, 908, and 758 cm^{-1}. It is noteworthy that all these changes are already visible in the spectrum of sample K (no Ag, plasma on), thus indicating that they are mostly due to the plasma effect and that the incorporation of AgO_x nanoparticles plays a less important role. The persistence of the main spectral features and the limited changes of the abovementioned peaks lead to rule out a damaging effect of both plasma and nanoparticle incorporation on the parylene chains, with the formation of molecular fragments during the deposition process. Instead, it is inferred that they can be related to the change of the crystalline structure of the parylene matrix in the plasma-deposited samples, as already pointed out by the XRD analysis, consisting in a decrease of the preferred orientation of parylene nanocrystallites. As a matter of fact, the surrounding chemical environment of any molecule affects the IR activity of its vibrational modes (i.e., the changes of the dipole moment as induced by IR radiation absorption). Therefore, the different proximity of parylene chains with nearby chains and AgO_x nanoparticles due to different structural arrangements can give rise to the effects observed in our samples. A similar behavior was also found in parylene C samples doped with an UV-absorbing compound [56].

Dielectric analysis: motivation for OFETs

For OFET applications, parylene C is often selected due to its numerous advantages, as clearly highlighted in a recent paper on the subject [3]. As discussed in the Introduction, one motivation here to develop NCPCs is the integration as gate insulating layer in such applications. A sufficiently high capacitance C_i of the gate insulating material is required for optimizing performances in OFETs [3]. C_i is given by:

$$C_i = \frac{\varepsilon_0 \varepsilon'}{t} S, \quad (1)$$

where ε_0 is the vacuum permittivity (8.85×10^{-12} $F \cdot m^{-1}$), t the thickness of the dielectric, S the surface of electrodes and ε' (often named k in the industry of microelectronics) is the dielectric constant (more rigorously called relative permittivity). As seen by this equation, the insulating gate capacitance C_i is directly proportional to ε'. Typically, for parylene C ε' = 3.15 (at 1 kHz and room temperature [34]) and an increase of this value will have a direct positive repercussion on the efficiency of the field effect.

We have developed our parylene stacks with a view to propose a new approach and a compromise to the solutions provided so far. The parylene layer doped with AgO_x nanoparticles increases the dielectric constant and responds to the increase in performance given in Equation 1. In order to maintain the good insulator/semiconducting interface and for keeping good band structures at the gate–insulator interface, the AgO_x-containing parylene C is encapsulated by undoped parylene C (samples A to F). In order to avoid an increase of the gate voltage to control the channel, we had the concern to keep a total thickness of our stack of the same order of magnitude as a single layer of parylene commonly encountered in applications. Thus, as reported in Table 1, thicknesses are in the range of 2 ± 1 µm.

Figure 6a reports the frequency dependence of the dielectric constant for pure parylene (samples O and K) and NCPC films (samples A to F).

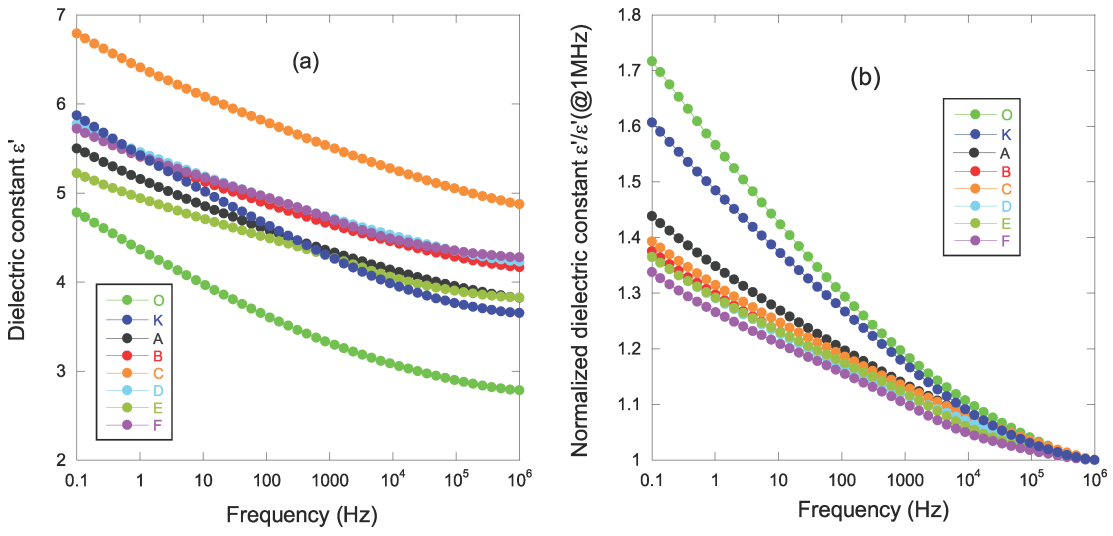

Figure 6: a) Dielectric constant ε' as a function of the frequency; b) normalized dielectric constant $\varepsilon'/\varepsilon'_{HF}$ (@1 MHz).

The general observation of an increase in the dielectric constant ε' with a decrease in frequency was clearly explained by the dipolar relaxation of the C–Cl bond (β-relaxation) [34]. Compared to the pure parylene sample (O) all other samples present a higher dielectric constant over the whole frequency range. Many factors could explain this result:

1. An increase in polymer thickness sometimes leads to an increase in the dielectric constant. This was observed for example in polyimide [67] and parylene C [65] films. It is attributed to the interaction between the polymer chains and the substrate and also to the orientation of polymer chains along this substrate. In our case, the change in the value of the dielectric constant is too big to consider such mechanisms.

2. The influence of the plasma must be taken into account as a significant effect. When comparing samples O and K, the plasma induces a mean ε' increase of 0.98 ± 0.12 over the whole frequency range. Referred to GIXRD analyses, sample K presents a higher degree of crystallinity than sample O, as highlighted by the shift of the (020) peak to a larger 2θ angle (Figure 3, left) and by the larger nanocrystallite size (reduction in the FWHM, see Table 2). Typically, when comparing two similar polymers with just a change in the degree of crystallinity, the most important parameter modifying the frequency trend of the β-relaxation is the dielectric strength $\Delta\varepsilon = \varepsilon'_{LF} - \varepsilon'_{HF}$ [62], where ε'_{LF} is the low-frequency dielectric constant (measured at 0.1 Hz in our case) and ε'_{HF} is the high-frequency dielectric constant (measured at 1 MHz in our case). Δε is associated to the number of dipoles participating in the β-relaxation process: the higher the degree of crystallinity for a given polymer, the lower the number of dipoles involved in the relaxation mechanism (as these dipoles are 'frozen' in the semi-crystalline state). Consequently, Δε decreases at increasing degrees of crystallinity [68]. For our results, $\Delta\varepsilon_{sample\ O} = 2$ and $\Delta\varepsilon_{sample\ K} = 2.2$. Moreover, as mentioned above, $\varepsilon'_{sample\ K} > \varepsilon'_{sample\ O}$ over the whole frequency range. Both results do not agree with the previous statement and another explanation must be explored.

As shown by RBS investigation, a decrease of film density and a larger amount of parylene are obtained when the plasma is switched on. The larger amount of parylene is accompanied by a larger amount of C–Cl bonds, which will then concur to increase both ε' and Δε. The β-relaxation is a local phenomenon and is expected to be little affected by the density of the film. Hence, we conclude that a greater amount of parylene explains the difference in ε' behavior between samples O and K. If one normalizes ε' to ε'_{HF} (Figure 6b), one can see that $\Delta\varepsilon_{normalized} = \Delta\varepsilon/\varepsilon'_{HF}$ is lower for sample K. The higher degree of crystallinity makes less C–Cl dipoles (in percentage) participate in β-relaxation.

3. Comparing all samples subjected to plasma, GIXRD reveals that the degree of crystallinity and the parylene crystallite size are not very different in the NCPC samples. Therefore, the origin of the difference in the dielectric behavior between all these samples has to be found in the presence of AgO_x nanoparticles in the parylene matrix. The incorporation of conductive particles into a dielectric matrix can lead to a consequent increase in the dielectric constant due to the high polarizability of these conductive particles [69]. A moderate amount of Ag-containing nanoparticles and the fact that these particles are in an oxide phase are the most likely cause of such a small change in the value of the dielectric constant in our present work. However, the values and frequency-dependence of ε' do not seem to follow a coherent trend as a function of the Ag content and, at first sight, irregular behavior appears.

To better clarify the influence of AgO_x nanoparticles on the dielectric response of NCPCs, let us first focus on the value of the high-frequency dielectric constant ε'_{HF}. No strict correlation appears between Ag content and ε'. Indeed, the sample C with Ag content of 3.8% presents the highest dielectric constant; samples B, D, F with respective Ag contents of 1.8%, 2.6%, 4.45% have similar dielectric values. Consequently, another parameter influences the results. In order to help the analysis of the results, we positioned the different samples on a graph in *x*-coordinate representing the average size of the Ag oxide nanoparticles and in *y*-coordinate representing the total amount of silver (Figure 7).

In this graph, we show for each sample the value of the high-frequency dielectric constant ε'_{HF} (Figure 7a) and the dielectric strength Δε (Figure 7b). As highlighted in Figure 7a, at a given average size of Ag oxide particles, ε'_{HF} increases with higher Ag content (comparison of samples A, B, D). A very low size of Ag oxide particles (≤5 nm) combined with a high Ag content increases ε'_{HF} very little (sample F compared to sample D). However, a combination of high Ag content and high average size of Ag oxide nanoparticles is expected to give rise to an improved ε'_{HF} as shown by sample C. Intermediate values of both Ag content and AgO_x size are not beneficial to obtain high values of ε'_{HF} (sample E).

Let us now focus on the frequency-dependence of the dielectric constant ε'. Using Figure 6b, we can clearly see that the presence of AgO_x nanoparticles induces a weaker $\Delta\varepsilon_{normalized}$ (38 ± 5%) than in the samples without nanoparticles (60% for sample K and 70% for sample O). This reflects that AgO_x nanoparticles generate chain entanglement or crosslinking of the

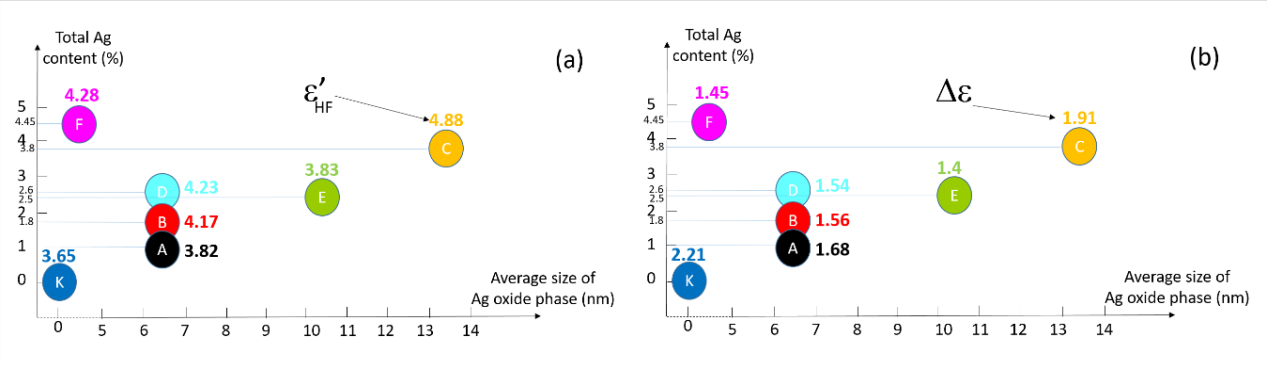

Figure 7: The amount of silver-oxide nanoparticles as a function of their average size. Additional information next to the sample symbol and in the same color of sample symbol: a) the high-frequency dielectric constant ε'_{HF} (value at 1 MHz); b) the dielectric strength Δε.

polymer chains thus decreasing the cooperative motion of chains and causing a reduction in the dielectric strength of the β-relaxation. An analogy to β-relaxation can be made by saying that the addition of AgO_x nanoparticles behaves as an overall increase in material crystallinity (i.e., $\Delta\varepsilon_{normalized}$ decreases). This analogy is emphasized when one compares sample K (absence of nanocomposites) to NCPCs (Figure 6b and Figure 7b). Clearly, Δε is higher revealing a lower global 'semi-crystalline state' for sample K. From Figure 7b, at a given average size of Ag oxide phase (samples A, B, D), Δε is reduced with higher Ag content, which is in line with our argument that adding nanoparticles effectively reduces the mobility of polymer chains. Comparing samples E and F (Figure 7b), they present a similar Δε, but the former has a lower amount of silver-oxide nanoparticles with a larger average size. Sample C stands out once again with a larger Δε than the other NCPCs. This last result seems surprising and contrary to our hypothesis of polymer chains restricted by the addition of nanoparticles and their size. However, let us not forget that the sample C has the greatest thickness (see Table 1) and therefore contains a larger 'reservoir' of dipoles available to participate in β-relaxation. TEM analysis should be carried out to assess the volume occupied by nanoparticles and possible agglomerations of AgO_x. This characterization was beyond the scope of this study but would deserve particular attention for future work.

It is well known that the addition of particles with a high dielectric constant to a polymeric material causes (as generally desired) an increase in the dielectric constant but is also accompanied by an unwanted increase of dielectric losses (imaginary part of the permittivity ε" and the dissipation factor tan δ = ε"/ε'), which limits their integration for the envisaged application. We have evaluated these losses in our materials and the results are shown in Figure 8.

Not surprisingly, the appearance of a broad peak over the entire frequency range for sample O is representative of β-relaxation

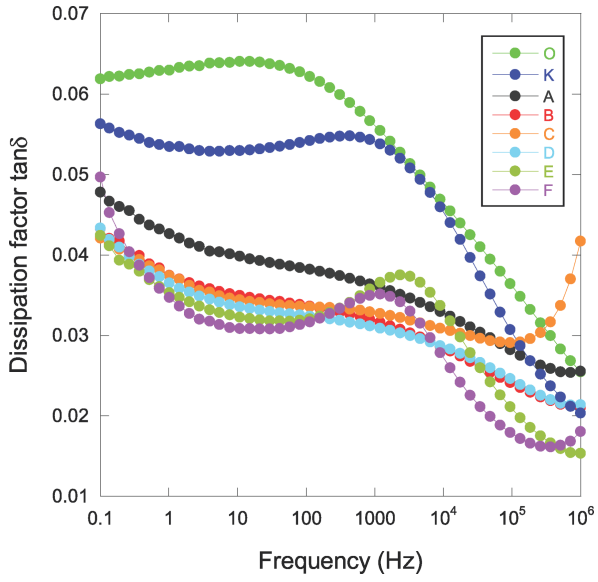

Figure 8: Frequency dependence of the dissipation factor for pure parylene C and NCPC samples.

[34]. The effect of plasma (sample K) results in a slight decrease in these losses over the entire frequency range. However, there is a slight increase in these losses at the lowest frequencies (less than 1 Hz) attributed to the manifestation of charge conduction or a new polarization mechanism. A temperature study would make it possible to decide on this rise.

It is worth noting that the addition of silver-oxide nanoparticles leads to a reduction in tan δ. Sample C, which has the highest dielectric constant, also shows a low tan δ. The increase in the dissipation factor at the higher frequencies for this sample is probably the consequence of a parasitic impedance at the electrode–polymer interface. This observation is related to the fact that this material has the highest roughness (see Table 2) and the deposition of the upper electrode for the measurement is probably impacted by the roughness.

The most pronounced effect of a moderate addition of nanoparticles appears to be an increase in the dielectric constant rather than a degradation (increase) in the imaginary part of the permittivity ε". These results indicate that silver oxide reduces the dielectric strength as related to the β-relaxation without bringing other inconveniences such as interfacial polarization mechanism or a long-range electrical conductivity induced by these nanoparticles. For this latter, we plotted the electrical ac-conductivity σ' as a function of the frequency (Figure 9).

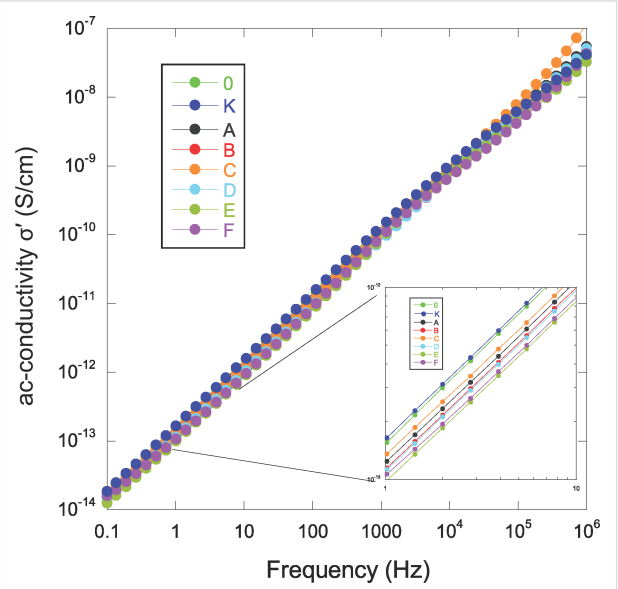

Figure 9: Electrical conductivity of pure parylene C and NCPCs.

The behavior is representative of short-range conduction (hopping) without significant effect of Ag nanoparticles besides a weaker improvement in σ' (see inset in Figure 9). In the range around 1 kHz, one observes a change in the slope of the ac-conductivity for sample F. This specific effect is well highlighted in the tan δ response (Figure 8) with the appearance of a peak for this sample and also for the sample E. It has to be remembered that these two samples have the weakest Δε (see Figure 7b), hence β-relaxation will mask less any other mechanism that may influence the dielectric response (or from another point of view: The other phenomenon drives the mechanism of β-relaxation much more, explaining the low Δε). The tan δ peak observed for the sample F could be justified by the large amount of Ag nanoparticles, while the reason why sample E exhibits similar behavior remains curious and would require additional work to be completely understood.

This dielectric analysis showed that an increase in the dielectric constant accompanied by a decrease of dissipation factor tan δ is possible when silver-oxide particles are embedded in a parylene C matrix. Thus, for OFET applications, NCPC thin films could constitute a new interesting route as insulating layer. Let us take Equation 1 and Figure 6a. To evaluate the improvement brought about by the addition of silver-oxide nanoparticles in the performance of the grid oxide for OFETs, we standardized (at each frequency) the curves in Figure 6a by the value of the dielectric constant obtained from the sample O (this latter uses a conventional deposition process for the growth of parylene C). Results are reported in Figure 10. Compared to the sample K (no Ag content), samples A and E have no advantages in terms of performance for C_i. Sample C has the highest insulating gate capacitance. However, an improvement in the roughness for this sample must be reached before integration for OFET as this structural parameter is critical in the deposition of organic semiconductor layers and will affect the performance [70,71].

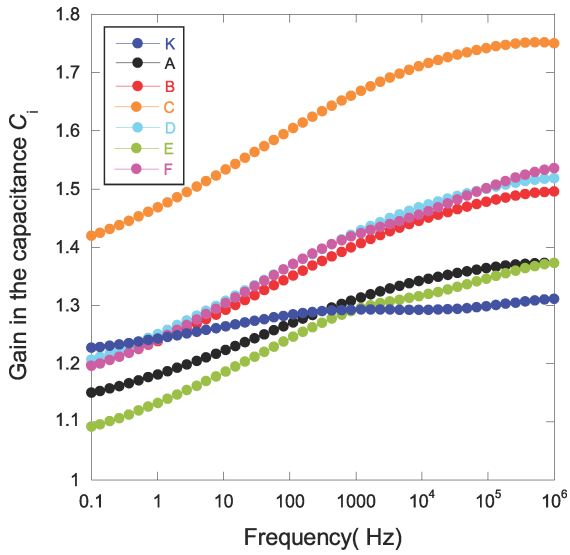

Figure 10: Gain in the gate insulation capacitance by replacing conventionally processed parylene C (sample O) with plasma-combined CVD process incorporating silver-oxide nanoparticles. Accuracy in the gain due to geometric dimensions of samples is in the range ±0.1 (sample F) to ±0.18 (sample C).

Conclusion

Nanocomposite–parylene C (NCPC) were synthetized at room temperature by chemical vapor deposition polymerization of parylene C combined with RF-sputtering of silver. It was demonstrated that the plasma itself induces changes in the density and semi-crystalline character of parylene C. A decrease in the density, an increase in the degree of crystallinity and an increase of about 60% in the size of parylene nanocrystallites were observed. The addition of silver-containing nanoparticles does not further modify the crystallinity of parylene C itself. These nanocomposites consist of a silver-oxide phase embedded inside the parylene C matrix. No trace of pure metal silver is found in all the NCPC samples. The roughness and the di-

electric properties of NCPC are significantly influenced by the presence of silver-oxide nanoparticles. The roughness increases from 10 nm (for undoped parylene C films) to values from 20 to 160 nm for NCPC, depending on the film thickness, size of silver-oxide nanoparticles and, to a lesser extent, Ag content. The dielectric performance appears suitable for the integration of these NCPC as gate insulating materials for OFETs. Simultaneously, it is possible to increase the dielectric constant (by a factor of 1.4) and to reduce (or to not degrade) the dissipation factor ($\tan \delta < 0.05$). Finally, the interest of NCPCs was proved for applications such as integration in OFETs, but improvements in the deposition process should be pursued. The possibility to tune the parameters of the CVD and plasma processes will allow for better controlling the semi-crystalline character of parylene C, the roughness, the thickness of the layers, the amount and the size of nanoparticles. Concerning possible aging effects on the properties of these NCPCs, the stability of both parylene C and silver oxide is a good premise for the achievement of a stable nanocomposite material. However, a specific study of this aspect will be carried out in the future.

Experimental

Parylene C/Ag nanocomposite deposition

To avoid the synthesis of the polymer nanocomposite in two stages, we propose a new clean method to simultaneously deposit both the organic compound (parylene C) and the inorganic compond (silver-containing nanoparticles). This method consists of two associated processes, i.e., primary vacuum-CVD and RF-magnetron sputtering.

The deposition process of NCPC involves three successive operations. The process begins with the deposition of parylene C. Some hundreds of nanometers of parylene C film are deposited firstly as an electrical passivation layer onto the metallic substrate (silicon, gold or aluminium). During this step, the RF-magnetron sputtering source is turned on in order to avoid the deposition of parylene C on the Ag target surface, but a shutter is placed between target and substrates to avoiding unwanted incorporation of Ag atoms in the deposited films. Then, the shutter is opened and the parylene C and the silver atoms are deposited at the same time in order to constitute the nanocomposite films (Figure 11). As a final step, the shutter is closed again leaving only the deposition of parylene C as a capping layer between the nanocomposite and the top metallic electrode or even as a coating layer for the nanocomposite.

Analogous to the description in [26], the parylene C deposition consists of three steps. First, the cyclic dimer (dichlorinated di-*p*-xylylene, 2.5 g, same amount for all the depositions) is sublimated at a temperature between 120 and 160 °C and a pressure of around 1–2 Pa in the first step. Then, the vapor of the dimer is cleaved into a reactive vapor monomer (monochlorinated *p*-xylylene) in a pyrolysis chamber at a temperature between 600 and 700 °C. Finally, the monomer molecules in the gaseous state enter the deposition zone to get deposited on substrates. When the RF sputtering process is enabled (open shutter), the silver atoms condense onto the substrates together with the monomer molecules and are then incorporated in the polymer matrix. Under these conditions, we have prepared

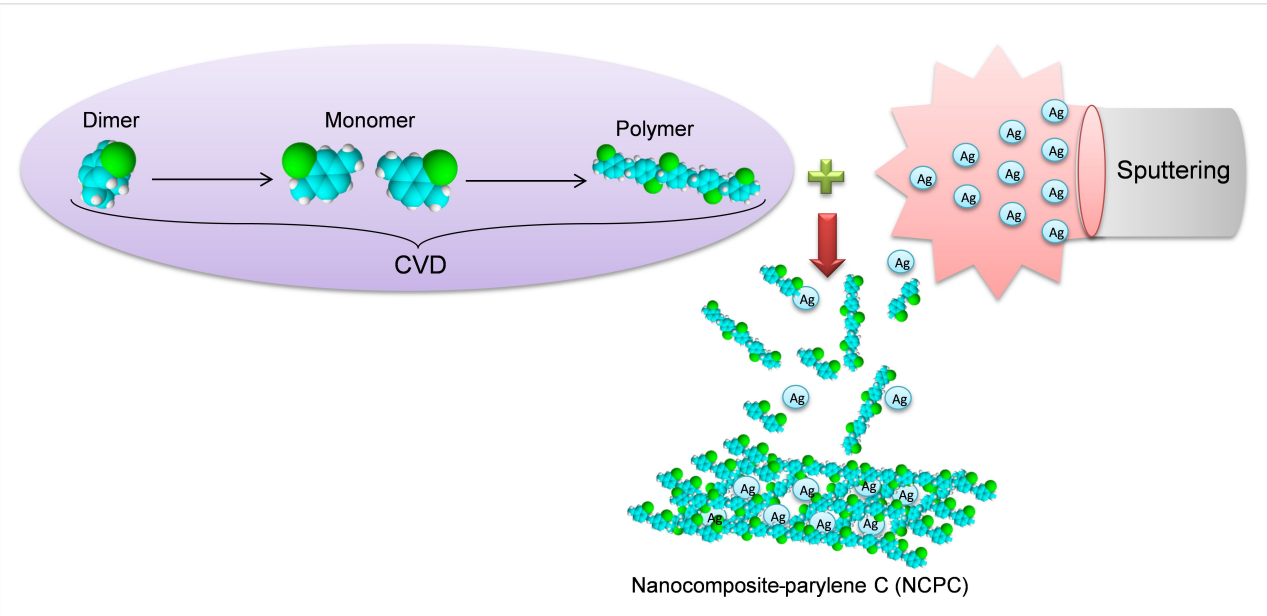

Figure 11: Depostion of nanocomposite–parylene C (NCPC) by a combined CVD and RF sputtering technique.

uniform nanocomposite thin films with thicknesses from 1 to 3 μm, as measured by a Tencor AlphaStep 200 profilometer. In order to obtain several, nominally identical samples for each deposition run, the substrates were put on a rotating carousel, with the rotation axis parallel to the Ag target surface and with a rotation period of 90 s. The sample holder can accommodate up to ten substrates so that at least two samples from each type were used for the different measurements carried out in this work. Different samples were produced by increasing the number of rotations from 0 to 6, as detailed above (see Results and Discussion). The minimum distance between the Ag target and the sample surface was fixed at 10.5 cm.

Parylene C/Ag nanocomposite characterization

The silver and chlorine content in the nanocomposite samples was quantified by Rutherford backscattering spectrometry (RBS). Ion beam analyses of the deposited films were performed using a 2.0 MeV $^4He^+$ beam at the Van de Graaf accelerator at the Laboratori Nazionali di Legnaro, with a scattering angle of 160°. We have to highlight that the Cl content measured with RBS (in atoms·cm^{-2}) is directly converted into the amount of parylene (in monomeric units·cm^{-2}), since each monomeric unit contains one Cl atom. RBS analysis was performed on coatings deposited on silicon substrates. Taking into account the desorption of Cl-containing species from the film occurring during ion beam analysis [72], RBS spectra were acquired by irradiating different spots of the pristine samples and collecting only 0.2 μC of charge on each spot until a total collected charge of a few microcoulombs was reached. A stylus profilometer (Tencor Instruments, model Alpha-Step 200) was used to measure the film thickness. Grazing incidence X-ray diffraction scans were carried out on a Philips diffractometer on the as-grown samples, using Ni-filtered Cu Kα radiation at 40 kV and 40 mA. The incidence angle was fixed at 0.5° for all the samples. Some spectra were also collected at 1° incidence in order to probe deeper the film structure. The surface morphology was analyzed using a non-contact mode AFM model C-21 (Danish Micro Engineering), mounting a DualScope Probe Scanner 95-50. Capacitance areas were defined in the top NCPC resulting in square 2 × 2 mm^2 contacts. In order to assure a homogeneous distribution of the potential during the dielectric measurements, top gold electrodes with a thickness of 100 nm were deposited by thermal evaporation with the sample held at room temperature. Chemical composition of pure parylene C films and NCPC thin films was investigated at room temperature by Fourier transform infrared spectrometer (FTIR, Nicolet 380) in reflectance mode at a resolution of 4 cm^{-1} in a wave number range from 400 to 3200 cm^{-1}. The spectra were obtained after a previous background subtraction with 32 scans for each sample to remove the contribution of H_2O and CO_2 molecules. Dielectric properties were measured using a Novocontrol broadband dielectric spectroscopy (BDS20) impedance meter in the frequency range of 0.1–10^6 Hz at room temperature.

ORCID® iDs

Gianluigi Maggioni - https://orcid.org/0000-0002-9367-7226
Sara M. Carturan - https://orcid.org/0000-0002-6702-2867
Alain Sylvestre - https://orcid.org/0000-0003-4048-1438

References

1. Liu, A.; Liu, G.; Zhu, H.; Song, H.; Shin, B.; Fortunato, E.; Martins, R.; Shan, F. *Adv. Funct. Mater.* **2015,** *25,* 7180–7188. doi:10.1002/adfm.201502612
2. Kololuoma, T.; Leppäniemi, J.; Majumdar, H.; Branquinho, R.; Herbei-Valcu, E.; Musat, V.; Martins, R.; Fortunato, E.; Alastalo, A. *J. Mater. Chem. C* **2015,** *3,* 1776–1786. doi:10.1039/c4tc02022g
3. Marszalek, T.; Gazicki-Lipman, M.; Ulanski, J. *Beilstein J. Nanotechnol.* **2017,** *8,* 1532–1545. doi:10.3762/bjnano.8.155
4. Metallo, C.; White, R. D.; Trimmer, B. A. *J. Neurosci. Methods* **2011,** *195,* 176–184. doi:10.1016/j.jneumeth.2010.12.005
5. Rodger, D. C.; Fong, A. J.; Li, W.; Ameri, H.; Ahuja, A. K.; Gutierrez, C.; Lavrov, I.; Zhong, H.; Menon, P. R.; Meng, E.; Burdick, J. W.; Roy, R. R.; Edgerton, V. R.; Weiland, J. D.; Humayun, M. S.; Tai, Y. C. *Sens. Actuators, B* **2008,** *132,* 449–460. doi:10.1016/j.snb.2007.10.069
6. Lee, T.; Lee, J.; Park, C. *Korean J. Chem. Eng.* **2002,** *19,* 722–727. doi:10.1007/bf02699324
7. Pokhodnya, K. I.; Bonner, M.; Miller, J. S. *Chem. Mater.* **2004,** *16,* 5114–5119. doi:10.1021/cm048872d
8. He, X.; Zhang, F.; Zhang, X. *Appl. Surf. Sci.* **2009,** *256,* 6–11. doi:10.1016/j.apsusc.2009.03.085
9. Spivack, M. A.; Ferrante, G. *J. Electrochem. Soc.* **1969,** *116,* 1592–1594. doi:10.1149/1.2411625
10. Ashimine, T.; Onoue, T.; Yasuda, T.; Fujita, K.; Tsutsui, T. *Mol. Cryst. Liq. Cryst.* **2007,** *471,* 221–227. doi:10.1080/15421400701548282
11. Shin, E.-Y.; Choi, E.-Y.; Noh, Y.-Y. *Org. Electron.* **2017,** *46,* 14–21. doi:10.1016/j.orgel.2017.04.005
12. Wu, J.; Fei, F.; Wei, C.; Chen, X.; Nie, S.; Zhang, D.; Su, W.; Cui, Z. *RSC Adv.* **2018,** *8,* 5721–5727. doi:10.1039/c8ra00023a
13. Yoon, Y. S.; Park, H. Y.; Lim, Y. C.; Choi, K. G.; Lee, K. C.; Park, G. B.; Lee, C. J.; Moon, D. G.; Han, J. I.; Kim, Y. B.; Nam, S. C. *Thin Solid Films* **2006,** *513,* 258–263. doi:10.1016/j.tsf.2006.01.015
14. Liao, C.; Zhang, M.; Yao, M. Y.; Hua, T.; Li, L.; Yan, F. *Adv. Mater. (Weinheim, Ger.)* **2015,** *27,* 7493–7527. doi:10.1002/adma.201402625
15. Yokota, T.; Zalar, P.; Kaltenbrunner, M.; Jinno, H.; Matsuhisa, N.; Kitanosako, H.; Tachibana, Y.; Yukita, W.; Koizumi, M.; Someya, T. *Sci. Adv.* **2016,** *2,* e1501856. doi:10.1126/sciadv.1501856
16. Hsu, J.-M.; Rieth, L.; Normann, R. A.; Tathireddy, P.; Solzbacher, F. *IEEE Trans. Biomed. Eng.* **2009,** *56,* 23–29. doi:10.1109/tbme.2008.2002155
17. Tszydel, I.; Marszalek, T.; Ulanski, J.; Nosal, A.; Gazicki-Lipman, M. *Surf. Coat. Technol.* **2016,** *290,* 21–27. doi:10.1016/j.surfcoat.2015.08.058

18. Chua, L.-L.; Zaumseil, J.; Chang, J.-F.; Ou, E. C.-W.; Ho, P. K.-H.; Sirringhaus, H.; Friend, R. H. *Nature* **2005,** *434,* 194–199. doi:10.1038/nature03376
19. Alt, M.; Melzer, C.; Mathies, F.; Deing, K.; Hernandez-Sosa, G.; Lemmer, U. *Appl. Phys. A: Mater. Sci. Process.* **2016,** *122,* 204. doi:10.1007/s00339-016-9678-6
20. Nair, S.; Kathiresan, M.; Mukundan, T.; Natarajan, V. *Microelectron. Eng.* **2016,** *163,* 36–42. doi:10.1016/j.mee.2016.06.001
21. Tewari, P.; Rajagopalan, R.; Furman, E.; Lanagan, M. T. *J. Colloid Interface Sci.* **2009,** *332,* 65–73. doi:10.1016/j.jcis.2008.12.060
22. Tewari, P.; Rajagopalan, R.; Furman, E.; Lanagan, M. T. *Langmuir* **2010,** *26,* 18817–18823. doi:10.1021/la1033367
23. Kahouli, A.; Jomni, F.; Sylvestre, A.; Yangui, B.; Legrand, J. *J. Phys. D: Appl. Phys.* **2011,** *44,* 505302. doi:10.1088/0022-3727/44/50/505302
24. Song, Q.; Sun, J.; Mu, Y.; Xu, Y.; Zhu, Q.; Jin, Q. *Sens. Actuators, B* **2018,** *256,* 1122–1130. doi:10.1016/j.snb.2017.10.006
25. Hassler, C.; Boretius, T.; Stieglitz, T. *J. Polym. Sci., Part B: Polym. Phys.* **2011,** *49,* 18–33. doi:10.1002/polb.22169
26. Kahouli, A.; Sylvestre, A.; Laithier, J.-F.; Pairis, S.; Garden, J.-L.; André, E.; Jomni, F.; Yangui, B. *J. Phys. D: Appl. Phys.* **2012,** *45,* 215306. doi:10.1088/0022-3727/45/21/215306
27. Sekitani, T.; Someya, T. *Jpn. J. Appl. Phys., Part 1* **2007,** *46,* 4300–4306. doi:10.1143/jjap.46.4300
28. Diallo, K.; Erouel, M.; Tardy, J.; André, E.; Garden, J.-L. *Appl. Phys. Lett.* **2007,** *91,* 183508. doi:10.1063/1.2802039
29. Ling, M.-m.; Bao, Z.; Li, D. *Appl. Phys. Lett.* **2006,** *88,* 033502. doi:10.1063/1.2166488
30. Han, S. H.; Kim, J. H.; Jang, J.; Cho, S. M.; Oh, M. H.; Lee, S. H.; Choo, D. J. *Appl. Phys. Lett.* **2006,** *88,* 073519. doi:10.1063/1.2174876
31. Ogawa, S.; Naijo, T.; Kimura, Y.; Ishii, H.; Niwano, M. *Appl. Phys. Lett.* **2005,** *86,* 252104. doi:10.1063/1.1949281
32. Sekitani, T.; Someya, T.; Sakurai, T. *J. Appl. Phys.* **2006,** *100,* 024513. doi:10.1063/1.2216883
33. Kiazadeh, A.; Gomes, H. L.; Barquinha, P.; Martins, J.; Rovisco, A.; Pinto, J. V.; Martins, R.; Fortunato, E. *Appl. Phys. Lett.* **2016,** *109,* 051606. doi:10.1063/1.4960200
34. Kahouli, A.; Sylvestre, A.; Ortega, L.; Jomni, F.; Yangui, B.; Maillard, M.; Berge, B.; Robert, J.-C.; Legrand, J. *Appl. Phys. Lett.* **2009,** *94,* 152901. doi:10.1063/1.3114404
35. Chen, F.-C.; Chu, C.-W.; He, J.; Yang, Y.; Lin, J.-L. *Appl. Phys. Lett.* **2004,** *85,* 3295–3297. doi:10.1063/1.1806283
36. Kim, P.; Jones, S. C.; Hotchkiss, P. J.; Haddock, J. N.; Kippelen, B.; Marder, S. R.; Perry, J. W. *Adv. Mater. (Weinheim, Ger.)* **2007,** *19,* 1001–1005. doi:10.1002/adma.200602422
37. Hashemi, A.; Bahari, A.; Ghasemi, S. *Appl. Surf. Sci.* **2017,** *416,* 234–240. doi:10.1016/j.apsusc.2017.04.154
38. Hashemi, A.; Bahari, A.; Ghasemi, S. *J. Electron. Mater.* **2018,** *47,* 3717–3726. doi:10.1007/s11664-018-6231-8
39. Lu, Y.; Lee, W. H.; Lee, H. S.; Jang, Y.; Cho, K. *Appl. Phys. Lett.* **2009,** *94,* 113303. doi:10.1063/1.3097010
40. Lee, J.; Kim, J. H.; Im, S. *J. Appl. Phys.* **2004,** *95,* 3733–3736. doi:10.1063/1.1650886
41. Zirkl, M.; Haase, A.; Fian, A.; Schön, H.; Sommer, C.; Jakopic, G.; Leising, G.; Stadlober, B.; Graz, I.; Gaar, N.; Schwödiauer, R.; Bauer-Gogonea, S.; Bauer, S. *Adv. Mater. (Weinheim, Ger.)* **2007,** *19,* 2241–2245. doi:10.1002/adma.200700831
42. Kanbur, Y.; Irimia-Vladu, M.; Głowacki, E. D.; Voss, G.; Baumgartner, M.; Schwabegger, G.; Leonat, L.; Ullah, M.; Sarica, H.; Erten-Ela, S.; Schwödiauer, R.; Sitter, H.; Küçükyavuz, Z.; Bauer, S.; Sariciftci, N. S. *Org. Electron.* **2012,** *13,* 919–924. doi:10.1016/j.orgel.2012.02.006
43. Schwabegger, G.; Ullah, M.; Irimia-Vladu, M.; Baumgartner, M.; Kanbur, Y.; Ahmed, R.; Stadler, P.; Bauer, S.; Sariciftci, N. S.; Sitter, H. *Synth. Met.* **2011,** *161,* 2058–2062. doi:10.1016/j.synthmet.2011.06.042
44. Veres, J.; Ogier, S.; Lloyd, G.; de Leeuw, D. *Chem. Mater.* **2004,** *16,* 4543–4555. doi:10.1021/cm049598q
45. Itaka, K.; Yamashiro, M.; Yamaguchi, J.; Haemori, M.; Yaginuma, S.; Matsumoto, Y.; Kondo, M.; Koinuma, H. *Adv. Mater. (Weinheim, Ger.)* **2006,** *18,* 1713–1716. doi:10.1002/adma.200502752
46. Feng, C.; Mei, T.; Hu, X. *Org. Electron.* **2011,** *12,* 1304–1313. doi:10.1016/j.orgel.2011.04.019
47. Nigam, A.; Schwabegger, G.; Ullah, M.; Ahmed, R.; Fishchuk, I. I.; Kadashchuk, A.; Simbrunner, C.; Sitter, H.; Premaratne, M.; Ramgopal Rao, V. *Appl. Phys. Lett.* **2012,** *101,* 083305. doi:10.1063/1.4747451
48. Chai, X.; Liu, J.; He, Q.; Peng, G.; Yang, C. *Appl. Surf. Sci.* **2011,** *257,* 10771–10774. doi:10.1016/j.apsusc.2011.07.095
49. He, Q.; Liu, J.-Q.; Yang, B.; Chen, X.; Yang, C.-S. *Surf. Coat. Technol.* **2014,** *252,* 120–125. doi:10.1016/j.surfcoat.2014.04.055
50. Xie, X.; Rieth, L.; Williams, L.; Negi, S.; Bhandari, R.; Caldwell, R.; Sharma, R.; Tathireddy, P.; Solzbacher, F. *J. Neural Eng.* **2014,** *11,* 026016. doi:10.1088/1741-2560/11/2/026016
51. Minnikanti, S.; Diao, G.; Pancrazio, J. J.; Xie, X.; Rieth, L.; Solzbacher, F.; Peixoto, N. *Acta Biomater.* **2014,** *10,* 960–967. doi:10.1016/j.actbio.2013.10.031
52. Jakabovič, J.; Kováč, J.; Weis, M.; Haško, D.; Srnánek, R.; Valent, P.; Resel, R. *Microelectron. J.* **2009,** *40,* 595–597. doi:10.1016/j.mejo.2008.06.029
53. Graz, I. M.; Lacour, S. P. *Appl. Phys. Lett.* **2009,** *95,* 243305. doi:10.1063/1.3265737
54. Kawasaki, N.; Kalb, W. L.; Mathis, T.; Kaji, Y.; Mitsuhashi, R.; Okamoto, H.; Sugawara, Y.; Fujiwara, A.; Kubozono, Y.; Batlogg, B. *Appl. Phys. Lett.* **2010,** *96,* 113305. doi:10.1063/1.3360223
55. RUMP: RBS Analysis and Plotting. http://www.genplot.com/doc/rump.htm (accessed Jan 7, 2019).
56. Maggioni, G.; Tessarollo, A.; Carturan, S. *Mater. Chem. Phys.* **2015,** *149–150,* 530–538. doi:10.1016/j.matchemphys.2014.11.003
57. Senkevich, J. J.; Desu, S. B. *Thin Solid Films* **1998,** *322,* 148–157. doi:10.1016/s0040-6090(97)00918-8
58. Patterson, A. L. *Phys. Rev.* **1939,** *56,* 978–982. doi:10.1103/physrev.56.978
59. Hanawalt, J. D.; Rinn, H. W.; Frevel, L. K. *Ind. Eng. Chem., Anal. Ed.* **1938,** *10,* 457–512. doi:10.1021/ac50125a001
60. Standke, B.; Jansen, M. *J. Solid State Chem.* **1987,** *67,* 278–284. doi:10.1016/0022-4596(87)90364-1
61. Salkind, A. J.; Zeek, W. C. *J. Electrochem. Soc.* **1959,** *106,* 366. doi:10.1149/1.2427349
62. Brese, N. E.; O'Keeffe, M.; Ramakrishna, B. L.; Von Dreele, R. B. *J. Solid State Chem.* **1990,** *89,* 184–190. doi:10.1016/0022-4596(90)90310-t
63. Standke, B.; Jansen, M. *Z. Anorg. Allg. Chem.* **1986,** *535,* 39–46. doi:10.1002/zaac.19865350406
64. Maggioni, G.; Castagliuolo, I. *Plasma Processes Polym.* **2014,** *11,* 489–495. doi:10.1002/ppap.201300145
65. Kahouli, A. *J. Appl. Phys.* **2012,** *112,* 064103. doi:10.1063/1.4752022

66. Silverstein, R. M.; Webster, F. X.; Kiemle, D. J. *Spectrometric Identification of Organic Compounds,* 7th ed.; Wiley: New York, NY, U.S.A., 2005.
67. Liang, T.; Makita, Y.; Kimura, S. *Polymer* **2001,** *42,* 4867–4872. doi:10.1016/s0032-3861(00)00881-8
68. Runt, J. P.; Fitzgerald, J. J. *Dielectric Spectroscopy of Polymeric Materials: Fundamentals and Applications;* American Chemical Society: Washington, DC, U.S.A., 1997.
69. Sylvestre, A.; Kukielka, S.; Nguyen, D. M.; Gulbiński, W.; Pauleau, Y. *Rev. Adv. Mater. Sci.* **2007,** *15,* 185–191.
70. Werkmeister, F. X.; Noever, S. J.; Nickel, B. A. *Org. Electron.* **2015,** *26,* 439–442. doi:10.1016/j.orgel.2015.08.009
71. Li, M.; An, C.; Marszalek, T.; Baumgarten, M.; Müllen, K.; Pisula, W. *Adv. Mater. (Weinheim, Ger.)* **2016,** *28,* 2245–2252. doi:10.1002/adma.201503552
72. Maggioni, G.; Campagnaro, A.; Carturan, S.; Quaranta, A. *Sol. Energy Mater. Sol. Cells* **2013,** *108,* 27–37. doi:10.1016/j.solmat.2012.08.009

License and Terms

BEILSTEIN JOURNAL OF NANOTECHNOLOGY

Ceria/polymer nanocontainers for high-performance encapsulation of fluorophores

Kartheek Katta[1], Dmitry Busko[1], Yuri Avlasevich[1], Katharina Landfester[1], Stanislav Baluschev[*1,2] and Rafael Muñoz-Espí[*1,3]

Full Research Paper

Open Access

Address:
[1]Max Planck Institute for Polymer Research, Ackermannweg 10, 55128 Mainz, Germany, [2]Optics and Spectroscopy Department, Faculty of Physics, Sofia University "St. Kliment Ochridski" 5 James Bourchier, 1164 Sofia, Bulgaria and [3]Institute of Materials Science (ICMUV), Universitat de València, c/ Catedràtic José Beltrán 2, 46980 Paterna, Spain

Email:
Stanislav Baluschev[*] - balouche@phys.uni-sofia.bg;
Rafael Muñoz-Espí[*] - rafael.munoz@uv.es

* Corresponding author

Keywords:
cerium oxide; crystallization; miniemulsion; nanocapsule; photoluminescence; singlet oxygen

Beilstein J. Nanotechnol. **2019,** *10,* 522–530.
doi:10.3762/bjnano.10.53

Received: 02 August 2018
Accepted: 24 January 2019
Published: 22 February 2019

This article is part of the thematic issue "Advanced hybrid nanomaterials".

Guest Editor: V. de Zea Bermudez

Abstract

We report the synthesis of high-performance organic–inorganic hybrid fluorescent nanocapsules comprising a polymer shell armored with an inorganic layer and a liquid core containing a fluorophore. The polymeric capsules are synthesized by free radical miniemulsion polymerization and contain covalently bound carboxylate surface functionalities that allow for the binding of metal ions through electrostatic interaction. A cerium(IV) oxide nanoparticle layer, formed in situ at the surface of the hybrid nanocapsules, acts as oxygen scavenger and keeps external reactive molecular oxygen from entering into the capsules, eventually resulting in a reduction of the photooxidation of encapsulated fluorescent molecules. This approach shows an increase in the fluorescence of the model organic fluorophore terrylene diimide by avoiding the ground-state molecular oxygen to react with electronically excited states of the fluorescent hydrocarbon molecule.

Introduction

Hybrid polymeric core–shell nanoparticles with encapsulated fluorescent dye molecules are frequently employed for life-science applications, such as cell labeling and drug delivery [1-5]. In recent years, polymeric hybrid nanoparticles and nanocapsules with tailored inorganic components on the surface have attracted great interest because of the possibility to tune size, composition, porosity, stability, surface functionality, and colloidal stability [6-12]. Generally, fluorescent dye molecules are sensitive to the external environment, which leads to unwanted chemical reactions [13]. Molecular oxygen is a well-known quencher of fluorescence. Consequently, the shell properties of the nanocontainers are often

customized to protect the fluorophore encapsulated into a liquid core.

Higher lying singlet states of a fluorophore are relatively short living and quickly relax to the lowest excited singlet state, relaxing further to the excited triplet state via an intersystem crossing process. The ground state of the oxygen molecule is a triplet state and the energy of the excited triplet state of the fluorophore can be transferred to the oxygen molecule. Thus, singlet oxygen is obtained through the process of fluorescence quenching [13-16].

Photooxidation significantly changes the emission properties of fluorophores because of an irreversible chemical reaction. In a simple description, the longer the fluorescence lifetime and the lower the fluorescence quantum yield of the fluorophore are, the stronger is the sensitivity to the presence of oxygen quenching [13]. The solubility of oxygen in organic solvents is also an important factor in the quenching process of a florescent molecule. The solubility of oxygen in organic solvents decreases with increasing alkyl chain length of the alkanes [17,18]. Furthermore, the oxygen quenching is less efficient in high-viscosity media [13]. In bulk fluorescent samples with a dye content between 10^{-4} and 10^{-5} M, oxygen quenching does not play a significant role. By applying standard degassing techniques such as nitrogen or argon bubbling and/or freeze–pump–thaw cycles, the oxygen content can be lowered. These techniques are efficient enough to suppress the oxygen quenching of fluorescence [13]. The case of fluorescent samples containing dyes encapsulated in nanoconfined materials is more complicated. In general, the encapsulation process of the dye leads to a drastic reduction of the total dye concentration in the sample and increases the amounts of dissolved molecular oxygen and encapsulated fluorescent dye.

A variety of methods have been applied to encapsulate the fluorescent materials into micro- and nanocapsules [19,20], with a concentration of hydrophobic dye of the order of 10^{-4} M and a total solid content of 1–5 wt %. In bulk fluorescent samples, the oxygen/dye molar concentration ratio is typically about 10:1, while for nanoconfined materials is of about 200:1. This huge excess of oxygen affects the optical response of nanometric systems not only by quenching dramatically the fluorescence but also by photooxidation of the organic dye [21]. This effect is an additional source of uncertainty for quantitative measurements in life sciences [22,23].

Near-infrared (NIR) light undergoes less diffuse scattering than visible light, causes less photodamage, and can penetrate deeper into tissues. Hence, it is preferred for life-science applications. Organic dyes that can be excited above 600 nm are highly favorable for live-cell imaging experiments, because the background signal obtained from the autofluorescence of living cells is negligible in the near-infrared region [24,25]. In this work, we have chosen a specific fluorescent dye molecule, i.e., terrylene diimide (TDI), which shows intense fluorescence in the NIR spectral region of the electromagnetic spectrum, to be encapsulated in polymeric nanocapsules [26,27]. TDI, which than can be excited with red light (λ_{exc} = 633 nm from a HeNe laser, for instance) and shows bright fluorescence at λ_{max} = 670–690 nm, is a suitable organic dye for patterning or imaging of biomaterials. This dye belongs to the rylene family [28], which is formed by extending the π-conjugated core system of highly fluorescent perylene-3,4:9,10-tetracarboxdimides. The rylene dyes have unique optical properties, such as high extinction coefficients, high thermal, chemical and photochemical stabilities, and exhibit brilliant colors [29,30]. Furthermore, in bulk samples, TDI demonstrates an excellent fluorescence quantum yield (ca. 90%) [24], less affected by the presence of molecular oxygen. Using the example of TDI, we aim to demonstrate that in nanoconfined geometries, quenching of the fluorescence of a dye becomes an important issue that needs to be taken into account. To obtain sustainable and reproducible results, the efficient protection against oxygen quenching cannot be neglected because the fluorescent response is used as a quantitative measure. Here, we focus on the development of an oxygen-protection strategy that is applicable for a broad range of encapsulated materials.

The core–shell structure of the hybrid organic–inorganic nanoparticles allows for the independent molecular design of each part. For instance, the oxygen permeability of the shell material can be lowered drastically by using semicrystalline nanocellulose [31]. Furthermore, a bovine serum albumin film at the oil–water interface [32] or rose bengal embedded in a microcapsule shell [33] can also be used to protect the encapsulated dye from molecular oxygen. Incorporating oxygen-scavenging materials such as WO_3 photocatalysts loaded with Pt [34], phosphonate coatings [35], organophosphates [36] or polyoxyethanyl α-tocopheryl sebacate [37] significantly reduces oxygen quenching. Last but not least, another possibility is to attach an oxygen scavenger (e.g., diphenylanthracene moieties) to the emissive dye itself [38]. Decoration of the molecular structure of cyanine dyes including a cyclodextrin complex, acetyl modification, fluoro- and cyano-substitution leads to increased photostability of the fluorophore [5]. However, unfortunately, all these oxygen-protection strategies affect the properties of core and shell materials that are used to form nanoconfined materials.

Our main goal is to develop a strategy to reduce the impact of reactive oxygen by applying an additional synthetic step, while

keeping unchanged all parameters involved in the synthesis of the initial nanoconfined materials. Exemplarily, polystyrene nanocontainers with a liquid hydrophobic core of hexadecane synthesized by using miniemulsion techniques will be protected by depositing metal-oxide particles on the surface, as proposed in a previous minireview from our team [21]. Deposition of metal-oxide particles on the surface of polymer hybrid nanoparticles via controlled surface crystallization was shown in previous works of our group [10,12]. The regular arrangement of functional groups on the nanocapsule surface can provide nucleation and structure-directing centers for the controlled crystallization of metal-oxide particles. We have chosen cerium(IV) oxide nanoparticles to be deposited on the nanocapsule surface in order to combine biocompatibility with a high oxygen-scavenging ability. Cerium oxide is a lanthanide metal oxide with a redox potential behavior that can easily switch between cerium(IV) and cerium(III) and has the capability to leave oxygen vacancies in the crystal lattice [39]. Cerium(IV) oxide exhibits excellent antioxidant properties, ideal for applications such as water-gas shift catalysis [40], combustion catalysis [41], oxygen ion conductors, and solid-oxide fuel cells [42]. Due to the valence and oxygen defect properties of cerium(IV) oxide, nanoparticles of this material are also used as efficient free-radical scavengers in biomedical applications as a potent therapeutic option for the treatment of disorders generated by reactive oxygen species, such as neurodegenerative disorders, retinal disorders and cancer [43-45].

In this work, we report the process of armoring anionically functionalized nanocontainers loaded with TDI by crystallizing cerium(IV) oxide nanoparticles on the nanocontainer surface. As a result, we obtain reproducible and sustained fluorescence of the nanocapsules, independently from the oxygen content of the external environment.

Experimental

Materials

Styrene (S, ≥99.0%) acrylic acid (AA, Sigma-Aldrich, 99%), hexadecane (Sigma-Aldrich, 99.0%), tetrahydrofuran (THF, Sigma-Aldrich, ≥99.9%), cerium(III) nitrate hexahydrate (Sigma-Aldrich, 99.99%), sodium hydroxide (Sigma-Aldrich, ≥97.0%), ammonia solution (28% aqueous solution, VWR), sodium dodecyl sulfate (SDS, Alfa Aesar, 99%), and 2,2'-azobis(2-methylbutyronitrile) (V59, Wako) were used as received. Styrene was passed over an aluminium oxide column to remove the stabilizer before use.

Synthesis of the dye and preparation of its stock solution

N,*N*'-(2,6-Diisopropylphenyl)-1,6,9,13-tetrakis[4-(1,1,3,3-tetramethylbutyl)phenoxy]terrylene-3,4,11,12-bis(dicarboximide) (TDI) was synthesized according to [26] (molecular structure and absorption/fluorescence emission spectra are given in Supporting Information File 1, Figures S1 and S2, respectively). The prepared TDI was dissolved in sufficient amounts of THF and transferred in hexadecane (4 g) to obtain a final concentration of 1×10^{-4} M. Afterwards, THF was completely removed by rotary evaporation (1 h at 70 mbar and 50 °C).

Synthesis of carboxyl-functionalized nanocapsules

Polystyrene nanocapsules were synthesized either under ambient conditions (sample NC) or under argon atmosphere [sample NC(Ar)] by free-radical miniemulsion polymerization [46]. The continuous phase contains SDS (30 mg) and demineralized water (30 g). The disperse phase contains styrene (1.8 g) and acrylic acid (0.2 g) as monomers, hexadecane (4 g) with the fluorescent dye TDI and the initiator V59 (100 mg). The two phases were mixed and pre-emulsified by stirring at 1000 rpm for 1 h. The emulsion was prepared by ultrasonication (Branson Digital Sonifier 450-D; 1/2″ tip, 90% intensity, 2 min) while cooling in an ice-water bath to avoid polymerization due to heating. The polymerization reaction was carried out in a closed flask at 72 °C for 18 h under constant stirring. The capsule content (polymer + hexadecane), determined gravimetrically by weighing 0.500 g of suspension before and after freeze-drying, was of ca. 15 wt %. The term “capsule content” is used as an analogous to the term “solid content” for solid capsules to take into account the fact that the hexadecane core is also weighted and counted. Since hexadecane is not solid under the conditions of measurement, the term “solid contend” would not be appropriate.

Synthesized nanocapsules were further used for the cerium-oxide crystallization experiments with specific concentration. The surface charge density was determined at pH 10 to ensure the complete deprotonation of the carboxylic groups.

Synthesis of CeO_2/polymer hybrid nanocapsules

The synthesized polymeric nanocapsules, NC and NC(Ar), were used in the crystallization experiments to obtain the hybrid samples, NC-CeO_2 and NC(Ar)-CeO_2, respectively. We apply an analogous procedure to the one used for solid particles [10,12]. The experiment was carried out at 35 °C in a closed flask under constant stirring while keeping the pH value constant during the whole procedure. First, the pH value of the dispersion was adjusted to pH 10 with a 28% ammonia solution. Then 5 mmol of metal salt per gram of dispersion nanocapsules was added and the dispersion was stirred for 2 h to allow for the binding of cerium ions to the surface of the capsules. Cerium(III) nitrate hexahydrate was dissolved in 2 mL of demineralized water and

200 µL of the latex dispersion was added to the solution. Afterwards, the precipitation of the oxide was carried out by adding dropwise 2 mL of aqueous NaOH solution (0.1 M) using a syringe pump (dropping speed of 1 $mL \cdot h^{-1}$). The addition of the base leads to the precipitation of $Ce(OH)_3$, which is insoluble in water. In an alkaline environment, $Ce(OH)_3$ is spontaneously oxidized to hydrated Ce(IV) ions by the oxygen of the environment, and then hydrolyzed to form hydroxocomplexes, which eventually evolve to CeO_2 [47]. The mixture was further stirred for 24 h to complete oxide formation. The loaded samples were freeze-dried for subsequent characterizations.

Characterization of the materials

Particle sizes of the prepared nanocapsules were determined by dynamic light scattering (DLS) using a Nicomp 380 PSS particle sizer (Santa Barbara, CA) at a fixed angle of 90°. Table 1 reports the different samples reported in this work with the corresponding particle sizes measured by DLS.

The surface charge density of the negatively charged latex nanocapsules was determined by direct polyelectrolyte titration with a roughly 0.001 N solution of poly(diallyldimethyl ammonium chloride), detecting the end point with an automatic streaming current detector with a particle-charge detector Mütek PCD-03 in combination with a Metrohm Titrino automatic titrator. The samples were diluted to a solid content of 0.1 wt % for titration and the surface charge density of 1.6 carboxylic groups per nm^2 was obtained for samples NC and NC(Ar).

Transmission electron microscopy (TEM) was carried out with a Jeol 1400 microscope at an acceleration voltage of 200 kV. Samples for TEM observation were prepared by dropping the diluted dispersions on carbon-coated copper grids and dried. Scanning electron microscopy (SEM) with a LEO Gemini 1530 field-emission microscope operated with an extractor voltage of 0.7 kV. Samples for SEM observation were prepared by dropping the diluted dispersions on small silicon wafers that were subsequently dried. EDX analysis combined with elemental mapping was carried out in a Hitachi SU8000 SEM microscope equipped with a Bruker AXS spectrometer with an operation voltage of 5 kV.

X-ray diffraction of the freeze dried sample was conducted on a Philips PW 1820 diffractometer with monochromatic Cu Kα radiation (λ = 1.5418 Å, 40 kV, 30 mA, 5 s, Δθ = 0.02). Thermogravimetric analysis of the freeze-dried sample was conducted using a Mettler Toledo TGA-851 at a heating rate of 10 $°C \cdot min^{-1}$.

Fluorescence spectra were recorded for the dispersions containing 0.75 wt % capsule content by using in a custom-built setup containing a diode laser with wavelength 635 nm (Roithner Lasertechnik GmbH, ADL-63201TL) with an excitation intensity of 0.2 $W \cdot cm^{-2}$. It is important to note that all fluorescence emission measurements were carried out by using the same batch of nanocapsules at the same capsule content. A first batch of nanocapsules was prepared under ambient conditions and an analogous one in argon atmosphere.

Results and Discussion

The objective of this work was to design colloidally stable polystyrene-based hybrid nanocapsules containing the fluorescent dye terrylene diimide (TDI) and being armored with metal-oxide nanoparticles on the polymer shell surface. Polymeric nanocapsules (labeled as sample NC) were prepared under ambient conditions by free radical miniemulsion polymerization of styrene and acrylic acid. The thickness of the shell of the formed nanocapsules was ca. 20 nm in average, and the weight ratio polymer/hexadecane was ca. 1:2. The fluorescent dye was dissolved in the liquid hexadecane core before polymerization of the shell. The nanocapsule formation takes place by phase separation between the formed polymer and hexadecane [46]. The surface of the nanocapsules was negatively charged, as proven by polyelectrolyte titration (surface charge density of 1.6 nm^{-2} at pH 10), which is a result of the used anionic surfactant (sodium dodecyl sulfate) and the hydrophilic co-monomer (acrylic acid). Acrylic acid plays a crucial role in binding the cerium ions to the surface of nanocapsules and is also helpful to increase the hydrophilic nature of the system.

The crystallization of cerium(IV) oxide nanoparticles on the surface of the polymer nanocapsules is depicted in Figure 1. First, the cerium ions from the precursor are complexed by the

Table 1: Characteristics of the samples reported in this work.

sample	material	atmosphere during synthesis	diameter (nm)[a]
NC	poly(styrene/acrylic acid)	air	140 (±23%)
NC(Ar)	poly(styrene/acrylic acid)	argon	153 (±29%)
NC-CeO_2	poly(styrene/acrylic acid) + CeO_2	air	146 (±30%)
NC(Ar)-CeO_2	poly(styrene/acrylic acid) + CeO_2	argon	159 (±18%)

[a]Determined by DLS.

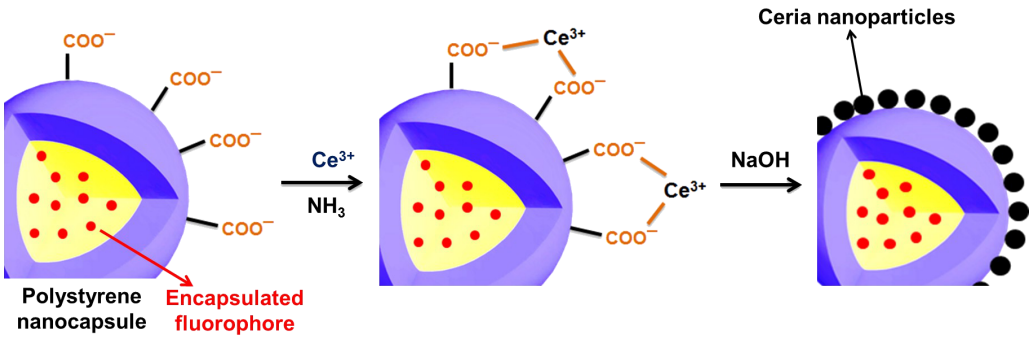

Figure 1: Schematic representation of the formation of cerium(IV) oxide on the surface of carboxylate functionalized fluorescent nanocapsules.

carboxylate functional groups and the crystallization occurs upon addition of NaOH at a controlled rate. The SEM and TEM images presented in Figure 2 demonstrate that the inorganic ceria nanoparticles were efficiently crystallized on the surface (Figure 2a,b shows the pristine sample NC and Figure 2c,d shows the hybrid sample, labeled as NC-CeO_2). The X-ray diffraction (XRD) pattern of the hybrid sample, shown in Figure 3, was unambiguously assigned to crystalline CeO_2 (ceria, JPCD card No. 34-0394). Elemental mapping by EDX also confirmed the presence of cerium in the investigated areas (see Supporting Information File 1, Figure S3). TEM images of ceria hybrid nanocapsules in Figure 4 indicate a homogeneous distribution of ceria nanocrystals on the surface of the capsules. The presence of bright spots in the dark field images (Figure 4b) confirms crystalline domains lying in the detection plane [10]. A corresponding high-resolution image of the hybrid

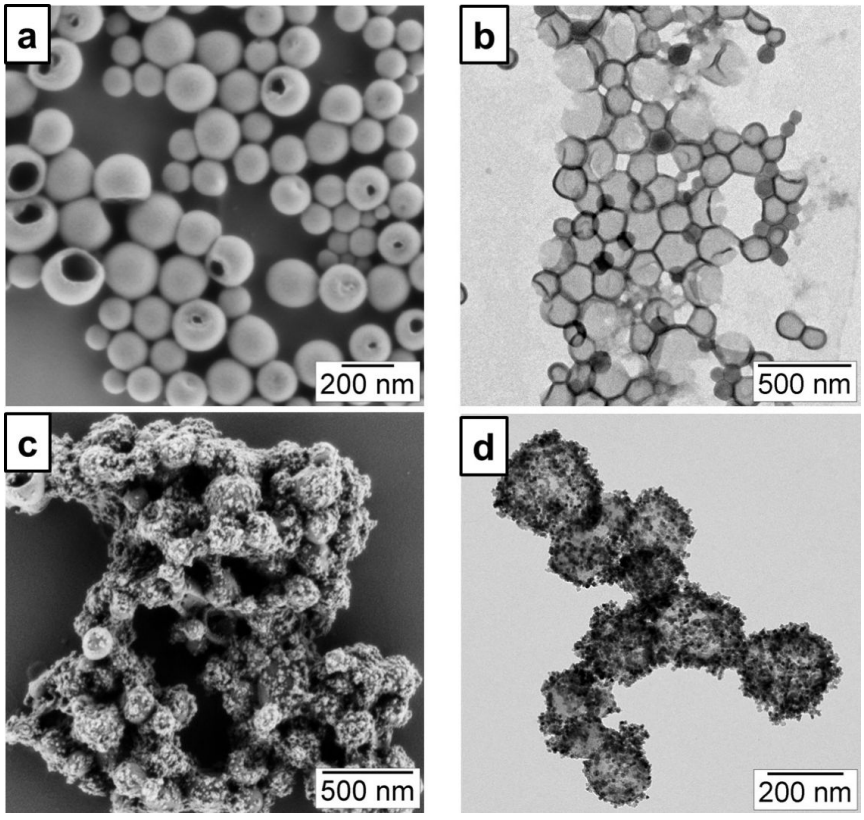

Figure 2: Electron micrographs of the prepared capsules: a) SEM and b) TEM of carboxylate-functionalized polystyrene hybrid nanocapsules (sample NC); c) SEM and d) TEM of ceria/polymer hybrid samples (sample NC-CeO_2) [21].

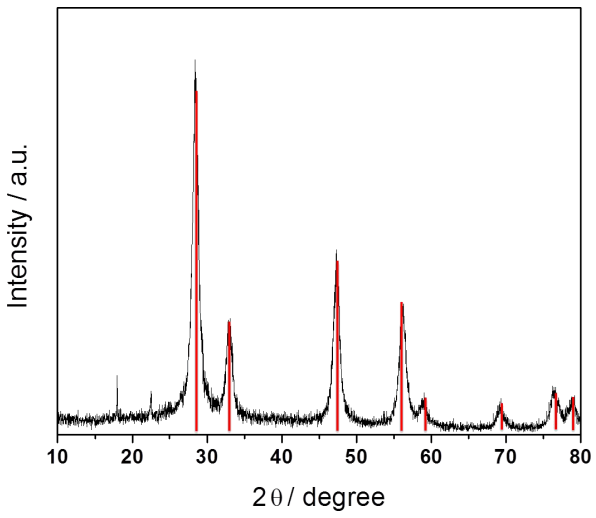

Figure 3: XRD pattern of hybrid polystyrene nanocapsules with cerium(IV) oxide on the surface (NC-CeO_2). Vertical lines indicates the position and relative intensity of cubic cerium(IV) oxide crystal phase (ICDD card no. 34-0394).

sample NC-CeO_2 is shown in Figure 4c,d. The ceria content for this sample was determined to be about 44 wt % by thermogravimetric analysis (see Supporting Information File 1, Figure S4).

The fluorescence spectrum measured under ambient conditions for the pure polymer nanocapsules (sample NC) is shown in Figure 5 (black line). An intense fluorescence emission from TDI with λ_{max} = 685 nm is observed. An important factor influencing the decrease of fluorescence efficiency is photooxida-

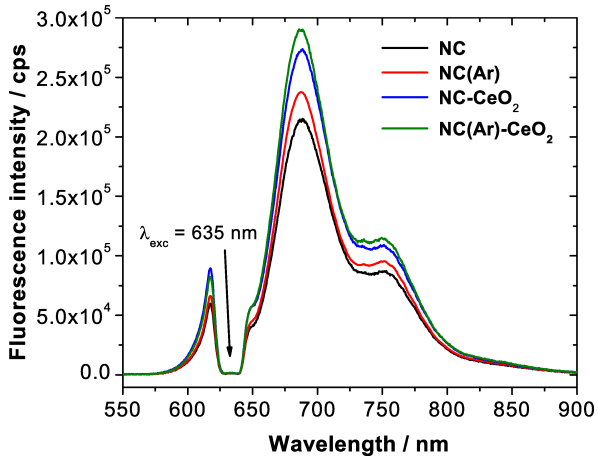

Figure 5: Fluorescence spectra of terylene diimide encapsulated in nanocapsules: NC (continuous black line, ambient conditions without cerium oxide), NC(Ar) (dashed red line, argon conditions without cerium oxide), NC-CeO_2 (dotted blue line, ambient conditions with CeO_2) and NC(Ar)-CeO_2 (dash-dotted green line, argon conditions with CeO_2).

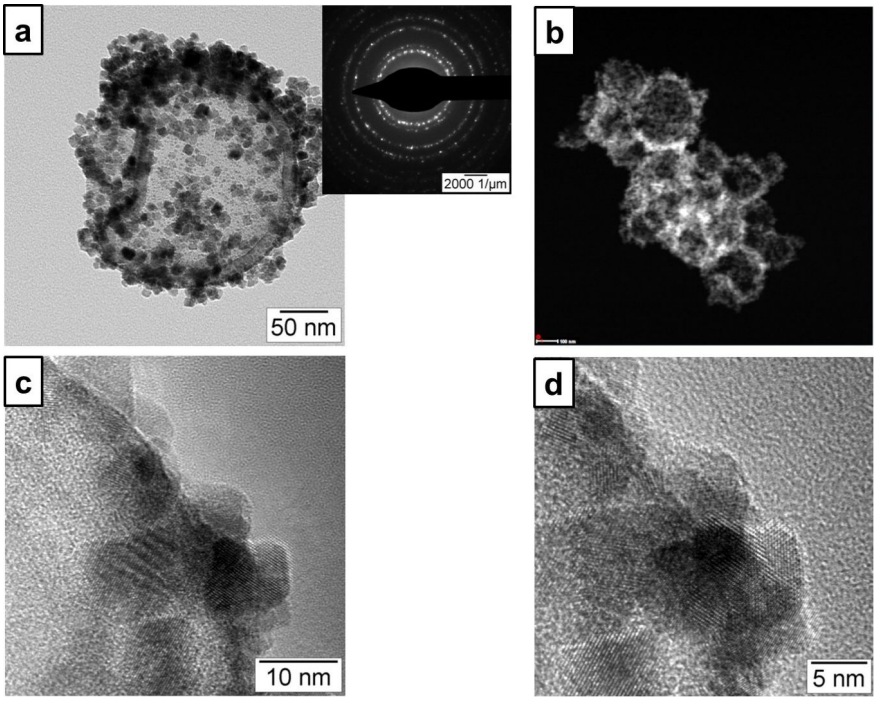

Figure 4: TEM micrographs of CeO_2/polystyrene hybrid nanocapsules (sample NC-CeO_2): a) bright-field image (inset shows the electron diffraction of the shown capsule); b) dark-field image; c, d) high-resolution images at different magnification.

tion. This kind of photochemical reaction is observed as a result of the interaction of the sample with singlet oxygen, which converts a fluorescent molecule into a state in which no longer absorbs and fluoresces. A possible explanation for the process of photooxidation in aromatic hydrocarbons is the non-zero probability for intersystem crossing. The excited triplet state is relatively long-lived, even at room temperature, and can serve as a source for generation of singlet oxygen.

In our case, during the encapsulation of TDI molecules the molecular oxygen present in the external environment (e.g., in the water phase) can enter into already formed polymer nanocapsules due to the permeability of the thin polymer shell. Thus, singlet oxygen is created by the process of interaction between electronic excited state of TDI and ground-state molecular oxygen within the encapsulated materials, which results in photo-oxidation processes. To overcome the limitations caused by oxygen influence, a sample named as NC(Ar) was prepared in a closed flask in argon atmosphere. The sample from the closed flask was transferred to a quartz cuvette under ambient conditions for further fluorescence measurements. As observed in Figure 5, the fluorescence efficiency of this sample is enhanced when compared to the sample prepared under ambient conditions, which is explained by the decrease of the oxygen concentration inside the capsules during polymerization. This decrease of oxygen content resulted also in a decreased rate of photodegradation of the TDI molecule.

To further minimize the effect of fluorescence quenching, cerium(IV) oxide was crystallized on the surface of polymer sample NC, which yielded the hybrid sample NC-CeO_2. The fluorescence intensity is higher than for nanocapsules synthesized under ambient conditions without CeO_2, but also even higher than for the sample NC(Ar) prepared under argon atmosphere. The oxygen vacancies present in the structure of cerium(IV) oxide nanoparticles are the most likely origin of the enhancement of the fluorescence, since they can scavenge oxygen molecules from the environment and prohibit molecular oxygen to enter into the nanocapsules.

Following these results, the deposition of cerium(IV) oxide was also carried out on nanocapsule samples prepared in inert atmosphere. The resulting sample was labeled as NC(Ar)-CeO_2. The corresponding fluorescence spectrum is shown by the green curve in Figure 5. Control experiments were carried out to confirm that the improvement of fluorescence efficiency originates from the formed cerium oxide and not from the cerium(III) precursor itself or any of the precipitating agents (see Supporting Information File 1, Figure S5). An enhancement of the fluorescence intensity took place only in the presence of the crystallized cerium(IV) oxide.

To investigate the effect of external oxygen, we recorded again the fluorescence emission spectra for all synthesized samples after having sealed the samples with argon in the glove box (see Supporting Information File 1, Figure S6). The spectra did not show any significant difference to samples prepared in an oxygen-free atmosphere.

Finally, photodegradation experiments were carried out in an oxygen-rich environment to investigate the stability of the fluorescence emission of pure polymer nanocapsules synthesized under ambient conditions (NC) and in argon atmosphere NC(Ar) in comparison to the analogous hybrid nanocapsules with cerium(IV) oxide crystallized on the surface (NC-CeO_2). The recorded spectra are shown in Figure 6. The fluorescence emission of NC(Ar) is less stable than that of NC-CeO_2. Simultaneously, the fluorescence of sample NC-CeO_2 is significantly more intense than the emission of the unprotected sample NC. After a sufficient time of excitation, sample NC(Ar) reaches the emission level of NC, while the CeO_2 protection layer prevents effectively the oxygen penetration, leading to stable and efficient fluorescence even under ambient conditions. All these experimental observations point out that the presence of oxygen inside the nanocapsules is the most likely reason for the reduced fluorescence stability and intensity.

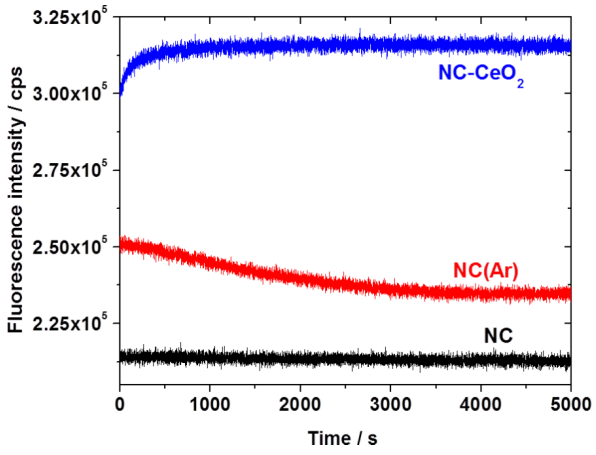

Figure 6: Photodegradation measurements of nanocapsules synthesized under different conditions without cerium oxide (sample NC at ambient conditions and sample NC(Ar) under argon) and with cerium oxide on the surface (sample NC-CeO_2 at ambient conditions).

Conclusion

In this work, we demonstrate that the armoring with CeO_2 of polystyrene nanocapsules containing a model fluorophore molecule results in a significant enhancement of the fluorescence. The in situ crystallization of the metal oxide on the surface of the nanocontainers suppresses the photobleaching of the fluorescent molecule by molecular oxygen. Hybrid CeO_2/polymer

samples simply prepared under ambient conditions exhibit an even fluorescence intensity than pure polymer nanocapsules carefully prepared in an oxygen-free atmosphere. The enhancement effect can be explained by the trapping of the quenching oxygen molecules on the metal oxide surface, which results in a reduction of the photo-oxidation.

Supporting Information

Supporting Information File 1

Chemical structure of TDI, absorption and emission spectra of TDI, EDX spectra, TGA, and additional photoluminescence emission spectra of samples.
[https://www.beilstein-journals.org/bjnano/content/supplementary/2190-4286-10-53-S1.pdf]

Acknowledgements

The source of this article is the doctoral dissertation of the first author, Dr. Katheek Katta (Uniform Resource Name: urn:nbn:de:hebis:77-diss-1000007157). Michael Steiert, Petra Räder, Gunnar Glaßer, and Katrin Kirchhoff are acknowledged for XRD, TGA, EDX, and high-resolution TEM measurements, respectively. The authors thank the International Research Training Group 1404 for financial support, as well as the Max Planck Society for funding of the Max Planck Partner Group on Colloidal Methods for Multifunctional Materials (CM3) at the University of Valencia, headed by R.M.E. S.B. and K.L. acknowledge the European Horizon 2020 Research and Innovation Programme (grant agreement no. 732794, project HYPOSENS) for the financial support. R.M.E. acknowledges the financial support from the Spanish Ministry of Economy and Competitiveness through a Ramón y Cajal grant (grant no. RYC-2013-13451).

ORCID® iDs

Yuri Avlasevich - https://orcid.org/0000-0002-2320-4976
Rafael Muñoz-Espí - https://orcid.org/0000-0002-8146-2332

References

1. Holzapfel, V.; Musyanovych, A.; Landfester, K.; Lorenz, M. R.; Mailänder, V. *Macromol. Chem. Phys.* **2005,** *206,* 2440–2449. doi:10.1002/macp.200500372
2. Burns, A.; Ow, H.; Wiesner, U. *Chem. Soc. Rev.* **2006,** *35,* 1028–1042. doi:10.1039/b600562b
3. Wang, L.; Wang, K.; Santra, S.; Zhao, X.; Hilliard, L. R.; Smith, J. E.; Wu, Y.; Tan, W. *Anal. Chem. (Washington, DC, U. S.)* **2006,** *78,* 646–654. doi:10.1021/ac0693619
4. Chinen, A. B.; Guan, C. M.; Ferrer, J. R.; Barnaby, S. N.; Merkel, T. J.; Mirkin, C. A. *Chem. Rev.* **2015,** *115,* 10530–10574. doi:10.1021/acs.chemrev.5b00321
5. Wu, X.; Zhu, W. *Chem. Soc. Rev.* **2015,** *44,* 4179–4184. doi:10.1039/c4cs00152d
6. Cong, H.-P.; Yu, S.-H. *Curr. Opin. Colloid Interface Sci.* **2009,** *14,* 71–80. doi:10.1016/j.cocis.2008.09.003
7. Lu, Y.; Hoffmann, M.; Yelamanchili, R. S.; Terrenoire, A.; Schrinner, M.; Drechsler, M.; Möller, M. W.; Breu, J.; Ballauff, M. *Macromol. Chem. Phys.* **2009,** *210,* 377–386. doi:10.1002/macp.200800608
8. Stuart, M. A. C.; Huck, W. T. S.; Genzer, J.; Müller, M.; Ober, C.; Stamm, M.; Sukhorukov, G. B.; Szleifer, I.; Tsukruk, V. V.; Urban, M.; Winnik, F.; Zauscher, S.; Luzinov, I.; Minko, S. *Nat. Mater.* **2010,** *9,* 101–113. doi:10.1038/nmat2614
9. Wu, S.; Dzubiella, J.; Kaiser, J.; Drechsler, M.; Guo, X.; Ballauff, M.; Lu, Y. *Angew. Chem., Int. Ed.* **2012,** *51,* 2229–2233. doi:10.1002/anie.201106515
10. Fischer, V.; Lieberwirth, I.; Jakob, G.; Landfester, K.; Muñoz-Espí, R. *Adv. Funct. Mater.* **2013,** *23,* 451–466. doi:10.1002/adfm.201201839
11. Hood, M. A.; Mari, M.; Muñoz-Espí, R. *Materials* **2014,** *7,* 4057–4087. doi:10.3390/ma7054057
12. Mari, M.; Müller, B.; Landfester, K.; Muñoz-Espí, R. *ACS Appl. Mater. Interfaces* **2015,** *7,* 10727–10733. doi:10.1021/acsami.5b01847
13. Valeur, B.; Berberan-Santos, M. N. *Molecular fluorescence: Principles and applications;* John Wiley & Sons: New York, NY, U.S.A., 2012. doi:10.1002/9783527650002
14. Wu, C.; Bull, B.; Christensen, K.; McNeill, J. *Angew. Chem., Int. Ed.* **2009,** *48,* 2741–2745. doi:10.1002/anie.200805894
15. Papkovsky, D. B.; Dmitriev, R. I. *Chem. Soc. Rev.* **2013,** *42,* 8700–8732. doi:10.1039/c3cs60131e
16. Wang, X.-d.; Wolfbeis, O. S. *Chem. Soc. Rev.* **2014,** *43,* 3666–3761. doi:10.1039/c4cs00039k
17. Fischer, K.; Wilken, M. *J. Chem. Thermodyn.* **2001,** *33,* 1285–1308. doi:10.1006/jcht.2001.0837
18. Sato, T.; Hamada, Y.; Sumikawa, M.; Araki, S.; Yamamoto, H. *Ind. Eng. Chem. Res.* **2014,** *53,* 19331–19337. doi:10.1021/ie502386t
19. Paiphansiri, U.; Dausend, J.; Musyanovych, A.; Mailänder, V.; Landfester, K. *Macromol. Biosci.* **2009,** *9,* 575–584. doi:10.1002/mabi.200800293
20. Zhang, X.; Rehm, S.; Safont-Sempere, M. M.; Würthner, F. *Nat. Chem.* **2009,** *1,* 623–629. doi:10.1038/nchem.368
21. Baluschev, S.; Katta, K.; Avlasevich, Y.; Landfester, K. *Mater. Horiz.* **2016,** *3,* 478–486. doi:10.1039/c6mh00289g
22. Gu, Z.; Yan, L.; Tian, G.; Li, S.; Chai, Z.; Zhao, Y. *Adv. Mater. (Weinheim, Ger.)* **2013,** *25,* 3758–3779. doi:10.1002/adma.201301197
23. Hung, C.-C.; Huang, W.-C.; Lin, Y.-W.; Yu, T.-W.; Chen, H.-H.; Lin, S.-C.; Chiang, W.-H.; Chiu, H.-C. *Theranostics* **2016,** *6,* 302–317. doi:10.7150/thno.13686
24. Jung, C.; Müller, B. K.; Lamb, D. C.; Nolde, F.; Müllen, K.; Bräuchle, C. *J. Am. Chem. Soc.* **2006,** *128,* 5283–5291. doi:10.1021/ja0588104
25. Lee, T. T.; García, J. R.; Paez, J. I.; Singh, A.; Phelps, E. A.; Weis, S.; Shafiq, Z.; Shekaran, A.; del Campo, A.; García, A. J. *Nat. Mater.* **2015,** *14,* 352–360. doi:10.1038/nmat4157
26. Nolde, F.; Qu, J.; Kohl, C.; Pschirer, N. G.; Reuther, E.; Müllen, K. *Chem. – Eur. J.* **2005,** *11,* 3959–3967. doi:10.1002/chem.200401177
27. Daehne, S.; Resch-Genger, U.; Wolfbeis, O. S., Eds. *Near-Infrared Dyes for High Technology Applications;* Springer Netherlands: Dordrecht, Netherlands, 1998. doi:10.1007/978-94-011-5102-3

28. Holtrup, F. O.; R. J. Müller, G.; Quante, H.; De Feyter, S.; De Schryver, F. C.; Müllen, K. *Chem. – Eur. J.* **1997,** *3,* 219–225. doi:10.1002/chem.19970030209
29. Kim, H. N.; Puhl, L.; Nolde, F.; Li, C.; Chen, L.; Basché, T.; Müllen, K. *Chem. – Eur. J.* **2013,** *19,* 9160–9166. doi:10.1002/chem.201300439
30. Piwoński, H.; Sokołowski, A.; Waluk, J. *J. Phys. Chem. Lett.* **2015,** *6,* 2477–2482. doi:10.1021/acs.jpclett.5b01060
31. Svagan, A. J.; Busko, D.; Avlasevich, Y.; Glasser, G.; Baluschev, S.; Landfester, K. *ACS Nano* **2014,** *8,* 8198–8207. doi:10.1021/nn502496a
32. Liu, Q.; Yin, B.; Yang, T.; Yang, Y.; Shen, Z.; Yao, P.; Li, F. *J. Am. Chem. Soc.* **2013,** *135,* 5029–5037. doi:10.1021/ja3104268
33. Kim, J.-H.; Deng, F.; Castellano, F. N.; Kim, J.-H. *ACS Photonics* **2014,** *1,* 382–388. doi:10.1021/ph500036m
34. Kim, J.-H.; Kim, J.-H. *J. Am. Chem. Soc.* **2012,** *134,* 17478–17481. doi:10.1021/ja308789u
35. Li, R.; Ji, Z.; Dong, J.; Chang, C. H.; Wang, X.; Sun, B.; Wang, M.; Liao, Y.-P.; Zink, J. I.; Nel, A. E.; Xia, T. *ACS Nano* **2015,** *9,* 3293–3306. doi:10.1021/acsnano.5b00439
36. Marsico, F.; Turshatov, A.; Peköz, R.; Avlasevich, Y.; Wagner, M.; Weber, K.; Donadio, D.; Landfester, K.; Baluschev, S.; Wurm, F. R. *J. Am. Chem. Soc.* **2014,** *136,* 11057–11064. doi:10.1021/ja5049412
37. Turshatov, A.; Busko, D.; Baluschev, S.; Miteva, T.; Landfester, K. *New J. Phys.* **2011,** *13,* 083035. doi:10.1088/1367-2630/13/8/083035
38. Filatov, M. A.; Heinrich, E.; Busko, D.; Ilieva, I. Z.; Landfester, K.; Baluschev, S. *Phys. Chem. Chem. Phys.* **2015,** *17,* 6501–6510. doi:10.1039/c4cp05025h
39. Trovarelli, A. *Catalysis by ceria and related materials;* World Scientific Publishing Inc.: Singapore, 2002; Vol. 2. doi:10.1142/p249
40. Fu, Q.; Saltsburg, H.; Flytzani-Stephanopoulos, M. *Science* **2003,** *301,* 935–938. doi:10.1126/science.1085721
41. Trovarelli, A.; de Leitenburg, C.; Boaro, M.; Dolcetti, G. *Catal. Today* **1999,** *50,* 353–367. doi:10.1016/s0920-5861(98)00515-x
42. Park, S.; Vohs, J. M.; Gorte, R. J. *Nature* **2000,** *404,* 265–267. doi:10.1038/35005040
43. Celardo, I.; Pedersen, J. Z.; Traversa, E.; Ghibelli, L. *Nanoscale* **2011,** *3,* 1411–1420. doi:10.1039/c0nr00875c
44. Li, Y.; He, X.; Yin, J.-J.; Ma, Y.; Zhang, P.; Li, J.; Ding, Y.; Zhang, J.; Zhao, Y.; Chai, Z.; Zhang, Z. *Angew. Chem., Int. Ed.* **2015,** *54,* 1832–1835. doi:10.1002/anie.201410398
45. Walkey, C.; Das, S.; Seal, S.; Erlichman, J.; Heckman, K.; Ghibelli, L.; Traversa, E.; McGinnis, J. F.; Self, W. T. *Environ. Sci.: Nano* **2015,** *2,* 33–53. doi:10.1039/c4en00138a
46. Katta, K.; Busko, D.; Avlasevich, Y.; Muñoz-Espí, R.; Baluschev, S.; Landfester, K. *Macromol. Rapid Commun.* **2015,** *36,* 1084–1088. doi:10.1002/marc.201400670
47. Tunusoğlu, Ö.; Muñoz-Espí, R.; Akbey, Ü.; Demir, M. M. *Colloids Surf., A* **2012,** *395,* 10–17. doi:10.1016/j.colsurfa.2011.11.026

License and Terms

BEILSTEIN JOURNAL OF NANOTECHNOLOGY

Topochemical engineering of composite hybrid fibers using layered double hydroxides and abietic acid

Liji Sobhana[1], Lokesh Kesavan[1,2], Jan Gustafsson[1] and Pedro Fardim[*1,3]

Full Research Paper

Open Access

Address:
[1]Laboratory of Fibre and Cellulose Technology, Åbo Akademi University, Porthansgatan 3, FI-20500, Åbo, Finland, [2]Laboratory of Materials Chemistry and Chemical Analysis, Turku University Centre for Materials and Surfaces (MatSurf), University of Turku, Vatselankatu 2, FI-20014 Turku, Finland and [3]Department of Chemical Engineering, KU Leuven, Celestijnenlaan 200F b,us 2424, B-3001 Leuven, Belgium

Email:
Pedro Fardim* - pfardim@abo.fi

* Corresponding author

Keywords:
abietic acid; composite hybrid fibers; high tensile pulp; hydrophobic pulp; layered double hydroxides

Beilstein J. Nanotechnol. **2019,** *10,* 589–605.
doi:10.3762/bjnano.10.60

Received: 10 October 2018
Accepted: 11 February 2019
Published: 28 February 2019

This article is part of the thematic issue "Advanced hybrid nanomaterials".

Guest Editor: A. Taubert

Abstract

Topochemical engineering of hybrid materials is an efficient way of synthesizing hydrophobic and highly tensile fiber composites by utilizing the intermolecular hydrogen bonds in natural materials. These materials include wood pulp fibers, abietic acid (resin acid) and inexpensive metal salts. In this work, a hybrid composite was created using bleached and unbleached kraft pulp fibers as cellulose platform. In situ co-precipitation of layered double hydroxide (LDH) was performed to grow LDH crystals on the surface of the cellulose fibers, followed by the immobilization of abietic acid (AA) on LDH-grafted cellulose. Here we aimed to benefit from the hydrogen bonding between –OH groups of cellulose and LDH, and the –COOH groups of AA to obtain charge-directed assembly of one material on the other material. Thus, composite hybrid fibers (C-HF) were produced and then characterized by optical (CAM), spectroscopic (XRD, IR) and microscopic techniques (SEM) to determine their average length and distribution, structure and purity, bonding, and morphology. These fibers further were tested for water contact angle (hydrophobicity), oil absorption (lipophilicity), tensile strength and ISO brightness measurements. The performance of C-HF was compared with unmodified reference fibers (REF), fibers composed with only AA (C-F) and LDH-hybridized fibers (HF). The results revealed a variety of correlations between materials and their properties due to characteristic surface morphology, functional groups, hydrogen bonding and natural co-materials such as lignin and hemicelluloses. Attractive and repulsive van der Waals forces between material entities play a crucial role in the resulting properties.

Introduction

Renewable chemicals or materials and their value addition are the current focus in the area of materials and applied chemistry, which strive to develop new end-products with novel functionalities via chemical bonds and physical interactions [1]. Wood pulp is one of these renewable materials. It is obtained from forest products industries and stands as a source of many polymeric materials such as cellulose, hemicelluloses, and lignin [2]. Cellulose, being one of the most abundant natural polymers, has been a target for basic and applied research [3]. It possesses chemically reactive and physically interactive, primary and secondary –OH groups on its molecular skeleton. This carbon-bonded –OH groups serve as the locations for any sort of modifications [4] in cellulose to produce customized end-use materials. They can be oxidized to –C=O, –CHO and –COOH or reduced to hydrocarbons depending on the aim of the application [5-7]. Physically, these –OH groups make cellulose hydrophilic [8]. In addition, these –OH groups facilitate binding between cellulose fibers strands in wood pulp via intermolecular hydrogen bonding. Thus, they contribute to the moderate inherent tensile strength of the fibers as well [9]. On the contrary, there has been always a research motivation to make cellulose hydrophobic [10-12] with high tensile strength [13].

Topochemical engineering is a method of designing the fractionation (disassembly) and fabrication (assembly) of highly engineered functional materials using a combination of molecular and supramolecular techniques. Topochemical engineering is inspired by bioassembly observed in natural systems such as trees and microorganisms [14]. The present work utilizes the approach of hydrogen bonding with external hydrophobic moieties in order to bring water-repelling properties to the cellulose fiber surface. In this work, abietic acid, a hydrophobic renewable material was combined with cellulose via a structure-directing agent, i.e., a layered double hydroxide (LDH). LDHs, inorganic ceramic materials carry symmetrically distributed charge centers/hydrogen bonds. This idea was the extrapolation of our earlier reported work, where introducing hydrophobicity was carried out by anchoring a hydrophobic moiety, namely stearic acid (SA), on wood pulp via a bridging LDH molecule. This led a new hybrid organic–inorganic–organic composite (SA-LDH-CEL) [15].

There are two different methods to make cellulose hydrophobic: (1) chemical methods such as esterification or etherification, and (2) physical methods such as composite development using hydrophobic moieties of silicones, fluorocarbons, or surfactants. The physical methods employed to make cellulose hydrophobic were applied only to regenerated cellulose and not to pristine wet-state cellulose. Our earlier reported work directly utilized the wet pulp fibers without any prior treatment. Moreover, anionic surfactants cause environmental pollution when the resultant acidic materials are washed out. Therefore, the choice of stearic acid was motivated by green-chemistry principles. This method differed from previous reported methods where hydrophobic molecules were directly incorporated into pulp fibers, insofar as it utilized the charge centers of LDH to make a conjugation with stearic acid on one side of the LDH molecules and cellulose on the other side. This way the amount of adhesion of hydrophobic molecules on pulp was carefully controlled as the adhesion was steered by self-directed –COOH···OH hydrogen bonding. This SA-LDH-CEL hybrid material offered superhydrophobicity.

We have decided to extend this research using another environmentally friendly natural fatty acid, namely abietic acid (AA). Abietic acid is a resin acid, abundantly present in pinewood and other coniferous plants [16]. Rosin, the colorful resin material used as pigments in inks, varnishes and adhesives, largely consists of abietic acid. It is highly hydrophobic and soluble only in organic solvents such as acetone, ethanol and diethyl ether. The reason for choosing AA was that it contains two more carbon atoms ($C_{20}H_{30}O_2$) in its skeleton (19 C-chain) with cyclic structure and unsaturated π-bonds. Moreover, compared to stearic acid, abietic acid is less flammable, insoluble in water and denser than water, and has a high melting temperature. These properties can yield improved hydrophobicity and mechanical strength to the fibers.

Layered double hydroxides are hydroxylated mixed metal salts (clay minerals) that have unique fascinating three-dimensional structures in which positively and negatively charged ions are stacked in a uniform fashion [17-19]. This makes the material employable for charge-directed self-assembly of any molecule of interest on its surface. The metals in this kind of inorganic solids, such as Ni, Mg, Zn, Al, Fe, usually have oxidation states of +2 and +3. The anions in these materials are commonly CO_3^{2-}, Cl^-, NO_3^-. These interlayer anionic sites are highly tunable, thus, they can be optimally replaced with anions of our interest [20-25]. The hydroxyl groups present on the brucite layers of LDHs are able to form hydrogen bonding with foreign molecules to increase stability. The present work focuses on stacking abietic acid and cellulose on each side of LDHs via van der Waals forces of hydrogen bonding. Thus, LDH works as an assembling agent.

The raw materials used in this study were bleached pine kraft pulp and unbleached spruce kraft pulp. Bleaching is a process in which pulp fibers are treated with strong oxidative chemicals such as peroxides or perchloric acid. This process removes most of the lignin and some hemicelluloses from the pulp, making it

soft and flexible. These co-materials are detrimental to functionalizing cellulose and its utilization as technical material. Both bleached and unbleached pulps further undergo refining. Refining is a process in which mechanical compression and shear forces are applied to the intact wet fiber network in order to increase the surface exposure and surface area. In addition, it opens up fibrils on the surface, which increase the surface roughness of the fibers and yield good adhesion properties. Bleached and unbleached fibers, refined and unrefined, were used as starting materials to synthesize direct composites (AA + fiber), hybrid fibers (LDH + fiber) and composite hybrid fibers (AA + LDH + fiber). We expect that these materials show different properties with regard to water repellency, oil absorption, tensile strength, and optical brightness. Composing renewable materials such as cellulose and abietic acid for customized product development is in the line of interests of circular-economy initiatives implemented by governments and research funding agencies all over the world.

The originality of this study is that it uses chemically (bleached)/mechanically (mill-refined) treated fibers in their pristine wet state. They are pine (bleached) and spruce (unbleached) kraft pulp fibers, in contrast to our previous study in which birch (unbleached) kraft pulp was used. The commercially acquired pulp fibers were first disintegrated, and further refined mechanically prior to LDH deposition. During LDH preparation, sodium carbonate was used as CO_3^{2-} source instead of urea. The AA-modified LDH-F hybrid material preparation method was slightly modified due to solubility difference between AA and SA. Also, in our earlier work, stearic acid treatment on HF was carried out for 24 h, whereas this work needs only 15 min to modify the surface of HF. Thus, the time spent on material development was drastically reduced. In the present work, the degree of refinement of fibers, fiber length distribution/average fiber length evidenced from optical microscopy and the optical brightness of the fibers were measured in a first attempt.

Experimental

Materials

Bleached and unbleached kraft pulps (wood fibers) from pine and spruce, respectively, were used as the platform materials for inducing hydrophobic behavior and high tensile strength. Both unrefined and refined pulps were investigated in the study. Abietic acid ($C_{19}H_{29}COOH$, Fluka) and sodium hydroxide (NaOH, 97%, VWR) were purchased. Metal nitrate salts (magnesium nitrate hexahydrate $Mg(NO_3)_2{\cdot}6H_2O$, aluminium nitrate nonahydrate $Al(NO_3)_3{\cdot}9H_2O$, ethanol C_2H_5OH) and sodium carbonate were procured from Sigma-Aldrich. All these chemicals were used as received without any further purification.

Methods

The present work employed some protocols that were already tried out in our earlier reported work. Those methods are 1) pulp disintegration, 2) LDH preparation in the presence of pulp fibers, 3) water contact angle measurements, 4) oil absorption measurements, 5) tensile strength measurements, 6) fiber handsheet making. The remainder of the protocols are reported here for the first time.

Wet disintegration of cellulose pulp

30 g of dry pulp (bleached/unbleached) was soaked in 2 L of water for 4 h followed by loading into a disintegrator with 30,000 revolutions (ISO 5263-1:2004) to break the intertwined cellulose fiber networks and disassemble the fibers from each other. The disintegrated pulp was dewatered by centrifugation to yield the free unbound cellulose fibers. These cellulose fibers were used for further grafting with LDH.

Refining of the pulps and Schopper–Riegler analysis

Refining of bleached and unbleached pulps was performed at a pulp concentration of 1.57% (w/w) according to ISO 5264-1:2012 using a Valley laboratory beater. The bleached pine and unbleached spruce pulps were refined for 60 min and 90 min, respectively, after which the pulps were collected for further analyses and treatment. In Table 1 the abbreviations used for the pulp fibers throughout the report are given.

Table 1: The following abbreviations will be used to distinguish the different pulps.

Abbreviation	Pulp sample
BKP	bleached kraft pulp of pine, unrefined
BKPR	bleached kraft pulp of pine, refined for 60 min
UBKP	unbleached kraft pulp of spruce, unrefined
UBKPR	unbleached kraft pulp of spruce, refined for 90 min

The water drainability of the refined pulps was determined according to ISO 5267-1:1999, the Schopper–Riegler method, in order to verify the refining degree of the pulps. The refining results in compression, fibrillation and finally intertwinement of the fibrils. Flattened well packed and stacked fibers that decrease the free path of water during filtration are obtained. Thus, refining increases water retention of the wet fiber mat during the Schopper–Riegler measurement, expressed as a higher value of the refining degree in °SR.

Grafting of LDH on cellulose fibers

The unbound cellulose fibers as prepared above were hybridized with Mg–Al LDH through in situ co-precipitation.

Typically, 3.0 g of disintegrated fibers (oven dry mass) was dispersed in a flask containing mixed metal-salt solutions (Mg and Al nitrate, molar ratio 3:1) under gentle stirring until a homogenous slurry was obtained. Aqueous solution of sodium carbonate was added dropwise to the reaction flask under constant magnetic stirring to ensure homogeneity of the reaction medium. The reaction was performed at room temperature and air atmosphere. The pH value of the co-precipitation medium was kept constant (pH 8.3 ± 0.3) by the simultaneous addition of 2 M NaOH. Then, the resultant slurry was aged in a digestion bomb at 120 °C for 24 h for the crystallization of LDH on cellulose fibers. Thus, Mg–Al LDH was synthesized in the presence of cellulose fibers and subsequently grafted on these fibers uniformly. The LDH-grafted cellulose fibers were filtered and washed repeatedly to remove any unbound LDH particles until a neutral pH value was attained. The recovered wet fibers were conjugated with Mg–Al CO_3 LDH. (Two more experiments were conducted with varying ratios between metal salts and sodium carbonate). All the experiments were repeated to confirm the reproducibility of the results.

Making of highly tensile hybrid fiber handsheets

The LDH–cellulose (LDH-F) inorganic–organic hybrid fibers were made into handsheets of hybrid fibers (HF) of 120.0 gm^{-2} grammage as follows: The hybrid fibers suspension was diluted to a total volume required to get a grammage of 120.0 $g{\cdot}m^{-2}$. Aliquots of 2 L of suspension were filled in a handsheet maker equipped with a 125 mesh size wire cloth. Water circulation was not applied in the handsheet maker as the fibers were already dispersed uniformly in the pulp solution. The newly formed wet hybrid fiber handsheets were pressed twice at a force of 400 ± 10 kPa between couch blotters for increased drying. Further, these handsheets were conditioned at 23 °C temperature in a room with 50% of relative humidity for 2 days.

Functionalization of LDH grafted cellulose fiber handsheets by abietic acid (AA)

On the surface of the 120.0 $g{\cdot}m^{-2}$ grammage hybrid fiber handsheets (HF) abietic acid (AA) was immobilized to induce hydrophobicity and increased tensile strength. The handsheets were immersed in a tray containing an ethanolic solution of abietic acid (0.1 M) for 15 min under ambient conditions to allow for the grafting between LDH and AA. Then the handsheets were gently taken out and allowed to dry at room temperature.

Characterization

Optical microscopy analysis: An optical microscope Nikon Eclipse E200 combined with a Nikon DS-Fi2 digital camera was used to visually analyze the fibrillation level of the fibers.

Fiber length distribution: The average fiber length and the length distribution were determined in diluted aqueous solution by using a Kajaani Fiber Lab fiber analyzer (Valmet Automation). The fiber length measurements were performed in duplicates. The contour length of the fibers (LC), i.e., the real length of a fiber, regardless of shape and the length weighted average fiber length, $L(l)$, were reported.

X-ray diffraction: Powder X-ray diffraction (PXRD) patterns of the fiber samples were recorded with a Siemens D501 diffractometer with Cu Kα radiation (λ = 0.15415 nm). Patterns were recorded in the 2θ range of 5–70° in steps of 0.04° with a counting time per step of 8 s. The modified fibers were analyzed by pressing them gently onto a copper sample holder.

ATR-FTIR analysis: Attenuated total reflectance Fourier transform infrared (ATR-FTIR) spectra were recorded for samples in the range of 400–4000 cm^{-1} in a Thermo Scientific Nicolet iS50 instrument (Thermo Scientific, Madison, WI, USA) equipped with a diamond crystal and a pressure gauge. A total of 64 scans was recorded and corrected by the Omnic spectral suite software that provided ambient background and ATR correction for 45° incidence angle and one refraction assuming a refractive index of 1.50 for all samples.

SEM analysis: A Leo Gemini 1530 field-emission scanning electron microscope with in-Lens detector (LEO Electron Microscopy, Oberkochen, Germany) was used for the characterization of fiber surfaces. The samples were coated with carbon in a Temcarb TB500 sputter coater (Emscope Laboratories, Ashford, UK), the optimum accelerating voltage was 2.70 kV.

Material testing

Water contact angle measurements

The hydrophobicity of reference and modified cellulose handsheets was assessed by contact angle measurements (CA). These were performed with an optical Contact Angle Meter, CAM 200 (KSV Instruments Ltd, Finland), using deionized water. A water droplet volume of 1.6 ± 0.2 μL was placed on a 1 × 10 cm^2 sample strip. Then the CA values were collected at 200 ms intervals in the beginning and subsequently at 1 s and 2 s intervals until either the water droplet was absorbed or no changes during wetting occurred. The results were analyzed and interpreted with Attention Theta software (Biolin Scientific, Sweden) based on the Young-Laplace function for iterative CA calculation.

Oil absorption capacity measurements

To investigate the hydrophobicity of the modified cellulose fibers, pine oil was selected for sorption experiments. The sorption experiments were carried out at room temperature as

follows: Small pieces of the pre-weighed cellulose handsheet samples were dipped in oil (10 mL) for approximately 15 min, and then hung in the air for 5 min to let the surface residual oil drip off before being weighed. The oil removal was optimized in such a way that after 5 min, there was no oil dripping from the sheet as well as no surface wetness of stagnant oil observed. Hence, the weight increase was purely by the immobilized oil on the sheets due to hydrophobicity. The increment in oil absorption was calculated as percentage value [(weight after oil absorption − weight before oil absorption)/weight before oil absorption] × 100.

Tensile strength measurements

The tensile strength measurements were conducted by using a L&W tensile tester SE 060 according to ISO 1924-2:2008, with a slight variation of elongation rate (12 mm·min^{-1}) and test span (100 mm). The tensile tests were performed at 23 °C and 50% RH. Tensile strength tests were also performed with an unmodified ISO standard (ISO 527-2 1BA) sample sheet for comparison. The tensile strength index, calculated as tensile strength divided by grammage, was defined as the inherent strength of the fiber network.

Optical brightness measurements

An Elrepho spectrophotometer (Elrepho SE070R, Lorentzen & Wettre) was used to determine the ISO brightness value of the dry fiber materials made into sheets. Both reference and modified fiber sheets were analyzed. The ISO brightness tests were performed at 23 °C and 50% RH.

Results and Discussion

Bleached (pine) and unbleached (spruce) kraft pulp fibers (F), refined (BKPR, UBKPR) and unrefined (BKP, UBKP), were modified to induce hydrophobicity and higher tensile strength by linking abietic acid (AA) via layered double hydroxide (LDH). The straightforward method to synthesize this composite hybrid fiber (CHF) would be to graft LDH on the fibers first by co-precipitation and to add AA in the same the solution environment under hydrothermal conditions afterwards. However, abietic acid is insoluble in the pre-formed LDH-F solution, and also lacks the capability to spread evenly to form a homogeneous handsheet. Hence, the LDH-F hybrid fibers were first pressed into handsheets (HF) and then modified by immersing it in ethanolic solution of AA. This way, randomly formed clots of AA on the surface of the HF sheets were avoided and the distribution of AA on the fiber surface was improved. Thus, composite hybrid fiber (C-HF) handsheet with homogenous surface and uniform appearance was obtained. Table 2 shows names of series of pulp fibers (control samples and final products) studied, with their abbreviations used throughout this section.

Macroscopic properties

Degree of refining of fibers

Schopper–Riegler (SR) analysis showed that refining the bleached kraft pulp of pine (BKPR) resulted in a slightly higher refining degree (higher Schopper–Riegler value) than refining the unbleached Kraft pulp of spruce (UBKPR). BKPR had a SR value of 26 °SR after 60 min refining, whereas the corresponding value for UBKPR pulp (after 90 min of refining) was 21 °SR. The ratio between the degree of refining values of BKPR and UBKPR was 1.24:1. Thus, the increase of refining degree due to bleaching was 24%. The refining degrees of both pulps were considered to be moderate. The refining time is of lesser importance than the refining degree (°SR). Spruce UBKP is a more durable material towards refining than pine BKP. Hence, spruce UBKP needs a longer refining time to reach the same treatment level as pine BKP. Consequently, similar refining degrees (26 °SR and 21 °SR for BKPR and UBKPR, respectively), were achieved. This enables us to exclude refining as an additional parameter to further analysis of the subsequent treatments of the refined fibers.

Fiber length

BKP, UBKP showed average fiber lengths of 2.18 mm and 3.00 mm, respectively (Figure 1a,b). As expected, the average fiber lengths $L(l)$ of BKPR and UBKPR were smaller (2.15 mm and 2.81 mm, respectively) than those of BKP and UBKP, due to the refinement. The magnitude of the refining effect was

Table 2: Samples studied in the present investigation. Note: Bleaching of the fibers was not done at the laboratory. They were obtained as such commercially. Whereas refining was done at the laboratory.

Sample	Pine		Spruce	
	BKP	BKPR	UBKP	UBKPR
reference fibers (unmodified fiber)	REF	REF	REF	REF
composite fibers (AA on fiber)	C-F	C-F	C-F	C-F
hybrid fibers (LDH on fiber)	HF	HF	HF	HF
composite hybrid fibers AA on (LDH-Fiber)	C-HF (0.15 M)	C-HF (0.15 M)	C-HF (0.15 M)	C-HF (0.15 M)
	C-HF (0.30 M)	C-HF (0.30 M)	C-HF (0.30 M)	C-HF (0.30 M)
	C-HF (0.45 M)	C-HF (0.45 M)	C-HF (0.45 M)	C-HF (0.45 M)

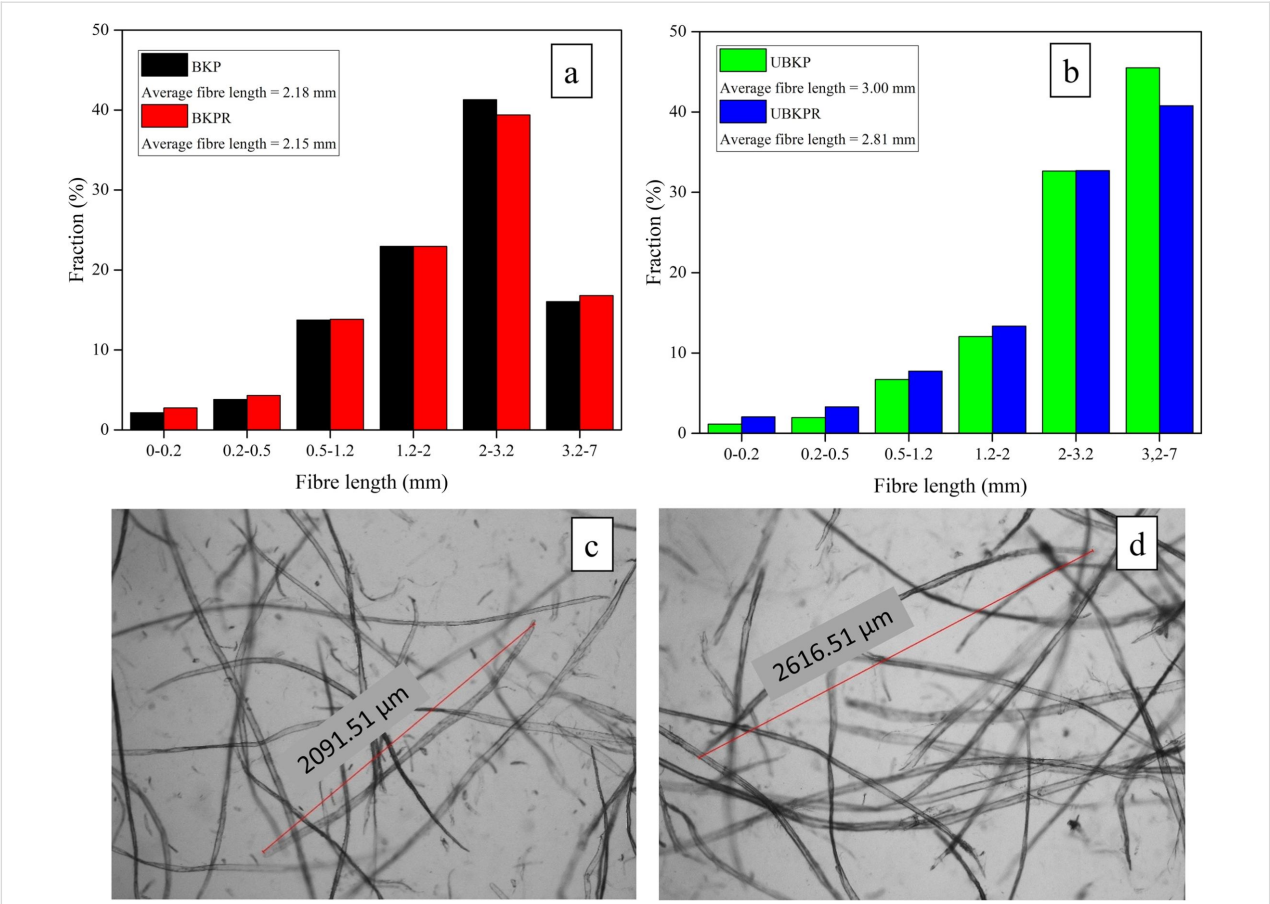

Figure 1: Fiber length distribution of (a) BKP and BKPR and (b) UBKP and UBKPR. Optical microscopy images (10× magnification) of (c) BKPR after 60 min of refining and (d) UBKPR after 90 min of refining.

larger for unbleached fibers ($\Delta L_{UBKP}(l)$ = 0.19) than for bleached fibers $\Delta L_{BKP}(l)$ = 0.03). This might be because bleached fibers were already softened and shortened during the chemical treatment.

The fiber length (LC) distribution and average fiber length $L(l)$ revealed that refining has shortened the average fiber length to some extent for both pulps BKPR and UBKPR. Both refined pulps showed a slight increase in the count of shorter fibers. The increase of these short fibers (0–0.5 mm) was from 3% to 5% for UBKPR (Figure 1b) and from 6% to 7 % for BKPR.

Optical microscopy pictures (10× magnification) showed that external fibrillation had occurred in both refined pulps, BKPR and UBKPR (Figure 1c,d). External fibrillation is the phenomenon in which fibrils stand out from the fiber surface but are still attached to the fiber strands. External fibrillation increases the specific surface area of the fibers and the number of sites for functionalization/grafting/adsorption. In addition, external fibrillation increases inter-fiber bonding which might lead to an increase in tensile strength of the fiber networks. Small separate pieces beaten out from fiber strands are also visible in the microscopy images of both the refined pulps, verifying the presence of the fine fractions (0–0.5 mm), measured in the fiber length investigations.

Spectroscopic studies

Structure and purity

X-ray diffraction patterns of the pulp fibers (REF, C-F, HF, C-$HF_{0.15M}$, C-$HF_{0.30M}$, and C-$HF_{0.45M}$) are shown in Figure 2.

The C-F and C-HF fibers exhibit characteristic peaks of AA at 15.51°. The presence of LDH in HF and C-HF was confirmed by its characteristic diffractions corresponding to the (003), (006), (012), (015), (018) planes [26]. These diffractions reveal the formation of a crystalline layer structure in the hybrid fibers (HF). The diffraction peaks at 14.5°, 16.5°, and 21.90° correspond to the (110) and (200) crystallographic planes of crystalline cellulose fibers (F) [27,28]. Thus, the presence of AA, LDH, and cellulose in C-F, HF, and C-HF materials, was confirmed by XRD. Out of these three components, AA and cellulose (pulp) were commercially obtained ingredients, whereas

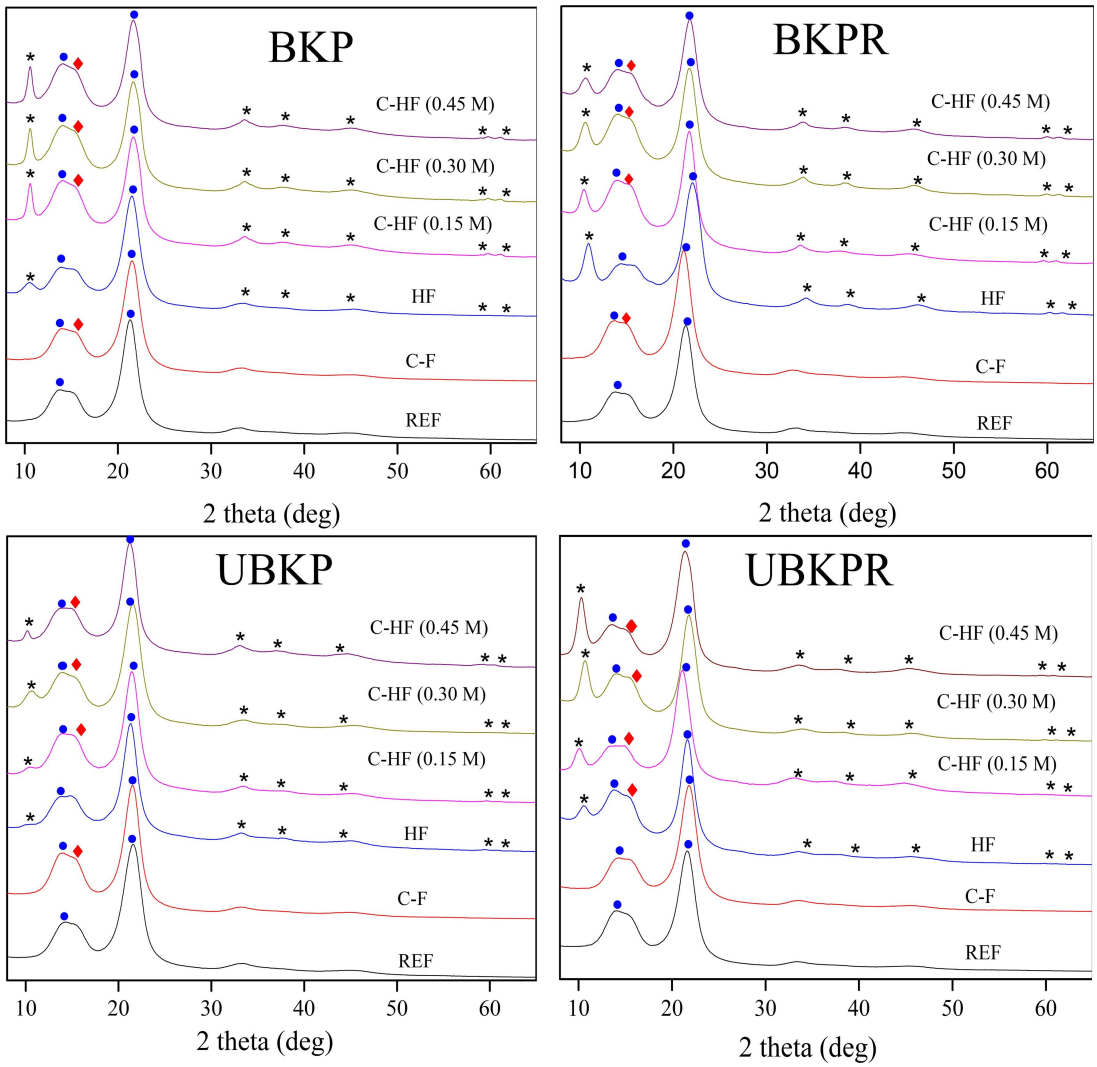

Figure 2: XRD spectra of pulp fibers (filled circles: fibers, asterisks: LDH, filled diamonds: abietic acid).

LDH was synthesized in situ. XRD might be helpful for gathering more information about formation, purity and grafting on cellulose of LDH.

The characteristic d_{003} line spacing of 0.77 nm in LDH disproves any undesirable anion exchange or chelation in the interlayer galleries of LDH. Layered double hydroxides are highly prone to ion displacement reactions at its interlayer anionic sites (e.g., NO_3^-, CO_3^{2-}) when it is synthesized in the presence of foreign molecules such as, in this case, cellulose. In this present work, cellulose existed in the neutral form and not as anion. In addition, abietic acid, which could form anions in solution, was only introduced after the hybrid fibers were transformed into sheets. Hence, abietate anions could not replace CO_3^{2-} in the LDH interlayers, causing contamination or reactions with cellulosic –OH groups.

AA was only connected to the HF fibers through freely available brucite layers (cations on the top plane) of LDH through hydrogen bonding between –OH groups of LDH and –COOH groups of AA. The –OH groups present in the bottom plane of LDH brucite layers were already utilized to graft cellulose through cellulosic O–H polarization. Thus, LDH act as a perfect structure-directing agent in C-HF materials. The XRD spectra of C-HF show a convergence of diffraction peaks of cellulose and AA at 14–16°, a shift from 14.77° to 15.20° and enhanced intensity, which confirm the AA-modification of HF.

Structure and bonding

The infrared absorption measurements were studied for the control samples (REF, C-F, HF) and the final material, hybrid fiber composites (C-$HF_{0.15M}$, C-$HF_{0.30M}$, and C-$HF_{0.45M}$, Figure 3. The control samples and composite hybrid fibers show

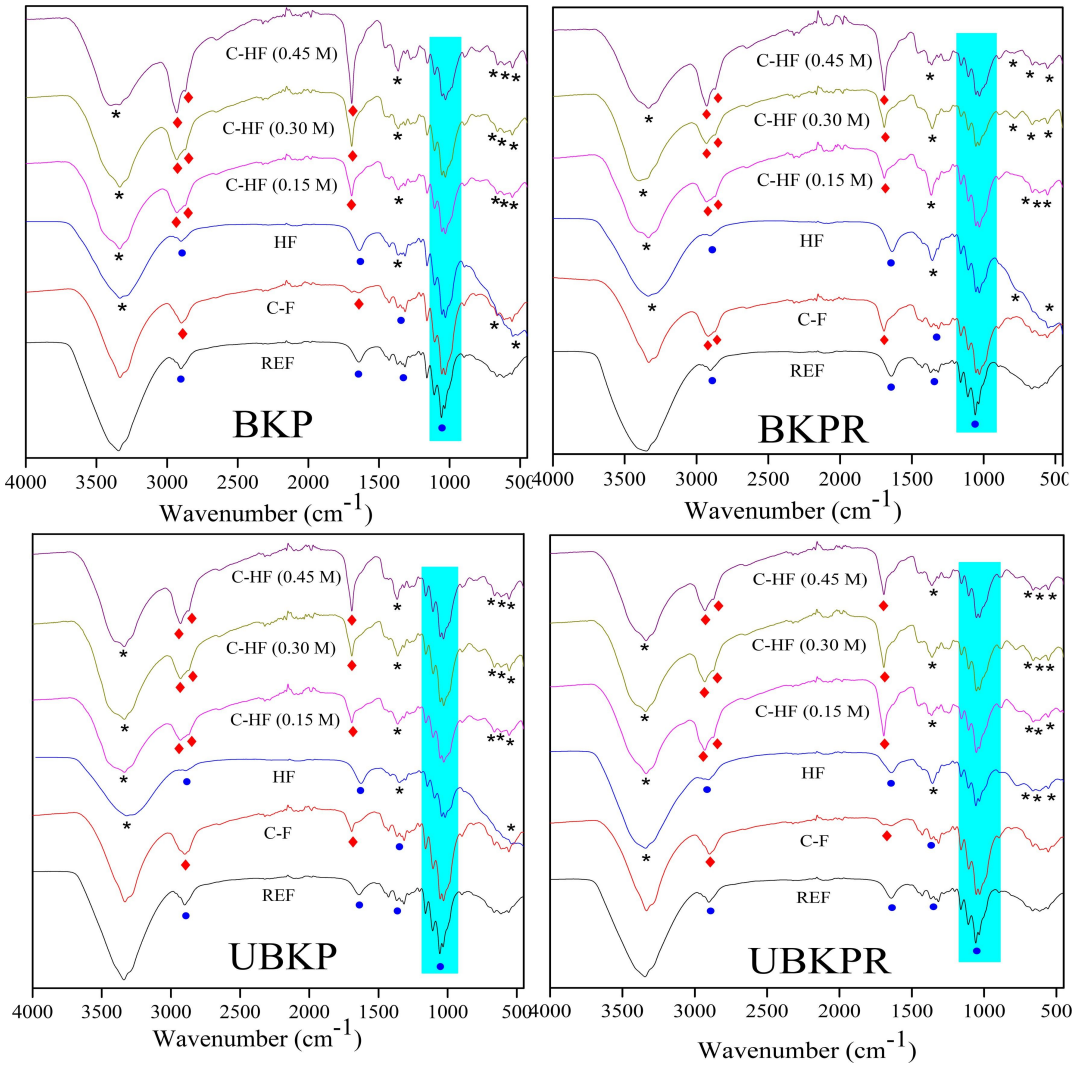

Figure 3: FTIR spectra of pulp fibers (filled circles: fibers, asterisks: LDH, filled diamonds: abietic acid).

their characteristic peaks at 3500–3000 cm^{-1} and 1640 cm^{-1}, which are due to stretching and bending of –OH bonds in cellulosic –OH groups/intramolecular hydrogen bonds and in adsorbed water, respectively. The peaks at 897 cm^{-1}, 1117 cm^{-1} and 1163 cm^{-1} were assigned to the C–O–C stretching in β-glycosidic bonds, C–C stretching and the C–O–C glycosidic ether band of cellulose, respectively. The cyan portion in Figure 3 denotes the cellulose fingerprint region.

HF and C-HF show a new vibration frequency at 1362 cm^{-1} that corresponds to asymmetric stretching of carbonate anions in LDH interlayer galleries. The frequencies at 617 cm^{-1}, 656 cm^{-1} and 783 cm^{-1} were attributed to M–O–M, M–OH, and O–M–O bond vibrations of LDH. The characteristic peaks of AA in C-HF are those at 2936 cm^{-1}, 2650 cm^{-1}, 1695 cm^{-1}, 1670 cm^{-1} and 1277 cm^{-1}. The vibration at 2936 cm^{-1} corresponds to C–H stretching absorption bands of $–CH_3$, $–CH_2–CH$ and =CH. The band at 2650 cm^{-1} is due to intermolecular hydrogen bonding in –OH of dimeric –COOH groups. The band at 1695 cm^{-1} is the outcome of C=O stretching vibrations of acid groups, whereas 1670 cm^{-1} is due to C=C conjugated bonds and 1277 cm^{-1} is from C–O deformation vibrations of –COOH. Consequently, the presence of characteristic vibrational frequencies of functional groups confirmed the presence of cellulose, LDH and AA in the respective materials.

Microscopic Studies

Morphology

Scanning electron microscopy (SEM) observations of the pulp fibers (REF, C-F, HF, C-$HF_{0.15M}$, C-$HF_{0.30M}$, and C-$HF_{0.45M}$) revealed how LDH is anchored on the fiber surface and the resin acid AA modifies the surface of hybrid fibers (HF).

Hybrid fibers (HF): The surface characterization of co-precipitated LDH on pulp fibers (HF of BKP, BKPR, UBKP, and UBKPR) revealed that LDH crystals had grown extensively on the fiber surface covering the fibers completely (Figure 4). The HF of bleached fibers (BKP, BKPR) show distinct fiber strand morphologies with LDH particles deposited like a tight continuous solid around the fibers (Figure 4a,b). Whereas HF of unbleached fibers (UBKP, UBKPR) do not show any fiber strands but only solid LDH grains (Figure 4c,d). The HF of refined fibers (BKPR, UBKPR) show LDH crystals with clear shapes like sand pebbles and hexagonal platelets on their surface. The refined fibers have numerous fibrils protruding from the pulp fiber strand. LDH grows around these fibrils and the inter-fibril spaces remain empty. Hence, the LDH crystals are slightly far apart and present in distinct shapes on the refined fibers. Thus, pure hybrid fibers (HF) obtained from direct co-precipitation of LDH on pulp fibers were confirmed by SEM.

BKP: The low-magnification images (Figure 5) of the reference (REF) show a dense, complex web of thin and long cellulose fibers. The surface of REF fibers directly modified by AA (C-F) looks like wax-smeared gauze. Although AA was coated directly on the fibers, it still reveals the complex web of fibers (Figure 5b). The REF fibers hybridized by LDH (HF) (Figure 5c) look very similar to unmodified reference fibers (REF). Figure 5d–f are images of AA-modified HFs, i.e., composite hybrid fibers (C-HF) with varying concentrations of LDH in increasing order (C-$HF_{0.15M}$, C-$HF_{0.30M}$, and C-$HF_{0.45M}$). All these images clearly portray the complete coverage of AA on hybrid fibers (C-HF), again like wax-smeared gauze. The high-magnification images (Figure S1, Supporting Information File 1) display a wrinkled surface of uncoated fibers (REF, HF, Figure S1a,c in Supporting Information File 1) and a very thick, smooth, and shiny layer of AA coating on C-F and C-HF fibers (Figure S1b and Figure S1d–f, Supporting Information File 1).

BKPR: Upon refining, the reference fibers (REF) showed fibrils protruding out from the surface (Figure 6a). It is suggested that the mechanical force applied on the BKPR fibers leads to dissociative fibrillation. This treatment is expected to have increased the surface area of the fibers. The low-magnification images of unmodified fibers (REF, HF, Figure 6a,c) showed again a complex network of very fine cellulose fibers, which are smudged by the AA layer upon modification either directly or through LDH (C-F, C-HF) (Figure 6b and Figure 6d–f). The microscopy images suggest that the refinement has reduced the size of the fibers in length and thickness. The high-magnification images (Figure S2, Supporting Information File 1) of these samples show heavily wrinkled fiber surfaces for REF, HF (Figure S2b,d in Supporting Information File 1) compared to unrefined counterparts (Figure S1a,c in Supporting Information File 1), and a very thick, smooth, and shiny layer of AA on fibers directly modified with AA (C-F, Figure S2b, Supporting Information File 1). In contrast, C-HF they display a thin, transparent and shiny layer of AA coating (Figure S2d–f, Supporting Information File 1). Thus, the difference in morphology between refined and unrefined bleached kraft pulp fibers (BKP, BKPR) could play a role in inducing hydrophobicity and tensile strength.

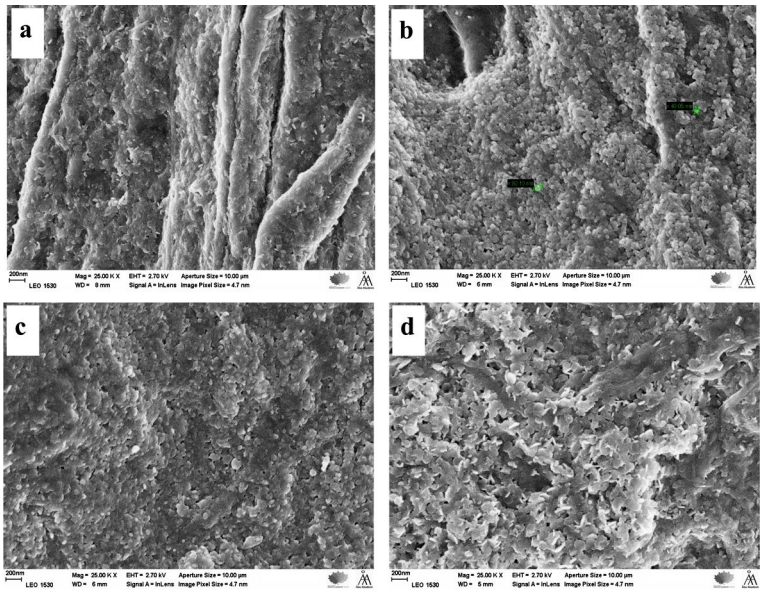

Figure 4: SEM images showing the hybridization of LDH particles on the fiber surfaces of (a) BKP, (b) BKPR, (c) UBKP and (d) UBKPR.

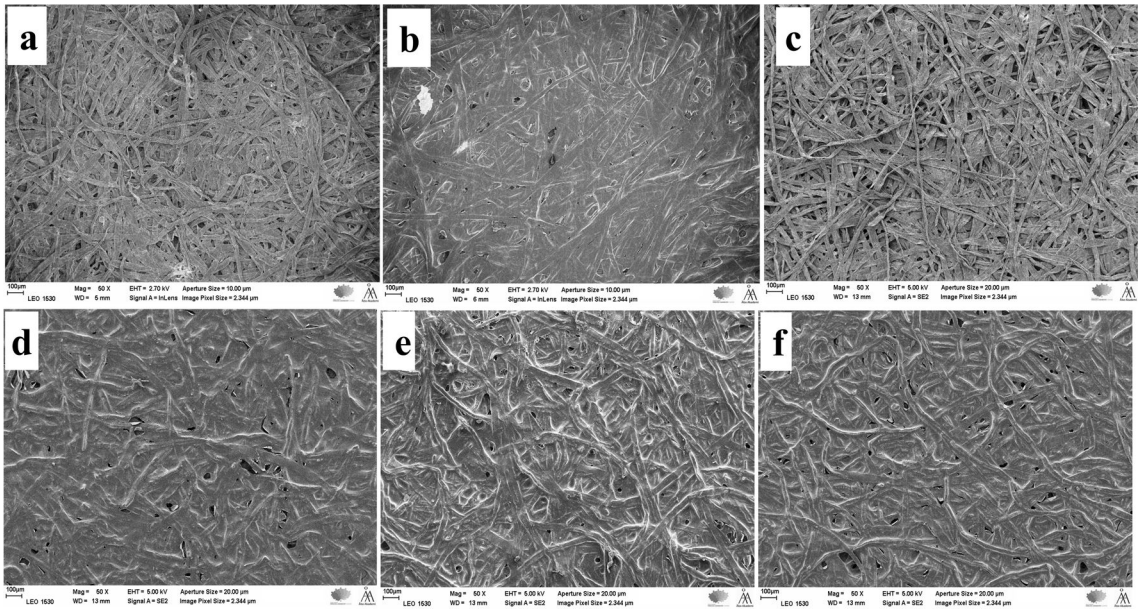

Figure 5: SEM images of the BKP fibers: (a) REF (b) C-F (c) HF (d) C-HF (0.15 M) (e) C-HF (0.30 M) (f) C-HF (0.45 M).

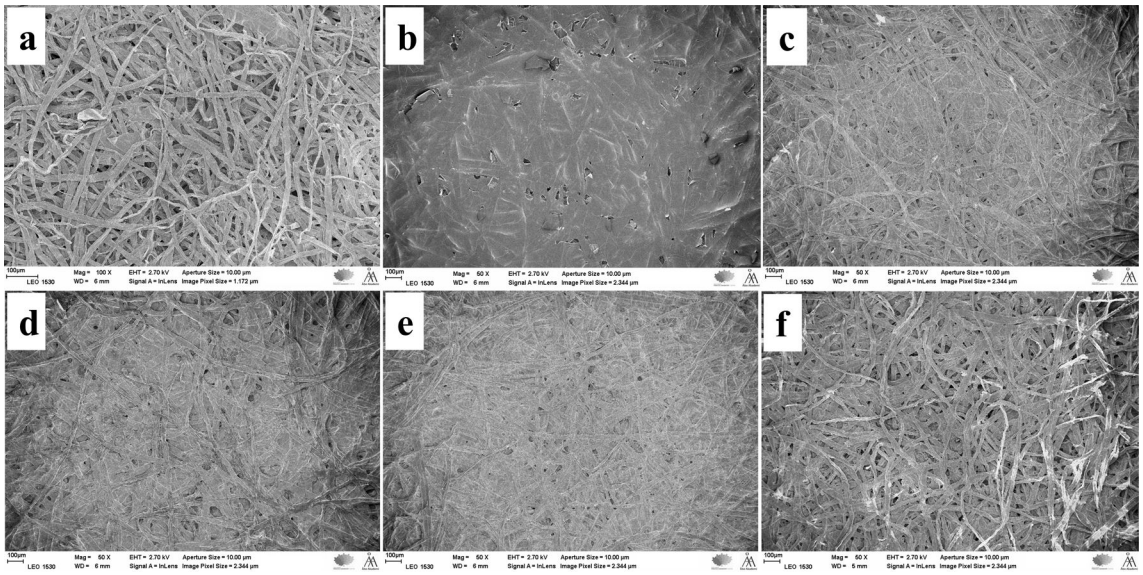

Figure 6: SEM images of the BKPR fibers: (a) REF (b) C-F (c) HF (d) C-HF (0.15 M) (e) C-HF (0.30 M) (f) C-HF (0.45 M).

UBKP: The reference fibers (REF) appear as tightly packed fiber bundles (Figure 7a). The HF show a web of thick fibers with LDH particles spread on the surface (Figure 7c). C-F fibers exhibit a thick covering of AA (Figure 7b). C-HF fibers reveal a moderately thick coating of AA (Figure 7d–f). The high-magnification images (Figure S3, Supporting Information File 1) reveal wrinkled surfaces or gel-like structures for all samples except C-F, which shows a very thick, smooth, and shiny coating of AA (Figure S3b, Supporting Information File 1). C-HF has a thick sticky glue-like coating of AA on the surface (Figure S3d–f, Supporting Information File 1).

UBKPR: REF fibers show a dense complex web of longer and thicker cellulose fibers having hairy projections on the surface (Figure 8a). HF displays a similar appearance but with few LDH crystals present on the surface (Figure 8c). C-F reveal a very thick AA layer (Figure 8b), whereas C-HF fibers show only a minimal AA coating (Figure 8d–f). At higher magnifica-

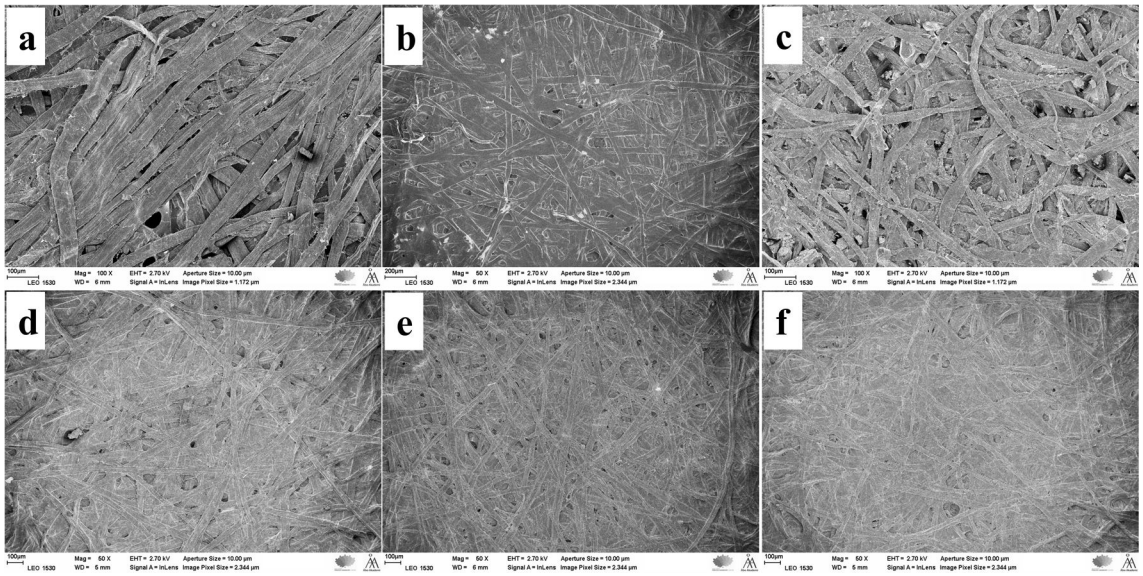

Figure 7: SEM images of the UBKP fibers: (a) REF (b) C-F (c) HF (d) C-HF (0.15 M) (e) C-HF (0.30 M) (f) C-HF (0.45 M).

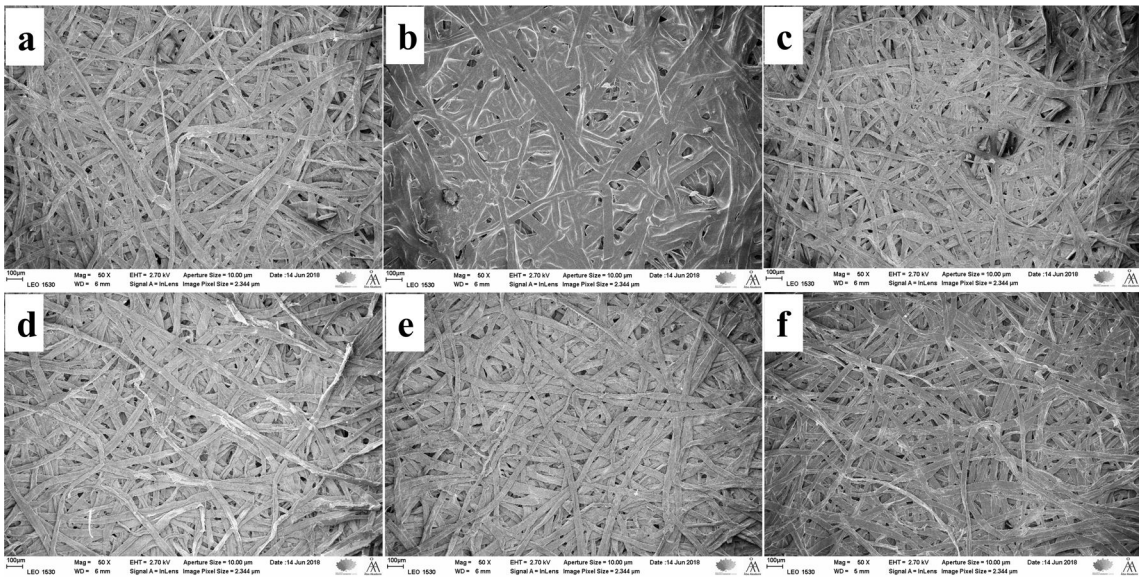

Figure 8: SEM images of the UBKPR fibers: (a) REF (b) C-F (c) HF (d) C-HF (0.15 M) (e) C-HF (0.30 M) (f) C-HF (0.45 M).

tion (Figure S4, Supporting Information File 1), the fibril projections of the refined fibers are clearly seen in all samples except C-F, which shows a very thick surface covering of AA wax (Figure S4b, Supporting Information File 1). C-HF fibers display a very thin covering of AA, compared to C-HF fibers from UBKP (Figure S4d–f, Supporting Information File 1).

The SEM characterization of materials suggests that unrefined fibers (BKP, UBKP) yield a better uptake of AA with uniform coating/adhesion than refined fibers (BKPR, UBKPR). SEM images of C-$HF_{0.30M}$ fibers from BKP, BKPR, UBKP, UBKPR are compared in Figure S5 (Supporting Information File 1). All these samples exhibited a wax-like coverage of abietic acid on the fiber skeleton. The thickness of the AA coverage may not be the same in all materials, quantitatively. Depending on the thickness of the AA coverage and intrinsic hydrophobic content such as hemicellulose and lignin, these materials showed different performance in CA_{water} and oil absorption studies.

Material Testing

Water contact angle (CA_{water})

The fibers REF, C-F, HF, C-$HF_{0.15M}$, C-$HF_{0.30M}$, and C-$HF_{0.45M}$ of all pulps were investigated with regard to their hydrophobicity in terms of water contact angle (Figure 9).

The REF fibers of BKPR, UBKPR exhibited higher CA_{water} values (20°, 36°) than the unrefined (BKP, UBKP) counterparts (19°, 19°, Figure 9). This suggests that the refining process opens up new fibrils on the surface of fibers, which increases the exposure of not only cellulosic –OH groups but also of hydrophobic lignin and hemicellulose. The latter increase the hydrophobicity of the fibers, and are removed during the bleaching process. Hence, the hydrophobicity is only associated with the intrinsic nature of cellulose.

Cellulose fibers directly modified with abietic acid (C-F) were also investigated. Refined C-F fibers (BKPR, UBKPR) showed a lower value of CA_{water} (40°, 66°) than the unrefined C-F fibers (BKP, UBKP) (65°, 86°). Refining caused a decrease in CA_{water} because of the deep diffusion and adsorption of AA inside the opened pores of the fibrillated surface. This leads to a smaller concentration of AA on the surface of the refined fibers. The same phenomenon occurs in bleached fibers. Hence, C-F fibers of UBKP were more hydrophobic (86°) than C-F fibers of BKP (65°). In contrast, unrefined unbleached fibers (UBKP) had a high concentration of AA on the surface and, hence, showed a higher value of CA_{water}.

The LDH hybridized cellulose fibers (HF) showed similar trends as the reference fibers (REF), with refined LDH-containing fibers of bleached and unbleached pulps (BKPR, UBKPR) exhibiting higher hydrophobicity (20°, 38°) than the unrefined counterparts (BKP, UBKP, 19°, 20°) due to the increased exposure of hydrophobic lignin and hemicellulose (Figure 9). Refining increased the CA_{water} value by about 18° from bleached to unbleached fibers. The reason for the identical trend was that the LDH material was grafted on cellulose at the hydrophilic sites because of its self-assembly on cellulosic –OH groups via hydrogen bonding. Although the cellulosic –OH groups were masked by –OH groups at the bottom planes of LDH, the freely exposed –OH groups at the top planes of LDH maintain the intrinsic hydrophilic character of cellulose fibers. Hence, there was no much change in the balance of the intrinsic hydrophobic character of the pulp fibers.

Composite hybrid fibers (C-HF) show higher water contact angle values than the two-component fibers, C-F and HF (Figure 9). The C-$HF_{0.15M}$, C-$HF_{0.30M}$, and C-$HF_{0.45M}$ fibers of BKP, UBKP have higher values of water contact angle (71°, 97°) (80°, 121°) (63°, 134°) than the refined counterparts (BKPR, UBKPR) (70°, 80°) (65°, 93°) (60°, 85°). These results were attributed to the fact that AA moieties diffuse deep inside the opened pores of the refined fibers leading to lower hydrophobicity. The unrefined fibers (BKP, UBKP) have a high amount of AA on the surface increasing hydrophobicity. Again, unbleached fibers are not free from hemicellulose and lignin. These hydrophobic moieties add up to the performance of the materials in CA_{water} measurements. Regarding the structure of C-HF fibers, –COOH groups of AA have directed the AA molecules towards the top-plane –OH groups of LDH through hydrogen bonding (Figure 10). Hence, the AA modification on pulp fibers via the linker material LDH (C-HF) is intact and stronger than the direct AA modification on pulp fibers (C-F).

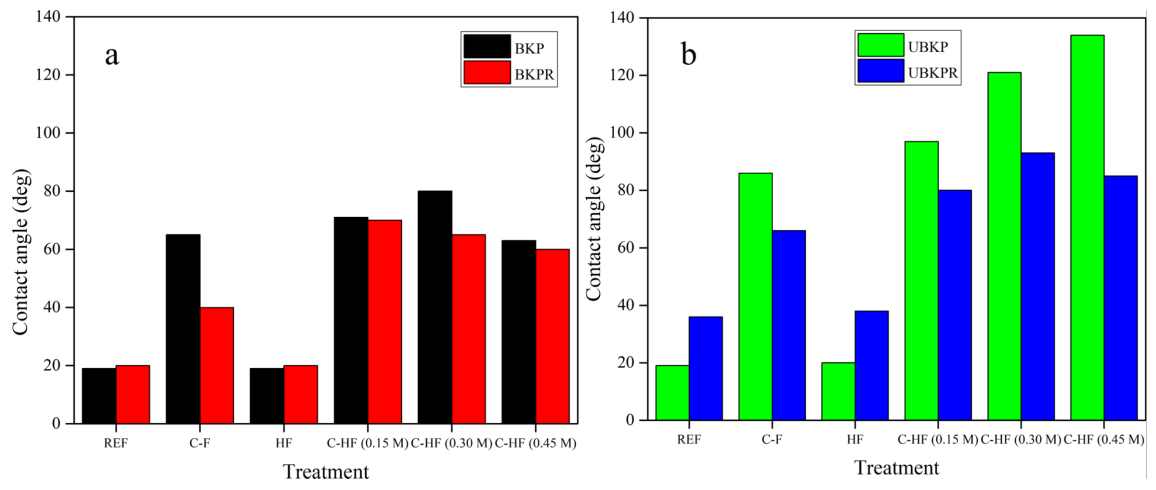

Figure 9: Water contact angle for (a) BKP and BKPR, (b) UBKP and UBKPR.

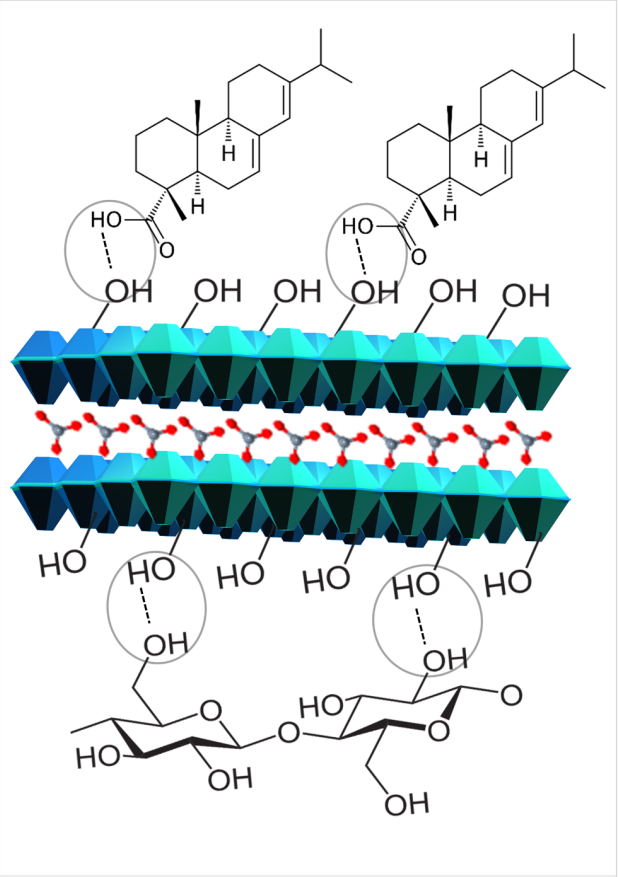

Figure 10: Hydrogen bonding directed assembly of AA on HF.

In C-F, there could be always repulsion between cyclic carbons of cellulose and AA, which will also diminish the AA grafting on pulp fibers.

Oil absorption capacity

The oil absorption experiments were carried out with the idea that when the material is hydrophobic it should also be lipophilic. The results show that the water contact angle is proportional to the oil absorption (Table 3). Higher CA_{water} values lead to a higher oil absorption. C-HF fibers have stood out as best candidates for oil absorption. Among all, the C-HF fibers of BKP and UBKP exhibited superior performance of 189% and 295% oil absorption, respectively (Table 3). These hydrophobic cellulose materials can be utilized as water-proof materials or oil sorbents [14].

Tensile strength

The reference and modified fibers was also studied with regard to tensile strength (Figure 11). The refined REF fibers of bleached and unbleached pulp (BKPR, UBKPR) show higher values of the tensile strength index (tensile strength divided by grammage) (50.18 and 72.10 $kNm{\cdot}kg^{-1}$) than the unrefined counterparts (BKP, UBKP) (16.21 and 8.93 $kNm{\cdot}kg^{-1}$) (Table S1, Supporting Information File 1). This observation was directly opposite to the trend obtained in the water contact angle/oil absorption measurements, where the unrefined fibers showed high hydrophobicity. However, it was highly reasonable that the refining process, which shortens the length of the fibers and opens up new fibrils on the surface, makes the fiber network very complex and tight binding. Moreover, the increased hydrogen bonding ($–CH_n–OH\cdots OH–CH_n–$) between newly exposed –OH groups in refined fibers caused improved tensile strength. Further, the higher tensile strength index of the refined fibers, compared to the unrefined fibers, was maintained even after the treatments, i.e., in C-F, HF, and C-HF.

Table 3: Water contact angle and oil absorption values of the pulp fibers.

Pulp fibers	BKP		BKPR	
	CA_{water} (°)	Oil absorption (%)	CA_{water} (°)	Oil absorption (%)
REF	19	45	20	55
C-F	65	57	40	78
HF	19	55	20	63
C-HF (0.15 M)	71	154	70	147
C-HF (0.30 M)	80	189	65	97
C-HF (0.45 M)	63	145	60	92
Pulp fibers	UBKP		UBKPR	
	CA_{water} (°)	Oil absorption (%)	CA_{water} (°)	Oil absorption (%)
REF	19	78	36	50
C-F	86	109	66	67
HF	20	90	38	54
C-HF (0.15 M)	97	128	80	102
C-HF (0.30 M)	121	184	93	153
C-HF (0.45 M)	134	295	85	132

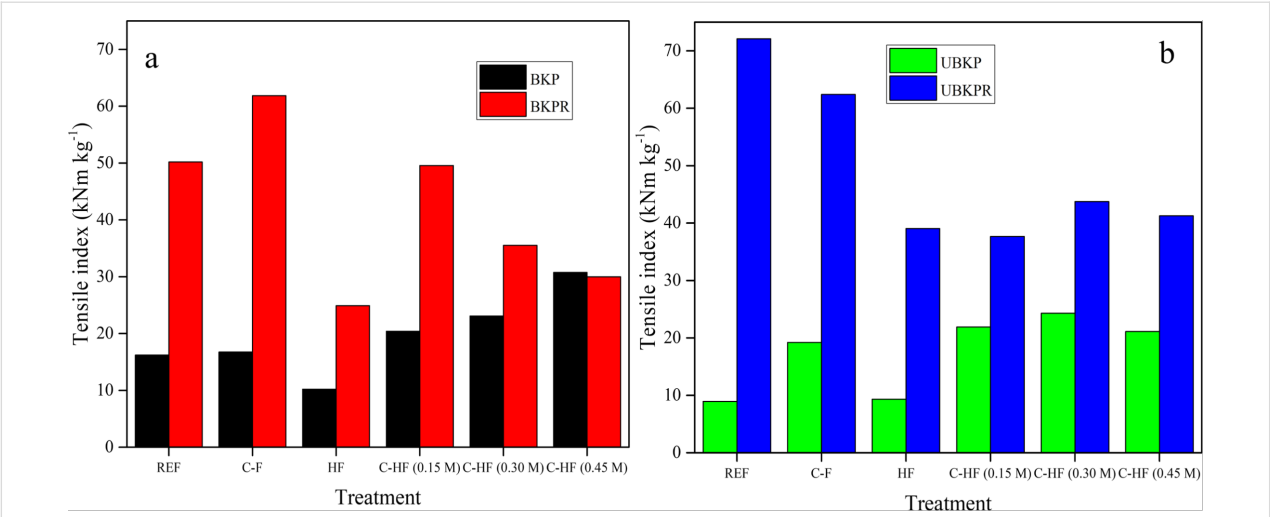

Figure 11: Tensile strength index for (a) BKP and BKP-R, (b) UBKP and UBKP-R.

Regarding a possible increased tensile strength, the treatments (LDH hybridization and AA modification) have positive effects only on unrefined fibers of bleached and unbleached pulp (C-HF of BKP, UBKP). The interaction with refined fibers of bleached and unbleached pulp (C-HF of BKPR, UBKPR) either maintains or reduces the existing tensile strength (Table S1, Supporting Information File 1). Hence, the refined fibers do not need any chemical treatment to increase the tensile strength, while the unrefined fibers need chemical functionalization.

In the case of fibers directly modified with AA (C-F), the AA treatment improved the tensile strength only for BKPR, UBKP but not for BKP, UBKPR pulps (Table S1, Supporting Information File 1). This suggests that AA forms a constructive composite only under the condition of low amounts of lignin or hemicellulose. However, the improved tensile strength was obtained only with BKPR and not with UBKP pulp. This revealed that AA not only needed low amounts of lignin or hemicellulose but also a high surface area. Although UBKPR has a high surface area, it has also increased amounts of lignin of hemicelluloses. Hence, AA has a negative effect on it. The more lignin or hemicelluloses are present, the higher the repulsion with AA, due to the aromatic carbon rings. Hence, the AA coverage on these fibers is smaller, which was evident from SEM as well. Therefore, there is less AA on the fiber surface to bind the fibers for improved tensile strength.

The sole LDH treatment of fibers and subsequent sheet forming (HF) showed a decrease in tensile strength indices for most of the pulps (Table S1, Supporting Information File 1) compared to the respective unmodified reference fibers (REF). The LDH particles are synthesized in the presence of disintegrated individual fibers, leading to a homogenous distribution of LDH particles on the surface of the fibers. These LDH particles completely cover the underlying fiber (polysaccharide material), which usually tend to form strong hydrogen bonds with other fiber strands. This direct hydrogen bonding from fiber to fiber ($–CH_n–OH\cdots OH–CH_n–$) is different and stronger than hydrogen bonding between LDH –OH groups and cellulosic –OH groups ($M^{n+}–OH\cdots OH–CH_n–$) or –COOH groups of AA ($M^{n+}–OH\cdots OHOC–CH_n–$), which plays a role in stacking AA and cellulose fibers above and below LDH, respectively. Thus, LDH hinders the inter-fiber bonding and reduces the tensile strength. However, this weakening of inter-fiber bonding was overcome by modifying hybrid fibers with AA. AA was self-assembled on LDH binding sites via hydrogen bonding ($M^{n+}–OH\cdots OHOC–CH_n–$). Then the adhesive action of AA on the fiber surface increased the binding between separate strands of fibers and improved the tensile strength. However, this type of action proved to be advantageous only with unrefined fibers. With refined fibers, the refining action itself was sufficient to increase the tensile strength. The results show that refined pulp fibers (REF of BKPR, UBKPR) and C-HF prepared from unrefined pulps (BKP and UBKP) can be utilized in reinforcement applications.

ISO brightness

As expected, the ISO brightness was found to be higher with bleached pulp compared to unbleached pulp (Figure 12). Bleaching essentially removes lignin and hemicelluloses that absorb light and cause the dark appearance of pulp. The refined fibers of bleached and unbleached pulp (BKPR, UBKPR) exhibited slightly less brightness (83.96%, 21.54%) than the unrefined counterparts (BKP, UBKP) (84.80%, 27.15%) (Table S2, Supporting Information File 1). This may be because the refined fibers have more empty spaces and pores than unre-

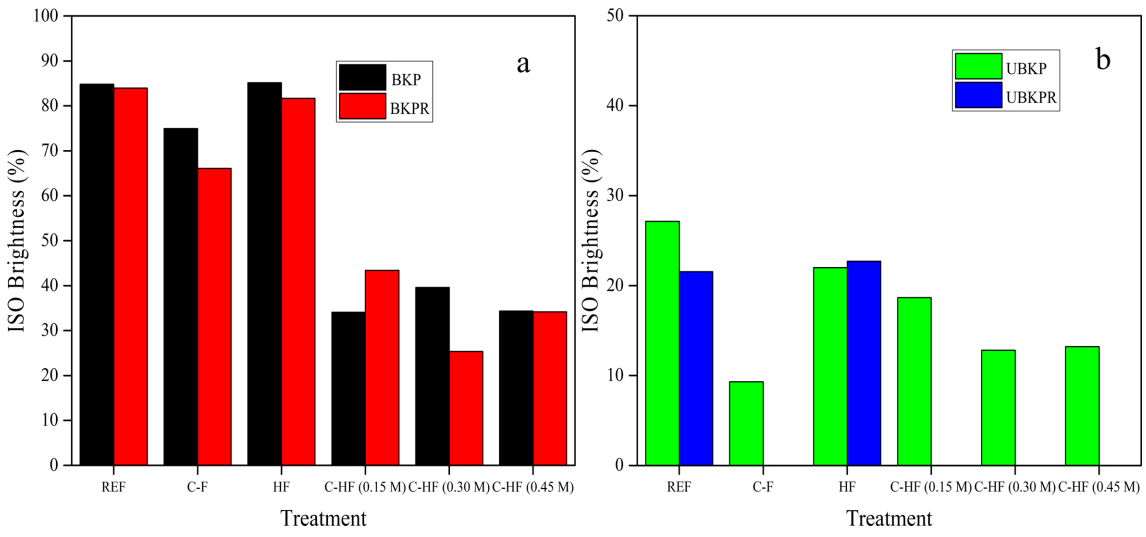

Figure 12: ISO Brightness of (a) BKP and BKP-R and (b) UBKP and UBKP-R.

fined fibers, which might reduce light scattering and reflectance. The brightness of unbleached pulps (UBKP, UBKPR) was markedly lower. UBKPR shows a very poor ISO brightness which sometimes could not be determined due the very weak reflectance (Table S2, Supporting Information File 1).

C-F fibers exhibit a lower brightness than the reference fibers (REF, Table S2, Supporting Information File 1). Again, the difference was huge with unbleached fibers for the reasons discussed above. AA, which is a resin acid with dull brown color, absorbed light even more. The hybrid fibers (HF) showed almost identical brightness values compared to reference fibers (REF) because LDH (white in color) reflects light. The combination of AA and LDH (C-HF) reduced the ISO brightness values (Table S2, Supporting Information File 1).

Comparing the data with our previous report

The use of abietic acid has significantly increased CA_{water} values and oil absorption, which we aimed for. In the experiments with stearic acid (SA) in our previous work, the composite material reach a maximum CA_{water} value of 150° after 24 h of treatment. In contrast, with abietic acid (AA) the HF material reach a CA_{water} value of 134° after only 15 min of treatment. The corresponding oil absorption percentage weight increases were 155% and 295%, respectively. This means AA-modified HF absorbs adsorb twice the amount of oil compared to SA-modified HF fibers. Another important reason to pick abietic acid was to improve the tensile strength, as the SA-modified HF lost 84% of its tensile strength compared to the reference fibers (REF). The tensile strength percentages after modification with AA are 90% increase, 1% decrease, 172% increase and 39% decrease for BKP, BKPR, UBKP and UBKPR, respectively. Thus, abietic acid has a better performance with regard to tensile strength than stearic acid.

Conclusion

The abietic acid (AA)-induced hydrophobicity on bleached pine kraft pulp and unbleached spruce kraft pulp fibers (F), refined and unrefined, requires a linker material, i.e., a layered double hydroxide (LDH). LDH, self-assembles on cellulose fiber surface through hydrogen bonding on the bottom plane and further directs AA to graft on it via hydrogen bonding but this time on the top plane. Thus, a sandwich composite hybrid material (C-HF) is formed. C-HF materials exhibit a better performance in water-contact angle (CA_{water}) and oil absorption measurements than unmodified/reference fibers, fibers modified with only AA (C-F) or only LDH (HF). C-HF obtained from unrefined fibers showed higher CA_{water} values than refined fibers, as the refined fibers have a reduced surface concentration of AA due to diffusion of AA inside the pores. In contrast, refined fibers exhibit higher tensile strength than unrefined fibers, due to the newly opened fibrils and surface –OH groups available for hydrogen bonding/inter-fiber binding. The refining is sufficient to achieve improved tensile strength in pulp fibers. Thus, treatment with LDH and AA is required only for improving the tensile strength of unrefined fibers. As expected, the ISO brightness of bleached fibers is higher than that of unbleached fibers due to the smaller content of lignin and hemicellulose. In addition, the unrefined fibers are brighter than refined fibers, as there are less empty space of pores that reduce the reflectance. The present investigation of pulp fibers can be taken to the next level at which the improved hydrophobicity and tensile strength could be utilized for applications in the field of sorption or reinforcement.

Supporting Information

Supporting Information contains additional SEM figures, and tensile strength and ISO brightness data that are relevant to the discussion part.

Supporting Information File 1

Additional experimental data.
[https://www.beilstein-journals.org/bjnano/content/supplementary/2190-4286-10-60-S1.pdf]

Acknowledgements

Author Liji Sobhana acknowledges Magnus Ehrnrooth Foundation for the post-doctoral financial support (2018). Lokesh Kesavan acknowledges the Turku Collegium for Science & Medicine (TCSM) and University of Turku for the funding aid and hosting his collaborative postdoctoral research.

ORCID® iDs

Liji Sobhana - https://orcid.org/0000-0002-3173-3798
Lokesh Kesavan - https://orcid.org/0000-0003-4945-5084
Pedro Fardim - https://orcid.org/0000-0003-1545-3523

References

1. Bozell, J. J., Ed. *Chemicals and Materials from Renewable Resources;* ACS Symposium Series, Vol. 784; American Chemical Society: Washington, DC, U.S.A., 2001. doi:10.1021/bk-2001-0784
2. Froschauer, C.; Hummel, M.; Iakovlev, M.; Roselli, A.; Schottenberger, H.; Sixta, H. *Biomacromolecules* **2013,** *14,* 1741–1750. doi:10.1021/bm400106h
3. Heinze, T.; Liebert, T. *Prog. Polym. Sci.* **2001,** *26,* 1689–1762. doi:10.1016/s0079-6700(01)00022-3
4. Ly, B.; Thielemans, W.; Dufresne, A.; Chaussy, D.; Belgacem, M. N. *Compos. Sci. Technol.* **2008,** *68,* 3193–3201. doi:10.1016/j.compscitech.2008.07.018
5. Ma, J.; Wang, X.; Fu, Q.; Si, Y.; Yu, J.; Ding, B. *ACS Appl. Mater. Interfaces* **2015,** *7,* 15658–15666. doi:10.1021/acsami.5b04741
6. Zemljič, L. F.; Peršin, Z.; Stenius, P.; Kleinschek, K. S. *Cellulose* **2008,** *15,* 681–690. doi:10.1007/s10570-008-9216-6
7. da Silva Perez, D.; Montanari, S.; Vignon, M. R. *Biomacromolecules* **2003,** *4,* 1417–1425. doi:10.1021/bm034144s
8. Takács, E.; Wojnárovits, L.; Borsa, J.; Rácz, I. *Radiat. Phys. Chem.* **2010,** *79,* 467–470. doi:10.1016/j.radphyschem.2009.09.012
9. Krässig, H.; Kitchen, W. *J. Polym. Sci.* **1961,** *51,* 123–172. doi:10.1002/pol.1961.1205115509
10. Sha, D.; Rui, H.; Mi, Z.; Feng, C.; Qiang, F. *Carbohydr. Polym.* **2016,** *154,* 129–138. doi:10.1016/j.carbpol.2016.07.101
11. S. Sobhanadhas, L.; Kesavan, L.; Lastusaari, M.; Fardim, P. *ACS Omega* **2019,** *4,* 320–330. doi:10.1021/acsomega.8b03061
12. Huang, X.; Wang, A.; Xu, X.; Liu, H.; Shang, S. *ACS Sustainable Chem. Eng.* **2017,** *5,* 1619–1627. doi:10.1021/acssuschemeng.6b02359
13. Lin, L.; Fu, F.; Qin, L. Cellulose fiber-based high strength composites. In *Advanced High Strength Natural Fibre Composites in Construction;* Fan, M.; Fu, F., Eds.; Woodhead Publishing, 2017; pp 179–203. doi:10.1016/b978-0-08-100411-1.00007-8
14. Sobhanadhas, L. S.; Kesavan, L.; Fardim, P. *Langmuir* **2018,** *34,* 9857–9878. doi:10.1021/acs.langmuir.7b04379
15. Sobhana, S. S. L.; Zhang, X.; Kesavan, L.; Liias, P.; Fardim, P. *Colloids Surf., A* **2017,** *522,* 416–424. doi:10.1016/j.colsurfa.2017.03.025
16. Norlin, L.-H. Tall Oil. *Ullmann's Encyclopedia of Industrial Chemistry;* Wiley-VCH: Weinheim, Germany, 2000. doi:10.1002/14356007.a26_057
17. Allmann, R. *Acta Crystallogr., Sect. B: Struct. Crystallogr. Cryst. Chem.* **1968,** *24,* 972–977. doi:10.1107/s0567740868003511
18. Dou, Y.; Xu, S.; Liu, X.; Han, J.; Yan, H.; Wei, M.; Evans, D. G.; Duan, X. *Adv. Funct. Mater.* **2014,** *24,* 514–521. doi:10.1002/adfm.201301775
19. Sobhana, S. S. L.; Bogati, D. R.; Reza, M.; Gustafsson, J.; Fardim, P. *Microporous Mesoporous Mater.* **2016,** *225,* 66–73. doi:10.1016/j.micromeso.2015.12.009
20. Yadollahi, M.; Namazi, H.; Barkhordari, S. *Carbohydr. Polym.* **2014,** *108,* 83–90. doi:10.1016/j.carbpol.2014.03.024
21. Huang, S.; Song, S.; Zhang, R.; Wen, T.; Wang, X.; Yu, S.; Song, W.; Hayat, T.; Alsaedi, A.; Wang, X. *ACS Sustainable Chem. Eng.* **2017,** *5,* 11268–11279. doi:10.1021/acssuschemeng.7b01717
22. Zhang, C.; Li, X.; Jiang, Z.; Zhang, Y.; Wen, T.; Fang, M.; Tan, X.; Alsaedi, A.; Hayat, T.; Wang, X. *ACS Sustainable Chem. Eng.* **2018,** *6,* 15644–15652. doi:10.1021/acssuschemeng.8b04146
23. Shuang, S.; Ling, Y.; Xiangxue, W.; Li, L.; Shuyi, H.; Rui, Z.; Tao, W.; Shujun, Y.; Dong, F.; Tasawar, H.; Xiangke, W. *Chem. Eng. J.* **2018,** *338,* 579–590. doi:10.1016/j.cej.2018.01.055
24. Ling, Y.; Yezi, H.; Ran, M.; Tao, W.; Xiangxue, W.; Baowei, H.; Zhimin, Y.; Tasawar, H.; Ahmed, A.; Xiangke, W. *Chem. Eng. J.* **2019,** *359,* 1550–1562. doi:10.1016/j.cej.2018.11.017
25. Pengcheng, G.; Sai, Z.; Xing, L.; Xiangxue, W.; Tao, W.; Riffat, J.; Ahmed, A.; Tasawar, H.; Xiangke, W. *Environ. Pollut.* **2018,** *240,* 493–505. doi:10.1016/j.envpol.2018.04.136
26. Franck, M.; Richard, I. W.; O'Hare, D. *J. Mater. Chem.* **2000,** 10. doi:10.1039/b002827o
27. Wada, M.; Okano, T. *Cellulose* **2001,** *8,* 183–188. doi:10.1023/a:1013196220602
28. Popescu, M.-C.; Popescu, C.-M.; Lisa, G.; Sakata, Y. *J. Mol. Struct.* **2011,** *988,* 65–72. doi:10.1016/j.molstruc.2010.12.004

BEILSTEIN JOURNAL OF NANOTECHNOLOGY

Outstanding chain-extension effect and high UV resistance of polybutylene succinate containing amino-acid-modified layered double hydroxides

Adam A. Marek[*1,2], Vincent Verney[1], Christine Taviot-Gueho[1], Grazia Totaro[3], Laura Sisti[3], Annamaria Celli[3] and Fabrice Leroux[1]

Full Research Paper

Open Access

Address:
[1]Institut de Chimie de Clermont-Ferrand (ICCF), SIGMA Clermont, CNRS, Université Clermont Auvergne, F-63000 Clermont-Ferrand, France, [2]Department of Organic Chemical Technology and Petrochemistry, Silesian University of Technology, 44100 Gliwice, Poland and [3]Dipartimento di Ingegneria Civile, Chimica, Ambientale e dei Materiali, Università di Bologna, Via Terracini 28, 40131 Bologna, Italy

Email:
Adam A. Marek[*] - adam.a.marek@polsl.pl

* Corresponding author

Keywords:
amino acid; layered double hydroxide; phenylalanine; polybutylene succinate

Beilstein J. Nanotechnol. **2019,** *10,* 684–695.
doi:10.3762/bjnano.10.68

Received: 15 September 2018
Accepted: 14 February 2019
Published: 12 March 2019

This article is part of the thematic issue "Advanced hybrid nanomaterials".

Associate Editor: C. T. Yavuz

Abstract

Polybutylene succinate (PBS) nanocomposite materials were prepared using a melt compounding process. The Mg_2Al-based PBS nanocomposites, dispersed with inorganic–organic hybrid materials (layered double hydroxides, LDHs), were functionalized with the amino acids L-histidine (HIS) and L-phenylalanine (PHE). The rheological and anti-ultraviolet (anti-UV) properties were investigated and compared to filler-free PBS as well as LDH Mg_2Al/nitrate as references. Both organo-modified LDHs exhibited a remarkable chain-extension effect for PBS with an outstanding increase in the zero-shear viscosity η_0 for PBS–Mg_2Al/PHE (two order of magnitude increase as compared to filler-free PBS). These results were compared to data found in the literature. Moreover, HIS and PHE anions embedded into the LDH structure can successfully prevent the chain scission reactions that usually occur during photo-ageing of PBS under UV radiation exposure. This highlights the outstanding performance of the LDH hybrid materials, and in particular, their application as a polymer chain extender and UV stabilizer for PBS, which can likely be extended to other biodegradable polymers.

Introduction

Polymer nanocomposite materials have been one of the leading scientific topics over the past decades [1-4]. Because many petrochemical sources are non-renewable and require raw materials for large-volume polymer production, many studies have been focused on the development of their substitutes. One of the most promising candidates to replace petroleum-based polymers is polybutylene succinate (PBS) – a biodegradable aliphatic polyester, obtained from the renewable sources succinic acid and butane-1,4-diol via a polycondensation process. Indeed PBS has mechanical characteristics similar to well-known polyolefins, such as low-density poly(ethylene) (LDPE). However, the drastic drawback of PBS for possible use in everyday life (e.g., packaging) is its rapid hydrolysis and UV degradation [5].

A classical approach to overcome these problems is to add a stabilizing agent that may act as an anti-moisture and UV stabilizer. The small organic molecules used [6-9] are typically prone to migrate out of the polymer, thus creating some porosity and subsequently causing potential disruption in the polymer barrier integrity. In addition to this, the possible release of the stabilizers is a key issue in terms of health since they may come in contact with the nutrient product. It is of great importance to avoid the migration of such chemical additives.

Today inorganic containers are thought to play the dual role of embedding a specific agent to avoid its ingress into a polymer as well as providing the complementary properties as a gas barrier and mechanical reinforcement for the polymer. Among the candidates, layered double hydroxides (LDH) appear to be a promising choice in endowing multiple properties to the polymer. This due to their versatility in terms of chemical composition and the relatively straightforward preparation involving soft chemistry routes.

Layered double hydroxides can be obtained as naturally existing materials or can be produced by synthetic routes (e.g., co-precipitation or ion exchange). They are also known as anionic clays or hydrotalcite-like materials and are described by the general formula $[M^{II}_{1-x}M^{III}_{x}–(OH)_2](A^{n-})_{x/n}\cdot mH_2O$, where M^{II} and M^{III} are di- and trivalent cations respectively and A^{n-} is an anion. The presence of trivalent cations results in a positive charge on the layers, which has to be balanced by diverse inorganic or organic anions intercalated between the layers [10,11]. LDHs are considered to be “green” and low environmental impact fillers [12], biocompatible [13] and food compatible [14].

Indeed the choice of organo-modified LDH using amino acids, and among them the protein-building amino acids, has already been demonstrated [15]. Having in mind that UV stabilization should require UV absorption properties for the organic molecule, any proteinogenic amino acids presenting cycle in their backbone will be preferentially considered. Tyrosine and tryptophan have been studied for their UV stabilizing properties; however, histidine (HIS) and (PHE) are rarely reported. One study reports the beneficial role of PHE interleaved into LDH as a self-healing agent for polymer coating in corrosion inhibition for aluminium substrates [16]. Due to the presence of benzene (for PHE) or the heterocyclic imidazole ring (for HIS), both organic molecules should absorb in the short to medium wavelength range of the ultraviolet C (UVC) and ultraviolet B (UVB) regions.

In the present work, Mg_2Al LDH materials were first organo-modified with histidine and phenylalanine using a co-precipitation method and then characterized by X-ray diffraction (XRD), Fourier transform infrared spectroscopy (FTIR) and thermogravimetric analysis (TGA). As expected, the UV–vis spectra showed absorbance in the UVC and UVB regions and the potential role as UV stabilizers. In a second part, PBS composites were prepared with 5 wt % of LDH filler by melt blending and once again fully characterized (XRD, TGA, DSC, DMTA and melt rheology). Impressively a pronounced chain-extension effect for PBS was observed with both organo-modified LDHs, especially in the case of PBS–LDH/PHE, for which the apparent molecular weight was almost 400 times higher than the pristine PBS. Finally, PBS composites were subjected to a photodegradation process, showing their resistance to UV irradiation.

Experimental

Materials and reagents

Aluminium nitrate $Al(NO_3)_3\cdot 9H_2O$, magnesium nitrate $Mg(NO_3)_2\cdot 6H_2O$, sodium nitrate $NaNO_3$, sodium hydroxide, the amino acids L-histidine (HIS) and L-phenylalanine (PHE) were purchased from Sigma-Aldrich. PBS (PBE003) was purchased from NaturePlast. All the materials were reagent grade and used as received.

Layered double hydroxide synthesis

The LDH hybrids with general formula $Mg_2Al(OH)_6$[amino acid]$\cdot 2H_2O$ were prepared by a co-precipitation method according to a similar procedure as described by Totaro et al. [17], for possible comparison. The solution of $Mg(NO_3)_2\cdot 6H_2O$ and $Al(NO_3)_3\cdot 9H_2O$ (molar ratio 2/1) in milli-Q water (100 mL) was added dropwise to the vigorously stirred water solution of organic guest (50 mL) for 3.5 h and the pH was kept constant (10.0 ± 0.1) with the addition of NaOH solution. When the addition of salts was finished, the reaction mixture was aged for 3.5 h at room temperature. Both the reaction and ageing pro-

cesses were performed under nitrogen atmosphere to avoid contamination by carbonate. The final products were centrifuged, washed several times with deionized water and vacuum dried at 40 °C for 24 h. Next, the solid LDH fillers were ground using a Retsch CryoMill machine and sieved to obtain a fraction with particles of diameter less than 50 μm.

Melt blending and film making

The PBS–LDH nanocomposites were obtained using a twin screw extruder Hakke MINILAB microcompounder (Thermo Electron Corporation). The melt extrusion process was performed at 120 °C with a roller speed of 100 rpm over 5 min. A LDH mass loading of 5 wt % was used as it appeared to be the right compromise to be detected by XRD, as formerly demonstrated [15]. This was also shown to endow the polymer composites with significantly improved properties as well as to envision a master-batch considering the observed state of dispersion.

PBS–LDH nanocomposite films with thickness of about 90–100 μm were prepared by compression moulding between two Teflon sheets under 100 bar at 120 °C for one minute.

Photodegradation

PBS and PBS–LDH nanocomposite films were placed on a rotating carousel in a SEPAP 12/24 chamber from ATLAS equipped with four 400 W mercury lamps with spectral rays above 300 nm. The accelerated photodegradation was studied at 60 °C and under air atmosphere.

Characterization methods

FTIR spectra of the LDH fillers were recorded using a Nicolet 380 FTIR spectrometer (DTGS detector) equipped with an attenuated total reflection single reflection diamond from Specac, and 32 scans and at a resolution of 4 cm^{-1} were collected.

LDH fillers and PBS–LDH nanocomposites were characterized by XRD using a Philips X-Pert Pro diffractometer with Cu Kα radiation. Data were collected at room temperature from $2\theta = 2.0–70.0°$ with a step size of 0.03° and a counting time of 10 s per step.

UV–vis spectra of the LDH substances and polymer nanocomposites were obtained using a Shimadzu UV-2101 PC spectrophotometer. Kubelka–Munk theory was applied to the LDH filler data to transform the diffuse reflectance spectra into absorption spectra.

The fluorescence spectra of PBS–LDH nanocomposites were recorded with a Perkin-Elmer LS-55 luminescence spectrophotometer equipped with a front surface accessory and pulsed xenon excitation source. The emission signal was collected with the monochromater from 200 to 600 nm at scan rate of 600 nm min^{-1} and excitation wavelength of 280 nm.

The thermal properties of the LDH fillers and polymer composites were characterized by differential scanning calorimetry (DSC) using a Perkin-Elmer DSC6 apparatus. The analyses were carried out under nitrogen, and firstly, the samples (≈10 mg) were heated from 40–150 °C at 20 °C min^{-1}, then kept at high temperature for 2 min, and then cooled down to −60 °C at 10 °C min^{-1}. After that, the thermal history of the samples was deleted and a second scan profile was performed by heating from −60 °C to 150 °C at 10 °C min^{-1}. The glass transition temperature (T_g), the melting temperature (T_m) and the enthalpy of fusion (ΔH_m) were measured from the second scan. T_g was taken as the midpoint of the heat capacity increment associated with the glass-to-rubber transition. The crystallization temperature (T_c) and the enthalpy of crystallization (ΔH_c) were measured during the cooling scan.

Thermogravimetric analysis (TGA) of LDH fillers and composites was performed in air atmosphere (gas flow 30 mL min^{-1}) using a Perkin Elmer TGA7 apparatus. The temperature range of 50–850 °C and heating rate 10 °C min^{-1} was applied. The onset degradation temperature (T_{onset}) was taken from the intersection of the tangent of the initial point and the inflection points. The 10% mass loss temperature ($T_{10}{}^{D}$) was also measured.

The melt rheological properties of the polymer composites were measured at 120 °C using a dynamic mechanical spectrometer (ARES Rheometric Scientific T&A Instruments) equipped with two parallel plate holders of 8 mm in diameter. The measurements were performed in oscillatory frequency sweep mode with the range of frequency sweeps from 0.1 to 100 rad s^{-1} and the gap between plates set at 1 mm. In all cases, the oscillatory shear stress amplitude was checked to ensure that measurements were performed inside the linear viscoelastic domain. The storage modulus (G'), loss modulus (G'') and tan δ (ratio of G'' and G') were monitored automatically against frequency.

The dynamic mechanical thermal properties were measured using a Rheometric Scientific DMTA IV dynamic mechanic thermoanalysis (DMTA) instrument with a dual cantilever testing geometry. Test samples were prepared by injection moulding at 140 °C using a Minimix Molder, obtaining small-sized bars (33 × 8 × 2 mm). Such samples were scanned from −150 °C to 80 °C (heating rate 3 °C min^{-1}, frequency 3 Hz, strain 0.01%).

Results and Discussion

Layered double hydroxide filler characterization

The organo-modified Mg_2Al LDH hybrid materials containing the levorotary form of amino acids: L-histidine (HIS) and L-phenylalanine (PHE) intercalated between metal cation layers were prepared by the co-precipitation method.

The synthesis and characterization of LDH–phenylalanine compounds has already been reported by Aisawa et al. [18]. However, we propose here a different interpretation of the XRD patterns based on a more detailed analysis of the position of the X-ray diffraction peaks and the matching between the surface area per unit charge of LDH host and the organic guest.

Mg_2Al/nitrate, as a reference sample, displays an X-ray diffraction pattern typical of lamellar compounds with a series of strong basal 00*l* reflections at low angles (Figure 1a). In the present case, the reflections are indexed assuming a three-layer 3R polytype with rhombohedral symmetry (space group *R*3*m*), generally observed in LDH systems. The interlayer distance can be determined in a straightforward way from the position of the first (00*l*) reflection indexed as (003), leading here to a value of ≈8.79 Å as expected for a nitrate-containing LDH. The position of the (110) reflection at high angles, near 2θ = 60° for Cu Kα radiation, allows the value of the lattice parameter *a* to be determined since $a = 2d_{110}$. Its value reflects the radii of the cations and the M^{2+}/M^{3+} ratio within the hydroxide layers. The value obtained here is ≈3.03 Å and suggests a Mg^{2+}/Al^{3+} molar ratio slightly lower than 2 [19].

For the synthesis performed in the presence of histidine and phenylalanine, we observed two series of (00*l*) reflections: one attributed to the desired Mg_2Al LDH hybrid phase and the other to a LDH/nitrate phase. In Figure 1, the Miller indices (*hkl*) were assigned to each reflection (assuming 3R polytypes) with positions marked by ticks under the peaks. The presence of this nitrate phase, also evidenced by FTIR analysis (see below), can be explained by either the small excess of the organic anion used during the synthesis or the large excess of nitrate anions in the reaction medium introduced by the reactants in the form of nitrate salts. The diffraction pattern obtained for LDH/HIS is poorly defined with only one (00*l*) reflection visible, from which the interlayer distance was estimated as ≈12.2 Å (Figure 1b). In the case of LDH/PHE, additional (00*l*) reflections are observed and their positions are consistent with an interlayer distance of ≈18.4 Å (Figure 1c). By subtracting both the thickness of the LDH hydroxide layer ≈2.1 Å and the hydrogen bond distances ≈2.7 Å from these interlayer distances, one can estimate the space available for the organic anion along the *c* direction. A value of ≈4.7 Å was thus obtained for LDH/HIS

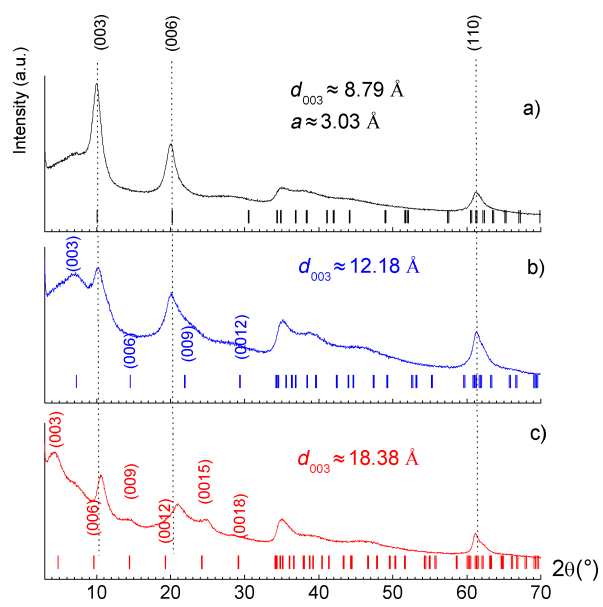

Figure 1: XRD patterns of Mg_2Al hybrids: a) LDH/nitrate, b) LDH/HIS and c) LDH/PHE. The ticks under the peaks give the positions of the Bragg reflections assuming 3R polytypes.

and ≈10.9 Å for LDH/PHE. A comparison with the dimensions of the organic anions (determined using ChemBio 3D ultra 13.0 suite software) leads us to propose a monolayer arrangement for LDH/HIS where the main plane of the molecule is oriented nearly parallel to the hydroxide layer (Figure 2). From the point of charge density, Mg_2Al hydroxide layers display an available surface area per unit charge of ≈24 $Å^2$, a value close to that required by histidine in a parallel orientation (≈26–29 $Å^2/e^-$). This interlayer arrangement suggests an important confinement of histidine molecules between LDH layers. This may explain the presence of co-intercalated nitrate ions, which decreases the constrained accommodation that would have resulted in the close proximity of the HIS molecules to one other.

On the other hand, the interlayer distance in the case of LDH/PHE must arise from a bilayer head-to-tail arrangement in the direction perpendicular to the hydroxide layer (Figure 3). A parallel orientation similar to histidine would require a surface area per unit charge of ≈35 $Å^2$, which is too high compared to the charge density of Mg_2Al host layers, thus supporting the perpendicular orientation. Actually, phenylalanine molecules are likely to be oriented in an inclined manner and partially interpenetrating at the aromatic rings, allowing for the structurally beneficial π–π interaction.

FTIR spectroscopy was applied to confirm the intercalation of HIS and PHE in the hybrid structures. The FTIR spectra of LDH/HIS and LDH/PHE in comparison to pristine amino acids are displayed in Figure 4. The large, broad bands with

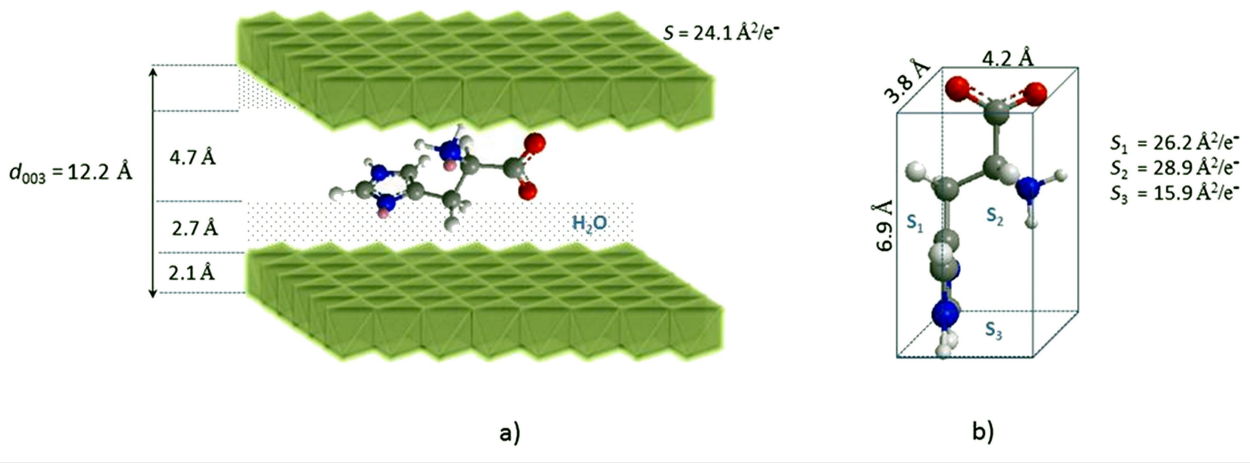

Figure 2: a) Structural model for Mg_2Al/HIS, b) molecular structure of L-histidine, dimensions and corresponding surface area per unit charge calculated by considering a rectangular parallelepiped shape.

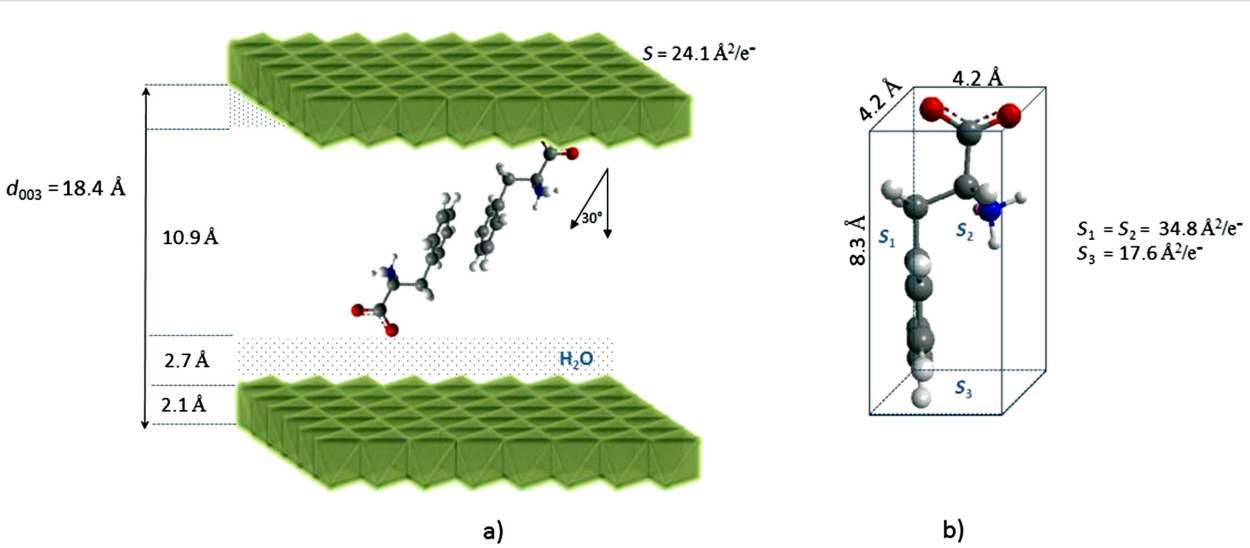

Figure 3: a) Structural model for Mg_2Al/PHE, b) molecular structure of L-phenylalanine, dimensions and surface area per unit charge calculated by considering a rectangular parallelepiped shape.

maximum around 3400 cm^{-1} correspond to the O–H stretching vibrations of the hydroxide layers and water molecules located in the interlayered spaces or physically adsorbed on the surface of hybrids. The typical signals from amide functional groups (N–H, C=O, C–N) overlap in the range of 1700–1480 cm^{-1} and the lattice vibration of M–O in the platelet structure can be depicted at a low wavenumber (800–650 cm^{-1}).

The experimental chemical composition of all synthesized LDHs has been estimated based on TGA analysis and collected in Table 1. All the thermogravimetric curves are shown in the Supporting Information File 1, Figure S1. The thermal decomposition of LDH occurs as a multiple step process. Firstly, the interlayer and surface adsorbed water molecules are removed up to around 200 °C. The weight change from 200–400 °C can be attributed to the removal of hydroxyl group OH^- associated with metal cations Al^{3+} and Mg^{2+}. Finally, the third weigh loss at >400 °C can be observed for the decomposition of amino acid or nitrate anions and the residual mass at 800 °C can be considered as the mass residue of $Mg_2AlO_{7/2}$. Evidently these residual mass losses are not equal because of the difference in molecular weight of the guest organic species as well as the different hydration rate.

The UV-absorbing properties of the LDH structure with amino acids are presented in Figure 5. The nitrate–inorganic derivative, which is used as a reference, presents a typical quite low absorption with a maximum at about 302 nm, coming from the

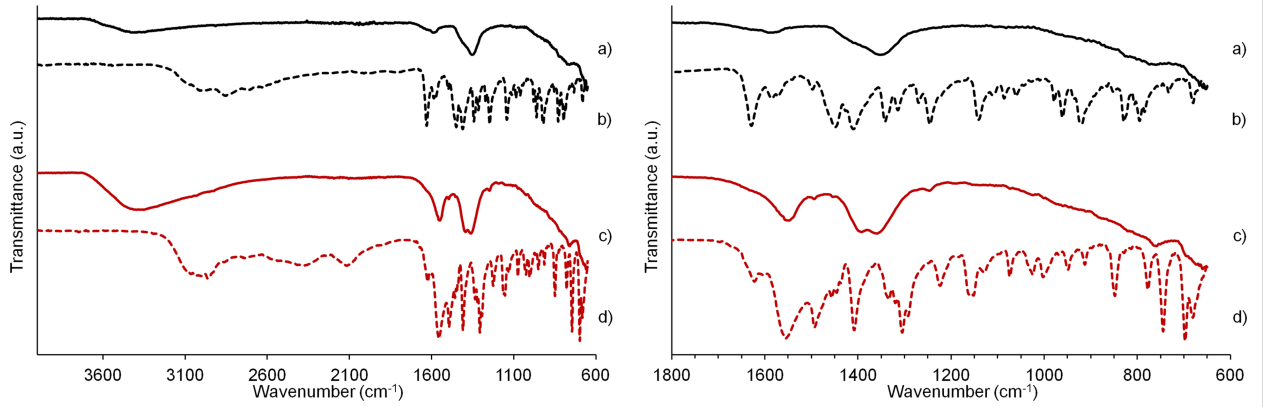

Figure 4: FTIR spectra of organo-modified Mg_2Al hybrids: (a) LDH/HIS, (c) LDH/PHE and pristine amino acids: (b) L-HIS, (d) L-PHE (left side), zoom region on the right side.

Table 1: Experimental chemical compositions of Mg_2Al LDHs.

Code	Experimental chemical composition[a]
LDH/nitrate	$[Mg_2Al(OH)_6](NO_3^-)_{1.0}{\cdot}0.75H_2O$
LDH/HIS	$[Mg_2Al(OH)_6](HIS^-)_{0.35}(NO_3^-)_{0.65}{\cdot}1.14H_2O$
LDH/PHE	$[Mg_2Al(OH)_6](PHE^-)_{0.65}(NO_3^-)_{0.35}{\cdot}2.21H_2O$

[a]Anions and water molecule content determined by TGA under air flow. Mass formulae are: 253.04 g mol^{-1} for Mg_2Al/nitrate, 346.26 g mol^{-1} for Mg_2Al/PHE and 292.4 g mol^{-1} for Mg_2Al/HIS. The procedure and detailed calculations are presented in Supporting Information File 1 and the TGA traces are displayed in Figure S1.

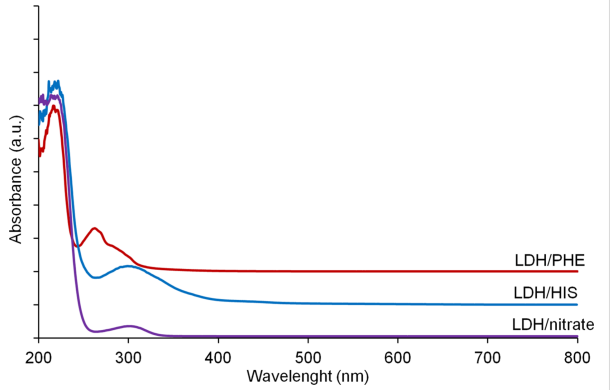

Figure 5: Diffuse reflectance UV–vis spectra (Kubelka–Munk functions) of Mg_2Al LDHs.

presence of nitrate anions in the interlayer space [20]. When PHE is inserted into the LDH inorganic structure, the absorption in the UV domain increases and a hypsochromic shift is observed with a maximum at 262 nm. In the case of LDH/HIS, the absorption is also more intense than for the nitrate reference, but the maximum shifts to 298 nm. As surmised, both cyclic amino acid organo-modified Mg_2Al LDHs should be effective as potential UV stabilizers.

PBS–LDH filler composites – characterization

PBS nanocomposites with 5 wt % of amino-acid-modified Mg_2Al LDHs and Mg_2Al LDH nitrate were prepared by melt extrusion. The XRD patterns are presented in Figure 6 together with PBS without filler as a reference.

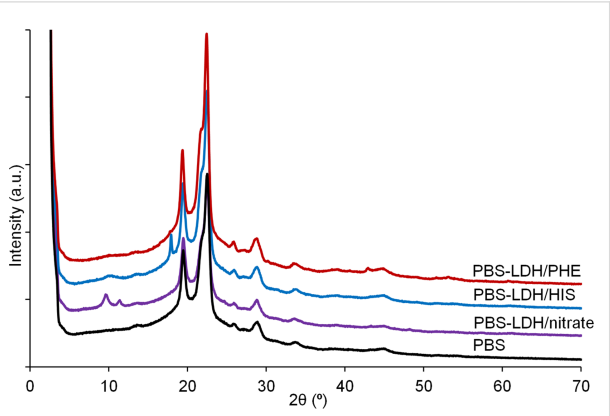

Figure 6: XRD patterns of PBS nanocomposites with 5 wt % Mg_2Al LDH fillers.

The diffraction peaks located at 2θ = 18–30°, which are characteristic for the crystallinity of PBS, seem to not be affected by the addition of the LDH hybrid materials. There is no reflection coming from pristine LDHs modified by amino acids. In contrast, the PBS–LDH nitrate composite exhibits an initial basal spacing of 0.84 nm. In the case of PBS composites with LDH/PHE or LDH/HIS, the absence of harmonic peaks from the layered filler structure can be explained by their lower crystallinity or by a partial exfoliation occurring during thermal processing. For PBS–LDH/HIS, there is an additional peak at 2θ = 18° that is difficult to assign. Its associated small full

width at half maximum (FWHM) may be attributed to rather structurally well ordered organic species. Tentatively it may be ascribed to some degradative effect coming from the imidazole cycle since there is no such effect for the other PBS composites. It is well known that imidazole cycle is prone to coordinate to metal ions as in metallo-proteins [21]. The temperature used during the extrusion may have induced a reaction of HIS weakly tethered onto the LDH platelets surface. Another possibility could be some reaction with PBS chains. However, this can be excluded since the calorimetric properties of PBS are maintained (Table 2).

The introduction of LDH fillers into PBS does not improve the thermal stability of the polymer and the decomposition process proceeds mainly in the range 300–450 °C. The determined T_{onset} and $T^{10}{}_{D}$ (temperature at which the polymer loses 10 wt %) measured for all nanocomposites are consistently lower than for PBS (Table 2). This trend has been previously observed and described in the literature [22,23]. It can be explained by the catalytic effect of Mg and Al ions on the intramolecular and intermolecular transesterifications of PBS and its hydrolysis due to water, which is released during the decomposition of the brucite-type layers. The calculated residual masses correspond with the filler loading. The addition of LDHs does not affect the melting temperature T_m which is quite constant at 115–114 °C. A slight decrease can be observed in the crystallization temperature T_c for nanocomposites with LDH/amino acids, from 85 °C (PBS) to 83 and 82 °C for PBS–LDH/HIS and PBS–LDH/PHE, respectively. Small differences are also observed in T_g, but without a regular trend. However, T_g will be discussed further in the next paragraph, because DMTA is a more sensitive method to detect this. TGA and DSC traces for all nanocomposites are shown in the Supporting Information File 1, Figure S2 and Figure S3.

Chain-extending effect and dynamic mechanical properties

The effect of synthesized amino acid LDH fillers on the chain extending and molecular weight evolution was measured using melt rheology. The rheological data were plotted in Cole–Cole plots – a model curve used to predict the variation in complex viscosity components, where the imaginary viscosity (η") versus real viscosity (η') is plotted as a circle arc in the complex plane. This representation is very helpful in the analysis of polymer and polymer composites [24-26]. By fitting and extrapolation of the Cole–Cole representation to the *x*-axis (η′ at η″ = 0), the Newtonian zero-shear viscosity η_0 can be calculated using Equation 1, which reflects even small changes in molecular mass.

$$\eta_0 \propto M_w{}^a \quad (1)$$

The effect of 5 wt % Mg_2Al LDH filler on the PBS chain extension is presented as η"–η' Cole–Cole plots in Figure 7. The addition of all LDH fillers causes the chain-extending effect associated with the non-miscible structure. The calculated values of the Newtonian zero-shear viscosity for PBS and nanocomposites with LDH/nitrate and LDH/HIS are 90, 274 and 584 Pa s. The best results were obtained for LDH/PHE with a calculated value of η_0 of 7174 Pa s which is almost 80 times higher than for PBS.

The role of layered double hydroxides modified with 3-(4-hydroxyphenyl)propionic acid and amino acids such as tyrosine, tryptophan as PBS chain-extenders has been known and described previously, however the results were not so spectacular [15,17,23]. The significant effect of LDH/PHE most likely results from chemical interaction between tethered amino acid molecules and PBS chains. Counterintuitively, the imidazole ring is found to induce less chain extension ability than the non-polar benzene ring. Indeed the NH functional group that can conjugate is a capto-proton, therefore this function is not suitable to interact strongly with the carbonyl groups present along the aliphatic polyester. The absence in both cases of chemical affinity between the cyclic backbone and the polymer chains suggests that the organic molecules tethered to LDH platelets may have a more jammed effect as evidenced previously [27]. The powdered flake structure of LDH/PHE observed by scanning electron microscopy (SEM) (Supporting Information

Table 2: Thermogravimetric and calorimetric data of PBS nanocomposites with 5 wt % of Mg_2Al LDHs fillers.

Sample	T_{onset} (°C)[a]	$T^{10}{}_{D}$ (°C)[a]	Res mass (%)[a]	T_C (°C)[b]	ΔH_C (J g^{-1})[b]	T_g (°C)[c]	T_m (°C)[c]	ΔH_m (J g^{-1})[c]
PBS	385	362	0.0	85	63	−31	115	47
PBS–LDH/nitrate	360	327	3.3	85	58	−31	115	48
PBS–LDH/HIS	362	347	2.5	83	61	−29	115	53
PBS–LDH/PHE	366	345	1.9	82	55	−33	114	37

[a]Determined by TGA at 10 °C min^{-1} in air. [b]Determined by DSC during the cooling scan from the melt at 10 °C min^{-1}. [c]Determined by DSC during the 2nd heating scan at 10 °C min^{-1}.

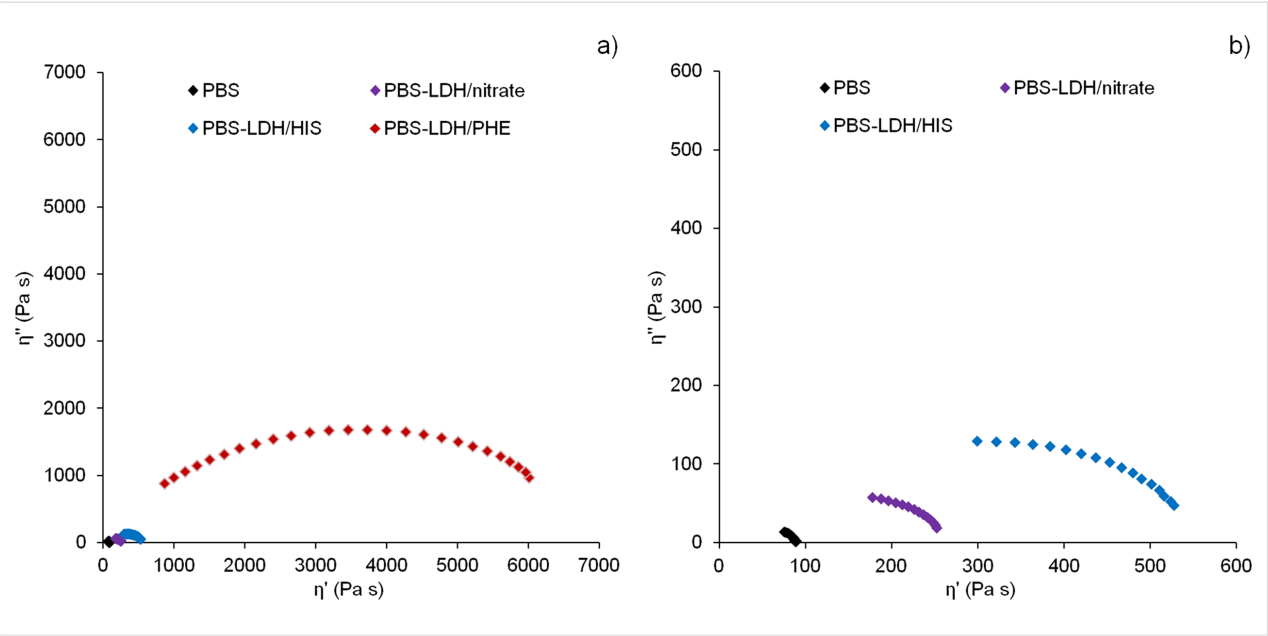

Figure 7: Cole–Cole plots of PBS and PBS nanocomposites with Mg_2Al LDH (a), zoom region (b).

File 1, Figure S4) may also contribute to the strong interaction with PBS chains.

With a value of a = 3.4 in Equation 1, the ratio of apparent molecular weight between the composite with Mg_2Al/PHE and filler-free PBS is of about 400 times (M_w(PBS–Mg_2Al/PHE)/M_w(PBS) = 397, resulting in a similar change in the average repeat units under melt state polymer rheology), thus underlining once again the outstanding effect of the filler in networking PBS chains. This occurs without a transition to a gel-like structure, which would be deleterious for the PBS processability.

Table 3 reports quasi-exhaustive data related to the effect of organo-modified LDHs on the chain extension for PBS nanocomposites. Nano-hybrid fillers (based on Mg_2Al or Zn_2Al LDH cations and with different anions from carboxylic and dicarboxylic acids, ascorbic acid and amino acids) were incorporated to PBS polymer by both methods: in situ polymerization and melt extrusion. Depending on the type of organic molecules, chain extension or plasticizing effects were observed.

In the case of in situ polymerization, an increase in the Newtonian zero-shear viscosity of nearly 20–28 times was observed when LDHs with embedded PBS oligomers were used, whereas the smaller molecules increased η_0 from 40–50 Pa s for unmodified PBS 400, 430, 450 and 790 Pa s for Mg_2Al/HPP, Mg_2Al/stearate, Mg_2Al/TRP and Zn_2Al/HPP, respectively (when used at 2.5–3 wt %).

The effectiveness of the LDHs was lower when they were added to the PBS in the melt extrusion process, most likely because LDH fillers were less dispersed in this case compared to the in situ polymerization approach. The best results were obtained for Zn_2Al/TYR and Zn_2Al/cinnamic LDHs (5 wt %), from 115 to 245 and 360 Pa s respectively, while in other cases the differences were smaller. Our present results are here spectacular, since an increase of 80 times for η_0 is observed, from 90 Pa s (unmodified PBS) up to more than 7,000 Pa s for Mg_2Al/PHE LDH (5 wt %), respectively. Moreover, the PBS nanocomposite composition displays the desired UV-stabilizing effect (described below), which was described previously but only for PBS composites with Zn_2Al/amino acid LDHs [15,31]. This work, however, used a different LDH platelet composition (Zn_2Al) that is known to present some UV screening due to Zn^{2+} cations. However, hydrotalcite-type Mg_2Al (as used in this work) has yet to be investigated.

The temperature and frequency-dependent mechanical relaxation data for the composites were recorded via the storage modulus (E') and tan δ, which is the ratio of the loss modulus to the storage modulus (Figure 8). With respect to PBS, the composites present moderate enhancement in the storage modulus E' over almost the entire temperature range, quantifiable as 6–12% and 17–26% from low temperature (−130 °C) up to RT, respectively. More detailed, at room temperature, the increase in E' is 26% for PBS–LDH/PHE, 20% for PBS–LDH/HIS and 17% for PBS–LDH/nitrate. The larger storage modulus with respect to PBS for such composites indicates a mechanical rein-

Table 3: Polymer processing and Newtonian zero-shear viscosity η_0 for PBS–LDH nanocomposites.

Polymer processing	LDH cations	Interleaved anions[b]	Loading (wt %)	η_0[a] (Pa s)	Ref.
in situ polymerization	Mg_2Al	succinate	3.0	250	[22]
	Mg_2Al	sebacate	3.0	150	
	Mg_2Al	adipate	3.0	–	
	Mg_2Al	lauryl sulfate	3.0	–	
	Mg_2Al	stearate	3.0	430	
	Zn_2Al	stearate	3.0	–	
	Mg_2Al	citric	3.0	55	
	Mg_2Al	ricinoleic	3.0	180	
in situ polymerization	Mg_2Al	PBS oligomer	3.0	1400	[28]
	Zn_2Al	PBS oligomer	3.0	1000	
in situ polymerization	Mg_2Al	HPP	3.0	400	[23]
	Zn_2Al	HPP	3.0	790	
in situ polymerization	Mg_2Al	HPP	2.5	331	[17]
	Mg_2Al	ASA	2.5	255	
	Mg_2Al	TRP	2.5	458	
	Mg_2Al	TYR	2.5	243	
extrusion	Zn_2Al	TRP	5.0	110	[15]
	Zn_2Al	TYR	5.0	245	
extrusion	Zn_2Al	cinnamic	5.0	360	[29]
	Zn_2Al	*p*-hydroxycinnamic	5.0	120	
	Zn_2Al	ferulic	5.0	190	
	Zn_2Al	cafeic	5.0	170	
extrusion	Zn_2Al	$CH_3(CH_2)_{6<n<16}COO^-$ (C8 to C18)	3.0	160 to 220	[30]
extrusion	Zn_2Al	TYR	5.0	171*	[31]
	Zn_2Al	TRP	5.0	179*	
	Zn_2Al	HPP	5.0	138*	
	Zn_2Al	NO_3	5.0	76*	
extrusion	Mg_2Al	HIS	5.0	584*	this article
	Mg_2Al	PHE	5.0	7174*	
	Mg_2Al	NO_3	5.0	274*	

[a]η_0 = 115 Pa s (*90 Pa s) for PBS by extrusion, η_0 = 40–50 Pa s for PBS by in situ polymerization. [b]HPP = 3-(4-hydroxyphenyl)propionic acid, ASA = L-ascorbic; TRP = L-tryptophan, TYR = L-tyrosine, NO_3 = nitrate, HIS = L-histidine, PHE = L-phenylalanine.

forcement of the matrix due to a better interfacial interaction filler/polymer achieved. Such results are consistent with rheology experiments. For all samples, the glass transition temperature is recognized by the large decrease in the storage modulus and by the corresponding peak maximum in tan δ. The values extrapolated (−15 °C for PBS, −10 °C for PBS–LDH/PHE, −9 °C for PBS–LDH/nitrate and PBS–LDH/HIS) highlight a slight increase with respect to the homopolymer, and therefore, the filler can be assumed to affect the mobility of the chains as a nucleating agent.

Photostability of PBS nanocomposites

Because all synthesized LDHs show absorption in the UV range (Figure 5), they should be more or less efficient as UV stabilizers. PBS and PBS nanocomposites with Mg_2Al LDHs were exposed to UV irradiation in an accelerated ageing chamber under aerobic conditions at 60 °C for 100 h. The variation in Newtonian viscosity η_0 as a function of time is presented in Figure 9. The filler-free PBS sample shows UV resistance for the first 60 h, which then begins to degrade fairly quickly. All three examined Mg_2Al samples seem to act as UV stabilizers

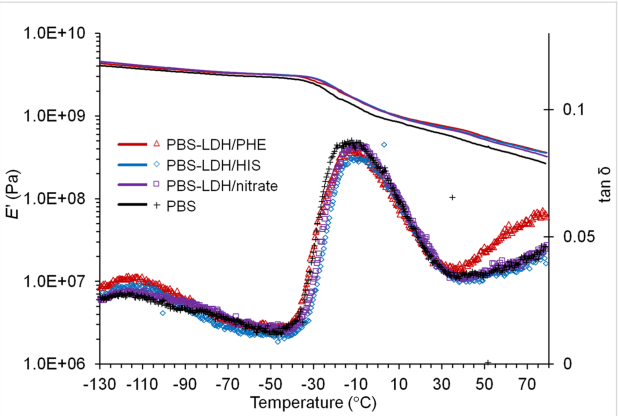

Figure 8: *E*' and tan δ as a function of temperature for PBS and PBS nanocomposites with Mg_2Al LDHs.

for the examined time period and the small fluctuations of composites with LDH/nitrate and LDH/HIS can result from the heterogeneity of the measured samples. In the case of the PBS nanocomposite with LDH/PHE, which shows the highest extending effect, a further increase in the Newtonian viscosity is observed, probably due to crosslinking reactions. The crosslinking phenomenon in the presence of LDH modified with amino acids has been previously observed and is described in the literature with reference to tryptophan [17].

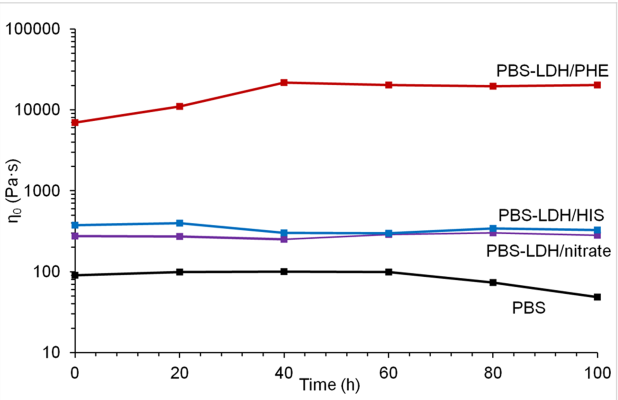

Figure 9: Evolution of zero-shear viscosity (in logarithmic scale) vs time for PBS and PBS nanocomposites with Mg_2Al LDH during photodegradation tests at 60 °C.

Up to now, no satisfactory proof was gathered to understand the better characteristics of PHE. Indeed the low content of organic molecules tethered to LDH (≈2 wt % considering the LDH mass loading and respective to LDH:PHE ration inside the hybrid filler) and the overlap of PBS impede any classical spectroscopic characterization. Nevertheless, considering the tethered molecular backbone of PHE as well as the Cole–Cole response indicative of a chain-extension effect rather than a gel-like transition, this may indicate the presence of a jamming structure due to mobility hindrance of PBS chains as observed for other LDH composites with polystyrene [27] rather that a possible covalent or hydrogen-type bonding between tethered PHE and PBS.

The worst behaviour in terms of UV stability for Mg_2Al/HIS (even if the UV absorption is similar between the two fillers (Figure 5)) may be explained by the strong networking of Mg_2Al/PHE and also to some degradative effects of Mg_2Al/HIS likely due to the presence of impurities (as evidenced by XRD), which may be affected under UV radiation of the polymer chains.

UV–vis transmittance spectra of PBS and the nanocomposites with 5 wt % of Mg_2Al LDHs are presented in Figure 10. The largest decrease in transmittance is observed for PBS–LDH/PHE, then for PBS–LDH/HIS. As mentioned for the hybrid LDH materials, the absorption band can be caused by the cycle phenyl or imidazole acting as a chromophore. Also, PBS with Mg_2Al/nitrate LDH shows lower transmittance, as described above. The evolution of the UV–vis transmittance of PBS and PBS nanocomposites was measured during photodegradation at 60 °C (Supporting Information File 1, Figure S5). The transmittance spectra for PBS are not modified during the entire period of irradiation. In the case of PBS nanocomposites with LDH/nitrate and LDH/HIS, the transmittance decreases during the first 20 h and then stabilizes. When the PBS nanocomposite with LDH/PHE is irradiated, the transmittance decreases during 40 h and then increases. This phenomenon may be caused by the transformation of amino acid molecules in the LDH structure or their interaction with the polymer matrix.

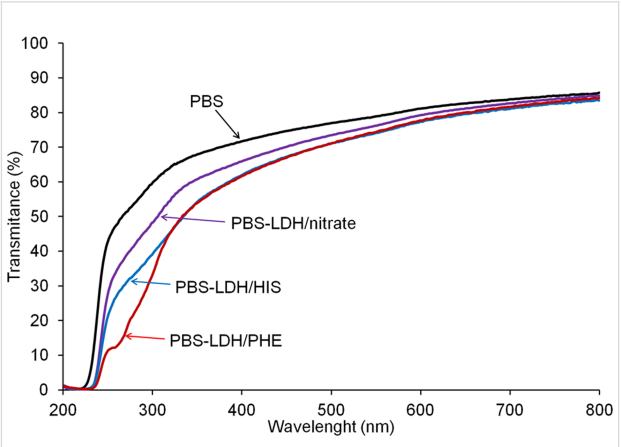

Figure 10: UV–vis transmittance spectra of PBS and PBS nanocomposites with Mg_2Al LDH fillers.

Similar trends have been also registered using fluorescence spectroscopy (Figure 11). The intense emission band centred at

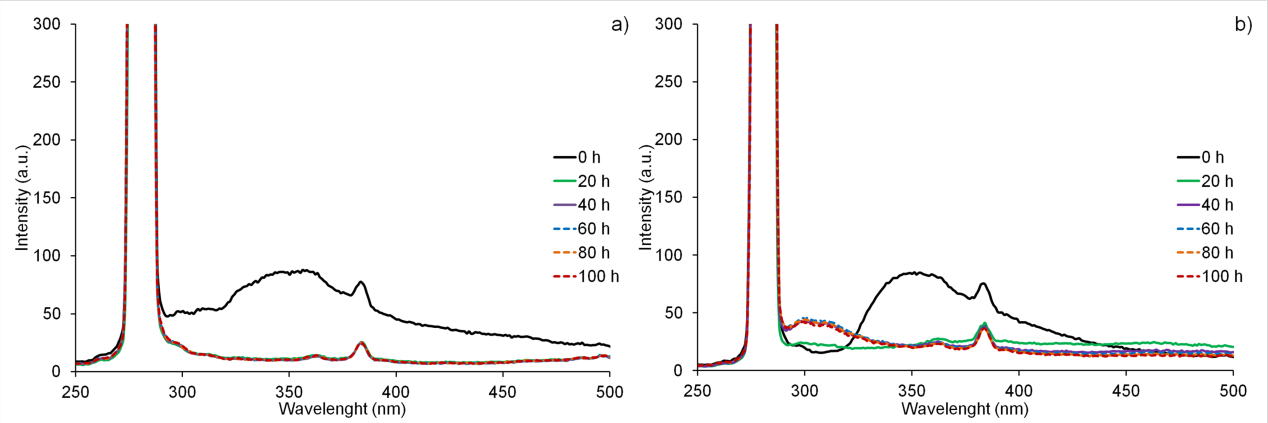

Figure 11: Fluorescence spectra of PBS nanocomposites with Mg_2Al LDH fillers, during photodegradation tests at 60 °C; (a) PBS–LDH/HIS and (b) PBS–LDH/PHE. The excitation wavelength was 280 nm.

350 nm can be observed for interlayered HIS and PHE (the small peak at 382 nm is instrumental noise). This band disappears after 20–40 h, which is in agreement with the decrease in the UV transmittance described above. In the case of the PBS nanocomposite with LDH/PHE, the emission band shifts towards lower wavelengths, at about 300 nm, which is characteristic for pristine amino acid.

A similar phenomenon was observed for the PBS composite with Zn_2Al/TYR LDH and is described in the literature [15]. It can be explained by the delamination of the LDH platelets and the presence of LDH filler in a different environment after UV irradiation.

Conclusion

Two amino acids, L-phenylalanine and L-histidine, have been interleaved into Mg_2Al layered double hydroxides and subsequently dispersed in PBS by melt blending. The XRD analysis indicated the presence of nitrate phase in the LDH structure, which can be explained by the large excess of nitrate anions in the reaction medium during co-precipitation. For this reason, the LDH framework with nitrate anions was also synthesized and applied for PBS as a reference.

The best results were obtained in the case of the LDH/PHE filler. By the use of melt rheology, an outstanding chain-extending effect was observed, with an increase of the Newtonian zero-shear viscosity of almost 90 times in comparison to filler-free PBS samples.

Moreover, the synthesized organo-modified LDHs were found to be effective as UV-stabilizers since they successfully prevent the chain scission reactions which usually occur during photoageing of PBS. Especially in the case of LDH/PHE, the UV-stabilizing effect is quite sustainable over time, thus making such a filler composition a good alternative in the design of polymer composites with these specific properties. These properties are important from the point of view of processability as well as for their prolonged shelf life and extended use.

Supporting Information

Supporting Information File 1

Additional experimental data and experimental schemes.
[https://www.beilstein-journals.org/bjnano/content/supplementary/2190-4286-10-68-S1.pdf]

Acknowledgements

The authors thank CNRS / DIRE for the financial support through the project PREMAT n°116 for research and founding a postdoc position for Adam Marek, and they want also to thank Dr. P. Breuilles, S. Essabaa and S. Guerreiro for their fruitful discussions.

ORCID® iDs

Adam A. Marek - https://orcid.org/0000-0002-1238-4123
Vincent Verney - https://orcid.org/0000-0002-3900-9366
Christine Taviot-Gueho - https://orcid.org/0000-0002-9468-2684
Grazia Totaro - https://orcid.org/0000-0002-7388-8894
Laura Sisti - https://orcid.org/0000-0003-4445-3880
Fabrice Leroux - https://orcid.org/0000-0002-4671-9630

References

1. Hussain, F.; Hojjati, M.; Okamoto, M.; Gorga, R. E. *J. Compos. Mater.* **2006,** *40,* 1511–1575. doi:10.1177/0021998306067321
2. Paul, D. R.; Robeson, L. M. *Polymer* **2008,** *49,* 3187–3204. doi:10.1016/j.polymer.2008.04.017

3. Feldman, D. *J. Macromol. Sci., Part A: Pure Appl. Chem.* **2016,** *53,* 55–62. doi:10.1080/10601325.2016.1110459
4. Zhao, X.; Lv, L.; Pan, B.; Zhang, W.; Zhang, S.; Zhang, Q. *Chem. Eng. J.* **2011,** *170,* 381–394. doi:10.1016/j.cej.2011.02.071
5. Sisti, L.; Totaro, G.; Marchese, P. PBS makes its entrance into the family of biobased plastics. In *Biodegradable and Biobased Polymers for Environmental and Biomedical Applications;* Kalia, S.; Averous, L., Eds.; John Wiley & Sons: Hoboken, NJ, U.S.A., 2016; pp 225–273. doi:10.1002/9781119117360.ch7
6. Li, B.; Wang, Z.-W.; Lin, Q.-B.; Hu, C.-Y. *J. Chromatogr. Sci.* **2016,** *54,* 939–951. doi:10.1093/chromsci/bmw025
7. Di Maio, L.; Scarfato, P.; Milana, M. R.; Feliciani, R.; Denaro, M.; Padula, G.; Incarnato, L. *Packag. Technol. Sci.* **2014,** *27,* 535–547. doi:10.1002/pts.2054
8. Schmidt, B.; Katiyar, V.; Plackett, D.; Larsen, E. H.; Gerds, N.; Koch, C. B.; Petersen, J. H. *Food Addit. Contam., Part A* **2011,** *28,* 956–966. doi:10.1080/19440049.2011.572927
9. Šimon, P.; Chaudhry, Q.; Bakoš, D. J. *J. Food Nutr. Res. (Bratislava, Slovakia)* **2008,** *47,* 105–113.
10. Rives, V.; Angeles Ulibarri, M. *Coord. Chem. Rev.* **1999,** *181,* 61–120. doi:10.1016/s0010-8545(98)00216-1
11. Nalawade, P.; Aware, B.; Kadam, V. J.; Hirlekar, R. *J. Sci. Ind. Res.* **2009,** *68,* 267–272.
12. Taviot-Guého, C.; Prévot, V.; Forano, C.; Renaudin, G.; Mousty, C.; Leroux, F. *Adv. Funct. Mater.* **2018,** *28,* No. 1703868. doi:10.1002/adfm.201703868
13. Del Hoyo, C. *Appl. Clay Sci.* **2007,** *36,* 103–121. doi:10.1016/j.clay.2006.06.010
14. Ghotbi, M. Y.; Hussein, M. Z. b.; Yahaya, A. H.; Rahman, M. Z. A. *J. Phys. Chem. Solids* **2009,** *70,* 948–954. doi:10.1016/j.jpcs.2009.05.007
15. Coelho, C.; Stimpfling, T.; Leroux, F.; Verney, V. *Eur. J. Inorg. Chem.* **2012,** *32,* 5252–5258. doi:10.1002/ejic.201200525
16. Stimpfling, T.; Vialat, P.; Hintze-Bruening, H.; Keil, P.; Shkirskiy, V.; Volovitch, P.; Ogle, K.; Leroux, F. *Eur. J. Inorg. Chem.* **2016,** *2016,* 2006–2016. doi:10.1002/ejic.201501161
17. Totaro, G.; Sisti, L.; Celli, A.; Aloisio, I.; Di Gioia, D.; Marek, A. A.; Verney, V.; Leroux, F. *Dalton Trans.* **2018,** *47,* 3155–3165. doi:10.1039/c7dt03914j
18. Aisawa, S.; Takahashi, S.; Ogasawara, W.; Umetsu, Y.; Narita, E. *J. Solid State Chem.* **2001,** *162,* 52–62. doi:10.1006/jssc.2001.9340
19. Troutier-Thuilliez, A.-L.; Taviot-Guého, C.; Cellier, J.; Hintze-Bruening, H.; Leroux, F. *Prog. Org. Coat.* **2009,** *64,* 182–192. doi:10.1016/j.porgcoat.2008.09.021
20. Tang, X.; Liu, Y.; Li, S. *RSC Adv.* **2016,** *6,* 80501–80510. doi:10.1039/c6ra14671f
21. Holm, R. H.; Kennepohl, P.; Solomon, E. I. *Chem. Rev.* **1996,** *96,* 2239–2314. doi:10.1021/cr9500390
22. Sisti, L.; Totaro, G.; Fiorini, M.; Celli, A.; Coelho, C.; Hennous, M.; Verney, V.; Leroux, F. *J. Appl. Polym. Sci.* **2013,** *130,* 1931–1940. doi:10.1002/app.39387
23. Totaro, G.; Sisti, L.; Celli, A.; Askanian, H.; Hennous, M.; Verney, V.; Leroux, F. *Eur. Polym. J.* **2017,** *94,* 20–32. doi:10.1016/j.eurpolymj.2017.06.031
24. Marek, A. A.; Verney, V. *Eur. Polym. J.* **2015,** *72,* 1–11. doi:10.1016/j.eurpolymj.2015.09.003
25. Friedrich, C.; Braun, H. *Rheol. Acta* **1992,** *31,* 309–322. doi:10.1007/bf00418328
26. Kumar, A.; Commereuc, S.; Verney, V. *Polym. Degrad. Stab.* **2003,** *81,* 333–339. doi:10.1016/s0141-3910(03)00104-6
27. Illaik, A.; Taviot-Guého, C.; Lavis, J.; Commereuc, S.; Verney, V.; Leroux, F. *Chem. Mater.* **2008,** *20,* 4854–4860. doi:10.1021/cm800212g
28. Totaro, G.; Sisti, L.; Celli, A.; Askanian, H.; Verney, V.; Leroux, F. *RSC Adv.* **2016,** *6,* 4780–4791. doi:10.1039/c5ra24031j
29. Coelho, C.; Hennous, M.; Verney, V.; Leroux, F. *RSC Adv.* **2012,** *2,* 5430–5438. doi:10.1039/c2ra20579c
30. Leroux, F.; Dalod, A.; Hennous, M.; Sisti, L.; Totaro, G.; Celli, A.; Coehlo, C.; Verney, V. *Appl. Clay Sci.* **2014,** *100,* 102–111. doi:10.1016/j.clay.2014.05.006
31. Marek, A. A.; Verney, V.; Totaro, G.; Sisti, L.; Celli, A.; Leroux, F. *J. Solid State Chem.* **2018,** *268,* 9–15. doi:10.1016/j.jssc.2018.08.026

License and Terms

BEILSTEIN JOURNAL OF NANOTECHNOLOGY

Towards rare-earth-free white light-emitting diode devices based on the combination of dicyanomethylene and pyranine as organic dyes supported on zinc single-layered hydroxide

Jeff L. Nyalosaso, Rachod Boonsin, Pierre Vialat, Damien Boyer*§, Geneviève Chadeyron, Rachid Mahiou and Fabrice Leroux

Full Research Paper

Open Access

Address:
Université Clermont Auvergne, CNRS, SIGMA Clermont, ICCF, F-63000 Clermont–Ferrand, France

Email:
Damien Boyer* - damien.boyer@sigma-clermont.fr

* Corresponding author
§ Fax: +33 (0)4 73 40 71 08; Tel: +33 (0)4 73 40 71 09

Keywords:
dicyanomethylene (DCM); hybrid luminescent films; light-emitting diode (LED); pyranine; zinc hydroxyacetate

Beilstein J. Nanotechnol. **2019,** *10,* 760–770.
doi:10.3762/bjnano.10.75

Received: 14 August 2018
Accepted: 06 March 2019
Published: 25 March 2019

This article is part of the thematic issue "Advanced hybrid nanomaterials".

Associate Editor: P. Leiderer

Abstract

A new luminescent composite film resulting from the dispersion of luminescent organic dyes in a single-layered hydroxide (SLH)-type inorganic matrix has been developed. Two fluorescent organic dyes emitting visible light upon blue LED excitation were investigated in this study: dicyanomethylene (DCM) and pyranine (HPTS). These dyes exhibit broad emission bands that cover a large part of the visible spectrum. The concept developed in our work consisted in keeping SLH in its wet form to ensure a good dispersion of the fluorescent dyes prior to immobilizing the hybrid materials in a silicone polymer to achieve luminescent composite films. We demonstrate that these coatings stacked upon each other and placed above a blue LED lead to white-light emission with suitable photometric parameters for applications in lighting or display devices: colour temperature of 5409 K and colour rendering index (CRI) of 81.

Introduction

Light-emitting diode (LED) devices are the most developed lighting systems today. 95% of LEDs found on the market generate white light by combining the blue light of a semiconductor diode (GaN or InGaN) with the broad yellow emission of the $Y_3Al_5O_{12}:Ce^{3+}$ (YAG:Ce) phosphor. The use of a phosphor is essential since, to date, no semiconductor diode has been found to emit directly into the white. The system YAG:Ce/blue LED gives a low colour-rendering index (CRI < 80) and a high correlated colour temperature (CCT > 5000 K), which requires the addition of expensive and moisture-sensitive red phosphors (fluoride or nitride) [1]. These phosphors involve rare-earth-doped inorganic phosphors that are extensively used in high-technology devices, LED lighting, mobile phones, flat panel display and wind turbines.

While a series of breakthroughs and advances have been made for efficient blue LEDs, currently the research on white LEDs is mainly focused on the development of rare-earth-free phosphors [2,3]. The worldwide demand for rare-earth elements (REEs), especially within the sectors of renewable energy, military, and consumer electronics, is projected to reach 200.000 tons per year by 2025 while the current annual supply is estimated to be only 113.000 tons. The attempt to increase the REE supply at a rate sufficiently high to meet the increase in demand faces economic, political and environmental limitations [4,5]. Over 95% of the global REE supply comes from China, which also has the largest demand for REEs at 65% of the total demand, even before the United States (15%). In 2010, China announced a 40% reduction in exports of REEs as it wants to reduce stress on its REE reserves. This led to a 600% price increase [6]. Moreover, the cost of a white LED lamp is strongly linked to the price of REEs as the latter represents 12% of the total.

The explosion of demand combined with a monopolistic supply source represents a real risk for the deployment of LED technology in the years to come. Developing rare-earth-free phosphors is therefore a major issue. In this context, it seems crucial to identify new cheap and REE-free phosphors capable of delivering cost-effective light energy conversion.

Luminescent organic dyes are a relevant alternative to REEs. Indeed, they are known to exhibit high luminous efficiency at low cost and may be associated with commercial blue or UV LEDs to generate coloured light and white light. However, most of them exhibit luminescence properties only in liquid solution when any aggregation-induced quenching is prevented. But we have shown recently that the dyes can exhibit fluorescence in the solid state when they are dispersed in an inorganic matrix such as silica [7]. Studies have been carried out on materials obtained by mixing a dye and a double-layered hydroxide solid compound [8-11]. Unfortunately, the optical properties of these materials, particularly their performance, are not yet satisfactory.

For all these reasons, we have studied the development of a rare-earth-free LED device by considering the use of stabilized synthetic organic dyes in an inorganic solid matrix to form a luminescent hybrid material. Some of these hybrid materials consist of a layered inorganic matrix, the role of which is to trap the organic molecules by intercalation so as to preserve their optical properties [10,11]. In the solid matrix the molecule dyes are arranged in the interlayer spaces by monolayer particle assembly and a direct anion-exchange procedure in organic media [12]. Depending on the nature of the layers, one can have structures of one, two or three dimensions [13].

Single-layered hydroxides (SLH), prepared by the polyol method [14,15], are part of the one-dimensional structures. Their general formula is $M(OH)_{2-y}X_y{\cdot}nH_2O$ in which M represents a cation of a divalent transition metal such as Zn^{2+}, Ni^{2+}, Co^{2+} and Cu^{2+} and X represents an interfoliary anion such as acetate or nitrate.

Similar to zinc basic salts, zinc hydroxyacetate $Zn_5(OH)_8(CH_3COO)_2{\cdot}2H_2O$ (Zn-SLH) is a white solid that is suitable for our study. Thanks to its positive lamellar charge, Zn-SLH can serve as a diluting solid allowing for the stabilization of negatively charged molecules or molecules with electron donor sites, i.e., double bonds [11].

The luminescent organic dye is selected so as to ensure good compatibility with the SLH compound and satisfy the synthesis conditions of the latter. It must therefore (i) exhibit negative charges or electron donor sites in order to interact with the positively charged SLH compound; (ii) be water-soluble in the reaction medium (generally water, ethanol or polyol); and (iii) be optically active at basic pH values, for which the formation of the SLH compound is favoured.

Among the organic dyes that meet these criteria, there are xanthene derivatives (fluorescein, rhodamine), acriflavines, arylsulfonates, cyanines and pyrans. Only a few organic dyes can be excited by a blue LED emission centred at 450 nm. Among these dyes, mention can be made of dicyanomethylene and pyranine (Figure 1).

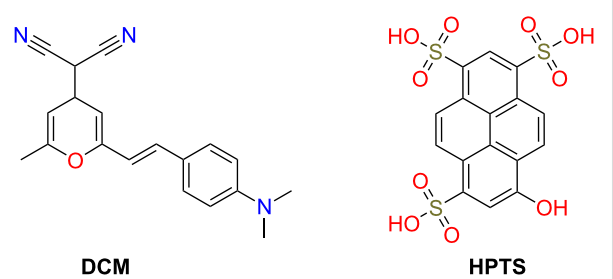

Figure 1: Dye molecules used for the preparation of the organic phosphor film.

Dicyanomethylene (4-(dicyanomethylene)-2-methyl-6-(4-dimethylaminostyryl)-4*H*-pyran, DCM) belongs to the pyran family (heterocycles in which five carbon atoms and one oxygen atom are present in the ring structure) while pyranine (trisodium 8-hydroxypyrene-1,3,6-trisulfonate, HPTS) belongs to the family of arylsulfonates. The first one exhibits, in ethanol solution, red emission with a maximum at 624 nm after excitation at 450 nm and the second one is water-soluble and characterized by a yellow-green emission with a maximum at 533 nm

after excitation at 450 nm. These organic dyes can be combined with the emission of a commercial blue LED (Figure 2a).

The emission spectrum of HPTS ranges from 465 to 625 nm, while that of DCM is wider and extends from 520 to 750 nm. By coupling their spectra with that of a blue LED (λ_{max} = 450 nm), we can expect a wider coverage of the visible spectrum that can generate white light. The combination of these two dyes is therefore of interest for the realization of white LEDs (WLEDs) (Figure 2b).

The chemical bond between these organic dyes and the Zn-SLH matrix should provide a good dispersion of the luminescent material in the silicone matrix while preventing at the same time the organic dyes from aggregation [16]. Indeed, the aggregation of organic molecules leading to the quenching of their fluorescence occurs when the hybrid compound (SLH-Dye) is prepared in the dry solid state. The originality of our preparation process lies in the dispersion of the organic dyes in the SLH matrix in its wet form. The resulting product consisting of dispersed hybrid sheets is then immobilized and dried in a polymer network such as silicone, so as to form a luminescent composite film. Another method reported in the literature to overcome the aggregation-induced quenching mechanism consists in modifying the structure of the organic dyes with units such as tetraphenylethene (TPE) in order to obtain aggregation-induced emission (AIE) mechanism [17].

The structural and morphological properties of Zn-SLH have been studied in order to highlight its lamellar structure. The optical properties of the luminescent wet hybrid materials and films were recorded. Finally, a down-conversion pseudo-white LED was designed by simply associating, in remote-phosphor configuration, silicone/SLH-dye composite film and a GaN LED emitting at 450 nm. Composite films with a single dye, HPTS or DCM, were tested as well as the combination of these two materials. Finally, the photometric parameters of these systems have been investigated under LED excitation.

Results and Discussion

Structural properties of Zn-SLH

The prepared Zn-SLH in the dry state is a white powder which, in a suspension medium, has a filamentous appearance reminding lamellar structures. Scanning electronic microscopy (Figure 3a) reveals that Zn-SLH compounds are aggregated sheets without any defined and regular shape.

Figure 3b shows the powder XRD pattern of the dried Zn-SLH, similar to the one reported by Poul and co-workers [14]. The most intense (001) peak at 2θ = 6.61° corresponds to an interlayer *d*-spacing of 1.33 nm where the intercalation of acetate anions occurs [1]. Such intense (001) reflections are characteristic of a layered structure. The other reflections, *hkl* with *h* or $k \neq 0$, are much weaker and exhibit usual asymmetrical enlargement for disordered pillared compounds [18]. Second-order (002) and third-order (003) peaks correspond to *d*-spacings of 0.68 nm and 0.44 nm, respectively. Moreover, the presence of the (110) diffraction line at 2θ = 59.3° is attributed to OH-edge-sharing platelets based on Zinc cations [18]. The XRD data evidenced the presence of a single phase with the following lattice parameters: *a* = 0.312 nm, *c* = 3.98 nm and *d* = 1.33 nm.

Structures of SLHs have been described by authors such as Rogez and co-workers [18]. The structure derived from botallackite or brucite consists of a quasi-planar triangular array of octahedral divalent metal ions separated by anions, e.g., acetate. Those anions coordinate the metal atoms and water molecules. The intercalation of new guest molecules or ions that substitute the acetate anions located in the interlayer space brings small variations in the molecular area of each metal atom.

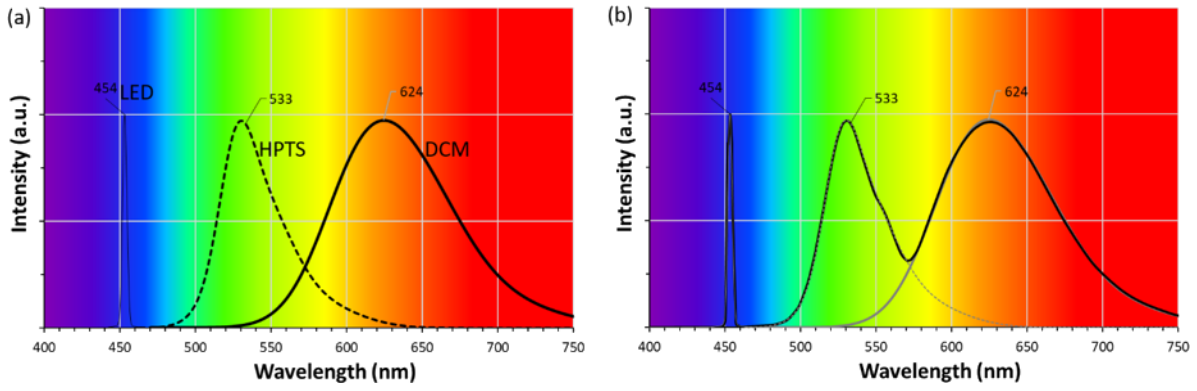

Figure 2: (a) Normalized emission spectra of blue LED light and selected dyes in ethanol solution: DCM and HPTS and (b) their predicted combined spectrum.

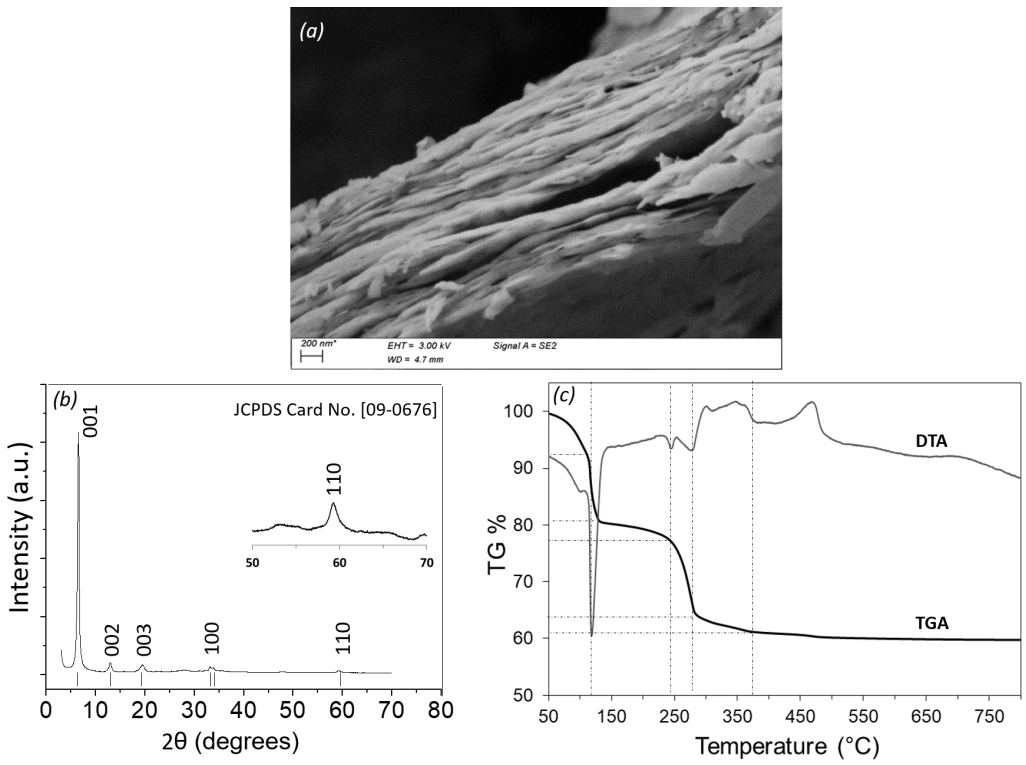

Figure 3: (a) SEM image, (b) XRD pattern and (c) TGA/DTA of zinc hydroxyacetate single-layered hydroxide.

TG-DTA measurements (Figure 3c) carried out on the dried Zn-SLH showed mass losses of 39% upon heating to 800 °C through the decomposition of zinc hydroxyacetate up to the fully inorganic ZnO. The associated thermal events are well documented [19] and correspond to the loss of two water molecules below 100 °C and four additional molecules below 250 °C, together with acetone and CO_2 as well as acetic anhydride to finally form ZnO. The TG-DTA data were used to verify the chemical formula of the compound $Zn_5(OH)_8(CH_3COO)_2{\cdot}nH_2O$. The mass formula at room temperature is related to $M(RT) = 5{\cdot}ZnO/(1 - 0.39)$ leading to 667.29 $g{\cdot}mol^{-1}$ (per 5·Zn) and corresponding to a hydration rate of $n = 4.79$, much higher than the value of 2 that is usually reported. It may be explained by a sample largely hydrated with weakly bonded water molecules as can be inferred from the mass loss between 50 and 100 °C. The theoretical mass loss of $4.79{\cdot}H_2O$ represents 12.92% while the loss of two acetate anions is 17.68%. These values are smaller than the measured mass loss. The mass loss below 150 °C is not only due to the evaporation of water molecules, some dehydroxylation may also occur.

Photoluminescence properties of the integrated dyes

Absolute quantum yield (QY_{ab}) is defined as the efficiency at which a given material re-emits by fluorescence a certain number of photons absorbed at a given wavelength. The parameters measured in a 3.3 inch integrating sphere provide information on the internal conversion (QY_{int}) and the absorbance (Abs) of the studied material. QY_{int} is defined as the ratio between photons emitted and photons absorbed by the material upon external excitation. The product of these two parameters gives the absolute quantum yield in percentage ($QY_{ab} = QY_{int} \times Abs \times 100\%$). Measuring the absolute quantum yield (through the scan mode of the software system) as a function of the excitation wavelength is used to plot the profile $[QY_{ab} = f(\lambda_{ex})]$ from which one can determine at which excitation wavelength the maximum of QY_{ab} occurs. QY_{ab} has a direct impact on the photoluminescence performance of the studied material. A fraction of the excitation light will be absorbed by the dye molecule, internally converted, transferred and emitted at a longer wavelength.

Figure 4 illustrates the recording of the evolution of photoluminescence QY_{ab} as a function of excitation wavelength for each wet luminescent hybrid material (WLHM) and white-emitting hybrid phosphor film (WEHP).

Thus, we have the value of QY_{ab} for a given excitation wavelength, in our case the one of the blue LED (450 nm). It can be seen that the organic dyes begin to be excited significantly at an excitation wavelength of 350 nm (near UV, see photographs of

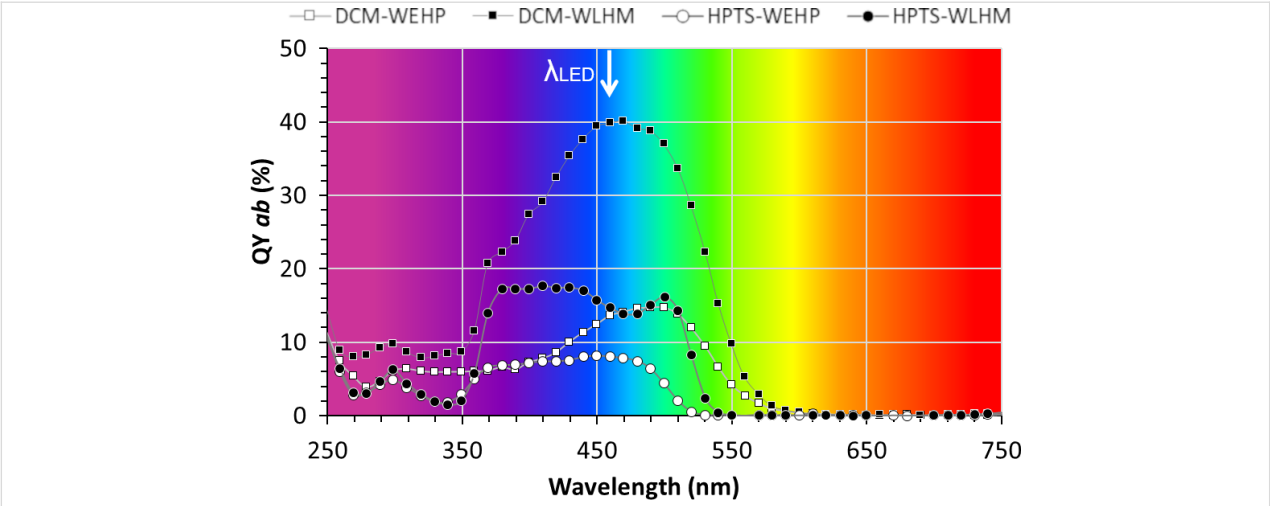

Figure 4: Photoluminescence excitation spectra. Absolute quantum yield (QY_{ab}) as a function of the excitation wavelength for DCM and HPTS in the wet hybrid compounds (WLHM) and in the silicon-based film (WEHP).

the fluorescent WEHP materials under UV light in Figure 5a,b). Then, they reach their maximum QY_{ab} in the region between 370 and 510 nm, mainly in the visible region.

The QY_{ab} of these dyes in both WLHM and WEHP films were measured at the wavelength of interest and the values are given in Table 1. The maximum values of QY_{ab} were measured at λ_{exc} 470 nm and 500 nm for DCM (40.2%) and HPTS (16.2%) dyes in their WLHM form, respectively. By moving from the wet state to the film form, QY_{ab} is reduced by more than 63% and 45% for DCM and HPTS dyes, respectively.

When excited, the organic dyes studied here exhibit strong fluorescence in diluted solution. In our study, these dyes were embedded in the inorganic Zn-SLH matrix in the wet state, before being immobilized in a dried silicone-based film.

It should be noted that the WLHM samples can distort the interpretation of QY_{ab} insofar as a part of dye that is in solution (free dyes existing in the wet compound) would dictate its photoluminescence properties (leading to higher QY_{ab} values), therefore masking those intrinsic to the solid (dyes actually supported on Zn-SLH). The measurements of QY_{ab} on the films are

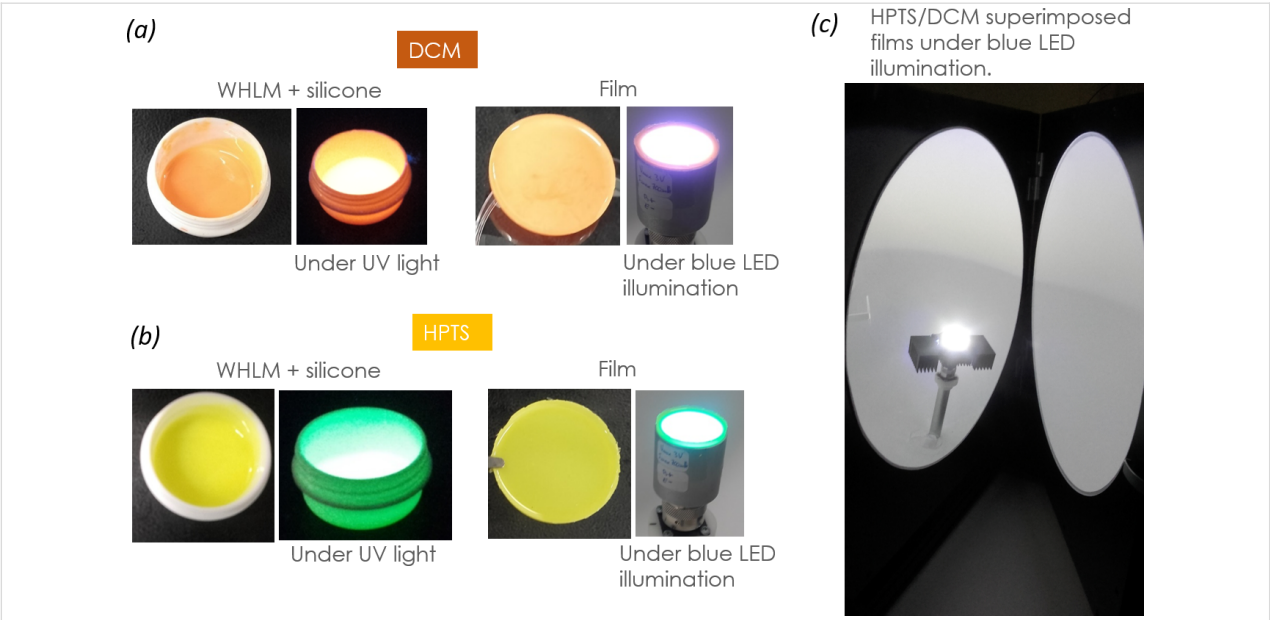

Figure 5: Photographs of (a) DCM- and (b) HPTS-based hybrid materials in the wet mixture containing pre-formed silicon film (with and without UV irradiation) and in the form of the completely formed film (with and without blue-LED illumination). (c) Photo of the two films superimposed (HPTS on DCM) under blue-LED illumination in the opened integrating sphere.

Table 1: Absolute quantum yield (QY_{ab}) values of DCM and HPTS dyes in the WLHMs and in WEHP films, excited at 450 nm. The excitation wavelength values corresponding to the highest values of QY_{ab} of each compound are given.

	DCM	HPTS
QY_{ab} in WLHM (%)	40.0	15.0
QY_{ab} max at λ (nm)	40.2% @ 470 nm	16.2% @ 500 nm
QY_{ab} in silicon film (%)	13.6	8.1
QY_{ab} max at λ (nm)	14.7% @ 500 nm	8.1 @ 450 nm

more representative of the intrinsic properties of supported dyes.

We focused our attention on the value of QY_{ab} at the excitation wavelength of 450 nm in order to assess the fluorescence of the organic dyes when they are placed on the LED that emits at this value. The films displayed QY_{ab} values of 13.6% and 8.1% for DCM and HPTS dyes, respectively. These QY_{ab} values are relatively weak but should be enough to convert a portion of the blue light into white light.

The emission spectra of each WEHP film placed on a 450 nm commercial LED in remote-phosphor configuration are shown in Figure 6. Taken individually, DCM and HPTS dyes have each different profile. We first observed the dominant emission band of the blue LED. Then, in the case of the DCM dye, the emission band, of low intensity, covers a wide visible range from 500 to 750 nm with a maximum at 600 nm (orange). In the case of HPTS dye, the emission band is centred at 517 nm (green).

When the films are stacked upon each other, the corresponding emission spectra represent the emission/excitation/re-emission phenomena between the films. Depending on the stacking order of the films, HPTS above DCM (HPTS/DCM) or DCM above HPTS (DCM/HPTS), the final emission spectra are different.

In the HPTS/DCM/LED configuration, the resulting emission spectrum resembles that of sole DCM but with an increase in the intensity in the wavelength range between 500 and 750 nm. In this configuration, the blue light will first excite the DCM dye-based film. The resulting fluorescence, which covers a wide visible range, will then excite the HPTS dye-based film. In this configuration, all visible colours are emitted relatively evenly.

In the other configuration, DCM/HPTS/LED, the fluorescence resulting from the interaction between the blue light of the LED and the HPTS dye-based film (the emission spectrum of which unevenly covers the visible region) will excite the DCM dye-based film. The resulting emission spectrum strongly resembles that of sole HPTS with a decrease in the contribution of green light.

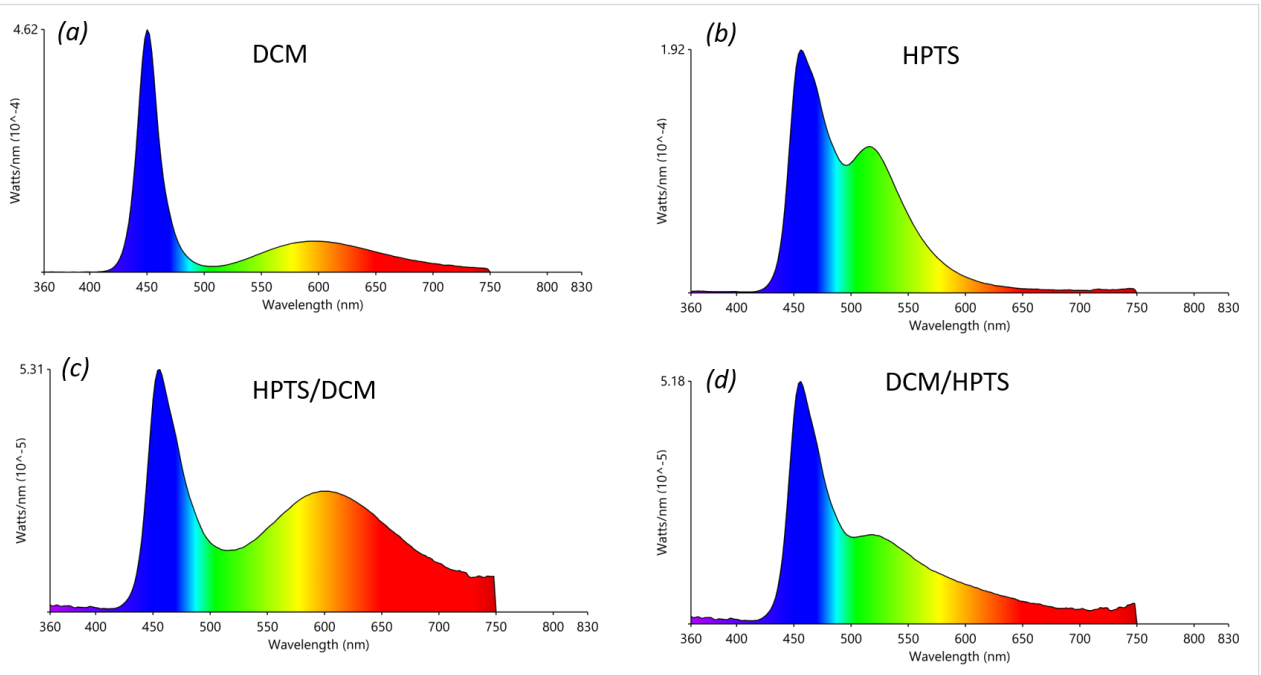

Figure 6: Emission spectra of the silicon films containing: (a) DCM, (b) HPTS, (c) HPTS over DCM and (d) DCM over HPTS; measured under 450 nm LED illumination (440 mA, 3 V). All films were placed in a remote-phosphor configuration at 0.3 cm from the LED chip.

We can otherwise interpret these results by the difference of QY_{ab} between that of the DCM film (14.7%) and that of HPTS (8.1%). It is therefore convenient to excite first the film that exhibits the strongest QY_{ab}.

The normalized two-dimensional colour coordinate systems (chromaticity) of the measured films are shown in Figure 7. The colour points of each film and their superimposition were defined according to the convention of the CIE (Commission Internationale de l'Éclairage, International Commission on Illumination).

The results showed that among all configurations, the HPTS/DCM/LED configuration is the one that yields a satisfactory emission in terms of CIE coordinates (0.33, 0.28). The corresponding colour rendering index (CRI or CIE R_a) rating map, illustrated in Figure 8, showed that, with this configuration, the LED device can render colours with a precision comparable to that of a commercial YAG:Ce-based LED.

The CRI describes how truly the colour of an object is represented by a light source compared to a black-body source. Fifteen standard colour swatches (termed R1 through R15) plus

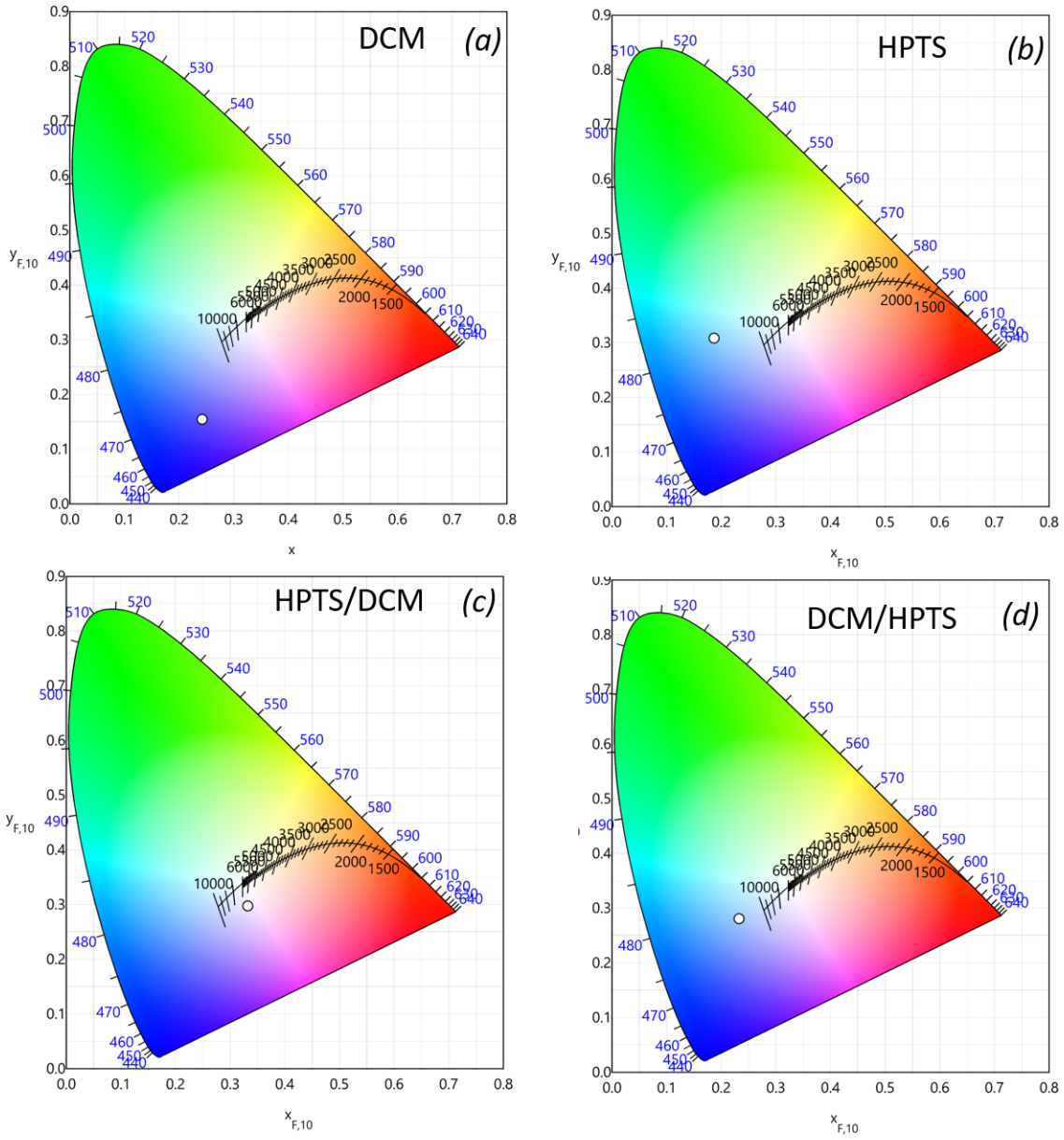

Figure 7: CIE chromaticity diagrams of films containing (a) DCM, (b) HPTS, (c) HPTS over DCM and (d) DCM over HPTS; measured under 450 nm LED illumination (440 mA, 3 V). All films were placed in a remote-phosphor configuration at 0.3 cm from the LED chip.

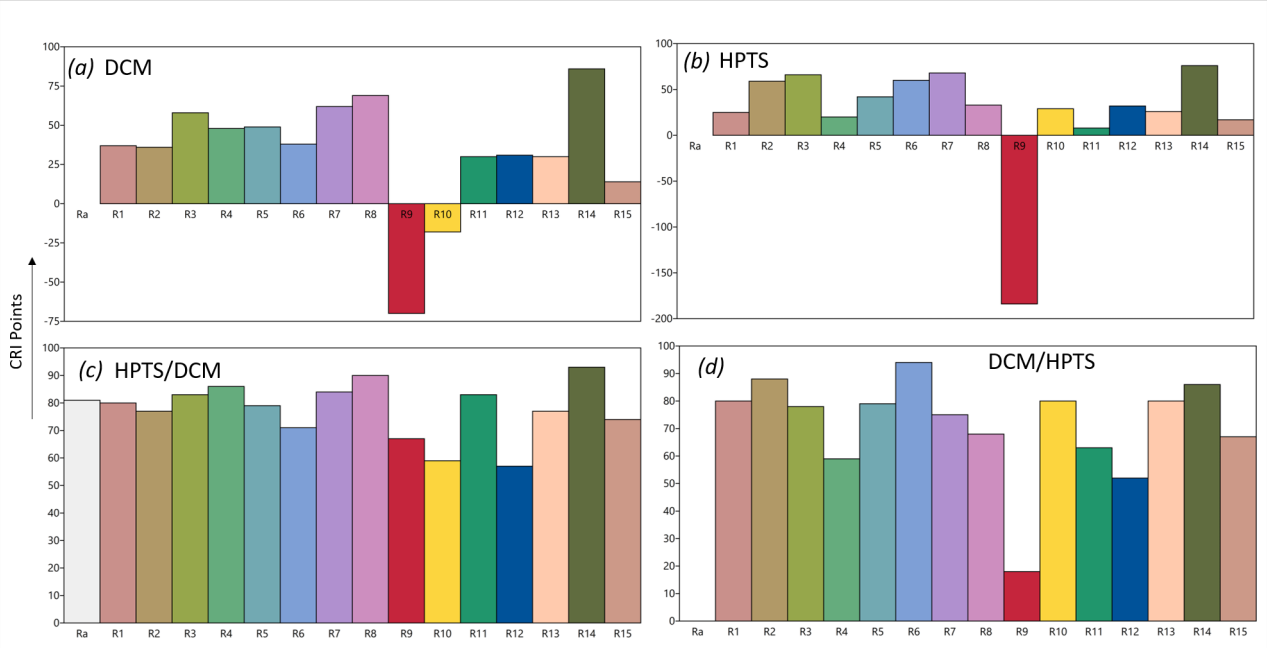

Figure 8: R-values charts for films containing: (a) DCM, (b) HPTS, (c) HPTS over DCM and (d) DCM over HPTS; measured under 450 nm LED illumination (440 mA, 3 V). All the films were placed in a remote-phosphor configuration at 0.3 cm from the LED chip.

the international standard colour rendering index R_a are represented in Figure 8. In the HPTS/DCM/LED configuration, all the colour indices values scored above 70 except R9, R10 and R12, which are assigned to strong saturated hues of red, yellow and blue. In the case of DCM/HPTS/LED configuration, R4 and R9 indices were comparatively low.

Red (R9) is a particularly difficult hue for YAG:Ce-based LEDs to render well. Red light is on the edge of the visible spectrum, where the human eye is less sensitive. A low R9 value leads to a low CRI. In the HPTS/DCM/LED configuration, we got a better CRI rating of 81. Note that a good daylight CRI rating is framed between 60 and 80 and an incandescent light bulb, considered a black-body radiator, exhibits a CRI of 100. Therefore, the HPTS/DCM/LED configuration exhibits a good CRI for lighting and display applications. The eyewitness account of a bright white light emitted by this system, suitable for indoor environments, is shown in the photograph in Figure 5c. In order to be considered as iso-energetic white, a LED device system needs to possess a correlated colour temperature (CCT) in the range of 2700–6000 K and the chromaticity coordinates falling on the black-body curve [20]. The apparent colour of the HPTS/DCM/LED configuration, determined by the CCT, was found to be 5409 K. This is assigned to a cool colour (bluish white) without infrared radiation, comparable to "vertical daylight" or an electronic flash. Table 2 reports all numeral values of photometric parameters for the HPTS/DCM/LED configuration in comparison to the DCM and HPTS films, as well as the DCM/HPTS/LED configuration.

Table 2: The luminous flux (Y2), colour rendering index (CRI), colour fidelity index R_f, colour temperature (CCT), CIE colour coordinates (x,y) and optical efficacy of films based on DCM, HPTS; HPTS over DCM and DCM over HPTS; measured under 450 nm LED illumination (440 mA, 3 V). All the films were placed in a remote-phosphor configuration at 0.3 cm from the LED chip.

		DCM	HPTS	HPTS/DCM	DCM/HPTS
luminous flux Y2 (lm)		3.1	4.1	1.5	1.0
CRI (R_a) [0–100]		33	7.60	81	44
R_f		56	43	72	67
CCT (K)		—	—	5409	—
chromaticity	x	0.25	0.18	0.33	0.23
	y	0.14	0.28	0.28	0.26
optical efficacy (lm/W)		7.6	9.9	3.0	2.0

In the HPTS/DCM/LED configuration, the optical efficiency was measured at 3.0 lm/W, which is very low. It was found to be 34.9 lm/W for the phosphor-free LED and for a LED covered with a dye-free silicone film (silicone/LED). A value of 29.3 lm/W was measured for the LED covered with a silicone film without dye but containing only Zn-SLH (Zn-SLH-silicone/LED). Noted that, good phosphor-based converters have values above 150 lm/W. The reason for the lower values obtained was due to the configuration chosen for our measurements, i.e., the use of a high-output LED.

To sum, except their weak optical efficacy, the HPTS/DCM/LED configuration exhibited photometric parameters comparable to the ones of commercial YAG:Ce white LEDs [21].

Conclusion

We have successfully developed luminescent composite films based on the mixture of a single-layered hydroxide and organic luminescent dyes. The organic dyes dicyanomethylene and pyranine were chosen according to their photoluminescent characteristics, which are excitation with blue light and an emission spectrum covering a wide range of the visible spectrum. The molecules were each dispersed in an inorganic matrix based on zinc hydroxyacetate single-layered hydroxide. In order to ensure good dispersion and avoid aggregation of the organic dyes, a composite preparation approach that kept the composite in its wet form prior to embedding in silicon second matrix was applied. The resulting films exhibit acceptable absolute quantum yields usable in LED devices. These films were placed on a 450 nm commercial LED in a remote-phosphor configuration to determine their photometric characteristics. The best results were obtained with the superposition of the pyranine film over that of dicyanomethylene. Both films were placed in a remote-phosphor configuration on top of a blue LED chip. The photometric parameters measured on this system [(CRI of 81, CCT of 5409 K, CIE coordinate of (0.33, 0.28)] were found to be very interesting for display applications. A bright white emission with cool colour temperature was obtained. Studies of the robustness of these luminescent films are underway with the aim to determine their mechanical and thermal stabilities. Furthermore, the stability of their optical properties will be investigated upon thermal and photonic stresses to demonstrate their ability for future applications.

Experimental

Materials

The hydrated zinc acetate $Zn(CH_3COO)_2{\cdot}2H_2O$ ($ZnAc_2$, 98% purity) was purchased from Alfa Aesar, absolute ethanol (EtOH, 100% purity), sodium hydroxide (NaOH), 4-(dicyanomethylene)-2-methyl-6-(4-dimethylaminostyryl)-4*H*-pyran (DCM, 98% purity) and trisodium 8-hydroxypyrene-1,3,6-trisulfonate (HPTS, 97% purity) were purchased from Sigma-Aldrich. The two-components Bluesil^{TM} RTV 141 A&B as silicon film precursors was purchased from Bluestar Silicones (Elkem France).

Synthesis procedures

Preparation of the zinc single-layered hydroxide (Zn-SLH)

The general procedure involves the dissolution of 50 mmol $ZnAc_2$ in 0.5 L absolute EtOH at 85 °C. After 1 h of agitation, the solution was cooled down to room temperature (RT) [14]. Then 12.22 mol of ultrapure milli-Q water was added to the solution under vigorous agitation. Hydrolysis occurs immediately and a white precipitate is formed progressively. After 1 h of ageing under magnetic stirring, the white product was centrifuged and washed several times with EtOH and stored after removing the supernatant solvent without drying.

A certain amount of the wet product was dried at 40 °C and weighed in order to determine the proportion of the dry extract (DE) to consider for the preparation of the luminescent hybrid material. The dry extract of the prepared Zn-SLH was evaluated at 16 wt %.

Preparation of wet luminescent hybrid materials (WLHM)

DCM and HPTS-containing Zn-SLH were prepared separately by impregnation before mixing the appropriate amount of each compound in the silicon film precursor in order to obtain the luminescent hybrid films.

In the impregnation procedure, each dye powder was previously dissolved in EtOH prior to mixing with the wet Zn-SLH. The composition of each mixture is given in Table 3. 1 wt % of dye in the DE-corresponding Zn-SLH was prepared in 15 mL of EtOH. After 24 h of impregnation under magnetic stirring at RT, the coloured wet mixture was recovered from the clear supernatant by centrifugation.

Table 3: Composition of each WLHM preparation.

	DCM	HPTS
concentration in EtOH (mg/mL)	1	1
wt % in WLHM	1	1
amount of wet HSL-Zn (*g*)	1	0.5
amount of DE HSL-Zn (16 wt % DE, g)	0.16	0.08
amount of dye (mg)	1.6	0.8
volume of dye (µL)	1600	800
total suspension volume adjustment (mL of EtOH)	15	15

Preparation of the white-emitting hybrid phosphor film (WEHP)

Each luminescent film was prepared by mixing the appropriate amount of each WLHM with the silicon polymer precursors, Bluesil^{TM} RTV 141 part A (90 wt %) and part B (10 wt %), with the consideration of their DE counterparts. Each mixture (WLHM and liquid silicon precursors) was prepared in a 3.5 cm diameter petri dish so as to obtain a film of 1.5 g weight and 3 mm thickness after drying in an oven overnight at 65 °C. The composition of WEHP preparation is given in Table 4.

Table 4: Composition of the white-emitting hybrid phosphor film (WEHP) preparation.

WLHM in the film		
	DCM/HSL-Zn	HPTS/HSL-Zn
wt % of DE for 1.5 g film	10%	2%
mass of DE for 1.5 g film (mg)	150	30
mass of WLHM to consider (g)	1	0.2
dye in the film		
	DCM	HPTS
wt % of Dye in the film	0.1	0.02
amount of dye in the film (mg)	0.15	0.03

Characterization methods

The scanning electron microscopy (SEM) images of Zn-SLH powder were taken using a ZEISS Supra 55 FEG-VP instrument at 2MAtech (Clermont-Ferrand, France). The observations were carried out under high vacuum at 3 kV and using an Everhart–Thornley secondary-electron detector. Prior to observation, the sample was attached to adhesive carbon and then coated with Au.

The X-ray diffraction (XRD) pattern of Zn-SLH was recorded with a Philips Xpert Pro diffractometer operating with Cu $K\alpha_1$ radiation (λ = 1.5406 Å) in the $2° < 2\theta < 70°$ range with a scanning speed (2θ) of 0.03°/min.

Thermogravimetry and differential thermal analysis (TG-DTA) experiments were carried out on a SETARAME TG-DTA92 thermogravimetric analyser. The dried Zn-SLH sample was heated in air (25 mL/min) from 25 to 800 °C at a rate of 5 °C/min. The measurements were performed with ca. 15 mg of the sample in an alumina crucible.

Quantum yields (QY) were measured using a C9920-02G PL-QY measurement system from Hamamatsu. The setup consisted of a 150 W monochromatized Xe lamp, an integrating sphere (Spectralon coating, φ = 3.3 inch) and a high-sensitivity CCD camera. Photoluminescence excitation (PLE) spectra were obtained by exciting the composite films from 250 to 500 nm with 5 nm increment and measuring their absolute QY. The absolute photoluminescence (PL) QYs were calculated by combining the QY values with the absorption coefficient (also measured by the apparatus) to plot the excitation spectra.

The main photometric parameters of silicone/HSL-Dye films [photoluminescence (PL), luminous flux, correlated colour temperature (CCT), International Commission on Illumination (CIE) colour coordinates (x,y) and colour rendering Index (CRI)] were measured at room temperature in an integrating sphere with a diode array rapid analyser system (GL Optic integrating sphere GLS 500). In order to carry out the measurements, the film was placed on a 450 nm LED at a distance of 0.3 cm from the chip (OCC-X010S01A Optogan GmbH type, 1000 lm at 1 A, T: 3000–5300 K, Fwd current: 700–2100 mA) so that it completely covers the circular aperture (φ = 2.9 cm) of the cylindrical support of the LED. This set is then placed inside the integrating sphere at the opposite part of the spectrometer. Input current and voltage of 440 mA and 3 V respectively were applied before the measurement.

Acknowledgements

The authors thank the Société d'accélération et de Transfert de Technologie "SATT" for financial support and Anne-Marie Gélinaud (2Matech, Aubière, France) for SEM observations.

ORCID® iDs

Jeff L. Nyalosaso - https://orcid.org/0000-0003-3753-1633
Pierre Vialat - https://orcid.org/0000-0002-9017-9328
Damien Boyer - https://orcid.org/0000-0003-2126-6468
Geneviève Chadeyron - https://orcid.org/0000-0002-8224-8979
Rachid Mahiou - https://orcid.org/0000-0003-2743-7045
Fabrice Leroux - https://orcid.org/0000-0002-4671-9630

References

1. Piquette, A.; Bergbauer, W.; Galler, B.; Mishra, K. C. *ECS J. Solid State Sci. Technol.* **2016,** *5,* R3146–R3159. doi:10.1149/2.0191601jss
2. Wang, M.-S.; Guo, G.-C. *Chem. Commun.* **2016,** *52,* 13194–13204. doi:10.1039/c6cc03184f
3. Mondal, T.; Mondal, S.; Bose, S.; Sengupta, D.; Ghorai, U. K.; Saha, S. K. *J. Mater. Chem. C* **2018,** *6,* 614–621. doi:10.1039/c7tc05215d
4. Moss, R.; Tzimas, E.; Kara, H.; Willis, P.; Kooroshy, J. Critical metals in strategic energy technologies- Assessing Rare Metals as Supply-Chain Bottlenecks in Low-Carbon Energy Technologies. *JRC-scientific and strategic reports;* 2011; JRC6559. doi:10.2790/35716

5. Alonso, E.; Sherman, A. M.; Wallington, T. J.; Everson, M. P.; Field, F. R.; Roth, R.; Kirchain, R. E. *Environ. Sci. Technol.* **2012,** *46,* 3406–3414. doi:10.1021/es203518d
6. Hatch, G. P. *Elements* **2012,** *8,* 341–346. doi:10.2113/gselements.8.5.341
7. Boonsin, R.; Chadeyron, G.; Roblin, J.-P.; Boyer, D.; Mahiou, R. *J. Mater. Chem. C* **2016,** *4,* 6562–6569. doi:10.1039/c6tc01039c
8. Marangoni, R.; Bouhent, M.; Taviot-Guého, C.; Wypych, F.; Leroux, F. *J. Colloid Interface Sci.* **2009,** *333,* 120–127. doi:10.1016/j.jcis.2009.02.001
9. Sun, Z.; Jin, L.; Shi, W.; Wei, M.; Duan, X. *Chem. Eng. J.* **2010,** *161,* 293–300. doi:10.1016/j.cej.2010.04.031
10. Aloisi, G. G.; Costantino, U.; Latterini, L.; Nocchetti, M.; Camino, G.; Frache, A. *J. Phys. Chem. Solids* **2006,** *67,* 909–914. doi:10.1016/j.jpcs.2006.01.003
11. Quites, F. J.; Germino, J. C.; Atvars, T. D. Z. *Colloids Surf., A* **2014,** *459,* 194–201. doi:10.1016/j.colsurfa.2014.07.009
12. Lee, J. H.; Jung, D.-Y.; Kim, E.; Ahn, T. K. *Dalton Trans.* **2014,** *43,* 8543–8548. doi:10.1039/c4dt00692e
13. Langry, A. Evaluation of IN SITU synthesis route of layered hydroxides in the presence of amphiphilic polymers in comparison with their corresponding physical mixtures. Ph.D. Thesis, Université Blaise Pascal, Clermont-Ferrand, France, 2015.
14. Poul, L.; Jouini, N.; Fiévet, F. *Chem. Mater.* **2000,** *12,* 3123–3132. doi:10.1021/cm991179j
15. Poul, L.; Ammar, S.; Jouini, N.; Fievet, F.; Villain, F. *J. Sol-Gel Sci. Technol.* **2003,** *26,* 261–265. doi:10.1023/a:1020763402390
16. Coronado, E.; Galán-Mascarós, J. R.; Gómez-García, C. J.; Laukhin, V. *Nature* **2000,** *408,* 447–449. doi:10.1038/35044035
17. Zhang, Y.; He, B.; Liu, J.; Hu, S.; Pan, L.; Zhao, Z.; Tang, B. Z. *Phys. Chem. Chem. Phys.* **2018,** *20,* 9922–9929. doi:10.1039/c8cp00260f
18. Rogez, G.; Massobrio, C.; Rabu, P.; Drillon, M. *Chem. Soc. Rev.* **2011,** *40,* 1031–1058. doi:10.1039/c0cs00159g
19. Moezzi, A.; McDonagh, A.; Dowd, A.; Cortie, M. *Inorg. Chem.* **2013,** *52,* 95–102. doi:10.1021/ic302328e
20. Bruckbauer, J.; Brasser, C.; Findlay, N. J.; Edwards, P. R.; Wallis, D. J.; Skabara, P. J.; Martin, R. W. *J. Phys. D: Appl. Phys.* **2016,** *49,* 405103. doi:10.1088/0022-3727/49/40/405103
21. Singh, G.; Mehta, D. S. *J. Inf. Disp.* **2014,** *15,* 91–98. doi:10.1080/15980316.2014.903211

License and Terms

The definitive version of this article is the electronic one which can be found at:
doi:10.3762/bjnano.10.75

BEILSTEIN JOURNAL OF NANOTECHNOLOGY

Tailoring the magnetic properties of cobalt ferrite nanoparticles using the polyol process

Malek Bibani[1], Romain Breitwieser[1], Alex Aubert[2], Vincent Loyau[2], Silvana Mercone[3], Souad Ammar[*1] and Fayna Mammeri[*1]

Full Research Paper

Open Access

Address:
[1]Université Paris Diderot, Sorbonne Paris Cité, ITODYS UMR CNRS 7086, [2]ENS Paris Saclay, SATIE UMR CNRS 8029, 61 Avenue du Président Wilson, 94235 Cachan Cedex, France and [3]Université Paris Nord, Sorbonne Paris Cité, LSPM CNRS UPR-3407, 99, Av. J. B. Clément, 93430 Villetaneuse, France

Email:
Souad Ammar[*] - ammarmer@univ-paris-diderot.fr; Fayna Mammeri[*] - fayna.mammeri@univ-paris-diderot.fr

* Corresponding author

Keywords:
cobalt ferrite; magnetocrystalline anisotropy; magnetostriction; nanoparticle; non-stoichiometry; polyol process

Beilstein J. Nanotechnol. **2019,** *10,* 1166–1176.
doi:10.3762/bjnano.10.116

Received: 09 October 2018
Accepted: 09 May 2019
Published: 04 June 2019

This article is part of the thematic issue "Advanced hybrid nanomaterials".

Guest Editor: A. Taubert

Abstract

Background: In extrinsically magnetoelectric materials made of two components, the direct magnetoelectric coupling arises from a mechanical strain transmission at the interface due to the shape change of the magnetostrictive component under an external magnetic field. Here, the size of the interface between the two components plays a crucial role. Therefore, the development of nanomaterials exhibiting large surface-to-volume ratios can help to respond to such a requirement. However, the magnetic nanoparticles (NPs) must be highly magnetostrictive and magnetically blocked at room temperature despite their nanometer-size. We describe here the use of the polyol process to synthesize cobalt ferrite ($Co_xFe_{3-x}O_4$) nanoparticles with controlled size and composition and the study of the relationship between size and composition and the magnetic behavior.

Methods: We used an improved synthesis of magnetostrictive $Co_xFe_{3-x}O_4$ NPs based on the forced hydrolysis of metallic salts in a polyol solvent, varying the fraction x. Stoichiometric NPs ($x = 1$) are expected to be highly magnetostrictive while the sub-stoichiometric NPs (particularly for $x \approx 0.7$) are expected to be less magnetostrictive but to present a higher magnetocrystalline anisotropy constant, as previously observed in bulk cobalt ferrites. To control the size of the NPs, in order to overcome the superparamagnetic limit, as well as their chemical composition, in order to get the desired magnetomechanic properties, we carried out the reactions for two nominal precursor contents ($x = 1$ and 0.67), using two different solvents, i.e., triethylene glycol (TriEG) and tetraethylene glycol (TetEG), and three different durations of refluxing (3, 6 and 15 h). The structure, microstructure and composition of the resulting NPs were then investigated by using X-ray diffraction (XRD), transmission electron microscopy (TEM) and X-ray fluorescence spectroscopy (XRF), respectively. The magnetic properties were also evaluated using standard magnetometry. To measure

the magnetostrictive response of the particles, the particles were sintered to dense pellets on which strain gauges were bonded, measuring the size variation radially, as a function of a dc magnetic field.

Findings: We found two samples, the first one being stoichiometric and magnetostrictive, and the second one being sub-stoichiometric and presenting a higher magnetization, that are appropriate to be used as ferromagnetic building blocks in nanostructured magnetoelectric materials, particularly materials based on polymers. We show that the polyol solvent and the reaction time are two key parameters to control the size and the magnetic properties of the resulting nanoparticles. We believe that these results provide relevant insights to the design of efficient magnetic and magnetostrictive nanoparticles that can be further functionalized by coupling agents, to be contacted with piezoelectric polymers.

Introduction

Recently, extrinsically (or artificially) magnetoelectric (ME) multiferroic (MF) materials have been seriously investigated for many applications in nanoelectronics [1] and energy harvesting [2,3]. They consist of two components, one being ferromagnetic, and the other being ferroelectric. A wide range of inorganic nanostructures, defined by their connectivity, have been prepared using different synthetic approaches. Andrew et al. published a critical viewpoint paper about the current limits of such nanostructures [4]. In these materials, the ME coupling arises from a mechanical transmission of strain originating from the shape change of the magnetostrictive component under an external magnetic field, or of the piezoelectric component under an external electrical field. Thus, the geometry of the connectivity has a huge impact on the ME efficiency and high ME coefficients are expected for extrinsic multiferroics with optimized interfaces. Despites these very enthusiastic theoretical predictions, most of the experimentally measured ME coefficients appear to be significantly smaller. This discrepancy is mainly due to the difficulties in producing hybrid materials with large and perfect interfaces [5]. The use of nanomaterials exhibiting large surface-to-volume ratios instead of bulk materials can help to overcome this limitation. To the best of our knowledge, the best improvements made in this sense were those achieved by Zheng et al., who succeeded in designing self-assembled ferromagnetic $CoFe_2O_4$ nanopillars embedded in a ferroelectric $BaTiO_3$ matrix [6], and by Acevedo et al. and Liu et al., who prepared $CoFe_2O_4$ and $BaTiO_3$ nanoparticles (NPs) separately and co-sintered them very quickly to avoid grain growth and coarsening [7,8]. Andrew et al. also managed to optimize and maximize the hybrid interface in polymer-based multiferroics, using 10 nm magnetic nanoparticles, prepared by coprecipitation and further embedded in ferroelectric polymer fibers, made by electrospinning [9]. Focusing on this latter class of materials, the polymer exhibiting the most interesting ferro- and piezoelectric properties is a semi-crystalline fluoropolymer: poly(vinylidene fluoride) or PVDF. Mixing PVDF with magnetic nanoparticles leads to a higher polymer crystallinity, with NPs acting as nucleating points. Also, as established by Costa et al., the presence of these NPs promotes the crystallization of PVDF in its β-phase, the most electroactive one, instead of its other allotropic forms [10].

Finally, another improvement consists in making the size of the ferromagnetic component as small as possible, while maintaining an efficient strain transmission (an amplitude of ca. 30 ppm is enough for many applications [11]). Currently, the size of such nanoparticles ranges above 30 nm in diameter. Bulk single crystalline cobalt ferrite, for instance, exhibits a magnetostriction amplitude of 590 ppm [12] while its nanoparticle counterparts exhibit an amplitude between 90 and 215 ppm, depending, e.g., on their synthesis conditions and their composition [13,14]. A few years ago, Nlebedim et al. demonstrated the influence of the composition (x) on the magnetocrystalline anisotropy of polycrystalline $Co_xFe_{3-x}O_4$. The anisotropy was found to be the highest for $x = 0.7$ and 0.8 and the lowest for $x = 0.2$. However, the most interesting magnetostriction effects were found at the composition of $x = 1$. Therefore, the stoichiometry appears to be a key-parameter to tailor the magnetostrictive properties of cobalt ferrite materials [15].

Among the several chemical techniques that can be used for synthesizing magnetic metal-oxide NPs (such as thermal decomposition [16], hydrothermal method [17], co-precipitation of precursors [18], combustion reaction [19]), the polyol process has emerged as promising and versatile chemical route for the preparation of highly crystalline, monodisperse particles that are isotropic in shape [20,21]. Polyols act not only of solvents, but also as complexing ligands, avoiding the presence of any surfactant. Hydrolysis ratio, nature of polyol, synthesis temperature and precursor concentration are determining the final products in composition, shape, and size. Cobalt ferrite nanoparticles (NPs) have already been produced by the polyol process in one or in several steps. However, little research has focused on the relationship between the NP size and the magnetic properties and there is no literature at all regarding non-stoichiometric NPs. Artus et al. produced stoichiometric NPs of various sizes (from 2.4 to 6.2 nm) depending on the hydrolysis ratio, starting from iron chloride and cobalt acetate in 1,2-

propane-diol [22]. The blocking temperature (T_B) of the samples was found to be between 141 K (smallest NPs) and 315 K (biggest NPs). Moreover, the biggest NPs exhibited a saturation magnetization very close to that of the bulk (85 emu·g^{-1} vs 90–95 emu·g^{-1}) indicating a very high crystallinity despite the small size of the NPs. Baldi et al. prepared stoichiometric NPs of different sizes, between 5 and 7 nm, in diethylene glycol, starting from iron and cobalt acetates, and using a seed-mediated growth approach [23]. They obtained monodisperse and stable particles, superparamagnetic at room temperature (RT), with, once again, high saturation magnetization values for the largest ones. Hyeon et al. succeeded to produce cobalt ferrite NPs of 12 nm in diameter and evidenced a blocked ferromagnetic behavior for these particles at RT (T_B = 320 K) [24]. They also used an etherdiol solvent as polyol during moderate heating.

Based on these former studies, sizes larger than 10–12 nm are necessary if one wants to obtain blocked cobalt ferrite particles at room temperature (T_B > RT) [25]. At the same time, the size must be as small as possible to extend the hybrid interface in the further nanostructured hybrid ME materials and to optimize the strain transmission as well as the ME coupling.

Here, we aim to control the size of the NPs through the choice of the solvent, triethylene glycol (TriEG) and tetraethylene glycol (TetEG) with different boiling temperatures (T_b = 285 and 325 °C, respectively, for TriEG and TetEG) and through the refluxing time (from 3 to 15 h), assuming that a higher reaction temperature and longer reaction times will yield larger particles. In addition, we will examine different chemical compositions of the particles, i.e., the stoichiometric composition (x = 1) and the non-stoichiometric composition (x = 0.67), expecting a higher magnetostrictive coefficient for the former and a higher magnetocrystalline energy constant for the latter.

Results and Discussion

Structural characterization of the $Co_xFe_{3-x}O_4$ nanoparticles

Nine samples have been prepared. They consist of $Co_xFe_{3-x}O_4$ nanoparticles distributed in two series: six of them are stoichiometric (x = 1) and the three others are sub-stoichiometric in cobalt (x = 0.67). For the first series (x = 1), triethylene glycol (TriEG) and tetraethylene glycol (TetEG) polyol have been used as solvents and the reaction was carried out over three different periods of time (3, 6 and 15 h). For the second series (x = 0.67), two attempts have been made in TriEG for 3 and 6 h, and only one in TetEG for 3 h. The main features of all prepared compositions are collected in Table 1.

We have recorded the X-ray diffraction (XRD) patterns of all cobalt ferrite samples (Figure 1). They are all matching very well with the cubic spinel structure (ICDD no. 98-003-9131). The crystal size of each sample has been estimated through computational Rietveld refinements using MAUD software [26] (Table 1). Then, the compositions have been checked by X-ray fluorescence (XRF) experiments (Figure 2).

The crystal sizes estimated from the XRD patterns are in good agreement with the mean diameters deduced from transmission electron microscopy (TEM) images (Table 1), meaning that the nanoparticles are monocrystalline. The micrographs given in Figure 3 and Figure 4 present the two series of nanoparticles (x = 1 and x = 0.67) as a function of the polyol and as a function of the reaction time. All of them appear to be quite uniform in size since the standard deviations do not exceed 20% of the average diameters. The particle size histograms presented in Figure 3 and Figure 4 have been made applying Sturges' rule [27]. They were then fitted using a log-normal function (Equation 1) and the median diameter D as well as the dispersion σ were determined (see Table 1).

Table 1: Main structural features of the $Co_xFe_{3-x}O_4$ nanoparticles, prepared by the polyol process.

sample	(x)	polyol	reaction time	d (nm) from XRD	d (nm) from TEM	cell parameter (Å) from XRD
Co-1-TriEG-3	1	TriEG	3	7 ± 1	5.6 ± 0.2	8.404 ± 0.002
Co-1-TriEG-6	1	TriEG	6	8 ± 1	6.7 ± 0.2	8.401 ± 0.002
Co-1-TriEG-15	1	TriEG	15	9 ± 1	8.4 ± 0.2	8.402 ± 0.002
Co-1-TetEG-3	1	TetEG	3	8 ± 1	7.8 ± 0.3	8.405 ± 0.002
Co-1-TetEG-6	1	TetEG	6	10 ± 1	9.6 ± 0.2	8.404 ± 0.002
Co-1-TetEG-15[a]	1	TetEG	15	13 ± 1	12.0 ± 0.3	8.399 ± 0.002
Co-0.67-TriEG-3	0.67	TriEG	3	12 ± 1	10.2 ± 0.2	8.397 ± 0.002
Co-0.67-TriEG-6	0.67	TriEG	6	13 ± 1	12.1 ± 0.2	8.397 ± 0.002
Co-0.67-TetEG-3	0.67	TetEG	3	13 ± 1	12.0 ± 0.3	8.398 ± 0.002

[a]Co-1-TetEG-15 shows traces of metallic Co.

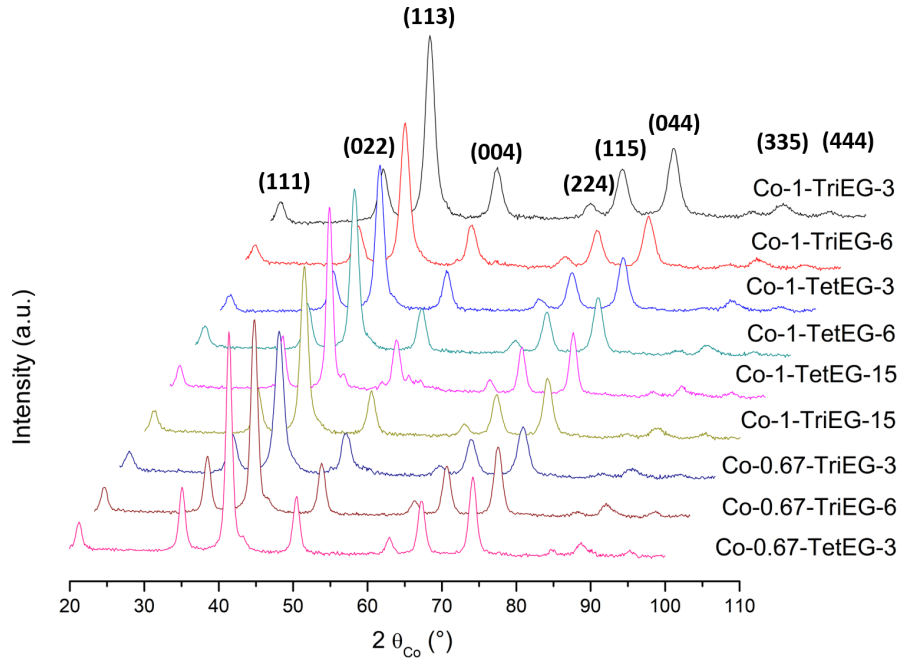

Figure 1: XRD patterns of all the produced $Co_xFe_{3-x}O_4$ powders.

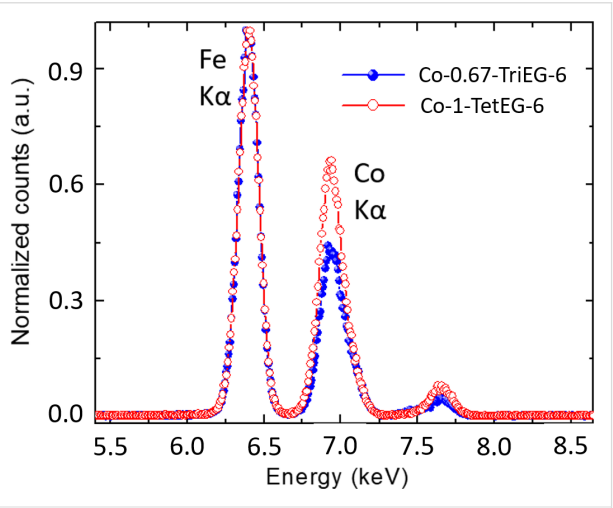

Figure 2: X-ray fluorescence experiments performed on two representative samples, Co-1-TetEG-6 and Co-0.67-TriEG-6.

$$f(D)=\frac{1}{\sqrt{2\pi}\sigma D}\times\exp\left[\frac{\ln^2\left(\frac{D}{D_0}\right)}{2\sigma^2}\right] \quad (1)$$

Then, the mean diameter <*D*> and standard deviation σ_D were calculated (Equation 2 and Equation 3).

$$\langle D\rangle = D_0\times\exp\left(\frac{\sigma^2}{2}\right) \quad (2)$$

$$\sigma_D = \langle D\rangle\times\left[\exp\left(\sigma^2-1\right)\right]^{1/2} \quad (3)$$

Influence of the time of synthesis

The reactions were carried out for different periods of time: 3, 6 and 15 h. Table 1 shows unambiguously that the NP diameter is increasing when the duration of the reaction increases, when the other conditions are the same.

Influence of the solvent

We used two polyols: TriEG and TetEG (Figure 4). The former presents a shorter backbone and a higher dielectric constant ($\varepsilon_{r(TriEG)}$ = 23.7 vs $\varepsilon_{r(TetEG)}$ = 20.4) while the latter exhibits a larger molecular weight and is assumed to be a little more polar (μ_{TetEG} = 5.84 *D* vs μ_{TriEG} = 5.58 *D*) [28]. Regardless of reaction time and composition, we observe that the NP diameter is higher when tetraethylene glycol is used instead of triethylene glycol. Dipolar moment and dielectric constant of the two molecules are very similar and we can assume that they both exhibit the same strength to dissolve the ionic precursors. TetEG has a longer backbone than TriEG and can chelate bigger colloidal species, which may promote the growth better than TriEG. Another parameter may contribute to explain this size difference between the TriEG- and the TetEG-derived particles, i.e., the reaction temperature and the boiling points of the polyols. Indeed, the refluxing temperature was observed to be lower for TriEG but not so much regarding the boiling points of the two polyols. Considering the very probable hypothesis that particle

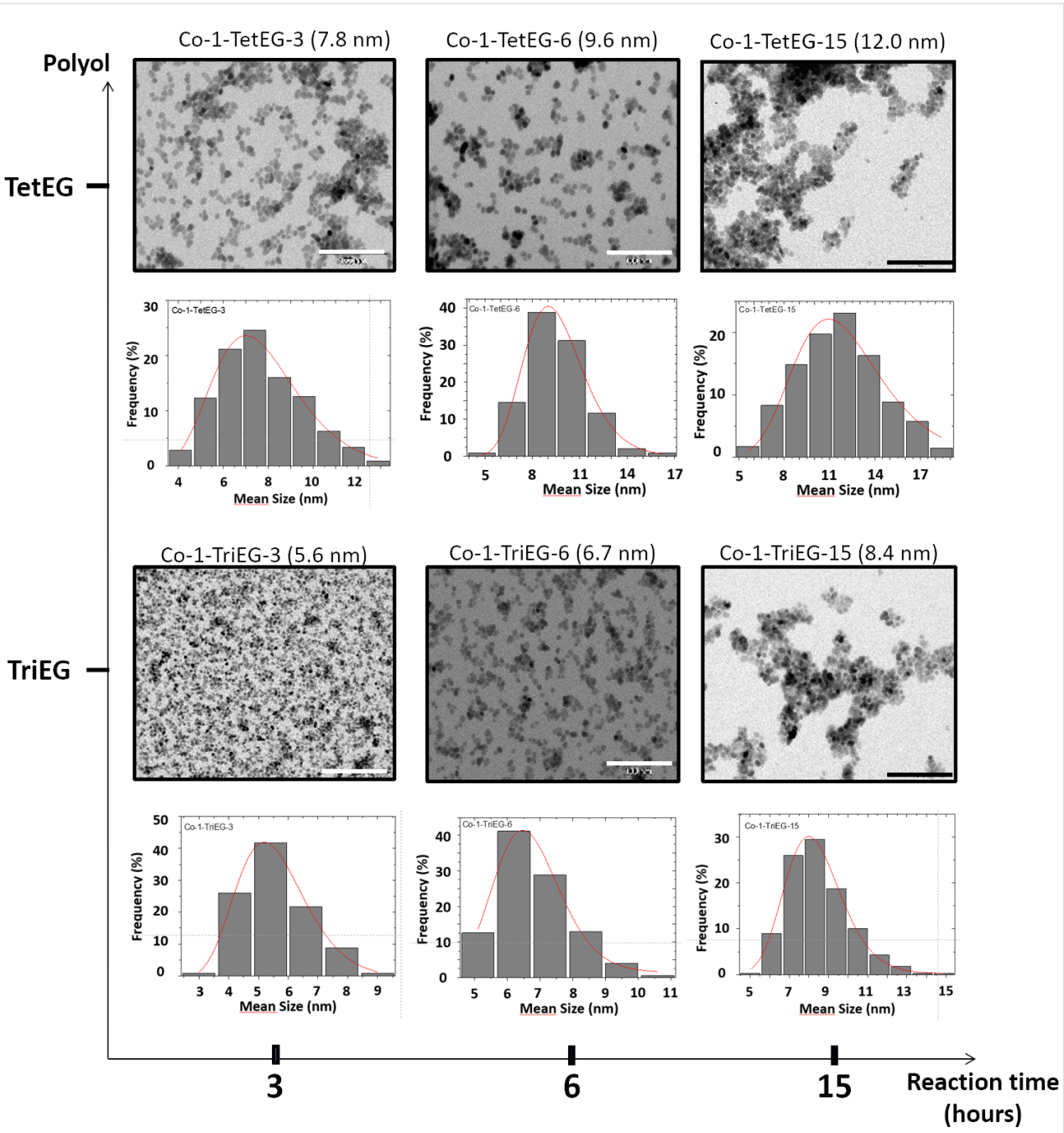

Figure 3: TEM images of $CoFe_2O_4$ NPs as a function of the polyol nature and the reaction time, and the corresponding diameter distributions and log-normal fits. Scale bar = 100 nm.

nucleation proceeds when the boiling temperature of the reaction medium is reached (leading to the lowest viscosity), one can expect the formation of much more nuclei when the reaction temperature is close to the boiling point of the solvent [29]. This was the case when TriEG was used. Thus, the crystal growth by solute diffusion occurred on a larger number of nuclei, leading to a smaller final particle size: In contrast, a smaller number of nuclei was produced in TetEG, since the reaction temperature was considerably lower than the boiling point.

Influence of the starting stoichiometry

Two chemical compositions of $Co_xFe_{3-x}O_4$ NPs have been prepared: $x = 1$ and $x = 0.67$. We observe that, for the same polyol used and the same time of reaction, the sub-stoichiometric nanoparticles are always bigger by at least 5 nm than the stoi-

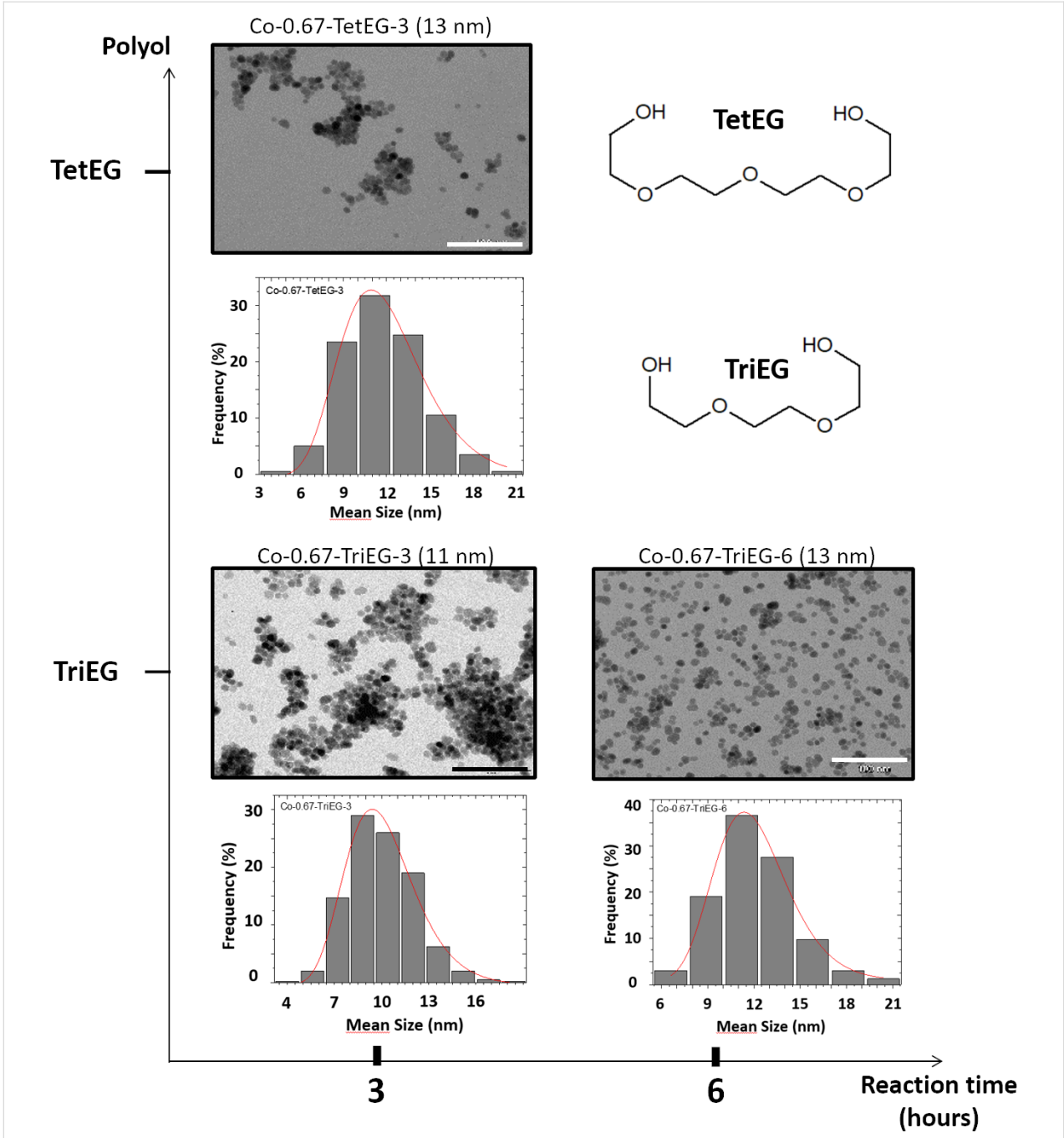

Figure 4: TEM images of $Co_{0.67}Fe_{2.33}O_4$ NPs as a function of the polyol nature and the reaction time, and the corresponding diameter distributions and log-normal fits. Scale bar = 100 nm. The formulas of the polyols are given in the insert.

chiometric ones. The dependence of the NP size on x is still poorly understood, and it would be interesting to investigate it. But at this stage of our study we only noticed it, with the aim of elucidating it in further experiments.

Aggregation

From the XRD and TEM measurements, we have deduced the average diameter of the produced particles, assuming them to be almost spherical single crystals uniform in size. Moreover, from TEM images, we can evaluate the morphology developed by the NPs. In the stoichiometric samples, the nanoparticles obtained after 15 h of reaction are clearly more aggregated than those obtained after 6 h, most likely due to stronger van der Waals and/or magnetostatic interactions between bigger nanoparticles (promoted by the drying of the NPs during the sample preparation for TEM) resulting in the clustering of particles. This ob-

servation has been made after syntheses with TetEG and TriEG, and after drop casting the same quantity of NPs under the same conditions. In the sub-stoichiometric series, Co-0.67-TriEG-3 NPs exhibit the highest degree of aggregation.

Magnetic properties

Standard magnetometry has been carried out on all $Co_xFe_{3-x}O_4$ NPs with a special emphasis on the biggest NPs, for which a blocked ferromagnetic behavior is expected at RT (T_B > RT).

The zero-field-cooled (ZFC) and field-cooled (FC) magnetization as a function of the temperature is shown in Figure 5. In general, the recorded magnetic behavior is that of ferrite particles in their single magnetic domain state. As it is summarized in Table 2, quite all the samples showed very high T_B values (>300 K). The only superparamagnetic nanoparticles at room temperature are the stoichiometric particles synthesized in TriEG for 6 h (Co-1-TriEG-6). In this case, T_B was found to be equal to 275 K; although the saturation magnetization value is pretty good for this composition at the nanoscale level (d = 8 nm), the superparamagnetic behavior observed at room temperature is not suitable for the targeted applications. Interestingly, such high T_B values confirm the high crystalline quality of the produced NPs. We pursued our investigations by plotting the variation of the magnetization of these particles as a function of the magnetic field at RT, typically T = 300 K (Figure 6). Low-temperature (T = 10 K) hysteresis behavior is not reported, as it is comparable to that at the RT; however, the coercive fields that have been measured at this temperature are summarized in Table 2, as well as those obtained at RT.

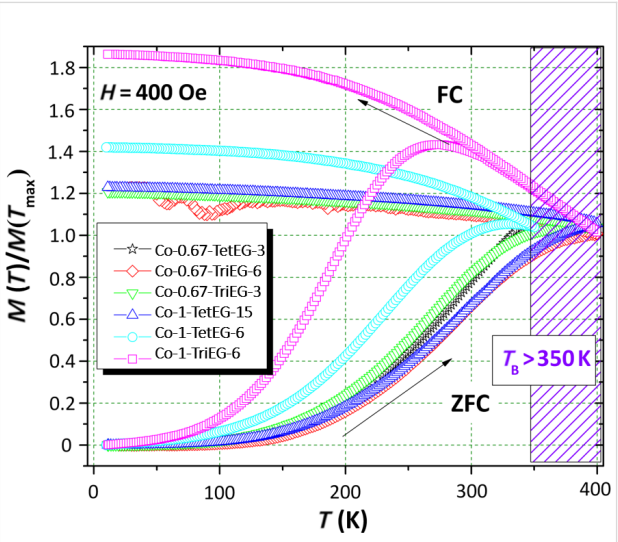

Figure 5: Thermal variation of the normalized DC magnetic magnetization measured in ZFC and FC conditions.

Higher values of coercivity have been observed for NPs synthesized in TetEG. Again, extending the reaction time in TriEG up to 6 h does not yield the high coercivity observed in TetEG at 300 and 10 K. Thus, for equal nanoparticle sizes, equal time of reaction and equal composition, the TetEG solvent seems to optimize the magnetic behavior of the nanopowders in regard to the targeted applications. Additionally, they present saturation magnetization values among the highest that can be found in the literature for this particle size [30,31].

Based on all these structural and magnetic results, we chose to focus on the following two samples: Co-1-TetEG-6 and Co-0.67-TriEG-6. As magnetostriction measurement requires bulk samples, the samples were sintered by using spark plasma sintering. We are aware that the measured magnetostrictive coefficients on the prepared pellets do not correspond exactly to those of the bare particles, but they are quite indicative of the magnetostrictive behavior of the starting powders. Magnetostriction measurements were performed by applying an in-plane external magnetic field (see the Experimental section). The results are presented in Figure 7.

For the Co-0.67-TriEG-6 consolidated derivative, a maximal radial magnetostrictive deformation $(L - L_0)/L_0$ of −76 ppm has been observed for the demagnetized state, when the magnetic field is applied for the first time (L_0 is the initial length of the material with H = 0). After the in-plane saturation of the magne-

Table 2: Blocking temperature (T_B), saturation magnetization (M_S) and coercive field (H_C) of the $Co_xFe_{3-x}O_4$ nanoparticles.

sample	T_B (K)	M_S (emu·g^{-1}) at 300 K	H_C (Oe) at 300 K	H_C (Oe) at 10 K
Co-1-TriEG-6	ca. 275	62	28	690
Co-1-TetEG-6	ca. 330	51	94	10041
Co-1-TetEG-15[a]	>350	67	220	13300
Co-0.67-TriEG-3	>350	71	60	8000
Co-0.67-TriEG-6	>350	77	220	780
Co-0.67-TetEG-3	>350	104	300	13700

[a]Co-1-TetEG-15 shows traces of metallic Co.

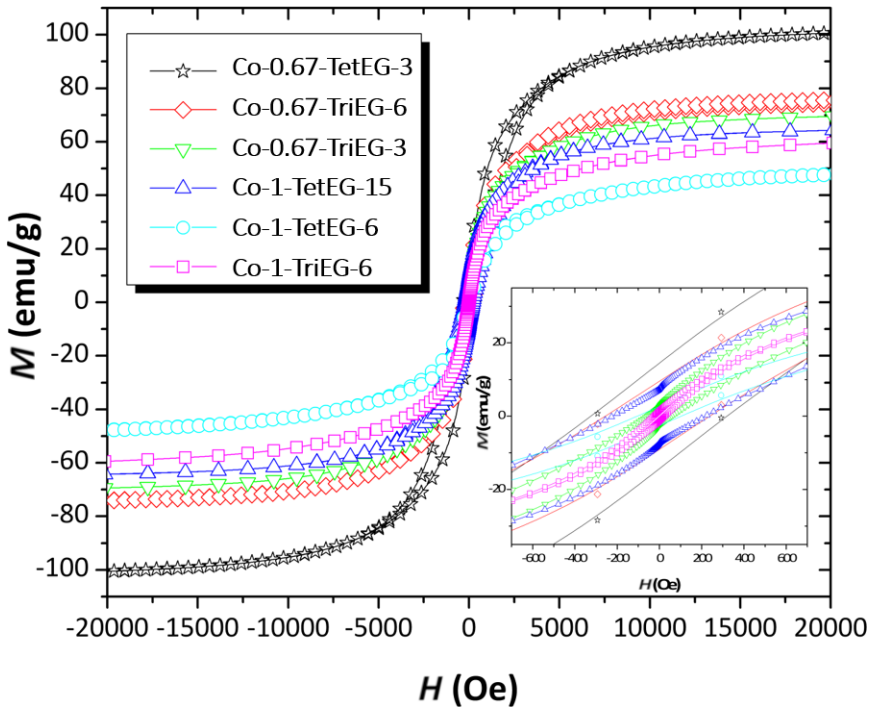

Figure 6: Magnetisation curves of NPs measured at 300 K. Inset: zoom-in of the coercive behavior.

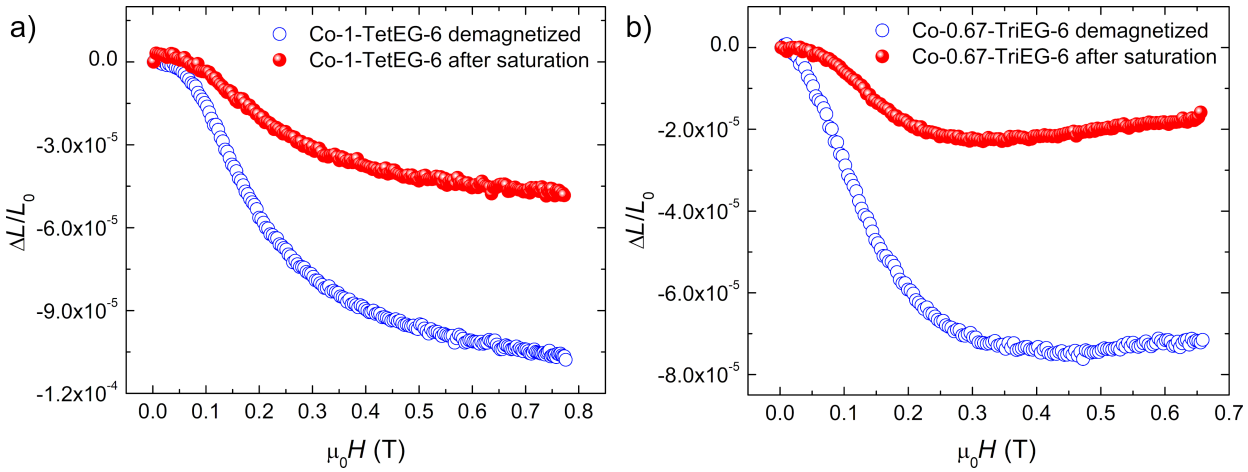

Figure 7: Radial magnetostriction as a function of the applied magnetic field for a) Co-1-TetEG-6 and b) Co-0.67-TriEG-6 consolidated derivatives, with measurements carried out from either the demagnetized (blue circles) or the in-plane saturated (red circles) state.

tization, a second measurement has been carried out showing a $\Delta L/L_0$ coefficient strongly reduced to −23 ppm due to the remanence effect of the magnetization. To recover the magnetostriction measured during the first cycle, it is necessary to preliminary demagnetize the sample or to saturate the magnetization along a transversal direction.

For the Co-1-TetEG-6 consolidated derivative, the highest magnetostrictive coefficient of −106 ppm has been obtained from the demagnetized state while the second cycle of measurements indicated a deformation of −47 ppm. We therefore observed that the magnetic history has similar effects on the magnetostrictive response of both samples. Moreover, reducing the Co amount in the initial powders by ca. 30% leads to a loss of ca. 30% of the magnetostrictive response. Such a result is quite reasonable since the magnetostriction of cobalt ferrites is induced by Co^{2+} ions in octahedral sites and the spin–orbit–lattice interaction with the distorted cubic crystal

field. The other striking conclusion is that the larger deformation of stoichiometric cobalt ferrites nanoparticles under magnetic field makes them more promising to enhance the ME properties of nanomaterials.

Conclusion

We have described here the synthesis procedures of magnetostrictive $Co_xFe_{3-x}O_4$ (x = 1 and x = 0.67) NPs, using the polyol process. The produced NPs have been well characterized using X-ray techniques (diffraction and fluorescence) and transmission electron microscopy. Most of the NPs are above 10 nm in size, magnetically stable and blocked at room temperature (T_B > RT). Moreover, they exhibit saturation magnetization values among the highest presented in literature for their typical size. For the syntheses, we used two different polyol solvents, TriEG and TetEG and carried out the reactions for three different periods of time (3, 6 and 15 h). We could identify two samples, the first one being stoichiometric and the second being sub-stoichiometric, appropriate for the use as ferromagnetic building blocks in nanostructured magnetoelectric materials, particularly polymer-based hybrid materials. We hope this work is providing some insight into the ability to design efficient magnetic and magnetostrictive particles that can be further functionalized by coupling agents such as phosphonic acids to be introduced in polymers [32,33].

Experimental

Synthesis of the nanoparticles

The synthesis of the $Co_xFe_{3-x}O_4$ nanoparticles (NPs) was carried out using the polyol process [22], starting from iron and cobalt acetates, $Fe(CH_3COO)_2$ and $Co(CH_3COO)_2{\cdot}4H_2O$ (Acros and Aldrich, respectively) in two nominal ratios (x = 1 or x = 0.67) [34]. We used two different polyols, TriEG and TetEG. The reaction mixture was heated up to reflux (270 or 290 °C, depending on the solvent) and maintained under reflux for 3, 6 or 15 h to obtain single-phase NPs of various sizes. After being cooled to RT, the black nanoparticle powders were recovered by several centrifugation cycles and washing with acetone. At the end, they were dried overnight in air at 50 °C. Table 1 is collecting all the main features of these samples.

Characterization of the nanoparticles

Structure

The XRD patterns of the recovered powders have been recorded on an X'Pert Pro PANanalytical diffractometer (Co Kα radiation), in the range of 10–100° (2θ) with a scan step of 0.02°. The morphology of the NPs has been determined by TEM observations, using a JEOL-100 CX II microscope operating at 100 kV. The mean diameter and standard deviation were inferred from image analysis of ca. 350–400 particles using ImageJ software and correlated to the microstructural information (mainly crystal size and micro-strain-induced lattice deformation) inferred from Rietveld analysis of the XRD data using MAUD software [26]. The chemical analysis of the particles was checked by XRF, using a Panalytical MINIPAL4 X-ray fluorescence spectrometer, equipped with a rhodium X-ray tube operating at 30 kV and 87 μA current emission. Quantification was determined from pre-plotted calibration curves using standard Co and Fe solutions.

Magnetic properties

Direct-current magnetic measurements were performed using a Quantum Design MPMS 3 superconducting quantum interference device working as a vibrational standard magnetometer. The thermal variation of the magnetic susceptibility $\chi(T)$ were recorded in both ZFC and FC modes, in the temperature range of 10–400 K under a magnetic field of 400 Oe. The magnetization as a function of the magnetic field $M(H)$ was also recorded at low temperature (10 K) and room temperature (300 K) cycling the magnetic field between −70 kOe and +70 kOe. A sampling tube made from a specific pod from Quantum Design has been used to mechanically block the analyzed powders (few milligrams) during the measurements.

Magnetostriction

Selected particles have been first consolidated into dense pellets by using spark plasma sintering, applying a uniaxial pressure of 100 MPa and heating the pressed powder up to 500 °C in a graphite die (more details are given in [35]). Then, a resistive strain gauge (EA-06-062TT-120, Micro-Measurements) was glued (with epoxy resin) on the top face of each polished pellet, to perform extensometry measurements in presence of a longitudinally applied magnetic field H (Figure 8b). The in-plane direction of H has been chosen to avoid demagnetizing field effects occurring in the out-of-plane direction, which is known to affect the ME response. Then, the relative strain $(L - L_0)/L_0$ of each pellet was deduced from the measurement of the resistance relative variation $(R - R_0)/R_0$ of the gauge following: $(L - L_0)/L = (1/K).\ (R - R_0)/R_0$, where K is the gauge factor (K = 2), R_0 = 120 Ω is the initial unstrained resistance of the gauge, and L_0 is the unstrained length of the active part of the gauge. The sample has been placed into an electromagnet, and a magnetic field varying from 0 up to 1 T has been applied. This is sufficient to reach the $Co_xFe_{3-x}O_4$ saturation magnetization (generally, $\mu_0 H_{sat}$ < 0.5 T at RT). In our measurements, $(L - L_0)/L$ coincides with the magnetostriction coefficient λ_{11} because the strain measurement is done along the direction of the applied field H. For magnetoelectric applications, one should note that the transverse magnetostrictive coefficient (λ_{21}) is also of interest. In case of isotropic samples, the transversal coefficient is expected to be half the longitudinal one and opposite in sign [36].

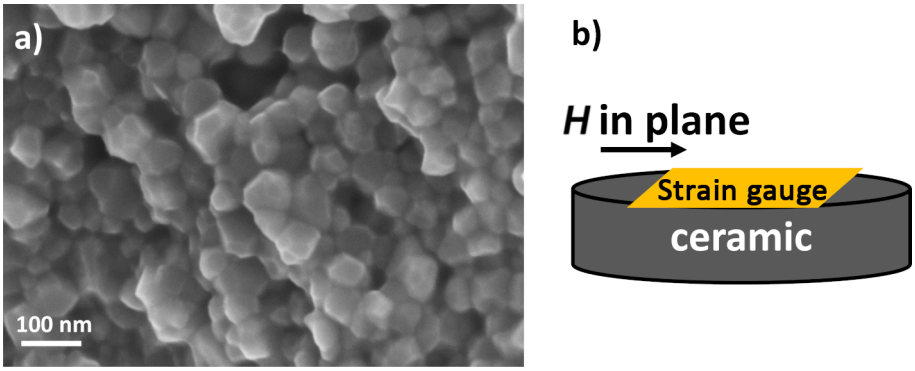

Figure 8: a) Representative scanning electron microscopy (SEM) image of the cobalt ferrite consolidated derivative and b) a schematic illustration of the custom-made magnetostriction measurement setup.

Using this procedure, we have evaluated the magnetostrictive properties of the two most interesting samples, i.e., $Co_{0.67}Fe_{2.33}O_4$, known to exhibit the highest magnetocrystalline anisotropy (Co-0.67-TriEG-6), and $CoFe_2O_4$, known to present the highest magnetostriction (Co-1-TetEG-6).

Acknowledgements

We would like to thank M. Ludovic Mouton and Dr. Sophie Nowak (Université Paris Diderot) for their technical support on TEM and XRF analysis, respectively. We would also like to thank Prof. Frédéric Mazaleyrat (ENS Paris-Saclay) for the fruitful discussions on nanomagnetism. The magnetic measurements performed by Dr. Silvana Mercone at ESPCI have been supported through grants from the Ile-de-France Regional Council. ANR (Agence Nationale de la Recherche) and CGI (Commissariat à l'Investissement d'Avenir) are gratefully acknowledged for their financial support of this work through Labex SEAM (Science and Engineering for Advanced Materials and devices), ANR 11 LBX 086, ANR 11 IDEX 05 02. ANR is also deeply acknowledged for the financial support to MULTIFERROFLEX Young Researcher project (ANR-14-CE08-0005-01) attributed to FM.

ORCID® iDs

Malek Bibani - https://orcid.org/0000-0002-0950-0875
Alex Aubert - https://orcid.org/0000-0002-0816-4566
Silvana Mercone - https://orcid.org/0000-0002-5790-1032
Souad Ammar - https://orcid.org/0000-0002-1656-0016

References

1. Chu, Y.-H.; Martin, L. W.; Holcomb, M. B.; Gajek, M.; Han, S.-J.; He, Q.; Balke, N.; Yang, C.-H.; Lee, D.; Hu, W.; Zhan, Q.; Yang, P.-L.; Fraile-Rodríguez, A.; Scholl, A.; Wang, S. X.; Ramesh, R. *Nat. Mater.* **2008,** *7,* 478–482. doi:10.1038/nmat2184
2. Wan, C.; Bowen, C. R. *J. Mater. Chem. A* **2017,** *5,* 3091–3128. doi:10.1039/c6ta09590a
3. Onuta, T.-D.; Wang, Y.; Long, C. J.; Takeuchi, I. *Appl. Phys. Lett.* **2011,** *99,* 203506. doi:10.1063/1.3662037
4. Andrew, J. S.; Starr, J. D.; Budi, M. A. K. *Scr. Mater.* **2014,** *74,* 38–43. doi:10.1016/j.scriptamat.2013.09.023
5. Liu, R.; Zhao, Y.; Huang, R.; Zhao, Y.; Zhou, H. *J. Mater. Chem.* **2010,** *20,* 10665–10670. doi:10.1039/c0jm02602f
6. Zheng, H.; Wang, J.; Lofland, S.; Ma, Z.; Mohaddes-Ardabili, L.; Zhao, T.; Salamanca-Riba, L.; Shinde, S.; Ogale, S.; Bai, F.; Viehland, D.; Jia, Y.; Schlom, D.; Wuttig, M.; Roytburd, A.; Ramesh, R. *Science* **2004,** *303,* 661–663. doi:10.1126/science.1094207
7. Acevedo, U.; Lopez-Noda, R.; Breitwieser, R.; Calderon, F.; Ammar, S.; Valenzuela, R. *AIP Adv.* **2017,** *7,* 055813. doi:10.1063/1.4974493
8. Liu, Y.; Xu, G.; Xie, Y.; Lv, H.; Huang, C.; Chen, Y.; Tong, Z.; Shi, J.; Xiong, R. *Ceram. Int.* **2018,** *44,* 9649–9655. doi:10.1016/j.ceramint.2018.02.192
9. Andrew, J. S.; Clarke, D. R. *Langmuir* **2008,** *24,* 8435–8438. doi:10.1021/la801617q
10. Martins, P.; Costa, C. M.; Benelmekki, M.; Botelho, G.; Lanceros-Méndez, S. *J. Mater. Sci.* **2013,** *48,* 2681–2689. doi:10.1007/s10853-012-7063-1
11. Affanni, A.; Guerra, A.; Dallagiovanna, L.; Chiorboli, G. Design and characterization of magnetostrictive linear displacement sensors. In *Proceedings of the 21st IEEE Instrumentation and Measurement Technology Conference (IEEE Cat. No.04CH37510),* IEEE Publishing: Piscataway, NJ, U.S.A., 2004; pp 206–209. doi:10.1109/imtc.2004.1351029
12. Bozorth, R. M.; Tilden, E. F.; Williams, A. J. *Phys. Rev.* **1955,** *99,* 1788–1798. doi:10.1103/physrev.99.1788
13. Nlebedim, I. C.; Ranvah, N.; Williams, P. I.; Melikhov, Y.; Snyder, J. E.; Moses, A. J.; Jiles, D. C. *J. Magn. Magn. Mater.* **2010,** *322,* 1929–1933. doi:10.1016/j.jmmm.2010.01.009
14. Nlebedim, I. C.; Snyder, J. E.; Moses, A. J.; Jiles, D. C. *J. Magn. Magn. Mater.* **2010,** *322,* 3938–3942. doi:10.1016/j.jmmm.2010.08.026
15. Nlebedim, I. C.; Snyder, J. E.; Moses, A. J.; Jiles, D. C. *IEEE Trans. Magn.* **2012,** *48,* 3084–3087. doi:10.1109/tmag.2012.2200884
16. Herrera, A. P.; Polo-Corrales, L.; Chavez, E.; Cabarcas-Bolivar, J.; Uwakweh, O. N. C.; Rinaldi, C. *J. Magn. Magn. Mater.* **2013,** *328,* 41–52. doi:10.1016/j.jmmm.2012.09.069

17. Repko, A.; Vejpravová, J.; Vacková, T.; Zákutná, D.; Nižňanský, D. *J. Magn. Magn. Mater.* **2015,** *390,* 142–151. doi:10.1016/j.jmmm.2015.04.090
18. Soler, M. A. G.; Lima, E. C. D.; da Silva, S. W.; Melo, T. F. O.; Pimenta, A. C. M.; Sinnecker, J. P.; Azevedo, R. B.; Garg, V. K.; Oliveira, A. C.; Novak, M. A.; Morais, P. C. *Langmuir* **2007,** *23,* 9611–9617. doi:10.1021/la701358g
19. Nakagomi, F.; da Silva, S. W.; Garg, V. K.; Oliveira, A. C.; Morais, P. C.; Franco Júnior, A.; Lima, E. C. D. *J. Appl. Phys.* **2007,** *101,* 09M514. doi:10.1063/1.2712821
20. Ammar, S.; Helfen, A.; Jouini, N.; Fiévet, F.; Rosenman, I.; Villain, F.; Molinié, P.; Danot, M. *J. Mater. Chem.* **2001,** *11,* 186–192. doi:10.1039/b003193n
21. Mammeri, F.; Mamèche, F.; Kataya, Z.; Yaacoub, N.; Slawska-Waniewska, A.; Menguy, N.; Grenèche, J.-M.; Ammar, S. *MRS Online Proc. Libr.* **2011,** *1359,* No. mrss11-1359-nn08-07. doi:10.1557/opl.2011.883
22. Artus, M.; Ben Tahar, L.; Herbst, F.; Smiri, L.; Villain, F.; Yaacoub, N.; Grenèche, J.-M.; Ammar, S.; Fiévet, F. *J. Phys.: Condens. Matter* **2011,** *23,* 506001. doi:10.1088/0953-8984/23/50/506001
23. Baldi, G.; Bonacchi, D.; Innocenti, C.; Lorenzi, G.; Sangregorio, C. *J. Magn. Magn. Mater.* **2007,** *311,* 10–16. doi:10.1016/j.jmmm.2006.11.157
24. Hyeon, T. *Chem. Commun.* **2003,** *8,* 927–934. doi:10.1039/b207789b
25. Dai, Q.; Nelson, A. *Chem. Soc. Rev.* **2010,** *39,* 4057–4066. doi:10.1039/b812669k
26. Lutterotti, L.; Matthies, S.; Wenk, H. R. *IUCr: Newsletter of the CPD* **1999,** *21,* 14–15.
27. Aragón, F. H.; Coaquira, J. A. H.; Villegas-Lelovsky, L.; da Silva, S. W.; Cesar, D. F.; Nagamine, L. C. C. M.; Cohen, R.; Menéndez-Proupin, E.; Morais, P. C. *J. Phys.: Condens. Matter* **2015,** *27,* 095301. doi:10.1088/0953-8984/27/9/095301
28. Fiévet, F.; Ammar-Merah, S.; Brayner, R.; Chau, F.; Giraud, M.; Mammeri, F.; Peron, J.; Piquemal, J.-Y.; Sicard, L.; Viau, G. *Chem. Soc. Rev.* **2018,** *47,* 5187–5233. doi:10.1039/c7cs00777a
29. Bailon, J. J.; Dorlot, L. M. *Des matériaux;* Ecole Polytechnique de Montréal: Québec, Canada, 1986.
30. Lu, R. E.; Chang, K. G.; Fu, B.; Shen, Y. J.; Xu, M. W.; Yang, S.; Song, X. P.; Liu, M.; Yang, Y. D. *J. Mater. Chem. C* **2014,** *2,* 8578–8584. doi:10.1039/c4tc01415d
31. Ajroudi, L.; Mliki, N.; Bessais, L.; Madigou, V.; Villain, S.; Leroux, C. *Mater. Res. Bull.* **2014,** *59,* 49–58. doi:10.1016/j.materresbull.2014.06.029
32. Ourry, L.; Mammeri, F.; Toulemon, D.; Gaudisson, T.; Delamar, M.; Ammar, S. *RSC Adv.* **2016,** *6,* 49973–49979. doi:10.1039/c6ra06963k
33. Ourry, L.; Toulemon, D.; Ammar, S.; Mammeri, F. *Beilstein J. Nanotechnol.* **2017,** *8,* 408–417. doi:10.3762/bjnano.8.43
34. Artus, M.; Ammar, S.; Sicard, L.; Piquemal, J.-Y.; Herbst, F.; Vaulay, M.-J.; Fiévet, F.; Richard, V. *Chem. Mater.* **2008,** *20,* 4861–4872. doi:10.1021/cm702464e
35. Gaudisson, T.; Artus, M.; Acevedo, U.; Herbst, F.; Nowak, S.; Valenzuela, R.; Ammar, S. *J. Magn. Magn. Mater.* **2014,** *370,* 87–95. doi:10.1016/j.jmmm.2014.06.014
36. Aubert, A.; Loyau, V.; Mazaleyrat, F.; LoBue, M. *J. Eur. Ceram. Soc.* **2017,** *37,* 3101–3105. doi:10.1016/j.jeurceramsoc.2017.03.036

License and Terms

The definitive version of this article is the electronic one which can be found at:
doi:10.3762/bjnano.10.116